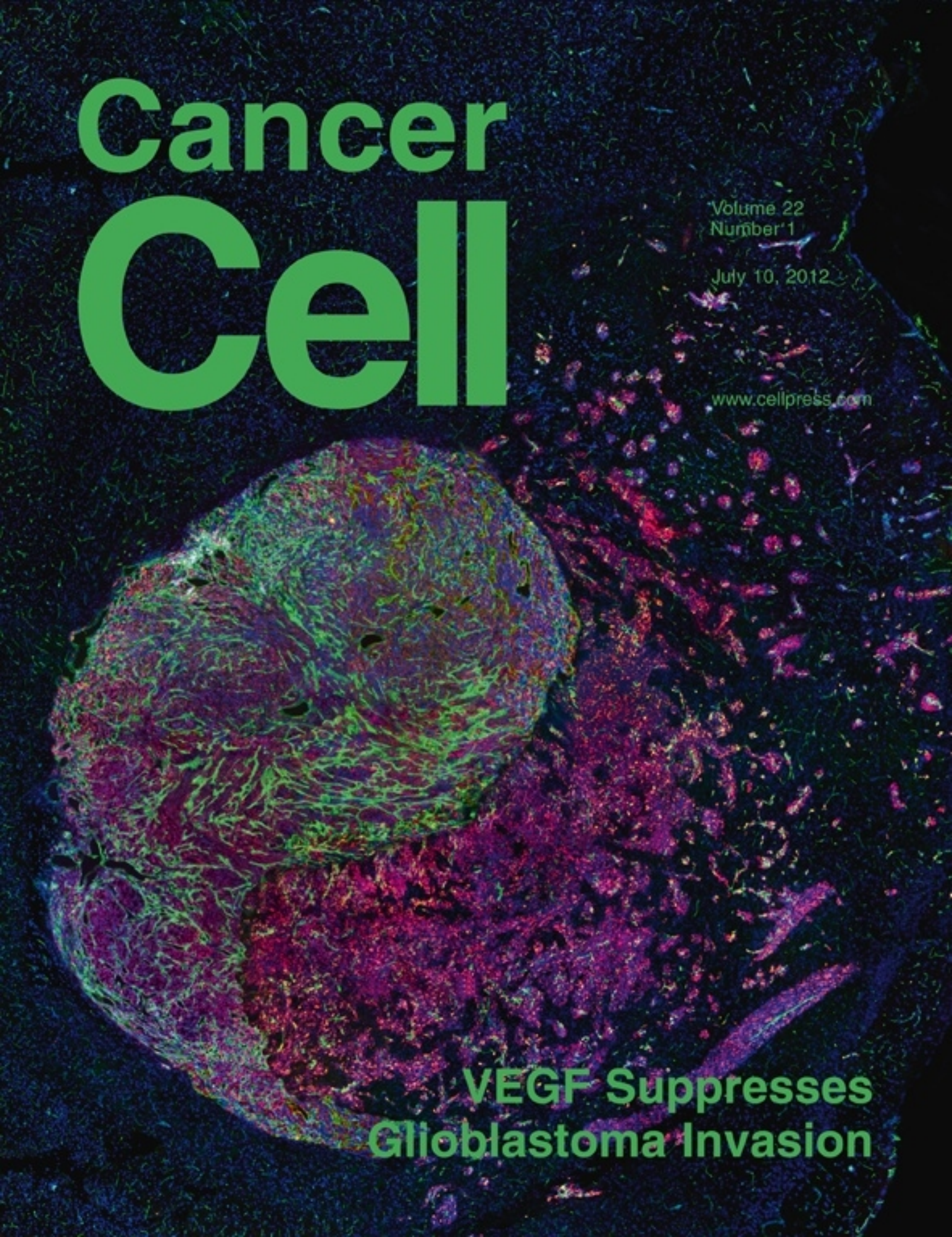
Cancer
Cell
Volume 22
Number 1
July 10, 2012
www.cellpress.com
VEGF Suppresses
Glioblastoma Invasion

Receptor Talk and Tumor Cell Walk in Glioblastoma

Lena Claesson-Welsh[1,*]
[1]Department Immunology, Genetics and Pathology, Uppsala University, Rudbeck Laboratory, 751 85 Uppsala, Sweden
*Correspondence: lena.welsh@igp.uu.se
http://dx.doi.org/10.1016/j.ccr.2012.06.011

In this issue of *Cancer Cell*, Lu et al. describe unconventional molecular interactions in glioblastoma cells that provide a mechanism for how anti-vascular endothelial growth factor therapy may promote mesenchymal transition of glioblastoma cells and increase tumor invasion.

Suppression of tumor angiogenesis using neutralizing antibodies against vascular endothelial growth factor (VEGF) initially appeared to be a straightforward strategy to starve the tumor and stop metastatic spread. Indeed, the anti-VEGF neutralizing antibody bevacizumab has been approved for the treatment of metastatic colorectal cancer, non-squamous non-small cell lung cancer, glioblastoma multiforme, and metastatic renal carcinoma. Disappointingly, a significant fraction of bevacizumab-treated patients carry tumors that are insensitive to this therapy or acquire resistance relatively quickly (Bergers and Hanahan, 2008). The worrisome findings that antiangiogenic therapy may increase tumor invasiveness and metastatic spread, described by the Kerbel and Casanova groups (Ebos et al., 2009; Pàez-Ribes et al., 2009), have further complicated the application of anti-VEGF treatment.

Data from the Bergers laboratory (Lu et al., 2012), in this issue of *Cancer Cell*, provide a possible explanation for the increased invasiveness seen with anti-VEGF therapy. Accordingly, blocking VEGF leads to increased activity of the hepatocyte growth factor (HGF) receptor MET, and elimination of both MET and VEGF expression from glioblastoma leads to increased survival in experimental models (Lu et al., 2012).

VEGF was originally described by Harvard Medical School researchers Donald Senger and Harold Dvorak as vascular permeability factor (VPF) and subsequently identified as an endothelial growth factor by Napoleone Ferrara (Dvorak, 2006). Overwhelming evidence in animal models and patients shows that bevacizumab suppresses pathological tumor vascularization. VEGF binds to two receptor tyrosine kinases, of which VEGF receptor 2 (VEGFR2) is primarily responsible for VEGF's effects on endothelial cells in blood vessels (Koch et al., 2011). Although initially perceived as endothelial cell-specific, refined reagents and analyses clearly show that VEGFR2 is expressed also in nonendothelial cells. Indeed, Lu et al. (2012) show that VEGFR2 is expressed in glioblastoma cells. VEGF-targeted therapy therefore may lead to adverse and unexpected effects by suppressing VEGFR2 on nonendothelial cells.

Glioblastoma multiforme is the most aggressive form of brain cancer, with a median survival of 18 months (Chamberlain, 2011). Treatment of recurrent glioblastoma with bevacizumab prolongs progression-free survival, particularly in older patients. The effect of bevacizumab is exerted atleast in part by reducing brain edema, demonstrating that neutralization of VEGF/VPF efficiently seals leaky tumor vessels. That the reduced permeability impairs contrast-enhanced magnetic resonance imaging, resulting in a false impression of reduced tumor dimensions, has confounded conclusions regarding the clinical benefit of bevacizumab therapy. In agreement with data from animal models (Ebos et al., 2009; Pàez-Ribes et al., 2009), there are indications for increased invasiveness of the cancer in bevacizumab-resistant glioblastoma, resulting in therapy-inaccessible, infiltrative growth along blood vessels (Chamberlain, 2011).

Interestingly, Lu et al. (2012) find that VEGFR2 is engaged in a constitutive complex with MET, which also includes a cytoplasmic phosphotyrosine phosphatase, PTP1B. PTPs, including PTP1B, serve dual roles in cancer and are implicated as both tumor suppressors and promoters of oncogenesis (Julien et al., 2011). In the scenario described by Lu et al. (2012), VEGFR2 directs the action of PTP1B toward HGF-activated MET, leading to MET dephosphorylation and thereby suppression of cell motility. Blocking VEGF through bevacizumab treatment unleashes HGF/MET activity by disengaging the phosphatase from the VEGFR2/MET complex. The fullblown MET activity in its turn promotes invasiveness (Figure 1), involving induction of a gene transcription program in the tumor, reminiscent of epithelial-to mesenchymal transition. Importantly, the Lu et al. (2012) study shows increased MET phosphorylation and, therefore, activity in gliomas from bevacizumab-treated patients.

The study by Lu et al. (2012) raises several critical questions regarding growth factor signaling. For example, does VEGFR2 signaling have cell-specific traits? VEGFR2 stimulates a wide spectrum of signaling pathways in endothelial cells resulting in survival, proliferation, migration, and formation of lumenized 3D vessel structures (Koch et al., 2011). This biology involves several of the most well-known signaling pathways, such as the RAS-RAF-ERK pathway and the PI3K/AKT pathway, which operate downstream of most growth factor receptors in most cell types. Surprisingly, VEGFR2 does not seem to contribute as a positive regulator in glioma cells. And why does VEGFR2 serve as a gate-keeper of MET activity in glioblastoma cells but not, as far as is known, in endothelial cells, which also express MET?

Furthermore, the PTP1B-mediated dephosphorylation is specific for MET and does not affect VEGFR2, even though the molecules exist in complex, implying a level of specificity that is difficult to comprehend in molecular terms. It does not seem to involve the famous VEGF coreceptor, neuropilin-1. Why, where, and how do these unconventional molecular complexes arise? Are they enriched in

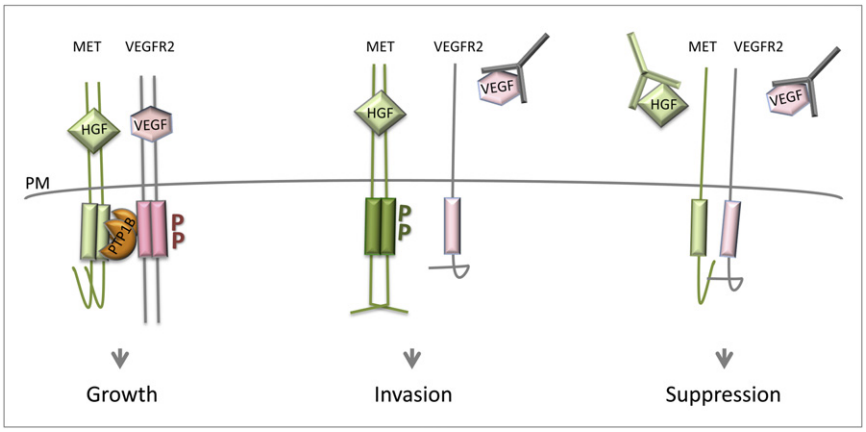

Figure 1. VEGF Suppresses MET Phosphorylation and Signaling via PTP1B
In glioblastoma cells, MET and VEGFR2 exist in a complex that also includes PTP1B, which allows growth of the tumor (left). Treatment with bevacizumab to neutralize VEGF reduces PTP1 activity and promotes MET signaling, leading to increased invasion (middle). Combined treatment to neutralize HGF and VEGF leads to efficient suppression of glioblastoma invasion (right). VEGFR2 (red) and MET (green) are indicated as monomers or dimmers, with the kinase domain shown as a rectangle, either phosphorylated (P) or not. The Pac-man symbol indicates PTP1B (orange). Intense colors indicate induction of enzymatic activities of kinases and the phosphatase. VEGF and HGF are shown either bound to their cognate receptors or as neutralized by specific antibodies against VEGF (middle) or HGF and VEGF (right). As an alternative to HGF antibodies, MET kinase inhibitors may be used clinically. PM, plasma membrane.

plasma membrane microdomains so densely packed with signal transducers that molecular interactions can occur also between unrelated receptor tyrosine kinases (Figure 1)? The interactions seem specific; at least Lu et al. (2012) could not detect any effects of PDGF and EGF on MET activity.

The study by Lu et al. (2012) has several novel implications with regard to optimization of treatment for glioblastoma multiforme and other forms of cancer. First, combined treatment with agents blocking HGF or MET in combination with bevacizumab should have the important double benefit of reducing edema and preventing invasiveness of the glioma cells. As the clinical development of efficient HRG and MET inhibitors is being actively pursued (Gherardi et al., 2012), combined treatment may be implemented very soon. Second, although there appear to be glioma-specific vascular aspects such as transdifferentiation of glioma stem cells to form vascular channels (Chamberlain, 2011), it is likely that VEGFR2 or other receptor tyrosine kinases also present PTP1B to MET in other types of malignancies. Indeed, Sennino et al. (2012) recently demonstrated that combined inhibition of MET and VEGF signaling suppresses tumor invasion and metastasis in neuroendocrine tumors in mouse models. Finally, the community is wise to expect further hurdles on the road toward efficient antiangiogenic therapy. Still, the obstacles we have encountered this far are, at least in hindsight, not very surprising, and are consistent with what we know about VEGF biology. High-quality basic research on VEGF and its mechanisms of action remains crucial for overcoming these hurdles, as demonstrated by Bergers and her colleagues.

ACKNOWLEDGMENTS

Work in the Claesson-Welsh laboratory is supported by grants from the Swedish Cancer Society, the Swedish Science Foundation, and the Knut and Alice Wallenberg Foundation.

REFERENCES

Bergers, G., and Hanahan, D. (2008). Nat. Rev. Cancer *8*, 592–603.

Chamberlain, M.C. (2011). Clin. Med. Insights Oncol. *5*, 117–129.

Dvorak, H.F. (2006). Exp. Cell Res. *312*, 522–526.

Ebos, J.M., Lee, C.R., Cruz-Munoz, W., Bjarnason, G.A., Christensen, J.G., and Kerbel, R.S. (2009). Cancer Cell *15*, 232–239.

Gherardi, E., Birchmeier, W., Birchmeier, C., and Vande Woude, G. (2012). Nat. Rev. Cancer *12*, 89–103.

Julien, S.G., Dubé, N., Hardy, S., and Tremblay, M.L. (2011). Nat. Rev. Cancer *11*, 35–49.

Koch, S., Tugues, S., Li, X., Gualandi, L., and Claesson-Welsh, L. (2011). Biochem. J. *437*, 169–183.

Lu, K.V., Chang, J.P., Parachoniak, C.A., Pandika, M.M., Aghi, M.K., Meyronet, D., Isachenko, N., Fouse, S.D., Phillips, J.J., Cheresh, D.A., et al. (2012). Cancer Cell *22*, this issue, 21–35.

Pàez-Ribes, M., Allen, E., Hudock, J., Takeda, T., Okuyama, H., Viñals, F., Inoue, M., Bergers, G., Hanahan, D., and Casanovas, O. (2009). Cancer Cell *15*, 220–231.

Sennino, B., Ishiguro-Oonuma, T., Wei, Y., Naylor, R.M., Williamson, C.W., Bhagwandin, V., Tabruyn, S.P., You, W.K., Chapman, H.A., Christensen, J.G., et al. (2012). Cancer Discov. *2*, 270–287.

Sensitizing Cancer Cells: Is It Really All about U?

Patrick J. Stover[1,*] and Robert S. Weiss[2,*]
[1]Division of Nutritional Sciences
[2]Department of Biomedical Sciences
Cornell University, Ithaca, New York, 14853, USA
*Correspondence: pjs13@cornell.edu (P.J.S.), rsw26@cornell.edu (R.S.W.)
http://dx.doi.org/10.1016/j.ccr.2012.06.010

In this issue of *Cancer Cell*, Hu et al. report that TMPK and RNR, two key enzymes in deoxyribonucleotide biosynthesis, co-localize to damaged DNA and produce nucleotides necessary for DNA repair while suppressing uracil incorporation. TMPK inhibition disrupts this balance and selectively sensitizes cancer cells to low-dose chemotherapy.

An ample and properly constituted supply of deoxyribonucleotides is required for the successful completion of DNA replication and repair. Consequently, the cellular enzymes responsible for nucleotide biosynthesis have long been recognized as possible targets for anti-cancer drugs; one such therapeutic is 5-fluorouracil (5-FU). 5-FU is converted intracellularly into toxic metabolites that are incorporated into nucleic acids and additionally inhibit thymidylate synthase (TS), a crucial enzyme for de novo dTTP biosynthesis (Figure 1) (Longley et al., 2003). 5-FU has been used in the clinic for over 50 years and is still being used for the treatment of colorectal and other cancers. However, 5-FU treatment has toxic side-effects, and its use is further limited by the occurrence of resistance. In this issue of *Cancer Cell*, Hu et al. (2012) describe exciting findings that identify thymidylate kinase (TMPK), another key player in thymidine nucleotide biosynthesis, as a promising target among the nucleotide biosynthetic machinery by virtue of its newly discovered role in generating dTDP for DNA repair directly at sites of DNA damage.

Of the four classical deoxyribonucleotides, thymidine is distinguished by both its metabolic regulation and the way it is utilized. Thymidine is the only nonessential deoxyribonucleotide for DNA synthesis, as DNA polymerases typically fail to distinguish between dTTP and dUTP during DNA replication and repair and can incorporate dUTP into DNA when dTTP is limiting. Furthermore, while the synthesis of cytosine and purine nucleosides through de novo and salvage pathways occurs in the cytoplasm, the salvage and folate-dependent de novo synthesis of thymidylate, catalyzed by thymidine kinase and TS respectively, occurs in the nucleus at sites of DNA synthesis (Anderson et al., 2012; Chen et al., 2010). Cellular dTTP pools are maintained at very low levels, and both pool depletion and expansion affect DNA integrity and human health (Samsonoff et al., 1997). There is increasing evidence that dTTP is synthesized "on-site and on-demand", and loss of the capacity to synthesize dTTP results in dU accumulation in DNA, causing genomic instability through futile cycles of DNA synthesis and repair (Blount et al., 1997).

Previous reports indicated that targeting dTTP production through TMPK depletion sensitizes cells to double strand DNA breaks (DSB) but, importantly, does not appear to impair cell viability in the absence of exogenous genotoxins (Hu and Chang, 2008). The present study extends those intriguing observations with the finding that TMPK knockdown leads to increased and persistent DNA lesions following treatment of cells with the clastogen doxorubicin. These effects were associated with increased uracil content in DNA and could be countered by overexpression of dUTPase, the enzyme that removes dUTP from the nucleotide pool.

The production of dUTP requires ribonucleotide reductase (RNR), a heteromultimer composed of large (R1) and small (R2) subunits that reduces NDPs to form dNDPs. The subcellular localization of mammalian RNR proteins has been a matter of debate (Pontarin et al., 2008), although recent evidence suggests that at least some RNR complexes localize to sites of DNA damage in the nucleus, where they can contribute to nucleotide production for DNA repair (Niida et al., 2010). Interestingly, the faulty DSB repair following TMPK knockdown could be rescued by disrupting RNR recruitment to DNA lesions, and additional experimental manipulation of RNR expression established RNR levels as a critical determinant of DSB repair proficiency following TMPK impairment. The authors proceed to show that TMPK, like RNR, is present in the nucleus at sites of DNA damage. The convergence of these pathways where DNA repair is occurring provides new insights into mechanisms of dUTP synthesis and incorporation into DNA during DSB repair. TMPK is essential for dTDP synthesis from both the de novo and salvage thymidylate synthesis pathways, whereas RNR generates dUDP in the process of producing dNDPs needed for DNA replication and repair, raising the possibility of coordinated regulation of dTDP and dUDP levels in the nucleus at sites of DNA damage.

Taken together, the results point toward a model (Figure 1) in which the balanced activity of TMPK, RNR, and other factors creates a local environment with a low ratio of dUTP to dTTP, limiting dUTP incorporation during DNA repair under normal circumstances. When this regulatory network is perturbed by inhibition of TMPK, dTTP levels decrease, leading to increased uracil incorporation during the DNA synthesis step of homologous recombinational repair. This results in an unproductive and ultimately lethal cycle of events in which the incorporated uracils are targeted for excision from the DNA, and the region is resynthesized under the same unfavorable nucleotide pool conditions with a high dUTP to dTTP ratio.

The translation of these findings to cancer therapy seems promising but remains to be proven. Inhibition of TS by 5-FU treatment is cytotoxic to both normal

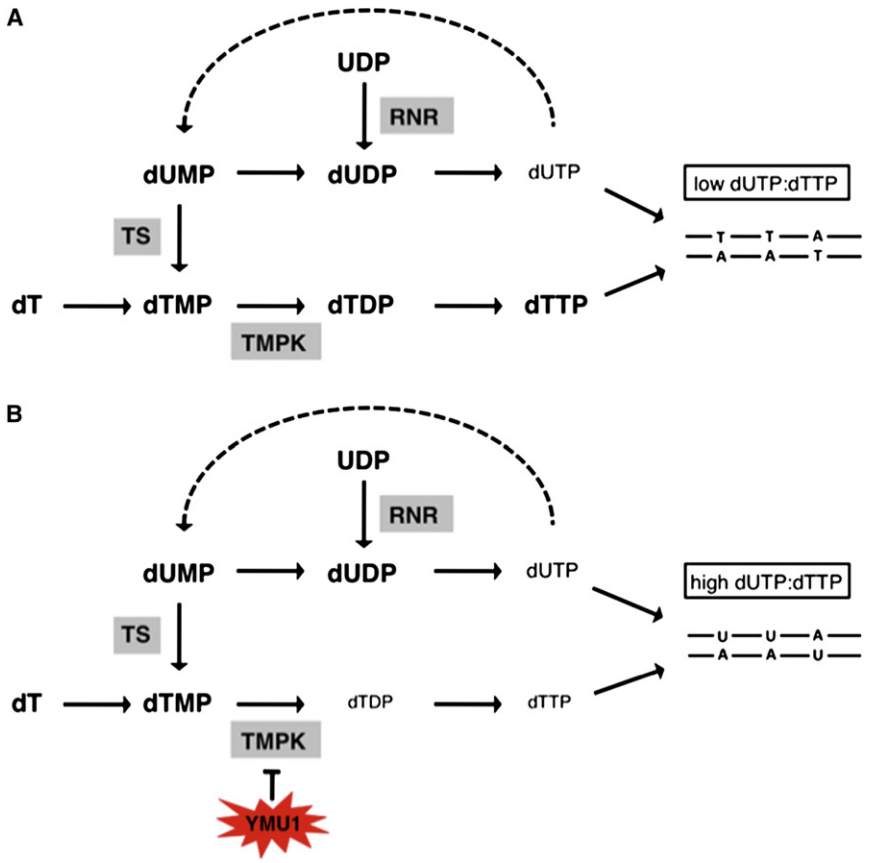

Figure 1. TMPK Co-Localizes with RNR at DNA Repair Sites to Limit Uracil Incorporation during DNA Synthesis

(A) Under normal conditions, a low dUTP:dTTP ratio is maintained in part through the breakdown of dUTP by dUTPase (dotted arrow) and TMPK-dependent dTTP biosynthesis.

(B) When TMPK is inhibited, such as by the small molecule YMU1, dTTP levels drop, resulting in a high dUTP:dTTP ratio that promotes uracil incorporation into DNA. Uracils in DNA are then targeted by uracil DNA glycosylase and excised, leading to futile repair cycles and DNA breakage (not shown).

RNR, ribonucleotide reductase; TMPK, thymidylate kinase; TS, thymidylate synthase.

and tumor cells, and its effects are associated with the incorporation of both dU and 5FdU into DNA. The authors propose that TMPK may be a more desirable target for specifically sensitizing tumor cells as compared to established therapeutic approaches directed against TS and the de novo thymidylate synthesis pathway without specificity for transformed cells (Longley et al., 2003). The authors propose that a cancer cell's Achilles heel is its elevated R2/TMPK ratio, leading to an increased dependence of cancer cells on TMPK activity to prevent uracil misincorporation in DNA. Moreover, R2 levels increase after DNA damage, such as that caused by doxorubicin and other chemotherapeutics, in part through a recently identified mechanism involving Cyclin F (D'Angiolella et al., 2012), potentially further tilting the dUTP:dTTP ratio at DNA damage sites in an unfavorable direction when TMPK is inhibited. These effects may be compounded in cancer cells because they often have cell cycle checkpoint defects and an increased S-phase fraction, which could contribute to high RNR activity as well as more opportunities for usage of homologous recombination for DNA repair.

The development of their lead compound, YMU1, offers some hope that this strategy could be realized. This selective, cell permeable TMPK inhibitor, identified by screening a small molecule library, has an IC_{50} of 0.6 μM. Similar to the effect of TMPK knockdown, treatment of cells with YMU1 alone does not significantly affect cell proliferation or cause cytotoxicity. It remains unclear why cells can tolerate TMPK inhibition in the absence of extrinsic stresses given the integral role of TMPK in dTDP production. The authors speculate that cells may produce variant isoforms of TMPK that could account for residual dTDP production after TMPK inhibition. Clearly, additional genetic and biochemical analyses are called for as TMPK continues to be explored as a drug target. Nevertheless, YMU1 sensitizes cultured tumor cells to low dose doxorubicin treatment, resulting in increased DNA damage and enhanced cell killing. Initial studies in a tumor xenograft mouse model further suggest that YMU1 in combination with doxorubicin suppresses tumor growth in vivo. Even before TMPK inhibitors are further evaluated for potential use in patients, the findings of Hu et al. (2012) suggest that monitoring the relative protein levels of R2 and TMPK in cancers could be predictive of chemosensitivity. While it remains to be seen whether this will be the case, the new focus on TMPK raised by this work has the potential to extend the long history of using the knowledge of the fundamentals of nucleotide metabolism for therapeutic benefit.

REFERENCES

Anderson, D.D., Woeller, C.F., Chiang, E.P., Shane, B., and Stover, P.J. (2012). J. Biol. Chem. *287*, 7051–7062.

Blount, B.C., Mack, M.M., Wehr, C.M., MacGregor, J.T., Hiatt, R.A., Wang, G., Wickramasinghe, S.N., Everson, R.B., and Ames, B.N. (1997). Proc. Natl. Acad. Sci. USA *94*, 3290–3295.

Chen, Y.L., Eriksson, S., and Chang, Z.F. (2010). J. Biol. Chem. *285*, 27327–27335.

D'Angiolella, V., Donato, V., Forrester, F.M., Jeong, Y.T., Pellacani, C., Kudo, Y., Saraf, A., Florens, L., Washburn, M.P., and Pagano, M. (2012). Cell *149*, 1023–1034.

Hu, C.-M., Yeh, M.-T., Tsao, N., Chen, C.-W., Gao, Q.-Z., Chang, C.-Y., Lee, M.-H., Fang, J.-M., Sheu, S.-Y., Lin, C.-J., et al. (2012). Cancer Cell *22*, this issue, 36–50.

Hu, C.M., and Chang, Z.F. (2008). Cancer Res. *68*, 2831–2840.

Longley, D.B., Harkin, D.P., and Johnston, P.G. (2003). Nat. Rev. Cancer *3*, 330–338.

Niida, H., Katsuno, Y., Sengoku, M., Shimada, M., Yukawa, M., Ikura, M., Ikura, T., Kohno, K., Shima, H., Suzuki, H., et al. (2010). Genes Dev. *24*, 333–338.

Pontarin, G., Fijolek, A., Pizzo, P., Ferraro, P., Rampazzo, C., Pozzan, T., Thelander, L., Reichard, P.A., and Bianchi, V. (2008). Proc. Natl. Acad. Sci. USA *105*, 17801–17806.

Samsonoff, W.A., Reston, J., McKee, M., O'Connor, B., Galivan, J., Maley, G., and Maley, F. (1997). J. Biol. Chem. *272*, 13281–13285.

To the Rescue: The Fanconi Anemia Genome Stability Pathway Salvages Replication Forks

George-Lucian Moldovan[1] and Alan D. D'Andrea[1,*]
[1]Department of Radiation Oncology, Dana-Farber Cancer Institute, Harvard Medical School, 450 Brookline Avenue, Boston, MA 02215, USA
*Correspondence: alan_dandrea@dfci.harvard.edu
http://dx.doi.org/10.1016/j.ccr.2012.06.006

DNA damage can arrest replication forks during S phase. Failure to stabilize and restart arrested forks results in fork collapse and genomic instability. In this issue of *Cancer Cell*, Schlacher et al. show that the Fanconi anemia and BRCA2 tumor suppressor pathways cooperate to protect stalled replication forks from degradation.

Patients with the rare genetic disorder Fanconi anemia (FA) exhibit increased cancer susceptibility, anemia, and developmental malformations (Crossan and Patel, 2012). The fifteen FA genes cooperate in a genome stability pathway that is essential for tolerance and repair of DNA crosslinks. Cells derived from FA patients are hypersensitive to DNA crosslinking agents and exhibit DNA damage checkpoint and mitosis defects. Monoubiquitination of the FA proteins FANCD2 and FANCI by a ubiquitin ligase complex, termed the FA core complex, is an essential step in the pathway and leads to the formation of active repair complexes on chromatin; thus, FANCD2 monoubiquitination is a biomarker of FA pathway activation. The FA pathway is activated not only by DNA crosslinks but also by treatment with other replication stalling agents, such as hydroxyurea (HU) or UV light. Paradoxically, FA patient cells are hypersensitive to crosslinks, but not these latter agents. The function of the FA pathway in the context of replication fork activity has remained elusive. In this issue of *Cancer Cell*, Schlacher et al. (2012) demonstrate that the FA pathway is required to stabilize stalled replication forks and protect them from nucleolytic degradation, thus suppressing genomic instability and tumorigenesis.

These investigators previously examined the function of the breast cancer susceptibility factor BRCA2 in replication fork protection (Schlacher et al., 2011). BRCA2 is known to function as a mediator of homologous recombination (HR) by inhibiting the ATPase activity of RAD51 and by catalyzing the formation of RAD51 nucleofilaments at processed double strand breaks (Heyer et al., 2010). By employing single DNA fiber analysis, the authors previously showed that BRCA2 is also required for the stabilization of stalled replication forks. BRCA2 achieves this function by promoting RAD51 nucleofilament formation at stalled forks; RAD51 coating confers protection against DNA degradation by the nuclease MRE11 (Schlacher et al., 2011).

In the current work, the authors extend these studies by examining the FANCD2 protein. Many genetic and biochemical findings connect the FA and HR pathways. FANCD2 and BRCA2 interact and co-localize in DNA damage-induced foci (Hussain et al., 2004). Several HR proteins, including BRCA2 itself, are encoded by FA genes that are inactivated through biallelic germline mutations in FA patients (Howlett et al., 2002; Walsh and King, 2007). These links, as well as the above-mentioned activation of the FA pathway by replication stalling agents such as HU and UV light, prompted the authors to investigate if FANCD2 and the FA core complex proteins are also required for promoting replication fork stability. Perhaps not surprisingly, they found that FA pathway deficient cells have a dramatic shortening of the nascent strand following replication fork stalling induced by HU treatment. This defect was associated with an increase in chromosomal aberrations observed in metaphase spreads, suggesting that the FA pathway protects stalled replication forks from degradation and thereby prevents genomic instability and transformation. Similar to BRCA2, FANCD2 promotes RAD51 nucleofilament formation at stalled forks and thereby prevents cleavage by the MRE11 nuclease (Figure 1). Importantly, the authors show that FANCD2, BRCA2, and RAD51 are epistatic in replication fork stabilization. These studies represent the most convincing functional data, so far, confirming that the upstream FA proteins and BRCA2/FANCD1 participate in a common pathway for tumor suppression, termed the FA/BRCA pathway.

Perhaps the most thought-provoking finding of this work is that gain of RAD51 function, by either expressing a mutant RAD51 that forms hyper-stable RAD51 filaments or overexpressing the wild-type RAD51, can compensate for FANCD2 deficiency. Overexpression rescues the length of the nascent replication tract in FANCD2-defective cells. This result suggests that promoting RAD51 accumulation at stalled replication forks is enough to alleviate the fork stabilization defect caused by FA/BRCA pathway mutations (Figure 1C).

It is unclear whether RAD51 overexpression also suppresses the spontaneous or DNA damage-induced chromosomal aberrations seen in FA patients. It will also be important to determine whether hyperactive RAD51 can alleviate the anemia phenotype that FA deficiency confers to organisms. The molecular mechanism that induces stem cell depletion in FA patients remains unclear. It is conceivable that this novel function of the FA pathway in protecting stalled replication forks against degradation is important for the maintenance and functionality of hematopoietic stem cells. Thus, the work of Schlacher et al. (2012) opens up the possibility for new therapeutic avenues for FA patients. The chemical compound RS-1 is known to promote the formation of RAD51 nucleofilaments (Jayathilaka et al., 2008). It will be interesting to investigate if this compound

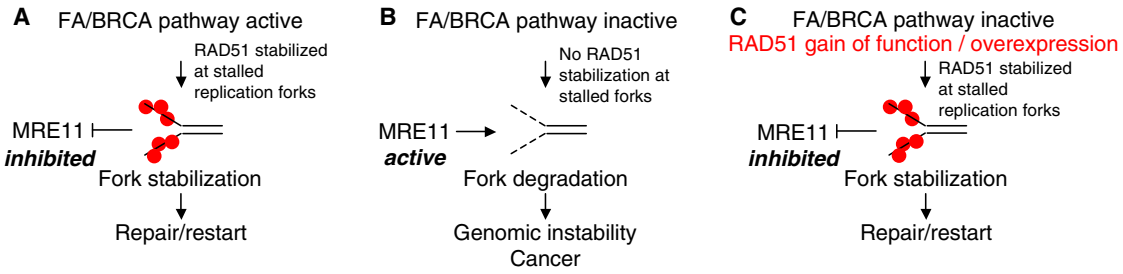

Figure 1. The Fanconi Anemia Pathway and BRCA2 Cooperate to Promote the Stability of Stalled Replication Forks
(A) FA proteins and BRCA2 protect stalled replication forks against degradation by stabilizing RAD51 filaments.
(B) In the absence of the FA/BRCA pathway, the MRE11 nuclease degrades stalled replication forks, promoting genomic instability.
(C) Fork protection in FA/BRCA pathway mutants can be rescued by stabilizing RAD51 filaments. RAD51 is represented by red dots.

can suppress the phenotypes of FA cells and patients. Moreover, the PARI protein was shown to disrupt the interaction between RAD51 and single stranded DNA, thus suppressing hyper-recombination (Moldovan et al., 2012). However, it is not clear if PARI can disrupt RAD51 replication fork filaments. Interestingly, PARI interacts with the replication protein PCNA, a master regulator of replication-coupled DNA repair processes. It is therefore possible that PARI may play a role in regulating replication fork stability by controlling RAD51 levels at stalled replication forks. PARI inhibition may result in stabilizing RAD51 at such structures, thereby representing yet another approach for FA therapy. Indeed, PARI depletion was shown to improve genomic stability of BRCA2- and FANCJ-deficient cells.

On the other hand, it is important to note that RAD51 is overexpressed in numerous tumor types (Klein, 2008). RAD51 overexpression in tumors is associated with resistance to genotoxic therapy. In model systems, RAD51 overexpression promotes toxic or deleterious recombination and genomic instability. Therefore, a delicate equilibrium between the different consequences of RAD51 hyper-activation must be achieved for such treatment strategies to succeed (Heyer et al., 2010).

By identifying this novel role of FA proteins, Schlacher et al. (2012) provide important insights into the mechanism of BRCA2-dependent fork stabilization. Still, several questions remain unanswered. Most importantly, how are stalled replication forks, which are covered by RAD51, ultimately repaired and restarted? HR may not be involved. Based on recent work in the FA field, FA proteins may recruit DNA polymerases to restart the fork and may recruit SLX4, a landing pad for nuclease activity, to process the fork. The poorly characterized template switching mechanism that requires multi-ubiquitination of PCNA at stalled forks may also be involved. DNA fiber assays following depletion of the factors involved in these processes should shed light on the pathway involved. Also intriguing is the involvement of MRE11; how this specific nuclease degrades stalled replication forks in the absence of RAD51 filaments is unclear. Are there other nucleases involved?

Although initially identified 85 years ago, FA remains a fatal genetic disease. The addition of yet another activity, namely the protection of stalled replication forks against nucleolysis, further underscores the multifaceted role of the FA pathway as an essential barrier against genomic instability and cancer.

REFERENCES

Crossan, G.P., and Patel, K.J. (2012). J. Pathol. *226*, 326–337.

Heyer, W.D., Ehmsen, K.T., and Liu, J. (2010). Annu. Rev. Genet. *44*, 113–139.

Howlett, N.G., Taniguchi, T., Olson, S., Cox, B., Waisfisz, Q., De Die-Smulders, C., Persky, N., Grompe, M., Joenje, H., Pals, G., et al. (2002). Science (New York), pp. 606–609.

Hussain, S., Wilson, J.B., Medhurst, A.L., Hejna, J., Witt, E., Ananth, S., Davies, A., Masson, J.Y., Moses, R., West, S.C., et al. (2004). Hum. Mol. Genet. *13*, 1241–1248.

Jayathilaka, K., Sheridan, S.D., Bold, T.D., Bochenska, K., Logan, H.L., Weichselbaum, R.R., Bishop, D.K., and Connell, P.P. (2008). Proc. Natl. Acad. Sci. USA *105*, 15848–15853.

Klein, H.L. (2008). DNA Repair (Amst.) *7*, 686–693.

Moldovan, G.L., Dejsuphong, D., Petalcorin, M.I., Hofmann, K., Takeda, S., Boulton, S.J., and D'Andrea, A.D. (2012). Mol. Cell *45*, 75–86.

Schlacher, K., Christ, N., Siaud, N., Egashira, A., Wu, H., and Jasin, M. (2011). Cell *145*, 529–542.

Schlacher, K., Wu, H., and Jasin, M. (2012). Cancer Cell *22*, this issue, 106–116.

Walsh, T., and King, M.C. (2007). Cancer Cell *11*, 103–105.

The Future of Cancer Treatment: Will It Include Immunotherapy?

Jeffrey A. Bluestone[1,2,*] and Eric J. Small[2]
[1]Diabetes Center
[2]Department of Medicine
University of California San Francisco, 513 Parnassus Ave, San Francisco, CA 94143, USA
*Correspondence: jeff.bluestone@ucsf.edu
http://dx.doi.org/10.1016/j.ccr.2012.06.009

Negative immune regulatory pathways inhibit anti-cancer T cell responses, preventing effective immune surveillance. Two clinical trials using monoclonal antibodies that antagonize the PD-1/PD-L1 pathway recently reported regression in several tumor types. In one of these trials, efficacy was linked to the expression of the PD-L1 biomarker on tumor cells.

Over the past few decades, we have often heard in the halls of cancer meetings, "Immunotherapy is the future of cancer treatment… and always will be." The idea that the immune system can be harnessed to destroy tumors has been a dream for over a century, ever since William Coley first injected toxins into patients to treat cancer. Reporting in a recent issue of *New England Journal of Medicine*, Topalian et al. (2012) and Brahmer et al. (2012) explore the clinical effects of two complementary means of achieving anti-tumor immunity in multiple cancers including, for the first time, lung cancer. These trials utilized monoclonal antibodies (mAbs) targeting a cell surface molecule programmed death-1 (PD-1) on T cells and its ligand PD-L1, which is overexpressed on cancer cells. The combination of these results and experiences with ipilimumab, an FDA-approved mAb that targets a related negative regulatory receptor cytotoxic T lymphocyte antigen 4 (CTLA-4), leaves no doubt that the future is here, and with it, a new era in the treatment of cancer.

The modern era of cancer immunology has focused on using immunotherapy to "boost" the immune system through vaccination and adoptive cellular immunotherapy based on the proposition that tumors express antigenic protein targets, but the anti-tumor T cells are not being activated due to limited T cell activation, growth factors, or immunosuppressive molecules secreted by cancer cells themselves. In many instances, these efforts have focused on promoting key positive co-stimulatory and innate immune pathways (such as ICOS, CD28, CD154, and TLR ligands) that are critical for a potent and sustained immune response. The general thinking was that the immune system was the lack of recognition and induction of an anti-tumor response. However, in the mid-90's, it became clear that the immune system did indeed recognize tumor antigens (mostly overexpressed self proteins) but remained quiescent in spite of the persistent presence of tumor antigens. This led to the hypothesis that there must be an active brake on the anti-tumor response that shuts down active immunity. The breakthrough came when it was discovered that negative regulatory T cell surface molecules (the first of which was CTLA-4) were upregulated in activated T cells to dampen their activity, resulting in less effective killing of tumor cells (Walunas et al., 1994, Leach et al., 1996). These inhibitory molecules, termed negative co-stimulatory molecules due to their homology with the quintessential T cell co-stimulatory molecule CD28, included a number of related family members including PD-1, B7-H4, B- and T-lymphocyte attenuator (BTLA), and their ligands (Bour-Jordan et al., 2011). The molecules function by multiple pathways, including the attenuation of early activation signals, competition for positive co-stimulation, and direct inhibition of the antigen presenting cells that would otherwise promote immune responses. The importance of these pathways was highlighted by studies showing that total blockade via genetic disruption led to massive T cell hyperproliferation and protracted multiorgan autoimmunity. Thus, it became increasing clear that there were a series of major pathways that the immune system employs to avoid unwanted autoimmune or hyperimmune responses. In various animal models, administration of immune checkpoint inhibitors (ICI) unleashed immunity to tumors, viruses, and other pathogens. These seminal studies ultimately led to the development and FDA approval of the first antibody-based immunotherapy that targets negative co-stimulation ipilimumab (Yervoy) in patients with metastatic melanoma (Hodi et al., 2010).

The first clinical trials of ICI-specific mAbs against the receptor PD-1 and its ligand PD-L1 included subjects with late-stage, heavily-pretreated kidney, lung, prostate, and colon cancer. They took advantage of newly conceived adaptive trial designs to move rapidly from a dose finding mode in multiple tumor types to rapid efficacy expansion cohorts (Wolchok et al., 2009). The data are quite encouraging and go beyond typical expectations. Overall, approximately 20%–25% of patients with metastatic melanoma, kidney (renal cell) and lung (non-small cell) cancer had partial or complete tumor shrinkage. Importantly, the durability of the responses was unparalleled as 65% of patients followed for greater than one year remained responsive (Topalian et al., 2012; Brahmer et al., 2012). The relatively low responses of the lung cancer patients to the PD-1 pathway immunotherapy is an important starting point for developing treatments that couple the ICIs with other therapies.

While these trials were highlighted for their success, it must be noted that the inherent risk in approaches that harness

the immune system to target anti-tumor immunity is the development of autoimmunity. While ipilimumab and these antibodies have not been directly compared, there appears to be less severe immune-related toxicity with the anti-PD-1 and anti-PD-L1 mAbs. Nevertheless, grade 3 and 4 toxicity did occur in 9% (Brahmer et al., 2012) and 11% (Topalian et al., 2012) of patients, and episodes of presumed autoimmune pneumonitis, including some with fatal outcomes, colitis, hepatitis, hypophysitis, and thyroiditis were noted. Importantly, autoimmunity can usually be treated with immune suppressive therapy without an apparent effect on anti-cancer immunity. The finding that the autoimmune side-effect profile is different between the different ICI drugs raises the question as to whether this is due to more ''downstream'' and specific roles of the PD-1-PD-L1 interaction in cancer.

It is important to note that the effect of these drugs represents a growing class effect, as demonstrated by the clinical activity of ipilimumab in renal cell carcinoma, prostate cancer, and melanoma. In addition, inhibitors of other targets, such as TIM-3, BTLA, etc., are working their way through pre-clinical and clinical development (Norde et al., 2012). As is the case with ipilimumab, treatment with anti-PD-1 and anti-PD-L1 mAbs did not appear to benefit patients with prostate or colon cancer. However, the responses in melanoma and kidney cancer were greater than that seen with ipilimumab. The reason for these differences remain unclear, but it is important to note that there appeared to be a correlation between patient response and the expression level of PD-L1 on the tumor cells in the anti-PD-1 study (Topalian et al., 2012). In preliminary results, 9 of 25 (36%) patients with PD-L1 positive cancers had an objective response, whereas none of the 17 patients whose tumors were PD-L1 negative had an objective response. The results suggest that receptor-target localization may define key differences in the efficacy of these agents, as CTLA-4 ligands and PD-1 ligands are differentially expressed on hematopoietic cells versus stromal cells, respectively. Moreover, the PD-1-PD-L1 pathway preferentially controls effector-memory $CD8^+$ T cell responses at the tissue site, while CTLA-4, via interaction with CD80 and CD86, has been shown to control early T cell responses in lymphoid tissues (Jin et al., 2011; Egan et al., 2002). Finally, the use of ICIs in combination with specific tumor and tumor antigen immunization may prove extremely effective in these therapeutic settings to boost existing responses and initiate de novo immunity.

In summary, these two studies provide compelling evidence that immunotherapy is no longer the future of cancer treatment, but is very much a current reality. The articles by Brahmer et al. (2012) and Topalian et al. (2012) provide critical insights into how further understanding of the basis of cancer immunology will lead to advances that benefit our patients.

REFERENCES

Bour-Jordan, H., Esensten, J.H., Martinez-Llordella, M., Penaranda, C., Stumpf, M., and Bluestone, J.A. (2011). Immunol. Rev. *241*, 180–205.

Brahmer, J.R., Tykodi, S.S., Chow, L.Q., Hwu, W.J., Topalian, S.L., Hwu, P., Drake, C.G., Camacho, L.H., Kauh, J., Odunsi, K., et al. (2012). N. Engl. J. Med. Published online June 2, 2012. http://dx.doi.org/10.1056/NEJMoa1200694.

Egan, J.G., Kuhns, M.S., and Allison, J.P. (2002). Nat. Immunol. *3*, 611–618.

Hodi, F.S., O'Day, S.J., McDermott, D.F., Weber, R.W., Sosman, J.A., Haanen, J.B., Gonzalez, R., Robert, C., Schadendorf, D., Hassel, J.C., et al. (2010). N. Engl. J. Med. *363*, 711–723.

Jin, H.T., Ahmed, R., and Okazaki, T. (2011). Curr. Top. Microbiol. Immunol. *350*, 17–37.

Leach, D.R., Krummel, M.F., and Allison, J.P. (1996). Science *271*, 1734–1736.

Norde, W.J., Hobo, W., van der Voort, R., and Dolstra, H. (2012). Blood. Published online May 4, 2012. http://dx.doi.org/10.1182/blood-2012-02-412510.

Topalian, S.L., Hodi, F.S., Brahmer, J.R., Gettinger, S.N., Smith, D.C., McDermott, D.F., Powderly, J.D., Carvajal, R.D., Sosman, J.A., Atkins, M.B., et al. (2012). N. Engl. J. Med. Published online June 2, 2012. http://dx.doi.org/10.1056/NEJMoa1200690.

Walunas, T.L., Lenschow, D.J., Bakker, C.Y., Linsley, P.S., Freeman, G.J., Green, J.M., Thompson, C.B., and Bluestone, J.A. (1994). Immunity *1*, 405–413.

Wolchok, J.D., Hoos, A., O'Day, S., Weber, J.S., Hamid, O., Lebbé, C., Maio, M., Binder, M., Bohnsack, O., Nichol, G., et al. (2009). Clin. Cancer Res. *15*, 7412–7420.

Cancer Cell
Review

Cancer Genetics and Epigenetics: Two Sides of the Same Coin?

Jueng Soo You[1] and Peter A. Jones[1,*]
[1]Departments of Urology and Biochemistry and Molecular Biology, USC Norris Comprehensive Cancer Center Keck School of Medicine, University of Southern California, Los Angeles, CA 90089, USA
*Correspondence: pjones@med.usc.edu
http://dx.doi.org/10.1016/j.ccr.2012.06.008

Epigenetic and genetic alterations have long been thought of as two separate mechanisms participating in carcinogenesis. A recent outcome of whole exome sequencing of thousands of human cancers has been the unexpected discovery of many inactivating mutations in genes that control the epigenome. These mutations have the potential to disrupt DNA methylation patterns, histone modifications, and nucleosome positioning and hence, gene expression. Genetic alteration of the epigenome therefore contributes to cancer just as epigenetic process can cause point mutations and disable DNA repair functions. This crosstalk between the genome and the epigenome offers new possibilities for therapy.

Cancer has traditionally been viewed as a set of diseases that are driven by the accumulation of genetic mutations that have been considered the major causes of neoplasia (Hanahan and Weinberg, 2011). However, this paradigm has now been expanded to incorporate the disruption of epigenetic regulatory mechanisms that are prevalent in cancer (Baylin and Jones, 2011; Sandoval and Esteller, 2012).

Both genetic and epigenetic views ultimately involve abnormal gene expression. The expression state of a particular gene is determined by the packaging of its DNA regulatory regions at promoters and/or enhancers and insulators in chromatin and by the presence of TFs and chromatin modifying enzymes. The genetic path to cancer is relatively straightforward: mutation of tumor suppressors and/or oncogenes causes either loss or gain of function and abnormal expression. The epigenetic pathway to cancer is not as simple and is determined by chromatin structure including DNA methylation, histone variants and modifications, nucleosome remodeling as well as small non-coding regulatory RNAs (Sharma et al., 2010). During tumor initiation and progression, the epigenome goes through multiple alterations, including a genome-wide loss of DNA methylation (hypomethylation), frequent increases in promoter methylation of CpG islands, changes in nucleosome occupancy, and modification profiles.

More recently, intriguing evidence has emerged that genetic and epigenetic mechanisms are not separate events in cancer; they intertwine and take advantage of each other during tumorigenesis. Alterations in epigenetic mechanisms can lead to genetic mutations, and genetic mutations in epigenetic regulators lead to an altered epigenome. In this review, we will discuss the collusion between epigenetics and genetics in cancer.

How Epigenetics Affect Genetics

Epigenetic mechanisms help establish cellular identities, and failure of the proper preservation of epigenetic marks can result in inappropriate activation or inhibition of various cellular signaling pathways leading to cancer. It is now generally accepted that human cancer cells harbor global epigenetic abnormalities and that epigenetic alterations may be the key to initiating tumorigenesis (Baylin and Jones, 2011; Sandoval and Esteller, 2012; Sharma et al., 2010). The cancer epigenome is characterized by substantial changes in various epigenetic regulatory layers; herein, we introduce some important examples of epigenetic disruptions that cause mutation of key genes and/or alteration of signaling pathways in cancer development.

Epigenetic Silencing Causes the Loss of Function of Genes and Predisposes to Genetic Mutation

Promoter hypermethylation of classic tumor suppressor genes is commonly observed in cancers, a phenomenon that has been implicated with driving tumorigenesis (Baylin and Jones, 2011). Genes controlling the cell cycle and DNA repair, such as *RB*, *BRCA1/2*, and *PTEN*, have all been reported to be hypermethylated or mutated/deleted in cancer (Hatziapostolou and Iliopoulos, 2011). There are also several genes that are seldom mutated but are silenced in cancer; promoter hypermethylation is the predominant mechanism for the loss of their functions (Baylin and Jones, 2011). *O6-methylguanine-DNA methyltransferase* (*MGMT*), which encodes a DNA repair gene, *Cyclin-dependent kinase inhibitor 2B* (*CDKN2B*), which encodes a cell cycle regulator p15, and *RASSF1A*, which encodes a protein that binds to the RAS oncogene all belong to this category, and they have been implicated with protective roles against tumorigenesis.

Several DNA repair genes are known to be subject to promoter methylation. MGMT removes carcinogen-induced O6-methylguanine adducts from DNA, which result in G to A transition mutations. Cancers with hypermethylated *MGMT* are susceptible to genetic mutation in critical genes such as *p53* or *KRAS* (Baylin and Jones, 2011; Esteller, 2007). The mismatch-repair gene *MLH1* plays an important role in genomic stability, and the loss of function of this gene by promoter hypermethylation causes microsatellite instability, which is a key factor in several cancers, including colorectal and endometrial cancers (Krivtsov and Armstrong, 2007). The *MLH1* promoter is already hypermethylated in normal colonic epithelium of some colorectal cancer patients, suggesting this epigenetic change is an early event of tumorigenesis and precedes downstream genetic mutation (Hitchins et al., 2011). Notably, SNVs of *MLH1* 5′UTR are correlated with the hypermethylation of its promoter, highlighting

a close relationship between genetic and epigenetic disruption in cancer (Hitchins et al., 2011).

Epigenetic Silencing Facilitates the Selection of Mutations in Key Signaling Pathways

Direct evidence for a close epigenetic-genetic cooperation is apparent in the colon cancer cell line HCT116 in which one allele of *MLH1* and *CDKN2A* is genetically mutated, whereas the other allele is silenced by DNA methylation (Baylin and Ohm, 2006). The lack of functional expression of MLH1 and CDKN2A causes defects in DNA mismatch repair and cell cycle regulation. Another example of epigenetic-genetic cooperation is in the WNT signaling pathway (Schepers and Clevers, 2012). In normal cells, secreted frizzled-related proteins (SFRPs) antagonize WNT signaling. Epigenetic silencing of *SFRPs* induces abnormal activation of this signaling pathway, further promoting the expression of several genes whose products are responsible for cell proliferation. As a result of survival and proliferative advantages, these cells accumulate genetic mutations in other components of the WNT signaling pathway. There are also several examples where epigenetic silencing allows abnormal proliferation pathways and increases the likelihood for mutation in genetic gate keepers and increases cancer risk (Baylin and Jones, 2011).

More recent results from The Cancer Genome Atlas project provide an integrative view of ovarian carcinoma based on integrated genomic analyses (Network, 2011). The mutation spectrum is unexpectedly simple, showing the predominance of *p53* mutations and other low frequency mutations in nine genes including *BRCA1*, *BRCA2*, and *RB*. On the other hand, promoter hypermethylation is observed in 168 genes, and those genes are epigenetically silenced and correlated with reduced expression. It is noteworthy that clustering of variable DNA methylation across tumors can identify subtypes. Indeed, the CpG island methylator phenotype (CIMP) is reported in colorectal cancer and glioblastoma, and this subgroup shows distinctive characters such as genetic and clinical features (Hinoue et al., 2012; Noushmehr et al., 2010). A CIMP-high subgroup is strongly associated with *MLH1* DNA hypermethylation and *BRAF* mutation, while a CIPM-low subgroup is related to *KRAS* mutation (Hinoue et al., 2012).

Role of 5-methylcytosine in Generating Disease-Causing Mutations

The methylation of cytosine residues in the germline has led to an approximately 75% decrease in the frequency of CpG methyl acceptor sites. This is thought to be due to the spontaneous hydrolytic deamination of 5-methylcytosine (5mC) to thymine rather than uracil, which is formed by deamination of cytosine. The resulting T:G mismatch is more difficult to repair, and about a third of all disease causing familial mutations and single nucleotide polymorphisms or variants (SNPs or SNVs) occur at methylated CpG sites. What is often overlooked is that the presence of 5mC in the gene bodies and coding regions of genes such as *p53* is responsible for generating inactivating C to T transition mutations, causing hotspots in somatic cells (Rideout et al., 1990). For example, as many as 50% of p53 point mutations in colon cancer occur at such sites, clearly demonstrating that an epigenetic mark (5mC) directly causes somatic mutations.

More interestingly, a somatic *DNMT3A* hotspot mutation in acute myeloid leukemia (AML) is caused by C to T transitions at a CpG site, possibly due to the methylation of its own exon by the enzyme (epigenetic alteration) and the subsequent deamination of 5mC (genetic mutation) (Ley et al., 2010) (Figure 1). The effect of the point mutation is not yet fully understood since methylation changes are not observed in the tumor. It is possible that this mutation alters DNMT3A function and/or activity and may further disrupt whole epigenetic regulation mechanism (Figure 1).

Role of MicroRNA in Tumorigenesis

MicroRNAs (miRNAs) are a class of small noncoding RNAs that play key roles in epigenetic regulation by controlling the translation and/or stability of mRNAs. There are over 1,000 human miRNAs and, interestingly, these miRNAs frequently target regions related to cancer development (Ryan et al., 2010). They have been classified as oncogenic, tumor-suppressive, or context-dependent miRNAs (Kasinski and Slack, 2011). Indeed, oncogenic miRNAs such as miR-155 or miR-21 are frequently overexpressed, and tumor suppressive miRNAs such as miR-146 or miR-15∼16 are deleted in cancers (Kasinski and Slack, 2011). Mutation in the miRNA can disrupt its recognition of binding targets and further result in oncogene activation and/or tumor suppressor repression. Additionally miRNAs including miR-101 and miR-29 target epigenetic modifiers such as EZH2 (Friedman et al., 2009; Varambally et al., 2008) and DNMT3A/B (Fabbri et al., 2007), respectively. This can result in further widespread epigenetic alterations (Fabbri and Calin, 2010; Kasinski and Slack, 2011) and might lead to the methylation of promoters of other miRNAs that target oncogenes. miR-127, which targets BCL6, is abnormally methylated and silenced in cancer (Saito et al., 2006), highlighting the reciprocal regulation of miRNAs, epigenetic modifiers, and genetic defects in cancer.

Given the importance of epigenetic silencing in the development of cancer, distinguishing "drivers" and "passengers" is becoming an important priority for the field. Driver genes must be essential for cancer causation, whereas passenger genes are not necessary (Kelly et al., 2010). With the improvement of technology, it may eventually be possible to specifically distinguish epigenetic disruptions of the driver genes (De Carvalho et al., 2012; Kalari and Pfeifer, 2010). Current evidence shows that epigenetic disruption plays a key role at every stage of tumorigenesis and has a significant impact on the underlying mechanisms of tumorigenesis and development of cancer therapy.

How Genetics Affect Epigenetics

While epigenetics and genetics can cooperate in cancer initiation and progression, the interconnectedness between of these two processes is becoming increasingly apparent with the realization that several epigenetic modifiers are mutated in human cancers (Kasinski and Slack, 2011; Rodríguez-Paredes and Esteller, 2011; Schuettengruber et al., 2011; Wilson and Roberts, 2011). Some examples of genetic mutations of epigenetic modifiers are shown in Table 1 and Figure 2. The mutation of epigenetic modifiers presumably leads to profound epigenetic changes, including aberrant DNA methylation, histone modifications, and nucleosome positioning, although this remains to be demonstrated. These epigenetic alterations can lead to abnormal gene expression and genomic instability, which may predispose to cancer (Rodríguez-Paredes and Esteller, 2011; Wilson and Roberts, 2011).

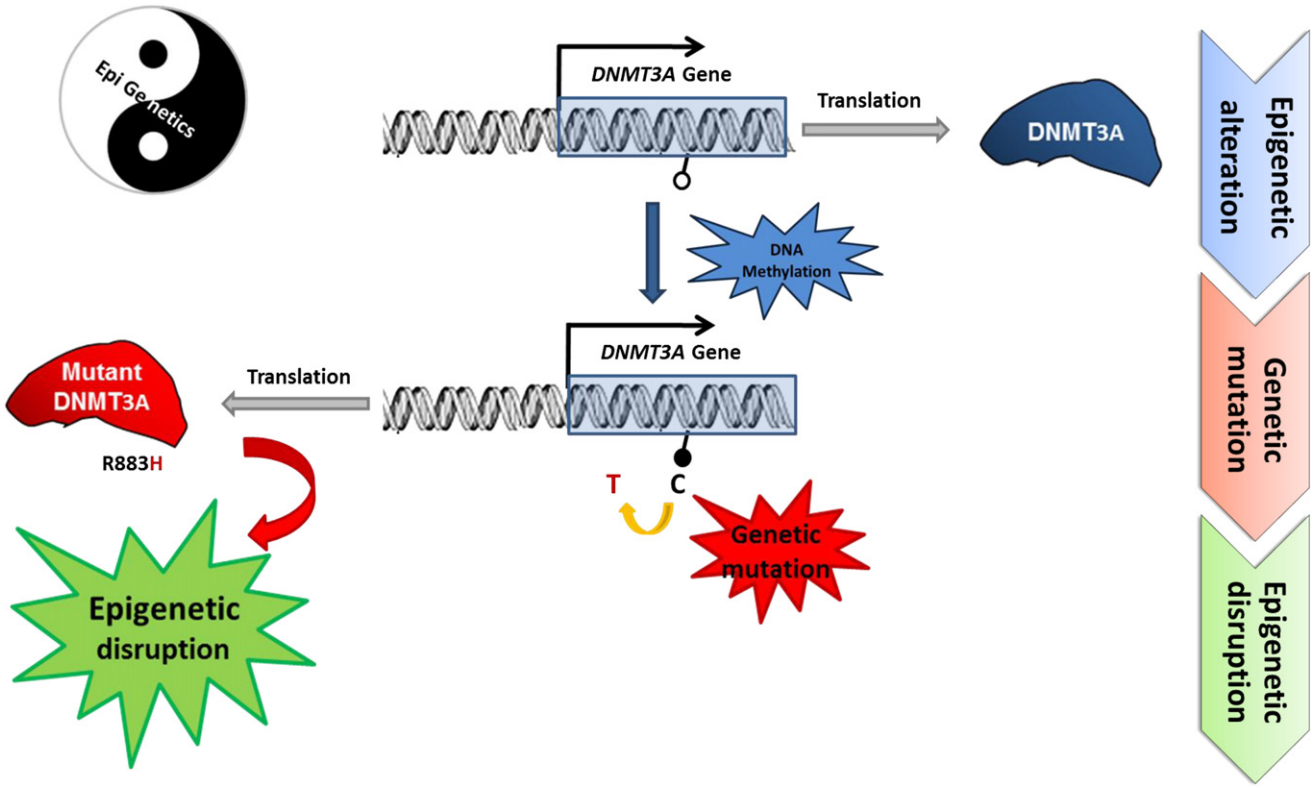

Figure 1. The Crosstalk between Cancer Genetics and Epigenetics

The methylation of CpG sites located in *DNMT3A* exons (epigenetic alteration, represented as a black circle) potentially leads to genetic mutation in somatic cells by the hydrolytic deamination of 5mC to form a C to T transition mutation. Although it is not known whether DNMT3A directly methylates its own exon and the effect of this genetic mutation is not yet fully understood, it is possible that the C to T transition alters DNMT3A function and/or activity and thereby disrupts the epigenetic landscape. The Yin-Yang diagram emphasizes how epigenetic and genetic interactions are required to achieve perfect balance and suggests that disruption of the balance can lead to disease.

DNA Methylation Machinery

While non-CpG methylation has been reported in pluripotent cells (Hawkins et al., 2010; Meissner et al., 2008), DNA methylation in mammals occurs predominantly at CpG dinucleotides, and methylation of CpG islands acts as a relatively stable gene silencing mechanism (Jones and Liang, 2009). The majority of the CpG islands, which represent over 50% of promoters, remain mostly unmethylated in somatic cells. DNA methylation is important for the regulation of non-CpG island as well as CpG island promoters and in repetitive sequences (LINE and/or SINE) to maintain genomic stability (De Carvalho et al., 2010; Jones and Liang, 2009). DNA methylation in mammalian cells is regulated by a family of DNA methyltransferases (DNMTs) that catalyze the transfer of methyl groups from S-adenosyl-L-methionine to the 5′ position of cytosine bases in the CpG dinucleotide. DNMT3A and DNMT3B, which are expressed throughout the cell cycle (Kinney and Pradhan, 2011), establish new DNA methylation patterns early in development. During replication, the original DNA methylation pattern is maintained largely by DNMT1 activity, which prefers hemi-methylated DNA over nonmethylated DNA as a substrate and which is also supported by recent structure study (Song et al., 2012) and is therefore responsible for the maintenance of methylation patterns during cell division, with some participation by DNMT3A and DNMT3B (Jones and Liang, 2009; Sharma et al., 2010).

DNMT1 mutations have been described in colorectal cancer (Kanai et al., 2003), and as previously noted, *DNMT3A* mutations are frequent in myelodysplastic syndromes (MDS) and AML (Ley et al., 2010; Yamashita et al., 2010; Yan et al., 2011). Germline mutations in *DNMT3B* underlie immunodeficiency-centromeric instability-facial anomalies (ICF) syndrome and chromosome instability (Wijmenga et al., 2000), and SNPs in *DNMT3B* have been suggested to be associated with risk of several cancers including breast and lung adenocarcinoma (Shen et al., 2002). In addition to the example in Figure 1, other mutations of *DNMT3A* occur at several positions and generally represent a loss of function, similar to *DNMT3B* mutations that are associated with ICF syndrome (Ley et al., 2010). Recent studies uncovered a role of DNMT3A in silencing self-renewal genes in hematopoietic stem cells (HSCs) to permit efficient hematopoietic differentiation, and its loss progressively impairs HSC differentiation (Challen et al., 2012; Trowbridge and Orkin, 2012). All known *DNMT3A* mutations are related to poor survival in AML (Ley et al., 2010; Yan et al., 2011), suggesting that these mutations prevent differentiation and have an important role in the progression of disease.

In addition to various mutations, DNMT1, DNMT3A, and DNMT3B are often overexpressed in various cancers and possibly contribute to ectopic hypermethylation (Wu et al., 2007). However, careful studies should be done to understand

Table 1. Epigenetic Modifiers in Cancer

	Gene	Function	Tumor Type	Alteration
DNA methylation	*DNMT1*	DNA methyltransferase	Colorectal, non-small cell lung, pancreatic, gastric, breast cancer	Mutation (Kanai et al., 2003)
				Overexpression (Wu et al., 2007)
	DNMT3A	DNA methyltransferase	MDS, AML	Mutation (Ley et al., 2010; Yamashita et al., 2010; Yan et al., 2011)
	DNMT3B	DNA methyltransferase	ICF syndrome, SNPs in breast and lung adenoma	Mutation (Wijmenga et al., 2000)
				Mutation (Shen et al., 2002)
	MBD1/2	Methyl binding protein	Lung and breast cancer	Mutation (Sansom et al., 2007)
	TET1	5′methylcytosine hydroxylase	AML	Chromosome translocation (De Carvalho et al., 2010; Wu and Zhang, 2010)
	TET2	5′methylcytosine hydroxylase	MDS, myeloid malignancies (AML), gliomas	Mutation/silencing (Tan and Manley, 2009)
	IDH1/2	Isocitrate dehydrogenase	Glioma, AML	Mutation (Figueroa et al., 2010; Lu et al., 2012; Turcan et al., 2012)
	AID	5′cytidine deaminase	CML	Aberrant expression (De Carvalho et al., 2010)
Histone modification	*MLL1/2/3*	Histone methyltransferase H3K4	Bladder TCC, ALL and AML, non-Hodgkin lymphoma, B cell lymphoma, prostate (primary)	Translocation, mutation, aberrant expression (Gui et al., 2011; Morin et al., 2011)
	BRD4	Bromodomain containing 4	Nuclear protein in testis, midline carcinoma, breast, colon, and AML	Translocation (fusion protein), aberrant expression (Filippakopoulos et al., 2010; Zuber et al., 2011)
	EZH2	Histone methyltransferase H3K27	Breast, prostate, bladder, colon, pancreas, liver, gastric, uterine tumors, melanoma, lymphoma, myeloma, and Ewing's sarcoma	Mutation, aberrant expression (Chase and Cross, 2011; Tsang and Cheng, 2011)
	ASXL	Enhancer of trithorax and polycomb group (EAP) Additional sex combs like 1	MDS and AML, Bohring-Opitz syndrome	Mutation (Gelsi-Boyer et al., 2012; Hoischen et al., 2011)
	BMI-1	PRC1 subunit	Ovarian, mantle cell lymphomas and Merkel cell carcinomas	Overexpression (Jiang et al., 2009; Lukacs et al., 2010)
	G9a	Histone methyltransferase H3K9	HCC, cervical, uterine, ovarian, and breast cancer	Aberrant expression (Varier and Timmers, 2011)
	PRMT1/5	Protein arginine methyltransferase	Breast/gastric	Aberrant expression (Miremadi et al., 2007)
	LSD1	Histone demethylase H3K4/H3K9	Prostate	Mutation (Rotili and Mai, 2011)
	UTX (*KDM6A*)	Histone demethylase H3K27	Bladder, breast, kidney, lung, pancreas, esophagus, colon, uterus, brain	Mutation (Rotili and Mai, 2011)
	JARID1B/C	Histone demethylase H3K4/H3K9	Testicular and breast, RCCC	Overexpression (Rotili and Mai, 2011)
	EP300	Histone deacetyltransferase	Breast, colorectal, pancreatic cancer	Mutation (Miremadi et al., 2007)
	CREBBP	Histone acetyltransferase	Gastric and colorectal, epithelial, ovarian, lung, esophageal cancer	Mutation, overexpression (Miremadi et al., 2007)
	PCAF	Histone acetyltransferase	Epithelial	Mutation (Miremadi et al., 2007)
	HDAC2	Histone deacetyltransferase	Colonic, gastric, endometrial cancer	Mutation (Ropero et al., 2006)
	SIRT1, *HDAC5/7A*	Histone deacetyltransferase	Breast, colorectal, prostate cancer	Mutation, aberrant expression (Miremadi et al., 2007)

Table 1. *Continued*

	Gene	Function	Tumor Type	Alteration
Chromatin remodeling	*SNF5* (*SMARCB1*, *INI1*)	BAF subunit	Kidney malignant rhabdoid tumors, atypical rhabdoid/teratoid tumors (extra-renal), epithelioid sarcomas, small cell hepatoblastomas, extraskeletal myxoid chondrosarcomas, and undifferentiated sarcomas	Mutation, silencing, loss of expression (Wilson and Roberts, 2011)
	BRG1 (*SMARCA4*)	ATPase of BAF	Lung, rhabdoid, medulloblastoma	Mutation, low expression (Wilson and Roberts, 2011)
	BRM (*SMARCA2*)	ATPase of BAF	Prostate, basal cell carcinoma	Mutation, low expression (de Zwaan and Haass, 2010; Sun et al., 2007)
	ARID1A (*BAF250A*)	BAF subunit	Ovarian clear cell carcinomas, 30% of endometrioid carcinomas, endometrial carcinomas	Mutation, genomic rearrangement, low expression (Guan et al., 2011; Jones et al., 2010)
	ARID2 (*BAF200*)	PBAF subunit	Primary pancreatic adenocarcinomas	Mutation (Li et al., 2011)
	BRD7	PBAF subunit	Bladder TCC	Mutation (Drost et al., 2010)
	PBRM1 (*BAF180*)	PBAF subunit	Breast tumors	Mutation (Varela et al., 2011)
	SRCAP	ATPase of SWR1	Prostate	Aberrant expression (Balakrishnan et al., 2007)
	P400/Tip60	ATPase of SWR1, acetylase of SWR1	Colon, lymphomas, head-and-neck, breast	Mutation, aberrant expression (Mattera et al., 2009)
	CHD4/5	ATPase of NURD	Colorectal and gastric cancer, ovarian, prostate, neuroblastoma	Mutation (Bagchi et al., 2007; Kim et al., 2011; Wang et al., 2011a)
	CHD7	ATP-dependent helicase	Gastric and colorectal	Mutation (Wessels et al., 2010)

MDS, myelodysplastic syndromes; AML, acute myeloid leukemia; TCC, transitional cell carcinoma; RCCC, renal clear cell carcinoma.

the relationship between the expression of DNMTs and methylation disruption since the overexpression of DNMTs may be a reflection of increased cell proliferation.

Methyl-binding domain (MBD) proteins, including MeCP2, MBD1, MBD2, and MBD4, bind to methylated CpG sites and might be involved in mediating transcriptional repression (Bogdanović and Veenstra, 2009). Genetic mutations in *MBD1* and *MBD2* increase the risk of lung and breast cancer, respectively (Sansom et al., 2007). MeCP2 and other MBD protein alterations have been reported in several cancers, however the mechanism is yet to be uncovered.

The field of DNA demethylation has been controversial (Ooi and Bestor, 2008), but recent evidence suggests that this demethylation can occur through two processes: active and passive (De Carvalho et al., 2010; Wu and Zhang, 2010). Passive DNA demethylation occurs when maintenance DNA methylation is impaired during DNA replication, resulting in loss of methylation of the newly synthesized DNA strand. In contrast, active DNA demethylation is dependent on the ability of one or more enzymes to hydroxylate, further oxidize, or deaminate 5mC and can occur independent of DNA replication (Bhutani et al., 2011; Wu and Zhang, 2010). Recently, several proteins have been implicated to be erasers of DNA methylation including *TET* (*ten-eleven-translocation*) and *AID* (*activation-induced cytidine deaminase*) (De Carvalho et al., 2010; Ko et al., 2010; Wu and Zhang, 2010). Active DNA demethylation is currently thought of as being a stepwise process—hydroxylation of 5mC (5hmC) by TET proteins followed by deamination by AID/APOBEC protein or carboxylation and entry in to the subsequent base excision repair pathway (Bhutani et al., 2011). Alternatively, 5hmC is not recognized by DNMT1 (Lao et al., 2010); replication of DNA containing this base would lead to loss of the 5mC mark in the subsequent S phase.

Three TET family members (TET1, TET2, and TET3) have been reported so far, and each protein seems to have a distinct function in different cellular contexts (Cimmino et al., 2011). Mutations in *TET2*, including frame shift, nonsense, and missense mutations, have been found in MDS and in myeloproliferative neoplasms (Tan and Manley, 2009). Notably, *TET2* loss-of-function mutations were mutually exclusive of mutations in *IDH1* (*isocitrate dehydrogenase1*) and *IDH2*, which are known to induce DNA hypermethylation and impair differentiation in hematopoietic cells (Figueroa et al., 2010). *IDH1/2* mutations in glioma and AML cause accumulation of 2-hydoxyglutarate which is called an "oncometabolite" and further impairs the DNA demethylation process and causes hypermethylation in glioma (Turcan et al., 2012). Remarkably, *IDH1/2* mutations also disrupt histone demethylation and block cell differentiation in nontransformed cells (Lu et al., 2012).

Considering that DNMTs/MBD proteins and enzymes involved in DNA demethylation contribute directly to the level of DNA methylation but also to nucleosome occupancy patterns, the alteration of these machineries in cancer development could be broader than previously realized.

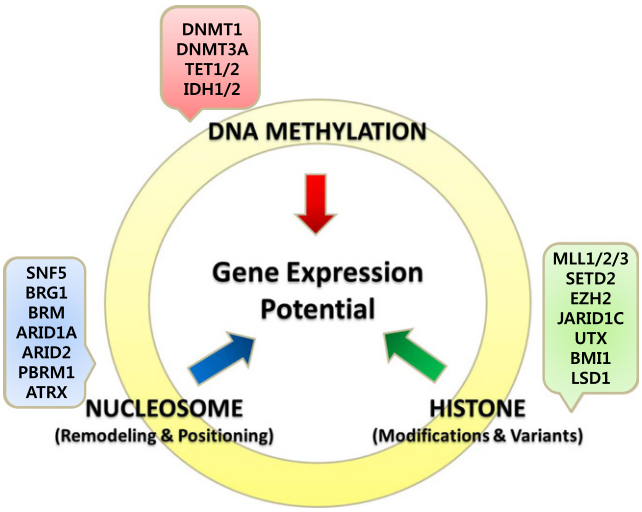

Figure 2. Genetic Mutations in Epigenetic Modifiers in Cancer
The drawing shows the interaction between epigenetic processes in specifying gene expression patterns. Recent whole exome sequencing studies show that mutations in the three classes of epigenetic modifiers is frequently observed in various types of cancers, further highlighting the crosstalk between genetics and epigenetics. Examples of some but not all of these mutations that are discussed in this review are shown. The mutations of epigenetic modifiers probably cause genome-wide epigenetic alterations in cancer, but these have yet to be demonstrated in a genome-wide scale. Understanding the relationship of genetic and the epigenetic changes in cancer will offer novel insights for cancer therapies.

Histone Modification Machinery

Nucleosomes, which are the basic building blocks of chromatin, contain DNA wrapped around histones (Luger et al., 1997). Histones are regulators of chromatin dynamics either by changing chromatic structure by altering electrostatic charge or providing protein recognition sites by specific modifications (Mills, 2010; Suganuma and Workman, 2011). Histone modifications at specific residues characterize genomic regulatory regions, such as active promoter regions which are enriched in trimethylated H3 at lysine 4 (H3K4me3), inactive promoters which are enriched in trimethylated H3 at lysine 27 (H3K27me3) or trimethylated H3 at lysine 9 (H3K9me3), and regulatory enhancers that are enriched in monomethylated H3 at lysine 4 (H3K4me1) and/or acetylated H3 at lysine 27 (H3K27ac) (Hawkins et al., 2011; Hon et al., 2009; Mills, 2010). These histone modification patterns are regulated by enzymes including histone acetyltransferases (HATs) and deacetylases (HDACs), which introduce and remove acetyl groups, respectively. Histone methyltransferases (HMTs) and demethylases (HDMs), on the other hand, introduce and remove methyl groups. During tumorigenesis, cells undergo global changes in histone modifications and in the distribution of histone variants such as H2A.Z (Conerly et al., 2010), which may affect the recruitment of TFs and often components of the transcription machinery, thereby contributing to aberrant gene expression (Mills, 2010; Sharma et al., 2010).

The acetylation of lysine residues on histones is generally associated with active gene transcription. HATs can be grouped into three categories based on their sequence similarities: Gcn5/PCAF, p300/CBP, and the MYST families (Yang, 2004). Mutations or translocations of these genes are observed in colon, uterine, and lung tumors and in leukemias (Esteller, 2007). Further, these HATs (p300, CBP, and MYST4) are commonly involved in chromosomal translocations in hematological cancers rather than in solid tumors (Iyer et al., 2004). For example, AML1-ETO, the fusion protein generated by the t(8;21) translocation, which is also the most common fusion protein in AML, requires its acetylation mediated by p300 for oncogenic activity (Wang et al., 2011b). HDACs remove acetyl groups from histone tails, and at least 18 HDAC genes have been identified in the human genome. HDACs as well as HATs function as part of large multi-protein complexes (Marks et al., 2001). HDACs have been implicated in cancer due to their aberrant binding and consequent silencing of tumor suppressor genes. For example, hypoacetylation of the *p21waf1/cif1* (*CDKN1A*) promoter results in its silencing and can be reversed by HDAC inhibitors (Ocker and Schneider-Stock, 2007). Germline mutations of HDACs increase the risk of breast and lung cancers, and abnormal HDAC overexpression has also been observed in various cancers (Miremadi et al., 2007). As a result, HDAC inhibitors have been developed as anti-cancer drugs (Shankar and Srivastava, 2008). Several independent reports have identified truncation mutations in HDAC2 in epithelial, colonic, gastric, and endometrial cancers, and these mutations confer resistance to HDAC inhibitors (Smith and Workman, 2009). Screening for these mutations may improve the efficacy of HDAC inhibitors. Conversely, there is evidence that HDACs may function as tumor suppressors by maintaining proper chromatin structure and further stabilizing the genome (Bhaskara et al., 2010). Potentially, either loss or gain of function mutations of HDACs could contribute to tumorigenesis.

In addition to chromatin modifying enzymes, chromatin binding proteins or so-called epigenetic ''readers'', such as the bromodomain proteins which read lysine acetylation marks, can also play an important during tumorigenesis. For example, the fusion of the bromodomain protein Brd4 with nuclear protein in testis (NUT) results in the development of aggressive NUT midline carcinoma (Filippakopoulos et al., 2010). Aberrant regulation of Brd4 has also been reported in other cancers such as colon and breast, suggesting that the selective inhibitors which target these kinds of epigenetic readers may give us a novel clue for cancer therapy (Filippakopoulos et al., 2010; Zuber et al., 2011).

Methylation of arginine and lysine residues on histones or nonhistone proteins such as TFs regulate chromatin structure and therefore gene expression (Greer and Shi, 2012). The best-known example of alterations in HMTs during tumorigenesis may be in the mixed lineage leukemia (MLL) protein, which introduces the active H3K4me3 mark and plays important roles in development. *MLL* is located on chromosome 11q23, which is a common region of chromosomal translocation in AML and ALL (Slany, 2009). Translocations of MLL with multiple different partners can result in the generation of fusion proteins that are frequently associated with tumorigenesis and poor prognosis by generating abnormal patterns of H3K4me3 and/or recruiting other epigenetic modifiers (Balgobind et al., 2011). These MLL fusion proteins have close relationships with other epigenetic modifiers and cause altered epigenetic programs in cancer. For example, the aberrant H3K79 methylation pattern mediated by DOT1L is required for the maintenance of the MLL

translocation-associated oncogenic program (Bernt et al., 2011). Inhibition of DOT1L activities decreases expression of MLL fusion-driven transcriptional programs and might have profound therapeutic implications (see the detailed discussion in Therapeutic Perspective). In addition, alternative splicing and mutations in *MLL1*, *MLL2*, and *MLL3* genes have been identified in bladder, breast, and pancreatic cancers and in glioblastoma (Gui et al., 2011; Morin et al., 2011).

The Polycomb group (PcG) of repressor proteins controls the accessibility of gene regulatory elements to the transcription machinery (Mills, 2010), This group is crucial for early development and often becomes deregulated in cancer. EZH2, together with SUZ12 and EED, form the polycomb repressive complex 2, which methylates H3K27. Overexpression of EZH2 has been reported in several cancers such as prostate, breast, lung, and bladder and seems to result in an increase in H3K27me3 (Chase and Cross, 2011). However, other studies show that there is no association between EZH2 and H3K27me3 in ovarian and pancreatic cancers (Füllgrabe et al., 2011). Downregulation of microRNA-101, a negative regulator of EZH2, has been described as a cause of overexpression of EZH2 in bladder and prostate cancers (Friedman et al., 2009; Varambally et al., 2008), and *EZH2* mutations have been reported in lymphoma and myeloid neoplasm (Chase and Cross, 2011). In lymphoma, a heterozygous missense mutation at amino acid Y641, within the SET domain, results in a gain of function, showing enhanced catalytic activity. The *EZH2* mutations in myeloid neoplasms are associated with poor prognosis, and the mutations frequently result in loss of function of HMT. Although the mechanism of action of EZH2 in cancer is not yet clear, it appears to play a role in growth control (Tsang and Cheng, 2011).

BMI-1, a component of PRC1, is indispensable for the regulation of self-renewal of normal and leukemic stem cells and for the differentiation of T cells (Nakayama and Yamashita, 2009; Sauvageau and Sauvageau, 2010). BMI-1 has been considered a key regulator of self-renewal in cancer stem cells (Jiang et al., 2009). More recently, overexpression of BMI-1 has been observed in solid tumors such as prostate cancer (Lukacs et al., 2010; Yang et al., 2010).

Subgroups of genes that are normally repressed by H3K27me3 in early development often acquire abnormal DNA methylation in cancers, a process which we have called ''epigenetic switching'' (Sharma et al., 2010). The differentiation of stem cells begins by turning off master regulators that define ''stemness'' (e.g., OCT4 in embryonic stem cells), followed by the expression of lineage specific genes, resulting in the acquisition of particular phenotypes (e.g., MYOD1 in muscle and NEUROG1 in neurons) (Young, 2011). Progress through these steps is often, but not always, controlled by PcG and does not involve DNA methylation. Once these key regulators become methylated, they become locked in a repressed state, and this prevents switching from one phenotype to another. The outcome of the ''epigenetic switch'' may therefore be an increase in the number of cancer initiating cells (Baylin and Jones, 2011). Full understanding of this mechanism remains to be clarified.

Other lysine HMTs (NSD1, SMYD3, and G9a) are aberrantly expressed in several cancers (Varier and Timmers, 2011). Evidence for the role of arginine HMTs (PRMTs) in tumorigenesis has not been as well established as that of lysine HMTs, although alteration of expression of PRMT1 in breast cancer and PRMT5 in gastric cancer has been reported (Lee and Stallcup, 2009).

Two distinct classes of HDMs have been defined based on their mechanism of action (Mosammaparast and Shi, 2010). Lysine-specific histone demethylase 1 (LSD1), lysine-specific demethylase 6A (KDM6A/UTX), and jumonji C-domain containing proteins (JARID1A-D) have all been implicated in tumorigenesis. Mutations in *LSD1* (prostate cancer) and *KDM6A/UTX* (various cancers including bladder, breast, kidney, and colon) have been reported (Rotili and Mai, 2011). Reintroduction of KDM6A/UTX in the UTX mutant cancer cells results in the slowing of proliferation, suggesting that genetic mutations of these enzymes reinforce the epigenetic deregulation in cancers.

The exact mechanism by which these histone modifying enzymes affect tumorigenesis remains to be elucidated; altered expression of histone modifiers caused by mutations may disrupt whole epigenetic regulation mechanisms and result in aberrant gene expression patterns. Indeed, the disruption of histone modifications has been linked to all the hallmarks of cancer, and it is important to be aware that a precise balance between the enzymes that write, read, and erase histone marks is crucial in preventing tumorigenesis.

Chromatin Remodeling Complexes

Nucleosome occupancy is a key mechanism for gene expression, and it has been known for some time that chromatin remodelers are responsible for regulating this process (Clapier and Cairns, 2009; Segal and Widom, 2009; Valouev et al., 2011). ATP dependent chromatin remodelers are generally divided into four main families: switch/sucrose non-fermenting (SWI/SNF), imitation SWI, inositol requiring 80, and nucleosome remodeling and deacetylation chromatin helicase DNA binding (NURD/Mi2/CHD) complexes (Ho and Crabtree, 2010). Although the ATPase domains are highly similar, the distinct chromatin interacting domains carry out specific roles and can be selectively targeted. These ATPase dependent remodelers act in the context of multisubunit complexes and have dual roles as activators and repressors of gene expression. The importance of chromatin remodeling machines is becoming apparent with the realization that many of them are mutated in several types of cancer (Hargreaves and Crabtree, 2011; Wilson and Roberts, 2011).

SWI/SNF is a large complex with 9 to 12 subunits including ATPases (BRG1 or BRM), core subunits (SNF5, BAF155, and BAF 170), and other accessory subunits (Ho and Crabtree, 2010). The variety of subunits allows for combinatorial assembly that leads to functional diversity as evidenced by the cellular stage-specific composition of SWI/SNF complexes (Hargreaves and Crabtree, 2011). SWI/SNF complexes remodel chromatin by changing nucleosome occupancy pattern, thereby contributing to either transcriptional activation or repression (Reisman et al., 2009; Wilson and Roberts, 2011).

SNF5 of the SWI/SNF core subunit is at the nexus of the link between chromatin remodeling and tumorigenesis, and many rhabdoid tumors contain inactivating mutations in this gene. Loss of SNF5 is also observed in renal carcinomas and melanomas, where it is correlated with poor survival rates (Lin et al., 2009). SNF5 loss affects expression of genes associated with cell proliferation and cell cycle, such as RB or p53 and Hedgehog-Gli, a key signaling pathway in early development

and cancer. Antagonism between EZH2 and SNF5 has also been reported during tumorigenesis (Jagani et al., 2010; Wilson and Roberts, 2011), and there is accumulating evident that SNF5 deletion plays a role in tumorigenesis, but the exact mechanism of SNF5 loss in tumorigenesis remains to be elucidated.

ARID1A/BAF250a mutations have been frequently observed in ovarian clear cell carcinoma (50%) and endometrioid carcinomas (30%) (Guan et al., 2011; Jones et al., 2010; Wiegand et al., 2010). More recently, *ARID1A/BAF250a* mutations have been observed in primary pancreatic adenocarcinomas, and transitional cell carcinoma and low ARID1A expression was found to be significantly associated with a specific subgroup of breast cancers (ER-/PR-/HER2-) (Zhang et al., 2011). In mice, ARID1B/ BAF250b-containing complexes, which include components of an E3 ubiquitin ligase and are mutually exclusive of ARID1A, have also been shown to play a role in the control of cell cycle and differentiation. Mutations in human *ARID1B/ BAF250b* have been reported very recently as a cause of Coffin-Siris syndrome (Santen et al., 2012; Tsurusaki et al., 2012).

The PBRM1/BAF180, BAF200, and BRD7 subunits belong to polybromo BRG1 associated factor (PBAF) complexes and facilitate transcriptional activation by nuclear receptors (Wilson and Roberts, 2011). Mutation of *PBRM/BAF180* has been identified in 41% renal cell carcinomas and in breast cancers, and this mutation affects senescence in human cells. Mutation in another PBAF specific subunit, *BRD7*, has been reported in breast cancers. Since BRD7 has a variety of binding partners including p53 and BRCA1, mutations in it may be important in tumorigenesis.

Mutations in SWI/SNF ATPase subunits *BRG1* or *BRM* have been reported in several cancers including lung, medulloblastoma, rhabdoid, and prostate tumors (Wilson and Roberts, 2011). Although BRG1 and BRM show some redundancy in vivo and in vitro, they seem to be mutually exclusive and have distinctive roles based on their expression changes during early development. Tumor suppressor properties of BRG1 and BRM have been reported in lung, breast, and prostate cancer cell lines (Roberts and Orkin, 2004) and, in vitro, BRG1 and BRM have been observed to interact with several tumor suppressors including BRCA1(Wang et al., 2007).

Mutation of BAF complexes is a frequent event in various cancers; however, the dependency between the subunits and whether mutation of one subunit results in a modification of the activity of the complex is not clear. In addition, mutations of BAF complex components frequently coexist with those of canonical oncogenes or tumor suppressors such as *KRAS*, *CDKN2A*, or *p53*, suggesting a synergistic effect on tumorigenesis (Wilson and Roberts, 2011).

In addition to SWI/SNF complexes, mutations of other ATP dependent chromatin remodelers are beginning to be identified in several cancers (Clapier and Cairns, 2009; Hargreaves and Crabtree, 2011; Ho and Crabtree, 2010). Despite emerging evidence that closely connects these ATPase remodelers in tumorigenesis, the direct causality and/or mechanism still remains to be explicated.

The Role of SNPs on Epigenetic Regulation and Cancer

Genome-wide association studies have identified a large number of SNPs associated with an increased risk of a variety of diseases including several cancers. Surprisingly, cancer-associated SNPs are significantly enriched at regions defined as functional enhancers in ES cells (Teng et al., 2011) and might confer cancer susceptibility by altering the chromatin landscape. Further, several genome-wide expression quantitative trait loci studies in humans have demonstrated a link between genetic variation and changes in gene regulation (Nica et al., 2010; Nicolae et al., 2010). More recently, these genetic variants were shown to modify the chromatin accessibility of TF binding sites, thereby leading to gene expression differences (Degner et al., 2012). Although allele-specific DNA methylation and allele-specific gene expression have been well studied in imprinting and X chromosome inactivation, recent studies show that these allele-specific phenomena are more pervasive to other cellular activities (Tycko, 2010). Notably, most of the allele-specific DNA methylation outside of imprinted genes shows a strong correlation with SNP genotypes that affect TF binding insulators and long-range chromosome structure. Conversely, SNPs can create or delete CpGs (termed as CpG SNPs), thereby influencing the binding of specific TFs (Tycko, 2010). Future studies aimed at understanding functional associations among epigenetic variation (epigenotype), genetic variation (genotype), and trait or disease (phenotype) may help us to determine the causality of diseases.

Therapeutic Perspective

An increasing number of nucleoside analogs/small molecules are being studied as anti-cancer drugs. Inhibitiors of DNMTs 5-azacytidine (5-Aza-CR; Vidaza; azacitidine) and 5-Aza-2-deoxycytidine (5-Aza-CdR; Dacogen; decitabine) or HDACs by SAHA or Rhomidepsin have been approved for cancer treatment by the FDA and proven to have therapeutic efficacy in a variety of malignancies (Kelly et al., 2010). Recently, several novel compounds have been reported to target epigenetic components and have therapeutic effects in the presence of specific genetic defects. The DOT1L inhibitor (EPZ004777) inhibits H3K79 methylation, prevents transcription of genes that are involved in leukemogenesis, and kills cancer cells bearing MLL translocations (Daigle et al., 2011). Selective bromodomain inhibitors (JQ1 or GSK525762) (Filippakopoulos et al., 2010; Nicodeme et al., 2010) inhibit transcription by MYC, which is overexpressed in a majority of cancers (Delmore et al., 2011). The presence of multiple genetic and epigenetic aberrations within a cancer suggests that effective cancer therapies will be most beneficial when combined with epigenetic and/or other anti-cancer strategies such as standard chemotherapy (Juergens et al., 2011; Matei and Nephew, 2010).

Conclusions

Recent whole exome sequencing of thousands of human cancers have come up with the unexpected results that mutations in genes that control the epigenome are surprisingly common in human cancers. The presence of these mutations was unknown and overlooked, which is surprising in view of the fact that were almost 1,000 cell lines recently analyzed by whole exome sequencing contain a large number of potential mutations in epigenetic modifiers (Barretina et al., 2012). The fact that the epigenome acts at the pinnacle of the hierarchy of gene control mechanisms means that the mutations probably

have effects on multiple pathways relevant to the cancer phenotype, and a single mutation could cause wide scale misregulation. This realization opens the door to further drug development since it might be possible to correct several pathways by altering or inhibiting one enzyme. These data also show a much closer Yin-Yang relationship between the genome and the epigenome, as indicated in this review. This has heralded the dawn of a new era in cancer research in which the way the genes are organized and controlled is being recognized as a major relevant factor for human carcinogenesis. Traditionally, cancer is diagnosed by pathologists using light microscopes to analyze the morphology of the nucleus among other cellular features. Understanding how epigenetic modifiers communicate with each other and alter nuclear architecture, and therefore gene expression, is a major challenge for the future but one which should yield better options for patients.

ACKNOWLEDGMENTS

We thank Jones lab members and Gerry Coetzee for helpful discussion of the manuscript. We apologize to those whose work has not been included because of space constraints. Funding for this work to P.A.J. was provided by NIH R37 CA-082422-12.

REFERENCES

Bagchi, A., Papazoglu, C., Wu, Y., Capurso, D., Brodt, M., Francis, D., Bredel, M., Vogel, H., and Mills, A.A. (2007). CHD5 is a tumor suppressor at human 1p36. Cell *128*, 459–475.

Balakrishnan, A., Bleeker, F.E., Lamba, S., Rodolfo, M., Daniotti, M., Scarpa, A., van Tilborg, A.A., Leenstra, S., Zanon, C., and Bardelli, A. (2007). Novel somatic and germline mutations in cancer candidate genes in glioblastoma, melanoma, and pancreatic carcinoma. Cancer Res. *67*, 3545–3550.

Balgobind, B.V., Zwaan, C.M., Pieters, R., and Van den Heuvel-Eibrink, M.M. (2011). The heterogeneity of pediatric MLL-rearranged acute myeloid leukemia. Leukemia *25*, 1239–1248.

Barretina, J., Caponigro, G., Stransky, N., Venkatesan, K., Margolin, A.A., Kim, S., Wilson, C.J., Lehár, J., Kryukov, G.V., Sonkin, D., et al. (2012). The Cancer Cell Line Encyclopedia enables predictive modelling of anticancer drug sensitivity. Nature *483*, 603–607.

Baylin, S.B., and Ohm, J.E. (2006). Epigenetic gene silencing in cancer - a mechanism for early oncogenic pathway addiction? Nat. Rev. Cancer *6*, 107–116.

Baylin, S.B., and Jones, P.A. (2011). A decade of exploring the cancer epigenome - biological and translational implications. Nat. Rev. Cancer *11*, 726–734.

Bernt, K.M., Zhu, N., Sinha, A.U., Vempati, S., Faber, J., Krivtsov, A.V., Feng, Z., Punt, N., Daigle, A., Bullinger, L., et al. (2011). MLL-rearranged leukemia is dependent on aberrant H3K79 methylation by DOT1L. Cancer Cell *20*, 66–78.

Bhaskara, S., Knutson, S.K., Jiang, G., Chandrasekharan, M.B., Wilson, A.J., Zheng, S., Yenamandra, A., Locke, K., Yuan, J.L., Bonine-Summers, A.R., et al. (2010). Hdac3 is essential for the maintenance of chromatin structure and genome stability. Cancer Cell *18*, 436–447.

Bhutani, N., Burns, D.M., and Blau, H.M. (2011). DNA demethylation dynamics. Cell *146*, 866–872.

Bogdanović, O., and Veenstra, G.J. (2009). DNA methylation and methyl-CpG binding proteins: developmental requirements and function. Chromosoma *118*, 549–565.

Challen, G.A., Sun, D., Jeong, M., Luo, M., Jelinek, J., Berg, J.S., Bock, C., Vasanthakumar, A., Gu, H., Xi, Y., et al. (2012). Dnmt3a is essential for hematopoietic stem cell differentiation. Nat. Genet. *44*, 23–31.

Chase, A., and Cross, N.C. (2011). Aberrations of EZH2 in cancer. Clin. Cancer Res. *17*, 2613–2618.

Cimmino, L., Abdel-Wahab, O., Levine, R.L., and Aifantis, I. (2011). TET family proteins and their role in stem cell differentiation and transformation. Cell Stem Cell *9*, 193–204.

Clapier, C.R., and Cairns, B.R. (2009). The biology of chromatin remodeling complexes. Annu. Rev. Biochem. *78*, 273–304.

Conerly, M.L., Teves, S.S., Diolaiti, D., Ulrich, M., Eisenman, R.N., and Henikoff, S. (2010). Changes in H2A.Z occupancy and DNA methylation during B-cell lymphomagenesis. Genome Res. *20*, 1383–1390.

Daigle, S.R., Olhava, E.J., Therkelsen, C.A., Majer, C.R., Sneeringer, C.J., Song, J., Johnston, L.D., Scott, M.P., Smith, J.J., Xiao, Y., et al. (2011). Selective killing of mixed lineage leukemia cells by a potent small-molecule DOT1L inhibitor. Cancer Cell *20*, 53–65.

De Carvalho, D.D., You, J.S., and Jones, P.A. (2010). DNA methylation and cellular reprogramming. Trends Cell Biol. *20*, 609–617.

De Carvalho, D.D., Sharma, S., You, J.S., Su, S.F., Taberlay, P.C., Kelly, T.K., Yang, X., Liang, G., and Jones, P.A. (2012). DNA methylation screening identifies driver epigenetic events of cancer cell survival. Cancer Cell *21*, 655–667.

de Zwaan, S.E., and Haass, N.K. (2010). Genetics of basal cell carcinoma. Australas J Dermatol. *51*, 81–92, quiz 93–84.

Degner, J.F., Pai, A.A., Pique-Regi, R., Veyrieras, J.B., Gaffney, D.J., Pickrell, J.K., De Leon, S., Michelini, K., Lewellen, N., Crawford, G.E., et al. (2012). DNaseI sensitivity QTLs are a major determinant of human expression variation. Nature *482*, 390–394.

Delmore, J.E., Issa, G.C., Lemieux, M.E., Rahl, P.B., Shi, J., Jacobs, H.M., Kastritis, E., Gilpatrick, T., Paranal, R.M., Qi, J., et al. (2011). BET bromodomain inhibition as a therapeutic strategy to target c-Myc. Cell *146*, 904–917.

Drost, J., Mantovani, F., Tocco, F., Elkon, R., Comel, A., Holstege, H., Kerkhoven, R., Jonkers, J., Voorhoeve, P.M., Agami, R., and Del Sal, G. (2010). BRD7 is a candidate tumour suppressor gene required for p53 function. Nat. Cell Biol. *12*, 380–389.

Esteller, M. (2007). Cancer epigenomics: DNA methylomes and histone-modification maps. Nat. Rev. Genet. *8*, 286–298.

Fabbri, M., and Calin, G.A. (2010). Epigenetics and miRNAs in human cancer. Adv. Genet. *70*, 87–99.

Fabbri, M., Garzon, R., Cimmino, A., Liu, Z., Zanesi, N., Callegari, E., Liu, S., Alder, H., Costinean, S., Fernandez-Cymering, C., et al. (2007). MicroRNA-29 family reverts aberrant methylation in lung cancer by targeting DNA methyltransferases 3A and 3B. Proc. Natl. Acad. Sci. USA *104*, 15805–15810.

Figueroa, M.E., Abdel-Wahab, O., Lu, C., Ward, P.S., Patel, J., Shih, A., Li, Y., Bhagwat, N., Vasanthakumar, A., Fernandez, H.F., et al. (2010). Leukemic IDH1 and IDH2 mutations result in a hypermethylation phenotype, disrupt TET2 function, and impair hematopoietic differentiation. Cancer Cell *18*, 553–567.

Filippakopoulos, P., Qi, J., Picaud, S., Shen, Y., Smith, W.B., Fedorov, O., Morse, E.M., Keates, T., Hickman, T.T., Felletar, I., et al. (2010). Selective inhibition of BET bromodomains. Nature *468*, 1067–1073.

Friedman, J.M., Liang, G., Liu, C.C., Wolff, E.M., Tsai, Y.C., Ye, W., Zhou, X., and Jones, P.A. (2009). The putative tumor suppressor microRNA-101 modulates the cancer epigenome by repressing the polycomb group protein EZH2. Cancer Res. *69*, 2623–2629.

Füllgrabe, J., Kavanagh, E., and Joseph, B. (2011). Histone onco-modifications. Oncogene *30*, 3391–3403.

Gelsi-Boyer, V., Brecqueville, M., Devillier, R., Murati, A., Mozziconacci, M.J., and Birnbaum, D. (2012). Mutations in ASXL1 are associated with poor prognosis across the spectrum of malignant myeloid diseases. J. Hematol. Oncol. *5*, 12.

Greer, E.L., and Shi, Y. (2012). Histone methylation: a dynamic mark in health, disease and inheritance. Nat. Rev. Genet. *13*, 343–357.

Guan, B., Mao, T.L., Panuganti, P.K., Kuhn, E., Kurman, R.J., Maeda, D., Chen, E., Jeng, Y.M., Wang, T.L., and Shih, IeM. (2011). Mutation and loss of expression of ARID1A in uterine low-grade endometrioid carcinoma. Am. J. Surg. Pathol. *35*, 625–632.

Gui, Y., Guo, G., Huang, Y., Hu, X., Tang, A., Gao, S., Wu, R., Chen, C., Li, X., Zhou, L., et al. (2011). Frequent mutations of chromatin remodeling genes in transitional cell carcinoma of the bladder. Nat. Genet. *43*, 875–878.

Hanahan, D., and Weinberg, R.A. (2011). Hallmarks of cancer: the next generation. Cell *144*, 646–674.

Hargreaves, D.C., and Crabtree, G.R. (2011). ATP-dependent chromatin remodeling: genetics, genomics and mechanisms. Cell Res. *21*, 396–420.

Hatziapostolou, M., and Iliopoulos, D. (2011). Epigenetic aberrations during oncogenesis. Cell. Mol. Life Sci. *68*, 1681–1702.

Hawkins, R.D., Hon, G.C., Lee, L.K., Ngo, Q., Lister, R., Pelizzola, M., Edsall, L.E., Kuan, S., Luu, Y., Klugman, S., et al. (2010). Distinct epigenomic landscapes of pluripotent and lineage-committed human cells. Cell Stem Cell *6*, 479–491.

Hawkins, R.D., Hon, G.C., Yang, C., Antosiewicz-Bourget, J.E., Lee, L.K., Ngo, Q.M., Klugman, S., Ching, K.A., Edsall, L.E., Ye, Z., et al. (2011). Dynamic chromatin states in human ES cells reveal potential regulatory sequences and genes involved in pluripotency. Cell Res. *21*, 1393–1409.

Hinoue, T., Weisenberger, D.J., Lange, C.P., Shen, H., Byun, H.M., Van Den Berg, D., Malik, S., Pan, F., Noushmehr, H., van Dijk, C.M., et al. (2012). Genome-scale analysis of aberrant DNA methylation in colorectal cancer. Genome Res. *22*, 271–282.

Hitchins, M.P., Rapkins, R.W., Kwok, C.T., Srivastava, S., Wong, J.J., Khachigian, L.M., Polly, P., Goldblatt, J., and Ward, R.L. (2011). Dominantly inherited constitutional epigenetic silencing of MLH1 in a cancer-affected family is linked to a single nucleotide variant within the 5′UTR. Cancer Cell *20*, 200–213.

Ho, L., and Crabtree, G.R. (2010). Chromatin remodelling during development. Nature *463*, 474–484.

Hoischen, A., van Bon, B.W., Rodríguez-Santiago, B., Gilissen, C., Vissers, L.E., de Vries, P., Janssen, I., van Lier, B., Hastings, R., Smithson, S.F., et al. (2011). De novo nonsense mutations in ASXL1 cause Bohring-Opitz syndrome. Nat. Genet. *43*, 729–731.

Hon, G.C., Hawkins, R.D., and Ren, B. (2009). Predictive chromatin signatures in the mammalian genome. Hum. Mol. Genet. *18* (R2), R195–R201.

Iyer, N.G., Ozdag, H., and Caldas, C. (2004). p300/CBP and cancer. Oncogene *23*, 4225–4231.

Jagani, Z., Mora-Blanco, E.L., Sansam, C.G., McKenna, E.S., Wilson, B., Chen, D., Klekota, J., Tamayo, P., Nguyen, P.T., Tolstorukov, M., et al. (2010). Loss of the tumor suppressor Snf5 leads to aberrant activation of the Hedgehog-Gli pathway. Nat. Med. *16*, 1429–1433.

Jiang, L., Li, J., and Song, L. (2009). Bmi-1, stem cells and cancer. Acta Biochim. Biophys. Sin. (Shanghai) *41*, 527–534.

Jones, P.A., and Liang, G. (2009). Rethinking how DNA methylation patterns are maintained. Nat. Rev. Genet. *10*, 805–811.

Jones, S., Wang, T.L., Shih, IeM., Mao, T.L., Nakayama, K., Roden, R., Glas, R., Slamon, D., Diaz, L.A., Jr., Vogelstein, B., et al. (2010). Frequent mutations of chromatin remodeling gene ARID1A in ovarian clear cell carcinoma. Science *330*, 228–231.

Juergens, R.A., Wrangle, J., Vendetti, F.P., Murphy, S.C., Zhao, M., Coleman, B., Sebree, R., Rodgers, K., Hooker, C.M., Franco, N., et al. (2011). Combination epigenetic therapy has efficacy in patients with refractory advanced non-small cell lung cancer. Cancer Discov. *1*, 598–607.

Kalari, S., and Pfeifer, G.P. (2010). Identification of driver and passenger DNA methylation in cancer by epigenomic analysis. Adv. Genet. *70*, 277–308.

Kanai, Y., Ushijima, S., Nakanishi, Y., Sakamoto, M., and Hirohashi, S. (2003). Mutation of the DNA methyltransferase (DNMT) 1 gene in human colorectal cancers. Cancer Lett. *192*, 75–82.

Kasinski, A.L., and Slack, F.J. (2011). Epigenetics and genetics. MicroRNAs en route to the clinic: progress in validating and targeting microRNAs for cancer therapy. Nat. Rev. Cancer *11*, 849–864.

Kelly, T.K., De Carvalho, D.D., and Jones, P.A. (2010). Epigenetic modifications as therapeutic targets. Nat. Biotechnol. *28*, 1069–1078.

Kim, M.S., Chung, N.G., Kang, M.R., Yoo, N.J., and Lee, S.H. (2011). Genetic and expressional alterations of CHD genes in gastric and colorectal cancers. Histopathology *58*, 660–668.

Kinney, S.R., and Pradhan, S. (2011). Regulation of expression and activity of DNA (cytosine-5) methyltransferases in mammalian cells. Prog. Mol. Biol. Transl. Sci. *101*, 311–333.

Ko, M., Huang, Y., Jankowska, A.M., Pape, U.J., Tahiliani, M., Bandukwala, H.S., An, J., Lamperti, E.D., Koh, K.P., Ganetzky, R., et al. (2010). Impaired hydroxylation of 5-methylcytosine in myeloid cancers with mutant TET2. Nature *468*, 839–843.

Krivtsov, A.V., and Armstrong, S.A. (2007). MLL translocations, histone modifications and leukaemia stem-cell development. Nat. Rev. Cancer *7*, 823–833.

Lao, V.V., Darwanto, A., and Sowers, L.C. (2010). Impact of base analogues within a CpG dinucleotide on the binding of DNA by the methyl-binding domain of MeCP2 and methylation by DNMT1. Biochemistry *49*, 10228–10236.

Lee, Y.H., and Stallcup, M.R. (2009). Minireview: protein arginine methylation of nonhistone proteins in transcriptional regulation. Mol. Endocrinol. *23*, 425–433.

Ley, T.J., Ding, L., Walter, M.J., McLellan, M.D., Lamprecht, T., Larson, D.E., Kandoth, C., Payton, J.E., Baty, J., Welch, J., et al. (2010). DNMT3A mutations in acute myeloid leukemia. N. Engl. J. Med. *363*, 2424–2433.

Li, M., Zhao, H., Zhang, X., Wood, L.D., Anders, R.A., Choti, M.A., Pawlik, T.M., Daniel, H.D., Kannangai, R., Offerhaus, G.J., et al. (2011). Inactivating mutations of the chromatin remodeling gene ARID2 in hepatocellular carcinoma. Nat. Genet. *43*, 828–829.

Lin, H., Wong, R.P., Martinka, M., and Li, G. (2009). Loss of SNF5 expression correlates with poor patient survival in melanoma. Clin. Cancer Res. *15*, 6404–6411.

Lu, C., Ward, P.S., Kapoor, G.S., Rohle, D., Turcan, S., Abdel-Wahab, O., Edwards, C.R., Khanin, R., Figueroa, M.E., Melnick, A., et al. (2012). IDH mutation impairs histone demethylation and results in a block to cell differentiation. Nature *483*, 474–478.

Luger, K., Mäder, A.W., Richmond, R.K., Sargent, D.F., and Richmond, T.J. (1997). Crystal structure of the nucleosome core particle at 2.8 A resolution. Nature *389*, 251–260.

Lukacs, R.U., Memarzadeh, S., Wu, H., and Witte, O.N. (2010). Bmi-1 is a crucial regulator of prostate stem cell self-renewal and malignant transformation. Cell Stem Cell *7*, 682–693.

Marks, P.A., Rifkind, R.A., Richon, V.M., Breslow, R., Miller, T., and Kelly, W.K. (2001). Histone deacetylases and cancer: causes and therapies. Nat. Rev. Cancer *1*, 194–202.

Matei, D.E., and Nephew, K.P. (2010). Epigenetic therapies for chemoresensitization of epithelial ovarian cancer. Gynecol. Oncol. *116*, 195–201.

Mattera, L., Escaffit, F., Pillaire, M.J., Selves, J., Tyteca, S., Hoffmann, J.S., Gourraud, P.A., Chevillard-Briet, M., Cazaux, C., and Trouche, D. (2009). The p400/Tip60 ratio is critical for colorectal cancer cell proliferation through DNA damage response pathways. Oncogene *28*, 1506–1517.

Meissner, A., Mikkelsen, T.S., Gu, H., Wernig, M., Hanna, J., Sivachenko, A., Zhang, X., Bernstein, B.E., Nusbaum, C., Jaffe, D.B., et al. (2008). Genome-scale DNA methylation maps of pluripotent and differentiated cells. Nature *454*, 766–770.

Mills, A.A. (2010). Throwing the cancer switch: reciprocal roles of polycomb and trithorax proteins. Nat. Rev. Cancer *10*, 669–682.

Miremadi, A., Oestergaard, M.Z., Pharoah, P.D., and Caldas, C. (2007). Cancer genetics of epigenetic genes. Hum. Mol. Genet. *16* (Spec No 1), R28–R49.

Morin, R.D., Mendez-Lago, M., Mungall, A.J., Goya, R., Mungall, K.L., Corbett, R.D., Johnson, N.A., Severson, T.M., Chiu, R., Field, M., et al. (2011). Frequent mutation of histone-modifying genes in non-Hodgkin lymphoma. Nature *476*, 298–303.

Mosammaparast, N., and Shi, Y. (2010). Reversal of histone methylation: biochemical and molecular mechanisms of histone demethylases. Annu. Rev. Biochem. *79*, 155–179.

Nakayama, T., and Yamashita, M. (2009). Critical role of the Polycomb and Trithorax complexes in the maintenance of CD4 T cell memory. Semin. Immunol. *21*, 78–83.

Network, C.G.A.R.; Cancer Genome Atlas Research Network. (2011). Integrated genomic analyses of ovarian carcinoma. Nature *474*, 609–615.

Nica, A.C., Montgomery, S.B., Dimas, A.S., Stranger, B.E., Beazley, C., Barroso, I., and Dermitzakis, E.T. (2010). Candidate causal regulatory effects by integration of expression QTLs with complex trait genetic associations. PLoS Genet. *6*, e1000895.

Nicodeme, E., Jeffrey, K.L., Schaefer, U., Beinke, S., Dewell, S., Chung, C.W., Chandwani, R., Marazzi, I., Wilson, P., Coste, H., et al. (2010). Suppression of inflammation by a synthetic histone mimic. Nature *468*, 1119–1123.

Nicolae, D.L., Gamazon, E., Zhang, W., Duan, S., Dolan, M.E., and Cox, N.J. (2010). Trait-associated SNPs are more likely to be eQTLs: annotation to enhance discovery from GWAS. PLoS Genet. *6*, e1000888.

Noushmehr, H., Weisenberger, D.J., Diefes, K., Phillips, H.S., Pujara, K., Berman, B.P., Pan, F., Pelloski, C.E., Sulman, E.P., Bhat, K.P., et al.; Cancer Genome Atlas Research Network. (2010). Identification of a CpG island methylator phenotype that defines a distinct subgroup of glioma. Cancer Cell *17*, 510–522.

Ocker, M., and Schneider-Stock, R. (2007). Histone deacetylase inhibitors: signalling towards p21cip1/waf1. Int. J. Biochem. Cell Biol. *39*, 1367–1374.

Ooi, S.K., and Bestor, T.H. (2008). The colorful history of active DNA demethylation. Cell *133*, 1145–1148.

Reisman, D., Glaros, S., and Thompson, E.A. (2009). The SWI/SNF complex and cancer. Oncogene *28*, 1653–1668.

Rideout, W.M., 3rd, Coetzee, G.A., Olumi, A.F., and Jones, P.A. (1990). 5-Methylcytosine as an endogenous mutagen in the human LDL receptor and p53 genes. Science *249*, 1288–1290.

Roberts, C.W., and Orkin, S.H. (2004). The SWI/SNF complex—chromatin and cancer. Nat. Rev. Cancer *4*, 133–142.

Rodríguez-Paredes, M., and Esteller, M. (2011). Cancer epigenetics reaches mainstream oncology. Nat. Med. *17*, 330–339.

Ropero, S., Fraga, M.F., Ballestar, E., Hamelin, R., Yamamoto, H., Boix-Chornet, M., Caballero, R., Alaminos, M., Setien, F., Paz, M.F., et al. (2006). A truncating mutation of HDAC2 in human cancers confers resistance to histone deacetylase inhibition. Nat. Genet. *38*, 566–569.

Rotili, D., and Mai, A. (2011). Targeting histone demethylases: a new avenue for the fight against cancer. Genes Cancer *2*, 663–679.

Ryan, B.M., Robles, A.I., and Harris, C.C. (2010). Genetic variation in microRNA networks: the implications for cancer research. Nat. Rev. Cancer *10*, 389–402.

Saito, Y., Liang, G., Egger, G., Friedman, J.M., Chuang, J.C., Coetzee, G.A., and Jones, P.A. (2006). Specific activation of microRNA-127 with downregulation of the proto-oncogene BCL6 by chromatin-modifying drugs in human cancer cells. Cancer Cell *9*, 435–443.

Sandoval, J., and Esteller, M. (2012). Cancer epigenomics: beyond genomics. Curr. Opin. Genet. Dev. *22*, 50–55.

Sansom, O.J., Maddison, K., and Clarke, A.R. (2007). Mechanisms of disease: methyl-binding domain proteins as potential therapeutic targets in cancer. Nat. Clin. Pract. Oncol. *4*, 305–315.

Santen, G.W., Aten, E., Sun, Y., Almomani, R., Gilissen, C., Nielsen, M., Kant, S.G., Snoeck, I.N., Peeters, E.A., Hilhorst-Hofstee, Y., et al. (2012). Mutations in SWI/SNF chromatin remodeling complex gene ARID1B cause Coffin-Siris syndrome. Nat. Genet. *44*, 379–380.

Sauvageau, M., and Sauvageau, G. (2010). Polycomb group proteins: multi-faceted regulators of somatic stem cells and cancer. Cell Stem Cell *7*, 299–313.

Schepers, A., and Clevers, H. (2012). Wnt signaling, stem cells, and cancer of the gastrointestinal tract. Cold Spring Harb. Perspect. Biol. *4*, a007989.

Schuettengruber, B., Martinez, A.-M., Iovino, N., and Cavalli, G. (2011). Trithorax group proteins: switching genes on and keeping them active. Nat. Rev. Mol. Cell Biol. *12*, 799–814.

Segal, E., and Widom, J. (2009). What controls nucleosome positions? Trends Genet. *25*, 335–343.

Shankar, S., and Srivastava, R.K. (2008). Histone deacetylase inhibitors: mechanisms and clinical significance in cancer: HDAC inhibitor-induced apoptosis. Adv. Exp. Med. Biol. *615*, 261–298.

Sharma, S., Kelly, T.K., and Jones, P.A. (2010). Epigenetics in cancer. Carcinogenesis *31*, 27–36.

Shen, H., Wang, L., Spitz, M.R., Hong, W.K., Mao, L., and Wei, Q. (2002). A novel polymorphism in human cytosine DNA-methyltransferase-3B promoter is associated with an increased risk of lung cancer. Cancer Res. *62*, 4992–4995.

Slany, R.K. (2009). The molecular biology of mixed lineage leukemia. Haematologica *94*, 984–993.

Smith, K.T., and Workman, J.L. (2009). Histone deacetylase inhibitors: anticancer compounds. Int. J. Biochem. Cell Biol. *41*, 21–25.

Song, J., Teplova, M., Ishibe-Murakami, S., and Patel, D.J. (2012). Structure-based mechanistic insights into DNMT1-mediated maintenance DNA methylation. Science *335*, 709–712.

Suganuma, T., and Workman, J.L. (2011). Signals and combinatorial functions of histone modifications. Annu. Rev. Biochem. *80*, 473–499.

Sun, A., Tawfik, O., Gayed, B., Thrasher, J.B., Hoestje, S., Li, C., and Li, B. (2007). Aberrant expression of SWI/SNF catalytic subunits BRG1/BRM is associated with tumor development and increased invasiveness in prostate cancers. Prostate *67*, 203–213.

Tan, A.Y., and Manley, J.L. (2009). The TET family of proteins: functions and roles in disease. J. Mol. Cell Biol. *1*, 82–92.

Teng, L., Firpi, H.A., and Tan, K. (2011). Enhancers in embryonic stem cells are enriched for transposable elements and genetic variations associated with cancers. Nucleic Acids Res. *39*, 7371–7379.

Trowbridge, J.J., and Orkin, S.H. (2012). Dnmt3a silences hematopoietic stem cell self-renewal. Nat. Genet. *44*, 13–14.

Tsang, D.P., and Cheng, A.S. (2011). Epigenetic regulation of signaling pathways in cancer: role of the histone methyltransferase EZH2. J. Gastroenterol. Hepatol. *26*, 19–27.

Tsurusaki, Y., Okamoto, N., Ohashi, H., Kosho, T., Imai, Y., Hibi-Ko, Y., Kaname, T., Naritomi, K., Kawame, H., Wakui, K., et al. (2012). Mutations affecting components of the SWI/SNF complex cause Coffin-Siris syndrome. Nat. Genet. *44*, 376–378.

Turcan, S., Rohle, D., Goenka, A., Walsh, L.A., Fang, F., Yilmaz, E., Campos, C., Fabius, A.W., Lu, C., Ward, P.S., et al. (2012). IDH1 mutation is sufficient to establish the glioma hypermethylator phenotype. Nature *483*, 479–483.

Tycko, B. (2010). Allele-specific DNA methylation: beyond imprinting. Hum. Mol. Genet. *19* (R2), R210–R220.

Valouev, A., Johnson, S.M., Boyd, S.D., Smith, C.L., Fire, A.Z., and Sidow, A. (2011). Determinants of nucleosome organization in primary human cells. Nature *474*, 516–520.

Varambally, S., Cao, Q., Mani, R.S., Shankar, S., Wang, X., Ateeq, B., Laxman, B., Cao, X., Jing, X., Ramnarayanan, K., et al. (2008). Genomic loss of microRNA-101 leads to overexpression of histone methyltransferase EZH2 in cancer. Science *322*, 1695–1699.

Varela, I., Tarpey, P., Raine, K., Huang, D., Ong, C.K., Stephens, P., Davies, H., Jones, D., Lin, M.L., Teague, J., et al. (2011). Exome sequencing identifies frequent mutation of the SWI/SNF complex gene PBRM1 in renal carcinoma. Nature *469*, 539–542.

Varier, R.A., and Timmers, H.T. (2011). Histone lysine methylation and demethylation pathways in cancer. Biochim. Biophys. Acta *1815*, 75–89.

Wang, G.G., Allis, C.D., and Chi, P. (2007). Chromatin remodeling and cancer, Part II: ATP-dependent chromatin remodeling. Trends Mol. Med. *13*, 373–380.

Wang, J., Chen, H., Fu, S., Xu, Z.M., Sun, K.L., and Fu, W.N. (2011a). The involvement of CHD5 hypermethylation in laryngeal squamous cell carcinoma. Oral Oncol. *47*, 601–608.

Wang, L., Gural, A., Sun, X.J., Zhao, X., Perna, F., Huang, G., Hatlen, M.A., Vu, L., Liu, F., Xu, H., et al. (2011b). The leukemogenicity of AML1-ETO is dependent on site-specific lysine acetylation. Science *333*, 765–769.

Wessels, K., Bohnhorst, B., Luhmer, I., Morlot, S., Bohring, A., Jonasson, J., Epplen, J.T., Gadzicki, D., Glaser, S., Göhring, G., et al. (2010). Novel CHD7 mutations contributing to the mutation spectrum in patients with CHARGE syndrome. Eur. J. Med. Genet. *53*, 280–285.

Wiegand, K.C., Shah, S.P., Al-Agha, O.M., Zhao, Y., Tse, K., Zeng, T., Senz, J., McConechy, M.K., Anglesio, M.S., Kalloger, S.E., et al. (2010). ARID1A mutations in endometriosis-associated ovarian carcinomas. N. Engl. J. Med. *363*, 1532–1543.

Wijmenga, C., Hansen, R.S., Gimelli, G., Björck, E.J., Davies, E.G., Valentine, D., Belohradsky, B.H., van Dongen, J.J., Smeets, D.F., van den Heuvel, L.P., et al. (2000). Genetic variation in ICF syndrome: evidence for genetic heterogeneity. Hum. Mutat. *16*, 509–517.

Wilson, B.G., and Roberts, C.W. (2011). SWI/SNF nucleosome remodellers and cancer. Nat. Rev. Cancer *11*, 481–492.

Wu, S.C., and Zhang, Y. (2010). Active DNA demethylation: many roads lead to Rome. Nat. Rev. Mol. Cell Biol. *11*, 607–620.

Wu, Y., Strawn, E., Basir, Z., Halverson, G., and Guo, S.W. (2007). Aberrant expression of deoxyribonucleic acid methyltransferases DNMT1, DNMT3A, and DNMT3B in women with endometriosis. Fertil. Steril. *87*, 24–32.

Yamashita, Y., Yuan, J., Suetake, I., Suzuki, H., Ishikawa, Y., Choi, Y.L., Ueno, T., Soda, M., Hamada, T., Haruta, H., et al. (2010). Array-based genomic resequencing of human leukemia. Oncogene *29*, 3723–3731.

Yan, X.J., Xu, J., Gu, Z.H., Pan, C.M., Lu, G., Shen, Y., Shi, J.Y., Zhu, Y.M., Tang, L., Zhang, X.W., et al. (2011). Exome sequencing identifies somatic mutations of DNA methyltransferase gene DNMT3A in acute monocytic leukemia. Nat. Genet. *43*, 309–315.

Yang, G.F., He, W.P., Cai, M.Y., He, L.R., Luo, J.H., Deng, H.X., Guan, X.Y., Zeng, M.S., Zeng, Y.X., and Xie, D. (2010). Intensive expression of Bmi-1 is a new independent predictor of poor outcome in patients with ovarian carcinoma. BMC Cancer *10*, 133.

Yang, X.J. (2004). The diverse superfamily of lysine acetyltransferases and their roles in leukemia and other diseases. Nucleic Acids Res. *32*, 959–976.

Young, R.A. (2011). Control of the embryonic stem cell state. Cell *144*, 940–954.

Zhang, X., Zhang, Y., Yang, Y., Niu, M., Sun, S., Ji, H., Ma, Y., Yao, G., Jiang, Y., Shan, M., et al. (2011). Frequent low expression of chromatin remodeling gene ARID1A in breast cancer and its clinical significance. Cancer Epidemiol. *36*, 288–293.

Zuber, J., Shi, J., Wang, E., Rappaport, A.R., Herrmann, H., Sison, E.A., Magoon, D., Qi, J., Blatt, K., Wunderlich, M., et al. (2011). RNAi screen identifies Brd4 as a therapeutic target in acute myeloid leukaemia. Nature *478*, 524–528.

Cancer Cell
Article

VEGF Inhibits Tumor Cell Invasion and Mesenchymal Transition through a MET/VEGFR2 Complex

Kan V. Lu,[1,3] Jeffrey P. Chang,[1,3] Christine A. Parachoniak,[5,6] Melissa M. Pandika,[1,3] Manish K. Aghi,[1,3,4] David Meyronet,[1,3] Nadezda Isachenko,[1,3] Shaun D. Fouse,[1,3] Joanna J. Phillips,[1,3,4] David A. Cheresh,[7] Morag Park,[5,6] and Gabriele Bergers[1,2,3,4,*]

[1]Department of Neurological Surgery
[2]Department of Anatomy
[3]Brain Tumor Research Center
[4]UCSF Comprehensive Cancer Center
University of California, Helen Diller Family Cancer Research Center, San Francisco, CA 94143, USA
[5]Department of Biochemistry
[6]Goodman Cancer Research Centre
McGill University, Montreal, QC H3G 1Y6, Canada
[7]Department of Pathology and Moore's UCSD Cancer Center, University of California, San Diego, CA 92093, USA
*Correspondence: gabriele.bergers@ucsf.edu
http://dx.doi.org/10.1016/j.ccr.2012.05.037

SUMMARY

Inhibition of VEGF signaling leads to a proinvasive phenotype in mouse models of glioblastoma multiforme (GBM) and in a subset of GBM patients treated with bevacizumab. Here, we demonstrate that vascular endothelial growth factor (VEGF) directly and negatively regulates tumor cell invasion through enhanced recruitment of the protein tyrosine phosphatase 1B (PTP1B) to a MET/VEGFR2 heterocomplex, thereby suppressing HGF-dependent MET phosphorylation and tumor cell migration. Consequently, VEGF blockade restores and increases MET activity in GBM cells in a hypoxia-independent manner, while inducing a program reminiscent of epithelial-to-mesenchymal transition highlighted by a T-cadherin to N-cadherin switch and enhanced mesenchymal features. Inhibition of MET in GBM mouse models blocks mesenchymal transition and invasion provoked by VEGF ablation, resulting in substantial survival benefit.

INTRODUCTION

Glioblastoma multiforme (GBM) are characterized by rapid and invasive growth throughout the brain. Despite standard and targeted therapies median overall survival of GBM patients remains just over one year (Furnari et al., 2007). GBM are also one of the most vascularized and edematous tumors as they express high levels of VEGF (Ferrara et al., 2003; Sundberg et al., 2001; van Bruggen et al., 1999). Encouragingly, bevacizumab, a humanized monoclonal antibody against VEGF, has demonstrated therapeutic benefit in many GBM patients when used alone or in combination with irinotecan (Friedman et al., 2009; Vredenburgh et al., 2007). This led to the accelerated approval of bevacizumab by the U.S. Food and Drug Administration in 2009 for use as a single agent in recurrent GBM, and its use in the frontline setting for newly diagnosed GBM is currently being evaluated.

Despite initial responsiveness, however, the beneficial effects of bevacizumab are transient, and GBM inevitably progress during anti-VEGF treatment by adapting and utilizing alternative pathways to sustain tumor growth, all while VEGF signaling remains inhibited (Bergers and Hanahan, 2008).

Significance

Bevacizumab has been approved for the treatment of GBM patients with recurrent disease and is currently being evaluated for frontline therapy. Most patients initially experience beneficial effects from the treatment, but all invariably confront tumor regrowth. About 20%–30% of recurrent tumors elicit an infiltrating and more diffuse growth pattern that renders surgical resection unfeasible and imparts detrimental effects. The ability to identify GBM patients who will benefit from antiangiogenic treatment without developing more invasive tumors is therefore pivotal. Here, we provide the molecular mechanisms by which VEGF ablation causes enhanced invasion. These findings support combined treatment strategies targeting both VEGF and MET in GBM patients to overcome proinvasive resistance and prolong survival.

Clinical evidence suggests that GBM relapse during anti-VEGF therapy can present with at least two differing radiographic patterns representing distinct mechanisms of evasion. Although most GBM patients develop characteristic local recurrences that regain the ability to induce neovascularization as observed by increased magnetic resonance imaging (MRI) contrast enhancement, up to 30% of GBM patients demonstrate a more extensive, infiltrative, and distant disease that lacks angiogenic induction and is noncontrast enhancing but is instead detectable by fluid-attenuated inversion recovery (FLAIR) MRI (de Groot et al., 2010; Iwamoto et al., 2009; Rose and Aghi, 2010). Whereas the incidence of invasion has been a subject of discussion because of the current lack of a standardized definition for radiographic relapse (Chamberlain, 2011; Wick et al., 2011), the frequency of invasive nonenhancing tumors nevertheless appears to be higher than would be expected in patients who do not receive bevacizumab (Iwamoto et al., 2009). This proinvasive recurrence encumbers surgical resection of recurrent GBM and challenges further therapeutic options for patients.

Similar to other studies using mouse models of GBM (de Groot et al., 2010; Kunkel et al., 2001; Rubenstein et al., 2000), we have observed that a more perivascular invasive phenotype, in which tumor cells move predominantly along blood vessels deep into the brain parenchyma, was induced when murine GBM were unable to initiate angiogenesis, a phenomenon that predicted the invasive relapse pattern seen in bevacizumab-treated human GBM (Blouw et al., 2003; Du et al., 2008a; Pàez-Ribes et al., 2009). The enhanced invasiveness was a result of impairing tumor angiogenesis either through genetic ablation of key angiogenic factors that drive VEGF-dependent neovascularization (HIF-1α, VEGF, MMP-9, MMP-2) (Blouw et al., 2003; Du et al., 2008a, 2008b) or by pharmacologic targeting of VEGF signaling (Pàez-Ribes et al., 2009). We further revealed an unexpected link between HGF and VEGF, in which VEGF reduced the chemotactic activity of GBM cells toward HGF in vitro (Du et al., 2008a). The HGF receptor MET, a receptor tyrosine kinase that is frequently deregulated in many cancers and promotes proliferation, scattering, invasion, survival, and angiogenesis (Birchmeier et al., 2003; Rong et al., 1992; Trusolino et al., 2010; Wang et al., 2001) is correlated with increased tumor invasion and poorer survival in GBM (Abounader and Laterra, 2005; Koochekpour et al., 1997; Lamszus et al., 1998).

Given that VEGF inhibition was a common denominator among the various genetic knockout models and pharmacologic treatments described above, we investigated whether VEGF itself might act as a regulatory switch for GBM invasion through regulating MET.

RESULTS

Intratumoral VEGF Levels Inversely Correlate with MET Phosphorylation and Invasion of GBM Tumor Cells

To test our hypothesis that VEGF regulates the HGF/MET axis in tumor cells, we used orthotopically implanted SV40 large T-antigen and H-ras-transformed mouse astrocytoma cell lines differing only in their VEGF expression levels: VEGFKO GBM, which are genetically ablated of VEGF expression; WT-GBM, which produce endogenous levels of VEGF; and VEGFKO-VEGF GBM, which are VEGFKO GBM cells expressing a high level of exogenous VEGF (Figures 1A and 1B). VEGFKO tumors were nonangiogenic and grew as extensively diffuse and invasive tumor cell clusters along normal blood vessels deep into the brain parenchyma (Figure 1A) (Blouw et al., 2003). In contrast, WT-GBM cells generated angiogenic tumors with locally infiltrative tumor cells characteristic of human GBM, and VEGFKO-VEGF cells produced highly vascular, tightly packed tumors with smooth borders (Figure 1A). We then assessed whether changes in MET expression and activation could account for differences in invasive capacity. Immunohistochemical staining and western blot analysis of total MET in orthotopic murine GBM xenografts and cell lines showed abundant and similar MET expression regardless of VEGF expression levels (Figure 1C; Figures S1A–S1C available online). In contrast, phospho-MET (P-MET) staining revealed strong positivity in invading clusters of VEGFKO GBM, marginal staining in a few invading tumor cells in WT-GBM, and no staining throughout VEGFKO-VEGF GBM (Figure 1D). These observations were recapitulated in another murine GBM model (NSCG), in which neural stem cells were isolated from the subventricular zone of Ink4a/Arf deficient mice and transduced with the constitutively active mutant receptor EGFRvIII (Phillips et al., 2012) (Figures S1D–S1F).

Importantly, when we assessed P-MET in GBM specimens from patients who had relapsed during bevacizumab therapy, we observed stronger and more abundant positivity in tumors posttreatment compared to matched pretreated samples in 7 out of 10 patients (Figures 1E and 1F). These data indicate that loss of VEGF induces MET activation in invading tumor cells without necessarily increasing MET expression and inferred a mechanism distinct from that of intratumoral hypoxia induced by anti-VEGF therapy causing transcription of hypoxia-regulated proinvasive genes, such as *Met* to perpetuate invasion.

VEGF Directly and Negatively Regulates GBM Invasion by Inhibiting MET Activation

We then asked whether VEGF could signal directly on tumor cells to affect MET activity and invasiveness. We first examined whether VEGF perturbed the HGF/MET signaling pathway. To test this, VEGFKO cells were stimulated with HGF alone or in combination with VEGF. HGF treatment resulted in robust phosphorylation of MET and of FAK, which were decreased by VEGF in a dose-dependent manner (Figure 2A). Similarly, MET and FAK activation induced by HGF were reduced when VEGFKO cells were incubated with VEGFKO-VEGF conditioned medium (CM) but not VEGFKO CM (Figure 2A). Total MET expression was unaltered by VEGF. In contrast, stimulation with increasing concentrations of HGF in the presence of high VEGF levels dose-dependently restored P-MET and P-FAK, supporting an antagonistic and dynamic interplay between VEGF and HGF on MET signaling (Figure 2A). VEGF also inhibited P-MET and P-FAK in human GBM43 cells derived from a GBM patient (Sarkaria et al., 2006) (Figure 2B). The antagonistic interaction between VEGF and HGF/MET appeared specific, as neither EGF nor PDGF suppress P-MET or P-FAK induced by HGF (Figure S2A). Treatment of GBM43 cells with the function-blocking anti-VEGF monoclonal antibody B20 (Liang et al., 2006) abrogated P-MET suppression by VEGF (Figure 2C), further supporting a specific role for VEGF in regulating MET activation.

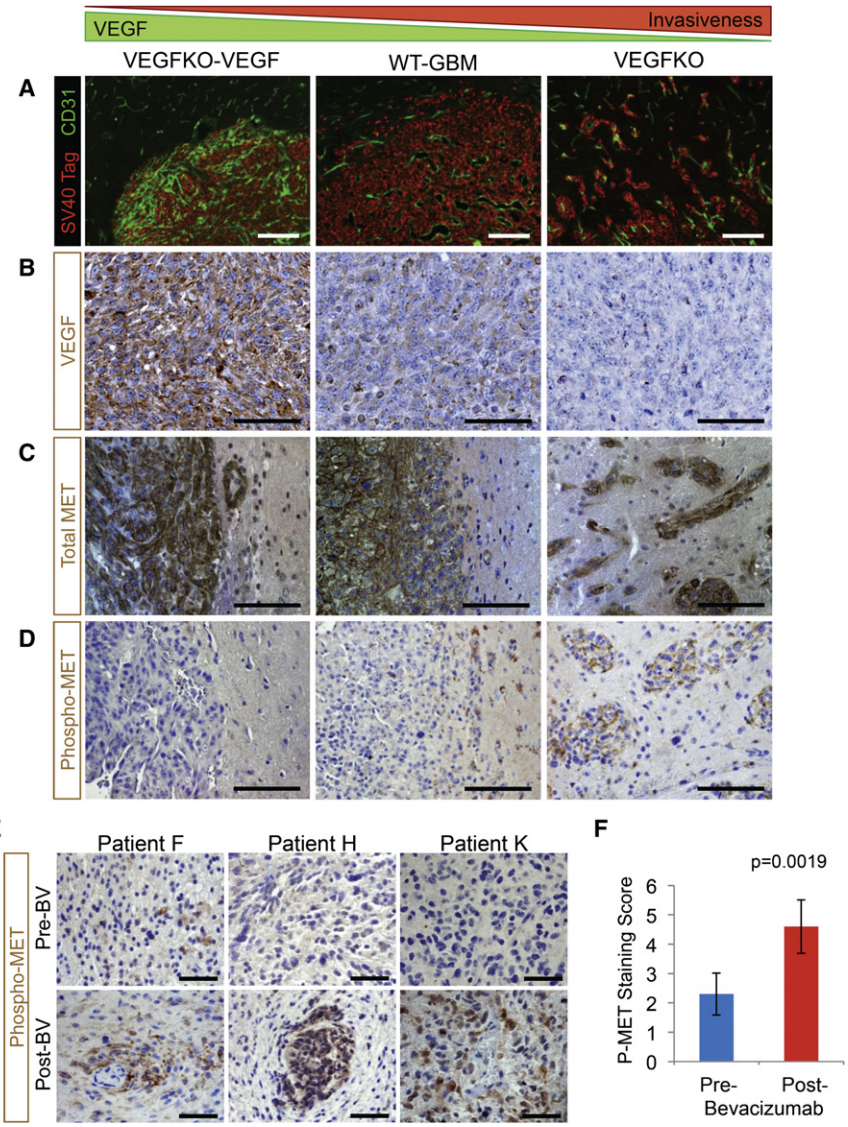

Figure 1. VEGF Expression Is Inversely Correlated with Perivascular Invasion and MET Phosphorylation

(A) Tumors from intracranial implantation of indicated murine GBM cells were fluorescently stained for SV40 large T-antigen and CD31 to detect tumor cells and vasculature, respectively. Scale bars, 200 μm.

(B–D) IHC staining for VEGF (B), total MET (C), and phospho-MET (D) in orthotopic murine GBM. Scale bars, 100 μm.

(E) IHC staining for phospho-MET in paired human GBM surgical specimens before and after bevacizumab (BV) treatment. Scale bars, 50 μm.

(F) P-MET staining score (mean ± SEM) of ten human GBM before and after bevacizumab treatment based on a composite score as described in the Supplemental Experimental Procedures.

See also Figure S1.

We next determined whether VEGF affected HGF-dependent GBM cell invasion by performing a wound-healing assay. HGF-treated VEGFKO cells closed nearly the entire wound area within 16 hr, whereas addition of exogenous VEGF significantly diminished their migration (Figure 2D). Similarly, VEGFKO-VEGF cells exhibited reduced migratory capacity, and application of VEGFKO-VEGF CM onto VEGFKO cells impeded cell migration (Figure 2D). Overexpression of VEGF or incubation with VEGFKO-VEGF CM also reduced P-MET in NSCG and GBM43 cells and hindered their migration (Figures S2B–S2C; Figure 2E). These studies demonstrate that VEGF directly impedes HGF-dependent MET signaling and migration in murine and human GBM cells.

VEGF Requires VEGFR2 to Inhibit MET Activation and Cell Motility

How does VEGF block HGF/MET signaling? One might envision that VEGF directly competes with HGF for MET binding or that VEGF antagonizes MET activity by signaling through VEGF receptors on tumor cells (Figure 3A). Congruent with reports that a variety of tumor cells express VEGF receptors (Lesslie et al., 2006; Spannuth et al., 2009; Wang et al., 2010), we found that murine and human GBM cells express VEGFR1 and VEGFR2 (Figures 3B, S3A and, S3B) and that many tumor cell lines representing other cancer types for which bevacizumab has been approved, also express VEGF receptors at various levels (Figure S3C).

Using neutralizing antibodies against VEGFR1 (MF1) and VEGFR2 (DC101), we found that VEGF-dependent suppression of HGF-mediated P-MET and P-FAK in GBM cells was abrogated by addition of DC101 but not MF1 (Figure 3C). Congruently, although VEGFKO cells treated with VEGFKO-VEGF CM were significantly less motile, DC101 treatment restored their ability to migrate, whereas MF1 did not (Figure 3D). We then stably silenced VEGFR2 in VEGFKO cells by shRNA (Figure 3E). Whereas scrambled shRNA had no effect on the negative regulation of P-MET by VEGF, shVEGFR2 resulted in sustained P-MET in the presence of VEGF (Figure 3F). Finally, addition of VEGF to HEK293T fibroblasts, which lack VEGFR2 expression, failed to suppress HGF-stimulated P-MET or P-FAK (Figures 3G and 3H), supporting the need for VEGFR2 and ruling out direct competition between HGF and VEGF for MET.

We then asked whether the VEGF coreceptor neuropilin-1 (NRP-1) is involved in mediating VEGF inhibition of P-MET. NRP-1 enhances signaling of the $VEGF_{165}$ isoform on VEGFR2 but is unable to bind the $VEGF_{121}$ isoform (Soker et al., 1998). VEGFKO cells stimulated with $VEGF_{121}$ were still able to diminish HGF-stimulated P-MET (Figure 3I), and NRP-1 did not coprecipitate with VEGFR2/MET (data not shown), indicating that the inhibitory effect of VEGF is independent of NRP-1.

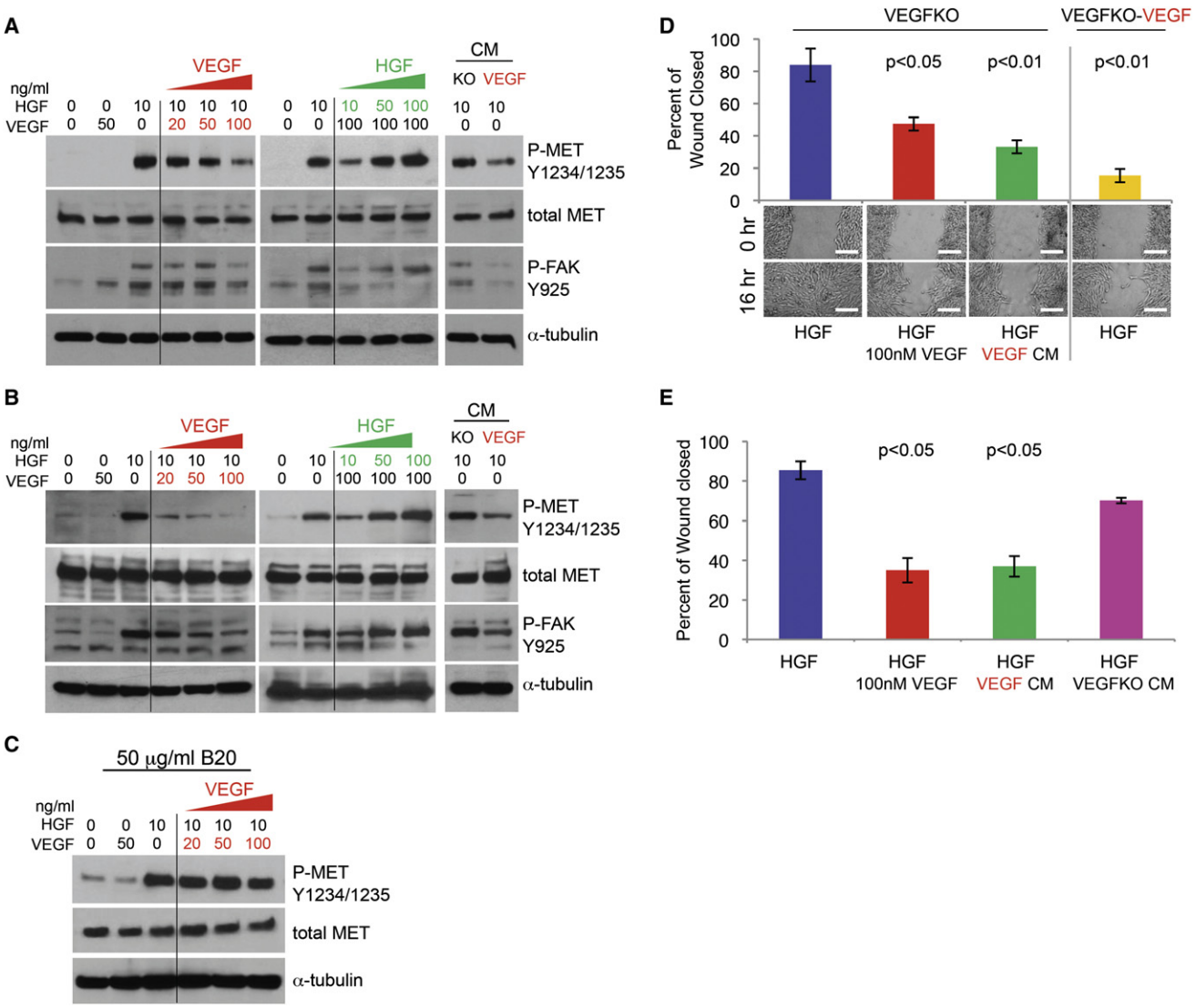

Figure 2. VEGF Suppresses HGF-Stimulated MET Phosphorylation and Cell Motility

(A) Western blot analysis of cell lysates from murine VEGFKO cells stimulated with various concentrations of HGF and/or VEGF for P-MET, total MET, and P-FAK. VEGFKO cells were also incubated with their own (KO) or VEGFKO-VEGF cells (VEGF) conditioned media (CM). α-tubulin was used for loading control.

(B) Western blot analysis of human primary GBM43 cells treated with HGF and/or VEGF for P-MET, total MET, P-FAK, and α-tubulin.

(C) Western blot analysis of human GBM43 cells treated with B20 and stimulated with HGF and/or VEGF.

(D) Wound-healing assay of HGF-stimulated VEGFKO cells or VEGFKO-VEGF cells. VEGFKO cells were treated with either exogenous VEGF or CM from VEGFKO-VEGF cells (VEGF CM). Top, quantification of wound closure (mean ± SEM). p values compared to VEGFKO cells stimulated with HGF only. Bottom, representative images of wounded cell monolayers. Scale bars, 150 μm.

(E) Wound-healing assay of GBM43 cells treated with exogenous VEGF, VEGF CM, and VEGFKO CM (mean ± SEM). p values compared to GBM43 cells stimulated with HGF only.

See also Figure S2.

Finally, given the negative regulation of VEGF on MET activation, we considered whether HGF could conversely affect VEGFR2 signaling. VEGF stimulation of GBM43 cells led to VEGFR2 phosphorylation and weak downstream activation of Akt and MAPK (Figure S3D), whereas HGF stimulation resulted in substantially more potent Akt and MAPK phosphorylation. Costimulation with HGF and VEGF did not perturb VEGFR2 phosphorylation (Figure S3D), suggesting that HGF/MET signaling does not negatively regulate VEGF/VEGFR2 signaling under these conditions.

Physical Association of MET and VEGFR2

We next evaluated whether VEGFR2 and MET physically associate with each other by performing reciprocal immunoprecipitation (IP) studies. IP of primary human GBM cells expressing detectable levels of MET and VEGFR2 with a VEGFR2 antibody followed by immunoblotting for MET revealed a physical interaction between these two endogenous proteins (Figure 4A). We then transduced VEGFKO and GBM43 cells with HA-tagged wild-type (WT)-VEGFR2 or a truncated VEGFR2 mutant lacking the C-terminal 450 amino acids encompassing key kinase and

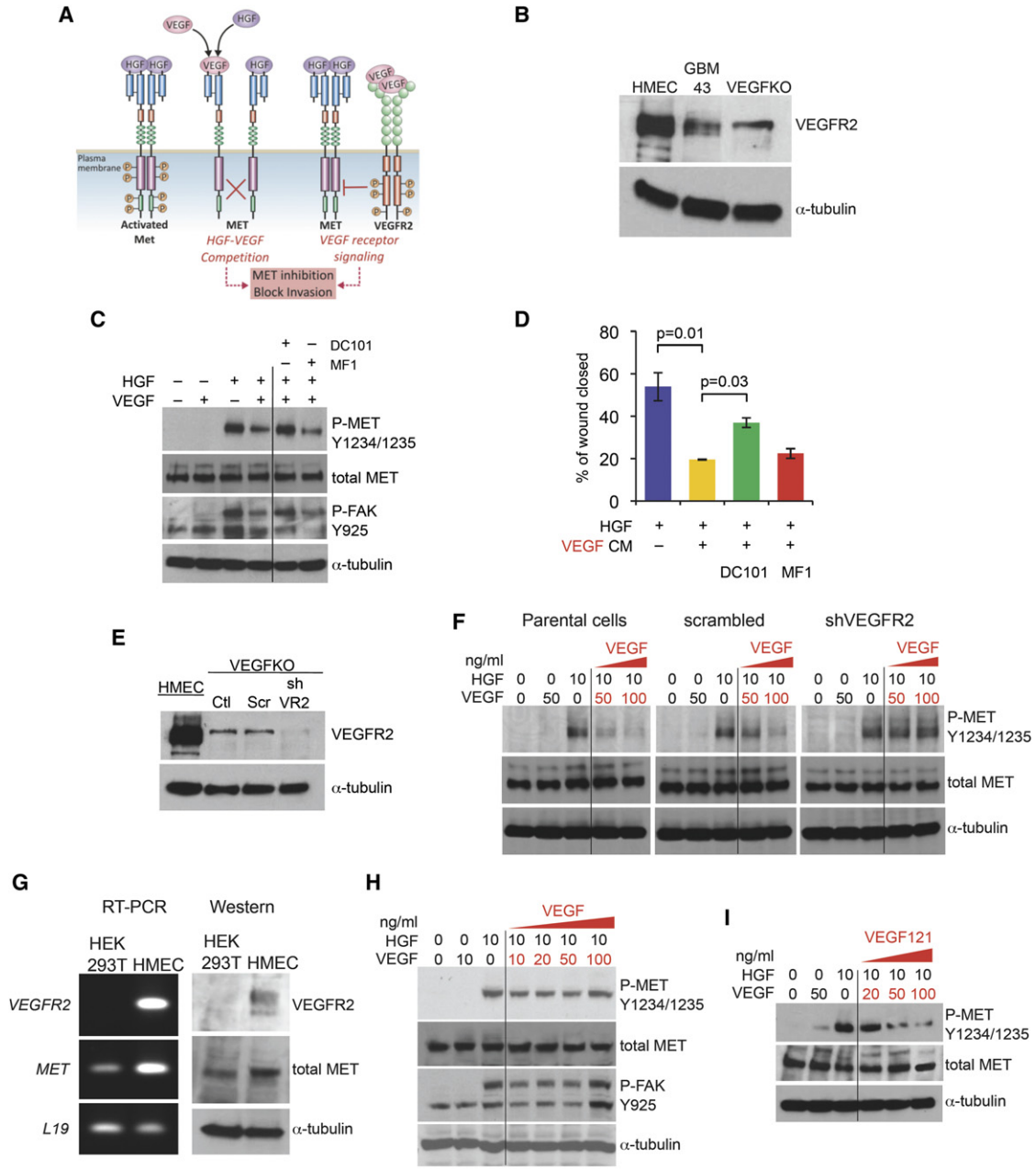

Figure 3. VEGFR2 Is Required for VEGF to Suppress HGF-Stimulated MET Phosphorylation and Cell Motility

(A) Schematic of possible ways by which VEGF can block MET activation.

(B) Western blot analysis detecting relative VEGFR2 expression in GBM43 and VEGFKO tumor cells. Human microvascular endothelial cells (HMEC) were used as a positive control.

(C) VEGFKO cells stimulated with HGF or VEGF as indicated were treated with 100 μg/ml of DC101 or 100 μg/ml of MF1 and lysates subjected to immunoblotting.

(D) Motility of VEGFKO cells incubated with VEGF CM and treated with either 100 μg/ml DC101 or MF1 was assessed in the wound-healing assay (mean ± SEM).

(E) Western blot analysis showing stable knockdown of VEGFR2 in VEGFKO cells transduced with VEGFR2 shRNA (shVR2). Parental control cells (Ctl) and a scrambled shRNA sequence (Scr) are also shown. HMEC were used as a positive control.

(F) Parental VEGFKO cells or VEGFKO cells transduced with scrambled shRNA or shRNA targeting VEGFR2 were stimulated with HGF and/or VEGF and subjected to immunoblotting as indicated.

(G) RT-PCR and western blot analyses for *VEGFR2* and *MET* expression in HEK293T fibroblasts. HMEC served as positive control for VEGFR2 expression. *L19* and α-tubulin were loading controls for RT-PCR and western blot, respectively.

(H) HEK293T cells stimulated with HGF and indicated concentrations of VEGF were subjected to western blot analysis as indicated.

(I) Western blot analysis of VEGFKO cells stimulated with HGF or VEGF121 as indicated.

See also Figure S3.

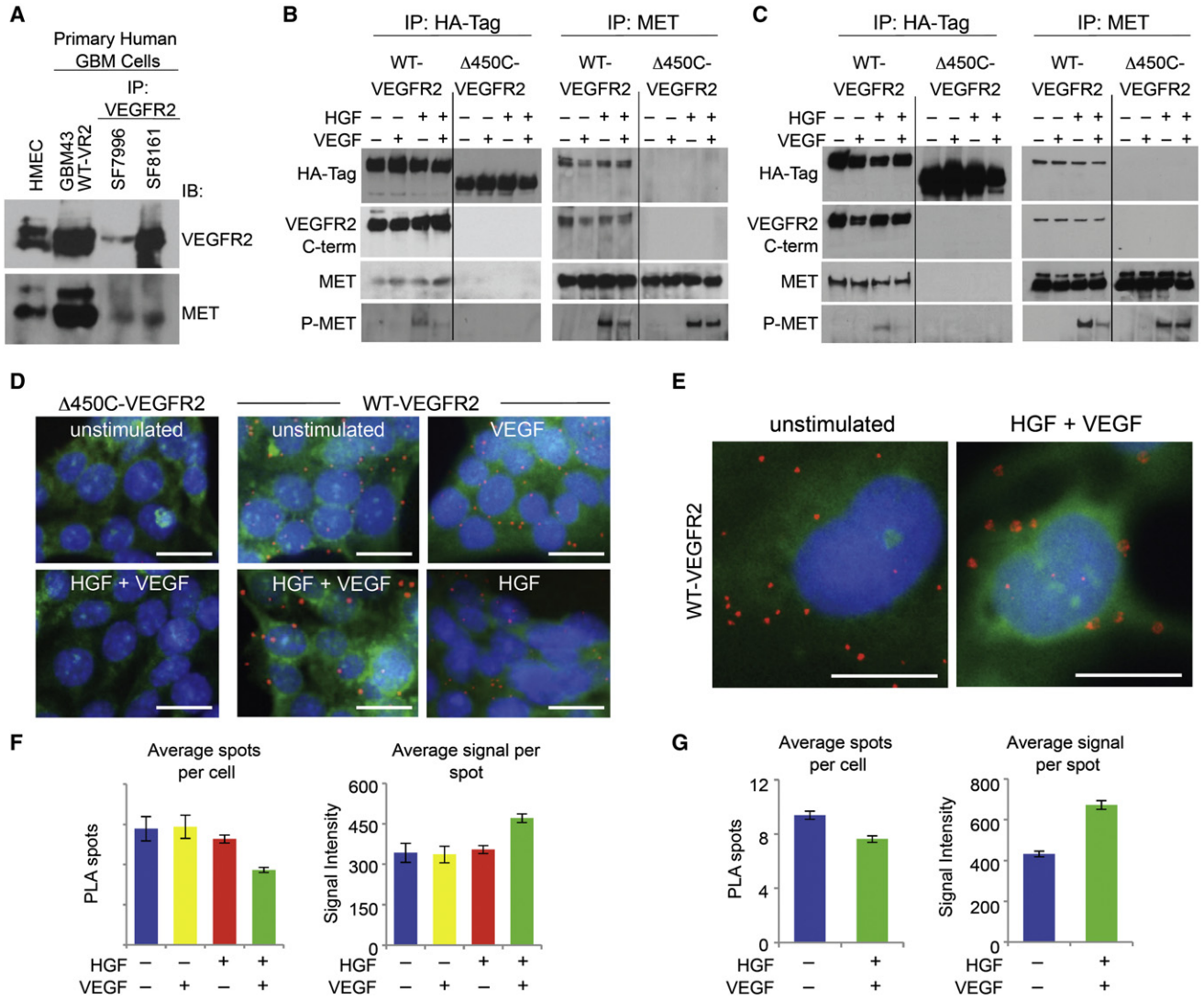

Figure 4. MET and VEGFR2 Associate in a Heterocomplex

(A) Coimmunoprecipitation (IP) of endogenous VEGFR and MET in two primary human GBM cultures (SF7796 and SF8161) as visualized by IP of VEGFR2 followed by immunoblotting for VEGFR2 and MET. Whole-cell lysates from HMEC and human primary GBM43 cells overexpressing VEGFR2 by adenoviral transduction (GBM43 WT-VR2) were run alongside as positive controls.

(B and C) Murine VEGFKO cells (B) or human GBM43 cells (C) transduced by adenovirus to overexpress HA-tagged WT-VEGFR2 or Δ450C-VEGFR2 with or without stimulation of HGF or VEGF as indicated were lysed and immunoprecipitated using indicated antibodies, and the immunoprecipitates were then immunoblotted as indicated.

(D and E) Representative images of PLA in murine VEGFKO (D) or human GBM43 (E) cells expressing WT-VEGFR2 or Δ450C-VEGFR2 after treatment with the indicated growth factors. Red spots are regions of signal amplification denoting VEGFR2 and MET interaction. Cytoskeletal staining (FITC-phalloidin) is green, and nuclear stain (DAPI) is blue. Scale bars, 20 μm.

(F and G) Quantification of PLA signals in murine VEGFKO (F) and human GBM43 (G) cells transduced with WT-VEGFR2 (mean ± SEM).

effector domains (VEGFR2-Δ450C). IP of these cells with a MET antibody or a HA-Tag antibody revealed an interaction of MET with WT-VEGFR2 but not with VEGFR2-Δ450C (Figures 4B and 4C), indicating that the C-terminal region of VEGFR2 is required for MET association. The physical association between MET and VEGFR2 was observed independent of stimulation of either receptor with its cognate ligand, but P-MET coprecipitated only when cells were stimulated with HGF, and addition of VEGF suppressed HGF-stimulated P-MET only when cells were transduced with WT-VEGR2, not VEGFR2-Δ450C (Figures 4B and 4C).

Similar to the IP studies, proximity ligation assay (PLA) (Söderberg et al., 2008) demonstrated an interaction between MET and WT-VEGFR2, but not with VEGFR2-Δ450C, in VEGFKO and GBM43 cells irrespective of stimulation with either ligand (Figures 4D and 4E). However, when GBM cells expressing WT-VEGFR2 were costimulated with HGF and VEGF, the number of PLA spots per cell was slightly reduced but the size of these spots increased (Figures 4D–4G). These results suggest that additional proteins might associate with and redistribute the complex when both ligands are present.

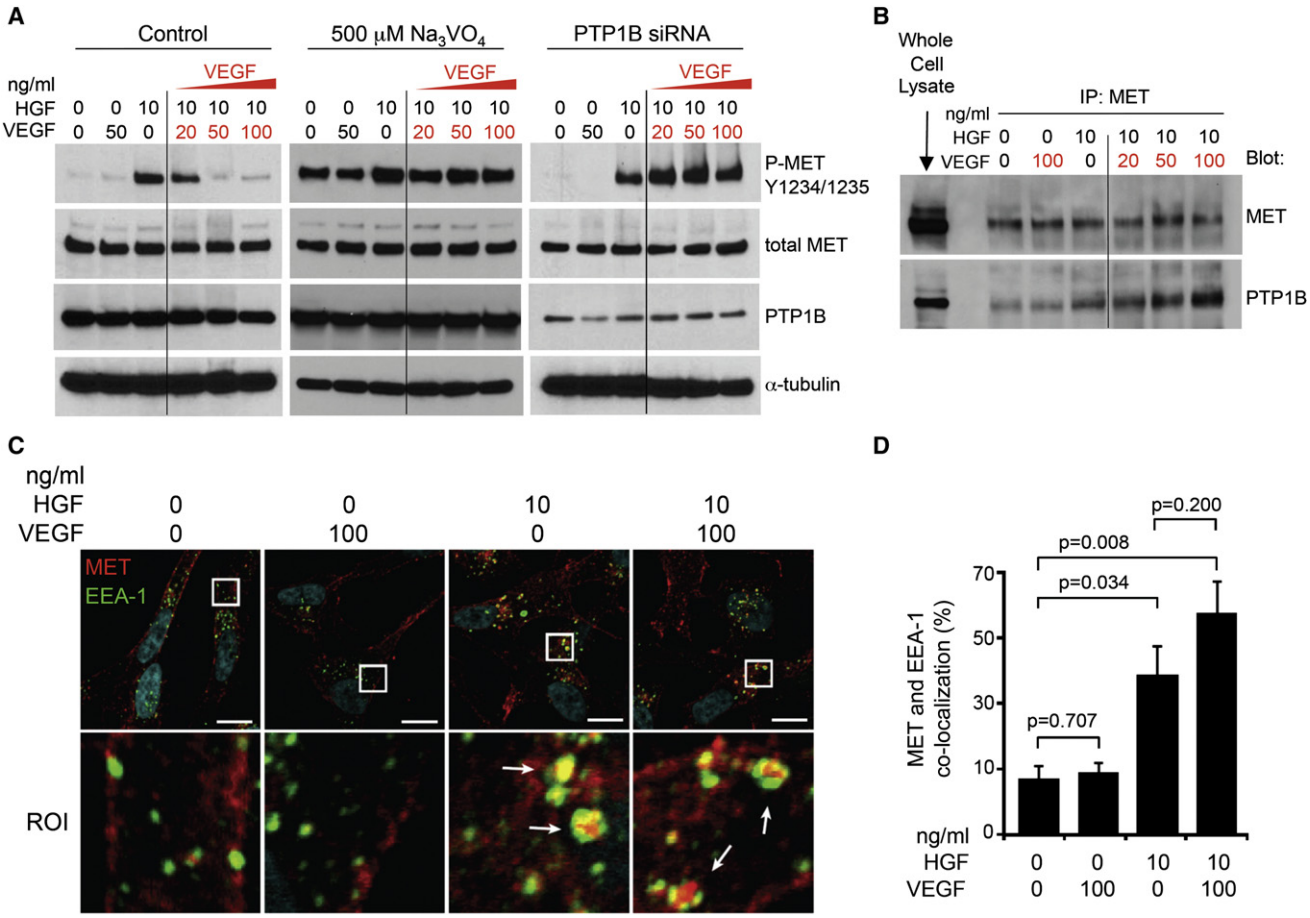

Figure 5. VEGF Signaling Increases PTP1B Recruitment to MET

(A) Control GBM43 cells, GBM43 cells treated with sodium orthovanadate (Na_3VO_4) for 30 min, or GBM43 cells transfected with PTP1B siRNA were stimulated with HGF, VEGF, or both ligands at the concentrations indicated and lysates analyzed by western blot for P-MET, total MET, and PTP1B.

(B) GBM43 cells stimulated with HGF and/or VEGF were crosslinked with the membrane-permeable and cleavable crosslinker DSP and 250 μg of each lysate immunoprecipitated with an anti-MET antibody, followed by immunoblotting for MET and PTP1B. GBM43 whole-cell lysate served as a positive control for analysis of the immunoprecipitates.

(C) Representative images of immunofluorescent staining of GBM43 cells treated with HGF and/or VEGF for MET (red), EEA-1 (green), and DAPI (blue). ROI: higher magnification of the indicated area. Arrows indicate colocalization of MET and EEA-1-positive vesicles. Scale bar = 10 μm.

(D) Quantification of colocalization between MET and EEA-1 staining (mean ± SEM).

See also Figure S4.

VEGF Enhances Recruitment of the Tyrosine Phosphatase PTP1B to MET and Facilitates Downregulation of HGF-Induced MET Phosphorylation

Several mechanisms for attenuation of MET signaling have been described, including internalization and degradation, as well as dephosphorylation by specific tyrosine phosphatases (Abella et al., 2005; Hammond et al., 2003; Sangwan et al., 2008). We found that VEGF stimulation did not decrease total MET over time (Figures 2A, 2B, and S4A–S4C) or enhance the phosphorylation of Ser985 of MET (data not shown), a negative regulatory site that suppresses MET tyrosine phosphorylation (Gandino et al., 1994). In contrast, treatment of GBM43 cells with the tyrosine phosphatase inhibitor sodium orthovanadate abrogated the suppressive effect of VEGF on P-MET (Figure 5A), indicating the involvement of a tyrosine phosphatase. Among the various tyrosine phosphatases known to modulate MET activity is the nonreceptor protein tyrosine phosphatase 1B (PTP1B), which can directly dephosphorylate various RTKs including MET and VEGFR2 (Nakamura et al., 2008; Sangwan et al., 2008). Knockdown of PTP1B in GBM43 cells abolished downregulation of P-MET by VEGF (Figure 5A), supporting a role for PTP1B in VEGF-dependent suppression of P-MET. We then asked whether the extent of interaction between PTP1B and MET was modulated in the presence of VEGF. Co-IP studies revealed low levels of PTP1B/MET interaction in untreated and VEGF-stimulated cells (Figure 5B). As expected, PTP1B/MET association was elevated when cells were stimulated with HGF and was further increased when cells were costimulated with HGF and VEGF (Figure 5B). These data indicate that VEGF enhances recruitment of PTP1B to MET and facilitates dephosphorylation of HGF-induced P-MET.

Upon HGF stimulation, MET enters the endocytic pathway and is either targeted for lysosomal degradation or recycled back to the cell surface (Abella et al., 2005; Hammond et al., 2003). We

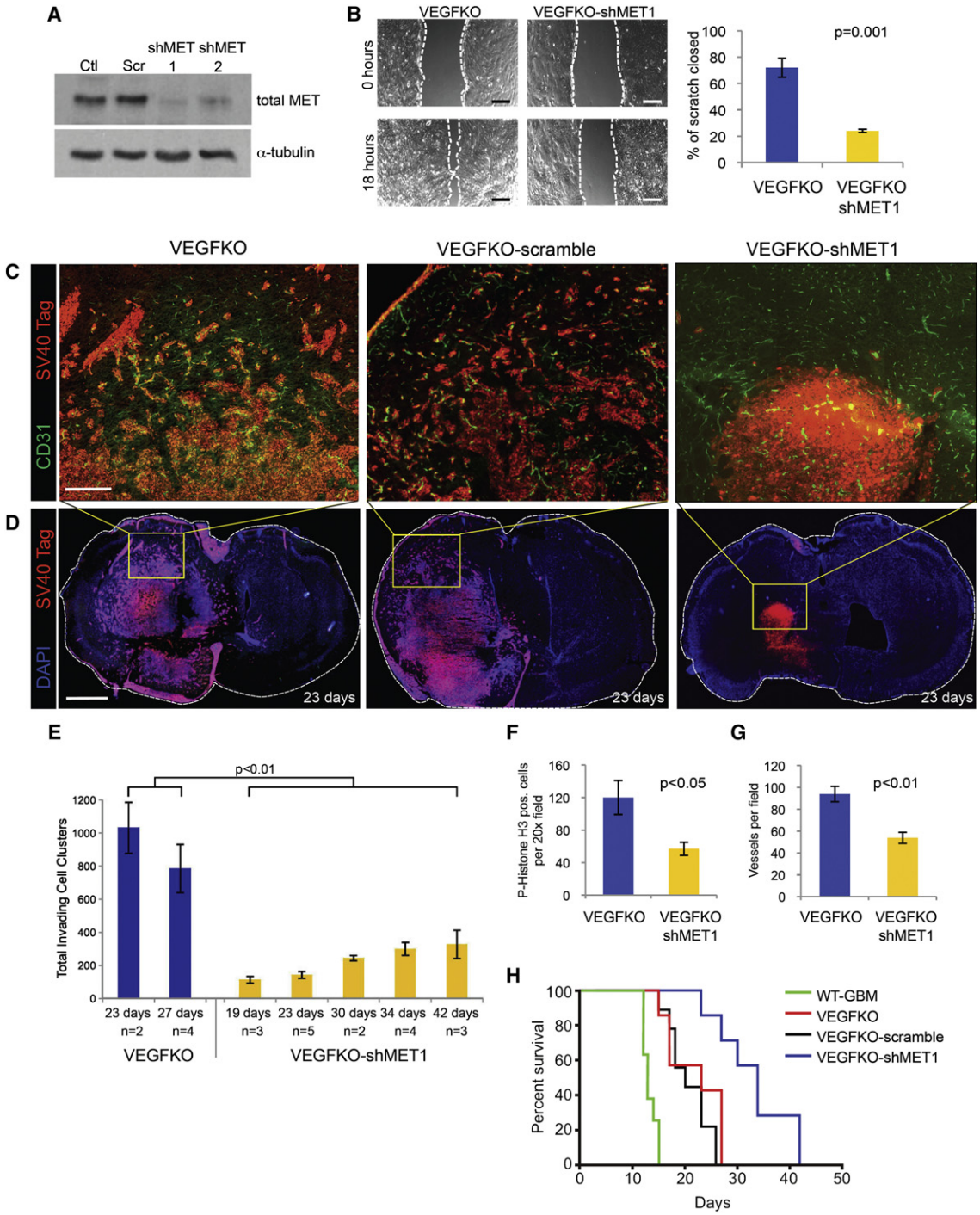

Figure 6. MET Knockdown Blocks Tumor Invasion and Promotes Survival of VEGF-Deficient Tumors

(A) Immunoblot analysis of MET expression in VEGFKO cells stably transduced with two independent shRNAs targeting MET. Parental VEGFKO cells (Ctl) and VEGFKO cells transduced with a scrambled shRNA (Scr) are also shown.

(B) Representative images (left) and quantification (right, mean ± SEM) of a wound-healing assay comparing migration of VEGFKO-shMET1 cells to VEGFKO cells. Dashed white lines indicate edge of wound. Scale bar, 100 μm.

(C and D) Immunohistochemical staining of intracranial VEGFKO, VEGFKO-scrambled, and VEGFKO-shMET1 tumors with SV40 large T-antigen (red) and CD31 (green) (C), or with SV40 large T-antigen (red) and DAPI (blue) (D), to visualize tumor cells and vasculature, respectively. Yellow boxes in (D) (scale bar, 1 mm) represent the region of magnification shown in (C) (scale bar, 200 μm). Images are representative of time-matched samples 23 days post-implantation.

(E) Quantification of total invasion from the primary tumor mass in VEGFKO or VEGFKO-shMET1 tumors over various time points (mean ± SEM). The number of mice analyzed for each condition and time point is indicated.

thus considered whether VEGF could enhance MET dephosphorylation by altering MET internalization and trafficking kinetics. To this end, we tracked MET colocalization with established endosomal markers indicative of different stages of trafficking (Stenmark, 2009). In serum-starved, unstimulated, or VEGF-treated GBM43 cells, MET was predominantly localized to the plasma membrane, whereas HGF stimulation caused MET internalization into EEA-1 positive endosomes (Figures 5C and 5D). Costimulation of GBM43 cells with VEGF and HGF provided a modest but not statistically significant increase in MET/EEA-1 colocalization (Figure 5D). Similar results were observed in VEGFKO cells (data not shown). We also studied colocalization of MET with GFP-fusion constructs of the early endosome markers Rab5 and Rab4, the late endosome marker Rab7, and the recycling endosome marker Rab11. Under the same stimulation conditions and time frame that revealed optimal VEGF-induced suppression of P-MET, we found MET predominantly in early endosomes upon stimulation with HGF irrespective of VEGF (Figures S4D–S4E). These results reveal that VEGF enhances recruitment of PTP1B to the VEGFR2/MET complex to facilitate MET dephosphorylation but does not alter endocytosis and trafficking.

MET Knockdown Blocks Invasiveness during VEGF Ablation and Prolongs Survival

If HGF/MET signaling is indeed a key mediator of GBM migration and invasion, MET inhibition should suppress tumor invasion provoked by VEGF ablation. Thus, we stably knocked down MET expression in VEGFKO cells using two independent shRNAs (VEGFKO-shMET1 and VEGFKO-shMET2) by 85% and 60%, respectively (Figure 6A). VEGFKO-shMET1 cells displayed significantly impaired in vitro motility (Figure 6B) and proliferation (Figure S5A). Most importantly, VEGFKO-shMET1 tumors growing intracranially in mice were substantially less invasive and grew as a solid mass even at end-stage (Figures S5B and S5C) in contrast to the extensive perivascular invasive phenotype of time-matched VEGFKO parental and scrambled-shRNA tumors (Figures 6C and 6D). Both the total number of invading cell clusters and invasion distance were considerably lower in VEGFKO-shMET1 tumors compared to VEGFKO tumors (Figures 6E and S5D–S5F). VEGFKO-shMET1 tumors also displayed lower in vivo proliferation (Figure 6F) and reduced vascular density (Figure 6G) compared to VEGFKO, indicating the pleiotrophic effects of MET signaling. These effects led to a 3-fold prolongation of survival compared to WT-GBM, surpassing the survival benefit observed in VEGFKO over WT-GBM (Figure 6H). Notably, because the silencing effect in VEGFKO-shMET2 was less effective, MET-positive tumor cells eventually emerged over time, leading to invasive progression (Figures S5A and S5H–S5J) and reduced survival benefit over control tumors (Figure S5G). These results underscore MET as a critical driver of GBM invasion and strongly encourage combined anti-VEGF and anti-MET therapy for GBM patients.

HGF/MET Signaling Induces an EMT-like Mesenchymal Phenotype in GBM

Knocking down MET in VEGFKO cells also changed their spindle-like, fibroblastic morphology toward one in which they clustered together into islands with minimal astrocytic processes (Figure 7A) reminiscent of epithelial cells undergoing a mesenchymal-to-epithelial transition (Kalluri and Weinberg, 2009; Thiery et al., 2009). Several recent studies have raised the notion that a mesenchymal gene expression signature is associated with poorer prognosis in GBM patients (Phillips et al., 2006; Tso et al., 2006; Verhaak et al., 2010). Therefore, we speculated that VEGF inhibition, and hence MET activation in GBM, may induce or enhance a switch to a more mesenchymal and aggressive state, analogous to the classical epithelial-to-mesenchymal transition (EMT) described in epithelial cells. Indeed, we found that VEGFKO cells gradually upregulated the EMT markers Snail and N-cadherin but suppressed T-cadherin over a 24 hr time course of HGF stimulation (Figure 7B). These effects were dependent on MET, as HGF-stimulated VEGFKO-shMET1 cells were unable to induce Snail and N-cadherin or downregulate T-cadherin (Figure 7B). Consistent with a report that T-cadherin promotes glioma cell growth arrest (Huang et al., 2003), T-cadherin expression was higher in less invasive and slower growing VEGFKO-shMET1 cells than in VEGFKO cells (Figure 7C). Upregulation of N-cadherin was not associated with suppression of E-cadherin as VEGFKO cells lack E-cadherin expression (data not shown). Importantly, when HGF-induced P-MET and P-FAK was tempered by VEGF in VEGFKO cells, N-cadherin was correspondingly suppressed (Figure 7D).

In vivo, N-cadherin staining was observed in the centers of VEGFKO tumors but was substantially stronger in invading cells at the tumor periphery in correlation with strong P-MET staining found only in invading cells (Figure 7E). Conversely, VEGFKO tumor centers were weakly positive for T-cadherin, and the invading cells were negative (Figure 7E). VEGFKO-shMET1 tumors had smooth borders and were positive for T-cadherin, whereas N-cadherin was weak in the tumor center and absent at the rim (Figure 7E).

We next tested whether increased MET activation due to VEGF ablation could indeed induce a more mesenchymal and aggressive phenotype. We pharmacologically inhibited VEGF and angiogenesis in orthotopic WT-GBM tumors with the anti-VEGF antibody B20, which imparted a significant survival benefit mirroring that which was observed in VEGFKO tumors (Figure S6A). As expected, treatment of WT-GBM-bearing mice with B20 increased cell invasion at the tumor periphery compared to control tumors (Figure 7F; Figure S6B). These invading cells were strongly positive for P-MET and correspondingly exhibited upregulation of N-cadherin and downregulation of T-cadherin (Figure 7F). In contrast, P-MET staining in control WT-GBM tumors was restricted to only a few infiltrating cells at the tumor periphery, similar to their limited pattern of N-cadherin

(F and G) Proliferation (F) and vessel density (G) in orthotopic VEGFKO and VEGFKO-shMET1 tumors 23 days after tumor inoculation as determined by phosphohistone H3 and CD31 staining, respectively (mean ± SEM).

(H) Kaplan-Meier survival curves of mice intracranially implanted with WT-GBM, VEGFKO, VEGFKO-scrambled, and VEGFKO-shMET1 cells. $p = 0.007$ for VEGFKO-shMET1 versus VEGFKO-scramble.

See also Figure S5.

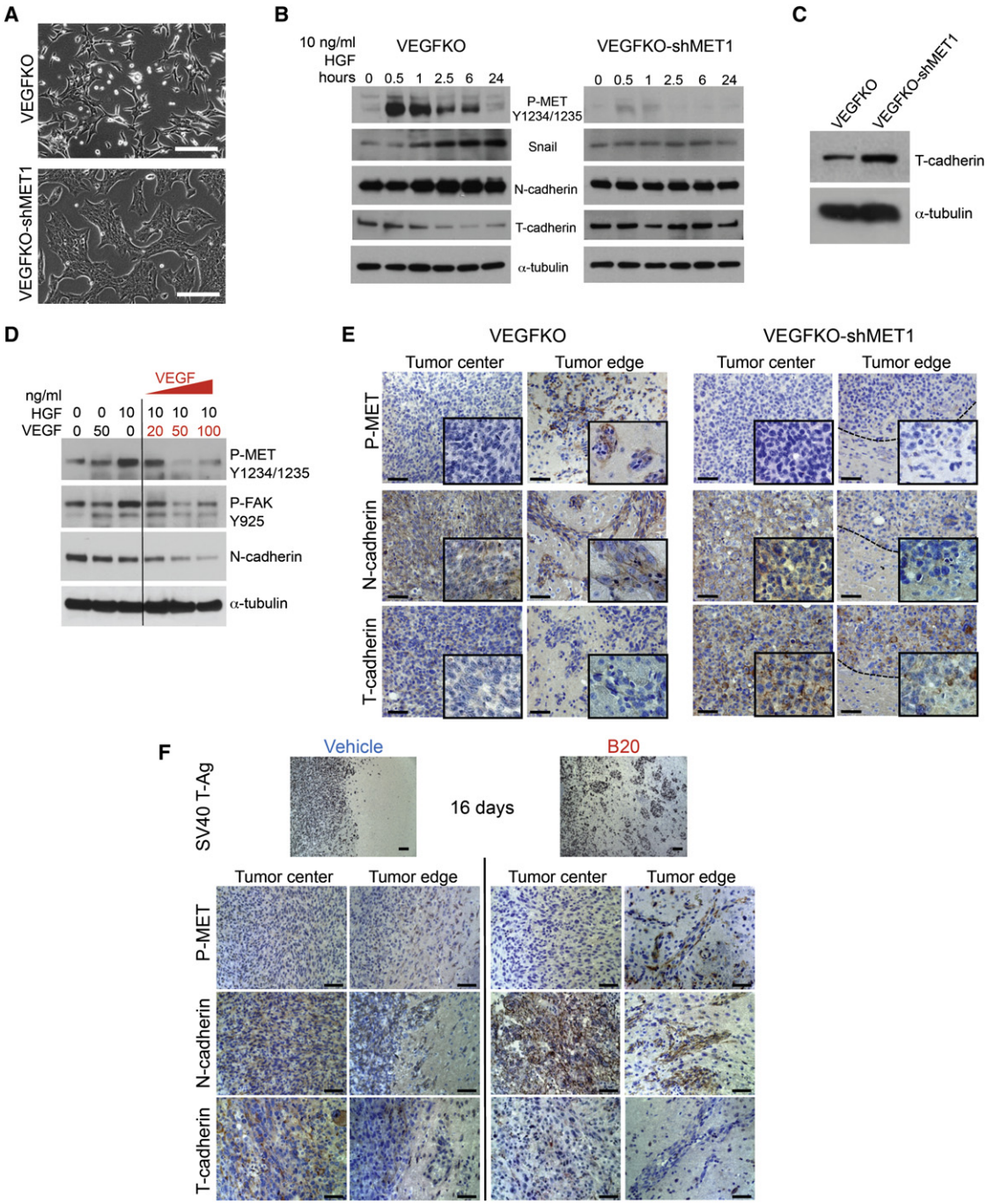

Figure 7. HGF/MET Signaling Induces an EMT-like Transition in GBM

(A) Representative phase contrast microscopy images of VEGFKO and VEGFKO-shMET1 cells. Scale bars, 100 μm.

(B) Immunoblot analysis of VEGFKO or VEGFKO-shMET1 cells stimulated with HGF for the indicated times for P-Met, Snail, N-cadherin, and T-cadherin expression.

(C) Immunoblot analysis of T-cadherin expression in VEGFKO-shMET1 cells and parental VEGFKO cells.

(D) Immunoblot analysis of VEGFKO cell lysates 6 hr after stimulation with HGF or indicated concentrations of VEGF.

(E and F) Immunohistochemical staining of intracranial mouse GBMs for P-MET, N-cadherin, and T-cadherin (brown). Sections were counterstained with hematoxylin (blue). Staining at the center of the main tumor mass or at the tumor rim is shown as indicated. (E) Representative images of time-matched (day 27) VEGFKO and VEGFKO-shMET1 tumors. Dashed lines indicate the smooth border of VEGFKO-shMET1 tumors. (F) Mice bearing orthotopic WT-GBM were treated with B20 or vehicle beginning 3 days after tumor implantation. Representative staining of tumors from mice sacrificed 16 days after tumor implantation are shown. Tumor cells were visualized by staining for SV40 Tag (top). Scale bars, 50 μm.

See also Figure S6.

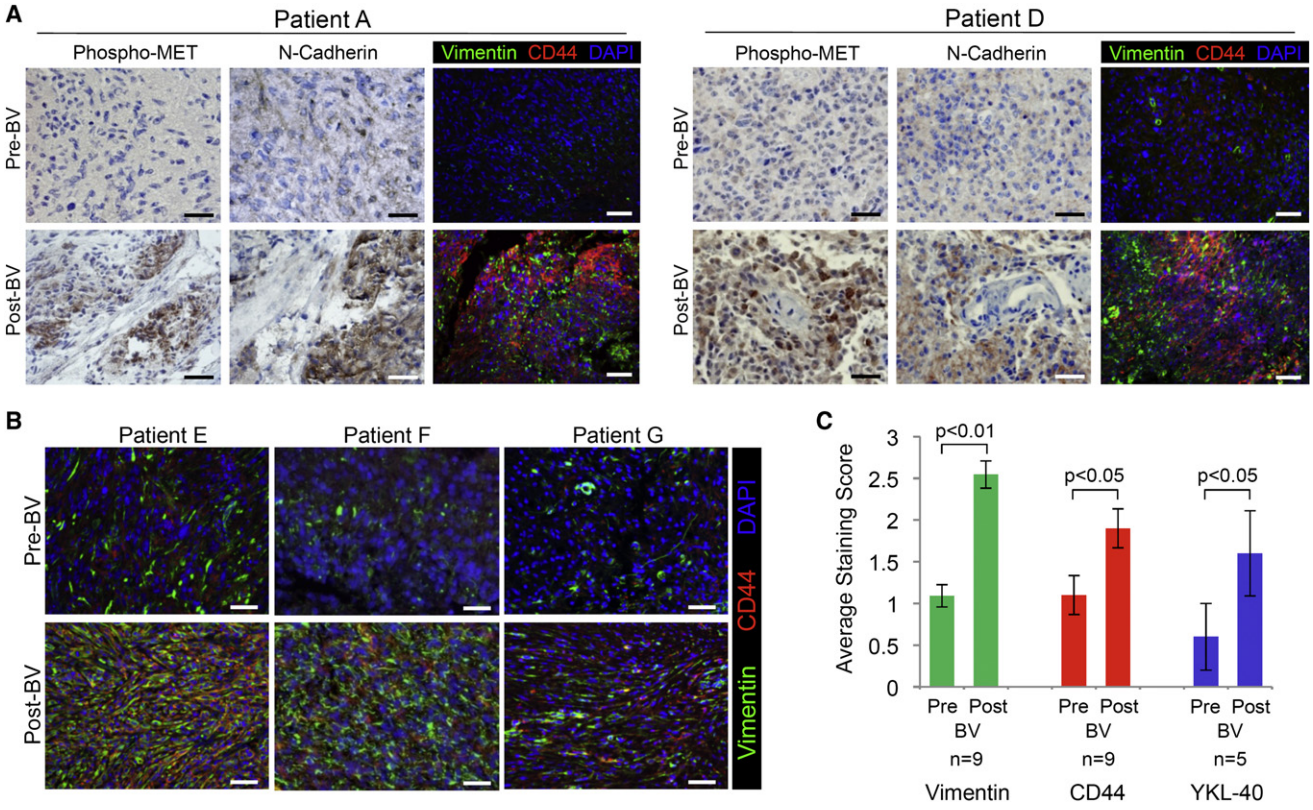

Figure 8. Bevacizumab-Resistant Human GBM Exhibit Increased P-MET and Expression of Mesenchymal Markers

(A and B) Paired human GBM samples obtained before and after treatment with bevacizumab (BV) were immunohistochemically stained for P-MET and N-cadherin (brown) and counterstained with hematoxylin (blue) (A). Representative images of staining from the same area of serial sections are shown. Tissues were also fluorescently costained for the mesenchymal markers vimentin (green) and CD44 (red) and nuclei visualized with DAPI (blue) (A and B). Scale bars, 50 μm.

(C) Staining scores (mean ± SEM) of the mesenchymal markers vimentin, CD44, and YKL-40 in paired human GBM specimens before and after BV. Each sample was scored on a scale of 0–3 and the number of paired patient samples analyzed for each marker is indicated.

expression (Figure 7F). T-cadherin was strongly expressed in many cells but not uniformly positive, with the frequency of positive cells diminishing toward the tumor edge (Figure 7F). Overall, MET phosphorylation was associated with tumor cell invasion, increased N-cadherin, and decreased T-cadherin expression. Similar results were observed when mice bearing WT-GBM tumors were treated with the broad-spectrum RTK inhibitor sunitinib, which also targets the VEGF pathway (Figure S6C). These results indicate that MET activation induces a mesenchymal transformation in GBM underscored by a T- to N-cadherin switch distinct from the classical E- to N-cadherin switch.

Bevacizumab-Resistant Human GBM Exhibit Increased MET Activation and Expression of Mesenchymal Markers

To determine whether mesenchymal markers are elevated in correlation with increased P-MET-positive invasive cell clusters in GBM patients after bevacizumab treatment, we examined our paired pre- and postbevacizumab treatment patient tumor specimens. Of seven relapsed tumors showing increased P-MET staining after treatment (Figures 1E and 1F), six exhibited a corresponding increase in the extent and intensity of N-cadherin staining (Figure 8A). Of these six tumors, five showed upregulation of the mesenchymal marker vimentin with three of them further displaying higher levels of CD44, a mesenchymal stem cell marker associated with GBM (Tso et al., 2006) (Figures 8A and 8B). In total, 8 of 9 analyzed tumor pairs demonstrated an increase in vimentin after bevacizumab treatment, while 6 of 9 exhibited increased CD44 (Figures 8A and 8B). Expression of YKL-40, a marker for the mesenchymal subtype of GBMs (Phillips et al., 2006), was also upregulated after bevacizumab treatment in 3 of 5 tumor pairs examined (Figure 8C). The mean staining intensities for vimentin, CD44, and YKL-40 were significantly higher in bevacizumab-resistant tumors than in paired pretreatment specimens (Figure 8C). These results suggest that human GBM treated with targeted VEGF therapy may progress by switching to a more mesenchymal phenotype involving upregulation of MET activity and expression of key mesenchymal genes and markers.

DISCUSSION

VEGF has been thought to act predominantly on the vasculature, given that its receptors are prevalent in endothelial cells and that deletion of either VEGF or VEGFR2 results in early embryonic lethality because of impaired hematopoietic and endothelial cell development (Ferrara, 2001; Olsson et al., 2006). The main signaling circuit of VEGF is thought to be

VEGFR2, which is implicated in all critical endothelial functions, including proliferation, migration, and vessel formation (Ferrara et al., 2003; Olsson et al., 2006; Shibuya, 2006). Emerging from these observations was the rationale to target the VEGF/VEGFR2 signaling pathway as an antiangiogenic strategy, a notion that has subsequently been supported by a wealth of preclinical data as well as clinical results (Crawford and Ferrara, 2009; Jain, 2008). However, more rigorous expression analyses recently have revealed the expression of VEGF receptors, specifically VEGFR2, on nonendothelial cells, including hematopoietic cells, megakaryocytes, pancreatic duct cells, pericytes, and even tumor cells of various origins (Dallas et al., 2007; Greenberg et al., 2008; Hamerlik et al., 2012; Matsumoto and Claesson-Welsh, 2001; Silva et al., 2011). This suggests that VEGF likely has additional effects on tumors besides promoting neovascularization.

VEGF Signaling in Tumor Cells

In this study we identified an autocrine VEGF/VEGFR2 loop in GBM cells that negatively affects MET activity through recruitment of the phosphatase PTP1B to a VEGFR2/MET heterocomplex. Indeed, evidence for crosstalk between VEGFR2 or MET and other receptor tyrosine kinases (RTKs) is growing. Most recently, VEGFR2 expression was identified on pericytes, where it physically associates with and suppresses PDGFRβ signaling, consequently ablating pericyte coverage of nascent vascular sprouts (Greenberg et al., 2008). These results are analogous to our own, conveying VEGF/VEGFR2 as a negative regulator of other RTKs by blocking their activation through direct interaction.

Both MET and VEGFR2 have been found to interact with a variety of other coreceptors and surface molecules as well (Birchmeier et al., 2003; Koch et al., 2011; Li et al., 2008; Trusolino et al., 2010). Notably, VEGFR2 and MET are each able to associate with neuropilin-1 (NRP-1), a receptor for class 3 semaphorins that is thought to enhance signaling of these two RTKs (Hu et al., 2007; Soker et al., 1998). However, our results suggest that NRP-1 is not a coreceptor of the VEGFR2/MET complex, which might not be unexpected because the heterocomplex blocks MET signaling, but we cannot rule out the association of other coreceptors within this complex.

The aforementioned results suggest that VEGF levels act as a sensor for the vascular and tumor cell compartments in part by sending signals through VEGFR2 complexes on endothelial cells and at least two distinct VEGFR2/RTK heterocomplexes (i.e., VEGFR2/MET on tumor cells and VEGFR2/PDGRβ on pericytes). One can speculate that the distinct associations of VEGFR2 with other RTKs might reflect a level of regulation by which VEGF can positively or negatively signal in different cell types. Although high levels of VEGF facilitate angiogenesis and thereby enable tumor cells to expand, low levels of VEGF lead to a reduction in tumor vessel growth and protection of remaining vessels and concomitantly promote signals for GBM cells to move away from these undesirable conditions.

Microenvironmental Regulation of MET Activity during Anti-VEGF Therapy

MET transcription is induced by the hypoxia-inducible factor HIF-1α in some tumor cells, including GBM (Eckerich et al., 2007; Pennacchietti et al., 2003), and MET expression was found to be upregulated in a subset of bevacizumab-treated patients (Rose and Aghi, 2010). Because reduction in vessel density causes low oxygen tension, it is conceivable that increased MET activity in response to anti-VEGF therapy might be regulated by hypoxia. However, we observed MET activity primarily at the invasive edges of tumors that are not hypoxic, rather than within the tumor mass, where low oxygen tension is more severe. We also observed that HIF1α-KO murine GBM were much more invasive than wild-type tumors, concomitant with high P-MET in the invasive areas (Blouw et al., 2003; Du et al., 2008a). Hence, these results demonstrate that the invasive phenotype cannot be exclusively driven by inadequate oxygen or nutrient supply.

Although we observed VEGFR2/MET complexes in the absence of ligand, the heterodimers appeared to coalesce into larger clusters only upon costimulation with HGF and VEGF, suggesting that additional proteins might further associate with the complex in the presence of both ligands. Indeed, we found that VEGF enhanced the recruitment of PTP1B to the VEGFR2/MET complex, which upon HGF stimulation, facilitated MET dephosphorylation. In addition to directly dephosphorylating ligand-stimulated RTK substrates, such as MET, VEGFR2, EGFR, insulin receptor, and PDGFR (Galic et al., 2005; Haj et al., 2003; Nakamura et al., 2008; Sangwan et al., 2008), PTP1B also regulates their endosomal trafficking and internalization into multivesicular bodies (Eden et al., 2010; Sangwan et al., 2011; Stuible and Tremblay, 2010). In the context of VEGF-driven suppression of MET activation, however, we observed no significant differences in MET endocytosis with VEGF treatment, suggesting that the principal role of PTP1B in this mechanism is to directly dephosphorylate MET. We found that MET was predominantly localized to early endosomes when cells were stimulated with HGF with or without VEGF. Because MET can continue to signal as it progresses along the endocytic pathway (Abella et al., 2005), VEGF-enhanced recruitment and activity of PTP1B may likely be important in maintaining suppression of P-MET in the endosomal compartments. Accordingly, lowering VEGF levels and/or increasing HGF levels would lead to rapid MET reactivation and enhanced tumor cell invasiveness.

VEGF Regulates HGF-Induced EMT-like Traits in GBM cells

Interestingly, activation of MET by genetic and pharmacologic VEGF inhibition increased invasion concomitant with induction of mesenchymal features. Similar to a recent report that MET signaling induces Snail (Grotegut et al., 2006), we observed Snail and N-cadherin upregulation in GBM cells, which was surprisingly associated with T-cadherin downregulation. The latter observation implies an alternative cadherin switch distinct from the classical E-cadherin to N-cadherin switch in epithelial cells (Kalluri and Weinberg, 2009). T-cadherin is an atypical member of the cadherin family devoid of a transmembrane domain but anchored to the surface of the plasma membrane via a glycosylphosphatidylinositol anchor (Andreeva and Kutuzov, 2010). Although it is expressed in many tumor vessels, downregulation of T-cadherin is observed in a variety of cancer cells and associated with a poorer prognosis (Andreeva and Kutuzov, 2010). In GBM cells, overexpression of T-cadherin suppresses proliferation and migration (Huang et al., 2003), consistent with

our observation that T-cadherin expression was higher in circumscribed, minimally invasive VEGFKO-shMET GBM but absent in invasive GBM with high MET activity. In addition we found that HGF stimulation suppressed T-cadherin within 6 hr, suggesting that HGF-induced EMT signals affect T-cadherin transcription. Further supporting a role for T-cadherin in an EMT-like acquisition in GBM is a recent report demonstrating that Zeb-1 suppresses T-cadherin and increases invasion in gallbladder cancer (Adachi et al., 2009).

Clinical Implication

These studies together suggest that one might be able to select GBM patients upfront who may likely develop a proinvasive recurrence during bevacizumab treatment by evaluating MET and VEGFR2 expression in the tumor. This is particularly instrumental in light of the fact that GBM are heterogeneous by nature and can be classified into four distinct molecular subtypes (Phillips et al., 2006; Verhaak et al., 2010). Moreover, our results suggest that patients whose GBM are positive for both MET and VEGFR2 might benefit from treatment modalities that block both VEGF and HGF signaling. As we found VEGFR2 and MET expression on various tumor cell types besides GBM, combined VEGF and MET inhibition might also be useful in other cancer types as recently shown (Sennino et al., 2012). Finally, although HGF/MET is a major signaling node in promoting invasion, it is likely that other proinvasive circuits are also involved in GBM invasion during the course of anti-VEGF therapy or induced when MET is blocked. It will be important to elucidate whether these pathways are also linked to VEGF.

EXPERIMENTAL PROCEDURES

Cell Culture and Reagents

Generation of murine WT-GBM and VEGFKO GBM has been previously described (Blouw et al., 2003). NSCGs were isolated from high-grade murine gliomas generated by transplantation of adult *Ink4/Arf*$^{-/-}$ neural stem cells expressing a constitutively active mutant of human EGFR, EGFRvIII (Phillips et al., 2012). Human GBM43 cells, which are primary cell cultures of patient-derived GBM specimens serially passaged as subcutaneous tumors in mice, have been previously described (Sarkaria et al., 2006). The primary human GBM cultures SF7996 and SF8161 were derived from freshly resected tumor specimens and expanded as glioma neural stem cell lines (Pollard et al., 2009). HEK293T fibroblast and BV-2 microglial cells were purchased from the American Type Culture Collection. HMEC cells have been previously described (Ades et al., 1992; Song et al., 2005). Overexpression and knockdown constructs are described in the Supplemental Experimental Procedures.

Human GBM Specimens

We analyzed paired sets of surgical specimens from ten patients with recurrent glioblastoma treated with bevacizumab at the University of California, San Francisco (UCSF), who demonstrated initial response but recurred while on therapy. Formalin-fixed and paraffin-embedded tumor specimens were collected during surgery from consenting patients, assigned a deidentifying number, and provided by the UCSF Brain Tumor Research Center Tissue Bank in accordance with a protocol approved by the UCSF Committee on Human Research. Patients were selected based on availability of paired tumor specimens from recurrent tumor before and after bevacizumab treatment. Immunohistochemistry on human tissues was performed as described in the Supplemental Experimental Procedures.

Animal Studies

Six- to eight-week-old FvBN Rag1ko mice were intracranially implanted with 2.5 μl of 1 × 10^5 murine WT-GBM, VEGFKO, VEGFKO-VEGF, VEGFKO-scramble, VEGFKO-shMET1 or 2, NSCG, NSCG-VEGF, or human GBM43 tumor cells as described previously (Blouw et al., 2003; Du et al., 2008a). Mice bearing WT-GBMs were treated with 5 mg/kg B20 (kindly provided by Genentech, South San Francisco, CA, USA) in PBS twice weekly by intraperitoneal injection beginning 3 days after tumor implantation until moribund. Sunitinib was administered to WT-GBM bearing mice at 40 mg/kg daily by oral gavage starting 4 days after tumor injection until moribund. Mice were sacrificed when they developed side effects of tumor burden, such as weight loss and lateral recumbency, or at predefined time points for comparative analysis. Tumors were isolated from the brain and prepared for immunohistochemical staining, flow cytometric analyses, or protein and RNA isolation as described in the Supplemental Experimental Procedures. All experiments involving animals in this study were reviewed and approved by the Institutional Animal Care and Use Committee at UCSF.

For further experimental details, see the Supplemental Experimental Procedures.

SUPPLEMENTAL INFORMATION

Supplemental Information includes seven figures, Supplemental Experimental Procedures, and Supplemental References and can be found with this article online at http://dx.doi.org/10.1016/j.ccr.2012.05.037.

ACKNOWLEDGMENTS

We thank Dr. Veena Sangwan for PTP1B siRNA, Bina Kaplan for technical assistance, Dr. Zena Werb for MF1, and Drs. Zena Werb, William Weiss, and Susan Chang for thoughtful discussion. This work was supported by grants from the National Institutes of Health (RO1CA099948, RO1CA113382, and U54CA163155 to G.B.) and the Canadian Institutes of Health Research (CTP-79857 to M.P.). K.V.L. was supported by a Leonard Heyman/American Brain Tumor Association Fellowship.

Received: October 26, 2011
Revised: April 8, 2012
Accepted: May 31, 2012
Published: July 9, 2012

REFERENCES

Abella, J.V., Peschard, P., Naujokas, M.A., Lin, T., Saucier, C., Urbé, S., and Park, M. (2005). Met/Hepatocyte growth factor receptor ubiquitination suppresses transformation and is required for Hrs phosphorylation. Mol. Cell. Biol. *25*, 9632–9645.

Abounader, R., and Laterra, J. (2005). Scatter factor/hepatocyte growth factor in brain tumor growth and angiogenesis. Neuro-oncol. *7*, 436–451.

Adachi, Y., Takeuchi, T., Nagayama, T., Ohtsuki, Y., and Furihata, M. (2009). Zeb1-mediated T-cadherin repression increases the invasive potential of gallbladder cancer. FEBS Lett. *583*, 430–436.

Ades, E.W., Candal, F.J., Swerlick, R.A., George, V.G., Summers, S., Bosse, D.C., and Lawley, T.J. (1992). HMEC-1: establishment of an immortalized human microvascular endothelial cell line. J. Invest. Dermatol. *99*, 683–690.

Andreeva, A.V., and Kutuzov, M.A. (2010). Cadherin 13 in cancer. Genes Chromosomes Cancer *49*, 775–790.

Bergers, G., and Hanahan, D. (2008). Modes of resistance to anti-angiogenic therapy. Nat. Rev. Cancer *8*, 592–603.

Birchmeier, C., Birchmeier, W., Gherardi, E., and Vande Woude, G.F. (2003). Met, metastasis, motility and more. Nat. Rev. Mol. Cell Biol. *4*, 915–925.

Blouw, B., Song, H., Tihan, T., Bosze, J., Ferrara, N., Gerber, H.P., Johnson, R.S., and Bergers, G. (2003). The hypoxic response of tumors is dependent on their microenvironment. Cancer Cell *4*, 133–146.

Chamberlain, M.C. (2011). Radiographic patterns of relapse in glioblastoma. J. Neurooncol. *101*, 319–323.

Crawford, Y., and Ferrara, N. (2009). VEGF inhibition: insights from preclinical and clinical studies. Cell Tissue Res. *335*, 261–269.

Dallas, N.A., Fan, F., Gray, M.J., Van Buren, G., 2nd, Lim, S.J., Xia, L., and Ellis, L.M. (2007). Functional significance of vascular endothelial growth factor receptors on gastrointestinal cancer cells. Cancer Metastasis Rev. *26*, 433–441.

de Groot, J.F., Fuller, G., Kumar, A.J., Piao, Y., Eterovic, K., Ji, Y., and Conrad, C.A. (2010). Tumor invasion after treatment of glioblastoma with bevacizumab: radiographic and pathologic correlation in humans and mice. Neuro-oncol. *12*, 233–242.

Du, R., Lu, K.V., Petritsch, C., Liu, P., Ganss, R., Passegué, E., Song, H., Vandenberg, S., Johnson, R.S., Werb, Z., and Bergers, G. (2008a). HIF1alpha induces the recruitment of bone marrow-derived vascular modulatory cells to regulate tumor angiogenesis and invasion. Cancer Cell *13*, 206–220.

Du, R., Petritsch, C., Lu, K., Liu, P., Haller, A., Ganss, R., Song, H., Vandenberg, S., and Bergers, G. (2008b). Matrix metalloproteinase-2 regulates vascular patterning and growth affecting tumor cell survival and invasion in GBM. Neuro-oncol. *10*, 254–264.

Eckerich, C., Zapf, S., Fillbrandt, R., Loges, S., Westphal, M., and Lamszus, K. (2007). Hypoxia can induce c-Met expression in glioma cells and enhance SF/HGF-induced cell migration. Int. J. Cancer *121*, 276–283.

Eden, E.R., White, I.J., Tsapara, A., and Futter, C.E. (2010). Membrane contacts between endosomes and ER provide sites for PTP1B-epidermal growth factor receptor interaction. Nat. Cell Biol. *12*, 267–272.

Ferrara, N. (2001). Role of vascular endothelial growth factor in regulation of physiological angiogenesis. Am. J. Physiol. Cell Physiol. *280*, C1358–C1366.

Ferrara, N., Gerber, H.P., and LeCouter, J. (2003). The biology of VEGF and its receptors. Nat. Med. *9*, 669–676.

Friedman, H.S., Prados, M.D., Wen, P.Y., Mikkelsen, T., Schiff, D., Abrey, L.E., Yung, W.K., Paleologos, N., Nicholas, M.K., Jensen, R., et al. (2009). Bevacizumab alone and in combination with irinotecan in recurrent glioblastoma. J. Clin. Oncol. *27*, 4733–4740.

Furnari, F.B., Fenton, T., Bachoo, R.M., Mukasa, A., Stommel, J.M., Stegh, A., Hahn, W.C., Ligon, K.L., Louis, D.N., Brennan, C., et al. (2007). Malignant astrocytic glioma: genetics, biology, and paths to treatment. Genes Dev. *21*, 2683–2710.

Galic, S., Hauser, C., Kahn, B.B., Haj, F.G., Neel, B.G., Tonks, N.K., and Tiganis, T. (2005). Coordinated regulation of insulin signaling by the protein tyrosine phosphatases PTP1B and TCPTP. Mol. Cell. Biol. *25*, 819–829.

Gandino, L., Longati, P., Medico, E., Prat, M., and Comoglio, P.M. (1994). Phosphorylation of serine 985 negatively regulates the hepatocyte growth factor receptor kinase. J. Biol. Chem. *269*, 1815–1820.

Greenberg, J.I., Shields, D.J., Barillas, S.G., Acevedo, L.M., Murphy, E., Huang, J., Scheppke, L., Stockmann, C., Johnson, R.S., Angle, N., and Cheresh, D.A. (2008). A role for VEGF as a negative regulator of pericyte function and vessel maturation. Nature *456*, 809–813.

Grotegut, S., von Schweinitz, D., Christofori, G., and Lehembre, F. (2006). Hepatocyte growth factor induces cell scattering through MAPK/Egr-1-mediated upregulation of Snail. EMBO J. *25*, 3534–3545.

Haj, F.G., Markova, B., Klaman, L.D., Bohmer, F.D., and Neel, B.G. (2003). Regulation of receptor tyrosine kinase signaling by protein tyrosine phosphatase-1B. J. Biol. Chem. *278*, 739–744.

Hamerlik, P., Lathia, J.D., Rasmussen, R., Wu, Q., Bartkova, J., Lee, M., Moudry, P., Bartek, J., Jr., Fischer, W., Lukas, J., et al. (2012). Autocrine VEGF-VEGFR2-Neuropilin-1 signaling promotes glioma stem-like cell viability and tumor growth. J. Exp. Med. *209*, 507–520.

Hammond, D.E., Carter, S., McCullough, J., Urbé, S., Vande Woude, G., and Clague, M.J. (2003). Endosomal dynamics of Met determine signaling output. Mol. Biol. Cell *14*, 1346–1354.

Hu, B., Guo, P., Bar-Joseph, I., Imanishi, Y., Jarzynka, M.J., Bogler, O., Mikkelsen, T., Hirose, T., Nishikawa, R., and Cheng, S.Y. (2007). Neuropilin-1 promotes human glioma progression through potentiating the activity of the HGF/SF autocrine pathway. Oncogene *26*, 5577–5586.

Huang, Z.Y., Wu, Y., Hedrick, N., and Gutmann, D.H. (2003). T-cadherin-mediated cell growth regulation involves G2 phase arrest and requires p21(CIP1/WAF1) expression. Mol. Cell. Biol. *23*, 566–578.

Iwamoto, F.M., Abrey, L.E., Beal, K., Gutin, P.H., Rosenblum, M.K., Reuter, V.E., DeAngelis, L.M., and Lassman, A.B. (2009). Patterns of relapse and prognosis after bevacizumab failure in recurrent glioblastoma. Neurology *73*, 1200–1206.

Jain, R.K. (2008). Lessons from multidisciplinary translational trials on anti-angiogenic therapy of cancer. Nat. Rev. Cancer *8*, 309–316.

Kalluri, R., and Weinberg, R.A. (2009). The basics of epithelial-mesenchymal transition. J. Clin. Invest. *119*, 1420–1428.

Koch, S., Tugues, S., Li, X., Gualandi, L., and Claesson-Welsh, L. (2011). Signal transduction by vascular endothelial growth factor receptors. Biochem. J. *437*, 169–183.

Koochekpour, S., Jeffers, M., Rulong, S., Taylor, G., Klineberg, E., Hudson, E.A., Resau, J.H., and Vande Woude, G.F. (1997). Met and hepatocyte growth factor/scatter factor expression in human gliomas. Cancer Res. *57*, 5391–5398.

Kunkel, P., Ulbricht, U., Bohlen, P., Brockmann, M.A., Fillbrandt, R., Stavrou, D., Westphal, M., and Lamszus, K. (2001). Inhibition of glioma angiogenesis and growth in vivo by systemic treatment with a monoclonal antibody against vascular endothelial growth factor receptor-2. Cancer Res. *61*, 6624–6628.

Lamszus, K., Schmidt, N.O., Jin, L., Laterra, J., Zagzag, D., Way, D., Witte, M., Weinand, M., Goldberg, I.D., Westphal, M., and Rosen, E.M. (1998). Scatter factor promotes motility of human glioma and neuromicrovascular endothelial cells. Int. J. Cancer *75*, 19–28.

Lesslie, D.P., Summy, J.M., Parikh, N.U., Fan, F., Trevino, J.G., Sawyer, T.K., Metcalf, C.A., Shakespeare, W.C., Hicklin, D.J., Ellis, L.M., and Gallick, G.E. (2006). Vascular endothelial growth factor receptor-1 mediates migration of human colorectal carcinoma cells by activation of Src family kinases. Br. J. Cancer *94*, 1710–1717.

Li, X., Claesson-Welsh, L., and Shibuya, M. (2008). VEGF receptor signal transduction. Methods Enzymol. *443*, 261–284.

Liang, W.C., Wu, X., Peale, F.V., Lee, C.V., Meng, Y.G., Gutierrez, J., Fu, L., Malik, A.K., Gerber, H.P., Ferrara, N., and Fuh, G. (2006). Cross-species vascular endothelial growth factor (VEGF)-blocking antibodies completely inhibit the growth of human tumor xenografts and measure the contribution of stromal VEGF. J. Biol. Chem. *281*, 951–961.

Matsumoto, T., and Claesson-Welsh, L. (2001). VEGF receptor signal transduction. Sci. STKE *2001*, re21.

Nakamura, Y., Patrushev, N., Inomata, H., Mehta, D., Urao, N., Kim, H.W., Razvi, M., Kini, V., Mahadev, K., Goldstein, B.J., et al. (2008). Role of protein tyrosine phosphatase 1B in vascular endothelial growth factor signaling and cell-cell adhesions in endothelial cells. Circ. Res. *102*, 1182–1191.

Olsson, A.K., Dimberg, A., Kreuger, J., and Claesson-Welsh, L. (2006). VEGF receptor signalling - in control of vascular function. Nat. Rev. Mol. Cell Biol. *7*, 359–371.

Pàez-Ribes, M., Allen, E., Hudock, J., Takeda, T., Okuyama, H., Viñals, F., Inoue, M., Bergers, G., Hanahan, D., and Casanovas, O. (2009). Antiangiogenic therapy elicits malignant progression of tumors to increased local invasion and distant metastasis. Cancer Cell *15*, 220–231.

Pennacchietti, S., Michieli, P., Galluzzo, M., Mazzone, M., Giordano, S., and Comoglio, P.M. (2003). Hypoxia promotes invasive growth by transcriptional activation of the met protooncogene. Cancer Cell *3*, 347–361.

Phillips, H.S., Kharbanda, S., Chen, R., Forrest, W.F., Soriano, R.H., Wu, T.D., Misra, A., Nigro, J.M., Colman, H., Soroceanu, L., et al. (2006). Molecular subclasses of high-grade glioma predict prognosis, delineate a pattern of disease progression, and resemble stages in neurogenesis. Cancer Cell *9*, 157–173.

Phillips, J.J., Huillard, E., Robinson, A.E., Ward, A., Lum, D.H., Polley, M.Y., Rosen, S.D., Rowitch, D.H., and Werb, Z. (2012). Heparan sulfate sulfatase SULF2 regulates PDGFRα signaling and growth in human and mouse malignant glioma. J. Clin. Invest. *122*, 911–922.

Pollard, S.M., Yoshikawa, K., Clarke, I.D., Danovi, D., Stricker, S., Russell, R., Bayani, J., Head, R., Lee, M., Bernstein, M., et al. (2009). Glioma stem cell lines expanded in adherent culture have tumor-specific phenotypes and are suitable for chemical and genetic screens. Cell Stem Cell *4*, 568–580.

Rong, S., Bodescot, M., Blair, D., Dunn, J., Nakamura, T., Mizuno, K., Park, M., Chan, A., Aaronson, S., and Vande Woude, G.F. (1992). Tumorigenicity of the met proto-oncogene and the gene for hepatocyte growth factor. Mol. Cell. Biol. *12*, 5152–5158.

Rose, S.D., and Aghi, M.K. (2010). Mechanisms of evasion to antiangiogenic therapy in glioblastoma. Clin. Neurosurg. *57*, 123–128.

Rubenstein, J.L., Kim, J., Ozawa, T., Zhang, M., Westphal, M., Deen, D.F., and Shuman, M.A. (2000). Anti-VEGF antibody treatment of glioblastoma prolongs survival but results in increased vascular cooption. Neoplasia *2*, 306–314.

Sangwan, V., Paliouras, G.N., Abella, J.V., Dubé, N., Monast, A., Tremblay, M.L., and Park, M. (2008). Regulation of the Met receptor-tyrosine kinase by the protein-tyrosine phosphatase 1B and T-cell phosphatase. J. Biol. Chem. *283*, 34374–34383.

Sangwan, V., Abella, J., Lai, A., Bertos, N., Stuible, M., Tremblay, M.L., and Park, M. (2011). Protein-tyrosine phosphatase 1B modulates early endosome fusion and trafficking of Met and epidermal growth factor receptors. J. Biol. Chem. *286*, 45000–45013.

Sarkaria, J.N., Carlson, B.L., Schroeder, M.A., Grogan, P., Brown, P.D., Giannini, C., Ballman, K.V., Kitange, G.J., Guha, A., Pandita, A., and James, C.D. (2006). Use of an orthotopic xenograft model for assessing the effect of epidermal growth factor receptor amplification on glioblastoma radiation response. Clin. Cancer Res. *12*, 2264–2271.

Sennino, B., Ishiguro-Oonuma, T., Wei, Y., Naylor, R.M., Williamson, C.W., Bhagwandin, V., Tabruyn, S.P., You, W.-K., Chapman, H.A., Christensen, J.G., et al. (2012). Suppression of tumor invasion and metastasis by concurrent inhibition of c-Met and VEGF signaling in pancreatic neuroendocrine tumors. Cancer Discov. *2*, 270–287.

Shibuya, M. (2006). Differential roles of vascular endothelial growth factor receptor-1 and receptor-2 in angiogenesis. J. Biochem. Mol. Biol. *39*, 469–478.

Silva, S.R., Bowen, K.A., Rychahou, P.G., Jackson, L.N., Weiss, H.L., Lee, E.Y., Townsend, C.M., Jr., and Evers, B.M. (2011). VEGFR-2 expression in carcinoid cancer cells and its role in tumor growth and metastasis. Int. J. Cancer *128*, 1045–1056.

Söderberg, O., Leuchowius, K.J., Gullberg, M., Jarvius, M., Weibrecht, I., Larsson, L.G., and Landegren, U. (2008). Characterizing proteins and their interactions in cells and tissues using the in situ proximity ligation assay. Methods *45*, 227–232.

Soker, S., Takashima, S., Miao, H.Q., Neufeld, G., and Klagsbrun, M. (1998). Neuropilin-1 is expressed by endothelial and tumor cells as an isoform-specific receptor for vascular endothelial growth factor. Cell *92*, 735–745.

Song, S., Ewald, A.J., Stallcup, W., Werb, Z., and Bergers, G. (2005). PDGFRbeta+ perivascular progenitor cells in tumours regulate pericyte differentiation and vascular survival. Nat. Cell Biol. *7*, 870–879.

Spannuth, W.A., Nick, A.M., Jennings, N.B., Armaiz-Pena, G.N., Mangala, L.S., Danes, C.G., Lin, Y.G., Merritt, W.M., Thaker, P.H., Kamat, A.A., et al. (2009). Functional significance of VEGFR-2 on ovarian cancer cells. Int. J. Cancer *124*, 1045–1053.

Stenmark, H. (2009). Rab GTPases as coordinators of vesicle traffic. Nat. Rev. Mol. Cell Biol. *10*, 513–525.

Stuible, M., and Tremblay, M.L. (2010). In control at the ER: PTP1B and the down-regulation of RTKs by dephosphorylation and endocytosis. Trends Cell Biol. *20*, 672–679.

Sundberg, C., Nagy, J.A., Brown, L.F., Feng, D., Eckelhoefer, I.A., Manseau, E.J., Dvorak, A.M., and Dvorak, H.F. (2001). Glomeruloid microvascular proliferation follows adenoviral vascular permeability factor/vascular endothelial growth factor-164 gene delivery. Am. J. Pathol. *158*, 1145–1160.

Thiery, J.P., Acloque, H., Huang, R.Y., and Nieto, M.A. (2009). Epithelial-mesenchymal transitions in development and disease. Cell *139*, 871–890.

Trusolino, L., Bertotti, A., and Comoglio, P.M. (2010). MET signalling: principles and functions in development, organ regeneration and cancer. Nat. Rev. Mol. Cell Biol. *11*, 834–848.

Tso, C.L., Shintaku, P., Chen, J., Liu, Q., Liu, J., Chen, Z., Yoshimoto, K., Mischel, P.S., Cloughesy, T.F., Liau, L.M., and Nelson, S.F. (2006). Primary glioblastomas express mesenchymal stem-like properties. Mol. Cancer Res. *4*, 607–619.

van Bruggen, N., Thibodeaux, H., Palmer, J.T., Lee, W.P., Fu, L., Cairns, B., Tumas, D., Gerlai, R., Williams, S.P., van Lookeren Campagne, M., and Ferrara, N. (1999). VEGF antagonism reduces edema formation and tissue damage after ischemia/reperfusion injury in the mouse brain. J. Clin. Invest. *104*, 1613–1620.

Verhaak, R.G., Hoadley, K.A., Purdom, E., Wang, V., Qi, Y., Wilkerson, M.D., Miller, C.R., Ding, L., Golub, T., Mesirov, J.P., et al.; Cancer Genome Atlas Research Network. (2010). Integrated genomic analysis identifies clinically relevant subtypes of glioblastoma characterized by abnormalities in PDGFRA, IDH1, EGFR, and NF1. Cancer Cell *17*, 98–110.

Vredenburgh, J.J., Desjardins, A., Herndon, J.E., 2nd, Dowell, J.M., Reardon, D.A., Quinn, J.A., Rich, J.N., Sathornsumetee, S., Gururangan, S., Wagner, M., et al. (2007). Phase II trial of bevacizumab and irinotecan in recurrent malignant glioma. Clin. Cancer Res. *13*, 1253–1259.

Wang, R., Ferrell, L.D., Faouzi, S., Maher, J.J., and Bishop, J.M. (2001). Activation of the Met receptor by cell attachment induces and sustains hepatocellular carcinomas in transgenic mice. J. Cell Biol. *153*, 1023–1034.

Wang, R., Chadalavada, K., Wilshire, J., Kowalik, U., Hovinga, K.E., Geber, A., Fligelman, B., Leversha, M., Brennan, C., and Tabar, V. (2010). Glioblastoma stem-like cells give rise to tumour endothelium. Nature *468*, 829–833.

Wick, W., Wick, A., Weiler, M., and Weller, M. (2011). Patterns of progression in malignant glioma following anti-VEGF therapy: perceptions and evidence. Curr. Neurol. Neurosci. Rep. *11*, 305–312.

Cancer Cell
Article

Tumor Cells Require Thymidylate Kinase to Prevent dUTP Incorporation during DNA Repair

Chun-Mei Hu,[1] Ming-Tyng Yeh,[4] Ning Tsao,[5] Chih-Wei Chen,[1] Quan-Ze Gao,[2] Chia-Yun Chang,[1] Ming-Hsiang Lee,[5] Jim-Min Fang,[4] Sheh-Yi Sheu,[2,3] Chow-Jaw Lin,[1] Mei-Chun Tseng,[6] Yu-Ju Chen,[6] and Zee-Fen Chang[1,*]
[1]Graduate Institute of Biochemistry and Molecular Biology
[2]Institute of Biomedical Informatics
[3]Department of Life Sciences and Institute of Genome Sciences
National Yang-Ming University, Taipei, 11221 Taiwan
[4]Department of Chemistry, National Taiwan University, Taipei, 10617 Taiwan
[5]Institute of Biochemistry and Molecular Biology, College of Medicine, National Taiwan University, Taipei, 10051 Taiwan
[6]Institute of Chemistry, Academia Sinica, Nankang, Taipei 115, Taiwan
*Correspondence: zfchang@ym.edu.tw
DOI 10.1016/j.ccr.2012.04.038

SUMMARY

The synthesis of dTDP is unique because there is a requirement for thymidylate kinase (TMPK). All other dNDPs including dUDP are directly produced by ribonucleotide reductase (RNR). We report the binding of TMPK and RNR at sites of DNA damage. In tumor cells, when TMPK function is blocked, dUTP is incorporated during DNA double-strand break (DSB) repair. Disrupting RNR recruitment to damage sites or reducing the expression of the R2 subunit of RNR prevents the impairment of DNA repair by TMPK intervention, indicating that RNR contributes to dUTP incorporation during DSB repair. We identified a cell-permeable nontoxic inhibitor of TMPK that sensitizes tumor cells to doxorubicin in vitro and in vivo, suggesting its potential as a therapeutic option.

INTRODUCTION

An important process during DNA repair is the availability of a supply in sufficient amounts of four dNTPs (Niida et al., 2010b). Ribonucleotide reductase (RNR)-mediated reduction directly generates dADP, dGDP, dCDP, and dUDP from their corresponding NDPs (Nordlund and Reichard, 2006). RNR is composed of the R1 and R2 subunits, with the level of R2 being subject to cell cycle regulation (Engström et al., 1985); R2 is often found to be elevated in tumor cells (Jensen et al., 1994; Zhang et al., 2009). It has been reported that R2 overexpression confers oncogenic potential (Fan et al., 1998). An analog of R2, p53R2, can be used to substitute for R2 in the RNR enzyme, and its function is important for DNA repair in quiescent cells (Håkansson et al., 2006; Pontarin et al., 2011). Nucleotide diphosphate kinase converts all dNDPs to dNTPs, including dUTP. Pyrophosphorolysis of dUTP by dUTPase or deamination of dCMP yields dUMP, which can then be converted to dTMP by thymidylate synthase. The action of thymidine kinase (TK) is also able to generate dTMP from thymidine. Thymidylate kinase (TMPK) subsequently catalyzes the formation of dTDP (Reichard, 1988). Thus, dTDP is the only dNDP formation that cannot be directly generated through the action of RNR.

Repair of double-strand breaks (DSBs) is mediated by the homologous recombination (HR), single-strand annealing (SSA), or nonhomologous end-joining (NHEJ) pathways (Hartlerode and Scully, 2009). NHEJ occurs during G1 phase and facilitates the direct ligation of the two DNA ends that are associated with DSBs (Lieber, 2010). Both the SSA and HR pathways involve 5′ resectioning from a DSB site to generate a long 3′ overhang (Mimitou and Symington, 2009). The SSA pathway repairs DSBs between or within linked direct repeats in which the 3′ overhangs are annealed in a way that is dependent on the presence of these repeat sequences in the same DNA duplex, and

Significance

The present study reveals that high levels of RNR at sites of DNA damage in tumor cells without coordination with TMPK seems to lead to dUTP incorporation during repair. Normal cycling cells, which have an intact checkpoint, express low levels of R2 after DNA damage, thereby dispensing with the requirement for TMPK during repair. Conventional cancer chemotherapy by DNA damage is unable to discriminate between tumor cells and rapidly dividing cells in normal tissues, which can often lead to unwanted side effects. This study offers a strategy by which TMPK is targeted as an adjunctive therapy that aims to minimizing side effects.

any unannealed sequences are then deleted followed by ligation to restore the continuous DNA duplex. HR repair at a DSB site produces a long 3′ single strand and employs DNA duplex containing a long homologous sequence as the template for strand exchange and resynthesis, which results in a repair of the DSB (San Filippo et al., 2008). The HR repair process is error free and mainly occurs during late S and G2 phases, when sister chromatids are available as the HR templates. The new synthesis of long strands during HR requires the incorporation of more than 10,000 dNTPs in order to repair a single DSB by strand invasion (Robert et al., 2011). The RNR-mediated supply of dNTPs is thus critical to successful HR repair (Burkhalter et al., 2009; Moss et al., 2010).

Because formation of dTDP specifically requires TMPK functionality, we have hypothesized that blocking TMPK should also reduce the efficiency of DSB repair and sensitize tumor cells to genotoxic insults. Using RNA interference, we have previously shown that TMPK knockdown significantly increases the sensitivity of HCT-116 colon cancer cells to doxorubicin, a topoisomerase II inhibitor that induces DSBs in DNA (Hu and Chang, 2008). In comparison, TS knockdown only sensitizes *p53*-deficient cells to doxorubicin to a limited extent because of complementation of TK-mediated dTMP formation. Importantly, we found that TMPK knockdown does not, on its own, activate DNA damage responses. It thus functions in a way that is quite distinct from that of the antimetabolites used in conventional anticancer therapies, which directly induce genotoxicity (Garg et al., 2010). For example, the thymidylate synthase inhibitors 5-FU and 5-FdUrd block the conversion of dUMP to dTMP, causing dUTP to accumulate and inducing the formation of 5-FdUTP (Longley et al., 2003). DNA polymerases are unable to discriminate between dUTP and dTTP (Bessman et al., 1958), and, therefore, excessive amounts of dUTP and 5-FdUTP are misincorporated into DNA, which triggers DNA damage-induced cell death (Ahmad et al., 1998). Consequently, such antimetabolites are highly toxic to normal cycling cells and potentially may induce the development of secondary tumors.

TMPK-knockdown cells are viable and capable of proliferating (Hu and Chang, 2008). Given the essential function of TMPK during dTDP formation, this suggests that human tumor cells have a TMPK isoform. However, it is hard to understand why TMPK knockdown profoundly affects DNA repair in tumor cells. Unlike TMPK knockdown, blocking RNR by itself induces a DNA damage response and blocks DNA repair (Shao et al., 2006). A recent report has demonstrated that RNR is recruited to sites of DNA damage as a result of an interaction with Tip60 via the C-terminal region of the R1 subunit (Niida et al., 2010a). Disruption of RNR recruitment to sites of DNA damage affects DSB repair in G1-phase cells but not in S-phase cells. The explanation for this is that the low levels of dNTPs in G0/G1-phase cells make the site-specific production of dNTPs by RNR critical to DNA repair (Håkansson et al., 2006). In this study, we have provided evidence linking the involvement of RNR at DNA damage sites to the functional requirement of TMPK for DNA repair in tumor cells. Additionally, we identified a cell-permeable inhibitor of hTMPK. Our results further demonstrate the potential of TMPK inhibitors to be part of mild anticancer therapies.

RESULTS

TMPK Contributes to the Repair of DSBs by Preventing dUTP Incorporation

To assess the role of TMPK in DSB repair, we silenced TMPK expression in U2OS cells harboring a DR-GFP reporter using siRNA and performed HR analysis (Pierce et al., 1999). In the presence of I-SceI endonuclease, which induces DSBs, HR repair generates intact GFP, which gives a fluorescent readout. Using flow cytometry analysis, it was found that TMPK knockdown significantly reduced the efficiency of HR repair, as determined by measuring the GFP-positive fraction (Figure 1A). Cell-cycle analysis showed that TMPK knockdown did not reduce the numbers of U2OS cells in the S and G2/M phases (Figure 1A and Figure S1A, which is available online), which excludes the possibility that TMPK knockdown reduces the number of HR-permissive cells. We also tested the effect of TMPK knockdown on the repair of doxorubicin-induced DNA lesions in MDA-MB231 breast cancer cells. Control and TMPK-knockdown cells were treated with a low dose of doxorubicin (0.1 μM) for 4 hr and then were washed thoroughly with growth medium. Initially, the number of DNA lesions, as indicated by γH2AX focus staining (Mah et al., 2010), was similar in these cells to the control (Figure 1B). After recovery for 24 hr, the number of doxorubicin-induced DNA lesions was reduced in the control cells, indicating that these cells were capable of repairing the DNA damage induced by exposure to low-dose doxorubicin. In contrast, the number of γH2AX foci in the TMPK-knockdown cells was relatively constant and significantly higher than in the control. Moreover, TMPK knockdown on its own had only a slight effect on the growth of MDA-MB231 cells, which contrasted with the marked reduction in cells growth found when cells were exposed to doxorubicin (Figures S1B and S1C). Thus, TMPK would seem to be essential for DNA repair in MDA-MB231 cells when they are exposed to low-dose doxorubicin.

Doxorubicin exposure-induced DSBs are repaired by HR. It is known that HR involves Rad 51 foci, which is where strand invasion takes place during repair (Holthausen et al., 2010). We tested the effect of TMPK knockdown on the formation and resolution of Rad 51 foci following exposure to doxorubicin. The results show that TMPK knockdown did not initially affect Rad51 focus formation. However, after 24 hr, the number of Rad 51 foci was significantly reduced in the control cells but not in TMPK-knockdown cells (Figure 1C). This indicates that TMPK knockdown prevents the repair of recombinogenic lesions. We also examined XRCC1 foci, which are known to be single-strand break-repair (SSBR) markers (Caldecott, 2008). As expected, very few XRCC1 foci were detected in control and TMPK knockdown cells immediately after exposure. At 24 hr after recovery, TMPK knockdown cells showed a marked increase in the number of XRCC1 foci (Figure 1D), which implies that blocking TMPK promotes the presence of DNA single-strand breaks (SSBs) formation during HR.

It is well established that SSBs are generated via the removal of erroneous bases by DNA glycosylases and via apurinic/apyrimidinic endonuclease (APE)-mediated cleavage at the abasic sites (Caldecott, 2008). Uracil DNA glycosylases, such as uracil N-glycosylase (UNG), remove uracil from DNA (Krokan

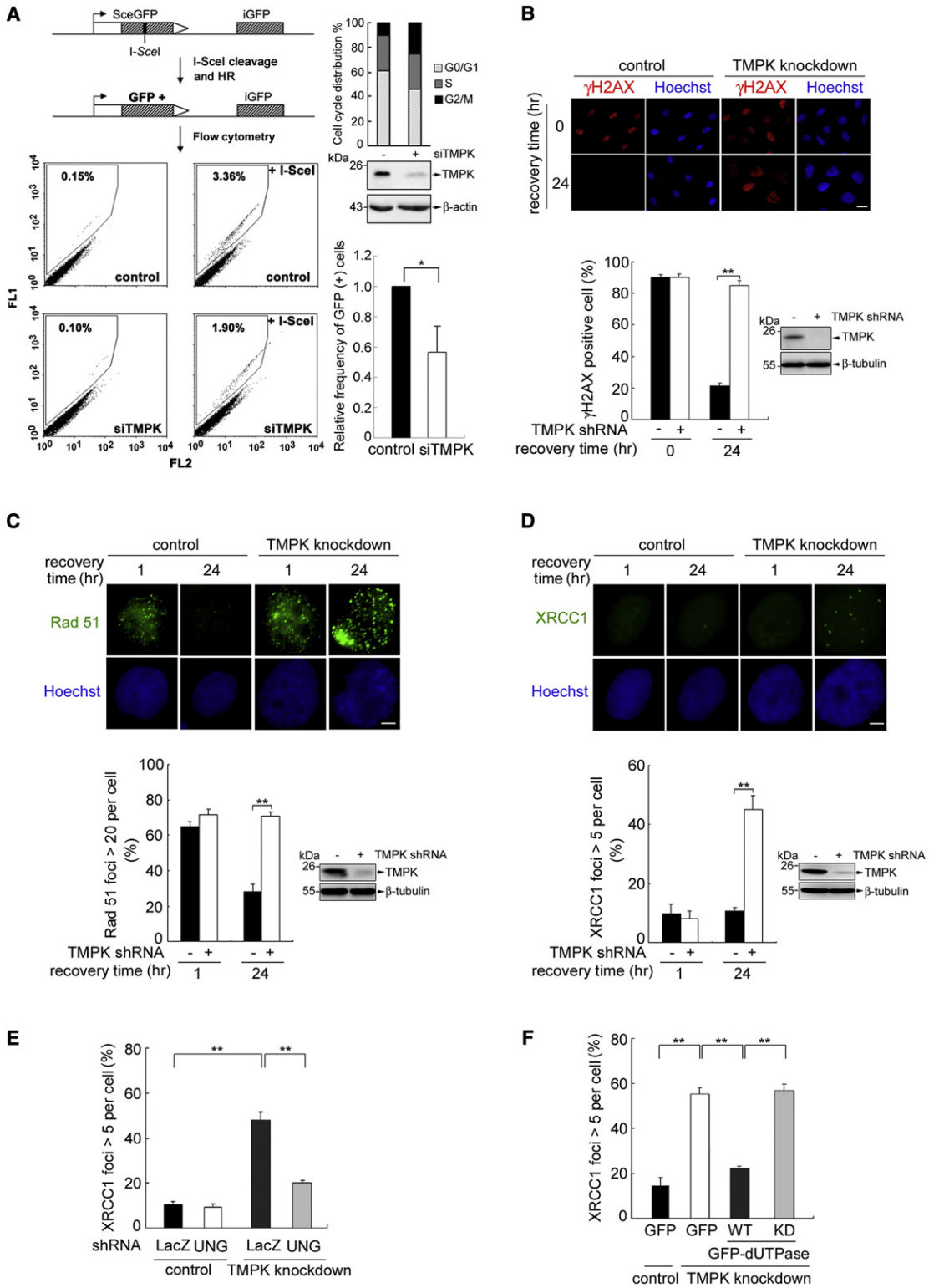

Figure 1. TMPK Knockdown Causes DSB Repair with dUTP Incorporation

(A) Following transfection with TMPK siRNA for 24 hr, U2OS-DR-GFP cells were transfected with pCBA-I-SceI plasmid for 48 hr. The frequency of GFP-positive cells was measured by FACS analysis. In parallel, cells were fixed with PI staining for FACS analysis and harvested for Western blot analysis.

(B–D) MDA-MB231 cells without and with TMPK shRNA stable expression were exposed to doxorubicin (0.1 μM) for 4 hr and then underwent recovery in refreshing medium to give γH2AX foci staining (B) (scale bar, 20 μm), Rad51 foci staining (C) (scale bar, 5 μm), and XRCC1 foci staining (D) (scale bar, 5 μm). Each cell containing γH2AX foci > 10, Rad51 foci > 20, and XRCC1 foci > 5 were counted and expressed as a percentage.

et al., 2002). To test whether the SSBs identified as XRCC1 foci resulted from the misincorporation of uracil, TMPK-knockdown cells were infected with lentiviral shRNA for UNG. After recovery from doxorubicin exposure, it was found that the number of XRCC1 foci was markedly reduced by UNG knockdown (Figure 1E and Figure S1D). To verify the presence of uracil in the genome of the cells after recovery from doxorubicin exposure, we isolated genomic DNA by in vitro UNG incubation and analyzed small molecules released from genomic DNA by mass spectrometric analysis. The mass spectrum showed the presence of uracil signal in the sample from TMPK knockdown but not control cells (Figure S1E). Thus, blocking TMPK promotes SSBs as a result of the presence of uracil in the genome during the repair of doxorubicin-induced DSBs.

We next tested whether the increase in uracil in the genome was a result of dUTP incorporation. Cellular levels of dUTP are primarily controlled by dUTPase, an enzyme responsible for hydrolyzing dUTP to dUMP and pyrophosphate (McIntosh et al., 1992). Wild-type GFP-dUTPase and a catalytically dead mutant form of GFP-dUTPase (Figure S1F) were expressed in TMPK-depleted MDA-MB231 cells. After recovery from doxorubicin exposure, expression of wild-type dUTPase was found to significantly reduce the number of XRCC1 foci in TMPK-knockdown cells compared to cells expressing the catalytically dead dUTPase, which retained a high level of XRCC1 foci (Figure 1F and Figure S1G). Consistently, γH2AX foci were abolished by overexpression of wild-type, but not catalytically dead, dUTPase (Figure S1H). In conclusion, our results show that TMPK is essential for preventing dUTP incorporation during the repair of DSBs.

Repair at Sites of DNA Damage Requires Coordination between RNR and TMPK

It has been estimated that the dUTP/dTTP ratio in cells is normally within the range 0.3% to 3% (Traut, 1994). TMPK-knockdown cells retain more than 60% of the dTTP pool and are able to proliferate albeit a slower rate (Figures S2A and S2B). Presumably, the cellular level of dTTP is still much higher in these cells than the level of dUTP. This prompted us to question why knockdown of TMPK should cause the incorporation of dUTP during DNA repair. To assess the functional requirements for this TMPK during DNA repair, MDA-MB231 breast cancer cells were transfected with pEGFP-TMPK(WT) or pEGFP-TMPK(D15R), a catalytically dead mutant (Figure S2C). Overexpression of TMPK(WT) resulted in an increased rate of disappearance of γH2AX foci after recovery from doxorubicin exposure. In contrast, overexpression of TMPK(D15R) resulted in the persistence of the γH2AX foci (Figure 2A). It should be mentioned that, when we overexpressed TMPK(D15R) in HeLa cells with high transfection efficiency, it was found that the steady-state level of dTTP was unaffected (Figures S2D and S2E). Given that functionality of endogenous TMPK does not seem to be significantly affected by the expression of TMPK(D15R), the inhibitory effect of TMPK(D15R) on DNA repair is thus unlikely to be related to the size of the dTTP pool.

The RNR-mediated reaction yields dUDP, which is converted to dUTP by NDP kinase (Mathews, 2006). TMPK knockdown results in the incorporation of dUTP during DNA repair, and, therefore, we examined the effect on repair of blocking the recruitment of RNR to sites of DNA damage in TMPK-knockdown MDA-MB231 cells. To this end, we overexpressed YFP fused to a 90-amino-acid C-terminal fragment of the R1 subunit (R1C–NLS–YFP), which interferes with the interaction between endogenous RNR and Tip60 that is required for recruitment to sites of damage (Niida et al., 2010a). Remarkably, overexpression of this R1C–NLS–YFP fusion protein abolished the effect of TMPK knockdown on the number of γH2AX foci during recovery from doxorubicin exposure (Figure 2B). The effect of TMPK(D15R) overexpression was also reversed by expression of R1C–NLS–YFP (Figure 2C). Thus, RNR functionality at sites of DNA damage requires functional coordination with TMPK in order to prevent dUTP-mediated lesions from persisting.

In order to determine whether TMPK and RNR are recruited to sites of DNA damage, we used laser microirradiation to damage DNA, and it was found that γH2AX and endogenous TMPK and R2 colocalized along the microirradiated line (Figure 2D). Consistently, R1 was also found colocalized with γH2AX (Figure S2F). In addition, we transfected cells with an expression vector encoding I-PpoI, which introduces specific DSB in chromosome 1 and ribosomal DNA (Flick et al., 1998). This system allows analysis of the recruitment of the repair proteins to specific DSB sites (Berkovich et al., 2007). We cotransfected cells with pFlag-TMPK to allow chromatin immunoprecipitation (ChIP). Quantitative ChIP analysis showed the presence of Flag-TMPK at the I-PpoI cleavage site in chromosome 1 but not at the c-*fos* promoter region. γH2AX and the R2 subunit of RNR were also present at the I-PpoI cleavage site, but histone 3 (H3) occupancy was not affected by I-PpoI cleavage (Figure 2E). Similar results were observed for ribosomal DNA compared to the control gene GAPDH using ChIP analysis, which additionally showed that the association of UBF, a specific rDNA-binding protein, was not affected by I-PpoI cleavage (Figure S2G). These results suggest that TMPK and RNR bind to sites of DNA damage where they coordinate the site-specific production of balanced amounts of the four dNTPs needed for repair.

High Levels of R2 Expression after DNA Damage Are a Determinant of Tumor Cells that Require TMPK for Repair

We further tested the requirement of TMPK for DNA repair in another breast cancer cell line, MCF-7, as well as in nontumorigenic cycling mammary H184B5F5/M10 and MCF10A cells. In

(E) Cells were infected with lentivirus of LacZ or UNG shRNA for 8 hr. After another 36 hr, cells were exposed to doxorubicin (0.1 μM) for 4 hr and allowed to recover in fresh medium for 24 hr before fixation and XRCC1 foci staining (scale bar, 5 μm). The inset indicates the Western blot data of UNG, TMPK, and GAPDH. For each experiment in (B–E), 100 cells were counted.

(F) Cells were transfected with wild-type and catalytic-dead dUTPase expression plasmids. After overnight incubation, the cells were treated with doxorubicin and recovered for XRCC1 staining as described in (E). The numbers of GFP-positive cells with > 5 XRCC1 foci per cells are shown in the upper panel. For each experiment, 100 GFP-positive cells were counted. All error bars represent SD (n = 3).

See also Figure S1.

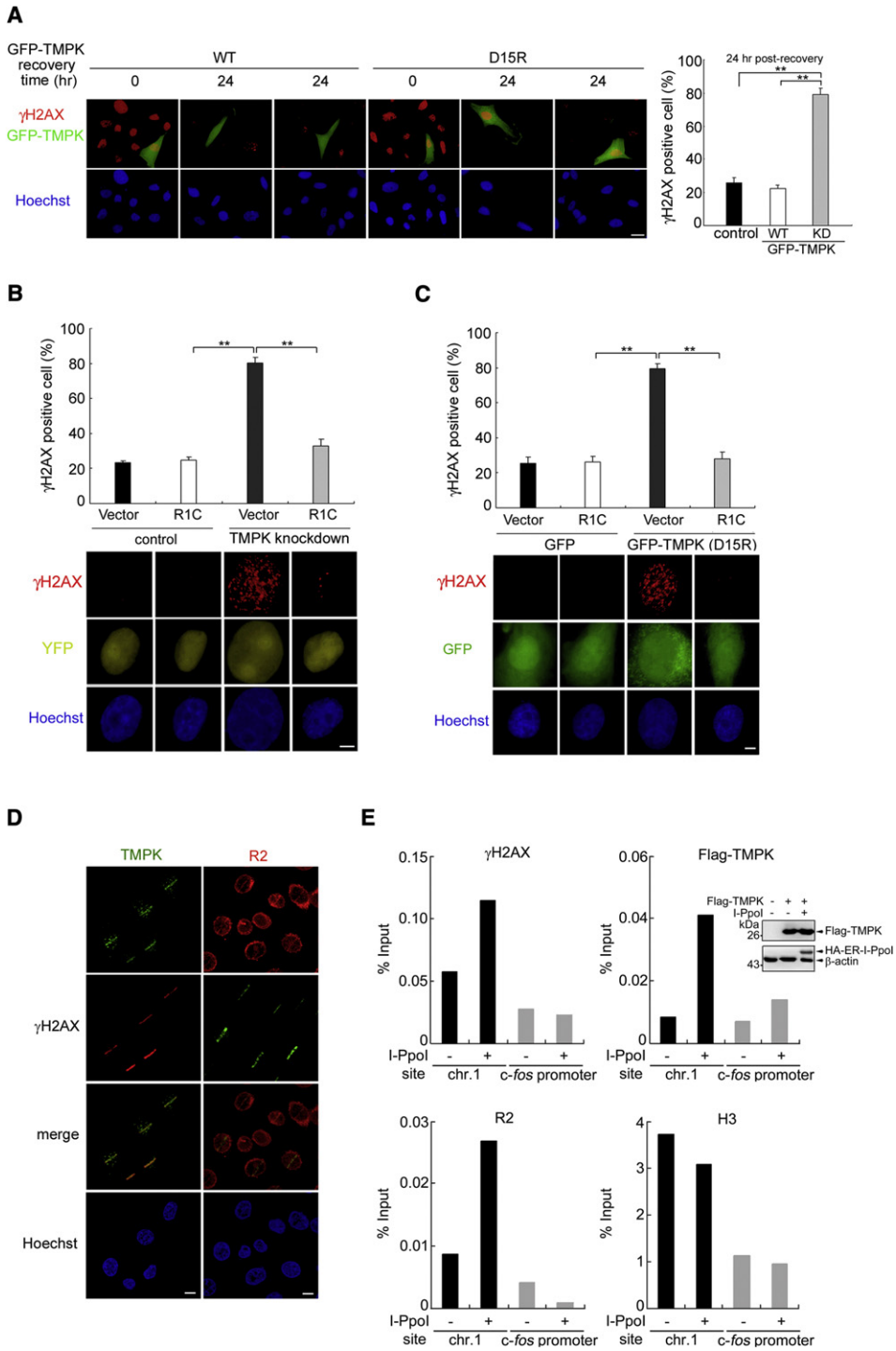

Figure 2. Coordination of TMPK with RNR at Sites of DNA Damage during Repair

(A) MDA-MB231 cells were transfected with pEGFP-TMPK (WT or D15R) followed by doxorubicin exposure and recovered as described in the legend to Figure 1B. Cells were fixed for γH2AX staining (scale bar, 20 μm). For each experiment, 100 GFP-positive cells were counted.

(B) Cells without and with stable TMPK shRNA expression were transfected with pCMV2-YFP-Nuc (vector) or pCMV2-YFP-Nuc-R1C (R1C) plasmid (scale bar, 5 μm).

(C) Cells were transfected with pEGFP-TMPK (D15R) in combination with pCMV2-YFP-Nuc-R1C (R1C) plasmid as indicated. Following doxorubicin exposure and recovery for 24 hr, these cells were analyzed by γH2AX foci staining (scale bar, 10 μm). For each experiment, 100 YFP- or GFP-positive cells were counted. All error bars represent SD (n = 3).

(D) HeLa cells were plated on glasses-like dishes for laser-micro-irradiation. After recovery for 5 min, cells were fixed for γH2AX, TMPK, and R2 immunofluorescence staining (scale bar, 10 μm).

a similar manner to that which occurred with MDA-MB231 cells, TMPK knockdown caused doxorubicin-induced γH2AX foci to persist in MCF-7 cells. In contrast, DNA repair was unaffected by TMPK knockdown in H184B5F5/M10 and MCF10A cells (Figure 3A). We compared expression levels of R2, p53R2, TMPK, and dUTPase during recovery from DNA damage in MDA-MB231, MCF-7, H184B5F5/M10, and MCF10A cells (Figure 3B). Expression of the R2 subunit of RNR and dUTPase was much higher in MCF-7 cells than in H184B5F5/M10 and MCF10A cells. In MDA-MB231 cells, the levels of R2 and dUTPase increased concomitantly between 12 and 48 hr after doxorubicin exposure, which contrasted with their continuous decline in H184B5F5/M10 and MCF10A cells. Expression of p53R2 was very low in MDA-MB231 cells because of the p53 functional deficiency. In MCF-7, H184B5F5/M10, and MCF10A cells, the expression of p53R2 increased during recovery from doxorubicin exposure (between 24 and 48 hr). Flow cytometry analysis demonstrated that the G0/G1-phase cell populations in H184B5F5/M10 and MCF10A cells were 2–3-fold higher than those in MDA-MB231 and MCF-7 cells during recovery from DNA damage (Figure 3C). The larger S and G2/M cell populations in MDA-MB231 and MCF-7 cells during recovery indicate a lower stringency of checkpoint control in response to genome insults in these cells. It has been shown that G2/M synchronization by nocodazole treatment promotes HR (Katada et al., 2012). We further treated H184B5F5/M10 cells with nocodazole overnight to block mitotic progression, which increased the G2/M cell population as confirmed by flow cytometry (Figure 3D and Figure S3A). It was noted that the level of R2 was decreased in nocodazole-treated cells (Figure 3D) probably because of mitotic degradation (Chabes et al., 2003). After washing out nocodazole, the released cells at 24 hr had less than 20% of G2/M population (Figure S3). Very differently, the nocodazole released cells after doxorubicin exposure, and recovery at 24 hr still contained more than 50% G2/M population. Under this situation, these H184B5F5/M10 cells with increased G2/M cell numbers were still insensitive to TMPK knockdown during DNA repair (Figure 3E). Therefore, the lack of TMPK sensitivity in DNA repair in H184B5F5/M10 cells is unlikely due to less HR-permissive cells after doxorubicin exposure. We also compared the cell growth rates of these four cell lines. Under our experimental conditions, H184B5F5/M10 and MCF10A cells proliferated more rapidly than did MDA-MB231 and MCF-7 cells (Figure S3B). These results indicate that the differences in sensitivity to TMPK knockdown in the context of DNA repair efficiency are not correlated with the proliferation rate of the cell lines nor are they determined by the cell cycle distribution.

Given that RNR at sites of DNA damage contributes to the incorporation of dUTP in TMPK-knockdown MDA-MB231 cells, we tested whether elevation of R2 levels in tumor cells is a major factor determining the requirement for TMPK during DNA repair. MCF-7 cells express high levels of R2 and contain p53R2 at a level similar to that found in H184B5F5/M10 and MCF10A cells. In this context, we reduced the R2 level in MCF-7 cells to a level that was similar to that found in H184B5F5/M10 cells by transfection with siRNA and then exposed the cells to doxorubicin (Figure 4A). Flow cytometric analysis showed that a reduction in R2 levels by siRNA transfection alone or in combination with TMPK knockdown did not decrease the S/G2 cell population significantly (Figure 4B and Figure S4A). At 24 hr after recovery, γH2AX foci were still present in cells transfected with either R2 siRNA alone or R2 and TMPK siRNAs (data not shown). However, at 36 hr after recovery, it was found that a reduction in R2 expression rescued DNA repair in TMPK-knockdown MCF-7 cells (Figures 4C and 4D). Therefore, it would seem that the level of R2 is able to determine whether TMPK knockdown affects DNA repair.

We next selected a MCF10A cell clone with constitutive elevation of R2 expression using a lentiviral vector of mCherry-R2. This cell line was then subjected to TMPK knockdown and DNA repair analysis (Figure 4E). The results showed that overexpression of R2 in combination with TMPK-knockdown caused Rad 51 foci to persist at 24 hr after recovery in MCF10A cells (Figure 4F and Figure S4B) and also promoted XRCC1 foci formation (Figure S4C). As a consequence of these changes, such cells remained γH2AX positive (Figure 4G). The cell-cycle analysis of these cells showed that constitutive elevation of R2 expression did not increase S/G2 cell population (Figure S4D). Thus, elevation of R2 expression renders DNA repair in MCF10A cells sensitive to TMPK knockdown without altering cell-cycle distribution. Taken together, the above results demonstrate that an increase in the level of R2 and the recruitment of RNR to sites of DNA damage are the key factors that make TMPK a critical factor for DNA repair in tumor cells. In other words, increased RNR activity at sites of DNA damage in tumor cells needs to be functionally coordinated with the presence of TMPK to prevent dUTP incorporation.

Screening and Characterization of YMU1 as an hTMPK Inhibitor

On the basis of the fact that there is a specific functional requirement for TMPK during DNA repair in tumor cells that have elevated levels of R2 expression, we next searched for inhibitors of hTMPK that might be useful as an approach to selectively sensitizing tumor cells to doxorubicin. Using a luciferase-coupled TMPK assay (Hu and Chang, 2010) in which the inhibition of TMPK leaves more ATP available for the generation of luminescence by luciferase (Figure 5A), we screened a library of 21,120 small molecules and identified one highly potent compound, YMU1, the structure of which is shown in Figure 5B. An enzymatic assay confirmed that YMU1 is an hTMPK inhibitor with an IC_{50} of 0.61 ± 0.02 μM (Figure 5C) and that the compound has no inhibitory effect on the activity of purified thymidine kinase 1 (TK1) (Figure 5D). To investigate the structure-activity relationship, two fragments of YMU1 (D3 and D6), one isomer

(E) HEK293T cells were transfected with HA-ER-I-PpoI or empty vector together with pFlag-TMPK. After 18 hr, cells were collected and used for qChIP analysis with the indicated antibody using a primer pair adjacent to the I-PpoI cleavage site (280 bp 5′ to the I-PpoI cut site) in chromosome 1. The c-*fos* promoter serves as a genomic DNA control because it has no I-PpoI site. Data were normalized by IgG control and calculated relative to total input (percentage) from two independent experiments.
See also Figure S2.

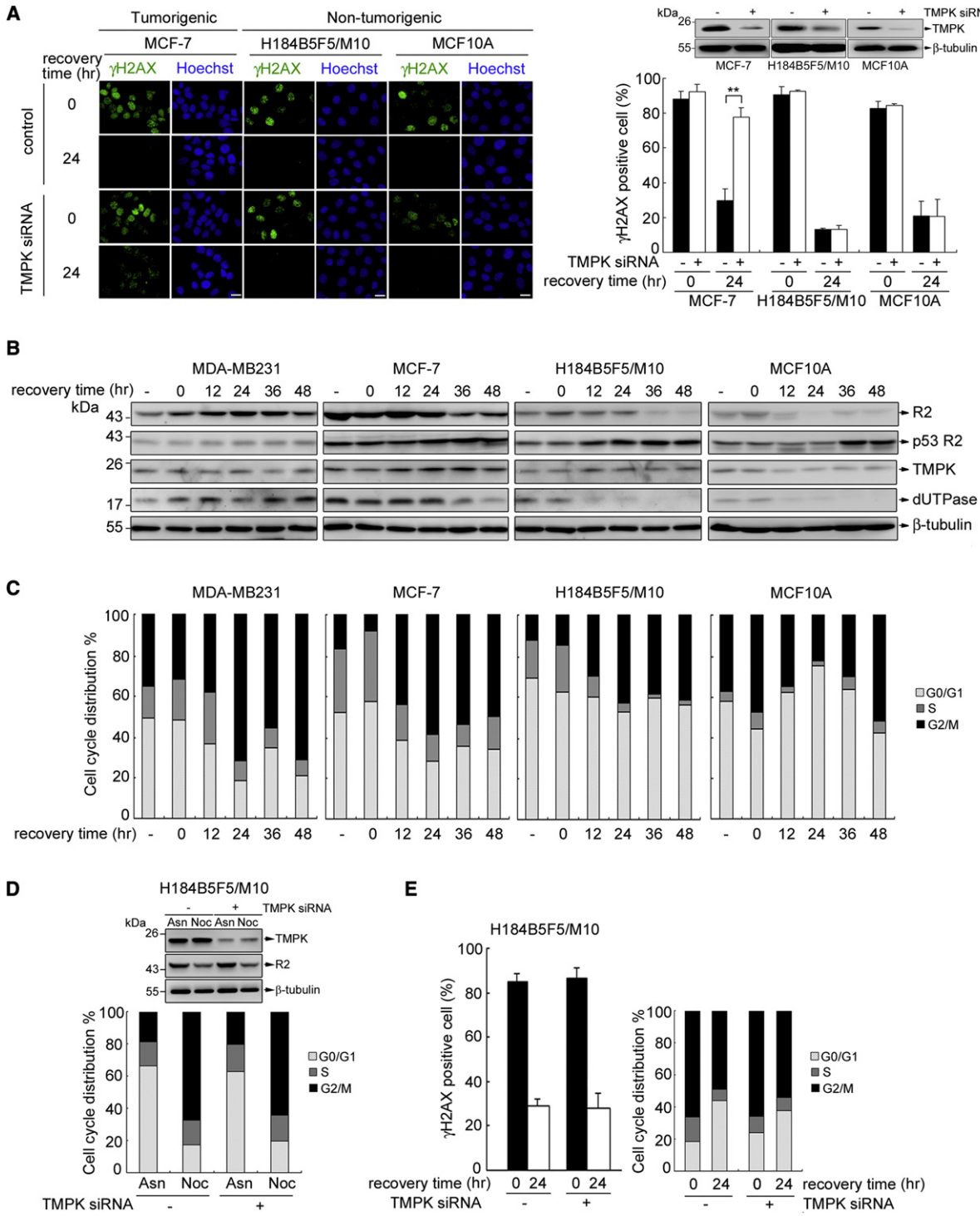

Figure 3. Correlation of the Cellular Level of R2 with the Requirement for TMPK during DNA Repair

(A) MCF-7, H184B5F5/M10, and MCF-10A cells were transfected with TMPK siRNA. These cells were exposed to doxorubicin and recovered for γH2AX foci staining (scale bar, 20 μm), as described in the legend to Figure 1B. For each experiment, 100 cells were counted.

(B and C) Cells were exposed to doxorubicin and then underwent recovery. Cells were harvested at the indicated time points for Western blot (B) and flow cytometry (C) analysis.

(D and E) H184B5F5/M10 cells were transfected with TMPK siRNA for 36 hr and then treated with 500 ng/ml of nocodazole overnight. (D) A proportion of cells were harvested for Western blot and FACS analysis. The rest of cells were exposed to doxorubicin (0.2 μM) for 2 hr and allowed to recover with fresh medium. (E) At the indicated time of recovery, cells were fixed for γH2AX foci staining and FACS analysis. For each experiment, 200 cells were counted.

See also Figure S3.

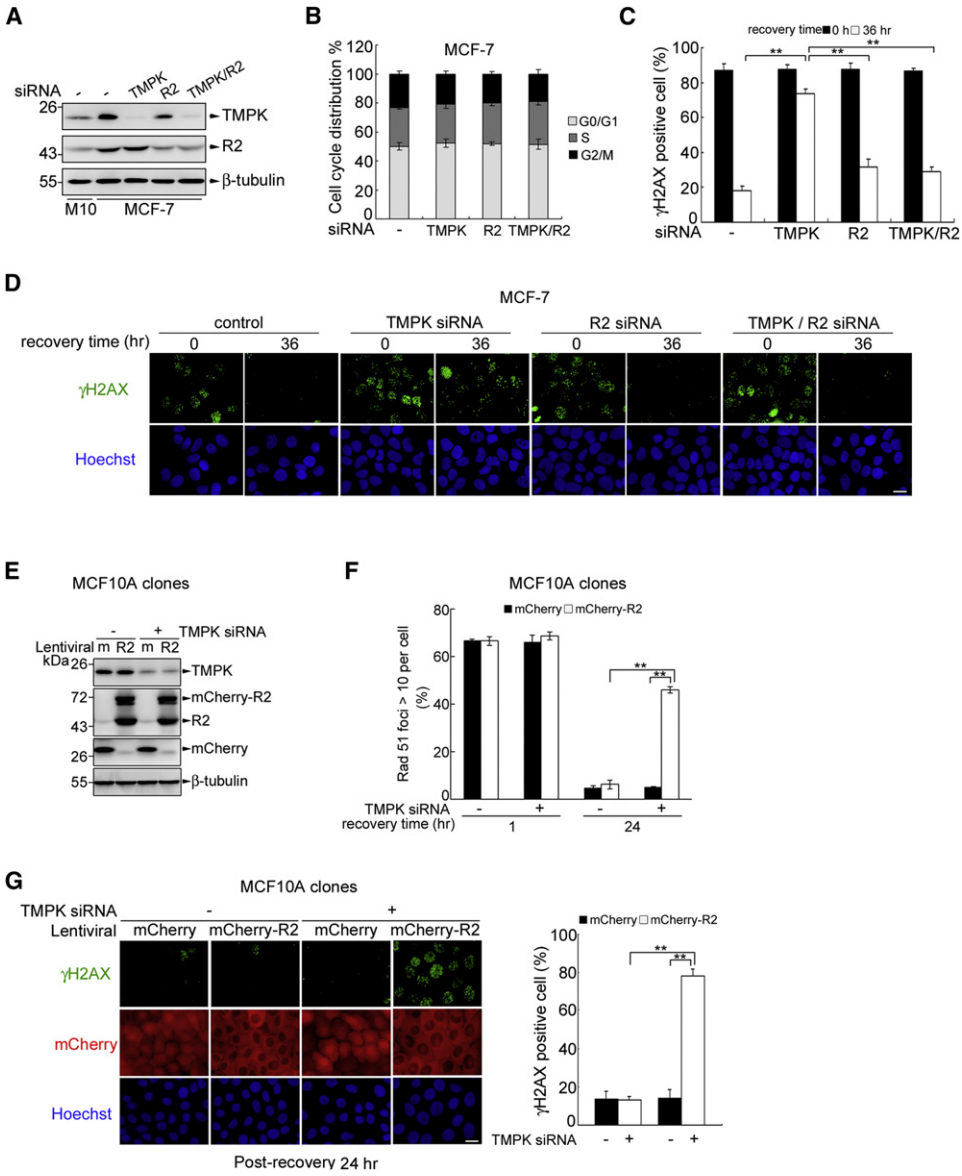

Figure 4. Effect of R2 Expression Level on DNA Repair in Response to TMPK Knockdown

(A and B) MCF-7 cells were transfected with siRNA of TMPK, R2, or TMPK/R2 for 36 hr. A proportion of cells were harvested for Western blot (A) and FACS (B) analysis. The rest of cells were exposed to doxorubicin (0.1 μM) for 4 hr.

(C and D) Cells at the indicated time points were analyzed by γH2AX foci staining, and 150 cells were counted to indicate the percentage of γH2AX foci-positive cells, and representative images are shown (D) (scale bar, 20 μm).

(E–G) MCF10A clones stably expressing mCherry or mCherry-R2 were selected and transfected with TMPK siRNA for 36 hr. (E) Western blot analysis of the cells. (F and G) After exposure to doxorubicin and recovery at indicated time, cells were fixed for Rad 51 (F) and γH2AX foci staining (G) (scale bar, 20 μm). For each experiment in (F) and (G), more than 150 cells were counted. All error bars represent SD (n = 3).

See also Figure S4.

of YMU1 (D7), and a benzeneisothiazolone derivative of YMU1 (D8) were synthesized (Figure 5B). Neither D6 (the piperazine fragment of YMU1) nor D7 (the O-alkylation isomer of YMU1) showed any inhibition of hTMPK, whereas D3 (the pyridinoisothiazolone fragment of YMU1) exhibited weak inhibitory activity. Interestingly and in contrast to the above three compounds, the benzeneisothiazolone derivative D8 also displayed considerable inhibitory activity.

The mode of inhibition of YMU1 was determined by preincubating different concentrations of YMU1 with purified hTMPK protein and measuring the initial velocity in a conventional TMPK assay. The K_m and V_{max} values were determined by nonlinear regression analysis and are summarized in Table 1. Preincubation with YMU1 reduced the V_{max} of hTMPK in a concentration-dependent manner while increasing the *K*m for ATP without significantly affecting the *K*m for TMP. The inhibition

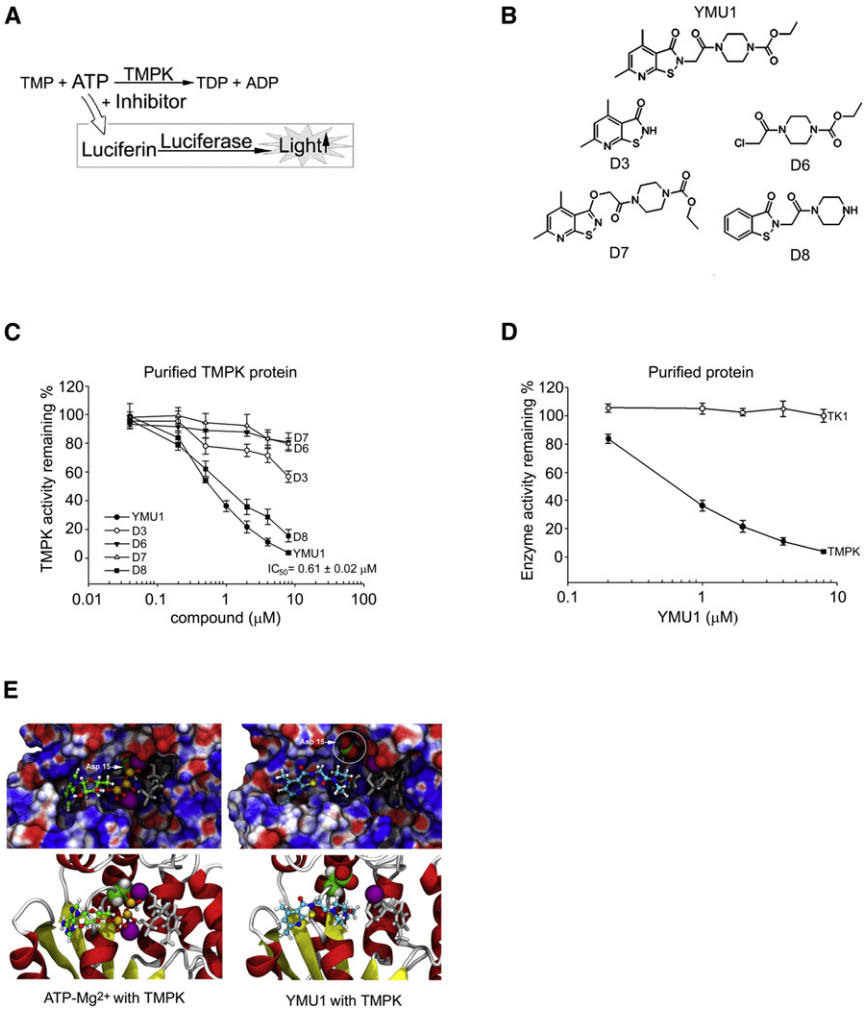

Figure 5. Identification of an hTMPK Inhibitor

(A) A screen for hTMPK inhibitors by luciferase-coupled assay.

(B) The chemical structures of YMU1 and related molecules. The chemical synthesis scheme of YMU1 and related compounds is presented in Supplemental Experimental Procedures.

(C) Effect of YMU1 and derivative compounds on hTMPK inhibition. Activity analysis of purified hTMPK protein (0.5 μg) after 10 min of preincubation with compounds using luciferase-coupled TMPK analysis.

(D) Activity of purified TMPK (0.5 μg) and GST-hTK1 protein (5 μg) that had been preincubated with YMU1 for 10 min prior to the activity assay. All error bars represent SD (n = 4).

(E) Molecular models of the TMPK-YMU1 complex. Left panel: TMPK/ATP/Mg^{2+}; right panel: TMPK/YMU1. The TMPK is represented as surface electrostatic potential (upper) and a structural ribbon (lower). ATP and YMU1 are shown as green and blue stick models, respectively, with colored atoms (O, red; S, yellow; P, orange). TMP is shown as a white backbone and Mg^{2+} is shown in purple. The arrow indicates the position of Asp15.

See also Figure S5.

constant (K_i) was determined by kinetic analysis to be 0.22 ± 0.03 μM (Table 1). Molecular docking studies were performed to analyze the mechanism of inhibition of TMPK by YMU1. The results of the kinetic studies suggest that YMU1 probably affects the ATP-binding pocket of TMPK. Using the crystal structure of TMPK with TMP and Mg^{+2}, it was possible to dock YMU1 into the ATP pocket. During this docking complex, YMU1 prevents one Mg^{+2} ion from interacting with the Asp15 residue in the catalytic domain (Figure 5E). Because a mutation of Asp15 to Arg is known to abrogate TMPK catalytic function, it is possible that preincubation of TMPK with YMU1 hinders the functionality of the Mg^{+2} ion pointing toward the catalytic Asp15 residue in the ATP pocket, thereby reducing catalytic efficiency. The docking of D3, D6, and D7 at these sites was found to not prevent Asp15 from interacting with Mg^{+2} and therefore suggests why these compounds do not inhibit TMPK.

YMU1 reduced cellular dTTP levels by about 30%–40% (Figure S5). Transfection of cells with siRNA to suppress TMPK expression reduced the size of the dTTP pool to a similar extent. YMU1 treatment did not cause any further reduction of the dTTP pool in TMPK-knockdown cells. The levels of dATP, dCTP, and dGTP were unaltered in both YMU1-treated and TMPK-knockdown cells (Figure S5). These results indicate that YMU1 specifically reduces dTTP level and that the ability of YMU1 to reduce dTTP level is dependent on the presence of TMPK in the cells.

YMU1 Is Not Toxic to the Genome and, Similar to TMPK Silencing, Impairs DSB Repair

Inhibition of TS by FdUrd causes genome toxicity (Longley et al., 2003). Given the shared role of TMPK and TS in dTTP synthesis, we next compared the effects of blocking TMPK and TS on the induction of DNA damage of either shRNA interference or inhibitor treatment. As indicated by γH2AX staining, TS silencing and FdUrd treatment induced severe DNA damage, whereas TMPK silencing and YMU1 treatment did not (Figure 6A). We also compared the effects of YMU1 and FdUrd on the viability of non-tumorigenic H184B5F5/M10 and MCF10A mammary cycling cells and MCF-7 and HCT-116 $p53^{-/-}$ tumor cells. A colony assay indicated that FdUrd, but not YMU1, caused cell death in all of these cells (Figure 6B). Therefore, unlike blocking TS, targeting TMPK does not, on its own, cause genome toxicity or cytotoxicity. We also performed MTS assays using human primary bone marrow mesenchymal stem cells (HBMSC), renal cortical epithelial cells (HRCE), mammary epithelial cells (HMEC), and breast tumor MDA-MB231 cells and found that YMU1 had very little effect on cell growth (Figure S6A).

We next examined the effect of YMU1 on the repair of doxorubicin-induced DNA lesions in MDA-MB231 and H184B5F5/M10 cells after recovery from low-dose doxorubicin treatment. Notably, in H184B5F5/M10 cells, YMU1 treatment did not affect the numbers of DNA lesions formed, as determined by γH2AX focus staining. Similar to TMPK knockdown, pretreatment with

Table 1. Effect of YMU1 on the Kinetic Parameters of Purified Human Thymidylate Kinase

YMU1 compound (μM)	*K*m for TMP (μM)	*V*max (nmol/min/mg)	*K*i (μM)
0	28.7 ± 2.4	376.6 ± 14.5	0.22 ± 0.03
0.125	26.5 ± 2.8	258.9 ± 12.4	
0.25	27.5 ± 4.0	180.6 ± 11.8	
0.5	28.0 ± 4.3	91.8 ± 6.4	
YMU1 compound (μM)	*K*m for ATP (μM)	*V*max (nmol/min/mg)	*K*i (μM)
0	25.7 ± 2.4	367.2 ± 9.4	0.18 ± 0.06
0.25	29.5 ± 5.6	212.0 ± 10.3	
0.5	41.2 ± 7.4	94.8 ± 6.9	
1	43.8 ± 3.3	55.7 ± 1.3	

For the *K*i value determination, YMU1 at the indicated concentration was preincubated with 0.5 μg of purified hTMPK protein for 10 min, and the initial velocity of the TMPK reaction was measured at different concentrations of TMP (2–200 μM) in the presence of ATP (1 mM) or at different concentrations of ATP (5–1000 μM) in the presence of TMP (200 μM) using a NADH-coupled TMPK assay. Data represent mean ± SD, n = 4. Data obtained from the nonlinear regression analysis were used to calculate the *K*m and *V*max. The *K*i value of YMU1 for hTMPK was calculated from the equation of $K_i = [I] / (V_{max} / V_{max}' - 1)$, where [I] and *V*max' are the YMU1 compound concentration and maximal velocity in the presence of YMU1, respectively. The *K*i value represents a mean value derived from three different YMU1 concentrations.

YMU1 caused over 70% of the MDA-MB231 cells to remain γH2AX positive at 48 hr after doxorubicin exposure (Figure 6C) but did not affect cell-cycle progression during recovery (Figure S6B). Comet assay analysis further confirmed that YMU1 treatment impaired DNA repair in MDA-MB231 cells exposed to doxorubicin (Figure S6C). Overexpression of GFP-TMPK rendered MDA-MB231 cells resistant to the YMU1-mediated persistence of DNA lesions, supporting the idea that YMU1 exerts its effect by targeting TMPK (Figure 6D). Overexpression of TMPK(WT) in YMU1-treated HeLa cells with high transfection efficiency restored the level of dTTP (Figure 6E). Similar to siRNA knockdown, YMU1 treatment also led to the persistence of Rad 51 foci and an increase in XRCC1 focus formation that was abolished by UNG depletion (Figures 6F–6H). The inhibitory effect of YMU1 on DNA repair was reversed by overexpression of either dUTPase or a 90-amino-acid C-terminal fragment of the R1 subunit of RNR (Figures 6I and 6J), which confirms that the effect of YMU1 on repair toxicity is dependent on the amount of dUTP present at damage sites and recruitment of RNR to the damage sites. Furthermore, YMU did not inhibit dUTPase in vitro (Figure S6D).

YMU1 Sensitizes Malignant Tumor Cells to Doxorubicin In Vitro and In Vivo

Next, various human cancer cell lines were treated with YMU1, the D6 compound, or the D7 compound for 72 hr to test the potential of TMPK inhibition in relation to doxorubicin sensitization. After exposure to different concentration of doxorubicin for 4 hr, cells were subjected to viability analysis, and the IC_{50} value for doxorubicin for each cell line was determined (Figure 7A). YMU1 treatment increased doxorubicin sensitivity in HT-29, HCT-116 $p53^{+/+}$, HCT-116 $p53^{-/-}$, H1299, CL1-0, U2OS, MDA-MB231, MDA-MB468, and SaoS2 cells by 3–35-fold. Two HR defective cell lines, HCC1937 and Capan1 deficient in BRCA1 and 2 (Nagaraju and Scully, 2007; Powell and Kachnic, 2003), were not responsive to YMU1 treatment. YMU1 had little effect on the doxorubicin IC_{50} of mammary cycling H184B5F5/M10 and MCF10A cells, IMR-90 embryonic lung fibroblasts, and primary HMEC and HRCE. The inactive compounds D6 and D7 shown in Figures 5B and 5C did not cause doxorubicin sensitization in any of these cell lines. Western blot analysis indicated that all tumor cells that were sensitized by YMU1 treatment showed elevated levels of R2 expression after doxorubicin exposure (Figure 7B). A colony assay further showed that YMU1 markedly enhanced the lethal effects of doxorubicin (0.1 μM) in HCT-116 and MCF-7 cells (Figure 7C). TMPK knockdown was unable to further sensitize YMU-treated MDA-MB231 cells to doxorubicin (Figure S7A), suggesting that the specificity of YMU1 in terms of doxorubicin sensitization is related to the drug targeting TMPK. Overexpression of wild-type dUTPase prevented YMU1/doxorubicin-induced apoptosis, as revealed by reduced Annexin V staining (Figure S7B).

We also used an in vivo xenograft model using HCT-116 $p53^{-/-}$ cells inoculated into nude mice to examine the effect of YMU1 as an adjuvant on sensitization to low-dose doxorubicin treatment. Tumor growth rates in mice treated with either doxorubicin alone or YMU1 alone were similar to those in control animals. In contrast, the growth of tumors was much slower in the YMU1/doxorubicin double-treated mice (Figure 7D). Two weeks after the last injections were administered, mice were sacrificed, and tumor weights measured. We observed excellent tumor suppression in the YMU1/doxorubicin double-treated mice, with an average tumor size that was 25% of the control mice (Figure 7E). Under these experimental conditions, the tumor sizes remained similar in mice treated with doxorubicin alone or YMU1 alone. In agreement with these tumor-growth data, the tumor proliferation index, determined by measuring Ki 67 immunostaining, was clearly reduced in the nude mice treated with both YMU1 and doxorubicin (Figure 7F). We also treated mice bearing larger tumors of various different sizes formed by HCT-116 $p53^{+/+}$ cell implantation. The results consistently showed that the joint therapy of YMU1 with doxorubicin significantly suppressed tumor growth (Figure S7C). Furthermore, Balb/c mice were treated with YMU1 for 4 weeks, using a 2-fold higher dose regimen than that used in the tumor xenograft study. YMU1 treatment did not alter mouse body weight over the course of 4 weeks. Additionally, the weights of various organs (heart, liver, spleen, lungs, and kidneys) and the results of hematological analyses of the YMU1-treated mice were similar to those of the control mice (Table S1). Taken together, these results indicate that, on its own, YMU1 seems to produce no obvious toxic effects in normal mice and that, in conjunction with low-dose doxorubicin, YMU1 suppresses tumor growth in mice.

DISCUSSION

In this study, we provide insights into the functional requirement of TMPK for DNA repair in tumor cells. Our results suggest that RNR at the sites of DNA damage may be responsible for the

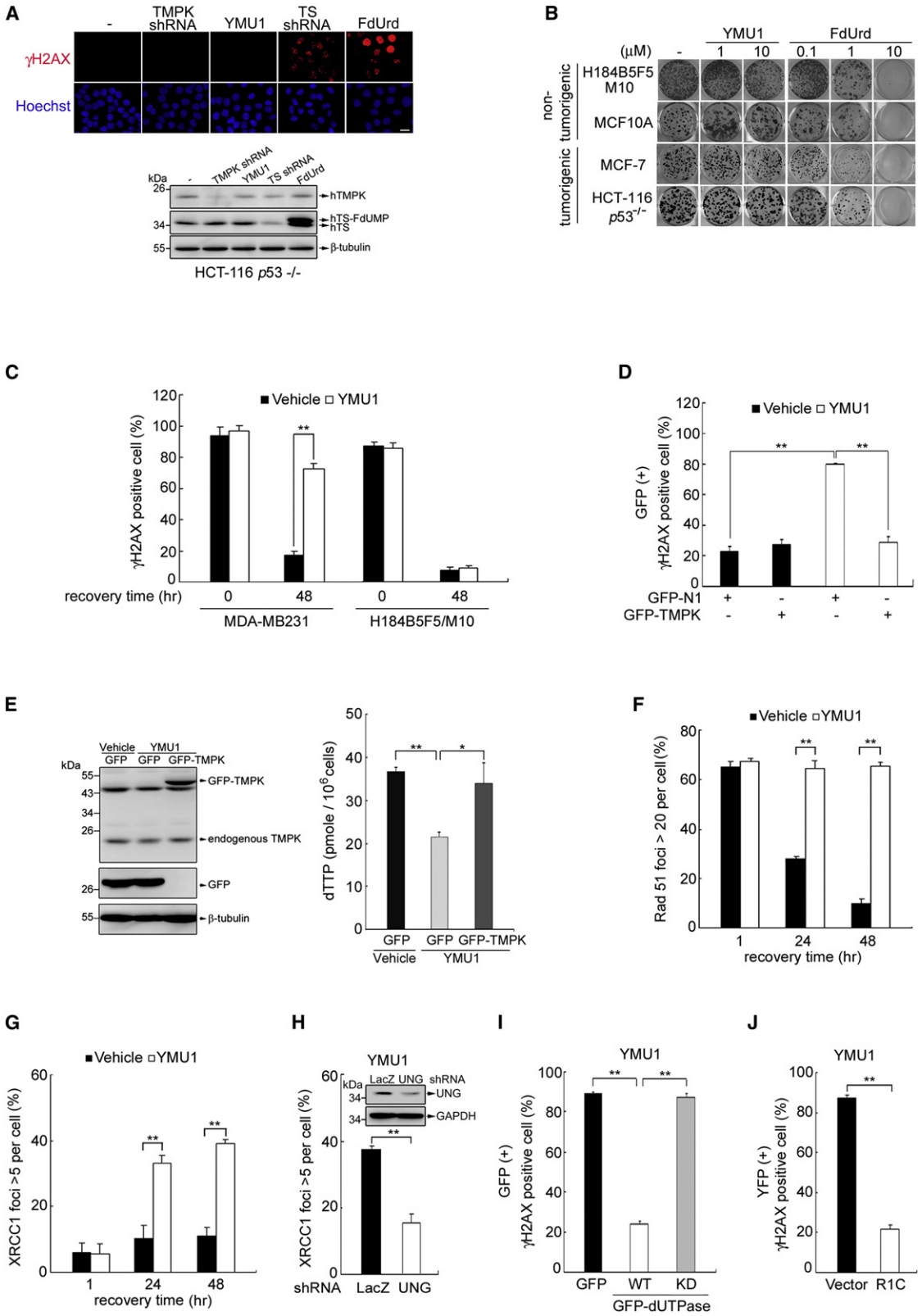

Figure 6. Effect of YMU1 on Genomic Toxicity and DNA Repair

(A) HCT-116 *p53*$^{-/-}$ cells were infected with lentivirus of TMPK or TS shRNA. In parallel, cells were treated with YMU1 (2 μM) for 2 days, or 5-fluoro-2′deoxyuridine (FdUrd, 2 μM) for 1 day. These cells were fixed for γH2AX foci staining (scale bar, 20 μm) and Western blot analysis.

site-specific production of dUTP. Theoretically, the formation of dUMP by dUTPase and the TS-mediated reaction that converts dUMP to dTMP should limit the amount of cellular dUTP. However, blocking TMPK function causes the incorporation of dUTP during DNA repair in tumor cells, a response that is dependent on the recruitment of RNR to the sites of damage; these findings reveal the physiological complexity of the site-specific production of dUTP by the RNR. We propose that blocking TMPK reduces the rate of dTTP formation at sites of damage, whereas increased RNR function is able to increase site-specific dUTP production. Because HR requires the incorporation of more than 10,000 dNTPs to repair each DSB, the probability of dUTP incorporation is increased, which leads to persistent lesions. Given that RNR activity is elevated in tumor cells after DNA damage, blocking TMPK function sensitizes tumor cells to doxorubicin (Figure 7G). In agreement with our hypothesis, we found that HR-defective tumor cells were not responsive to the blocking of TMPK during the repair of doxorubicin-induced lesions.

Expression of the R2 subunit of RNR and dUTPase is cell-cycle regulated, peaking during the S and G2/M phases (Ladner and Caradonna, 1997; Nordlund and Reichard, 2006). Malignant tumor cells have cell-cycle checkpoint defects (Kastan and Bartek, 2004). Therefore, tumor cells recovering from low dosage of DNA damage have greater S-phase and G2/M-phase populations, during which HR-mediated DNA repair can take place with an increase of R2 expression, and this has a requirement for TMPK functionality. In contrast, the S-phase population is reduced in nontumorigenic cycling cells during recovery from DNA damage because of the presence of an intact checkpoint control. As a result, these cycling cells express even lower amounts of R2, which may further limit dUDP formation.

Because nontumorigenic cycling cells after DNA damage have fewer S/G2 cells, the question is whether the R2 level or cell-cycle phase permissive for HR determines the requirement for TMPK during DNA repair. In this study, we provide evidence that the manipulation of increasing the G2/M-phase cell does not make nontumorigenic cycling cells sensitive to TMPK knockdown during DNA repair, whereas enforced expression of R2 does. Because MCF10A and H184B5F5/M10 nontumorigenic cells do not grow any slower than MDA-MB231 and MCF7 cells, these results led us to conclude that the elevation of R2 after DNA damage is a key factor affecting the requirement for TMPK in the repair of doxorubicin-induced DNA lesions. In view of the elevation of R2 expression in tumor cells being associated with their continued S/G2 progression after low dosage of DNA damage, checkpoint defects in tumor cells would seem to be closely related to the requirement for TMPK during DNA repair. If so, it is possible that patients with tumor containing a high R2/TMPK ratio should be more responsive to doxorubicin therapy. Because expression levels of R2 and TMPK are controlled by transcription and proteolysis, it is necessary to generate new TMPK antibody applicable for immunohistochemical analysis. In addition, such an analysis in tumor samples from patients before chemotherapy may not be informative for predicting response, because some tumors do not express high levels of R2 until with genotoxic treatment.

Notably, normal cycling cells contain appreciable levels of the p53R2 subunit, which is capable of forming functional RNR at sites of DNA damage. This opens up the question as to why DNA repair in normal cycling cells is not affected by TMPK knockdown. One plausible explanation is that R2 has a 4.7-fold higher binding affinity for R1 than does p53R2 (Shao et al., 2004). It is possible that the low affinity of p53R2 for the R1 subunit reduces the efficiency of the RNR and minimizes the site-specific production of dUTP in normal cycling cells. This would thereby abolish the functional requirement for TMPK at sites of DNA damage repair. Indeed, enforced expression of R2 in normal cycling cells causes an impairment of DNA repair in TMPK knockdown cells, which supports our conclusion that DNA repair toxicity induced by TMPK knockdown is linked to an increase in RNR functionality. Expression of R2 and p53R2 has been found to be upregulated in many types of cancer cells in patients (Yanamoto et al., 2003; Zhang et al., 2009). Tumors form in transgenic mice overexpressing R2 or p53R2 in the lungs (Xu et al., 2008). Whether the side effects of dUTP formation by RNR at sites of DNA damage are related to their oncogenic potential remains to be investigated. Nevertheless, it is noteworthy that p53R2 predicts better survival in patients with colorectal cancer, whereas R2 level is correlated with increased aggressiveness of tumors (Liu et al., 2011). Expression of an RNR mutant defective in dATP feedback inhibition in yeast causes elevation of dNTP, which is accompanied by an inhibition of cell-cycle progression and the DNA damage

(B) H184B5F5/M10 cells were seeded at 5,000 cells/100 mm-dish. MCF10A, MCF-7, and HCT-116 $p53^{-/-}$ cells were seeded onto 6-well plates at the density of 600 cells/well. Following an overnight incubation, the cells were treated with YMU1 or FdUrd at the indicated concentration twice a week. After 14 days, colonies were fixed and stained by crystal violet.
(C) Cells were pretreated with vehicle or YMU1 (2 μM) for 72 hr and then exposed to doxorubicin (0.1 μM) for 4 hr. After replacing with fresh medium, the cells were fixed for γH2AX foci staining at the indicated time.
(D) MDA-MB231 cells after vehicle or YMU1 (2 μM) treatment for 48 hr were transfected with pEGFP-N1or pEGFP-TMPK plasmid. After incubation overnight, the cells were exposed to doxorubicin and recovered as described above. At 24 hr, the cells were analyzed by γH2AX foci staining.
(E) HeLa cells were treated with vehicle or YMU1 (10 μM) for 24 hr and transfected with GFP or GFP-TMPK (WT). After 48 hr, cells were harvested for Western blot and dTTP level analysis.
(F and G) MDA-MB231 cells pretreated with vehicle or YMU1 (2 μM) for 72 hr, then exposed to doxorubicin, followed by recovery as described above for Rad51 foci (F) and XRCC1 foci (G) staining.
(H) Cells were infected with lentivirus carrying LacZ or UNG shRNA for 8 hr. After exposure to doxorubicin and recovery for 24 hr, the cells were fixed for XRCC1 foci staining. Inset indicates the levels of UNG protein by Western blotting analysis. For each experiment in (C–G), more than 100 of the cells were counted.
(I and J) MDA-MB231 cells pretreated with YMU1 (2 μM) for 48 hr were transfected with indicated plasmid or shRNA. After overnight incubation, the cells were exposed to doxorubicin and then underwent recovery as described above. After 24 hr, the cells were analyzed by γH2AX foci staining. For each experiment, 100 GFP-positive or YFP-positive cells were counted. Error bars represent SD (n = 3).
See also Figure S6.

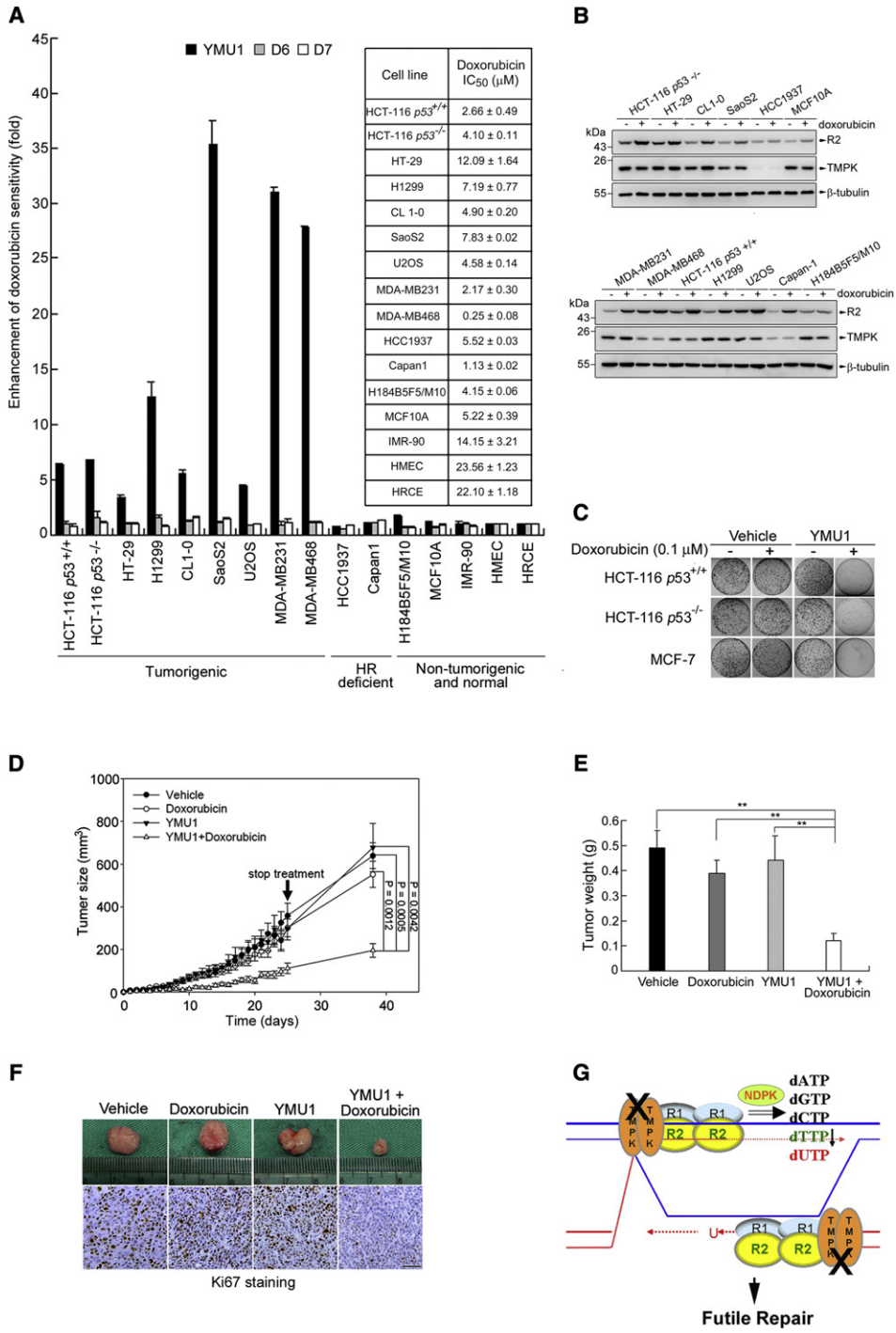

Figure 7. In Vitro and In Vivo Effect of YMU1 on Doxorubicin Sensitization

(A) Various cell lines were pretreated with vehicle, YMU1, D6, or D7 for 3 days. D6 and D7 are inactive molecules shown in Figure 5B. The cells were exposed to different concentration of doxorubicin for 4 hr. After 48 hr of recovery from doxorubicin exposure, the cells were subjected to MTS assay in quadruplicate, and the IC_{50} for doxorubicin was determined. The enhancement (fold) of doxorubicin sensitivity for each cell line was calculated. Error bars represent SD (n = 3). The inset indicates the IC_{50} value of doxorubicin for each cell line.

(B) Cells (1×10^6) were plated in a 60 mm dish. After an overnight incubation, cells were exposed to without or with doxorubicin (0.5 μM) for 4 hr and allowed to recover in fresh medium for 16 hr. The cells were then harvested for western blot analysis.

(C) After treatment with vehicle or YMU1 for 72 hr, the cells were exposed to 0.1 μM doxorubicin for 4 hr and then seeded onto a 100 mm-dish at 5,000 cells/dish. Following an overnight incubation, the cells were refreshed with growth medium for 14 days of incubation for colony formation.

(D) HCT-116 $p53^{-/-}$ cells were subcutaneously implanted in the right flank of Balb/c nude mice. The arrow indicated the time when drug treatment was stopped. The tumor volume was determined.

checkpoint (Chabes and Stillman, 2007). Whether this phenomenon involves dUTP formation is also worthy of investigation.

Our findings suggest that a tumor context with checkpoint defect to allow an R2 elevation after DNA damage makes TMPK an Achilles heel for doxorubicin sensitization. To substantiate this idea, we identified a TMPK inhibitor, YMU1. We found that YMU1 increases doxorubicin sensitivity in a variety of tumor cells. The mice therapy experiments also prove that YMU1 in conjunction with sublethal dose of doxorubicin greatly suppresses tumor growth. Most importantly, YMU1 on its own did not produce genotoxic effects in cells or mice. Although TS inhibitors and other nucleotide metabolite blockers have also been used as chemosensitizers (Garg et al., 2010), it should be emphasized that these anticancer agents are toxic to the genomic DNA in normal cycling cells as well. Their therapeutic effect stems solely from their ability to cause extensive DNA damage by which they produce nonspecific toxicity. We propose that the therapeutic advantage of a TMPK inhibitor over these conventional compounds is the fact that it shows a specific toxicity toward malignant cells that contain DNA lesions with increased levels of R2 expression. Here, we proposed that YMU1 is a promising lead compound for the development of a very mild chemosensitization regimen that primes tumor cells and makes them sensitive to sublethal doses of doxorubicin; the result should involve lethality that targets these tumor cells while causing minimal side effects with respect to normal cycling cells.

EXPERIMENTAL PROCEDURES

Chemistry

Compound YMU1, ethyl 4-(2-(4,6-dimethyl-3-oxoisothiazolo[5,4-b]pyridin-2(3H)-yl)acetyl)piperazine-1-carboxylate, was synthesized using 2-chloro-4,6-dimethylnicotinonitrile as a starting material. See Supplemental Experimental Procedures for synthetic schemes and procedures; additional characterization data are available upon request.

Homologous Recombination Assay

U2OS DR-GFP cells with the integrated homologous recombination reporter DR-GFP (Pierce et al., 1999) were transfected with TMPK siRNA, which was followed by transfection with the I-SceI expression vector (pCBA-I-SceI) for 48 hr. The recombination efficiency was examined by flow cytometric analysis of the frequency of GFP^+ cells.

In Vivo Chemotherapy

All mice experiments were approved by the biosafety committee of National Yang-Ming University and conformed to the national guidelines and regulations. Female BALB/c AnN.Cg-Foxnl^{nu}/Crl Nurl mice 6–8 weeks of age (National Laboratory Animal Center, Taiwan) were used for the tumor xenograft model. HCT-116 $p53^{-/-}$ cells (1×10^6) were subcutaneously implanted in the right flank of each mouse. Treatment began when the tumor size was about 1 mm^3. Mice (n = 32) were randomly allocated to four groups, namely vehicle (15% TEG), doxorubicin (1.25 mg/kg twice a week), YMU1 (5 mg/kg thrice a week), and YMU (5 mg/kg thrice a week) combined with doxorubicin (1.25 mg/kg twice a week). Mice were administered with the indicated treatment by intraperitoneal injection for four weeks, after which the mice were kept in a drug-free condition for additional two weeks. The tumor size was measured every day after the initiation of drug treatment by electronic caliper. Tumor volume = length (mm) × width^2 (mm^2) / 2.

Statistical Analyses

A two-tailed Student's t test was used to assess DNA lesions, tumor size, and tumor weight (*$p < 0.05$, **$p < 0.01$). Data are presented as mean ± SD. All other experimental procedures are described in the Supplemental Experimental Procedures.

SUPPLEMENTAL INFORMATION

Supplemental Information includes seven figures, one table, Supplemental Experimental Procedures, and Supplemental References and can be found with this article online at doi:10.1016/j.ccr.2012.04.038.

ACKNOWLEDGMENTS

We thank B. Vogelstein (The Johns Hopkins University Medical Institutions), M.B. Kastan (St. Jude Children's Research Hospital, Memphis), A.J. Pierce (University of Kentucky, Lexington), S.Y. Shieh (Institute of Biomedical Sciences, Academia Sinica, Taiwan), C.H. Lin (Institute of Biological Chemistry, Academia Sinica, Taiwan), W.H. Lee (Department of Biological Chemistry University of California, Irvine USA), C.L. Hsieh (Graduate Institute of Cancer Biology, China Medical University Hospital, Taiwan), and O.K. Lee (Stem Cell Research Center, National Yang-Ming University, Taiwan) for providing $p53^{+/+}$, $p53^{-/-}$ HCT-116 cell lines, I-PpoI, the I-SceI expression vectors, the U2OS stably expressing DR-GFP reporter, Capan-1, HCC1937, MCF-10A H184B5F5/M10, HRCE, and HBMSC, respectively. The authors are indebted to Y.J. Lee, P.S. Jiang, and T.Y. Huang at National Yang-Ming University for their technical assistance and P.-Y. Lin (Mass spectrometry facility, Academia Sinica, Taiwan) for her help in mass spectrum analysis. We are also grateful to C.H. Wong and Y.T. Wu (Genome Center, Academia Sinica) for generously providing the chemical library and technical support. This study was supported by grants NHRI-EX-100-10005NI from National Health Research Institute and NSC 100-2325-B-010-001 from National Science Council, Taiwan, and a grant from Aim for the Top University plan in National Yang-Ming University supported by the Ministry of Education, Taiwan.

Received: August 23, 2011
Revised: January 3, 2012
Accepted: April 24, 2012
Published: July 9, 2012

REFERENCES

Ahmad, S.I., Kirk, S.H., and Eisenstark, A. (1998). Thymine metabolism and thymineless death in prokaryotes and eukaryotes. Annu. Rev. Microbiol. *52*, 591–625.

Berkovich, E., Monnat, R.J., Jr., and Kastan, M.B. (2007). Roles of ATM and NBS1 in chromatin structure modulation and DNA double-strand break repair. Nat. Cell Biol. *9*, 683–690.

Bessman, M.J., Lehman, I.R., Adler, J., Zimmerman, S.B., Simms, E.S., and Kornberg, A. (1958). Enzymatic synthesis of deoxyribonucleic acid. III. The incorporation of pyrimidine and purine analogues into deoxyribonucleic acid. Proc. Natl. Acad. Sci. USA *44*, 633–640.

(E) After 2 weeks recovered from treatment, the mice were sacrificed to allow tumor weight measurement. All error bars in (D) and (E) represent SEM (n = 8).
(F) Ki 67 proliferation marker staining of a tumor is shown in the lower panel (scale bar, 50 μm).
(G) Model of doxorubicin sensitization by YMU1 in malignant cancer cells. Both R2/R1 and TMPK are recruited to the site of doxorubicin-induced double-strand breaks, where dATP, dGTP, dCTP, dTTP, and dUTP are synthesized in a site-specific manner. Inhibition of TMPK decreases dTTP formation at the DNA damage sites, which causes futile DNA repair due to dUTP incorporation.
See also Figure S7 and Table S1.

Burkhalter, M.D., Roberts, S.A., Havener, J.M., and Ramsden, D.A. (2009). Activity of ribonucleotide reductase helps determine how cells repair DNA double strand breaks. DNA Repair (Amst.) *8*, 1258–1263.

Caldecott, K.W. (2008). Single-strand break repair and genetic disease. Nat. Rev. Genet. *9*, 619–631.

Chabes, A., and Stillman, B. (2007). Constitutively high dNTP concentration inhibits cell cycle progression and the DNA damage checkpoint in yeast *Saccharomyces cerevisiae*. Proc. Natl. Acad. Sci. USA *104*, 1183–1188.

Chabes, A.L., Pfleger, C.M., Kirschner, M.W., and Thelander, L. (2003). Mouse ribonucleotide reductase R2 protein: a new target for anaphase-promoting complex-Cdh1-mediated proteolysis. Proc. Natl. Acad. Sci. USA *100*, 3925–3929.

Engström, Y., Eriksson, S., Jildevik, I., Skog, S., Thelander, L., and Tribukait, B. (1985). Cell cycle-dependent expression of mammalian ribonucleotide reductase: differential regulation of the two subunits. J. Biol. Chem. *260*, 9114–9116.

Fan, H., Villegas, C., Huang, A., and Wright, J.A. (1998). The mammalian ribonucleotide reductase R2 component cooperates with a variety of oncogenes in mechanisms of cellular transformation. Cancer Res. *58*, 1650–1653.

Flick, K.E., Jurica, M.S., Monnat, R.J., Jr., and Stoddard, B.L. (1998). DNA binding and cleavage by the nuclear intron-encoded homing endonuclease I-PpoI. Nature *394*, 96–101.

Garg, D., Henrich, S., Salo-Ahen, O.M., Myllykallio, H., Costi, M.P., and Wade, R.C. (2010). Novel approaches for targeting thymidylate synthase to overcome the resistance and toxicity of anticancer drugs. J. Med. Chem. *53*, 6539–6549.

Håkansson, P., Hofer, A., and Thelander, L. (2006). Regulation of mammalian ribonucleotide reduction and dNTP pools after DNA damage and in resting cells. J. Biol. Chem. *281*, 7834–7841.

Hartlerode, A.J., and Scully, R. (2009). Mechanisms of double-strand break repair in somatic mammalian cells. Biochem. J. *423*, 157–168.

Holthausen, J.T., Wyman, C., and Kanaar, R. (2010). Regulation of DNA strand exchange in homologous recombination. DNA Repair (Amst.) *9*, 1264–1272.

Hu, C.M., and Chang, Z.F. (2008). Synthetic lethality by lentiviral short hairpin RNA silencing of thymidylate kinase and doxorubicin in colon cancer cells regardless of the p53 status. Cancer Res. *68*, 2831–2840.

Hu, C.M., and Chang, Z.F. (2010). A bioluminescent method for measuring thymidylate kinase activity suitable for high-throughput screening of inhibitor. Anal. Biochem. *398*, 269–271.

Jensen, R.A., Page, D.L., and Holt, J.T. (1994). Identification of genes expressed in premalignant breast disease by microscopy-directed cloning. Proc. Natl. Acad. Sci. USA *91*, 9257–9261.

Kastan, M.B., and Bartek, J. (2004). Cell-cycle checkpoints and cancer. Nature *432*, 316–323.

Katada, H., Harumoto, T., Shigi, N., and Komiyama, M. (2012). Chemical and biological approaches to improve the efficiency of homologous recombination in human cells mediated by artificial restriction DNA cutter. Nucleic Acids Res. *40*, e81.

Krokan, H.E., Drabløs, F., and Slupphaug, G. (2002). Uracil in DNA—occurrence, consequences and repair. Oncogene *21*, 8935–8948.

Ladner, R.D., and Caradonna, S.J. (1997). The human dUTPase gene encodes both nuclear and mitochondrial isoforms: differential expression of the isoforms and characterization of a cDNA encoding the mitochondrial species. J. Biol. Chem. *272*, 19072–19080.

Lieber, M.R. (2010). The mechanism of double-strand DNA break repair by the nonhomologous DNA end-joining pathway. Annu. Rev. Biochem. *79*, 181–211.

Liu, X., Lai, L., Wang, X., Xue, L., Leora, S., Wu, J., Hu, S., Zhang, K., Kuo, M.L., Zhou, L., et al. (2011). Ribonucleotide reductase small subunit M2B prognoses better survival in colorectal cancer. Cancer Res. *71*, 3202–3213.

Longley, D.B., Harkin, D.P., and Johnston, P.G. (2003). 5-fluorouracil: mechanisms of action and clinical strategies. Nat. Rev. Cancer *3*, 330–338.

Mah, L.J., El-Osta, A., and Karagiannis, T.C. (2010). gammaH2AX: a sensitive molecular marker of DNA damage and repair. Leukemia *24*, 679–686.

Mathews, C.K. (2006). DNA precursor metabolism and genomic stability. FASEB J. *20*, 1300–1314.

McIntosh, E.M., Ager, D.D., Gadsden, M.H., and Haynes, R.H. (1992). Human dUTP pyrophosphatase: cDNA sequence and potential biological importance of the enzyme. Proc. Natl. Acad. Sci. USA *89*, 8020–8024.

Mimitou, E.P., and Symington, L.S. (2009). DNA end resection: many nucleases make light work. DNA Repair (Amst.) *8*, 983–995.

Moss, J., Tinline-Purvis, H., Walker, C.A., Folkes, L.K., Stratford, M.R., Hayles, J., Hoe, K.L., Kim, D.U., Park, H.O., Kearsey, S.E., et al. (2010). Break-induced ATR and Ddb1-Cul4(Cdt)^2 ubiquitin ligase-dependent nucleotide synthesis promotes homologous recombination repair in fission yeast. Genes Dev. *24*, 2705–2716.

Nagaraju, G., and Scully, R. (2007). Minding the gap: the underground functions of BRCA1 and BRCA2 at stalled replication forks. DNA Repair (Amst.) *6*, 1018–1031.

Niida, H., Katsuno, Y., Sengoku, M., Shimada, M., Yukawa, M., Ikura, M., Ikura, T., Kohno, K., Shima, H., Suzuki, H., et al. (2010a). Essential role of Tip60-dependent recruitment of ribonucleotide reductase at DNA damage sites in DNA repair during G1 phase. Genes Dev. *24*, 333–338.

Niida, H., Shimada, M., Murakami, H., and Nakanishi, M. (2010b). Mechanisms of dNTP supply that play an essential role in maintaining genome integrity in eukaryotic cells. Cancer Sci. *101*, 2505–2509.

Nordlund, P., and Reichard, P. (2006). Ribonucleotide reductases. Annu. Rev. Biochem. *75*, 681–706.

Pierce, A.J., Johnson, R.D., Thompson, L.H., and Jasin, M. (1999). XRCC3 promotes homology-directed repair of DNA damage in mammalian cells. Genes Dev. *13*, 2633–2638.

Pontarin, G., Ferraro, P., Rampazzo, C., Kollberg, G., Holme, E., Reichard, P., and Bianchi, V. (2011). Deoxyribonucleotide metabolism in cycling and resting human fibroblasts with a missense mutation in p53R2, a subunit of ribonucleotide reductase. J. Biol. Chem. *286*, 11132–11140.

Powell, S.N., and Kachnic, L.A. (2003). Roles of BRCA1 and BRCA2 in homologous recombination, DNA replication fidelity and the cellular response to ionizing radiation. Oncogene *22*, 5784–5791.

Reichard, P. (1988). Interactions between deoxyribonucleotide and DNA synthesis. Annu. Rev. Biochem. *57*, 349–374.

Robert, T., Vanoli, F., Chiolo, I., Shubassi, G., Bernstein, K.A., Rothstein, R., Botrugno, O.A., Parazzoli, D., Oldani, A., Minucci, S., and Foiani, M. (2011). HDACs link the DNA damage response, processing of double-strand breaks and autophagy. Nature *471*, 74–79.

San Filippo, J., Sung, P., and Klein, H. (2008). Mechanism of eukaryotic homologous recombination. Annu. Rev. Biochem. *77*, 229–257.

Shao, J., Zhou, B., Zhu, L., Qiu, W., Yuan, Y.C., Xi, B., and Yen, Y. (2004). In vitro characterization of enzymatic properties and inhibition of the p53R2 subunit of human ribonucleotide reductase. Cancer Res. *64*, 1–6.

Shao, J., Zhou, B., Chu, B., and Yen, Y. (2006). Ribonucleotide reductase inhibitors and future drug design. Curr. Cancer Drug Targets *6*, 409–431.

Traut, T.W. (1994). Physiological concentrations of purines and pyrimidines. Mol. Cell. Biochem. *140*, 1–22.

Xu, X., Page, J.L., Surtees, J.A., Liu, H., Lagedrost, S., Lu, Y., Bronson, R., Alani, E., Nikitin, A.Y., and Weiss, R.S. (2008). Broad overexpression of ribonucleotide reductase genes in mice specifically induces lung neoplasms. Cancer Res. *68*, 2652–2660.

Yanamoto, S., Kawasaki, G., Yoshitomi, I., and Mizuno, A. (2003). Expression of p53R2, newly p53 target in oral normal epithelium, epithelial dysplasia and squamous cell carcinoma. Cancer Lett. *190*, 233–243.

Zhang, K., Hu, S., Wu, J., Chen, L., Lu, J., Wang, X., Liu, X., Zhou, B., and Yen, Y. (2009). Overexpression of RRM2 decreases thrombspondin-1 and increases VEGF production in human cancer cells in vitro and in vivo: implication of RRM2 in angiogenesis. Mol. Cancer *8*, 11.

Cancer Cell
Article

Inhibition of RNA Polymerase I as a Therapeutic Strategy to Promote Cancer-Specific Activation of p53

Megan J. Bywater,[1,3] Gretchen Poortinga,[1,6] Elaine Sanij,[1,4] Nadine Hein,[1] Abigail Peck,[1] Carleen Cullinane,[1] Meaghan Wall,[7] Leonie Cluse,[1] Denis Drygin,[8] Kenna Anderes,[8] Nanni Huser,[8] Chris Proffitt,[8] Joshua Bliesath,[8] Mustapha Haddach,[8] Michael K. Schwaebe,[8] David M. Ryckman,[8] William G. Rice,[8] Clemens Schmitt,[9,10] Scott W. Lowe,[11] Ricky W. Johnstone,[1,3,4] Richard B. Pearson,[1,3,5,12] Grant A. McArthur,[1,2,3,6,14] and Ross D. Hannan[1,2,3,5,12,13,*]

[1]Division of Cancer Research
[2]Division of Cancer Medicine
Peter MacCallum Cancer Centre, St. Andrews Place, East Melbourne, Victoria 3002, Australia
[3]Sir Peter MacCallum Department of Oncology
[4]Department of Pathology
[5]Department of Biochemistry and Molecular Biology
The University of Melbourne, Parkville, Victoria, 3010, Australia
[6]Department of Medicine, St. Vincent's Hospital, University of Melbourne, Fitzroy, Victoria, 3065, Australia
[7]Victorian Cancer Cytogenetics Service, St. Vincent's Hospital, Fitzroy, Victoria, 3065, Australia
[8]Cylene Pharmaceuticals, Suite 200/5820 Nancy Ridge Drive, San Diego, CA 92121, USA
[9]Charité-Universitätsmedizin Berlin/Molekulares Krebsforschungszentrum-MKFZ, Berlin, Germany
[10]Max-Delbrück-Center for Molecular Medicine, Berlin, Germany
[11]Howard Hughes Medical Institute, Cold Spring Harbor Laboratory, 1 Bungtown Road, Cold Spring Harbor, NY 11724, USA
[12]Department of Biochemistry and Molecular Biology, Monash University, Clayton, Victoria, 3800, Australia
[13]School of Biomedical Sciences, University of Queensland, St Lucia, Queensland, 4072, Australia
[14]These authors contributed equally to this work
*Correspondence: ross.hannan@petermac.org
http://dx.doi.org/10.1016/j.ccr.2012.05.019

SUMMARY

Increased transcription of ribosomal RNA genes (rDNA) by RNA Polymerase I is a common feature of human cancer, but whether it is required for the malignant phenotype remains unclear. We show that rDNA transcription can be therapeutically targeted with the small molecule CX-5461 to selectively kill B-lymphoma cells in vivo while maintaining a viable wild-type B cell population. The therapeutic effect is a consequence of nucleolar disruption and activation of p53-dependent apoptotic signaling. Human leukemia and lymphoma cell lines also show high sensitivity to inhibition of rDNA transcription that is dependent on p53 mutational status. These results identify selective inhibition of rDNA transcription as a therapeutic strategy for the cancer specific activation of p53 and treatment of hematologic malignancies.

INTRODUCTION

Pol I-dependent transcription of the 47S rDNA dynamically responds to growth signaling and cellular stresses to establish the abundance of the ribosomal RNAs and directly regulates cellular protein translational capacity and thus proliferative growth rate (Jorgensen et al., 2002; Larminie et al., 1998). rDNA transcription takes place in specialized subnuclear domains termed nucleoli that are formed around actively transcribed rDNA repeats in early G1 before being disassembled in

Significance

Morphologic abnormalities of the nucleolus, the site of ribosomal gene (rDNA) transcription by RNA Polymerase I (Pol I), have been recognized as diagnostic for cancer for over a century. Nevertheless, an unresolved question has been whether the accelerated ribosome biogenesis responsible for the nucleolar changes is required for malignancy. Here we provide the definitive evidence, both genetic and pharmacologic, that accelerated rDNA transcription and nucleolar integrity are necessary for oncogenic activity. Further, we show that Pol I transcription can be targeted in vivo to treat lymphoma and leukemia through the nongenotoxic activation of p53-dependent apoptosis, while sparing normal cells. Thus, selective inhibition of Pol transcription, can serve as a therapeutic strategy for the treatment of cancer.

mitosis when rDNA transcription is halted. Strikingly, elevated rDNA transcription by Pol I is a stalwart feature of cancer (Barna et al., 2008; Ruggero and Pandolfi, 2003; White, 2005), and enlarged nucleoli, a consequence of hyper-activated rDNA transcription, have been used by pathologists since the late 19th century as a marker of aggressive tumors (Derenzini et al., 2009).

In addition to rRNA and factors associated with ribosome biogenesis, nucleoli are enriched with a large number of other proteins, many of which have no direct function in the synthesis of ribosomes. In many cases, regulated sequestration of these proteins in the nucleoli controls their cellular activity. Because of this, the nucleolus has the potential to control a broad range of cellular functions in addition to rDNA transcription. In particular, nucleolar localization regulates the function of key oncogenes and tumor suppressors such as ARF and MDM2, both of which are critical for the regulation of p53 (TP53) (Boisvert et al., 2007). Thus, Pol I-dependent transcription and nucleolar integrity are pivotal determinants for numerous processes required for the excessive proliferation of cancer cells.

Surprisingly, despite its constant activation in cancer and potential to control critical determinants of malignant transformation, the importance of accelerated Pol I transcription and nucleolar integrity for cancer and their potential as therapeutic targets, remains undefined (Ruggero and Pandolfi, 2003; White, 2005). From a clinical perspective, a key question is whether targeted inhibition of rDNA transcription, generally considered a ''housekeeping process'' universally required for cell growth and proliferation, can show selectivity for killing malignant cells over normal cells. Furthermore, it is critical to understand the mechanism(s) by which such selectivity might be achieved and identify the tumor types that may therapeutically respond.

MYC is a potent oncogene whose dysregulated expression plays a significant role in human cancer development. MYC also plays a fundamental role in the biogenesis of ribosomes through transcriptional upregulation of 47S rRNA, and transcription of a select group of factors involved in rRNA processing, rRNA transport, and ribosome assembly. Due to the function that MYC plays in regulating Pol I activity and ribosome biogenesis (Arabi et al., 2005; Dai and Lu, 2008; Dang et al., 2006; Grandori et al., 2005; Grewal et al., 2005; Poortinga et al., 2004, 2011; Shiue et al., 2009; van Riggelen et al., 2010), models of MYC driven oncogenesis provide an ideal setting to explore the dependencies between Pol I transcription, ribosome biogenesis, and cancer.

In this study, we used both genetic approaches and a small molecule selective inhibitor of Pol I transcription (CX-5461) (Drygin et al., 2011) to investigate the dependence of tumors on Pol I activity in a murine model of spontaneous lymphoma driven by MYC (Eμ-*Myc*) (Adams et al., 1985). In addition, we explored the therapeutic potential of inhibiting Pol I transcription in various human hematologic malignancies.

RESULTS

rRNA Transcription and Ribosome Biogenesis Are Accelerated in Eμ-*Myc* Lymphoma Cells

To investigate the role of Pol I transcription in malignancy, we employed a murine model of spontaneous lymphoma (Eμ-*Myc*) in which MYC is overexpressed in lymphocytes of the B lineage. This genetic model reproduces many of the clinical aspects of Burkitt's lymphoma in humans, including reciprocal chromosomal translocations that juxtapose the c-*myc* proto-oncogene on chromosome 8 to the immunoglobulin heavy chain locus on chromosome 14, or the κ or λ light chain locus on chromosomes 2 or 22 (Adams et al., 1985; Klein, 1993). As expected from MYC's well-defined role in promoting growth, premalignant B220+ splenic B cells from 4- to 6-week-old Eμ-*Myc* mice had increased cell volume, increased protein content, and highly accelerated proliferation rates compared to B cells from wild-type littermates (Figure S1 available online) (Iritani and Eisenman, 1999). Despite their much faster cell doubling time, the Eμ-*Myc* B cells also exhibited higher amounts of both total RNA and ribosomal RNA (rRNA) per cell (Figures 1A and 1B), suggesting that Pol I transcription and cell growth were highly accelerated. Consistent with these findings, B cells from Eμ-*Myc* mice exhibited robust increases in the level of transcription of rDNA by Pol I, as determined by measuring the abundance of pre-rRNA, which is rapidly processed (half-life of 10–30 min) to mature rRNA (half-life of days to weeks) and can therefore be used as indirect measure of rRNA synthesis rate (White, 2005) (Figure 1C).

MYC regulates transcription of rDNA through direct activation of Pol I (Arabi et al., 2005; Grandori et al., 2005; Shiue et al., 2009) and by transcriptionally increasing the level of the Pol I subunits and Pol I-specific transcription factors (Grewal et al., 2005; Poortinga et al., 2004, 2011). Consistent with this, both the mRNA and protein abundance of key Pol I specific components including UBF (UBTF), a factor involved in pre-initiation complex formation and rDNA chromatin remodeling (Sanij et al., 2008), RRN3 (also termed TIF-1A), an essential Pol I initiation factor (Yuan et al., 2005), and POLR1B, the second largest subunit of Pol I (Hannan et al., 1998), were all highly elevated in premalignant Eμ-*Myc* transgenic B cells compared to normal B cells isolated from wild-type littermates (Figures 1D and 1E). Furthermore, this increased expression of Pol I-specific components was perpetuated in malignant B cells isolated from tumor bearing Eμ-*Myc* mice, indicating the continued elevation of this pathway with the development of lymphoma (Figure 1E). This demonstrates that the increased levels of the Pol I factors and rDNA transcription occur during cellular transformation and tumor initiation and are not simply a consequence of transformation.

Accelerated rDNA Transcription Is Required for Survival Eμ-*Myc* Lymphoma Cells

We used RNAi-mediated knockdown of UBF and RRN3 to examine the extent to which the increased rate of Pol I transcription exhibited by the Eμ-*Myc* B cells was necessary for their proliferative capacity and survival. Eμ-*Myc* lymphoma cells isolated from tumor bearing mice that grow in culture and are wild-type for p53 were retrovirally transduced with microRNA-based short hairpins (shRNA-mirs) targeting *Ubf* (shUBF) or *Rrn3* (shRRN3) (Sanij et al., 2008). Coexpression of GFP allowed for FACS-based sorting of transduced cells. Transduction efficiency was titered to reduce *Ubf* and *Rrn3* mRNA and protein abundance in the lymphoma cells to near those found in

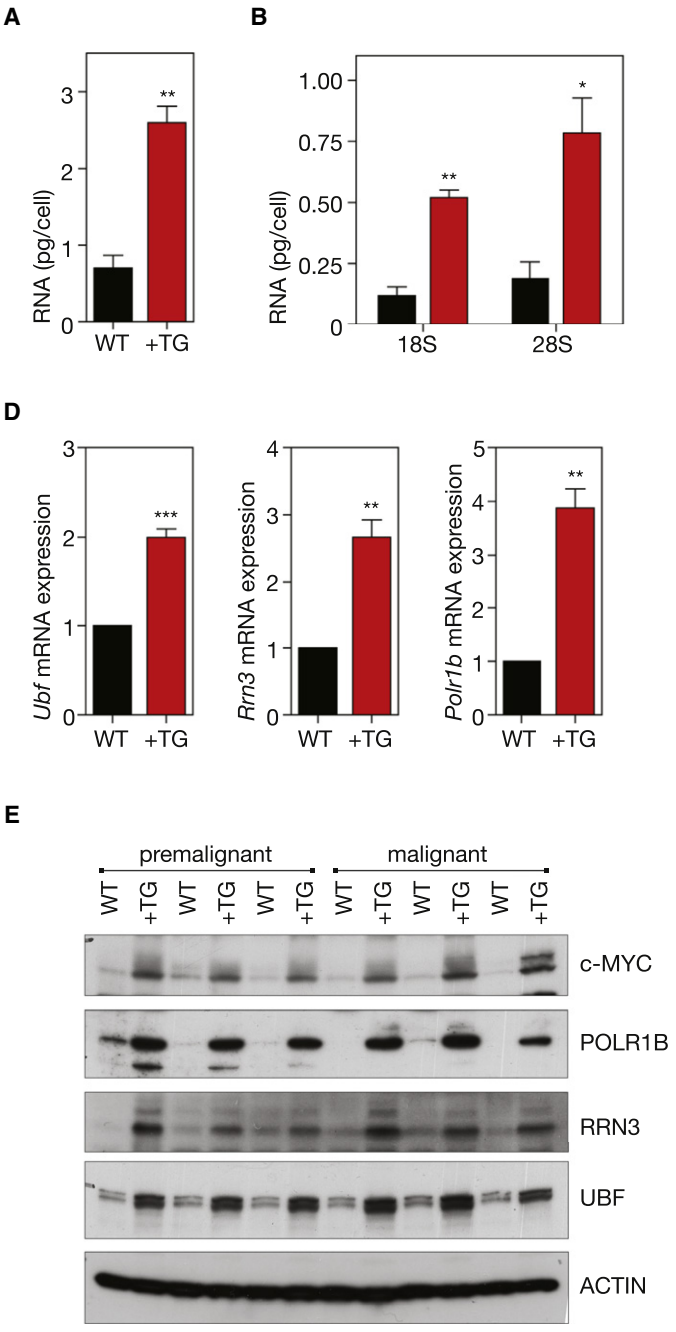

Figure 1. Regulation of Pol I Transcription in Transgenic Eμ-*Myc* B Cells

(A) Premalignant B220+ splenic B cells were isolated from premalignant (4- to 6-week-old) Eμ-*Myc* mice (+TG) and their respective wild-type littermates (WT), lysed, and total RNA content per cell determined ($p < 0.01$, $n = 3$).

(B) Total 18S ($p < 0.01$, $n = 3$) and 28S ($p < 0.05$, $n = 3$) rRNA per cell, as determined using an Agilent Bioanalyzer.

(C) Pre-rRNA expression determined by quantitative reverse transcription real-time (qRT) PCR of the internally transcribed spacer 1 (ITS1) (+742 to +874) of the 47S pre-rRNA ($p < 0.05$; $n = 5$).

(D) Relative mRNA expression of Pol I transcription factors *Ubf*, *Rrn3*, and *Polr1b*, determined by qRT-PCR (*Ubf*, $p < 0.001$; *Rrn3*, $p < 0.01$; *Polr1b*, $p < 0.01$; $n = 5$).

(E) Western blot analysis of ACTIN, c-MYC and Pol I transcription factors, UBF, RRN3 and POL1RB in premalignant and malignant (tumor bearing) B220+ B cells isolated from +TG mice and their respective WT littermates. Student's two-tailed t test for all comparisons. Error bars represent SEM.

See also Figure S1.

normal B cells (Figures 2A and 2B). Individual knockdown of UBF or RRN3 resulted in a reduction in Pol I transcription by 35%–40%, but notably, not below levels observed in normal B cells (Figures 2C and 2D). To gauge the effect of normalizing Pol I transcription on the proliferation and survival of Eμ-*Myc* lymphoma cells we performed an in vitro GFP competition assay in which mock transduced Eμ-*Myc* lymphoma cells were mixed with equal numbers of Eμ-*Myc* lymphoma cells transduced with either LMS vector alone (adapted from Dickins et al., 2005), (Eμ-*Myc*/LMS), LMS-shUBF (Eμ-*Myc*/LMS-shUBF), or LMS-shRRN3 (Eμ-*Myc*/LMS-shRRN3) and maintenance of the transduced population was followed by FACS. Eμ-*Myc*/LMS-shUBF and Eμ-*Myc*/LMS-shRRN3 cells exhibited a profound disadvantage with regard to proliferation and/or survival (Figure 2E). Likewise, expression of shUBF and shRRN3 caused an increased sub-G1 population (Figure 2F) and a 2–3-fold increase in markers of apoptosis including loss of mitochondrial membrane potential (decrease in tetramethylrhodamine ethyl [TMRE] retention; Figure S2A) and increased AnnexinV/PI staining (Figure S2B). This suggested that the Eμ-*Myc* lymphoma cells were eliminated by apoptosis following normalization of Pol I transcription levels. Consistent with the survival disadvantage resulting from an induction of apoptosis, enforced expression of the anti-apoptotic protein BCL-2 (Figure S2C) significantly reduced the disadvantage of the Eμ-*Myc*/LMS-shUBF and Eμ-*Myc*/LMS-shRRN3 cells (Figure 2G). Moreover, a long-term competition assay with Eμ-*Myc*/LMS-shRRN3 cells expressing BCL2 demonstrated that their proliferative capacity was similar to control cells (Figure S2D). These results reveal that a ~35% reduction in Pol I transcription in Eμ-*Myc* lymphoma cells results in induction of apoptosis that is not linked to a reduction in proliferation rate. Together these data demonstrate that the process of malignant transformation and cancer cell survival is considerably more dependent upon maintenance of elevated levels of Pol I activity than previously appreciated.

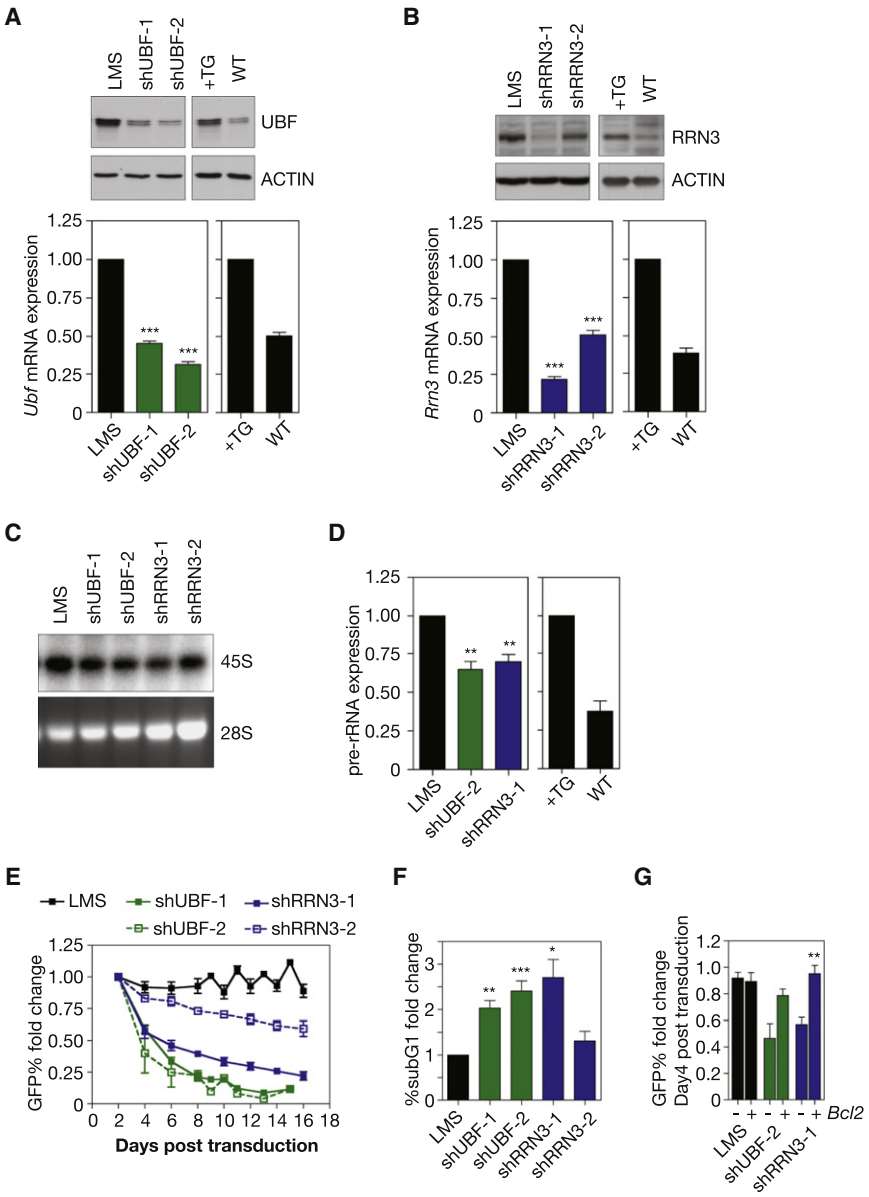

Figure 2. Reducing Pol I Transcription Rates in Eμ-*Myc* Lymphoma Cells Using shRNA-mirs Against UBF or RRN3 Strongly Activates Programmed Cell Death

(A) Western blot analysis of UBF in cultured in Eμ-*Myc* lymphoma cells transduced with one of two independent shRNA-mirs targeting UBF (shUBF-1 and -2) or empty vector (LMS), and in B220+ splenic B cells isolated from 4- to 6-week-old Eμ-*Myc* mice (+TG) and their respective wild-type littermates (WT). Relative *Ubf* mRNA expression determined by qRT-PCR (LMS versus shUBF-1, $p < 0.001$; LMS versus shUBF-2, $p < 0.001$; $n = 3$).

(B) Western blot analysis of RRN3 as for UBF in (a) utilizing two independent shRNA-mirs targeting RRN3 (shRRN3-1 and -2). Relative *Rrn3* mRNA expression determined by qRT-PCR (LMS versus shRRN3-1, $p < 0.001$; LMS versus shRRN3-2, $p < 0.001$; $n = 4$).

(C) 47S pre-rRNA synthesis determined by [^{32}P] orthophosphate labeling in cells transduced with shRNA-mirs targeting UBF or RRN3 as compared to LMS alone (representative of $n = 2$).

(D) Pre-rRNA expression determined by qRT-PCR of the ITS1 in cells transduced with select shRNA-mirs and B cells described in (a) (LMS versus shUBF-2, $p < 0.01$; LMS versus shRRN3-1, $p < 0.01$; $n = 4$).

(E) GFP competition assay of GFP+, transduced Eμ-*Myc* lymphoma cells (LMS, shUBF, shRRN3) cocultured with GFP−, mock transduced Eμ-*Myc* lymphoma cells. Data expressed as fold change in percentage of GFP+ cells compared to Day 2 posttransduction ($n = 3$).

(F) Percentage of apoptotic cells determined by subG1 DNA content analysis expressed as fold change over LMS (6.3% ± 0.61 SEM) (LMS versus shUBF-1, $p < 0.01$; LMS versus shUBF-2, $p < 0.001$; $n = 3$) (LMS versus shRRN3-1, $p < 0.05$; $n = 6$). See also Figures S2A and S2B.

(G) GFP competition assay in Eμ-*Myc* lymphoma cells with BCL2 overexpression, expressed as fold change in percentage of GFP+ cells on Day 4 compared to Day 2 posttransduction (shRRN3-1 $p < 0.01$; $n = 3$). One-way ANOVA with Tukey's multiple comparison posttest (a,b,d,f). Student's two-tailed t test (g). Error bars represent SEM. See also Figures S2C and S2D.

CX-5461, A Selective Inhibitor of Pol I Transcription Induces p53-Dependent Apoptotic Cell Death of Eμ-*Myc* Lymphoma Cells

The profound sensitivity of Eμ-*Myc* lymphoma cells to reductions in Pol I transcription led us to question whether this could be exploited therapeutically to treat B cell lymphoma. To test this approach, we utilized a highly selective agent (CX-5461) that inhibits Pol I-driven transcription in the low nanomolar range by preventing the association of the Pol I-specific transcription initiation selectivity factor SL-1 with the rDNA promoter, exhibiting >200-fold selectivity relative to the inhibition of Pol II-driven transcription (Drygin et al., 2011). Eμ-*Myc* lymphoma cells that had been isolated from tumor-bearing mice and cultured in vitro were exquisitely sensitive to CX-5461 with an IC_{50} of 27.3 nM ± 8.1 nM for Pol I transcription after 1 hr (Figures 3A, 3B, S3A, and S3B) and IC_{50} of 5.4 nM ± 2.1 nM for cell death after 16 hr (Figure 3C). Under these conditions, transcription of the Pol II-dependent gene, β2m, was not affected (Figure S3C), attesting to the selectively of CX-5461 for Pol I.

Loss or mutations of p53 or ARF are frequent lesions in Eμ-*Myc* driven lymphomagenesis (Eischen et al., 1999), so we tested a panel of Eμ-*Myc* lymphomas with variable p53 and ARF status for sensitivity to CX-5461. We observed that the ability of CX-5461 to kill lymphoma cells at low nM concentrations ($IC_{50} < 10$ nM) was dependent on intact p53 pathway but independent of ARF, which is frequently associated with oncogenic stress-dependent activation of p53. Cells, mutant or null for *p53* exhibited a 180-fold decreased sensitivity to CX-5461 (Figure 3C). Importantly this was not due to elevated basal rates of Pol I transcription as the Eμ-*Myc* clones on the different

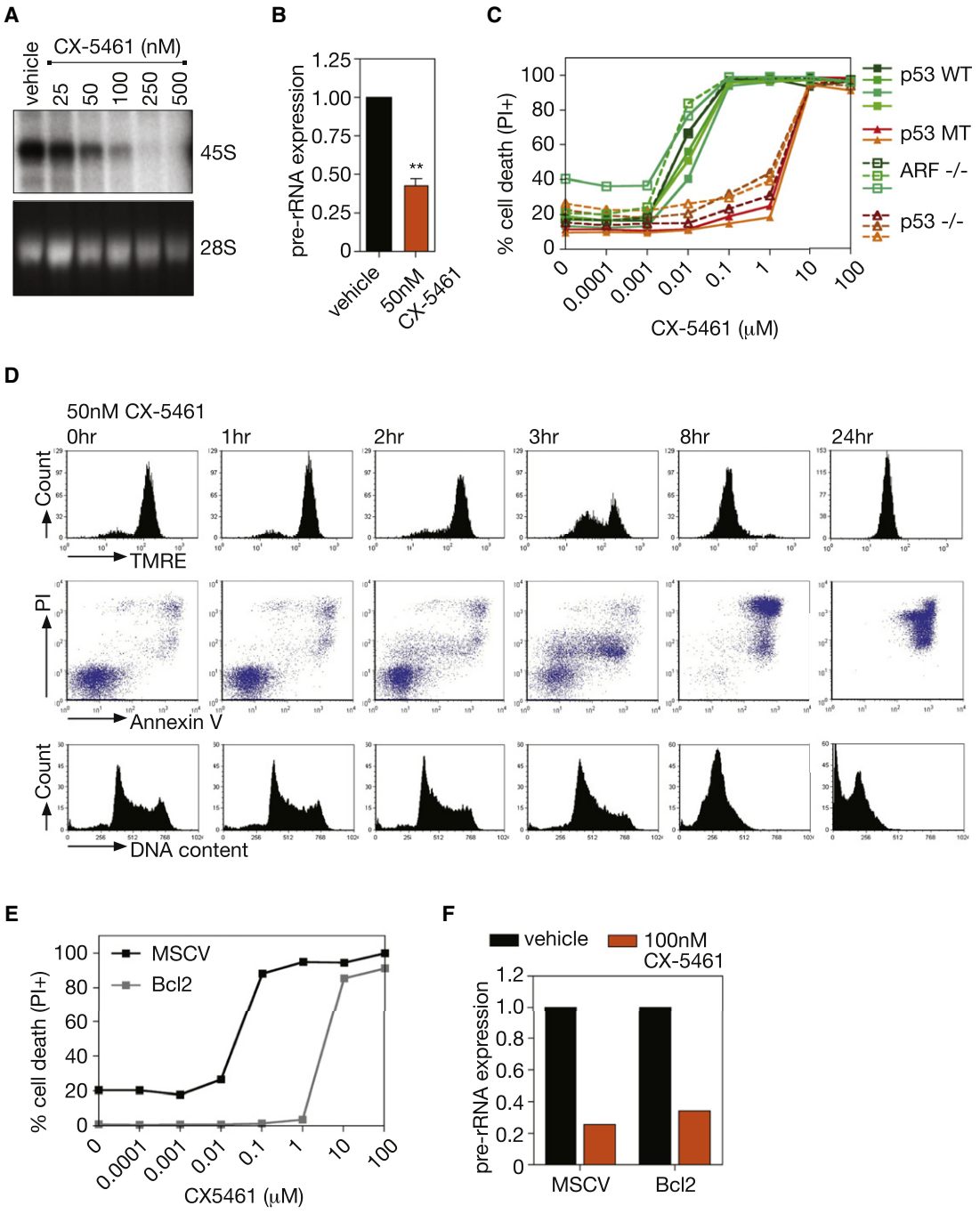

Figure 3. CX-5461 Induces Rapid, p53-Dependent, Apoptotic Cell Death of Eμ-*Myc* Lymphoma Cells

(A) 47S pre-rRNA synthesis in cultured Eμ-*Myc* lymphoma cells treated with increasing nM concentrations of CX-5461, determined by [^{32}P] orthophosphate labeling (representative of n = 3). See also Figure S3A.

(B) Pre-rRNA expression determined by qRT-PCR in cells treated with 50 nm CX-5461 as compared to vehicle alone ($p < 0.01$; n = 3). See also Figures S3B and S3C.

(C) CX-5461 cell death curve of cultured Eμ-*Myc* lymphoma cell lines (including wild-type [WT], mutant [MT], and homozygous deleted [−/−] for indicated genes) 16 hr posttreatment, quantified by percentage of cells incorporating PI (representative of n = 3). See also Figures S3D and S3E.

(D) Induction of apoptosis in cultured Eμ-*Myc* lymphoma cells treated with 50 nM CX-5461, shown by loss of TMRE staining; increased Annexin V/PI costaining; increased cells with subG1 DNA content. See also Figures S3F–S3H.

(E) CX-5461 cell death curve of a p53 WT Eμ-*Myc* lymphoma cell line overexpressing BCL2 at 16 hr posttreatment, quantified by percentage of cells incorporating PI (representative of n = 2).

(F) Pre-rRNA expression in an Eμ-*Myc* lymphoma cell line overexpressing BCL2 in comparison to vector alone (MSCV), and treated with 100 nM CX-5461 as compared to vehicle as determined by qRT-PCR (n = 1). Student's two-tailed t test for all comparisons. Error bars represent SEM.

genetic backgrounds exhibited similar Pol I transcription rates prior to treatment (Figure S3D). Moreover, consistent with our previous study demonstrating that CX-5461 is nongenotoxic, Eμ-*Myc* lymphoma cells null for ATM, a mediator of DNA damage response, exhibited a comparable level of sensitivity to CX-5461 as Eμ-*Myc* lymphoma cells wild-type for ATM and p53 (Figure S3E).

Cell death in *p53* wild-type lymphoma cells in response to CX-5461 was rapid and concomitant with induction of apoptotic markers, including progressive loss of mitochondrial membrane potential, increased AnnexinV/PI staining, and an increased percentage of cells with subG1 DNA content (Figures 3D and S3F–S3H). Enforced expression of BCL-2 in *p53* wild-type Eμ-*Myc* cells reduced the cell death sensitivity to CX-5461 by over 130-fold despite exhibiting comparative inhibition of Pol I transcription (Figures 3E and 3F). Thus, repression of Pol I transcription in Eμ-*Myc* lymphoma cells by a small molecule inhibitor of Pol I induces rapid p53-dependent cell death by apoptosis.

Inhibition of Pol I Transcription by CX-5461 Induces p53-Mediated Death of Lymphoma Cells via Activation of the Rp-MDM2-p53 Nucleolar Surveillance Pathway

As Pol I transcription rates ultimately determine ribosome levels, it was possible that the apoptotic death of the Eμ-*Myc* lymphoma cells in response to suppression of Pol I transcription was an indirect response to ribosome insufficiency and thus defects in translation. Indeed, a recent study demonstrated that aberrant translation downstream of MYC hyperactivation is required for MYC's oncogenic potential (Barna et al., 2008). Alternatively, acute perturbations related to many aspects of ribosome biogenesis have been shown to contribute to a "nucleolar stress response," also called the nucleolar surveillance pathway, which leads to rapid activation of p53, in an ARF-independent manner, and induction of apoptosis well before ribosome insufficiency and translation defects can occur (Boisvert et al., 2007; Boulon et al., 2010; Deisenroth and Zhang, 2010; Lohrum et al., 2003; Macias et al., 2010; Zhang et al., 2003). We examined these mechanisms and found that induction of apoptotic signaling was an immediate response to repression of Pol I transcription and not driven by ribosome insufficiency.

Treatment of Eμ-*Myc* lymphomas with CX-5461 for as little as 1 hr increased p53 levels followed by transactivation of p53 target genes, *p21* (*Cdkn1a*) and *Puma* (*Bbc3*), and cleavage and activation of CASPASE 3 (CASP3) at 2 hr (Figures 4A, 4B, and S4A), despite the fact that total RNA levels, which reflect ribosome abundance, were not decreased at these time points (Figure 4C). Notably, neither levels of MYC protein or expression of the MYC transcriptional targets *ornithine decarboxylase 1* (*Odc1*) and *mTert* were affected, demonstrating that the cell death was not due to alterations in MYC activity (Figures 4A and 4B). These findings are consistent with the induction of apoptosis being a direct result of disruption of Pol I transcription, and activation of nucleolar stress, rather than an indirect effect of ribosome insufficiency. To further examine this mechanism we monitored nucleolar integrity using a prototypical nucleolar marker protein fibrillarin (FBL), nucleophosmin (B23), and nucleolin (NCL), which demonstrate both nucleolar and nuclear localization, and by fluorescence in situ hybridization (FISH) for the 47S rDNA repeats. Within 1 hr of treatment with 50 nM CX-5461, the multiple nucleoli normally found in Eμ-*Myc* lymphoma cells had fused to form a single nucleolus per cell that exhibited reduced FBL staining (Figure 4D). Further analysis revealed that the altered FBL staining was accompanied by relocalization of a proportion of B23 and NCL to the periphery of the single nucleoli (Figure S4B). This correlated with condensation of the rDNA within the nucleoli to punctate foci, which is characteristic of a reduced Pol I transcription rate (Figures 4E and S4C) (McStay and Grummt, 2008). Activation of p53 by the Rp-MDM2-p53 nucleolar surveillance pathway has been attributed in part to the release of ribosomal proteins (RP), in particular RPL5 and RPL11, from the nucleolus and their binding to MDM2, a p53 E3 ubiquitin ligase. This results in the release of p53 from MDM2 and the subsequent accumulation of p53 (Deisenroth and Zhang, 2010). To test if CX-5461 acts, in part through the nucleolar surveillance pathway to activate p53, we immunoprecipitated MDM2 from Eμ-*Myc* lymphoma cells following CX-5461 treatment and examined the levels of RPL5 and RPL11 that coimmunoprecipitated with MDM2. Because MDM2 is a transcriptional target of p53, it was important to avoid possible confounding effects of increased levels of immunoprecipitated MDM2. A time course following treatment of cells with CX-5461 demonstrated that MDM2 expression increased dramatically beyond the 1 hr time point (Figure S4D); therefore we performed the coimmunoprecipitation experiments after 1hr treatment, prior to changes in MDM2 levels. Consistent with a nucleolar surveillance mechanism, coimmunoprecipitation experiments demonstrated an increase in the amount of RPL5 and RPL11 associated with MDM2 in p53 wild-type Eμ-*Myc* lymphoma cells in response to 1 hr treatment with CX-5461 relative to vehicle-treated cells (Figure 4F). Together with the data shown in Figures 1, 2, and 3, these findings provide independent lines of evidence for an absolute dependence of Eμ-*Myc* lymphoma cells on high rates of Pol I transcription for their survival, whereby perturbations in rRNA synthesis result in immediate induction of a nucleolar stress response leading to p53-dependent apoptotic cell death.

Inhibition of Pol I Transcription by CX-5461 Selectively Induces p53-Mediated Cell Death of Lymphoma Cells In Vivo while Sparing Normal B Cells

We next examined whether inhibition of Pol I transcription and thus activation of the Rp-MDM2-p53 nucleolar stress pathway could be used to selectively kill malignant B cells in vivo. C57BL/6 mice with established disease from transplanted Eμ-*Myc* lymphoma that is wild-type for p53 (Clone 4242) were treated with a single oral dose of CX-5461 (50 mg/kg) or vehicle. The Eμ-*Myc* tumor cells infiltrating the lymph nodes showed marked sensitivity to CX-5461, with cells exhibiting an 84% repression in Pol I transcription at 1 hr posttreatment (Figure 5A), also confirmed by RNA chromogenic in situ hybridization (CISH) for 47S pre-rRNA levels in the spleen (Figures S5A and S5B). Moreover, CX-5461 induced a rapid reduction in tumor burden in the lymph nodes (3.1% GFP-tagged malignant cells ± 0.20 for CX-5461-treated versus 34% GFP-tagged malignant cells ± 5.5 for vehicle-treated mice at 24 hr post therapy, $p < 0.01$) (Figures 5B and S5C) and a concomitant reduction of spleen size to within the normal range (0.14 g ± 0.01 for

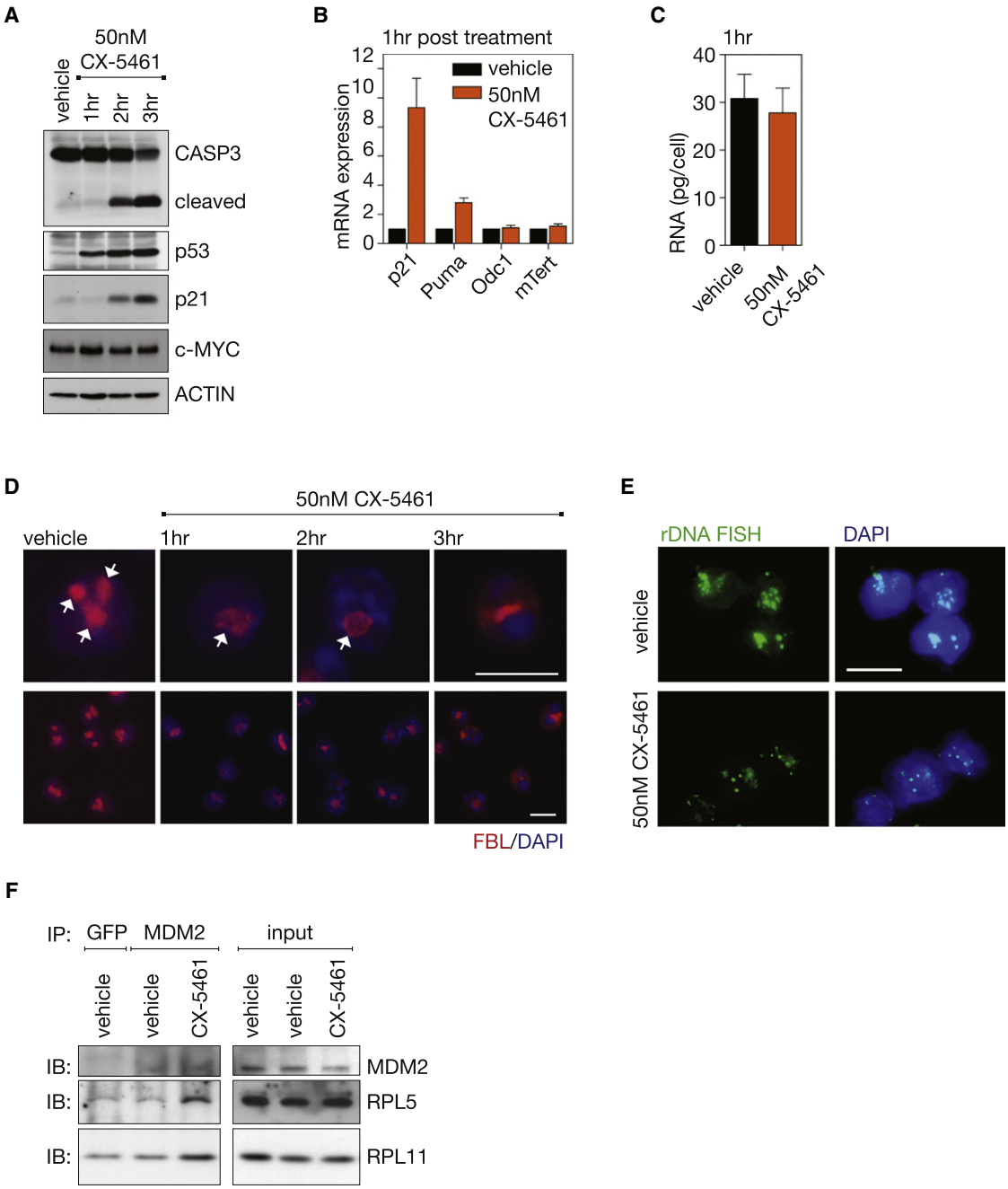

Figure 4. CX-5461 Activates p53 via the Nucleolar Stress Response in Eμ-*Myc* Lymphoma Cells

(A) Western blot analysis over 3 hr of cleavage of CASPASE 3 (CASP3), total p53, p21, and c-MYC in a p53 wt wild-type Eμ-*Myc* lymphoma cell line treated with 50 nM CX-5461 in culture. See also Figure S4A.

(B) Relative *p21*, *Puma*, *Odc1*, and *mTert* mRNA expression determined by qRT-PCR (n = 3).

(C) Total RNA per cell ($p > 0.05$; n = 3) in cells from (a) at 1 hr of CX-5461 treatment.

(D) Nucleolar disruption shown in cells from (a) by fibrillarin (FBL) immunofluorescence with DAPI counterstain, nucleoli indicated by white arrows. See also Figure S4B.

(E) rDNA fluorescent in situ hybridization (FISH) with DAPI counterstain 2 hr post CX-5461 treatment. See also Figures S4C and S4D.

(F) Coimmunoprecipitation of ribosomal proteins L5 (RPL5) and L11 (RPL11) with MDM2 (as compared to GFP control) in vehicle-treated Eμ-*Myc* lymphoma cells overexpressing BCL2 cells versus cells treated with 500 nM CX-5461, as shown by western immunoblot (IB) analysis. Images taken at 60× magnification. Scale bar represents 10 μm. Student's two-tailed t test for all comparisons. Error bars represent SEM. See also Figure S4D.

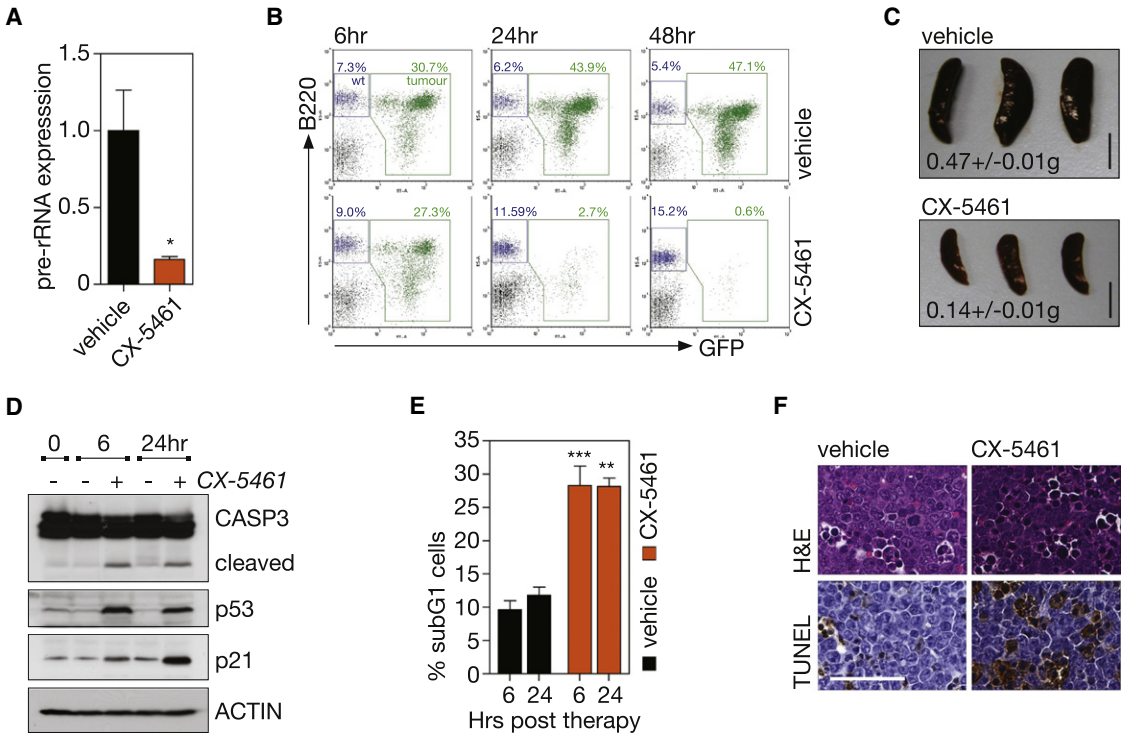

Figure 5. Therapeutic Administration of CX-5461 Selectively Kills Transplanted p53 Wild-type Eμ-*Myc* Lymphoma Cells In Vivo

(A) Pre-rRNA expression in tumor bearing lymph nodes of mice transplanted with p53 wild-type Eμ-*Myc* lymphoma cells (clone 4242) 1 hr posttreatment with 50 mg/kg CX-5461, determined by qRT-PCR ($p < 0.05$; n = 4). See also Figures S5A and S5B.

(B) FACS analysis of tumor burden in lymph node; stained with antibody against pan B cell marker B220, tumor cells GFP+ (green) (representative of n = 3). See also Figure S5C.

(C) Mean spleen weight ± SEM at 24 hr post therapy ($p < 0.001$; n = 3). Scale bar represents 1 cm.

(D) Western blot analysis at 6 and 24 hr of cleavage of CASP3, total p53, and p21 in the lymph node.

(E) Quantitation of apoptotic cells in lymph node, determined by subG1 DNA content analysis (vehicle versus CX-5461, $p < 0.001$ at 6 hr, $p < 0.01$ at 24 hr; n = 3). See also Figure S5D.

(F) Hematoxylin and eosin (H&E) and TUNEL stained lymph node sections at 6 hr post therapy; images taken at 40× magnification. Scale bar represents 50 μm. Student's two-tailed t test (a). One-way ANOVA with Tukey's multiple comparison posttest (c,e). Error bars represent SEM.

CX-5461-treated versus 0.47 g ± 0.01 for vehicle-treated mice at 24 hr posttherapy, $p < 0.001$) (Figure 5C). Consistent with the in vitro studies, reduction in malignant B cell numbers in vivo in response to CX-5461 therapy was preceded by the rapid activation of p53 and p21 and markers of apoptosis within 6 hr of drug administration (Figures 5D–5F and S5D).

Although CX-5461 activated p53 and induced apoptosis among malignant cells, it did not trigger these responses in the normal spleen cells of wild-type nontumor bearing mice (Figures 6A and 6B) and did not affect either spleen size or B cell numbers (Figures 6C and 6D). The lack of a cytotoxic effect in normal spleens cells was not due to lack of inhibition of Pol I transcription as CISH demonstrated robust reductions in 47S pre-rRNA levels in the spleens of wild-type nontumor bearing mice as observed in tumor bearing mice (Figures 6E and S6A) Furthermore, the nucleolar integrity of normal bone marrow cells from mice treated with CX-5461 was maintained, as determined by FBL and B23 immunofluorescence (Figure 6F). By comparison, exposure of nontumor bearing mice to 5Gy of γ-irradiation, a clinically appropriate dose for hematologic malignancies, resulted in marked elevation of p53 levels, apoptosis, reduced spleen weight, and B cell numbers (Figures 6A–6D). We also examined the response of B220+ B cells from the spleens and bone marrow of 4- to 6-week-old premalignant Eμ-*Myc* mice. These cells also demonstrated profound sensitivity to CX-5461 as characterized by p53 activation and markers of apoptotic cell death (increased CASP3 cleavage and sub-G1 cells) whereas the normal B cells from age-matched littermate mice failed to show p53 activation or increased cell death (Figures S6B–S6E). Together these data demonstrate the therapeutic response to inhibition of Pol I transcription by CX-5461 in vivo is highly selective for premalignant and malignant cells, which differentiates CX-5461 from genotoxic therapies such as γ-irradiation.

To further demonstrate the therapeutic effect of CX-5461 in this model, mice with established transplanted p53 wild-type Eμ-*Myc* lymphoma (clone 107) were treated with three doses of CX-5461 at 50 mg/kg once every 3 days. This regimen significantly prolonged the survival of the tumor-bearing mice (Figure 7A, $p < 0.0001$) and restored the white blood cell count to within the normal range (Figure 7B). Indeed, the day following the last dose of CX-5461, there were few identifiable GFP-tagged tumor cells in the peripheral blood (Figures 7C

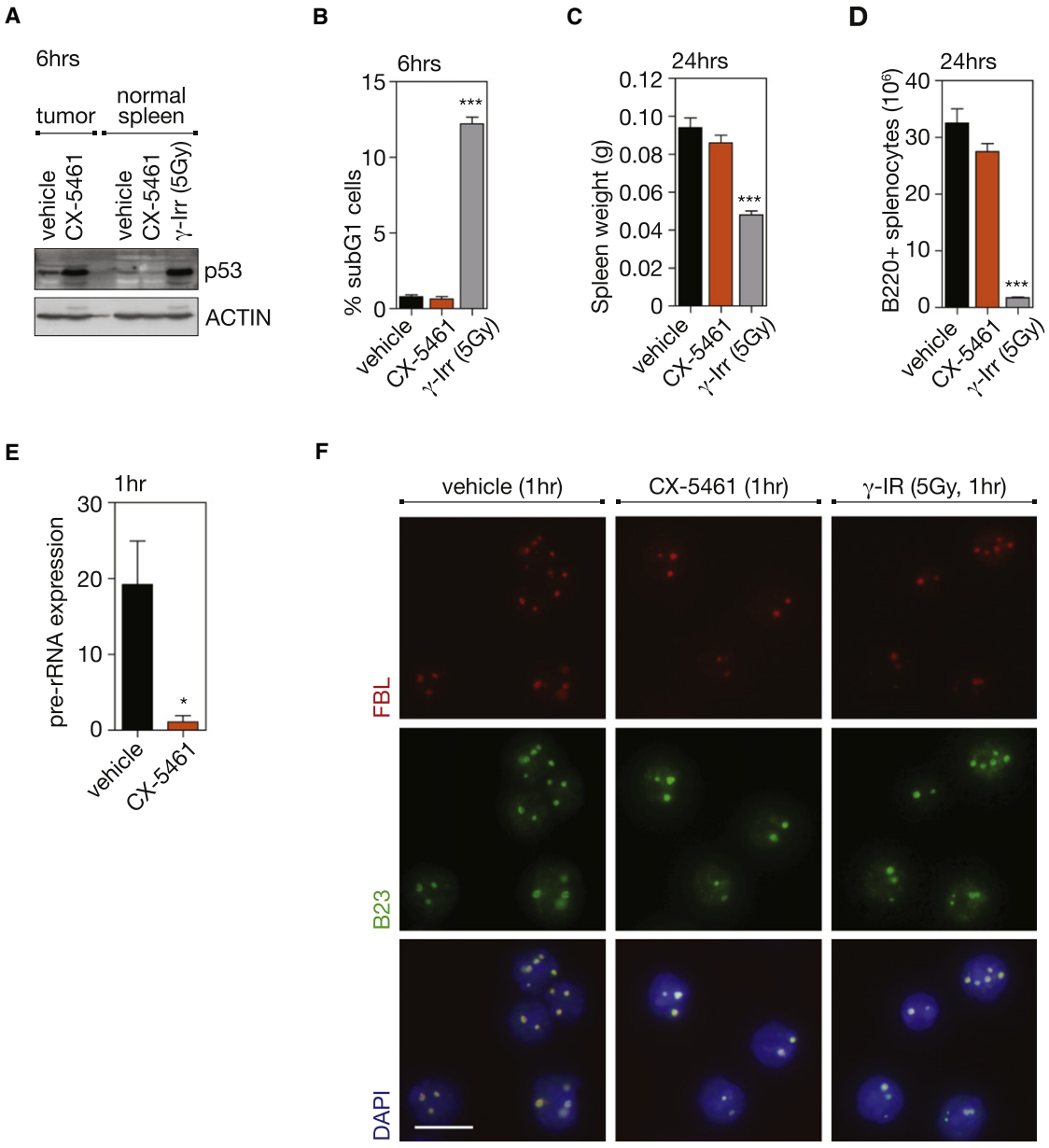

Figure 6. Therapeutic Administration of CX-5461, in Contrast to γ-Irradiation, Does Not Kill Normal B Cells In Vivo

(A) Western blot analysis of total p53 in tumor-bearing lymph nodes (tumor) (Figure 5) or spleen from wild-type (WT) mice (normal spleens) treated for 6 hr with vehicle, 40 mg/kg CX-5461, or 5 Gy γ-irradiation (γ-Irr).

(B) Quantitation of apoptotic cells in spleens of WT mice treated with vehicle, 40 mg/kg CX-5461 or 5 Gy γ-Irr; determined by subG1 DNA content analysis (vehicle versus γ-Irr, $p < 0.001$; $n = 5$).

(C) Spleen weight of WT mice treated for 24 hr with vehicle, 40 mg/kg CX-5461 or 5 Gy γ-Irr (vehicle versus γ-Irr, $p < 0.001$; $n = 5$).

(D) Number of B220+ cells in WT spleen at 24 hr post therapy, as determined by FACS and comparative cell counts on whole organ suspensions (vehicle versus γ-Irr, $p < 0.001$; $n = 5$).

(E) Pre-rRNA expression in spleen from WT mice at 1 hr posttreatment with vehicle or 40 mg/kg CX-5461, as determined by CISH using an anti-sense probe to the ITS1 ($p < 0.05$; $n = 3$ spleens, mean of six fields of comparative regions per spleen; %threshold area). See also Figure S6A.

(F) FBL and B23 immunofluorescence with DAPI counterstain on bone marrow from WT mice 1 hr posttreatment with vehicle, 40 mg/kg CX-5461, or 5 Gy γ-Irr; images taken at 60× magnification. Scale bar represents 10 μm. One-way ANOVA with Tukey's multiple comparison posttest (b–d). Student's two-tailed t test (e). Error bars represent SEM. See also Figure S6.

and 7D). Notably, there was preservation and restoration of the recipient-derived nonmalignant normal B cell population, again indicating selective eradication of malignant disease (Figure 7C, bottom panel). Moreover, more prolonged dosing with CX-5461 also showed minimal effects on normal B cells (data not shown). CX-5461 had no discernible adverse effect on the health of the

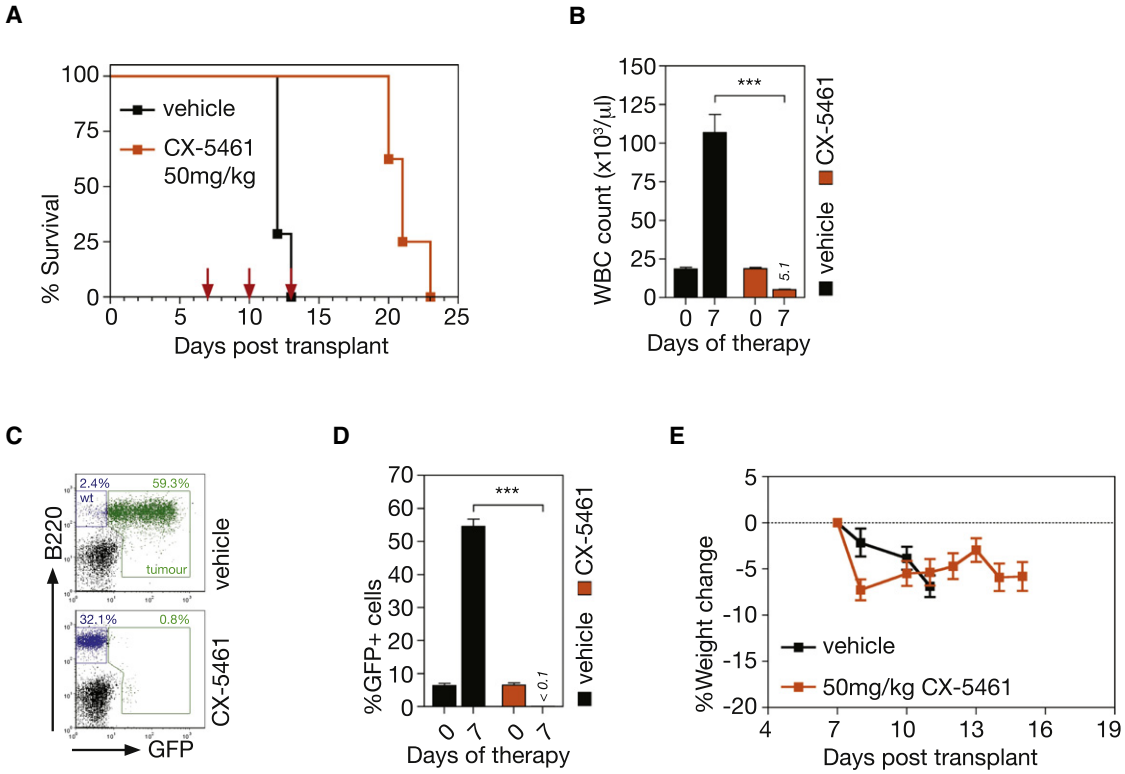

Figure 7. Therapeutic Administration of CX-5461 Increases Survival from Transplanted p53 Wild-type Eμ-*Myc* Lymphoma

(A) Kaplan-Meier curves showing increased survival of mice transplanted with p53 wild-type Eμ-*Myc* lymphoma (clone 107) treated with three doses of CX-5461 at 50 mg/kg in comparison to vehicle (dosing day indicated by arrows) ($p < 0.0001$; vehicle, n = 7; drug, n = 8).

(B) White blood cell (WBC) count at 0 and 7 days poststart of therapy (Day7 vehicle versus Day7 CX5461 $p < 0.001$; vehicle, n = 7; drug, n = 8).

(C) FACS analysis of tumor burden as measured by GFP+ B cells (B220+) in peripheral blood at 7 days posttherapy.

(D) Quantitation of FACS analysis (c) of tumor burden in the peripheral blood at 7 days poststart of therapy ($p < 0.0001$; vehicle, n = 7; drug, n = 8).

(E) Percent change in body weight of mice on therapy (vehicle, n = 7; drug, n = 8). Logrank test (a). One-way ANOVA with Tukey's multiple comparison posttest (b,d). Error bars represent SEM. See also Figure S7.

mice and the measured body weights showed minimal deviation below that at the commencement of therapy and in comparison to vehicle-treated mice (Figure 7E). To assess the ability of prolonged dosing of CX-5461 to extend survival, mice transplanted with p53 wild-type Eμ-*Myc* tumors (clone 4242) were maintained on continuous repeat dosing of CX-5461 at 40 mg/kg once every 3 days (Figure S7A). This treatment regimen reproducibly increased the average survival compared to the three repeat dose regimen with the mice going through a stage of apparent disease remission (no detectable tumor cells in peripheral blood at day 7/8) before eventually relapsing (Figures S7B–S7E). CX-5461 was also evaluated in a murine genetic model of acute myeloid leukemia (AML1/ETO9a+Nras) that reproduces many of the clinical aspects of leukemias in human patients that carry *AML1/ETO* fusion genes (Zuber et al., 2009). As with therapy in the Eμ-*Myc* model, transplanted AML1/ETO9a+Nras leukemic cells showed marked sensitivity to CX-5461 in vivo, undergoing p53-dependent apoptotic cell death within 6 hr of treatment of a single 40 mg/kg dose of CX-5461 (Figures S7F–S7I). This apoptotic response was comparable to 100 mg/kg cytarabine, a cytotoxic drug frequently used in treatment of patients with AML.

Inhibition of Pol I Transcription by CX-5461 Induces Apoptotic Cell Death of Human Hematological Malignancies with Sensitivity Correlating with p53 Mutational Status

To translate our findings with CX-5461 to human hematologic malignancies, we evaluated CX-5461 against a genetically diverse panel of cells derived from human hematologic cancers. Consistent with the data from the murine models (Figure 3C), viability assays demonstrated that human hematologic cancer cells wild-type for p53 were significantly more sensitive to CX-5461 (median IC_{50} = 12 nM) than p53 mutant cells (median IC_{50} = 230 nM) (Figure 8A). Three cell lines, SR (large cell immunoblastic lymphoma), MV 4;11 (biphenotypic B myelomonocytic leukemia), and K562 (chronic myelogenous leukemia) were examined in further detail. Although all three cell lines exhibited similar $IC_{50\ s}$ for Pol I transcription in response to CX-5461 (Figure 8B), the cell viability IC_{50} for the SR and MV 4;11 cell lines (IC_{50} = 5 nM and 12 nM, respectively) that are wild-type for p53, were 10–20-fold less than for K562 cells (IC_{50} = 104 nM) that carry a c.406_407insC nonsense mutation in p53 and hence do not express a stable p53 transcript. Consistent with this, CX-5461 induced rapid p53 accumulation and induction of the p53

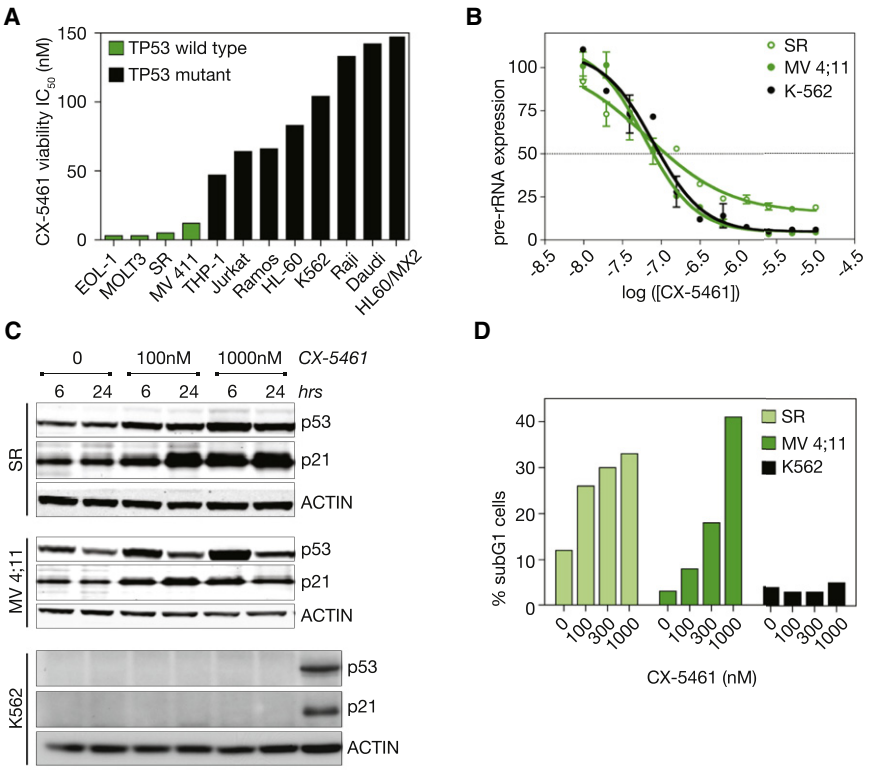

Figure 8. Human Leukemia and Lymphoma Cell Lines Treated with CX-5461

(A) The result of 96 hr treatment with CX-5461 on viability of human leukemia and lymphoma cell lines with different p53 status ($p < 0.0009$ comparing TP53 wild-type [WT] IC_{50} to TP53 mutant IC_{50}).

(B) Effect of CX-5461 on Pol I transcription in human cancer cell lines, as determined by qRT-PCR to the 5′ externally transcribed spacer (5′ ETS) region of the 47S pre-rRNA. Error bars represent SEM.

(C) CX-5461 induces p53 and p21 in p53 WT SR and MV 4;11 cell lines, but not in the p53 null K562 cell line, as determined by western blot analysis. A549 cell lysates used as positive control for p53 and p21 in K562 blots (far right lane).

(D) CX-5461 induces apoptosis in p53 WT SR and MV 4;11 cell lines, but not in the p53 null K562 cell line, as determined by subG1 DNA content analysis. See also Figures S8A and S8B.

(E) Activity of CX-5461 in vivo against MV 4;11 xenograft model as measured by increased tumor volume over days of therapy (n = 10). Error bars represent SEM. See also Figure S8C.

(F) CX-5461 induces p21 in MV 4;11 xenografts, as determined by western blot analysis of p21 normalized to ACTIN using densitometry ($p < 0.001$; n = 5). Student's two-tailed t test.

target p21 (Figure 8C), in addition to nucleolar disruption (Figure S8B) and subsequent induction of apoptosis as determined by induction of a subG1 population (Figure 8D) and Caspase 3/7 activity (after 24 hr) in both the SR and MV 4:11 lines (Figure S8A). In contrast, the p53-deficient K562 cells did not undergo apoptosis in response to CX-5461 (Figures 8D and S8A).

To determine whether this apoptotic response of cells derived from human hematologic malignancies following inhibition of Pol I transcription could be translated into a therapeutic index in vivo, MV 4:11 cells were transplanted subcutaneously into nude mice and the effect of CX-5461 on tumor growth examined. Notably, CX-5461 administered once weekly for 3 weeks demonstrated potent antitumor activity (Figure 8E), was associated with increased tumor levels of the p53 transcriptional target gene p21 (Figure 8F), and was well tolerated (Figure S8C).

Together these studies establish that Pol I transcription can be selectively targeted in vivo using a small molecule inhibitor of Pol I to preferentially eradicate hematologic malignant cells by activation of p53, while simultaneously maintaining a normal populations of cells of the same lineage.

DISCUSSION

Herein we have used RNAi to the essential Pol I-specific transcription factors UBF and RRN3 to provide robust genetic evidence that accelerated Pol I transcription is required for survival of malignant cells. Specifically we have show that reductions in rDNA transcription rate by as little as 35% result in apoptotic cell death of Eμ-*Myc* lymphoma cells rather than slower growing tumor cells as might be predicted. Using a newly described small molecule inhibitor of Pol I transcription, CX-5461, we extended these findings to demonstrate that dysregulation of the synthesis of rRNA plays an essential role in cancer cell biology in vivo, thus providing an important alternative approach for the treatment of malignant diseases. One of the most striking and unanticipated findings of these studies was the demonstration that the apoptotic death induced by reductions in Pol I transcription occurred rapidly as the result of immediate activation of p53 following perturbations of the nucleolus rather than an indirect effect resulting from reduced ribosome accumulation and defective protein translation. This is in contrast to what was previously demonstrated in the Eμ-*Myc* lymphoma model following ribosomal protein haploinsufficiency (Barna et al., 2008). Indeed when apoptosis was blocked in Rrn3 knockdown Eμ-*Myc* cells, the resultant

35% reduction in rDNA transcription rate did not result in a proliferative disadvantage of these cells. Thus contrary to the commonly accepted belief, rDNA transcription rates are not always rate limiting for optimal proliferative growth of mammalian cells. Our data demonstrate that MYC's control of Pol I transcription and nucleolar integrity is required for its oncogenic potential, independent of its function in regulating ribosome levels, protein translation, and proliferative growth. These findings also lend strong support for the evolving paradigm of the nucleolus being a key regulator of biology of the cancer cell distinct from its role in determining the abundance of ribosomes (Boisvert et al., 2007).

The rapid disruption of the nucleolus and subsequent induction of p53-mediated apoptotic cell death in response to CX-5461 is consistent with induction of the nucleolar stress pathway (also called the ribosome biogenesis surveillance/sensing pathway) (Boulon et al., 2010; Deisenroth and Zhang, 2010; Fumagalli et al., 2009) that acutely monitors the integrity of ribosome biogenesis pathway and activates p53 when the fidelity of this complex process is dysregulated. This pathway can be initiated by the accumulation of free ribosomal proteins following perturbation of ribosome biogenesis (Boulon et al., 2010; Deisenroth and Zhang, 2010) or MYC activation (Macias et al., 2010). The release of free ribosomal proteins from the nucleolus has been shown to sequester the p53 ligase MDM2 leading to elevated p53 levels and to directly increase p53 translation, the net result of which is induction of apoptosis (Boulon et al., 2010; Deisenroth and Zhang, 2010). Thus, the ribosome surveillance pathway (ribosomal protein-MDM2-p53) works independently of ARF and functions in parallel and cooperatively with ARF-dependent MYC oncogenic stress pathways to restrain MYC oncogenesis (Macias et al., 2010). Most likely, not only does impaired ribosome biogenesis act as a trigger to induce p53, but ribosome biogenesis is also a homeostatic regulator in normal cells, tightly linking on-going production of newly synthesized ribosomes with p53 levels (Boulon et al., 2010; Deisenroth and Zhang, 2010; Fumagalli et al., 2009). Here we show how this process can be exploited as a therapeutic strategy to selectively kill malignant cells. Moreover, as a nongenotoxic, cancer-specific activator of p53, CX-5461 is ~300-fold more potent at killing Eμ-*Myc* lymphoma cells (IC_{50} for cell death of 5.4 nM) than Nutlin-3A, a selective small-molecule MDM2 antagonist and p53 activator (IC_{50} for cell death of 1600 nM, results not shown), that is currently in clinical trials (Saha et al., 2010).

The data herein also demonstrate that Pol I transcription can be therapeutically targeted to selectively activate p53 and kill malignant cells of hematologic origin in vivo while maintaining a viable population of wild-type cells of the same lineage. Indeed, normal B cells isolated from the bone marrow of wild-type mice treated in vivo with CX-5461 at doses sufficient to kill malignant Eμ-*Myc* B cells, did not exhibit disruption of their nucleoli, activation of p53 or induction of apoptosis despite having a significantly reduced rate of Pol I transcription. In contrast, treatment of wild-type mice with doses of γ-irradiation similar to those used therapeutically for human hematologic malignancies induced robust apoptotic cell death associated with p53 activation in normal B cells. This striking tumor cell selective activity following inhibition of Pol I transcription by CX-5461 is most likely a function of the robust upregulation of ribosome biogenesis we have shown to occur during MYC driven lymphomagenesis sensitizing cells to the induction of the nucleolar stress pathway. The MYC-induced upregulation of rRNA synthesis also requires a stoichiometric elevation in the levels of ribosomal proteins in the nucleolus. Inhibition of rRNA synthesis in cancer cells would result in excessive accumulation of free ribosomal proteins and subsequent activation of the nucleolar stress pathway and p53 as described above. Consistent with this model, treatment of Eμ-*Myc* lymphoma cells with CX-5461 promoted enhanced association of ribosomal proteins L5 and L11 with MDM2 and subsequent activation of p53. Furthermore, premalignant B cells of 4- to 6-week-old Eμ-*Myc* transgenic mice also displayed p53-mediated increased sensitivity to CX-5461 providing evidence that MYC overexpression alone, independent of a fully malignant phenotype, may serve to prime the nucleolar stress pathway in cells. Given that a range of other oncogenes including PI3K, AKT, and Ras also play important roles regulating ribosome biogenesis (Chan et al., 2011; Hannan et al., 2003; Ruggero and Pandolfi, 2003; Stefanovsky et al., 2001; White, 2005), our findings indicate that selective activation of the ribosome biogenesis surveillance pathway to activate p53 using small molecule inhibitors of Pol I is likely to be therapeutically useful in the treatment of a wide range of tumors in addition to those under control of MYC. Indeed, we demonstrated that CX-5461 potently induced p53-dependent apoptosis of non-MYC driven tumor cells in vivo using a transgenic model of AML in which the leukemic cells coexpress the AML/ETO9a fusion protein with NRas. However, we note that increased expression of MYC is common in hematologic malignancies even when it is not the primary driving event (for example AML/ETO9a leukemia cells have elevated MYC levels). Thus we cannot discount the possibility that MYC may be a common factor in conferring sensitivity to apoptotic death in hematologic malignancies in response to Pol I inhibition.

We also demonstrated that CX-5461 also exhibits potent antigrowth capacity in a broad range of human hematological tumor cell lines with sensitivity being dependent on the genetic and functional status of p53. Importantly, p53 gene mutations are rare at diagnosis in common cancers of hematopoietic origin (Saha et al., 2010), suggesting that inhibition of Pol I may be a broadly applicable therapeutic approach for treatment of numerous human hematological cancers. In support of this, CX-5461 demonstrated potent antitumor activity in a xenograft model of biphenotypic B myelomonocytic leukemia. Intriguingly, human cell lines from solid tumors do not generally demonstrate p53 dependent apoptotic responses following Pol I transcription inhibition (Drygin et al., 2011) but instead undergo senescence and autophagy. This differential response highlights the dissimilarity in the crosstalk between the nucleolar stress and cell death in different types of cancer. It is possible that hematological malignancies have a unique nucleolar biology that makes them especially susceptible to activation of p53 and apoptotic cell death following acute perturbations of ribosome biogenesis. In support of this notion, mutations in genes encoding ribosomal proteins that cause defects in ribosome biogenesis and activate p53 is emerging as a shared paradigm among bone marrow failure syndromes such as Diamond Blackfan Anemia (DBA) and the acquired 5q syndrome myelodysplastic syndrome

(del [5q] MDS) that both exhibit increased cancer susceptibility. Together these data suggest that patients with hematologic malignancies represent a highly sensitive population for the initial trial of CX-5461 in humans.

In summary, our work demonstrates that hematologic tumor cells depend upon hyperactivated rDNA transcription and integrity of Pol I transcription for survival and this dependency is vulnerable to perturbations that induce apoptosis via a process that is independent of ribosome levels or effects on proliferation. Further, we show that a selective inhibitor of Pol I transcription, CX-5461, causes cancer-specific activation of p53 and induction of apoptosis that results in the improvement of outcome in in vivo models of leukemia and lymphoma.

EXPERIMENTAL PROCEDURES

Eμ-*Myc* Transgenic Mice, B Cell Purification, and Lymphoma Cell Lines

All animal work was performed with approval from the Peter MacCallum Cancer Centre Animal Experimentation Ethics Committee and Cylene Pharmaceuticals' Institutional Animal Care and Use Committee. Eμ-*Myc* mice were maintained as heterozygote on a C57BL/6 background. Primary B cells were purified from the spleen of transgenic mice and their wild-type littermates with anti-B220 conjugated microbeads (Miltenyi Biotech) using the autoMACS system (Miltenyi Biotech) according to manufacturer's instructions. Lymphoma cell lines were generated from lymph nodes of tumor bearing Eμ-*Myc*/+, Eμ-*Myc*/*p53*$^{+/-}$, Eμ-*Myc*/*Arf*$^{+/-}$ mice, and Eμ-*Myc*/*Atm*$^{-/-}$. Cell lines were determined as mutant for p53 via sequencing or assessment of protein molecular weight via western blotting, in addition to exhibiting resistance to etoposide. For in vivo drug studies, 1 × 10^5 Eμ-*Myc* lymphoma cells were injected into the tail veins of wild-type C57BL/6 mice. Peripheral blood was sampled by retro-orbital bleeding into 10 mM EDTA. For in vivo drug studies with the mouse model of AML, Scott Lowe generously provided leukemia cells isolated from the spleens of tumor-bearing mice. Leukemia cells (1 × 10^6), AML1/ETO9a NRas p53 wt, or p53−/−, were injected into the tail vein of irradiated (2 × 3 Gy) recipient C57BL/6 mice. Leukemia onset/progression was monitored by peripheral blood analysis and single dose of 40 mg/kg CX-5461 was administrated when ~40%–50% GFP+ cells in the peripheral blood were detectable. Lymphoma cell lines were maintained in Anne Kelso DMEM supplemented with 10% FBS, 100 μM L-asparagine (Sigma), 0.5% β-mercaptoethanol, and penicillin/streptomycin/glutamine (GIBCO). Cell volume was determined using a Beckman Coulter Z series. shRNA-mediated knockdown was achieved via retroviral transduction as described (Schmitt et al., 2000) using the CSHL vector system LMS (Dickins et al., 2005) with the short-hairpin sequences listed in Supplemental Experimental Procedures. Transduced populations were selected by sorting for GFP expression on a BD FACS Vantage SE. Bcl2 overexpression was achieved by sorting for Cherry expression following retroviral transduction with a MSCV vector expressing *Bcl2* cDNA.

Orthophosphate Labeling

Lymphoma cells (1.5 × 10^6) were cultured in 3 ml media in the presence of 500 μCi of ^{32}P orthophosphate for 20 min. Cells were harvested on ice and RNA extracted using the QIAGEN RNAeasy kit, according to the manufacturer's instructions. RNA (7 μg) was run overnight on a 1.2% MOPS/formaldehyde agarose gel. The gel was dried using a Bio-Rad gel dryer, exposed overnight to a phospho imager screen and scanned using a Typhoon TRI variable mode imager (GE Healthcare). The radioactivity of each band was determined using the Image Quant TL software (GE Healthcare).

Immunofluorescence and FISH

For immunofluorescence, cells were fixed in a 2% paraformaldehyde suspension and spun onto slides. Cells were stained with antibodies listed in Supplemental Experimental Procedures followed by the appropriate secondary, either 594 conjugated goat anti-rabbit IgG (Molecular Probe, A21442) or 488 conjugated goat anti-mouse IgG1 (Jackson ImmunoResearch Laboratories). Stained cells were fixed again with 4% formaldehyde, counterstained with DAPI, and visualized on an Olympus BX-51 microscope, with images captured using the SPOT Advance image acquisition software (Diagnostic Instruments). For FISH, 1 μg of BAC clone (RP23-225M6) was biotin-labeled using a nick translation kit (Roche), according to the manufacturer's instructions. Labeled probe (100 ng) was precipitated in ethanol together with 30 μg salmon sperm DNA and 18 μg COT1 carrier DNA (Invitrogen) and dissolved in 30 μl hybridization buffer (50% formamide, 20% dextran sulfate in 2× SSC). Probes were denatured at 95°C for 5 min then incubated at 37°C for 1 hr. Cells were fixed in paraformaldehyde and spun onto slides as described above. Slides were fixed in methanol/acetic acid (3:1) for 5 min at room temperature and dried then dehydrated through an ethanol series. Slides were incubated in 70% formamide/2× SSC for 10 min at 83°C and then dehydrated through an ethanol series. Slides were hybridized overnight at 37°C in a humidified chamber and then washed in 50% formamide/2× SSC at 42°C for 15 min and 0.1× SSC at 60°C for 15 min. Streptavidin-Alexa fluor 488 was added for 1 hr at 37°C and slides were then washed in 0.05% Tween-20/4× SSC for 15 min. Slides were mounted in DAPI and microscopy was performed as above. Quantitation was performed using MetaMorph (Molecular Devices, Sunnydale, CA).

Histology

Harvested tissues were fixed in 10% neutral buffered formalin overnight followed by paraffin wax embedding. Hematoxylin and eosin staining (H&E) was performed on 4 μm sections. TUNEL staining was performed on 4 μm sections using an Apoptag Peroxidase In Situ Apoptosis Detection kit (Chemicon, S7100), according to the manufacturer's instructions. For CISH, 4 μm sections were dewaxed in xylene followed by an ethanol series. Epitope recovery was performed with incubation at 120°C in 10 mM sodium citrate (pH 6.0) followed by the addition of proteinase K (12.5 ng/ml) and finally, fixation in formaldehyde (4%). Hybridization was performed overnight at 37°C with digoxigenin-labeled oligonucleotide rRNA anti-sense probe to the ITS1. Sense probe hybridization was performed under identical conditions on serial sections as a negative control. Sections were incubated with anti-Digoxigenin-alkaline phosphatase (Roche, 11093274910) and signal was detected in 100 mM NaCl, 100 mM Tris (pH 9.5) buffer containing 0.18 mg/ml BCIP, 0.34 mg/ ml NBT (Roche, 11 681 451 001), and 240 μg/ml levamisole (Sigma). Tissues were counter stained with nuclear fast red stain. Sections were visualized on an Olympus BX-51 and images captured using the SPOT Advance image acquisition software. Quantitation was performed using MetaMorph (Molecular Devices).

MV 4;11 Xenograft Model

Female immunocompromised mice CrTac:Ncr-Foxn1nu (6–8 weeks old) were obtained from Taconic Farms (Germantown, NY). Animals were maintained under clean room conditions in sterile filter top cages. Animals received sterile rodent chow and water ad libitum. All procedures were conducted in accordance with the Institute for Laboratory Animal Research Guide: The Care and Use of Laboratory Animals. Xenografts were initiated by subcutaneous injection of 5 × 10^6 MV 4;11 cells into the right hind flank region of each mouse. When tumors reached a designated volume of ~150 mm^3, animals were randomized and divided into Vehicle (50 mM NaH_2PO_4, pH 4.5) or CX-5461 treatment groups of 10 mice per group. CX-5461 was administered intraperitoneally once a week at 125 mg/kg for the length of 25 days. Tumor volumes and body weights were measured twice weekly. The length and width of the tumor were measured with calipers and the volume calculated using the following formula: tumor volume = (length × $width^2$)/2. Tumor growth inhibition (TGI) was determined on the last day of study according to the formula: TGI (%) = [100 − (Vf^D − Vi^D)/(Vf^V − Vi^V) × 100], where Vi^V is the initial mean tumor volume in vehicle-treated group, Vf^V is the final mean tumor volume in vehicle-treated group, Vi^D is the initial mean tumor volume in drug-treated group, and Vf^D is the final mean tumor volume in drug-treated group.

SUPPLEMENTAL INFORMATION

Supplemental Information includes eight figures and Supplemental Experimental Procedures and can be found with this article online at http://dx.doi.org/10.1016/j.ccr.2012.05.019.

ACKNOWLEDGMENTS

This work was supported by the National Health and Medical Research Council (NHMRC) of Australia project grants; NHMRC Research Fellowship to R.D.H.; NHMRC Postgraduate Research Scholarship, GSK Postgraduate Research Scholarship and Leukaemia Foundation Postdoctoral Fellowship to M.J.B.; Cancer Council of Victoria Sir Edward Weary Dunlop Clinical Research Fellowship and NHMRC Research Fellowship to G.A.M.; The John T. Reid Charitable Trusts and Mrs. Margaret Ross AM; and in part by Cylene Pharmaceuticals. We thank Joseph Trapani and James Whisstock for critical evaluation of the manuscript, Brian McStay for anti-sera to RRN3 and Sinisa Volarevic for anti-sera to rpL5. We also thank Rachael Walker, Kym Stanley, Analia Lesmana, Kerry Ardley, Susan Jackson, Jeannette Valentan, Kathryn Kinross, Petranel Ferrao, Ralph Rossi, and Sarah Ellis for technical assistance.

M.J.B., G.P., G.A.M., and R.D.H. were responsible for the overall concept and design of experiments. D.D., K.A., M.H., M.K.S., D.M.R., W.G.R., S.W.L., and R.W.J provided essential materials. M.J.B., G.P., E.S., N.Hein, A.P., C.C., L.C., N.H., C.P., J.B., D.D., G.A.M., and R.D.H. were responsible for the collection and assembly of data. M.J.B., G.P., E.S., N.Hein, C.C., M.W., D.D., K.A., R.W.J., R.B.P., G.A.M., and R.D.H. were involved in data analysis and interpretation. M.J.B., G.P., E.S., C.C., M.W., D.D., K.A., W.G.R., S.W.L., R.W.J., R.B.P., G.A.M., and R.D.H. were involved in the writing of the manuscript and all authors approved the final form. D.D., K.A., N.H., C.P., J.B., M.H., M.K.S., D.M.R., and W.G.R. are affiliated with Cylene Pharmaceuticals in being current or past employees of the company. However, this did not influence the conduct of the research described in this manuscript and had no bearing on the decision to submit this paper for publication.

Received: September 8, 2011
Revised: March 2, 2012
Accepted: May 15, 2012
Published: July 9, 2012

REFERENCES

Adams, J.M., Harris, A.W., Pinkert, C.A., Corcoran, L.M., Alexander, W.S., Cory, S., Palmiter, R.D., and Brinster, R.L. (1985). The c-myc oncogene driven by immunoglobulin enhancers induces lymphoid malignancy in transgenic mice. Nature *318*, 533–538.

Arabi, A., Wu, S., Ridderstråle, K., Bierhoff, H., Shiue, C., Fatyol, K., Fahlén, S., Hydbring, P., Söderberg, O., Grummt, I., et al. (2005). c-Myc associates with ribosomal DNA and activates RNA polymerase I transcription. Nat. Cell Biol. *7*, 303–310.

Barna, M., Pusic, A., Zollo, O., Costa, M., Kondrashov, N., Rego, E., Rao, P.H., and Ruggero, D. (2008). Suppression of Myc oncogenic activity by ribosomal protein haploinsufficiency. Nature *456*, 971–975.

Boisvert, F.M., van Koningsbruggen, S., Navascués, J., and Lamond, A.I. (2007). The multifunctional nucleolus. Nat. Rev. Mol. Cell Biol. *8*, 574–585.

Boulon, S., Westman, B.J., Hutten, S., Boisvert, F.M., and Lamond, A.I. (2010). The nucleolus under stress. Mol. Cell *40*, 216–227.

Chan, J.C., Hannan, K.M., Riddell, K., Ng, P.Y., Peck, A., Lee, R.S., Hung, S., Astle, M.V., Bywater, M., Wall, M., et al. (2011). AKT promotes rRNA synthesis and cooperates with c-MYC to stimulate ribosome biogenesis in cancer. Sci. Signal. *4*, ra56.

Dai, M.S., and Lu, H. (2008). Crosstalk between c-Myc and ribosome in ribosomal biogenesis and cancer. J. Cell. Biochem. *105*, 670–677.

Dang, C.V., O'Donnell, K.A., Zeller, K.I., Nguyen, T., Osthus, R.C., and Li, F. (2006). The c-Myc target gene network. Semin. Cancer Biol. *16*, 253–264.

Deisenroth, C., and Zhang, Y. (2010). Ribosome biogenesis surveillance: probing the ribosomal protein-Mdm2-p53 pathway. Oncogene *29*, 4253–4260.

Derenzini, M., Montanaro, L., and Treré, D. (2009). What the nucleolus says to a tumour pathologist. Histopathology *54*, 753–762.

Dickins, R.A., Hemann, M.T., Zilfou, J.T., Simpson, D.R., Ibarra, I., Hannon, G.J., and Lowe, S.W. (2005). Probing tumor phenotypes using stable and regulated synthetic microRNA precursors. Nat. Genet. *37*, 1289–1295.

Drygin, D., Lin, A., Bliesath, J., Ho, C., O'Brien, S., Proffitt, C., Omori, M., Haddach, M., Schwaebe, M., Siddiqui-Jain, A., et al. (2011). Targeting RNA polymerase I with an oral small molecule CX-5461 inhibits ribosomal RNA synthesis and solid tumor growth. Cancer Res. *71*, 1418–1430.

Eischen, C.M., Weber, J.D., Roussel, M.F., Sherr, C.J., and Cleveland, J.L. (1999). Disruption of the ARF-Mdm2-p53 tumor suppressor pathway in Myc-induced lymphomagenesis. Genes Dev. *13*, 2658–2669.

Fumagalli, S., Di Cara, A., Neb-Gulati, A., Natt, F., Schwemberger, S., Hall, J., Babcock, G.F., Bernardi, R., Pandolfi, P.P., and Thomas, G. (2009). Absence of nucleolar disruption after impairment of 40S ribosome biogenesis reveals an rpL11-translation-dependent mechanism of p53 induction. Nat. Cell Biol. *11*, 501–508.

Grandori, C., Gomez-Roman, N., Felton-Edkins, Z.A., Ngouenet, C., Galloway, D.A., Eisenman, R.N., and White, R.J. (2005). c-Myc binds to human ribosomal DNA and stimulates transcription of rRNA genes by RNA polymerase I. Nat. Cell Biol. *7*, 311–318.

Grewal, S.S., Li, L., Orian, A., Eisenman, R.N., and Edgar, B.A. (2005). Myc-dependent regulation of ribosomal RNA synthesis during Drosophila development. Nat. Cell Biol. *7*, 295–302.

Hannan, K.M., Brandenburger, Y., Jenkins, A., Sharkey, K., Cavanaugh, A., Rothblum, L., Moss, T., Poortinga, G., McArthur, G.A., Pearson, R.B., and Hannan, R.D. (2003). mTOR-dependent regulation of ribosomal gene transcription requires S6K1 and is mediated by phosphorylation of the carboxy-terminal activation domain of the nucleolar transcription factor UBF. Mol. Cell. Biol. *23*, 8862–8877.

Hannan, R.D., Hempel, W.M., Cavanaugh, A., Arino, T., Dimitrov, S.I., Moss, T., and Rothblum, L. (1998). Affinity purification of mammalian RNA polymerase I. Identification of an associated kinase. J. Biol. Chem. *273*, 1257–1267.

Iritani, B.M., and Eisenman, R.N. (1999). c-Myc enhances protein synthesis and cell size during B lymphocyte development. Proc. Natl. Acad. Sci. USA *96*, 13180–13185.

Jorgensen, P., Nishikawa, J.L., Breitkreutz, B.J., and Tyers, M. (2002). Systematic identification of pathways that couple cell growth and division in yeast. Science *297*, 395–400.

Klein, G. (1993). Multistep evolution of B-cell-derived tumors in humans and rodents. Gene *135*, 189–196.

Larminie, C.G., Alzuherri, H.M., Cairns, C.A., McLees, A., and White, R.J. (1998). Transcription by RNA polymerases I and III: a potential link between cell growth, protein synthesis and the retinoblastoma protein. J. Mol. Med. *76*, 94–103.

Lohrum, M.A., Ludwig, R.L., Kubbutat, M.H., Hanlon, M., and Vousden, K.H. (2003). Regulation of HDM2 activity by the ribosomal protein L11. Cancer Cell *3*, 577–587.

Macias, E., Jin, A., Deisenroth, C., Bhat, K., Mao, H., Lindström, M.S., and Zhang, Y. (2010). An ARF-independent c-MYC-activated tumor suppression pathway mediated by ribosomal protein-Mdm2 Interaction. Cancer Cell *18*, 231–243.

McStay, B., and Grummt, I. (2008). The epigenetics of rRNA genes: from molecular to chromosome biology. Annu. Rev. Cell Dev. Biol. *24*, 131–157.

Poortinga, G., Hannan, K.M., Snelling, H., Walkley, C.R., Jenkins, A., Sharkey, K., Wall, M., Brandenburger, Y., Palatsides, M., Pearson, R.B., et al. (2004). MAD1 and c-MYC regulate UBF and rDNA transcription during granulocyte differentiation. EMBO J. *23*, 3325–3335.

Poortinga, G., Wall, M., Sanij, E., Siwicki, K., Ellul, J., Brown, D., Holloway, T.P., Hannan, R.D., and McArthur, G.A. (2011). c-MYC coordinately regulates ribosomal gene chromatin remodeling and Pol I availability during granulocyte differentiation. Nucleic Acids Res. *39*, 3267–3281.

Ruggero, D., and Pandolfi, P.P. (2003). Does the ribosome translate cancer? Nat. Rev. Cancer *3*, 179–192.

Saha, M.N., Micallef, J., Qiu, L., and Chang, H. (2010). Pharmacological activation of the p53 pathway in haematological malignancies. J. Clin. Pathol. *63*, 204–209.

Sanij, E., Poortinga, G., Sharkey, K., Hung, S., Holloway, T.P., Quin, J., Robb, E., Wong, L.H., Thomas, W.G., Stefanovsky, V., et al. (2008). UBF levels determine the number of active ribosomal RNA genes in mammals. J. Cell Biol. *183*, 1259–1274.

Schmitt, C.A., Rosenthal, C.T., and Lowe, S.W. (2000). Genetic analysis of chemoresistance in primary murine lymphomas. Nat. Med. *6*, 1029–1035.

Shiue, C.N., Berkson, R.G., and Wright, A.P. (2009). c-Myc induces changes in higher order rDNA structure on stimulation of quiescent cells. Oncogene *28*, 1833–1842.

Stefanovsky, V.Y., Pelletier, G., Hannan, R., Gagnon-Kugler, T., Rothblum, L.I., and Moss, T. (2001). An immediate response of ribosomal transcription to growth factor stimulation in mammals is mediated by ERK phosphorylation of UBF. Mol. Cell *8*, 1063–1073.

van Riggelen, J., Yetil, A., and Felsher, D.W. (2010). MYC as a regulator of ribosome biogenesis and protein synthesis. Nat. Rev. Cancer *10*, 301–309.

White, R.J. (2005). RNA polymerases I and III, growth control and cancer. Nat. Rev. Mol. Cell Biol. *6*, 69–78.

Yuan, X., Zhou, Y., Casanova, E., Chai, M., Kiss, E., Gröne, H.J., Schütz, G., and Grummt, I. (2005). Genetic inactivation of the transcription factor TIF-IA leads to nucleolar disruption, cell cycle arrest, and p53-mediated apoptosis. Mol. Cell *19*, 77–87.

Zhang, Y., Wolf, G.W., Bhat, K., Jin, A., Allio, T., Burkhart, W.A., and Xiong, Y. (2003). Ribosomal protein L11 negatively regulates oncoprotein MDM2 and mediates a p53-dependent ribosomal-stress checkpoint pathway. Mol. Cell. Biol. *23*, 8902–8912.

Zuber, J., Radtke, I., Pardee, T.S., Zhao, Z., Rappaport, A.R., Luo, W., McCurrach, M.E., Yang, M.M., Dolan, M.E., Kogan, S.C., et al. (2009). Mouse models of human AML accurately predict chemotherapy response. Genes Dev. *23*, 877–889.

Cancer Cell
Article

Nrf2 Redirects Glucose and Glutamine into Anabolic Pathways in Metabolic Reprogramming

Yoichiro Mitsuishi,[1,2,6] Keiko Taguchi,[1,6] Yukie Kawatani,[1] Tatsuhiro Shibata,[4] Toshihiro Nukiwa,[2] Hiroyuki Aburatani,[5] Masayuki Yamamoto,[1,*] and Hozumi Motohashi[3,*]
[1]Department of Medical Biochemistry
[2]Department of Respiratory Medicine
[3]Center for Radioisotope Sciences
Tohoku University Graduate School of Medicine, 2-1 Seiryo-machi, Aoba-ku, Sendai, Miyagi, 980-8575, Japan
[4]Division of Cancer Genomics, Center for Medical Genomics, National Cancer Center Research Institute, 5-1-1, Tsukiji, Chuo-ku, Tokyo, 104-0045, Japan
[5]Research Center for Advanced Science and Technology, The University of Tokyo, 4-6-1, Komaba, Meguro-ku, Tokyo, 153-8904, Japan
[6]These authors contributed equally to this work
*Correspondence: masiyamamoto@med.tohoku.ac.jp (M.Y.), hozumim@med.tohoku.ac.jp (H.M.)
DOI 10.1016/j.ccr.2012.05.016

SUMMARY

Cancer cells consume large quantities of nutrients and maintain high levels of anabolism. Recent studies revealed that various oncogenic pathways are involved in modulation of metabolism. Nrf2, a key regulator for the maintenance of redox homeostasis, has been shown to contribute to malignant phenotypes of cancers including aggressive proliferation. However, the mechanisms with which Nrf2 accelerates proliferation are not fully understood. Here, we show that Nrf2 redirects glucose and glutamine into anabolic pathways, especially under the sustained activation of PI3K-Akt signaling. The active PI3K-Akt pathway augments the nuclear accumulation of Nrf2 and enables Nrf2 to promote metabolic activities that support cell proliferation in addition to enhancing cytoprotection. The functional expansion of Nrf2 reinforces the metabolic reprogramming triggered by proliferative signals.

INTRODUCTION

Metabolic activities in proliferating cells are fundamentally different from those in quiescent cells (DeBerardinis et al., 2008). Quiescent cells invest large amounts of energy in the maintenance of functional and morphological integrity against extrinsic and intrinsic insults, including oxidative stress. In contrast, proliferating cells take up abundant nutrients, including glucose and glutamine, and shunt their metabolites into anabolic pathways. The signals that promote cell proliferation direct the reprogramming of metabolic activities, which pushes quiescent cells into proliferative states. Recent studies have revealed that oncogenic pathways involving oncogenes and tumor suppressor genes, such as *c-Myc*, *p53*, and *PI3K-Akt*, directly promote the uptake and metabolism of glucose and glutamine, resulting in metabolic features that are unique to proliferating cells (Kroemer and Pouyssegur, 2008; Tong et al., 2009; Dang, 2010).

The pentose phosphate pathway (PPP) generates ribose 5-phosphate (R5P), a critical substrate for the nucleotide synthesis, and NADPH as reducing equivalents. Although the PPP is a well-established metabolic pathway, a direct regulator that activates the PPP during metabolic reprogramming has yet to be identified. One of the p53 targets, TIGAR, inhibits glycolysis and diverts the carbon flux into the PPP, resulting in the passive promotion of the PPP activity (Bensaad et al., 2006). However, because glycolysis is often facilitated in proliferating cells, alternative mechanisms that actively promote the PPP are expected to be involved.

Significance

Nrf2 is an inducible transcription activator for cytoprotection from xenobiotic and oxidative stresses. Increasing attention has been paid to the role of Nrf2 in cancer cells because the constitutive stabilization of NRF2 has been observed in many human cancers that have poor prognoses. Recent studies revealed that antioxidant and detoxification activities carried out by Nrf2 confer growth advantages on cancer cells. In this study, we show that Nrf2 directly or indirectly facilitates the metabolic pathways that enhance cell proliferation in the presence of active PI3K-Akt signaling. Thus, Nrf2 contributes to cancer development by modulating metabolism in addition to enhancing cellular stress response. This study expands upon current knowledge regarding the role of Nrf2 in the malignant evolution of cancers.

Nrf2 is a master transcriptional activator of cytoprotective genes. It activates transcription in response to electrophiles and reactive oxygen species (ROS) (Itoh et al., 1997; Uruno and Motohashi, 2011). Under normal conditions, Nrf2 is constantly ubiquitinated by Keap1 and degraded by the proteasome. Exposure to the stimuli inactivates Keap1 and stabilizes Nrf2. Nrf2 then translocates into the nucleus, binds to the antioxidant response element (ARE) and activates the transcription of many cytoprotective genes that encode detoxifying enzymes and antioxidant proteins. The induction of these genes confers resistance against xenobiotic and oxidative stresses. Recently, the constitutive stabilization of NRF2 was found in various human cancers (Singh et al., 2006; Shibata et al., 2008; Wang et al., 2008; Kim et al., 2010; Solis et al., 2010; Zhang et al., 2010). Cancers with high NRF2 levels are associated with poor prognosis (Shibata et al., 2008; Solis et al., 2010) not only because of the chemo- and radio-resistance but also the aggressive proliferation (Singh et al., 2008; Zhang et al., 2010). The molecular mechanisms that allow Nrf2 to promote cell proliferation have not yet been fully elucidated. To clarify how Nrf2 contributes to cell proliferation, we explored Nrf2 target genes in cancer cells. Hypothesizing that Nrf2 plays distinct roles in proliferating cells and quiescent cells, we attempted to identify a signal that modifies the Nrf2 function.

RESULTS

Nrf2 Activates Genes Involved in the PPP, De Novo Nucleotide Synthesis, and NADPH Production

NRF2 knockdown repressed the proliferation of cancer cell lines with constitutive NRF2 accumulation (A549, H2126, LK2 and EBC1 cells) (Figure 1A), suggesting that NRF2 accelerates the proliferation of these cells. Knockdown efficiency was monitored by the reduced expression of NAD(P)H:quinone oxidoreductase 1 (*NQO1*), one of the typical target genes of NRF2 (Figure 1B; Figure S1A available online).

To identify the target genes of NRF2 responsible for cell proliferation, we performed microarray analysis in A549 cells treated with *NRF2* siRNA or control siRNA. A549 is a lung cancer cell line in which NRF2 is constitutively stabilized due to a somatic mutation in the *KEAP1* gene (Taguchi et al., 2008) and the hypermethylation of the *KEAP1* promoter (Wang et al., 2008). We used three independent *NRF2* siRNAs and selected genes whose expression levels were reduced to less than 66.7% of that of the control sample by all three siRNAs to minimize off-target effects (Table S1). In addition to the typical target genes of NRF2 encoding detoxifying enzymes and antioxidant proteins (cytoprotective genes), genes whose products are involved in the PPP (glucose-6-phosphate dehydrogenase [*G6PD*], phosphogluconate dehydrogenase [*PGD*], transketolase [*TKT*], and transaldolase 1 [*TALDO1*]) and de novo nucleotide synthesis (phosphoribosyl pyrophosphate amidotransferase [*PPAT*] and methylenetetrahydrofolate dehydrogenase 2 [*MTHFD2*]) were decreased by the *NRF2* knockdown (Figure 1B). Genes encoding enzymes for NADPH synthesis (malic enzyme 1 [*ME1*] and isocitrate dehydrogenase 1 [*IDH1*]) were also decreased (Figure 1B). The *NRF2* knockdown did not affect the expression levels of four unrelated genes (*MDM2*, *CREBBP*, *EGFR*, and *ERBB2*) or the abundance of the ribosomal RNA primary transcript (pre-rRNA) (Figure 1B). These results indicate that the genes involved in the metabolism (metabolic genes) were specifically repressed by the *NRF2* knockdown and exclude the possibility that cell activities were generally impaired in *NRF2*-knockdown cells. We also confirmed the reduction of the enzyme proteins encoded by these genes in the *NRF2*-knockdown cells (Figure 1C). A time-course of the gene expression was consistent with the blunted increase in cell number (Figure S1B and Figure 1A).

We then performed global mapping of NRF2 binding sites in A549 cells using ChIP-seq analysis (to be published elsewhere). By integrating the results of the ChIP-seq and microarray analyses, we found that NRF2 directly activates *G6PD*, *PGD*, *TKT*, *TALDO1*, *ME1*, and *IDH1* through well-conserved AREs (Figures 1D and S1C). The ChIP-seq results were validated for each locus using quantitative polymerase chain reaction (PCR) (Figure 1E). The expression of these genes depended on NRF2 in three other cell lines with constitutively stabilized NRF2 (Figure S1A). Although the peaks in the *PPAT* and *MTHFD2* loci from the ChIP-seq analysis were not validated by quantitative PCR (data not shown), the abundance of *PPAT* and *MTHFD2* mRNAs was similarly decreased by *NRF2* knockdown in these cell lines (Figure S1A).

Nrf2 Promotes Purine Nucleotide Synthesis and Glutamine Metabolism

To elucidate the contribution of NRF2 to cellular metabolic activities, we performed metabolomic profiling using capillary electrophoresis mass spectrometry (CE-MS) in A549 cells treated with *NRF2* siRNA or control siRNA (Figure 2). Consistent with our finding that NRF2 activates the expression of enzymes for PPP and nucleotide synthesis (Figure 2A), *NRF2* knockdown significantly increased the levels of glycolytic intermediates, such as G6P, F6P, DHAP, pyruvate, and lactate (Figure 2B). The effect was more obvious at 48 hr after siRNA introduction than at 24 hr (Figure 2B; Tables S2 and S3). PRPP and IMP, the first product of the purine nucleotide synthesis, were decreased whereas the PPP intermediates (i.e., 6-PG, Ru5P, R5P and S7P) were increased (Figure 2C). These results were validated by a tracer study using [U-$^{13}C_6$] glucose (Figure 2D; Table S4). Importantly, 100% of IMP detected in the tracer study was [$^{13}C_5$] IMP, suggesting that the ribose ring (C_5) of IMP is all derived from glucose in A549 cells (Table S4). Thus, the decrease in IMP in the *NRF2*-knockdown cells indicates that NRF2 is required for the efficient purine nucleotide synthesis from glucose. We did not detect a significant contribution of NRF2 to the pyrimidine nucleotide synthesis.

To exclude the effect of the salvage pathway of the nucleotide synthesis, we performed a tracer study with [U-$^{13}C_6$] glucose using dialyzed fetal bovine serum (FBS) to remove purine bases from the medium (Figure S2; Table S5). In the *NRF2*-knockdown cells, [$^{13}C_5$] IMP and [$^{13}C_5$] ADP significantly decreased while metabolites in the PPP, glycolysis, TCA cycle, and serine synthesis pathway tended to increase, suggesting that the overall distribution of the glucose-derived ^{13}C was shifted away from the purine nucleotide synthesis. These results demonstrated that the steps from R5P to IMP via PRPP (the post-R5P steps) were delayed and that the PPP intermediates stagnated in the *NRF2*-knockdown cells.

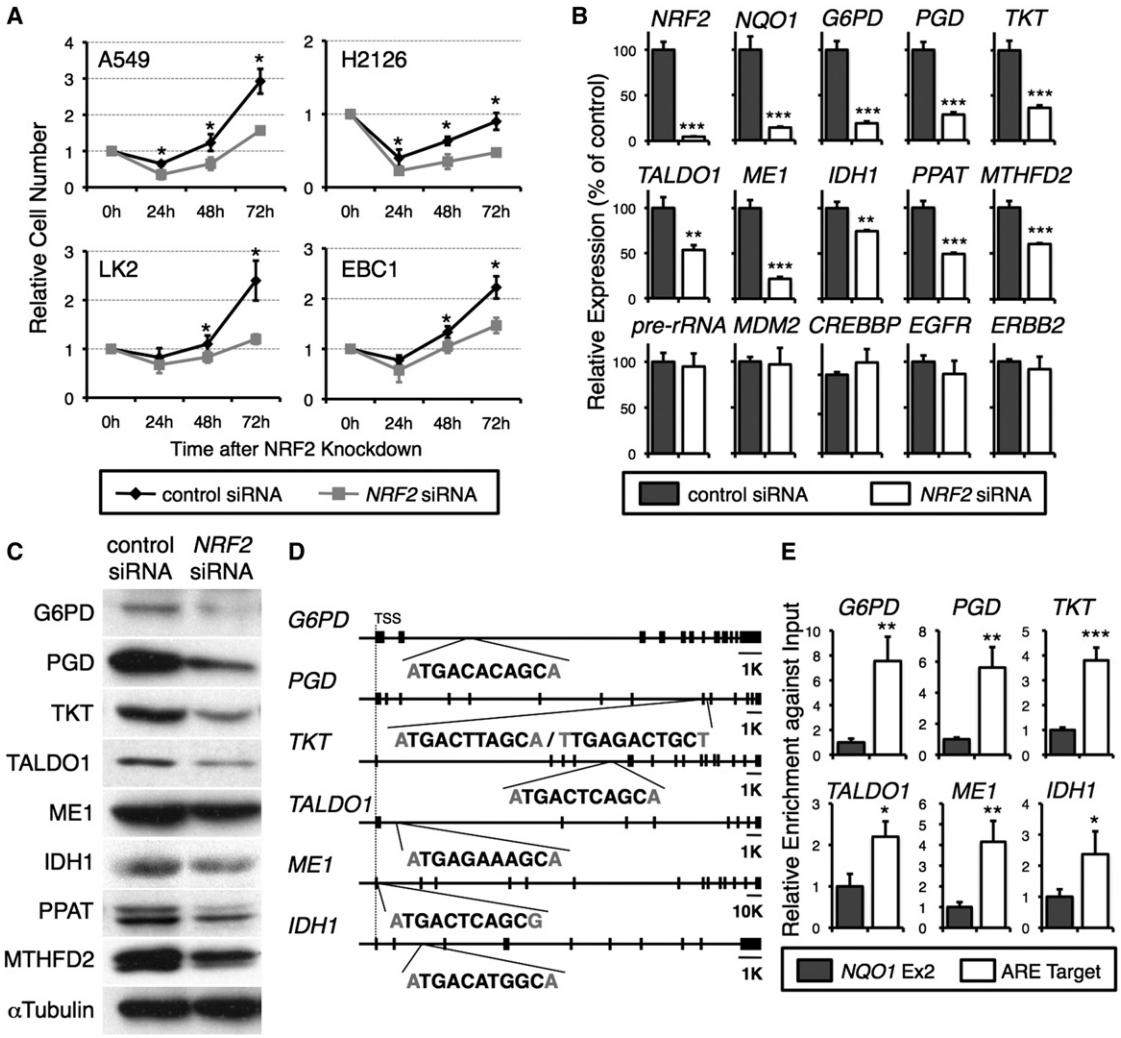

Figure 1. NRF2 Activates Genes Involved in the PPP, Nucleotide Synthesis, and NADPH Production

(A) Effects of *NRF2* knockdown on cell proliferation in cancer cell lines with the constitutive stabilization of NRF2. Cells were transfected with siRNA targeting *NRF2* (*NRF2* siRNA) or scrambled control siRNA (control siRNA). Initial cell numbers were set to 1.

(B) Effects of *NRF2* knockdown on gene expression in A549 cells. The mRNA expression was analyzed at 24 hr after the siRNA transfection. Each panel shows one representative result from three independent experiments. Average values and SDs were calculated from triplicate samples. Average values for cells treated with the control siRNA were set to 100. See also Table S1, Figures S1A and S1B.

(C) Immunoblot detection of the PPP enzymes and other metabolic enzymes in A549 cells. Cells were analyzed at 48 hr after the siRNA transfection. αTubulin was detected as a loading control.

(D) Position and sequence of AREs within each target locus. TSS, transcription start site. Scale bars indicate 1 kbp (1K) or 10 kbp (10K). See also Figure S1C.

(E) Relative enrichment against the input of each locus. The second exon of the *NQO1* gene (*NQO1* Ex2) was used as a negative control locus, whose enrichment was set to 1. One representative result from three independent experiments is shown. Average values and SDs were calculated from triplicate samples.

*$p < 0.05$; **$p < 0.01$; ***$p < 0.001$ (A, B, and E).

One unexpected finding was a marked increase in glutamine and glutamate in the *NRF2*-knockdown cells (Figure 2F), which was suggestive of the critical contribution of Nrf2 to glutamine metabolism. The tracer study using [U-$^{13}C_5$] glutamine demonstrated the primary distribution of carbons derived from glutamine (Table S6). The two major directions of the metabolite flux were toward the glutathione synthesis and TCA cycle (Figure 2E). Remarkably, *NRF2* knockdown affected glutathione synthesis, decreasing the levels of ^{13}C-labeled GSH and GSSG (Figure 2G). This result is consistent with previous reports demonstrating that Nrf2 activates both genes encoding the catalytic and regulatory subunits of gamma-glutamyl-cysteinyl-ligase (GCL), a rate-limiting enzyme of glutathione synthesis (Lu, 2009). Indeed, the knockdown of *KEAP1* and *NRF2* in HaCaT cells increased and decreased glutathione, respectively (MacLeod et al., 2009), indicating that Nrf2 plays an important role in glutathione synthesis. Another notable result of *NRF2* knockdown was an increase in [U-$^{13}C_4$] malate and a decrease in [U-$^{13}C_3$] lactate (Figure 2G), suggesting that lactate production from glutamine is inhibited. This result likely reflects the reduced activity of ME1 (Figures

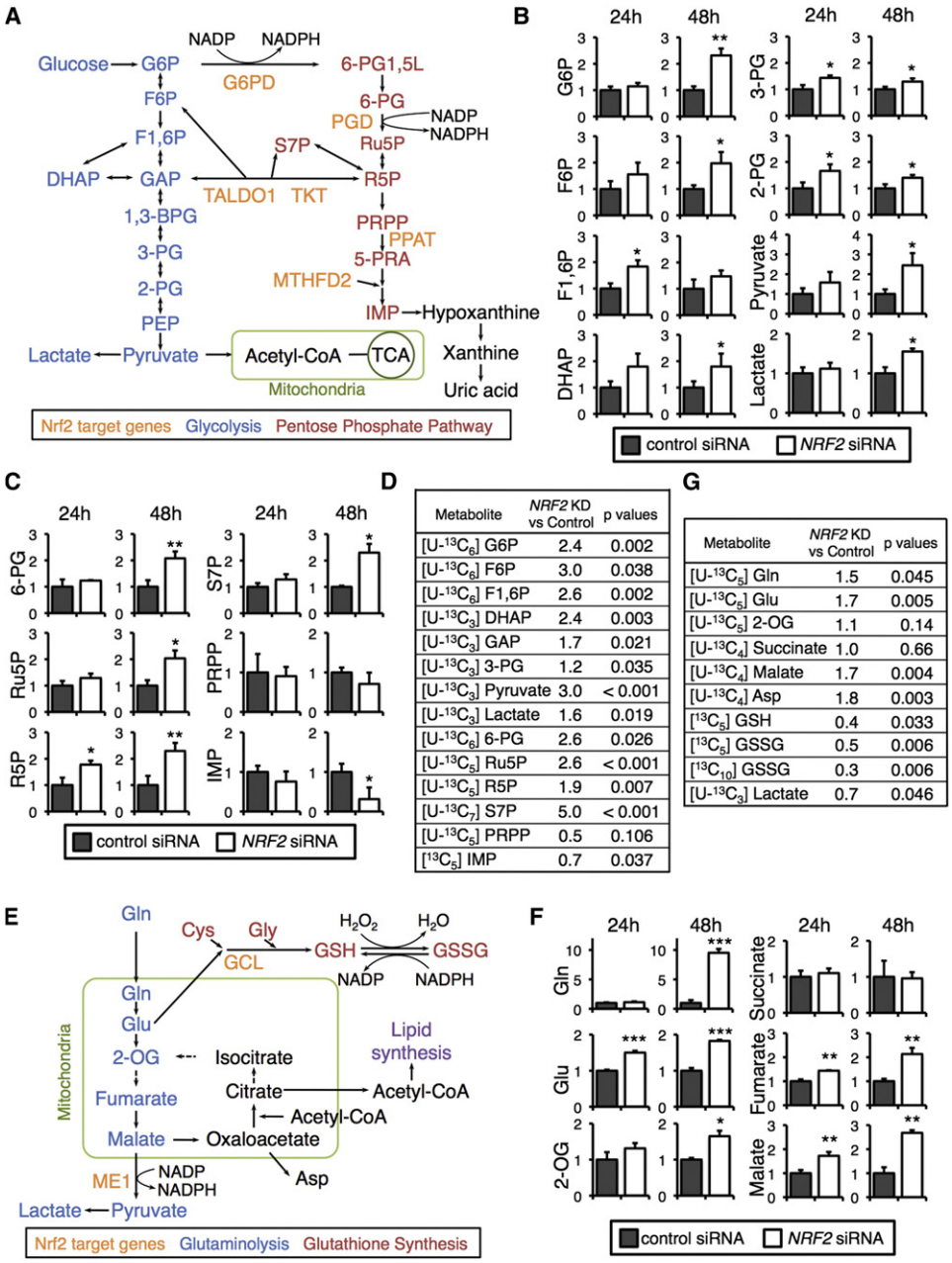

Metabolite	*NRF2* KD vs Control	p values
[U-$^{13}C_6$] G6P	2.4	0.002
[U-$^{13}C_6$] F6P	3.0	0.038
[U-$^{13}C_6$] F1,6P	2.6	0.002
[U-$^{13}C_3$] DHAP	2.4	0.003
[U-$^{13}C_3$] GAP	1.7	0.021
[U-$^{13}C_3$] 3-PG	1.2	0.035
[U-$^{13}C_3$] Pyruvate	3.0	< 0.001
[U-$^{13}C_3$] Lactate	1.6	0.019
[U-$^{13}C_6$] 6-PG	2.6	0.026
[U-$^{13}C_5$] Ru5P	2.6	< 0.001
[U-$^{13}C_5$] R5P	1.9	0.007
[U-$^{13}C_7$] S7P	5.0	< 0.001
[U-$^{13}C_5$] PRPP	0.5	0.106
[$^{13}C_5$] IMP	0.7	0.037

Metabolite	*NRF2* KD vs Control	p values
[U-$^{13}C_5$] Gln	1.5	0.045
[U-$^{13}C_5$] Glu	1.7	0.005
[U-$^{13}C_5$] 2-OG	1.1	0.14
[U-$^{13}C_4$] Succinate	1.0	0.66
[U-$^{13}C_4$] Malate	1.7	0.004
[U-$^{13}C_4$] Asp	1.8	0.003
[$^{13}C_5$] GSH	0.4	0.033
[$^{13}C_5$] GSSG	0.5	0.006
[$^{13}C_{10}$] GSSG	0.3	0.006
[U-$^{13}C_3$] Lactate	0.7	0.046

Figure 2. *NRF2* Knockdown Alters Glucose and Glutamine Metabolism in A549 Cells

(A) Metabolic enzymes regulated by NRF2 in glucose metabolism.

(B and C) Quantification of metabolic intermediates in glycolysis (B) and the PPP and purine nucleotide synthesis (C). Metabolite concentrations were quantified at 24 and 48 hr after the transfection of siRNAs. See also Tables S2 and S3.

(D) Tracer study using [U-$^{13}C_6$] glucose. A549 cells transfected with control siRNA or *NRF2* siRNA were incubated with [U-$^{13}C_6$] glucose for 1 hr and analyzed. Ratios of isotopomer concentrations in *NRF2*-knockdown (KD) samples versus control samples are shown. See also Tables S4 and S5 and Figure S2.

(E) Metabolic enzymes regulated by NRF2 in glutamine metabolism.

(F) Quantification of metabolic intermediates in glutathione synthesis and glutaminolysis. Metabolite concentrations were quantified at 24 and 48 hr after the transfection of siRNAs. See also Tables S2 and S3.

(G) Tracer study using [U-$^{13}C_5$] glutamine. A549 cells transfected with control siRNA or *NRF2* siRNA were incubated with [U-$^{13}C_5$] glutamine for 6 hr and analyzed. Ratios of isotopomer concentrations in *NRF2* KD samples versus control samples are shown. See also Table S6.

All samples were analyzed in triplicate. Error bars indicate SDs. *$p < 0.05$; **$p < 0.01$; ***$p < 0.001$ (B, C and F).

1,3-BPG, 1,3-bisphosphoglycerate; 2-OG, 2-oxoglutarate; 2-PG, 2-phosphoglycerate; 3-PG, 3-phosphoglycerate; 6-PG, 6-phosphogluconate; 6-PG1,5L, 6-phosphoglucono-1,5-lactone; 5-PRA, β-5-phosphorybosylamine; DHAP, dihydroxyacetone phosphate; F1,6P, fructose 1,6-bis-phosphate; F6P, fructose 6-phosphate; G6P, glucose 6-phosphate; GSSG, glutathione (oxidized); GSH, glutathione (reduced); GAP, glyceraldehyde 3-phosphate; IMP, inosine 5′-monophosphate; PEP, phosphoenolpyruvate; PRPP, phosphoribosyl pyrophosphate; R5P, ribose 5-phosphate; Ru5P, ribulose 5-phosphate; S7P, sedoheptulose 7-phosphate.

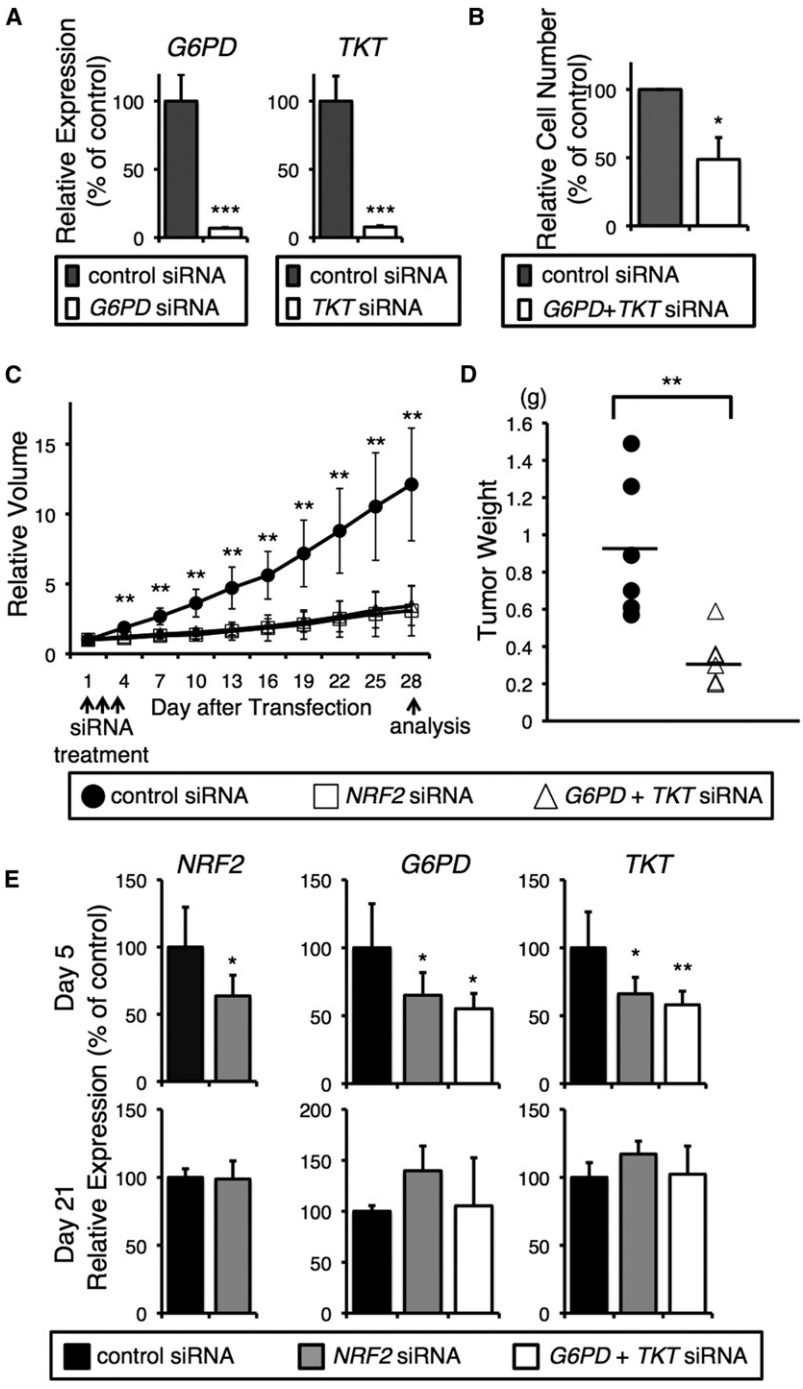

Figure 3. Functional Contribution of the PPP Enzymes to Cell Proliferation In Vitro and In Vivo

(A) Knockdown efficiencies of *G6PD* and *TKT* in A549 cells were examined by quantitative RT-PCR. Average values for cells treated with the control siRNA were set to 100.

(B) Effect of simultaneous knockdown of *G6PD* and *TKT* on cell proliferation. Relative cell numbers are shown. Cells were counted at 72 hr after transfection.

(C) Effect of simultaneous knockdown of *G6PD* and *TKT* on tumor growth in vivo. Mice transplanted with A549 cells were treated with control siRNA (n = 6), *NRF2* siRNA (n = 5), or *G6PD*+*TKT* siRNA (n = 6).

(D) Tumor weight on day 28 after the first siRNA treatment.

(E) mRNA expression of siRNA targets (*NRF2*, *G6PD*, and *TKT*) in tumors. The tumors were injected with control siRNA (n = 6 for day 5; n = 3 for day 21), *NRF2* siRNA (n = 6 for day 5; n = 3 for day 21), or *G6PD*+*TKT* siRNA (n = 5 for day 5; n = 3 for day 21) and processed for RNA purification at 5 or 21 days after the initial injection.

Average values and SDs were calculated from triplicate samples. Average values for cells treated with control siRNA were set to 100. *p < 0.05; **p < 0.01; ***p < 0.001 (A-E).

1B and 1C), which catalyzes the oxidative decarboxylation of malate and the production of NADPH. Indeed, the enzymatic activity of ME1 has been suggested to be responsible for glutaminolysis (DeBerardinis et al., 2007). Nrf2 thus facilitates glutaminolysis by activating ME1.

Nrf2 Requires the PPP Enzymes to Accelerate Tumor Growth

Since the inhibitory effect of the *NRF2* knockdown on the post-R5P steps seemed to dominate over that on the PPP in the metabolite analysis, we separately evaluated the significance of the PPP for Nrf2-dependent proliferation. We examined the necessity of the PPP activity in NRF2-overexpressing cells by knocking down *G6PD* and *TKT*, which are involved in the oxidative and non-oxidative arms of the PPP, respectively (Figure 3). We used A549 cells in which NRF2 is abundantly expressed. The simultaneous knockdown of *G6PD* and *TKT* significantly repressed cell number increase after 72 hr of transfection (Figures 3A and 3B). The knockdown effect on tumor growth in vivo was examined in a xenograft experiment. Four weeks after A549 cells were transplanted into nude mice, the siRNA was injected into the tumor. Tumor growth was dramatically repressed by the injection of *NRF2* siRNA (Figure 3C). A previous study reported the therapeutic efficacy of the local injection of *NRF2* siRNA in a xenograft experiment (Singh et al., 2008), which was reproducible in our system. We further examined the efficacy of the double knockdown of *G6PD* and *TKT*. The simultaneous injection of siRNAs against *G6PD* and *TKT* was also effective for the inhibition of tumor growth (Figure 3C). The average tumor weight was significantly reduced by the double knockdown compared with the control samples (Figure 3D). Thus, the highly expressed NRF2 in A549 cells was insufficient to overcome the inhibitory effect on cell proliferation resulting from the *G6PD* and *TKT* knockdown. These data are consistent with a model in which G6PD and TKT are requisite downstream targets for NRF2 to support A549 cell proliferation.

The siRNA treatment of the tumor reduced the expression of the respective gene by approximately 40%–50% on day 5 (Figure 3E, upper panels), whereas no difference was detected on day 21 (Figure 3E, lower panels). These results suggest that

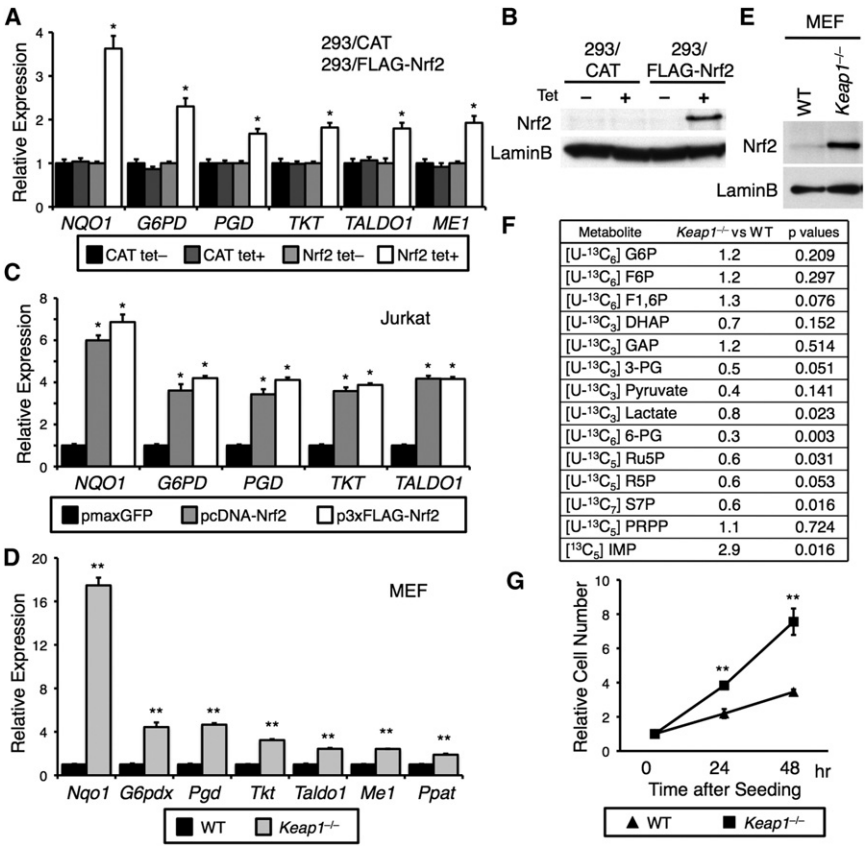

Metabolite	*Keap1*$^{-/-}$ vs WT	p values
[U-$^{13}C_6$] G6P	1.2	0.209
[U-$^{13}C_6$] F6P	1.2	0.297
[U-$^{13}C_6$] F1,6P	1.3	0.076
[U-$^{13}C_3$] DHAP	0.7	0.152
[U-$^{13}C_3$] GAP	1.2	0.514
[U-$^{13}C_3$] 3-PG	0.5	0.051
[U-$^{13}C_3$] Pyruvate	0.4	0.141
[U-$^{13}C_3$] Lactate	0.8	0.023
[U-$^{13}C_6$] 6-PG	0.3	0.003
[U-$^{13}C_5$] Ru5P	0.6	0.031
[U-$^{13}C_5$] R5P	0.6	0.053
[U-$^{13}C_7$] S7P	0.6	0.016
[U-$^{13}C_5$] PRPP	1.1	0.724
[$^{13}C_5$] IMP	2.9	0.016

Figure 4. Effects of Nrf2 Overexpression in Cultured Cells

(A) Gene expression in 293/CAT and 293/FLAG-Nrf2 cells. Cells were treated with or without 1 μg/ml tetracycline for 24 hr. Average values for each cell without tetracycline were set to 1.

(B) Immunoblot analysis of Nrf2 in nuclear fractions of 293/CAT and 293/FLAG-Nrf2 cells. LaminB was detected as a loading control. Cells were treated with or without 1 μg/ml tetracycline for 24 hr.

(C) Gene expression in Jurkat cells transfected with pmaxGFP, pcDNA3-mNrf2 and p3xFLAG-Nrf2. Cells were harvested at 24 hr after the transfection. Average values for cells transfected with pmaxGFP were set to 1.

(D) Gene expression in WT and *Keap1*$^{-/-}$ MEFs. Average values for the WT MEFs were set to 1.

(E) Immunoblot analysis of Nrf2 in WT and *Keap1*$^{-/-}$ MEFs. LaminB was detected as a loading control.

(F) Tracer study using [U-$^{13}C_6$] glucose. WT and *Keap1*$^{-/-}$ MEFs were cultured with dialyzed FBS and incubated with [U-$^{13}C_6$] glucose for 1 hr. Ratios of isotopomer concentrations in *Keap1*$^{-/-}$ MEFs versus WT MEFs are shown. All samples were analyzed in triplicate. See also Table S7 and Figure S3.

(G) Cell proliferation of WT and *Keap1*$^{-/-}$ MEFs. Initial cell numbers were set to 1.

Average values and SDs were calculated from triplicate samples. *$p < 0.01$; **$p < 0.001$ (A, C, D and G).

the suppression of NRF2 activity or the PPP activity for a limited period sufficiently delayed tumor outgrowth and had a prolonged effect on tumor size.

Increased Expression of Nrf2 Alters Metabolic Activities and Enhances Proliferation in Cultured Cells

We next examined the effect of the increased Nrf2 on gene expression. 293/FLAG-Nrf2 and 293/CAT are stable cell lines that inducibly express FLAG-tagged Nrf2 and chloramphenicol acetyltransferase (CAT), respectively. After the induction with tetracycline, *NQO1*, one of the cytoprotective genes, and the metabolic genes were elevated in 293/FLAG-Nrf2 cells but not in 293/CAT cells (Figure 4A). The nuclear accumulation of Nrf2 was confirmed in 293/FLAG-Nrf2 cells treated with tetracycline (Figure 4B). When Nrf2 was overexpressed in Jurkat cells, in which Nrf2-mediated antioxidant response was augmented due to a frame-shift mutation in the *PTEN* gene (Sakamoto et al., 2009), *NQO1* and the metabolic genes were upregulated with the exception of ME1, whose expression was not detected in Jurkat cells (Figure 4C). We then examined the effect of the forced stabilization of endogenous Nrf2 by adopting *Keap1*$^{-/-}$ mouse embryonic fibroblasts (MEFs). *Keap1*$^{-/-}$ MEFs displayed abundant nuclear accumulation of Nrf2 and higher expression of the metabolic genes than wild-type (WT) MEFs (Figures 4D and 4E). Thus, Nrf2 activates the metabolic genes when it is highly expressed in cultured cells.

To examine the effect of Nrf2 increase on the nucleotide synthesis, *Keap1*$^{-/-}$ and WT MEFs were subjected to the tracer study using [U-$^{13}C_6$] glucose and dialyzed FBS. In *Keap1*$^{-/-}$ MEFs, [$^{13}C_5$] IMP, [$^{13}C_5$] AMP, and [$^{13}C_5$] ATP significantly increased while metabolites in the PPP, glycolysis, TCA cycle and serine synthesis pathway tended to decrease, suggesting that the overall distribution of the glucose-derived ^{13}C was shifted toward the purine nucleotide synthesis (Figures 4F and S3; Table S7). The post-R5P steps were facilitated in *Keap1*$^{-/-}$ MEFs, which was just opposite to the effect of *NRF2*-knockdown in A549 cells.

We then examined the effect of Nrf2 accumulation on cell proliferation. The cell number increase was much faster in *Keap1*$^{-/-}$ MEFs than in WT MEFs (Figure 4G). When the exogenous Nrf2 was transiently expressed in 293T cells, in which the basal Nrf2 protein is hardly detected (Figure 5A, left panel), the cell number increase was significantly accelerated (Figure 5B), and the Nrf2 target genes were activated (Figure 5C). These effects were not observed when the mutant Nrf2 (Nrf2 CT) lacking the activation domain was expressed (Figures 5A, right panel, 5B and 5C). Thus, Nrf2 enhanced the proliferation of 293T cells, which depended on its transcriptional activation ability.

Since 293T cells turned out to display Nrf2-dependency in cell proliferation, we used 293T cells for analyzing the contribution of the PPP to proliferation as a downstream pathway of Nrf2. The cell number increase was significantly accelerated upon the expression of the exogenous G6PD or TKT (Figures 5D and 5E), indicating that selective increase of G6PD or TKT accelerated proliferation without activating the other Nrf2 target genes. Thus, the enhancement of the PPP activity accounts for the Nrf2-dependent cell proliferation at least in part.

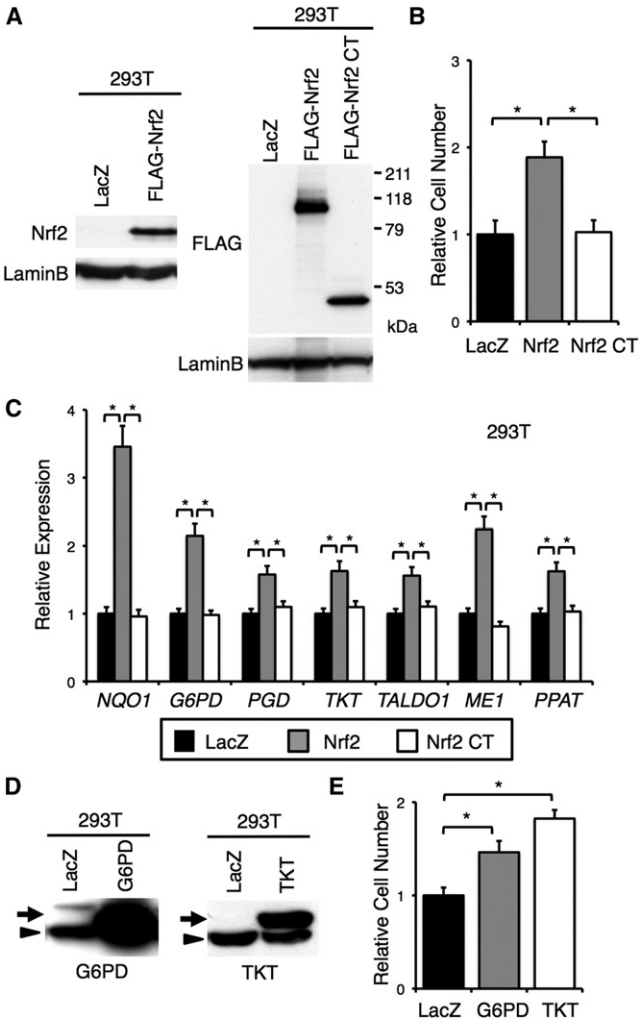

Figure 5. Increased Expression of Nrf2 or the PPP Enzymes Accelerates Cell Proliferation

(A) Immunoblot analysis of 293T cells expressing FLAG-Nrf2 and FLAG-Nrf2 CT. FLAG-Nrf2 was detected with anti-Nrf2 (left panel) and anti-FLAG (right panel) antibodies. LaminB was detected as a loading control.

(B) Effect of increased expression of Nrf2 on cell proliferation. FLAG-Nrf2 or FLAG-Nrf2 CT was expressed in 293T cells. Relative cell numbers are shown. The number of cells expressing LacZ was set to 1. Cells were counted at 96 hr after transfection.

(C) Gene expression in 293T cells transfected with an expression vector encoding LacZ, FLAG-Nrf2 or FLAG-Nrf2 CT. Cells were harvested at 48 hr after the transfection. Average values for cells expressing LacZ were set to 1.

(D) Immunoblot analysis of 293T cells expressing exogenous G6PD (left) and TKT (right). Arrowheads and arrows indicate endogenous and exogenous enzymes, respectively.

(E) Effect of increased expression of G6PD or TKT on cell proliferation. Relative cell numbers are shown. The number of cells expressing LacZ was set to 1. Cells were counted at 96 hr after transfection.

Average values and SDs were calculated from triplicate samples. *$p < 0.01$ (B, C and E).

Nrf2 Accumulation Promotes Cell Proliferation in the Forestomach Epithelium

Our next question was how Nrf2 contributes to the cell proliferation in normal cells in vivo. We utilized *Keap1*$^{F/-}$ mice as a source of non-cancer cells with abundant Nrf2 protein (Taguchi et al., 2010). While the expression of *Nqo1* was clearly higher in *Keap1*$^{F/-}$ mice in all the tissues examined, the metabolic genes were significantly activated in the forestomach and intestine but not in the liver (Figure 6A). These results suggest that Nrf2 induces the metabolic genes in the forestomach and intestine but does not do so efficiently in the liver. Comparison of *Nrf2*$^{-/-}$ and WT livers suggested that Nrf2 contributes to the basal expression rather than the inducible expression of the metabolic genes in the liver (Figure S4).

Because of the most marked induction of the metabolic genes by Keap1 reduction, we focused on the forestomach. Corresponding to the elevated gene expression, the enzyme protein levels were dramatically higher in the *Keap1*$^{F/-}$ forestomachs than the control samples (Figure 6B). The metabolic intermediates of glycolysis and the PPP were all decreased in the *Keap1*$^{F/-}$ forestomachs (Figure 6C). Hypoxanthine, xanthine and uric acid were all robustly increased in place of IMP (Figure 6C), implying that the excessive IMP may have been converted to uric acid (Figure 2A). These results were almost consistent with the metabolite pattern in *Keap1*$^{-/-}$ MEFs.

We then histologically examined the cell proliferation in the forestomach epithelia. In the *Keap1*$^{F/-}$ forestomach, the epithelial layer was hypertrophic, and abundant Nrf2 accumulation was clearly observed (Figure 6D). These results are consistent with those of our previous reports (Wakabayashi et al., 2003; Taguchi et al., 2010). The incorporation of BrdU was enhanced in the *Keap1*$^{F/-}$ forestomach (Figure 6D), suggesting that the accumulated Nrf2 provokes cell proliferation leading to the epithelial hypertrophy.

To validate the Nrf2-dependency of the phenotypes caused by the Keap1 reduction, we examined the forestomach epithelia in *Keap1*$^{-/-}$::*Nrf2*$^{-/-}$ mice. The expression of the metabolic genes in the forestomach was mostly comparable between *Nrf2*$^{-/-}$ and *Keap1*$^{-/-}$::*Nrf2*$^{-/-}$ mice (Figure 6E) and between WT and *Nrf2*$^{-/-}$ mice (Figure S4), indicating that *Keap1*$^{-/-}$::*Nrf2*$^{-/-}$ mice showed no or only marginal increase of the metabolic genes compared with WT mice. Neither epithelial hypertrophy nor enhanced incorporation of BrdU was seen in the *Keap1*$^{-/-}$::*Nrf2*$^{-/-}$ mice (Figure 6D). These results indicate that the accumulated Nrf2 is responsible for the phenotypes observed in *Keap1*$^{F/-}$ mice. Thus, Nrf2 activates metabolic genes, modulates the metabolite pattern and provokes cell proliferation when it accumulates in forestomach epithelial cells.

Nrf2 Enhances Metabolic Gene Expression in the Presence of Active PI3K-Akt Signaling

We were curious why Nrf2 accumulation had different effects on different tissues in terms of the metabolic gene activation (Figure 6A). Considering that epithelial tissues of the forestomach and intestine are composed of proliferating cells and that approximately 80% of the liver is composed of normally quiescent hepatocytes (Taub, 2004), we assumed that Nrf2 could effectively activate metabolic genes in the presence of proliferative signals.

The PI3K-Akt signaling pathway is one of the major contributors to cancer development because it promotes cancer cell growth, survival, and metabolism (Elstrom et al., 2004; Engelman, 2009). We compared the activities of the PI3K-Akt pathway

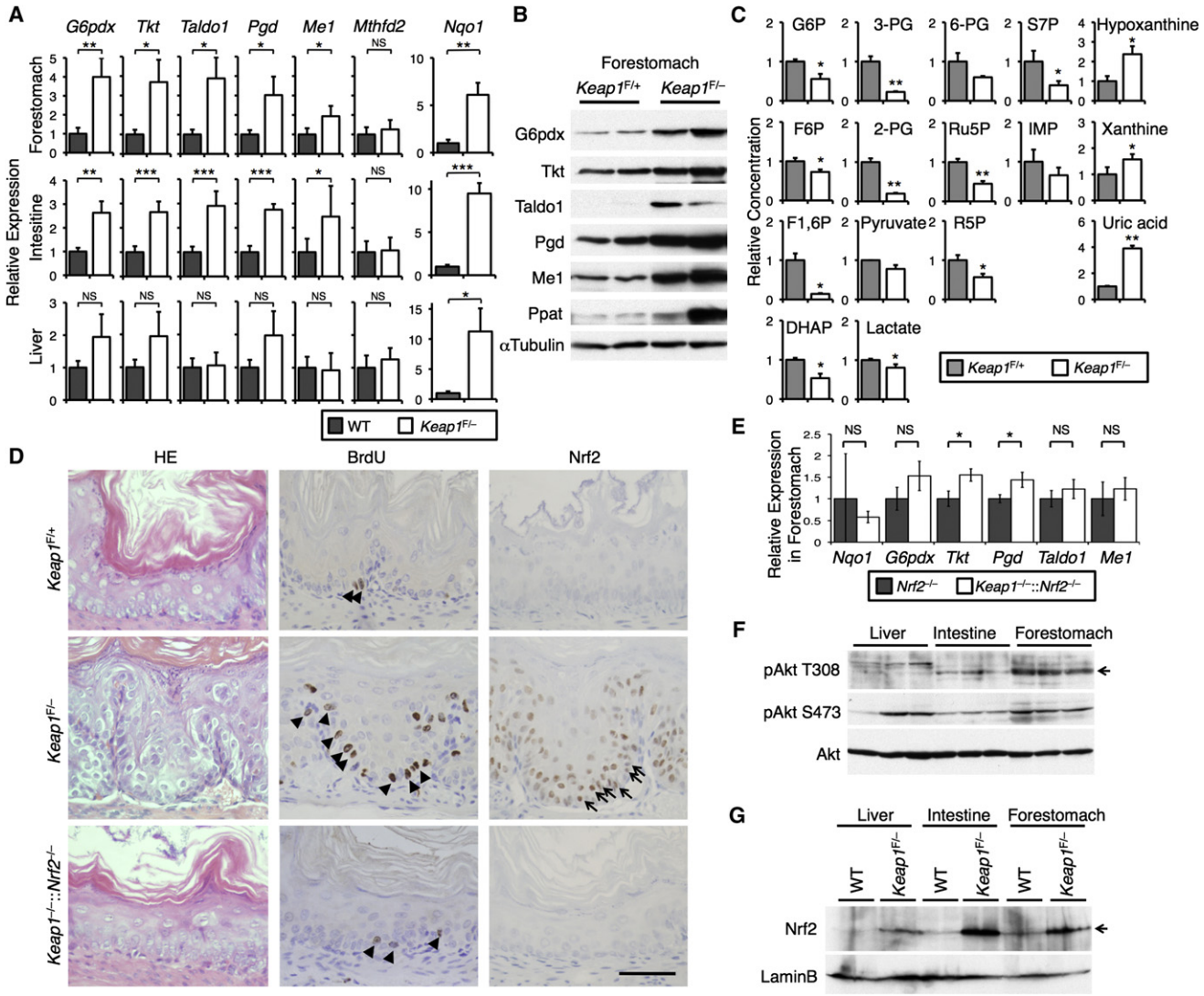

Figure 6. Effects of Nrf2 Accumulation in Forestomach Epithelia

(A) Gene expression in the forestomach, intestine and liver of WT (n = 6) and *Keap1*$^{F/-}$ (n = 4) mice. See also Figure S4.

(B) Immunoblot detection of the PPP and NADPH production enzymes in the forestomach epithelia of *Keap1*$^{F/+}$ and *Keap1*$^{F/-}$ mice. αTubulin was detected as a loading control.

(C) Quantification of metabolic intermediates of glycolysis and the PPP. IMP and its derivatives were also measured. Forestomach epithelia of *Keap1*$^{F/+}$ (n = 3) and *Keap1*$^{F/-}$ (n = 3) mice were analyzed.

(D) Histological analysis of the forestomach of *Keap1*$^{F/+}$ (n = 4), *Keap1*$^{F/-}$ (n = 4) and *Keap1*$^{-/-}$::*Nrf2*$^{-/-}$ (n = 3) mice. BrdU and Nrf2 were detected with specific antibodies (middle and right columns, respectively). Hematoxylin and eosin (HE) staining is shown in the left column. Representative micrographs are shown. A scale bar corresponds to 50 μm.

(E) Gene expression in the forestomach of *Nrf2*$^{-/-}$ (n = 3) and *Keap1*$^{-/-}$::*Nrf2*$^{-/-}$ (n = 3) mice.

(F) Phosphorylation of Akt in the forestomach, intestine, and liver of *Keap1*$^{F/-}$ mice. An arrow indicates the phosphorylated Akt at T308.

(G) Immunoblot analysis of Nrf2 in the forestomach, intestine and liver of WT and *Keap1*$^{F/-}$ mice. An arrow indicates Nrf2. LaminB was detected as a loading control.

Average values are shown, and error bars indicate SDs (A, C, and E). Average values for WT (A), *Keap1*$^{F/+}$ (C) or *Nrf2*$^{-/-}$ (E) were set to 1. *p < 0.05; **p < 0.01; ***p < 0.001 compared with WT (A), *Keap1*$^{F/+}$ (C) or *Nrf2*$^{-/-}$ (E).

in the *Keap1*$^{F/-}$ mouse tissues by monitoring the phosphorylation of Akt (Figure 6F). While the phosphorylation at S473 showed individual variability, the levels of T308 phosphorylation were markedly different among tissues; they were the highest in the forestomach, intermediate in the intestine, and almost undetectable in the liver. The phosphorylation at T308 is essential for the activation of Akt because T308 is positioned at the activation loop of the kinase (Casamayor et al., 1999). The Akt in the forestomach was likely to possess the highest activity. The cultured cells, including A549, 293, Jurkat, and MEFs, where Nrf2 activates the PPP, also showed the high levels of Akt phosphorylation at both sites (Figures 7A–7C and 7E). When the PI3K-Akt signaling was turned off by serum starvation, the highly expressed metabolic genes in *Keap1*$^{-/-}$ MEFs were decreased

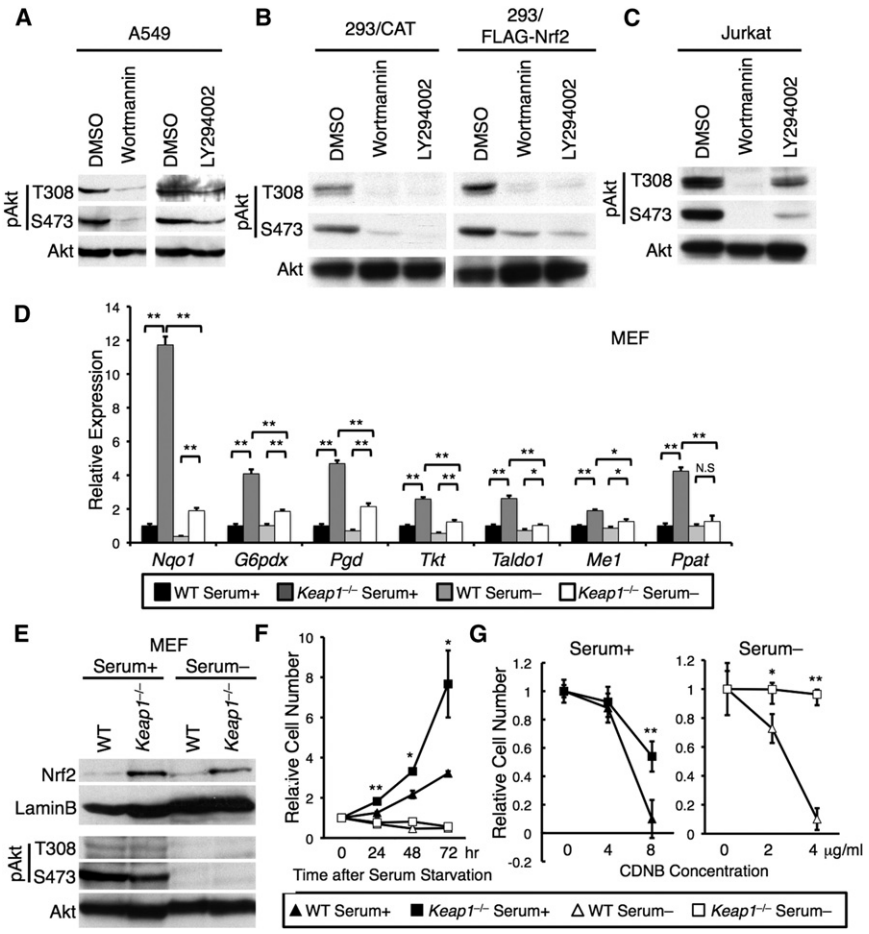

Figure 7. Nrf2 Enhances Metabolic Gene Expression in the Presence of Active PI3K-Akt Signaling in Cultured Cells

(A–C) Phosphorylation of Akt in cytoplasmic fractions of A549 cells (A), 293/CAT and 293/FLAG-Nrf2 cells (B), and Jurkat cells (C). Cells were treated with 5 μM Wortmannin (A–C) or LY294002 (20 μM for A and 50 μM for B and C) for 48 hr (A) and 3 hr (B and C).

(D) Gene expression in WT and *Keap1*$^{-/-}$ MEFs. Cells were cultured in the presence or absence of serum for 48 hr. Average values for the WT MEFs with serum were set to 1.

(E) Immunoblot analysis of Nrf2 and phosphorylated Akt in WT and *Keap1*$^{-/-}$ MEFs. Cells were cultured in the presence or absence of the serum for 48 hr. LaminB and total Akt were detected as loading controls.

(F) Cell number increase of WT and *Keap1*$^{-/-}$ MEFs cultured in the presence or absence of serum. The time was measured from the start of serum starvation. Initial cell numbers were set to 1.

(G) Susceptibility to CDNB treatment in WT and *Keap1*$^{-/-}$ MEFs under normal condition or serum starvation.

Average values and SDs were calculated from triplicate samples. *$p < 0.05$; **$p < 0.001$ (D, F and G).

closer to the WT levels (Figures 7D and 7E). Thus, we speculated that Nrf2 requires cooperation from active PI3K-Akt signaling to fully activate the metabolic genes.

It should be noted that both *Keap1*$^{-/-}$ and WT MEFs ceased proliferation under serum starvation, indicating that Nrf2 promotes cell proliferation only in the presence of proliferative signals (Figure 7F). In contrast, *Keap1*$^{-/-}$ MEFs were more resistant to the toxicity of 1-chloro-2,4-dinitrobenzene (CDNB) than WT MEFs with or without serum (Figure 7G), indicating that Nrf2 enhances cytoprotection irrespective of the activity of proliferative signals. These results implicate the functional expansion of Nrf2 in the presence of active PI3K-Akt signaling.

Forced Activation of PI3K Allows Nrf2 to Activate Metabolic Genes

To test this hypothesis, we activated the PI3K-Akt signaling pathway by deleting *Pten* in the liver and examined the gene expression (Figure 8A, left four bars). The livers of mice with four different genotypes were compared; *Pten*$^{F/F}$ (Control), *Pten*$^{F/F}$::*Alb*-Cre (*P-Alb*), *Keap1*$^{F/F}$::*Alb*-Cre (*K-Alb*) and *Pten*$^{F/F}$::*Keap1*$^{F/F}$::*Alb*-Cre (*P/K-Alb*). Because the *P/K-Alb* mice were lethal at approximately 3 weeks after birth due to unknown reasons, all the mice were examined on day 15 (P15). The *K-Alb* liver showed a modest increase in the metabolic gene expression but a robust increase in *Nqo1*, which is consistent with the results observed in the *Keap1*$^{F/-}$ liver (Figure 6A). While the *P-Alb* liver showed only a slight increase in the expression of the genes examined, the *P/K-Alb* liver showed a marked increase in metabolic gene expression, even for *Mthfd2*, which was not elevated in *Keap1*$^{F/-}$ tissues (Figure 6A). A comparison of *P-Alb* and *P/K-Alb* showed that the *Keap1* deletion robustly increased the metabolic gene expression in addition to *Nqo1* in the absence of *Pten*, suggesting that the *Pten* deletion potentiates Nrf2 function and augments the induction of the ARE-driven genes by Nrf2.

To verify the contribution of Nrf2 to the expression of the metabolic genes, we examined the livers of mice in the *Nrf2* null background; *Pten*$^{F/F}$::*Nrf2*$^{-/-}$ (*Nrf2*-KO), *Pten*$^{F/F}$::*Alb*-Cre::*Nrf2*$^{-/-}$ (*P-Alb/N*), *Pten*$^{F/F}$::*Keap1*$^{F/F}$::*Alb*-Cre::*Nrf2*$^{-/-}$ (*P/K-Alb/N*), and *Pten*$^{F/F}$::*Keap1*$^{F/F}$::*Alb*-Cre::*Nrf2*$^{+/-}$ (*P/K-Alb/N*-h) (Figure 8A, right four bars). The gene expression in the *P/K-Alb/N* liver was much lower than that in the *P/K-Alb* liver and as low as that in the *P-Alb* liver, indicating that Nrf2 is essential for the marked elevation of the gene expression in the *P/K-Alb* liver. The expression levels of *Me1* and *Nqo1* of the *P/K-Alb/N*-h liver were intermediate between the *P/K-Alb* and *P/K-Alb/N* livers. The expression of the rest of the genes in the *P/K-Alb/N*-h liver was as low as that observed in the *P/K-Alb/N* liver. These results indicate that the transcriptional activation of the metabolic genes requires higher Nrf2 activity than the cytoprotective genes.

We further examined the effect of active PI3K-Akt signaling on the Nrf2 function to modulate the metabolic activity in the liver. The metabolic intermediates were measured in the livers of Control, *P-Alb*, *K-Alb*, *P/K-Alb* and *P/K-Alb/N* mice using CE-MS (Figure 8B). The abundance of PPP intermediates, IMP and

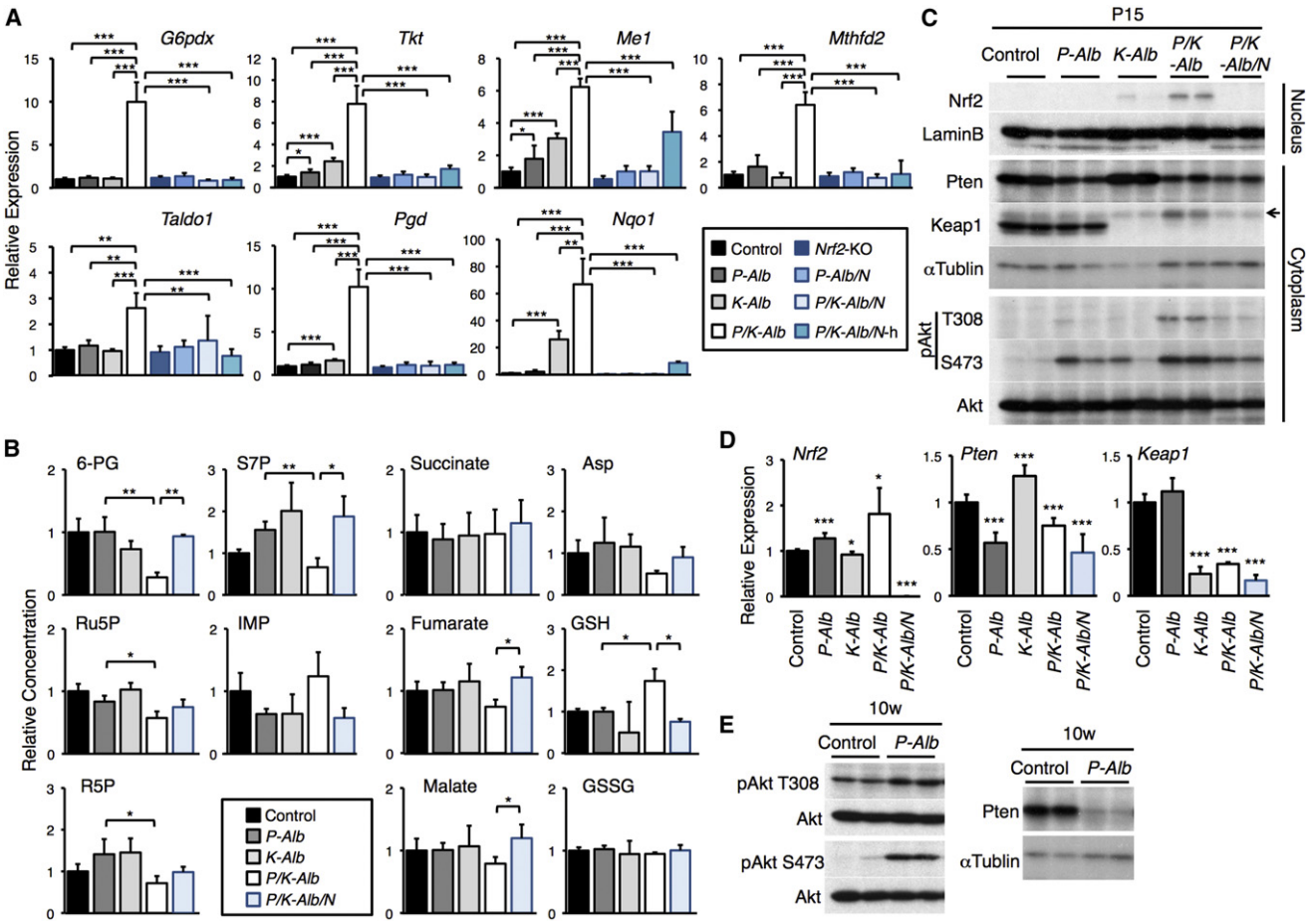

Figure 8. Forced Activation of PI3K-Akt Signaling in the Liver Enhances Nrf2 Activity

(A) Gene expression in the liver of Control (n = 3), *P-Alb* (n = 4), *K-Alb* (n = 4), *P/K-Alb* (n = 3), *Nrf2*-KO (n = 6), *P-Alb/N* (n = 5), *P/K-Alb/N* (n = 4), and *P/K-Alb/N*-h (n = 4) mice.

(B) Quantification of the intermediates of the PPP and glutamine metabolism and IMP in the liver of Control (n = 3), *P-Alb* (n = 3), *K-Alb* (n = 3), *P/K-Alb* (n = 3), and *P/K-Alb/N* (n = 3) mice.

(C) Immunoblot detection of Nrf2, Pten, Keap1, and phosphorylated Akt in the liver of Control, *P-Alb*, *K-Alb*, *P/K-Alb* and *P/K-Alb/N* mice at P15. LaminB and αTubulin were detected as loading controls.

(D) mRNA expression of *Nrf2*, *Pten*, and *Keap1* in the liver of Control (n = 3), *P-Alb* (n = 4), *K-Alb* (n = 4), *P/K-Alb* (n = 3), and *P/K-Alb/N* (n = 4) mice.

(E) Immunoblot detection of Pten and phosphorylated Akt in the livers of Control and *P-Alb* mice at 10 weeks. αTubulin was detected as a loading control.

Average values are shown, and error bars indicate SDs. Average values for Control samples were set to 1 (A, B, and D). *p < 0.05; **p < 0.01; ***p < 0.001 (compared with Control in panel D).

GSH were almost comparable between Control and *K-Alb* livers, suggesting that simple Nrf2 accumulation does not alter the metabolite pattern. Importantly, the PPP intermediates were significantly lower in *P/K-Alb* liver than in *P-Alb* liver, and the decrease was restored in *P/K-Alb/N* liver. IMP tended to be higher in *P/K-Alb* than *P-Alb*, and the increase was not observed in *P/K-Alb/N*. Similarly, GSH was significantly higher in *P/K-Alb* than *P-Alb*, and the increase was canceled in *P/K-Alb/N*. These results implied that Nrf2 accumulation affects the metabolite pattern in the presence of active PI3K-Akt pathway.

Forced Activation of PI3K Enhances the Nuclear Availability of Nrf2

To elucidate the underlying mechanisms of the functional potentiation of Nrf2, we examined the protein abundance of Nrf2 in liver nuclear extracts (Figure 8C). Whereas *K-Alb* liver showed slight increases in Nrf2 compared with the Control and *P-Alb* livers, nuclear extracts from the *P/K-Alb* liver contained dramatically increased Nrf2. We also found that *Nrf2* mRNA was more abundant in the *P/K-Alb* liver compared with the rest of the mice, suggesting the increased production of Nrf2 in the *P/K-Alb* liver (Figure 8D). Thus, the quantitative increase in nuclear Nrf2 is regarded to be the primary cause of the elevated expression of Nrf2 target genes in the *P/K-Alb* mice. Importantly, Keap1 protein was barely detectable in either the *K-Alb* or *P/K-Alb* livers (Figure 8C), which indicates that the enhanced nuclear accumulation of Nrf2 is independent of Keap1 deficiency but dependent on the disruption of the *Pten* gene. Consistently, the Nrf2 protein was more abundant in the tissues and cells with higher activity of PI3K-Akt signaling; the forestomach and intestine accumulates

more Nrf2 than the liver in *Keap1*$^{F/-}$ mice (Figure 6G), and *Keap1*$^{-/-}$ MEFs with serum accumulates more Nrf2 than those without serum (Figure 7E).

We then examined the phosphorylation of Akt, which was present at low levels in the *P-Alb* liver at P15 (Figure 8C) but was markedly increased at 10 weeks (Figure 8E, left panel). Considering the postnatal expression of Cre recombinase driven by the albumin promoter, the *Pten* gene was not fully disrupted at P15, and *Pten* mRNA was present in the *P-Alb*, *P/K-Alb*, and *P/K-Alb/N* livers by 50% of the control liver (Figure 8D). Accordingly, the *P-Alb*, *P/K-Alb*, and *P/K-Alb/N* livers at P15 showed approximately 50% reduction of the Pten protein compared with that in the control liver (Figure 8C), whereas it was hardly detected in the 10-week-old *Pten-Alb* liver (Figure 8E, right panel). Despite the partial depletion of Pten, Akt phosphorylation, especially at T308, was markedly enhanced in the *P/K-Alb* liver but not in the *P-Alb* liver (Figure 8C). Therefore, the augmented Akt phosphorylation is independent of Pten reduction but is attributed to the disruption of the *Keap1* gene. The enhancement of Akt phosphorylation in the *P/K-Alb* liver was absent in the *P/K-Alb/N* liver, which indicates that accumulated Nrf2 is responsible for the increased phosphorylation of Akt. Nrf2 accumulation may have augmented the Akt phosphorylation in the *Keap1*$^{F/-}$ forestomach and intestine (Figure 6F). Thus, the activation of the PI3K-Akt pathway enhances Nrf2 activity by increasing its nuclear availability, and the activated Nrf2 in turn promotes the further activation of the PI3K-Akt pathway. This positive feedback is one of the molecular mechanisms underlying the aggravating role of Nrf2 in cancer progression.

DISCUSSION

This study demonstrated a contribution of Nrf2 to cellular metabolic activities in proliferating cells. While being a key regulator of redox homeostasis in quiescent cells, Nrf2 activates the metabolic genes in addition to the cytoprotective genes in proliferating cells, which is advantageous for proliferation and survival. Metabolomic profilings revealed that Nrf2 promotes the purine nucleotide synthesis and glutamine metabolism in the presence of active PI3K-Akt signaling.

We identified six genes involved in the PPP and NADPH production pathways as direct targets of Nrf2. Some of these genes were listed as Nrf2 targets in previous microarray analyses conducted in mouse and human (Thimmulappa et al., 2002; MacLeod et al., 2009). These genes, except for *Me1*, were also listed as direct target genes of Nrf2 in an earlier ChIP-seq analysis with anti-Nrf2 antibody using MEFs (Malhotra et al., 2010). While a previous study focused on a cytoprotective aspect of the PPP by analyzing the NADPH production as reducing equivalents for the ROS elimination (Wu et al., 2011), this study showed that the increase of the PPP activity accounts for the Nrf2-dependent proliferation. We further identified the PI3K-Akt pathway as one of the proliferative signals augmenting Nrf2-dependent transcription. Since the PPP genes are strongly activated by Nrf2 in proliferating cells in which PI3K-Akt pathway is active, it is pertinent that the increased expression of the PPP genes contributes to cell proliferation.

In addition to the PPP, or the pre-R5P steps of the nucleotide synthesis, our metabolomic profilings revealed that Nrf2 strongly enhances the latter part of the nucleotide synthesis, or the post-R5P steps. Although we currently do not know the molecular mechanisms how Nrf2 promotes the post-R5P steps, we speculate that the functional enhancement of Ppat and Mthfd2 is one of the regulatory targets of Nrf2 (see Figures 1B, 4D, 6B, and 8A). Nrf2 may also promote the glutamine-utilizing reactions in the post-R5P steps, which could partly explain the glutamine consumption mediated by Nrf2. We surmise that the post-transcriptional regulation of key enzymes catalyzing the reactions in the post-R5P steps explains the discordance between the Nrf2-dependent transcriptome and metabolome. In addition, Nrf2 may indirectly promote the synthesis of 10-formyl-tetrahydrofolate (THF), which is an important substrate in post-R5P steps, though supplying NADPH for the THF production. With these possibilities, Nrf2 directly and/or indirectly controls the complex multilayered regulation of the post-R5P steps.

The importance of glutathione has been recognized from the viewpoint of the detoxification of xenobiotics and ROS. However, recent studies have revealed that glutathione is critical for cell proliferation (Reddy et al., 2007; 2008; Ishimoto et al., 2011). Intriguingly, glutathione could not be replaced with N-acetylcysteine for the proliferation-promoting activity, suggesting that glutathione does more than simply correct the redox balance to fully support cell proliferation (Reddy et al., 2008). The metabolomic profiling showed that a substantial amount of glutamine is directed into glutathione synthesis, to which Nrf2 makes a large contribution. Nrf2 induces GCL, a key enzyme for glutathione synthesis, by directly activating the genes encoding the catalytic and regulatory subunits, *GCL catalytic subunit* (*GCLC*) and *GCL modifier subunit* (*GCLM*) (Moinova and Mulcahy, 1999; Solis et al., 2002; Bea et al., 2003; Sekhar et al., 2003). Nrf2 also increases the supply of cysteine by directly activating the gene encoding xCT (*SLC7A11*), a subunit of the cystine transporter (Sasaki et al., 2002). Because Nrf2 strongly activates *Gclc*, *Gclm*, and *Slc7a11* in the presence of active PI3K-Akt signaling (K.T., unpublished data), the enhancement of glutathione synthesis is an important downstream of Nrf2 in accelerating proliferation.

The functional interaction between the Keap1-Nrf2 pathway and Pten-PI3K-Akt pathway has been reported in several studies using cell lines. The pharmacological inhibition of the PI3K-Akt pathway represses the nuclear translocation of Nrf2 (Harrison et al., 2006; So et al., 2006). Consistent with these reports, we have shown that activation of the PI3K-Akt pathway increases the abundance of nuclear Nrf2. Recently GSK-3 was shown to promote Keap1-independent degradation of Nrf2 (Rada et al., 2011). Because Akt phosphorylates GSK-3 and inhibits its activity (Cross et al., 1995), the active PI3K-Akt signaling should stabilize Nrf2 through repressing GSK-3.

Unexpectedly, Akt phosphorylation was robustly augmented in the *P/K-Alb* mice in Nrf2-dependent manner, which is consistent with the previous report that Nrf2 positively regulates the activation of Akt (Beyer et al., 2008). Considering that SREBP has been suggested to induce the PPP genes when mTORC1 is activated (Düvel et al., 2010), Nrf2 could indirectly activate the PPP through the Akt-mTORC1-SREBP axis in addition to its role in the direct regulation of the PPP.

The genetic inactivation of PTEN leading to the constitutive activation of PI3K-Akt signaling has been identified in many

human cancers (Li et al., 1997). Many oncogenic signals also activate the PI3K-Akt signaling pathway (Yuan and Cantley, 2008). This study demonstrated the positive feedback loop between the Pten-PI3K-Akt and Keap1-Nrf2 pathways, which appears to be one of the most substantial mechanisms for promoting the malignant evolution of cancers. Efficient cancelation of the feedback would be an effective strategy for anti-cancer therapy. It should be noted that a high level of Nrf2 accumulation, which is achieved by the functional impairment of Keap1 combined with the sustained activation of PI3K-Akt pathway, allows Nrf2 to get involved in the modulation of metabolism under pathological conditions. In contrast, temporary accumulation of Nrf2 at a low level is sufficient for Nrf2 to exert the cytoprotective function under physiological conditions. The marked difference in Nrf2 activities between cancers and normal tissues may provide a clue to the selective inhibition of Nrf2 in cancers.

EXPERIMENTAL PROCEDURES

Cell Culture

Two cell lines with *KEAP1* mutations (A549 and H2126) and two cell lines with *NRF2* mutations (LK2 and EBC1) were used. 293/CAT cells and 293/FALG-Nrf2 cells were established previously (Zhang et al., 2007). MEFs were established from *Keap1*$^{-/-}$ and WT mouse embryos (Wakabayashi et al., 2003).

Microarray Analysis

Total RNA from A549 cells was labeled with Cy3. Samples were hybridized to the Human Oligo Microarray (Agilent) according to the manufacturer's protocol. Arrays were scanned using the G2539A Microarray Scanner system (Agilent), and the resulting data were analyzed using GeneSpring GX software (Agilent).

Tumor Xenograft Experiment

A549 cells were subcutaneously injected into the upper back region of eight-week-old male nude mice (BALB/C nu/nu). Tumor size was measured every three days using calipers.

Animals

The generation of *Nrf2*$^{+/-}$, *Keap1*$^{+/-}$, *Keap1*$^{F/+}$, and *Pten*$^{F/+}$ mice has been described (Itoh et al., 1997; Wakabayashi et al., 2003; Okawa et al., 2006; Horie et al., 2004). *Pten*$^{F/+}$ mice were a kind gift from Dr. Akira Suzuki (Kyushu University). *Alb*-Cre transgenic mice were purchased from Jackson Laboratory. All mice were kept under specific pathogen-free conditions and treated according to the regulations presented in The Standards for Human Care and Use of Laboratory Animals of Tohoku University and Guidelines for Proper Conduct of Animal Experiments by the Ministry of Education, Culture, Sports, Science, and Technology of Japan. All the animal experiments were approved at The Tohoku University Committee for Laboratory Animal Research.

Cell Viability Assay

MEFs were seeded at the initial density of 1×10^4 cells/well in 96-well plates and cultured for 24 hr in the presence of 10% FBS or in the absence of FBS. Cells were then treated with 1-chloro-2,4-dinitrobenzene (CDNB; WAKO Pure Chemicals). After 12 hr of culturing, viable cell numbers were quantified with the Cell Counting Kit-8 (Dojindo Molecular Technologies, Inc.) according to the manufacturer's protocol.

BrdU Assay

BrdU was intraperitoneally injected into mice at the dose of 100 mg/kg body weight. One hour after the injection, mice were sacrificed and analyzed using BrdU Immunohistochemistry System (Merck Calbiochem).

Metabolite Measurements

Extracts were prepared from 2 to 6×10^6 cells or approximately 50 mg of tissues with methanol containing Internal Standard Solution (Human Metabolime Technoligies) and analyzed using a capillary electrophoresis (CE)-connected ESI-TOFMS system.

Statistical Analyses

All differences were analyzed with Student's t test. A p value less than 0.05 was considered to be statistically significant.

ACCESSION NUMBERS

The GEO database accession number for the microarray data is GSE28230.

SUPPLEMENTAL INFORMATION

Supplemental Information includes four figures, seven tables, Supplemental Experimental Procedures, and Supplemental References and can be found with this article online at doi:10.1016/j.ccr.2012.05.016.

ACKNOWLEDGMENTS

We would like to thank Drs. Akihiko Muto, Kai Takaya and Maki Goto for providing us the technical advice and key materials. We also thank Ms. Eriko Naganuma and the Biomedical Research Core of the Tohoku University Graduate School of Medicine for their technical support. This work was supported by Grants-in-Aid for Creative Scientific Research (M.Y.) and Scientific Research (K.T., M.Y., and H.M.) from the JSPS; Grants-in-Aid for Scientific Research on Innovative Areas (K.T., M.Y., and H.M.) from the MEXT; the Tohoku University Global COE for the Conquest of Signal Transduction Diseases with Network Medicine (K.T. and M.Y.); JST, CREST (M.Y. and H.M.); and a research grant from the Princess Takamatsu Cancer Research Fund 09-24118 (H.M.).

Received: April 22, 2011
Revised: September 21, 2011
Accepted: May 14, 2012
Published: July 9, 2012

REFERENCES

Bea, F., Hudson, F.N., Chait, A., Kavanagh, T.J., and Rosenfeld, M.E. (2003). Induction of glutathione synthesis in macrophages by oxidized low-density lipoproteins is mediated by consensus antioxidant response elements. Circ. Res. *92*, 386–393.

Bensaad, K., Tsuruta, A., Selak, M.A., Vidal, M.N., Nakano, K., Bartrons, R., Gottlieb, E., and Vousden, K.H. (2006). TIGAR, a p53-inducible regulator of glycolysis and apoptosis. Cell *126*, 107–120.

Beyer, T.A., Xu, W., Teupser, D., auf dem Keller, U., Bugnon, P., Hildt, E., Thiery, J., Kan, Y.W., and Werner, S. (2008). Impaired liver regeneration in Nrf2 knockout mice: role of ROS-mediated insulin/IGF-1 resistance. EMBO J. *27*, 212–223.

Casamayor, A., Morrice, N.A., and Alessi, D.R. (1999). Phosphorylation of Ser-241 is essential for the activity of 3-phosphoinositide-dependent protein kinase-1: identification of five sites of phosphorylation in vivo. Biochem. J. *342*, 287–292.

Cross, D.A.E., Alessi, D.R., Cohen, P., Andjelkovich, M., and Hemmings, B.A. (1995). Inhibition of glycogen synthase kinase-3 by insulin mediated by protein kinase B. Nature *378*, 785–789.

Dang, C.V. (2010). Glutaminolysis: supplying carbon or nitrogen or both for cancer cells? Cell Cycle *9*, 3884–3886.

DeBerardinis, R.J., Mancuso, A., Daikhin, E., Nissim, I., Yudkoff, M., Wehrli, S., and Thompson, C.B. (2007). Beyond aerobic glycolysis: transformed cells can engage in glutamine metabolism that exceeds the requirement for protein and nucleotide synthesis. Proc. Natl. Acad. Sci. USA *104*, 19345–19350.

DeBerardinis, R.J., Lum, J.J., Hatzivassiliou, G., and Thompson, C.B. (2008). The biology of cancer: metabolic reprogramming fuels cell growth and proliferation. Cell Metab. *7*, 11–20.

Düvel, K., Yecies, J.L., Menon, S., Raman, P., Lipovsky, A.I., Souza, A.L., Triantafellow, E., Ma, Q., Gorski, R., Cleaver, S., et al. (2010). Activation of a metabolic gene regulatory network downstream of mTOR complex 1. Mol. Cell *39*, 171–183.

Elstrom, R.L., Bauer, D.E., Buzzai, M., Karnauskas, R., Harris, M.H., Plas, D.R., Zhuang, H., Cinalli, R.M., Alavi, A., Rudin, C.M., and Thompson, C.B. (2004). Akt stimulates aerobic glycolysis in cancer cells. Cancer Res. *64*, 3892–3899.

Engelman, J.A. (2009). Targeting PI3K signalling in cancer: opportunities, challenges and limitations. Nat. Rev. Cancer *9*, 550–562.

Harrison, E.M., McNally, S.J., Devey, L., Garden, O.J., Ross, J.A., and Wigmore, S.J. (2006). Insulin induces heme oxygenase-1 through the phosphatidylinositol 3-kinase/Akt pathway and the Nrf2 transcription factor in renal cells. FEBS J. *273*, 2345–2356.

Horie, Y., Suzuki, A., Kataoka, E., Sasaki, T., Hamada, K., Sasaki, J., Mizuno, K., Hasegawa, G., Kishimoto, H., Iizuka, M., et al. (2004). Hepatocyte-specific Pten deficiency results in steatohepatitis and hepatocellular carcinomas. J. Clin. Invest. *113*, 1774–1783.

Ishimoto, T., Nagano, O., Yae, T., Tamada, M., Motohara, T., Oshima, H., Oshima, M., Ikeda, T., Asaba, R., Yagi, H., et al. (2011). CD44 variant regulates redox status in cancer cells by stabilizing the xCT subunit of system xc(-) and thereby promotes tumor growth. Cancer Cell *19*, 387–400.

Itoh, K., Chiba, T., Takahashi, S., Ishii, T., Igarashi, K., Katoh, Y., Oyake, T., Hayashi, N., Satoh, K., Hatayama, I., et al. (1997). An Nrf2/small Maf heterodimer mediates the induction of phase II detoxifying enzyme genes through antioxidant response elements. Biochem. Biophys. Res. Commun. *236*, 313–322.

Kim, Y.R., Oh, J.E., Kim, M.S., Kang, M.R., Park, S.W., Han, J.Y., Eom, H.S., Yoo, N.J., and Lee, S.H. (2010). Oncogenic NRF2 mutations in squamous cell carcinomas of oesophagus and skin. J. Pathol. *220*, 446–451.

Kroemer, G., and Pouyssegur, J. (2008). Tumor cell metabolism: cancer's Achilles' heel. Cancer Cell *13*, 472–482.

Li, J., Yen, C., Liaw, D., Podsypanina, K., Bose, S., Wang, S.I., Puc, J., Miliaresis, C., Rodgers, L., McCombie, R., et al. (1997). PTEN, a putative protein tyrosine phosphatase gene mutated in human brain, breast, and prostate cancer. Science *275*, 1943–1947.

Lu, S.C. (2009). Regulation of glutathione synthesis. Mol. Aspects Med. *30*, 42–59.

MacLeod, A.K., McMahon, M., Plummer, S.M., Higgins, L.G., Penning, T.M., Igarashi, K., and Hayes, J.D. (2009). Characterization of the cancer chemopreventive NRF2-dependent gene battery in human keratinocytes: demonstration that the KEAP1-NRF2 pathway, and not the BACH1-NRF2 pathway, controls cytoprotection against electrophiles as well as redox-cycling compounds. Carcinogenesis *30*, 1571–1580.

Malhotra, D., Portales-Casamar, E., Singh, A., Srivastava, S., Arenillas, D., Happel, C., Shyr, C., Wakabayashi, N., Kensler, T.W., Wasserman, W.W., and Biswal, S. (2010). Global mapping of binding sites for Nrf2 identifies novel targets in cell survival response through ChIP-Seq profiling and network analysis. Nucleic Acids Res. *38*, 5718–5734.

Moinova, H.R., and Mulcahy, R.T. (1999). Up-regulation of the human gamma-glutamylcysteine synthetase regulatory subunit gene involves binding of Nrf-2 to an electrophile responsive element. Biochem. Biophys. Res. Commun. *261*, 661–668.

Okawa, H., Motohashi, H., Kobayashi, A., Aburatani, H., Kensler, T.W., and Yamamoto, M. (2006). Hepatocyte-specific deletion of the keap1 gene activates Nrf2 and confers potent resistance against acute drug toxicity. Biochem. Biophys. Res. Commun. *339*, 79–88.

Rada, P., Rojo, A.I., Chowdhry, S., McMahon, M., Hayes, J.D., and Cuadrado, A. (2011). SCF/beta-TrCP promotes glycogen synthase kinase 3-dependent degradation of the Nrf2 transcription factor in a Keap1-independent manner. Mol. Cell. Biol. *31*, 1121–1133.

Reddy, N.M., Kleeberger, S.R., Cho, H.Y., Yamamoto, M., Kensler, T.W., Biswal, S., and Reddy, S.P. (2007). Deficiency in Nrf2-GSH signaling impairs type II cell growth and enhances sensitivity to oxidants. Am. J. Respir. Cell Mol. Biol. *37*, 3–8.

Reddy, N.M., Kleeberger, S.R., Bream, J.H., Fallon, P.G., Kensler, T.W., Yamamoto, M., and Reddy, S.P. (2008). Genetic disruption of the Nrf2 compromises cell-cycle progression by impairing GSH-induced redox signaling. Oncogene *27*, 5821–5832.

Sakamoto, K., Iwasaki, K., Sugiyama, H., and Tsuji, Y. (2009). Role of the tumor suppressor PTEN in antioxidant responsive element-mediated transcription and associated histone modifications. Mol. Biol. Cell *20*, 1606–1617.

Sasaki, H., Sato, H., Kuriyama-Matsumura, K., Sato, K., Maebara, K., Wang, H., Tamba, M., Itoh, K., Yamamoto, M., and Bannai, S. (2002). Electrophile response element-mediated induction of the cystine/glutamate exchange transporter gene expression. J. Biol. Chem. *277*, 44765–44771.

Sekhar, K.R., Crooks, P.A., Sonar, V.N., Friedman, D.B., Chan, J.Y., Meredith, M.J., Starnes, J.H., Kelton, K.R., Summar, S.R., Sasi, S., and Freeman, M.L. (2003). NADPH oxidase activity is essential for Keap1/Nrf2-mediated induction of GCLC in response to 2-indol-3-yl-methylenequinuclidin-3-ols. Cancer Res. *63*, 5636–5645.

Shibata, T., Ohta, T., Tong, K.I., Kokubu, A., Odogawa, R., Tsuta, K., Asamura, H., Yamamoto, M., and Hirohashi, S. (2008). Cancer related mutations in NRF2 impair its recognition by Keap1-Cul3 E3 ligase and promote malignancy. Proc. Natl. Acad. Sci. USA *105*, 13568–13573.

Singh, A., Misra, V., Thimmulappa, R.K., Lee, H., Ames, S., Hoque, M.O., Herman, J.G., Baylin, S.B., Sidransky, D., Gabrielson, E., et al. (2006). Dysfunctional KEAP1-NRF2 interaction in non-small-cell lung cancer. PLoS Med. *3*, e420.

Singh, A., Boldin-Adamsky, S., Thimmulappa, R.K., Rath, S.K., Ashush, H., Coulter, J., Blackford, A., Goodman, S.N., Bunz, F., Watson, W.H., et al. (2008). RNAi-mediated silencing of nuclear factor erythroid-2-related factor 2 gene expression in non-small cell lung cancer inhibits tumor growth and increases efficacy of chemotherapy. Cancer Res. *68*, 7975–7984.

So, H.S., Kim, H.J., Lee, J.H., Lee, J.H., Park, S.Y., Park, C., Kim, Y.H., Kim, J.K., Lee, K.M., Kim, K.S., et al. (2006). Flunarizine induces Nrf2-mediated transcriptional activation of heme oxygenase-1 in protection of auditory cells from cisplatin. Cell Death Differ. *13*, 1763–1775.

Solis, W.A., Dalton, T.P., Dieter, M.Z., Freshwater, S., Harrer, J.M., He, L., Shertzer, H.G., and Nebert, D.W. (2002). Glutamate-cysteine ligase modifier subunit: mouse Gclm gene structure and regulation by agents that cause oxidative stress. Biochem. Pharmacol. *63*, 1739–1754.

Solis, L.M., Behrens, C., Dong, W., Suraokar, M., Ozburn, N.C., Moran, C.A., Corvalan, A.H., Biswal, S., Swisher, S.G., Bekele, B.N., et al. (2010). Nrf2 and Keap1 abnormalities in non-small cell lung carcinoma and association with clinicopathologic features. Clin. Cancer Res. *16*, 3743–3753.

Taguchi, K., Shimada, M., Fujii, S., Sumi, D., Pan, X., Yamano, S., Nishiyama, T., Hiratsuka, A., Yamamoto, M., Cho, A.K., et al. (2008). Redox cycling of 9,10-phenanthraquinone to cause oxidative stress is terminated through its monoglucuronide conjugation in human pulmonary epithelial A549 cells. Free Radic. Biol. Med. *44*, 1645–1655.

Taguchi, K., Maher, J.M., Suzuki, T., Kawatani, Y., Motohashi, H., and Yamamoto, M. (2010). Genetic analysis of cytoprotective functions supported by graded expression of Keap1. Mol. Cell. Biol. *30*, 3016–3026.

Taub, R. (2004). Liver regeneration: from myth to mechanism. Nat. Rev. Mol. Cell Biol. *5*, 836–847.

Thimmulappa, R.K., Mai, K.H., Srisuma, S., Kensler, T.W., Yamamoto, M., and Biswal, S. (2002). Identification of Nrf2-regulated genes induced by the chemopreventive agent sulforaphane by oligonucleotide microarray. Cancer Res. *62*, 5196–5203.

Tong, X., Zhao, F., and Thompson, C.B. (2009). The molecular determinants of de novo nucleotide biosynthesis in cancer cells. Curr. Opin. Genet. Dev. *19*, 32–37.

Uruno, A., and Motohashi, H. (2011). The Keap1-Nrf2 system as an in vivo sensor for electrophiles. Nitric Oxide *25*, 153–160.

Wakabayashi, N., Itoh, K., Wakabayashi, J., Motohashi, H., Noda, S., Takahashi, S., Imakado, S., Kotsuji, T., Otsuka, F., Roop, D.R., et al. (2003). Keap1-null mutation leads to postnatal lethality due to constitutive Nrf2 activation. Nat. Genet. *35*, 238–245.

Wang, R., An, J., Ji, F., Jiao, H., Sun, H., and Zhou, D. (2008). Hypermethylation of the Keap1 gene in human lung cancer cell lines and lung cancer tissues. Biochem. Biophys. Res. Commun. *373*, 151–154.

Wu, K.C., Cui, J.Y., and Klaassen, C.D. (2011). Beneficial role of Nrf2 in regulating NADPH generation and consumption. Toxicol. Sci. *123*, 590–600.

Yuan, T.L., and Cantley, L.C. (2008). PI3K pathway alterations in cancer: variations on a theme. Oncogene *27*, 5497–5510.

Zhang, J., Hosoya, T., Maruyama, A., Nishikawa, K., Maher, J.M., Ohta, T., Motohashi, H., Fukamizu, A., Shibahara, S., Itoh, K., and Yamamoto, M. (2007). Nrf2 Neh5 domain is differentially utilized in the transactivation of cytoprotective genes. Biochem. J. *404*, 459–466.

Zhang, P., Singh, A., Yegnasubramanian, S., Esopi, D., Kombairaju, P., Bodas, M., Wu, H., Bova, S.G., and Biswal, S. (2010). Loss of Kelch-like ECH-associated protein 1 function in prostate cancer cells causes chemoresistance and radioresistance and promotes tumor growth. Mol. Cancer Ther. *9*, 336–346.

Cancer Cell
Article

Proapoptotic Activation of Death Receptor 5 on Tumor Endothelial Cells Disrupts the Vasculature and Reduces Tumor Growth

Nicholas S. Wilson,[1,5] Annie Yang,[1,5] Becky Yang,[1] Suzana Couto,[2] Howard Stern,[2] Alvin Gogineni,[3] Robert Pitti,[1] Scot Marsters,[1] Robby M. Weimer,[3] Mallika Singh,[4] and Avi Ashkenazi[1,*]
[1]Department of Molecular Oncology
[2]Department of Pathology
[3]Department of Biomedical Imaging
[4]Department of Molecular Biology
Genentech, Inc., South San Francisco, CA 94080, USA
[5]These authors contributed equally to this work
*Correspondence: aa@gene.com
http://dx.doi.org/10.1016/j.ccr.2012.05.014

SUMMARY

The proapoptotic death receptor DR5 has been studied extensively in cancer cells, but its action in the tumor microenvironment is not well defined. Here, we uncover a role for DR5 signaling in tumor endothelial cells (ECs). We detected DR5 expression in ECs within tumors but not normal tissues. Treatment of tumor-bearing mice with an oligomeric form of the DR5 ligand Apo2L/TRAIL induced apoptosis in tumor ECs, collapsing blood vessels and reducing tumor growth: Vascular disruption and antitumor activity required DR5 expression on tumor ECs but not malignant cells. These results establish a therapeutic paradigm for proapoptotic receptor agonists as selective tumor vascular disruption agents, providing an alternative, perhaps complementary, strategy to their use as activators of apoptosis in malignant cells.

INTRODUCTION

Apoptosis, or type I programmed cell death, is essential for normal development, tissue homeostasis, and tumor suppression in higher organisms (Strasser et al., 2000). The ability of the proapoptotic receptor ligand Apo2L/TRAIL (TNFSF10) to kill malignant cells selectively has prompted an intensive effort to explore its therapeutic potential. Various agonists of the cognate death receptors DR4 and DR5 have been developed, and several have been studied in human cancer clinical trials (Ashkenazi and Herbst, 2008; Johnstone et al., 2008). Referred to as proapoptotic receptor agonists (PARAs) (Ashkenazi, 2008a), these agents include recombinant human Apo2L/TRAIL (dulanermin) and several agonistic antibodies targeting DR4 or DR5. Although certain cancer cells undergo apoptosis in response to PARAs, others exhibit partial or total resistance (Abdulghani and El-Deiry, 2010; Yang et al., 2010). Preclinical studies with these agents have relied mainly on cultured human cancer cells or mouse-xenografted human tumors. However, because most PARAs target human receptors but not their mouse counterparts (Ashkenazi, 2002), the effects of death-receptor engagement on the tumor microenvironment are not well understood.

Some previous studies have used MD5-1, an antibody directed against murine DR5 (or TRAIL-R), the only Apo2L/TRAIL death receptor present in the mouse. MD5-1 is reported to induce apoptosis of cancer cells in vitro; however, its tumoricidal efficacy in vivo requires aspects of innate and adaptive host immunity (Frew et al., 2008; Haynes et al., 2010; Takeda et al., 2004; Uno et al., 2006). Other studies have examined the ability of Apo2L/TRAIL to induce apoptosis in endothelial cells: these were performed mainly by in vitro culture of endothelial cells

Significance

Cancer therapies typically attack the malignant cells of a tumor, but targeting the nonmalignant tumor microenvironment may augment antitumor efficacy. Various types of cancer cells express the proapoptotic death receptor DR5. DR5 agonists induce apoptosis of certain malignant cells and thereby can exert antitumor activity. Here we show that endothelial cells within tumor blood vessels can selectively express DR5. Activation of DR5 on tumor endothelial cells triggers apoptosis: This disrupts the integrity of tumor blood vessels and decreases tumor growth even in the absence of DR5 expression in the malignant cell compartment. Our findings suggest a unique, perhaps complementary, utility for proapoptotic receptor agonists as vascular disruption agents in cancer therapy.

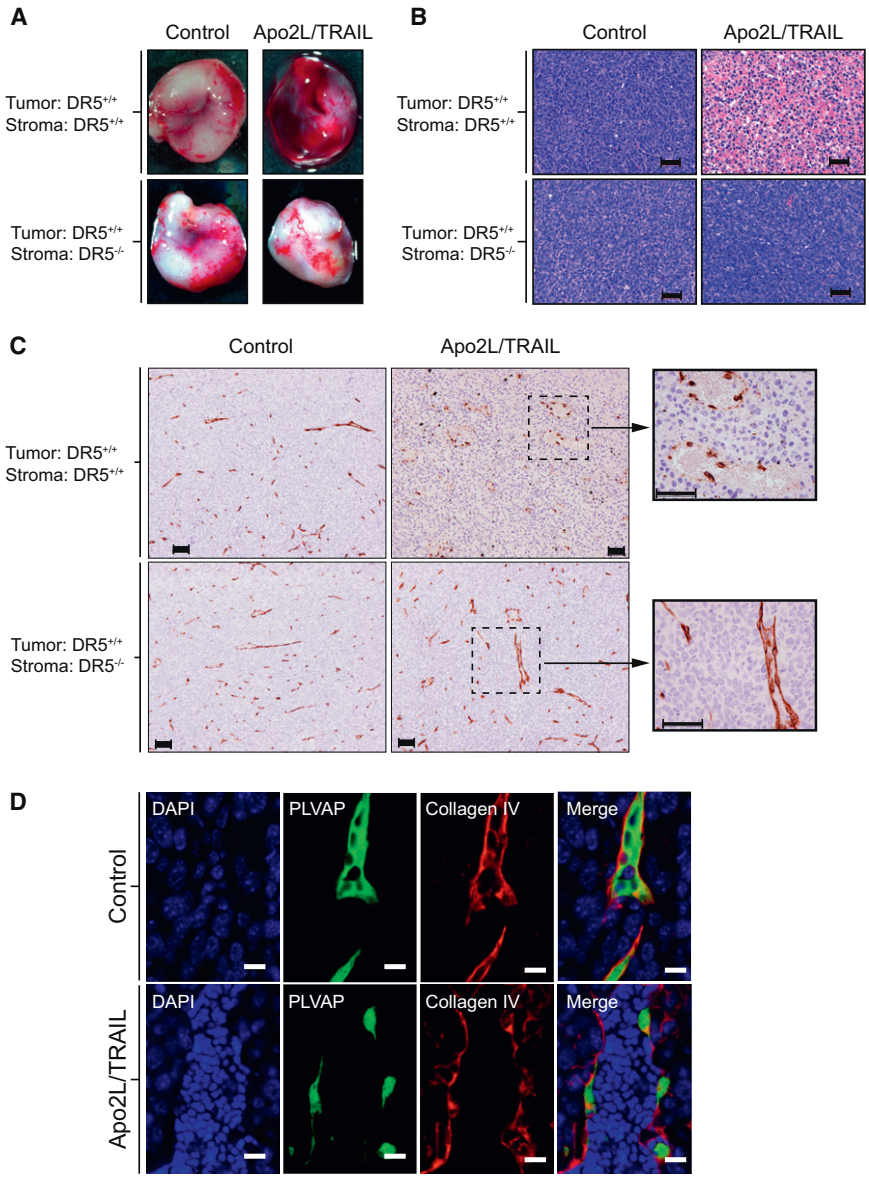

Figure 1. DR5-Dependent Disruption of the Tumor Vasculature by Apo2L/TRAIL

(A) Lewis lung carcinoma (LLC) tumors (>500 mm^3) grown in WT ($DR5^{+/+}$) or DR5-KO ($DR5^{-/-}$) mice were dosed with an intraperitoneal (i.p.) injection of 10 mg/kg of Apo2L/TRAIL (consisting of 10 mg/kg of Flag-tagged Apo2L/TRAIL and 10 mg/kg anti-Flag antibody, given sequentially) or PBS. Tumors were examined macroscopically 24 hr after treatment for the appearance of vascular disruption.

(B) Hematoxylin and eosin (H&E) staining of sections from LLC tumors grown in WT or DR5-KO mice and treated with Apo2L/TRAIL.

(C) Anti-PLVAP staining was used to visualize the tumor endothelium; representative images show disrupted blood vessels (inset = higher magnification image) in tumors from Apo2L/TRAIL-treated WT, but not DR5-KO or untreated (control), mice. Scale bars, 50 μm.

(D) Immunofluorescence colocalization of DAPI (blue), PLVAP (green), and collagen IV (red) on LLC tumor sections from control or Apo2L/TRAIL-treated, WT mice. Single-channel as well as merged images are shown. Scale bar, 10 μm. Data in Figure 1 are representative of two or more independent experiments.

See also Figure S1.

and arrived at conflicting conclusions as to whether this ligand induced apoptosis or proliferation in these cells (Chan et al., 2010; Chen and Easton, 2010; Li et al., 2003). Indeed, the prevailing paradigm for PARAs as anticancer therapeutics remains centered on their ability to induce apoptosis directly in malignant cells.

In the present study, we investigated the biological activity of an oligomeric form of Apo2L/TRAIL capable of activating DR5 in both the malignant and stromal compartments of tumors.

RESULTS

DR5-Dependent Disruption of the Tumor Vasculature by Crosslinked Apo2L/TRAIL

Although murine cancer cells often express DR5, they do not respond to dulanermin, the trimeric recombinant soluble version of human Apo2L/TRAIL that has been studied in clinical trials (Ashkenazi et al., 1999; Herbst et al., 2010) (Figure S1A available online; data not shown). However, we found that crosslinking of a Flag epitope-tagged version of Apo2L/TRAIL with an anti-Flag antibody into higher order oligomers enabled the ligand to induce apoptosis in a range of mouse cancer cell lines: These included Renca331 cells (Figure S1B), which are particularly sensitive to membrane-bound Apo2L/TRAIL (Seki et al., 2003), as well as Lewis lung carcinoma (LLC) cells (Figure S1C). To determine the efficacy of this oligomeric DR5-ligand in vivo, we implanted LLC cells into C57BL/6 wild-type recipient mice and treated the animals with a single dose of crosslinked Apo2L/TRAIL (Apo2L/TRAIL hereafter). Surprisingly, we observed a striking hemorrhagic appearance in tumors within 24 hr of treatment (Figure 1A). Histological examination confirmed extensive tumor hemorrhage, as well as widespread tumor-cell death (Figure 1B). Such effects were not induced by dulanermin (Figure S1D), consistent with its lack of activity toward mouse DR5. Immunohistochemical staining with the Meca-32 antibody (Hallmann et al., 1995), which recognizes the plasmalemma vesicle-associated protein (PLVAP; also PV-1)—an endothelial marker—revealed severe disruption of the tumor vasculature in response to Apo2L/TRAIL. Tumor blood vessels in treated mice showed evidence of congestion, discontinuity in ECs lining the vessel, and blood-cell leakage (Figure 1C). To evaluate this further, we performed immunofluorescence staining for PLVAP in conjunction with collagen IV, a marker for the basement membrane. In tumors

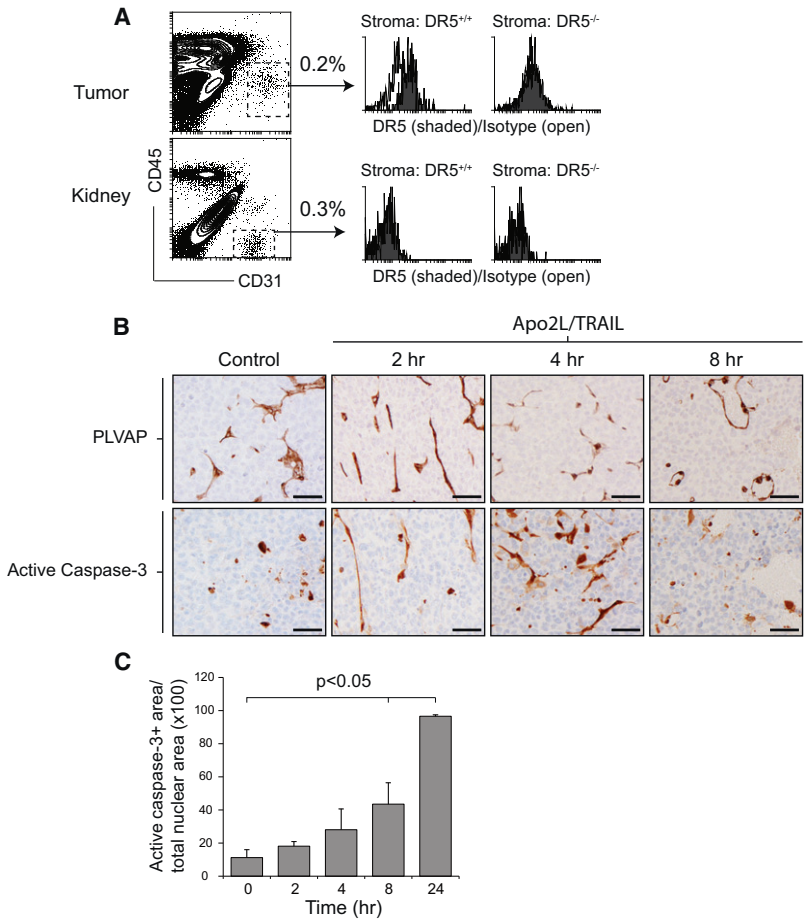

Figure 2. DR5-Mediated Apoptosis in Tumor-Associated Endothelial Cells

(A) Top, analysis of DR5 expression by CD45^{low}CD31^{high} expressing tumor endothelial cells (ECs) in LLC tumors grown in WT (DR5$^{+/+}$) or DR5-KO (DR5$^{-/-}$) mice. DR5 expression (shaded) versus isotype control (open) on cell lines are shown from a pooled cell fraction generated from WT (n = 4) or DR5-KO LLC tumors. Bottom, analysis of DR5 expression by CD45^{low}CD31^{high} expressing, "normal" kidney endothelial cells isolated from WT or DR5-KO mice. Pooled kidney cell fractions were generated from the same mice that were analyzed above.

(B) Anti-PLVAP and activated capsase-3 (CC3) staining in serial LLC tumor sections collected from WT or DR5-KO mice treated for the indicated times with Apo2L/TRAIL or PBS (control).

(C) Quantitation of cleaved caspase-3 immunohistochemical staining on LLC tumor sections from a time course of Apo2L/TRAIL treatment. The average of n = 5 tumors for each time point is plotted; error bars indicate the SEM. Student's t test was used to calculate statistical significance. Data in Figure 2 are representative of two or more independent experiments.

See also Figure S2.

from untreated mice, blood vessels were characterized by a contiguous layer of PLVAP-positive cells within the collagen IV-stained basement membrane (Figure 1D); in contrast, tumors from mice treated with Apo2L/TRAIL for 24 hr displayed congested blood vessels, with only occasional PLVAP-positive cells and with large areas of "naked" basement membrane. These observations suggest that Apo2L/TRAIL treatment leads to ablation and detachment of ECs lining blood vessels within tumors, thereby perturbing the integrity of these vessels.

DR5-Dependent Apoptosis Activation in Tumor Endothelial Cells

Remarkably, implantation of LLC tumor cells in DR5-deficient mice completely abrogated the effects of Apo2L/TRAIL on the tumor vasculature (Figures 1A–1C). We therefore hypothesized that the proapoptotic ligand might be exerting a direct biological effect on the tumor-stromal compartment. To evaluate this possibility, we dissociated LLC tumors grown in wild-type (WT) or DR5-knockout (KO) recipients and stained the isolated cells for flow cytometric analysis with antibodies to three markers: DR5; the leukocyte common antigen, CD45; and the endothelial cell-associated antigen, CD31 (Tang et al., 1993). We used differential CD45 and CD31 expression to broadly define tumor-associated leukocytes (CD45^{high}), a tumor epithelial-cell enriched fraction (CD45^{low}CD31^{low}), and tumor ECs (CD45^{low}CD31^{high}). We detected DR5 protein expression on CD45^{low}CD31^{low} malignant epithelial cells from tumors grown in WT or DR5-KO mice, but not on CD45^{high} leukocytes from tumors grown in mice with either DR5 genotype (Figure S2A) (Tang et al., 1993). Importantly, we also observed DR5 expression on CD45^{low}CD31^{high} endothelial cells from tumors grown in WT but not DR5-KO mice (Figure 2A). By contrast, we did not detect significant DR5 expression on CD45^{low}CD31^{high} endothelial cells isolated from the kidneys of normal WT mice (Figure 2A). Immunohistochemistry confirmed DR5 expression on ECs within the tumor stroma of WT mice (Figure S2B).

ECs in various tissues are phenotypically and functionally diverse, with differential surface-marker expression and distinct adherens and tight junctional complexes (Dejana, 2004; Jain, 2005; Pober and Sessa, 2007). Consistent with the lack of DR5 expression by ECs in normal tissues, we did not observe any evidence of vascular disruption or hemorrhage outside of the tumor microenvironment in Apo2L/TRAIL-treated mice. The apparent selectivity of DR5 expression on tumor ECs as compared to normal-tissue ECs may reflect local stressful conditions within the tumor such as hypoxia, which has been shown to increase DR5 expression in cancer cells (Mahajan et al., 2008). To assess proapoptotic signaling in tumor ECs, we monitored the appearance of apoptotic markers over time in LLC tumors from mice treated with Apo2L/TRAIL. Serial sections of tumor tissue were stained for PLVAP to localize tumor ECs, or with an antibody specific to active (cleaved) caspase-3 as an indicator of proapoptotic signaling. Some areas of active caspase-3 staining appeared in tumor epithelial cells regardless of treatment (Figure 2B), suggesting spontaneous focal apoptosis as is commonly seen in mouse tumors. However, we detected rapid generation of active caspase-3 in tumor ECs, within 2 hr after

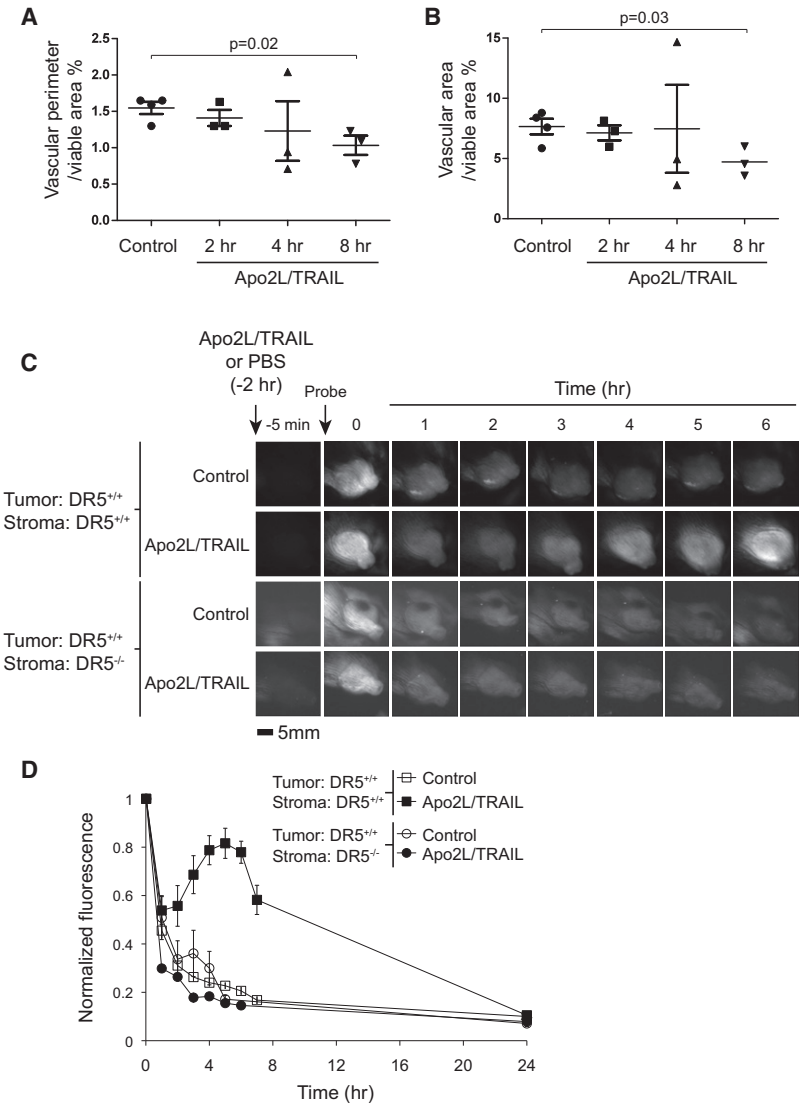

Figure 3. Temporal Analysis of Tumor-Vascular Changes Induced by Apo2L/TRAIL

Quantitation of anti-PLVAP immunostaining was performed on tumor sections from mice treated with Apo2L/TRAIL for the indicated time period.

(A) Vascular perimeter (presented as vessel perimeter in μm, divided by viable area in μm^2 multiplied by 100). Horizontal bars indicate the mean ± SEM. Statistical significance was calculated using a two-tailed, independent samples t test.

(B) Vascular area (presented as vessel area in μm^2, divided by viable area in μm^2 multiplied by 100). Vascular perimeter and area were calculated as described in Supplemental Experimental Procedures. Horizontal bars indicate the mean ± SEM. Statistical significance was calculated using a two-tailed, independent samples t test.

(C) LLC tumor-bearing WT or DR5-KO mice (n = 3–5/group) were treated with PBS or Apo2L/TRAIL. Two hr after treatment, mice were injected intravenously with the fluorescent blood pool probe AngioSense680IVM. Distribution of the fluorescent probe in the tumor was monitored at the indicated times on anesthetized mice. Shown are representative images from a time course following injection of the probe.

(D) Quantification from (C). Error bars indicate the SEM. See also Figure S3.

Apo2L/TRAIL treatment. By 8 hr, there was evidence of vessel congestion and hemorrhage (indicated by the presence of blood cells outside of PLVAP-marked vascular spaces). Distinct changes in EC morphology were also apparent, with cell bodies rounded and protruding into the lumen (Figure 2B). By 24 hr after Apo2L/TRAIL treatment, extensive active caspase-3 staining could be seen throughout the tumor (Figure 2C; Figure S2C). Remarkably, at early time points, little caspase-3 activity was present within malignant epithelial cells (Figures 2B and 2C), suggesting that Apo2L/TRAIL-induced apoptosis in tumor ECs preceded, and was independent of, apoptosis in the malignant-cell compartment. Apo2L/TRAIL did not induce EC apoptosis in LLC tumors grown in DR5-deficient mice (Figure S2C), confirming direct DR5-dependent signaling in tumor ECs.

In contrast to Apo2L/TRAIL, the MD5-1 antibody, which targets mouse DR5, did not induce discernible effects on the tumor vasculature. LLC tumors from mice treated with MD5-1 showed no evidence of hemorrhage (Figure S2D), and activation of caspase-3 in these tumors by MD5-1 was significantly weaker than stimulation by Apo2L/TRAIL (Figure S2E). However, MD5-1 did inhibit tumor growth in vivo (Figure S2F). These results suggest that the enhanced potency achieved by crosslinking of Apo2L/TRAIL, perhaps better mimicking the transmembrane form of this ligand, is important for activation of DR5-mediated apoptosis in tumor ECs. Nevertheless, additional mechanisms supported by MD5-1, such as innate or adaptive immune-cell functions (Frew et al., 2008; Haynes et al., 2010; Takeda et al., 2004; Uno et al., 2006), may mediate generation of an apoptotic signal by this anti-DR5 antibody in tumor cells.

Temporal Analysis of DR5-Mediated Tumor-Vascular Disruption

We next asked whether the apoptotic effects of Apo2L/TRAIL on ECs were associated with changes in tumor-vascular density. Using a method previously described (Brey et al., 2003), we quantitated PLVAP immunostaining in control and Apo2L/TRAIL-treated tumor specimens over time. By 8 hr after treatment with Apo2L/TRAIL, both the vascular perimeter and area significantly decreased (Figures 3A and 3B), indicating diminished tumor-vascular density. This decrease was consistent with the changes in vessel morphology seen at the same timepoint (Figure 2B), suggesting a cumulative effect of EC apoptosis over time.

To examine the kinetics of tumor-vascular disruption more closely, we used noninvasive, near-infrared imaging of a fluorescent macromolecular blood-pool probe. Intravenous (i.v.)

A

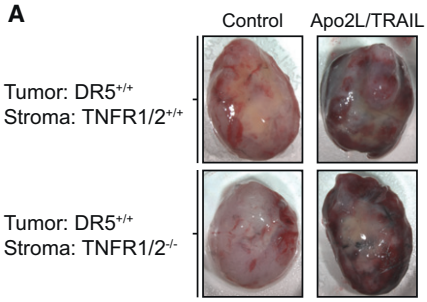

B

Recipient	Treatment	Tumor Hemorrhage	(n)
Wildtype	Control	0%	14
Wildtype	Apo2L/TRAIL	100%	12
DR5-deficient	Control	0%	15
DR5-deficient	Apo2L/TRAIL	0%	14
TNFR1/2-deficient	Control	0%*	10
TNFR1/2-deficient	Apo2L/TRAIL	100%	10

* Untreated tumors in TNFR1/2-deficient exhibited small areas of hemorrhage

C

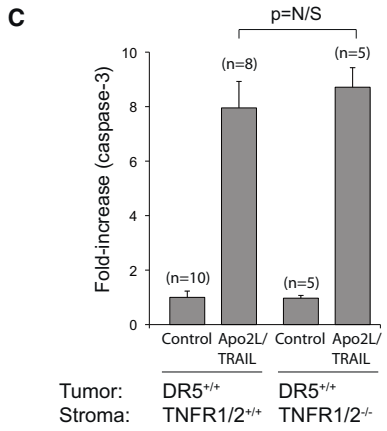

Figure 4. DR5-Mediated Vascular Disruption Is Independent of TNFR Signaling

(A) LLC tumors (>500 mm^3) grown in WT or TNFR1/2-double-KO (TNFR1/$2^{-/-}$) mice were dosed intraperitoneally with 10 mg/kg of Apo2L/TRAIL or PBS. Tumors were examined macroscopically 24 hr after treatment for the appearance of vascular disruption.

(B) Table summarizing the incidence of hemorrhage in tumors grown in recipient mice with the indicated genotypes.

(C) LLC tumor cells were implanted in C57BL/6 WT or TNFR1/2-double-KO mice. After a 24 hr treatment with Apo2L/TRAIL or PBS (control), tumors were harvested and flow cytometry was used to measure cleaved caspase-3 in tumor cells. Caspase-3 activation is represented as fold over control (PBS). Error bars indicate the SEM. Student's t test was used to calculate statistical significance. N/S, not significant. Data in Figure 4 are representative of two or more independent experiments.

administration of macromolecular probes enables longitudinal assessment of vascular permeability, because probe distribution within tumors is governed by endothelial permeability and the differential rates of clearance between the vascular and interstitial compartments (for further discussion see Figure S3). In untreated tumor-bearing mice, fluorescence intensity within tumors decreased exponentially following i.v. probe injection (Figures 3C and 3D), consistent with the expected systemic half-life of the probe. By contrast, in animals treated with ApoL2/TRAIL 2 hr before probe injection, tumor-associated fluorescence decreased initially, comparable to control, but then increased between 2 and 6 hr. Both the timing and characteristics of the phenotype were consistent with an acute change in vascular permeability (Figure S3C), rather than vascular normalization due to an antiangiogenic effect (Jain, 2005; McKeage and Baguley, 2010). Apo2L/TRAIL treatment of DR5-KO tumor-bearing mice did not result in abnormal probe clearance, confirming that the disruption of tumor-vascular integrity required stromal DR5. Together, these data suggest that Apo2L/TRAIL induces DR5-dependent changes in the tumor vasculature within 4 hr of treatment.

DR5-Mediated Tumor-Vascular Disruption Is Independent of TNFR Signaling

In addition to proapoptotic signaling, engagement of DR5 under certain circumstances may activate nonapoptotic pathways, such as the nuclear factor-κB (NF-κB) cascade, which promotes cytokine and chemokine production, among other cellular effects (Wilson et al., 2009). Tumor necrosis factor alpha (TNFα), often induced by NF-κB stimulation, has been reported to trigger dramatic tumor-vascular effects (Corti and Ponzoni, 2004; ten Hagen et al., 2008). This raised the possibility that the impact of DR5 activation on the tumor vasculature might be exerted indirectly, via TNFα. To examine this notion, we implanted TNF receptor (TNFR) 1 and 2 double-KO mice with LLC tumors and treated them with Apo2L/TRAIL. The appearance and incidence of tumor-vascular disruption induced by Apo2L/TRAIL in TNFR1/2-KO mice were indistinguishable from those in WT mice, yet were absent in DR5-KO recipients (Figures 4A and 4B). In accordance, TNFR1/2 deficiency in the stromal compartment had no impact on Apo2L/TRAIL-induced caspase-3 activation in tumor epithelial cells (Figure 4C). These results indicate that Apo2L/TRAIL exerts its tumor-vascular effects independently of TNFR signaling.

Tumor-Vascular Disruption Is Independent of DR5 Expression in Malignant Cells

Our findings suggested that DR5 ligation on tumor ECs might directly induce apoptotic death of these cells; alternatively, proapoptotic signaling in DR5-expressing malignant cells might indirectly mediate the observed apoptotic outcome in tumor ECs. To interrogate this, we generated methylcholanthrene (MCA)-induced fibrosarcomas in WT and DR5-KO mice and established cell lines from the resulting tumors. We confirmed significant DR5 expression or its absence by flow cytometric analysis of the corresponding tumor cell lines (Figure 5A). We then generated WT or DR5-KO MCA tumors by implanting these fibrosarcoma cells in WT or DR5-KO recipient mice. Induction of tumor hemorrhage by Apo2L/TRAIL required DR5 expression in the stroma, but not the malignant tumor-cell compartment (Figure 5B; Figure S4). Immunostaining with anti-PLVAP and anti-active caspase-3 antibodies confirmed proapoptotic signaling in tumor ECs, regardless of DR5 expression status in the malignant cells (Figures 5C and 5D). Hence, disruption of the tumor vasculature by Apo2L/TRAIL occurs independently of DR5 engagement in cancer cells.

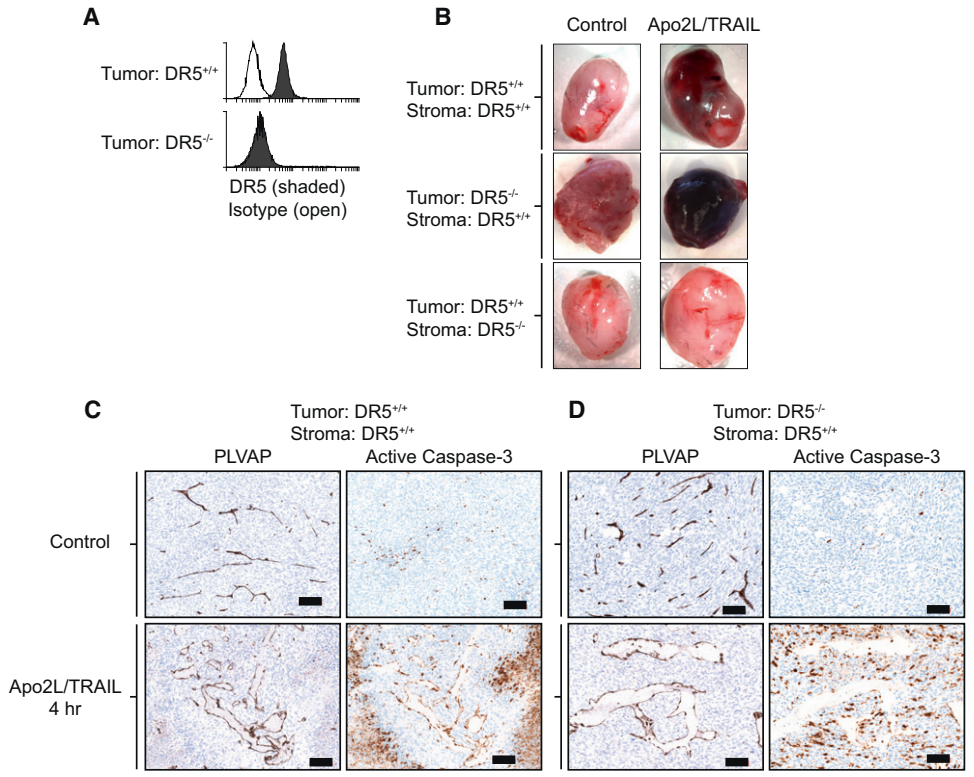

Figure 5. Effect of Apo2L/TRAIL on the Tumor Vasculature Is Independent of DR5 Expression in Malignant Cells

(A) Methylcholanthrene (MCA)-induced fibrosarcoma cell lines were derived from WT ($DR5^{+/+}$) or DR5-KO ($DR5^{-/-}$) C57BL/6 mice and assayed for DR5 expression by flow cytometry.

(B) Images are shown of $DR5^{+/+}$ or $DR5^{-/-}$ fibrosarcoma tumors, grown in C57BL/6 $DR5^{+/+}Rag2^{-/-}$ (top and middle panels), or C57BL/6 $DR5^{-/-}$ (bottom panels), recipients. Tumors were harvested at 24 hr post-treatment with Apo2L/TRAIL and compared with PBS-treated controls.

(C and D) Apoptosis in tumor vasculature of MCA-induced tumors. $DR5^{+/+}$ (C) or $DR5^{-/-}$ (D) MCA-induced fibrosarcoma cells were implanted in C57BL/6 $DR5^{+/+}Rag2^{-/-}$ recipients and treated with Apo2L/TRAIL (10 mg/kg) for 4 hr. Serial sections from tumors were stained with antibodies specific for PLVAP or cleaved casapse-3 to localize endothelial and apoptotic cells, respectively. Scale bars, 100 μm. Data in Figure 5 are representative of two or more independent experiments.

See also Figure S4.

DR5-Mediated Vascular Disruption Reduces Tumor Growth

The induction of DR5-mediated apoptosis in tumor ECs suggested that it might be possible to harness this activity for therapeutic gain. To assess this, we compared the ability of Apo2L/TRAIL to inhibit tumor growth in WT mice bearing either DR5-expressing or DR5-deficient tumors. In vitro analysis of caspase-8 and caspase-3/7 activation and loss of cell viability confirmed a lack of proapoptotic signaling in DR5-KO MCA tumor cells (Figure 6A). Consistent with the immunohistochemical evidence (Figures 5C and 5D), both DR5-expressing and DR5-KO fibrosarcomas showed significant caspase-3 activation in vivo in response to Apo2L/TRAIL (Figure 6B). This result suggested that the death of malignant cells occurred as an indirect consequence of tumor-vascular disruption. Supporting this hypothesis, the growth of pre-established fibrosarcomas possessing either DR5 genotype was significantly attenuated by Apo2L/TRAIL (Figures 6C and 6D). Moreover, in both cases, extensive hemorrhagic tumor necrosis occurred (Figure S4). Thus, DR5-mediated apoptosis in tumor ECs can contribute to antitumor efficacy in a manner that is distinct and separable from DR5-dependent malignant-cell apoptosis. We also evaluated vascular density and morphology at an "end of study" time point (i.e., when control and Apo2L/TRAIL-treated tumors had grown to similar size). Although overall vascular density was significantly reduced in tumors exposed to Apo2L/TRAIL as compared with controls, vascular morphology was indistinguishable (Figures S5A and S5B). Hence, although repeat dosing of Apo2L/TRAIL exerts a long-term effect on tumor-vascular density, treatment cessation allows the tumor vasculature to reform.

Consistent with its modest proapoptotic activity toward the fibrosarcoma and LLC cell lines in vitro (Figure 6A; Figure S1C), Apo2L/TRAIL did not induce significant proapoptotic signaling in the malignant-cell compartment of corresponding tumors in DR5-KO mice (Figure 6E; Figure S5C). Although DR5 status in the recipient mice did not affect tumor initiation or growth (data not shown), antitumor activity of Apo2L/TRAIL required DR5 expression in the stromal compartment (Figures S5D and S5E). Therefore, in these particular models, DR5 engagement on tumor ECs may be the primary mechanism mediating the inhibition of tumor growth by Apo2L/TRAIL. The

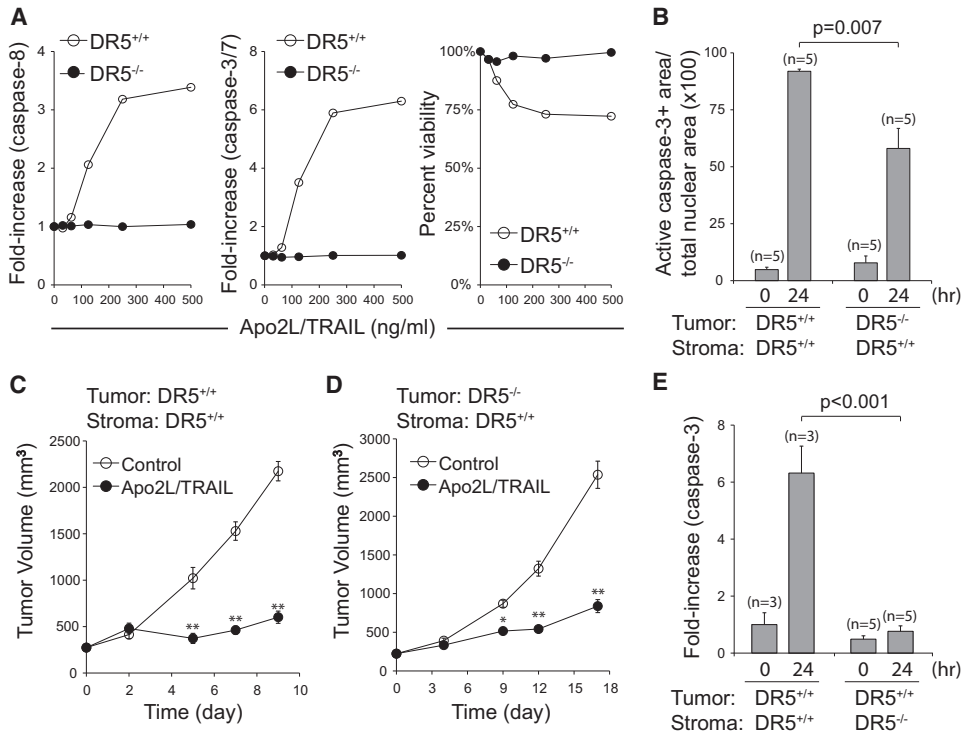

Figure 6. Vascular Disruption by Apo2L/TRAIL Contributes to Antitumor Effects In Vivo

(A) DR5$^{+/+}$ or DR5$^{-/-}$ fibrosarcoma cell lines were treated in vitro with a dose titration of Apo2L/TRAIL. Caspase-8 and caspase 3/7 activity was quantified 4 hr after treatment using luminescent substrate assays. Cell viability was determined 24 hr after Apo2L/TRAIL treatment using an ATP-based Cell Titer Glo assay.

(B) DR5$^{+/+}$ or DR5$^{-/-}$ fibrosarcoma cell lines were grown in DR5$^{+/+}$Rag2$^{-/-}$ recipient mice, treated with a single dose (10 mg/kg) of Apo2L/TRAIL, and harvested for immunohistochemical (IHC) staining with antibodies against cleaved caspase-3. Graph shows quantitation of cleaved caspase-3 IHC staining on tumor sections from control (0 hr) or Apo2L/TRAIL-treated (24 hr) mice. The mean of n = 5 tumors for each group is plotted; error bars indicate the SEM. Student's t test was used to calculate statistical significance.

(C and D) C57BL/6 DR5$^{+/+}$Rag2$^{-/-}$ mice bearing wild-type (C) or DR5$^{-/-}$ (D) MCA-induced tumors were treated with Apo2L/TRAIL five times per week for two weeks, and tumor growth was compared with untreated controls. Error bars indicate the SEM (n = 8–10 mice/group). p values were calculated using Student's t test; asterisk indicates $p < 0.01$; double asterisks indicate $p < 0.001$.

(E) DR5$^{+/+}$ MCA-induced fibrosarcoma cells were grown in DR5$^{+/+}$ or DR5$^{-/-}$ C57BL/6 mice. Tumors were harvested 24 hr after treatment with Apo2L/TRAIL, and flow cytometry was used to measure cleaved caspase-3 in tumor cells. Caspase-3 activation is shown as fold increase over control (0 hr). Error bars indicate the SEM (n = 3–5 mice/group). Data in Figure 6 are representative of two or more independent experiments.

See also Figure S5.

lack of malignant-cell apoptosis in the absence of stromal DR5 could be attributed alternatively to a nonoptimal distribution of the crosslinked ligand into the tumor in this context. To address this, we used H2122 human lung carcinoma cells, which exhibit strong sensitivity to Apo2L/TRAIL (Wagner et al., 2007). We established H2122 tumor xenografts in Rag2-deficient mice with DR5-WT or DR5-KO stromal compartments. In the presence of stromal DR5, but not in its absence, Apo2L/TRAIL induced H2122 tumor hemorrhage similar to that seen in the fibrosarcoma and LLC models (Figure S5F). Nonetheless, activation of caspase-3 in H2122 tumor cells was comparable in both DR5 genotypic backgrounds (Figure S5G). Hence, antibody-crosslinked Apo2L/TRAIL can access the malignant tumor cells to induce apoptosis independently of stromal DR5 expression or effects on the tumor vasculature. These data suggest that DR5-mediated vascular disruption represents an alternative, possibly complementary, mechanism of antitumor efficacy of Apo2L/TRAIL.

Apo2L/TRAIL Disrupts the Tumor Vasculature in a Genetic Model of Pancreatic Cancer

Our results demonstrated that DR5 engagement could disrupt the tumor vasculature in murine syngeneic tumor models (Figures 2, 3, 4, and 5) as well as in mouse xenograft models of human lung and breast cancer (Figure S5F; data not shown). Genetically engineered mouse models of cancer have been increasingly recognized for their ability to recapitulate many aspects of human cancer, including pathogenesis and response to therapy. Therefore, to assess more rigorously the ability of Apo2L/TRAIL to disrupt tumor vessels, we turned to a previously established, genetically engineered mouse model of pancreatic ductal adenocarcinoma (Singh et al., 2010). Seven out of eight (87.5%) tumors from *KrasLSL−G12D; p16/p19$^{fl/fl}$; Pdx1-Cre* mice treated with a single dose of Apo2L/TRAIL showed extensive hemorrhage (Figures 7A and 7B), similar to that seen in syngeneic or xenografted tumor models. Anti-PLVAP staining confirmed tumor-vessel disruption in Apo2L/TRAIL-treated

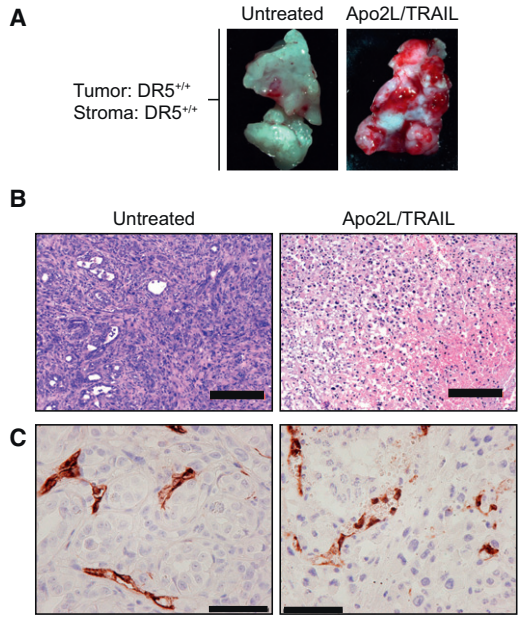

Figure 7. Vascular Disruption by Apo2L/TRAIL in a Mouse Genetic Model of Human Pancreatic Cancer

(A) Tumor-bearing *KrasLSL-G12D; p16/19$^{fl/fl}$; Pdx1-Cre* mice were dosed intraperitoneally with 10 mg/kg of Apo2L/TRAIL or PBS. Tumors were examined macroscopically 24 hr after treatment for the appearance of vascular disruption.

(B) H&E staining of sections from pancreatic ductal adenocarcinomas resected from Apo2L/TRAIL or untreated mice. Representative images show widespread hemorrhaging observed in 7 of 8 tumors from mice treated with Apo2L/TRAIL. Scale bars, 200 μm.

(C) Anti-PLVAP staining was used to visualize the tumor endothelium; representative images show disrupted blood vessels in tumors from Apo2L/TRAIL-treated but not in control mice. Scale bars, 50 μm.

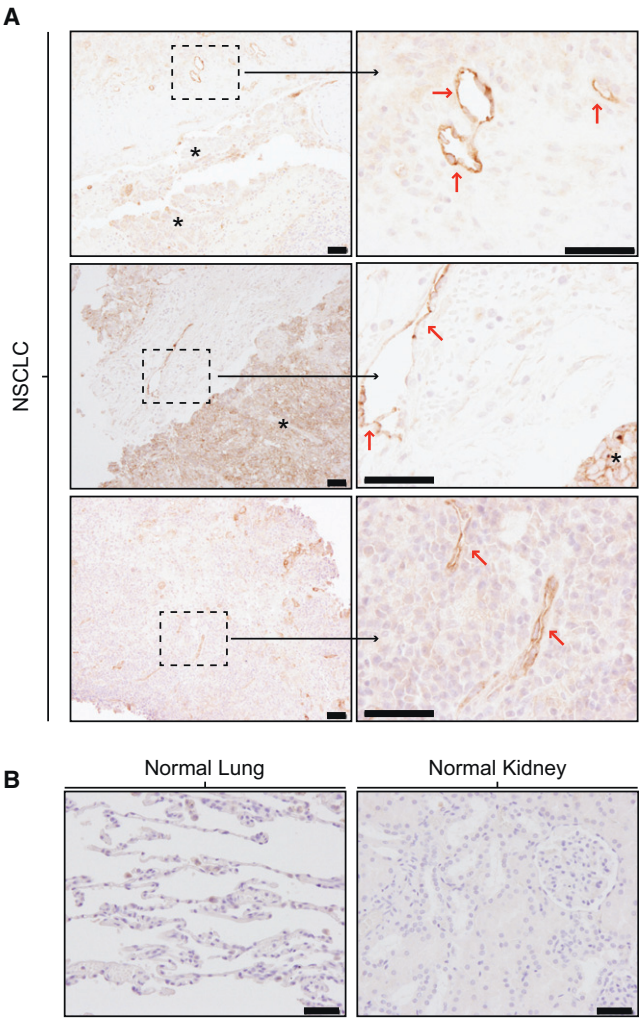

Figure 8. Analysis of DR5 Expression in Human Tumor Endothelial Cells

(A) Representative sections from three separate human nonsmall cell lung cancer (NSCLC) specimens with DR5 expression in the tumor endothelium. Dashed boxes indicate areas shown at higher magnification (right panels). Red arrows indicate focal DR5-positive tumor endothelial cells.

(B) Representative sections from normal human lung and kidney, respectively. Scale bars, 50 μm.

See also Figure S6.

mice (Figure 7C). The ability of Apo2L/TRAIL to trigger vascular disruption in a range of tumor types and contexts supports the potential relevance of this activity for treating human cancer.

Evidence for DR5 Expression in Human Tumor Endothelial Cells

To evaluate the frequency of DR5 expression in ECs within human tumors, we analyzed a panel of surgical tissue specimens from nonsmall cell lung cancer (NSCLC) patients by DR5 immunohistochemistry. Of 43 samples, four (~10%) showed focal regions of DR5 expression in the tumor endothelium (Figure 8A). We also surveyed a panel of normal tissues from human and mouse: With the exception of some staining in human stomach, DR5 expression was not detected in the endothelium or in other cell types of normal tissues (Figure 8; Figure S6). Consistent with the lack of DR5 expression in nontumor vasculature, repeated dosing of naive C57BL/6 mice with Apo2L/TRAIL did not significantly affect body weight or survival, despite some small, transient elevations in liver enzyme activity, detected in serum from some of the animals (Figures S6C–S6E and data not shown). These findings suggest that endothelial expression of DR5 is present in a subset of human NSCLC tumors. In contrast, expression in normal tissues is rarely detected, permitting repeated administration of crosslinked Apo2L/TRAIL in mice without significant adverse effects.

DISCUSSION

The current experimental paradigm for PARAs as cancer-therapeutic agents is based on their ability to induce direct cancer-cell apoptosis via DR5 and/or DR4 (Ashkenazi, 2002, 2008b; Johnstone et al., 2008). Yet, clinical studies with PARAs to date have suggested that malignant cells are relatively refractory to death-receptor engagement, suggesting that various mechanisms of apoptosis evasion may limit the efficacy of such agents in patients with cancer (Yang et al., 2010). In the

present study, we show that an oligomeric form of Apo2L/TRAIL, which displays more potent agonistic activity toward DR5 and is capable of engaging the murine receptor, can achieve antitumor effects by directly perturbing the tumor vasculature. Oligomeric Apo2L/TRAIL induced vascular disruption in several tumor settings and models.

Our data suggest that DR5 activation in tumor ECs induces apoptotic death of these cells, thereby compromising vascular integrity and causing vessel congestion, intratumoral hemorrhage, decreased vascular density, and diminished tumor growth. Several lines of evidence indicate that Apo2L/TRAIL can act directly on the tumor stroma: First, its effects on the vasculature and on tumor growth in the fibrosarcoma model persisted even when DR5 was genetically ablated from the malignant cell compartment. Conversely, the effects on the tumor vasculature were abolished upon genetic ablation of DR5 the stroma, diminishing antitumor efficacy in both the fibrosarcoma and LLC models. Second, Apo2L/TRAIL induced significant levels of caspase-3 activation in tumor ECs prior to engaging apoptosis in the malignant cell compartment. Considering that other stromal cells (e.g., immune infiltrates) did not show appreciable DR5 expression, our data demonstrate the ability of Apo2L/TRAIL to induce direct, DR5-dependent apoptosis in tumor ECs.

Importantly, DR5-mediated vascular disruption exerted antitumor activity even in the absence of DR5 in malignant cells, thus highlighting the potential for attacking tumors that otherwise might be expected to resist PARA therapy. Although vascular disruption appears to be the primary mechanism for antitumor effects in the fibrosarcoma and LLC models studied here, this may not apply to all tumors. Indeed, direct effects of PARAs on cancer cells are well established and further supported by the activity of Apo2L/TRAIL against H2122 human xenografts in the absence of stromal DR5 expression and tumor-vascular disruption. Thus, DR5-mediated perturbation of the tumor vasculature may constitute an alternative, and perhaps complementary, antitumor strategy to the current PARA-based approach of directly inducing tumor-cell apoptosis.

Several vascular disrupting agents (VDAs) are in clinical development for cancer treatment. However, there is concern that the therapeutic utility of these agents might be limited by adverse events, such as on-target effects against normal vasculature, as well as a lack of efficacy (Heath and Bicknell, 2009; Lara et al., 2011; Lorusso et al., 2011; McKeage and Baguley, 2010). Certain effects of Apo2L/TRAIL on the tumor vasculature—namely, the rapid disruption of existing vessels and ensuing intratumoral hemorrhage—are similar to those of other VDAs. However, despite these similarities, there are key differences in the mechanisms of action of Apo2L/TRAIL versus known VDAs. One class of VDAs, including combretastatin and its analogs, acts primarily by inhibiting tubulin polymerization and inducing changes in EC shape (McKeage and Baguley, 2010; Siemann et al., 2009). Although its specific molecular target is unknown, another clinically tested VDA, the flavonoid ASA404, induces vascular permeabilization and EC apoptosis via TNFα-dependent mechanisms (Baguley, 2011). In contrast to these agents, Apo2L/TRAIL disrupts the tumor vasculature strictly through direct DR5-mediated apoptosis in tumor ECs. This mechanistic difference may have important implications for both safety and efficacy outcomes in patients. Nevertheless, additional studies will be necessary to understand more fully the impact of DR5 activation in tumor ECs and the longer-term effects on vascular function.

An additional consideration is that specific PARAs exhibit differences in potency that may affect their biological activity and potential toxicity. The enhanced activity of oligomeric Apo2L/TRAIL toward mouse DR5 suggests that this form of the protein may better mimic the endogenous transmembrane ligand. It is possible that the noncrosslinked trimeric Apo2L/TRAIL molecule represented by dulanermin, as well as DR5 agonistic antibodies, although active against malignant cells, do not achieve the signaling threshold required to induce significant apoptosis in tumor ECs. Thus, variants of PARAs with greater potency might display stronger vascular disrupting activity. Although more potent variants may not be as well tolerated as dulanermin (Lawrence et al., 2001), the lack of systemic toxicity in mice with the oligomeric Apo2L/TRAIL used here is encouraging, and suggests that a significant therapeutic window may be achievable. This is further supported by the apparent absence of DR5 expression in most normal vasculature and tissues. However, more focused studies on the nontumor vasculature, quiescent or inflamed, may reveal additional examples of DR5 modulation besides the tumor stroma. Regardless, any clinical development of more potent PARAs would necessitate extensive testing in animals, including nonhuman primates, to exclude potential side effects on normal tissues including the vasculature.

Only a minority (~10%) of human NSCLC specimens showed endothelial DR5 expression. However, given the very high prevalence of this lethal malignancy, our data suggest significant impact for potential clinical translation and provide a compelling rationale for assessing endothelial DR5 expression in other human cancers. Furthermore, it will be interesting to determine what specific features of the tumor microenvironment drive endothelial DR5 expression and whether DR5 levels can be manipulated by certain combinatorial treatment regimes. To date, clinical efficacy with PARAs has not been observed in unselected patients, with the exception of some individual subjects (Ashkenazi and Herbst, 2008; Yang et al., 2010). In future clinical studies, it will be important to assess more specifically whether DR5 expression in tumor ECs correlates with responsiveness to PARAs, and whether efficacy in individual patients is associated with tumor-vascular disruption.

In conclusion, our studies uncover DR5-mediated proapoptotic signaling in tumor ECs. We propose that PARAs may act as a unique class of tumor-selective vascular disruption agents, even for tumors in which the malignant cell compartment is resistant to direct apoptosis induction via DR5.

EXPERIMENTAL PROCEDURES

Mouse Models

C57BL/6 (wild-type) mice were obtained from the Jackson Laboratory, and C57BL/6.Rag2$^{-/-}$ mice were obtained from Taconic, Inc. C57BL/6.DR5$^{-/-}$ (Diehl et al., 2004), C57BL/6.TNFR1$^{-/-}$TNFR2$^{-/-}$, Rag2$^{-/-}$;DR5$^{-/-}$ and *KrasLSL−G12D; p16/p19fl/fl; Pdx1-Cre* (Singh et al., 2010) mice were bred and maintained at Genentech, Inc. under specific pathogen-free conditions. All animal experiments were reviewed and approved by the Institutional Animal Care and Use Committee (IACUC) at Genentech, Inc.

Human Tissue Samples

Archival formalin fixed paraffin embedded (FFPE) tissue specimens of nonsmall cell lung cancer (NSCLC) were collected and used in this study in accordance with the protocol (APM4074 g) approved by the Institutional Review Board of Kaiser Permanente Medical Center, (Vallejo CA and Portland, OR), Ohio State University (Columbus, OH), Medical College of Wisconsin (Milwaukee WI), and M. D. Anderson Cancer Center (Houston TX), and written informed consent was obtained from patients in all cases at time of enrollment. Normal tissue specimens were purchased from Biomax Inc., (Rockville, MD). In all analyses, a slide was H&E stained and verified by a board-certified pathologist.

Fibrosarcoma Tumor Initiation

C57BL/6 (wild-type) or C57BL/6.DR5$^{-/-}$ mice were inoculated subcutaneously in the hind flank with 200 μg of methylcholanthrene (MCA) (Sigma-Aldrich) in 0.1 ml of corn oil, as previously described (Koebel et al., 2007). Mice were assessed weekly for tumor development from 90 days after MCA treatment.

In Vivo Dosing

Dulanermin (trimeric Apo2L/TRAIL) and recombinant soluble Flag-tagged human Apo2L/TRAIL was prepared according to a published method (Ashkenazi et al., 1999; Kischkel et al., 2000). Tumor-bearing mice were dosed intraperitoneally with 60 mg/kg of dulanermin, or 10 mg/kg of Apo2L/TRAIL followed by 10 mg/kg of the anti-Flag antibody (M2) (Sigma). For tumor growth studies and the end-of-study experiment in Figure S5, mice were dosed with 1 or 2 cycles of Apo2L/TRAIL (10 mg/kg) as indicated. Each cycle consisted of 5 days of consecutive treatment, with 2 days of no treatment in between cycles.

Cell Lines and Tumor Transplant Models

Lewis lung carcinoma, fibrosarcoma, and H2122 cells were maintained in RPMI medium supplemented with L-glutamine and 10% fetal bovine serum (FBS) under conditions of 5% CO_2 at 37°C. Mice were injected subcutaneously with 5×10^6 cancer cells. Tumors were measured in two dimensions using a caliper. Tumor volume was calculated using the formula: $V = 0.5a \times b^2$, where a and b are the long and the short diameters of the tumor, respectively. Additional details are available in Supplemental Experimental Procedures.

Cell Viability and Caspase-3 Assays

Cell viability following Apo2L/TRAIL treatment was determined in vitro using the Cell-titer Glo cell viability assay (Promega). Caspase-3/7 or 8 activity was measured in vitro using the Caspase-Glo 3/7 or Caspase-Glo 8 assay (Promega), according to the manufacturer's instructions. For in vitro viability and caspase assays, Apo2L and M2 were combined sequentially at a 1:1 molar ratio. Ex vivo caspase-3 processing in tumor cells was monitored by flow cytometry using the cleaved caspase-3-specific antibody (clone C92-605, BD PharMingen). Caspase-3 activation is represented as a fold-increase relative to control treated mice.

Immunohistochemistry for Mouse Specimens

Primary antibodies were used at 10 μg/ml for mouse DR5 (clone MD5-1, BD Biosciences; Franklin Lakes, NJ), 2 μg/ml for PLVAP (clone MECA-32, BD Biosciences, NJ), and 0.06 μg/ml for cleaved caspase 3 (Asp175) (Cell Signaling Technologies; Danvers, MA). Quantitation of caspase-3 and PLVAP immunostaining and additional details are described in Supplemental Experimental Procedures.

In Vivo Near Infrared Fluorescence Imaging

Two hr after treatment with Apo2L/TRAIL or PBS, mice (n = 3–5/treatment group) were injected intravenously with the fluorescent blood pool marker AngioSense680IVM (PerkinElmer). The temporal distribution of AngioSense680IVM within tumors and neighboring tissue was measured by visualizing fluorescence (650 nm excitation/700 nm emission) with a Kodak 4000 FX Pro imaging system (CareStream Health) and quantifying fluorescence intensities within regions of interest placed over tumor or adjoining tissue normalized to time = 0, $(I_{ROIt=x} - I_{BG}) / (I_{ROIt=0} - I_{BG})$. At each indicated time point, animals were anesthetized under isoflurane, with body temperature maintained at 37°C, and were imaged.

SUPPLEMENTAL INFORMATION

Supplemental Information includes six figures, Supplemental Experimental Procedures, and Supplemental References and can be found with this article online at http://dx.doi.org/10.1016/j.ccr.2012.05.014.

ACKNOWLEDGMENTS

We thank Weilan Ye, as well as members of the Ashkenazi laboratory, for helpful discussion and insight. We are also grateful for technical support from Sharon Yee, Sheila Bheddah, Jeffrey Eastham-Anderson, and the Pathology facility at Genentech. We thank Astar Winoto (University of California, Berkeley), for providing DR5-KO mice. N.S.W. and A.Y. contributed equally to this work, designed and performed experiments, analyzed data, wrote, and edited the paper. B.Y. initiated and performed experiments and analyzed data. S.C. and H.S. performed experiments and analysis relating to the immunohistochemistry data in the paper. S.M. designed and generated reagents used in this study. A.G. and R.P. initiated and performed experiments in the paper. M.S. and R.W. designed experiments and edited the paper. A.A. designed experiments, and wrote and edited the paper. All authors are present or former employees of Genentech, Inc.

Received: June 15, 2011
Revised: February 22, 2012
Accepted: May 4, 2012
Published: July 9, 2012

REFERENCES

Abdulghani, J., and El-Deiry, W.S. (2010). TRAIL receptor signaling and therapeutics. Expert Opin. Ther. Targets *14*, 1091–1108.

Ashkenazi, A. (2002). Targeting death and decoy receptors of the tumour-necrosis factor superfamily. Nat. Rev. Cancer *2*, 420–430.

Ashkenazi, A. (2008a). Directing cancer cells to self-destruct with pro-apoptotic receptor agonists. Nat. Rev. Drug Discov. *7*, 1001–1012.

Ashkenazi, A. (2008b). Targeting the extrinsic apoptosis pathway in cancer. Cytokine Growth Factor Rev. *19*, 325–331.

Ashkenazi, A., and Herbst, R.S. (2008). To kill a tumor cell: the potential of proapoptotic receptor agonists. J. Clin. Invest. *118*, 1979–1990.

Ashkenazi, A., Pai, R.C., Fong, S., Leung, S., Lawrence, D.A., Marsters, S.A., Blackie, C., Chang, L., McMurtrey, A.E., Hebert, A., et al. (1999). Safety and antitumor activity of recombinant soluble Apo2 ligand. J. Clin. Invest. *104*, 155–162.

Baguley, B.C. (2011). Preclinical efficacy of vascular disrupting agents in non-small-cell lung cancer. Clin. Lung Cancer *12*, 81–86.

Brey, E.M., Lalani, Z., Johnston, C., Wong, M., McIntire, L.V., Duke, P.J., and Patrick, C.W., Jr. (2003). Automated selection of DAB-labeled tissue for immunohistochemical quantification. J. Histochem. Cytochem. *51*, 575–584.

Chan, J., Prado-Lourenco, L., Khachigian, L.M., Bennett, M.R., Di Bartolo, B.A., and Kavurma, M.M. (2010). TRAIL promotes VSMC proliferation and neointima formation in a FGF-2-, Sp1 phosphorylation-, and NFkappaB-dependent manner. Circ. Res. *106*, 1061–1071.

Chen, P.L., and Easton, A.S. (2010). Evidence that tumor necrosis factor-related apoptosis inducing ligand (TRAIL) inhibits angiogenesis by inducing vascular endothelial cell apoptosis. Biochem. Biophys. Res. Commun. *391*, 936–941.

Corti, A., and Ponzoni, M. (2004). Tumor vascular targeting with tumor necrosis factor alpha and chemotherapeutic drugs. Ann. N Y Acad. Sci. *1028*, 104–112.

Dejana, E. (2004). Endothelial cell-cell junctions: happy together. Nat. Rev. Mol. Cell Biol. *5*, 261–270.

Diehl, G.E., Yue, H.H., Hsieh, K., Kuang, A.A., Ho, M., Morici, L.A., Lenz, L.L., Cado, D., Riley, L.W., and Winoto, A. (2004). TRAIL-R as a negative regulator of innate immune cell responses. Immunity *21*, 877–889.

Frew, A.J., Lindemann, R.K., Martin, B.P., Clarke, C.J., Sharkey, J., Anthony, D.A., Banks, K.M., Haynes, N.M., Gangatirkar, P., Stanley, K., et al. (2008).

Combination therapy of established cancer using a histone deacetylase inhibitor and a TRAIL receptor agonist. Proc. Natl. Acad. Sci. USA *105*, 11317–11322.

Hallmann, R., Mayer, D.N., Berg, E.L., Broermann, R., and Butcher, E.C. (1995). Novel mouse endothelial cell surface marker is suppressed during differentiation of the blood brain barrier. Dev. Dyn. *202*, 325–332.

Haynes, N.M., Hawkins, E.D., Li, M., McLaughlin, N.M., Hämmerling, G.J., Schwendener, R., Winoto, A., Wensky, A., Yagita, H., Takeda, K., et al. (2010). CD11c+ dendritic cells and B cells contribute to the tumoricidal activity of anti-DR5 antibody therapy in established tumors. J. Immunol. *185*, 532–541.

Heath, V.L., and Bicknell, R. (2009). Anticancer strategies involving the vasculature. Nat. Rev. Clin. Oncol. *6*, 395–404.

Herbst, R.S., Eckhardt, S.G., Kurzrock, R., Ebbinghaus, S., O'Dwyer, P.J., Gordon, M.S., Novotny, W., Goldwasser, M.A., Tohnya, T.M., Lum, B.L., et al. (2010). Phase I dose-escalation study of recombinant human Apo2L/TRAIL, a dual proapoptotic receptor agonist, in patients with advanced cancer. J. Clin. Oncol. *28*, 2839–2846.

Jain, R.K. (2005). Normalization of tumor vasculature: an emerging concept in antiangiogenic therapy. Science *307*, 58–62.

Johnstone, R.W., Frew, A.J., and Smyth, M.J. (2008). The TRAIL apoptotic pathway in cancer onset, progression and therapy. Nat. Rev. Cancer *8*, 782–798.

Kischkel, F.C., Lawrence, D.A., Chuntharapai, A., Schow, P., Kim, K.J., and Ashkenazi, A. (2000). Apo2L/TRAIL-dependent recruitment of endogenous FADD and caspase-8 to death receptors 4 and 5. Immunity *12*, 611–620.

Koebel, C.M., Vermi, W., Swann, J.B., Zerafa, N., Rodig, S.J., Old, L.J., Smyth, M.J., and Schreiber, R.D. (2007). Adaptive immunity maintains occult cancer in an equilibrium state. Nature *450*, 903–907.

Lara, P.N., Jr., Douillard, J.Y., Nakagawa, K., von Pawel, J., McKeage, M.J., Albert, I., Losonczy, G., Reck, M., Heo, D.S., Fan, X., et al. (2011). Randomized phase III placebo-controlled trial of carboplatin and paclitaxel with or without the vascular disrupting agent vadimezan (ASA404) in advanced non-small-cell lung cancer. J. Clin. Oncol. *29*, 2965–2971.

Lawrence, D., Shahrokh, Z., Marsters, S., Achilles, K., Shih, D., Mounho, B., Hillan, K., Totpal, K., DeForge, L., Schow, P., et al. (2001). Differential hepatocyte toxicity of recombinant Apo2L/TRAIL versions. Nat. Med. *7*, 383–385.

Li, J.H., Kirkiles-Smith, N.C., McNiff, J.M., and Pober, J.S. (2003). TRAIL induces apoptosis and inflammatory gene expression in human endothelial cells. J. Immunol. *171*, 1526–1533.

Lorusso, P.M., Boerner, S.A., and Hunsberger, S. (2011). Clinical development of vascular disrupting agents: what lessons can we learn from ASA404? J. Clin. Oncol. *29*, 2952–2955.

Mahajan, S., Dammai, V., Hsu, T., and Kraft, A.S. (2008). Hypoxia-inducible factor-2alpha regulates the expression of TRAIL receptor DR5 in renal cancer cells. Carcinogenesis *29*, 1734–1741.

McKeage, M.J., and Baguley, B.C. (2010). Disrupting established tumor blood vessels: an emerging therapeutic strategy for cancer. Cancer *116*, 1859–1871.

Pober, J.S., and Sessa, W.C. (2007). Evolving functions of endothelial cells in inflammation. Nat. Rev. Immunol. *7*, 803–815.

Seki, N., Hayakawa, Y., Brooks, A.D., Wine, J., Wiltrout, R.H., Yagita, H., Tanner, J.E., Smyth, M.J., and Sayers, T.J. (2003). Tumor necrosis factor-related apoptosis-inducing ligand-mediated apoptosis is an important endogenous mechanism for resistance to liver metastases in murine renal cancer. Cancer Res. *63*, 207–213.

Siemann, D.W., Chaplin, D.J., and Walicke, P.A. (2009). A review and update of the current status of the vasculature-disabling agent combretastatin-A4 phosphate (CA4P). Expert Opin. Investig. Drugs *18*, 189–197.

Singh, M., Lima, A., Molina, R., Hamilton, P., Clermont, A.C., Devasthali, V., Thompson, J.D., Cheng, J.H., Bou Reslan, H., Ho, C.C., et al. (2010). Assessing therapeutic responses in Kras mutant cancers using genetically engineered mouse models. Nat. Biotechnol. *28*, 585–593.

Strasser, A., O'Connor, L., and Dixit, V.M. (2000). Apoptosis signaling. Annu. Rev. Biochem. *69*, 217–245.

Takeda, K., Yamaguchi, N., Akiba, H., Kojima, Y., Hayakawa, Y., Tanner, J.E., Sayers, T.J., Seki, N., Okumura, K., Yagita, H., and Smyth, M.J. (2004). Induction of tumor-specific T cell immunity by anti-DR5 antibody therapy. J. Exp. Med. *199*, 437–448.

Tang, D.G., Chen, Y.Q., Newman, P.J., Shi, L., Gao, X., Diglio, C.A., and Honn, K.V. (1993). Identification of PECAM-1 in solid tumor cells and its potential involvement in tumor cell adhesion to endothelium. J. Biol. Chem. *268*, 22883–22894.

ten Hagen, T.L., Seynhaeve, A.L., and Eggermont, A.M. (2008). Tumor necrosis factor-mediated interactions between inflammatory response and tumor vascular bed. Immunol. Rev. *222*, 299–315.

Uno, T., Takeda, K., Kojima, Y., Yoshizawa, H., Akiba, H., Mittler, R.S., Gejyo, F., Okumura, K., Yagita, H., and Smyth, M.J. (2006). Eradication of established tumors in mice by a combination antibody-based therapy. Nat. Med. *12*, 693–698.

Wagner, K.W., Punnoose, E.A., Januario, T., Lawrence, D.A., Pitti, R.M., Lancaster, K., Lee, D., von Goetz, M., Yee, S.F., Totpal, K., et al. (2007). Death-receptor O-glycosylation controls tumor-cell sensitivity to the proapoptotic ligand Apo2L/TRAIL. Nat. Med. *13*, 1070–1077.

Wilson, N.S., Dixit, V., and Ashkenazi, A. (2009). Death receptor signal transducers: nodes of coordination in immune signaling networks. Nat. Immunol. *10*, 348–355.

Yang, A., Wilson, N.S., and Ashkenazi, A. (2010). Proapoptotic DR4 and DR5 signaling in cancer cells: toward clinical translation. Curr. Opin. Cell Biol. *22*, 837–844.

Cancer Cell
Article

Endothelial CCR2 Signaling Induced by Colon Carcinoma Cells Enables Extravasation via the JAK2-Stat5 and p38MAPK Pathway

Monika Julia Wolf,[1,12] Alexandra Hoos,[4,12] Judith Bauer,[5] Steffen Boettcher,[2] Markus Knust,[6,7] Achim Weber,[3] Nicole Simonavicius,[5] Christoph Schneider,[8] Matthias Lang,[6] Michael Stürzl,[9] Roland S. Croner,[9] Andreas Konrad,[9] Markus G. Manz,[2] Holger Moch,[3] Adriano Aguzzi,[1] Geert van Loo,[10] Manolis Pasparakis,[11] Marco Prinz,[6] Lubor Borsig,[4,13,*] and Mathias Heikenwalder[1,5,13,*]

[1]Institute of Neuropathology
[2]Division of Hematology
[3]Institute of Surgical Pathology
University Hospital Zurich, CH-8091 Zurich, Switzerland
[4]Institute of Physiology, Zurich Center for Integrative Human Physiology, University of Zurich, CH-8057 Zurich, Switzerland
[5]Institute of Virology, Technische Universität München/Helmholtz Zentrum München, D-81675 Munich, Germany
[6]Department of Neuropathology & BIOSS Centre for Biological Signaling Studies, University of Freiburg, D-79106 Freiburg, Germany
[7]Faculty of Biology, University of Freiburg, D-79104 Freiburg, Germany
[8]Institute of Integrative Biology, ETH Zurich, CH-8952 Schlieren, Switzerland
[9]Division of Molecular and Experimental Surgery, Department of Surgery, University Hospital Erlangen, D-91054 Erlangen, Germany
[10]Department for Molecular Biomedical Research, VIB Gent, B-9052 Gent-Zwijnaarde, Belgium
[11]Institute of Genetics, Centre for Molecular Medicine (CMMC) and Cologne Excellence Cluster on Cellular Stress Responses in Aging-Associated Diseases (CECAD), University of Cologne, D-50674 Cologne, Germany
[12]These authors contributed equally to this work
[13]These authors contributed equally to this work
*Correspondence: lborsig@access.uzh.ch (L.B.), heikenwaelder@helmholtz-muenchen.de (M.H.)
http://dx.doi.org/10.1016/j.ccr.2012.05.023

SUMMARY

Increased expression of the chemokine CCL2 in tumor cells correlates with enhanced metastasis, poor prognosis, and recruitment of CCR2^{+}Ly6C^{hi} monocytes. However, the mechanisms driving tumor cell extravasation through the endothelium remain elusive. Here, we describe CCL2 upregulation in metastatic UICC stage IV colon carcinomas and demonstrate that tumor cell-derived CCL2 activates the CCR2^{+} endothelium to increase vascular permeability in vivo. CCR2 deficiency prevents colon carcinoma extravasation and metastasis. Of note, CCR2 expression on radio-resistant cells or endothelial CCR2 expression restores extravasation and metastasis in *Ccr2*$^{-/-}$ mice. Reduction of CCR2 expression on myeloid cells decreases but does not prevent metastasis. CCL2-induced vascular permeability and metastasis is dependent on JAK2-Stat5 and p38MAPK signaling. Our study identifies potential targets for treating CCL2-dependent metastasis.

INTRODUCTION

Metastasis, the spread of tumor cells to vital organs, is the leading cause of cancer-related death in humans (Gupta and Massagué, 2006). Understanding the mechanisms driving metastasis is therefore essential for developing new therapeutic strategies. Metastasis is a multistage process comprising tumor cell dissemination, survival in the circulation, extravasation, and ultimately colonization of distant organs (Chambers et al., 2002; Joyce and Pollard, 2009). Tumor cell extravasation, colonization

Significance

Metastasis is the primary cause of cancer-related mortality. Elevated expression of CCL2 attracts CCR2^{+}Ly6C^{hi} monocytes and enhances metastasis. We show that metastatic UICC stage IV colon carcinomas upregulate CCL2. Using both in vivo and in vitro models, we demonstrate that colon carcinoma-derived CCL2 activates endothelial cells through CCR2 and is dependent on JAK2-Stat5 and p38MAPK phosphorylation. Our results show that a tumor cell-derived chemokine induces vascular permeability and enables efficient tumor cell extravasation, suggesting a so-far undescribed role for chemokines in tumor cell extravasation. Moreover, we identified two targets for the suppression of CCL2-dependent tumor cell extravasation during colon carcinoma metastasis. Chemokine-dependent control of vascular permeability during metastasis is likely to occur in various cancers.

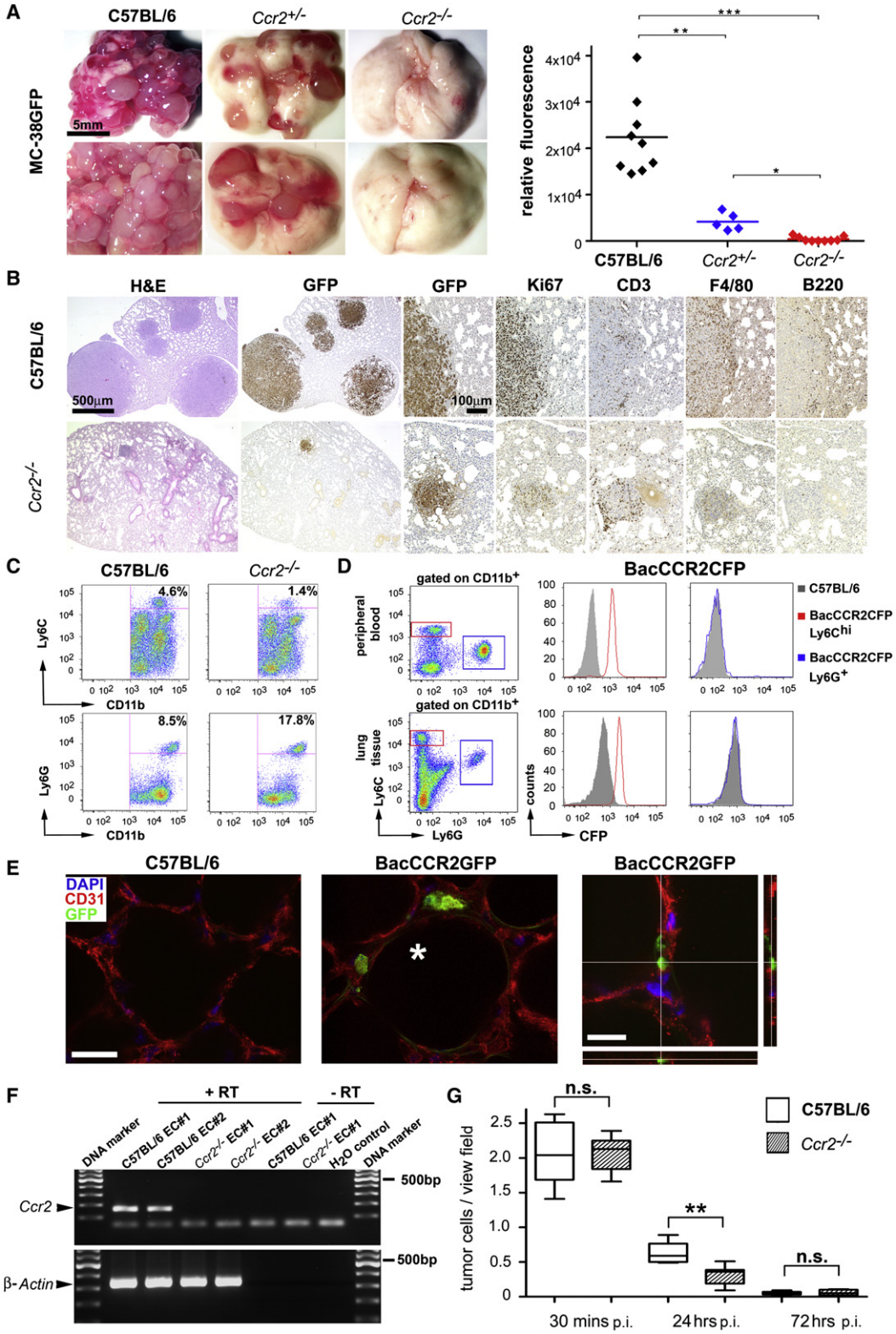

Figure 1. CCR2 Determines Susceptibility to Experimental Lung Metastasis in a Dose-Dependent Manner

(A) Macroscopy of lungs derived from C57BL/6 (n = 9), *Ccr2*$^{+/-}$ (n = 5), *Ccr2*$^{-/-}$ mice (n = 9) on day 28 p.i. with MC-38GFP cells. Size of scale bar is indicated (left panel). Quantification of tumor load by GFP fluorescence in lung homogenates (right panel).

(B) Histological analysis of colon carcinoma tumors (MC-38GFP) in C57BL/6 and *Ccr2*$^{-/-}$ lungs at 28 d.p.i. Low and high magnifications (scale bars) are indicated. H&E, hematoxylin and eosin; GFP, tumor cells; Ki67, proliferating cells; CD3, T cells; F4/80, macrophages, B220: B cells.

as well as outgrowth are considered to be the limiting steps in metastasis (Chambers et al., 2002). It has long been recognized that the tumor cell microenvironment, composed of fibroblasts, endothelial cells, and leukocytes, significantly contributes to metastatic dissemination (Joyce and Pollard, 2009). In particular, myeloid-derived monocytes/macrophages, commonly found in various types of malignant cancers were shown to facilitate tumor cell extravasation and metastatic outgrowth (Peinado et al., 2011; Qian and Pollard, 2010). Analysis of the metastasis-supporting niche revealed that soluble factors derived from the local environment and from tumors are responsible for mobilization of bone marrow (BM)-derived cells during metastasis (Peinado et al., 2011).

Chemokines and their receptors were found to be involved in metastasis and also to be direct targets of oncogene activation (Allavena et al., 2011; Hiratsuka et al., 2006). Stromal cells, infiltrating leukocytes and tumor cells themselves were identified as sources of cytokines and chemokines, both at primary tumors and metastatic sites (Läubli and Borsig, 2010; Mishra et al., 2011; O'Hayre et al., 2008). Highly metastatic cells have been shown to induce BM-derived macrophages to express cytokines and chemokines emphasizing the role of a reciprocal crosstalk of tumor cells with the microenvironment to actively shape the metastatic niche (Kim et al., 2009). Local activation of endothelia by metastasizing tumor cells induced CCL5 expression, which was associated with monocyte recruitment during the initial phase of metastasis. Accordingly, inhibition of CCL5 reduced metastasis (Läubli et al., 2009). Recently, CCL2 has been identified as the major factor facilitating breast cancer metastasis to the lung (Qian et al., 2011). Clinical evidence clearly associated elevated levels of CCL2 and CCL5 with poor prognosis in breast, colon, prostate, and cervix cancer patients due to metastatic progression (Soria et al., 2011; Yoshidome et al., 2009; Zhang et al., 2010; Zijlmans et al., 2006). Monocytes recruited to tumors through the CCL2-CCR2 axis can be polarized to an alternatively activated M2-phenotype thereby contributing to immunosuppression and enhanced tumor cell survival (Loberg et al., 2007; Mantovani and Sica, 2010). CCL2 has been shown to induce angiogenic activation of endothelial cells along with inflammatory responses (Salcedo et al., 2000), and CCL2-mediated recruitment of inflammatory monocytes promoted metastasis (Qian et al., 2011). Similarly, overexpression of CCL2 in PC-3 prostate cancer cells led to increased bone metastasis associated with elevated accumulation of macrophages (Mizutani et al., 2009). Consequently, CCL2-neutralizing antibody treatment significantly prolonged survival of tumor-bearing mice due to inhibition of metastasis (Lu and Kang, 2009; Mizutani et al., 2009; Qian et al., 2011; Salcedo et al., 2000). Although elevated CCL2 expression is clearly linked to metastasis through the recruitment of monocytes/macrophages, the exact mechanisms by which CCL2 signaling facilitates tumor cell extravasation at the endothelial barrier and subsequent metastatic colonization remain elusive.

Here, we investigate the role of the CCL2-CCR2 chemokine axis during metastatic dissemination and the involvement of the endothelium in this process.

RESULTS

CCR2 Promotes Metastasis of Colon Carcinoma Cells

To determine whether tumor cell extravasation and growth was altered in the absence of CCR2, C57BL/6 and *Ccr2*$^{-/-}$ mice were intravenously (i.v.) injected with syngeneic GFP^{+} colon carcinoma cells (MC-38GFP) and lungs were macroscopically scored for the presence of metastatic foci 28 days postinjection (d.p.i.). *Ccr2*$^{-/-}$ lungs displayed fewer tumors than C57BL/6 lungs ($p < 0.001$; Figure 1A; Figure S1A available online). Development of tumors depended on CCR2 expression levels in the recipient host, since *Ccr2*$^{+/-}$ lungs contained fewer metastases than C57BL/6 ($p < 0.01$) but still more than *Ccr2*$^{-/-}$ ($p < 0.05$; Figures 1A, S1A, and S1B). This was corroborated by measurement of relative GFP fluorescence in lung homogenates (Figure 1A). Immunohistochemistry revealed no obvious differences in the relative composition of Ki67^{+}, CD3^{+}, F4/80^{+}, and B220^{+} cells within the tumors (Figure 1B).

Next, we investigated whether differences in the immune cell composition could influence metastasis. No differences in numbers of CD4^{+} or CD8^{+} T cells, CD19^{+} B cells, NK1.1^{+}, or F4/80^{+} cells could be identified between naive C57BL/6 and *Ccr2*$^{-/-}$ lungs by flow cytometry (Figure S1C). However, *Ccr2*$^{-/-}$ lungs displayed reduced numbers of CD11b^{+}Ly6C^{hi}Ly6G^{-} monocytes ($p < 0.001$; denoted as Ly6C^{hi}) and a relative increase in CD11b^{+}Ly6G^{+} cells ($p < 0.01$; Figures 1C, S1D, and S1E). To identify which cells express CCR2, we performed flow cytometry on blood and lung tissue from BacCCR2CFP reporter mice, expressing CFP under the CCR2 promoter (Hohl et al., 2009). Almost all CD11b^{+}Ly6C^{hi} cells were CFP positive, whereas CD11b^{+}Ly6G^{+}, CD19^{+}, CD4^{+}, and CD8^{+} cells were CFP negative (Figures 1D and S1F). We next investigated whether nonhematopoietic cells in lungs express CCR2. Confocal microscopy of BacCCR2GFP mice revealed that CD31^{+} lung endothelial cells expressed GFP (Figures 1E and S1G), as confirmed by transcriptional analysis of purified primary endothelial cells from C57BL/6 and *Ccr2*$^{-/-}$ lungs (Figures 1F, S1I, and S1J).

Altered numbers of colon carcinoma cells in lungs of *Ccr2*$^{-/-}$ mice could explain the observed inability to form tumors. However, no differences in the amount and distribution of

(C) Flow cytometry analysis of monocytes in naive lungs of *Ccr2*$^{-/-}$ and C57BL/6 mice.
(D) Flow cytometry of CFP^{+} cells in blood and lung tissue of BacCCR2CFP transgenic mice shows that most Ly6C^{hi} (red) but no Ly6G (blue) cells express CFP.
(E) Confocal microscopy analysis on lung tissue of C57BL/6 and BacCCR2GFP mice for the expression of GFP. Endothelial cells are positive for GFP (green) and CD31 (red); nuclei are stained in blue (DAPI). The asterisk indicates the alveolar space; scale bars: 20 μm (low magnification); 15 μm (high magnification); Z-stacks are indicated.
(F) RT-PCR of *Ccr2* expression in CD31-sorted primary endothelial cells isolated from lungs of C57BL/6 and *Ccr2*$^{-/-}$ mice. Two samples for each genotype are shown (+RT), including controls without reverse transcriptase treatment (-RT). *β-actin* served as control (bp, base pairs).
(G) Time course analysis of tumor cell survival in lung tissue. Numbers of tumor cells/view field were analyzed on sections of C57BL/6 and *Ccr2*$^{-/-}$ lungs 30 min, 24 hr and 72 hr p.i. (n = 3, each; mean with min/max is shown). Statistics: ***$p < 0.001$; **$p < 0.01$; *$p < 0.05$; n.s., not significant.
See also Figure S1.

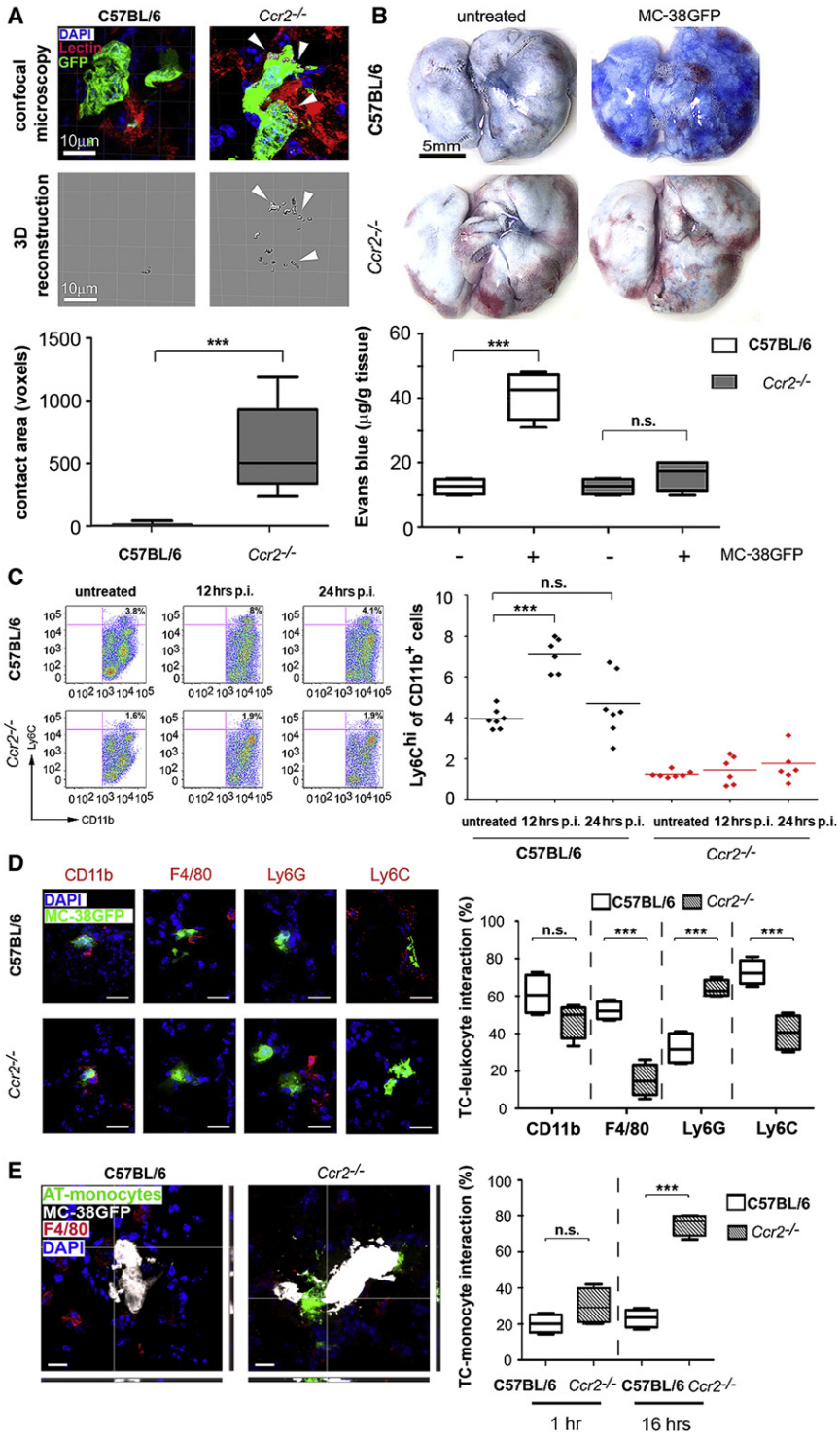

Figure 2. CCR2 Deficiency Reduces Tumor Cell Extravasation and Vascular Permeability and Affects Myeloid-Tumor Cell Interaction

(A) Confocal microscopy of MC-38GFP cells (green) and endothelial cells (red; lectin$^+$) in C57BL/6 and *Ccr2*$^{-/-}$ lungs (n = 5) 24 hr p.i. with MC-38GFP cells (upper row). Size of scale bar is indicated. Three-dimensional reconstruction of the interaction of both cell types (lower row). Quantification of the 3D contact area in voxels is shown as percentiles.

(B) Macroscopy of naive C57BL/6 and *Ccr2*$^{-/-}$ lungs (upper row) as well as 24 hr p.i. with MC-38GFP cells (lower row) upon Evans blue administration. Size of scale bar is indicated. Spectrophotometric quantification of Evans blue extracted from C57BL/6 and *Ccr2*$^{-/-}$ lungs (n = 6, each).

(C) Flow cytometry analysis for CD11b$^+$Ly6C^{hi} cells in lung tissue upon tumor cell challenge of C57BL/6 and *Ccr2*$^{-/-}$ mice over time (left panel). Quantification of Ly6C^{hi} cells is presented in the right panel (n = 6–7).

(D) Confocal microscopy images of the interaction of myeloid cells (CD11b, F4/80, Ly6G, Ly6C; all stained in red) with MC-38GFP cells (green) in C57BL/6 and *Ccr2*$^{-/-}$ mice 24 hr p.i. are shown. Nuclei are stained in blue (DAPI; left panel). Quantification of the myeloid-tumor cell interaction in lungs; percentiles are indicated (n = 3, each). Scale bar: 20 μm (right panel).

(E) Confocal microscopy analysis of the interaction of adoptively transferred, PKH26-labeled monocytes (green) with MC-38GFP cells (white) and endogenous F4/80$^+$ macrophages (red) in C57BL/6 and *Ccr2*$^{-/-}$ mice (n = 3) 16 hr p.i. (left panel). Scale bar: 10 μm; Z-stacks are indicated. Quantification of myeloid-tumor cell interaction in lungs; percentiles are indicated (right panel; mean with min/max). Statistics: ***p < 0.001; n.s., not significant.

See also Figure S2.

MC-38GFP cells in the lung vasculature were found in either genotype as early as 30 min p.i. (Figure 1G). At later time points (24, 72 hr), numbers of MC-38GFP cells in lung tissue decreased in both genotypes, though slightly more pronounced in *Ccr2*$^{-/-}$ mice at 24 hr. Besides, no significant changes were found in the structure and organization of the CD31$^+$ alveolar vasculature in both genotypes (Figure S1H).

CCR2 Controls Endothelial Permeability and Tumor Cell Extravasation

Reduced lung metastasis in *Ccr2*$^{-/-}$ mice could be explained by an impaired ability of MC-38GFP cells to extravasate into parenchyma of *Ccr2*$^{-/-}$ lungs. Confocal microscopy revealed that MC-38GFP cells remained associated with tomato lectin-stained endothelium of blood vessels in *Ccr2*$^{-/-}$ lungs at 24 hr p.i. (Figure 2A). In contrast, there was minimal contact of MC-38GFP cells with endothelia in C57BL/6 mice at 24 hr p.i., indicating that tumor cells had already extravasated from blood vessels. Three-dimensional reconstruction of confocal images showed increased contact of MC-38GFP cells with endothelium in *Ccr2*$^{-/-}$ lungs compared to C57BL/6 (p < 0.001; Figure 2A). To determine whether reduced capacity of MC-38GFP cells to extravasate in *Ccr2*$^{-/-}$ lungs was due to decreased vascular permeability, we

tested the ability of Evans blue to permeate lung tissue. No Evans blue leakage occurred in naive lungs of either genotype, indicating full vascular integrity (Figure 2B). However, 24 hr p.i. with MC-38GFP cells C57BL/6 lungs readily took up Evans blue, whereas *Ccr2*$^{-/-}$ lungs remained white, indicating no increase in vascular permeability (Figure 2B). Quantification of Evans blue confirmed the macroscopic data ($p < 0.001$; Figures 2B and S2C). The increase in vascular permeability upon injection of MC-38GFP cells was transient, as revealed by time course analyses (Figures S2A and S2B).

Next, the hypothesis whether reduced capacity of MC-38GFP cells to extravasate in *Ccr2*$^{-/-}$ lungs correlates with reduced recruitment of leukocytes was tested (Läubli et al., 2006; Qian et al., 2011). Flow cytometry of lungs from mice injected with MC-38GFP cells revealed recruitment of Ly6C^{hi} cells in C57BL/6 mice that was strongly reduced in *Ccr2*$^{-/-}$ mice (Figure 2C). The increase of Ly6C^{hi} cells in C57BL/6 lungs persisted for approximately 12–24 hr p.i. No significant increase of other immune cell types (e.g., CD4^{+}, CD8^{+}, CD11c^{+}, NK1.1^{+}) was found (data not shown).

In addition, we investigated whether lung-infiltrating myeloid cell populations are recruited to MC-38GFP cells at sites of vascular arrest. F4/80^{+}, CD11b^{+}, and Ly6C^{+} cells associated less with tumor cells in *Ccr2*$^{-/-}$ lungs compared to C57BL/6. In contrast, increased association of Ly6G^{+} cells with MC-38GFP cells was observed in *Ccr2*$^{-/-}$ lungs ($p < 0.001$; Figure 2D).

Finally, to test whether MC-38GFP cells injected into *Ccr2*$^{-/-}$ mice would still efficiently recruit myeloid cells, we adoptively transferred myeloid cells to mice 6 hr post-tumor cell injection. MC-38GFP cells recruited transferred myeloid cells in *Ccr2*$^{-/-}$ but not in C57BL/6 lungs ($p < 0.001$; Figure 2E) as MC-38GFP cells in C57BL/6 lungs had already recruited endogenous myeloid cells.

CCR2 Expression on Radio-Resistant Cells Enables Efficient Metastasis

We next tested whether reconstitution of *Ccr2*$^{-/-}$ mice with CCR2^{+} BM cells could restore the ability of MC-38GFP cells to extravasate and metastasize into lungs. Reciprocal BM reconstitutions (C57BL/6 → *Ccr2*$^{-/-}$; *Ccr2*$^{-/-}$ → C57BL/6) and controls (C57BL/6 → C57BL/6; *Ccr2*$^{-/-}$ → *Ccr2*$^{-/-}$) were performed and blood was analyzed for the presence of CCR2^{+}Ly6C^{hi} monocytes 6–8 weeks after reconstitution (Figures 3A and S3A). MC-38GFP cells were administered to reconstituted mice (efficiency >90%) and analyzed for tumor growth in lungs (Figures 3A and S3B). C57BL/6 → C57BL/6 mice displayed robust metastasis similar to control C57BL/6 mice, whereas *Ccr2*$^{-/-}$ → *Ccr2*$^{-/-}$ mice lacked or had strongly reduced metastasis. CCR2 expression on radio-resistant cells (*Ccr2*$^{-/-}$ → C57BL/6) resulted in more metastasis when compared to mice devoid of CCR2 expression in the stromal compartment (C57BL/6 → *Ccr2*$^{-/-}$; $p < 0.05$). This indicates that both, hematopoietic and stromal CCR2 expression is required for efficient metastasis.

To delineate the role of stromal CCR2 expression during metastasis, we assessed whether endothelial cell-restricted CCR2 expression (i.e., Tie2CCR2/*Ccr2*$^{-/-}$ mice; (Mildner et al., 2009) would enable tumor cell extravasation and metastasis. Tie2CCR2/*Ccr2*$^{-/-}$ mice lacked Ly6C^{hi} monocytes in blood and lung tissue and lacked CCR2 expression on CD11b^{+}, CD19^{+} or CD3^{+} cells in blood, spleen and BM (Figures 3B and S3C). Transcriptional analysis indicated *Ccr2* expression in whole lung tissue and in purified lung endothelial cells in Tie2CCR2/*Ccr2*$^{-/-}$ mice (Figures S3D and S3E). Upon injection with MC-38GFP cells, tumor cell extravasation and metastasis was partially restored in Tie2CCR2/*Ccr2*$^{-/-}$ compared to C57BL/6 mice (Figure 3C). Quantification of metastatic foci, GFP fluorescence and immunohistochemistry confirmed these data (Figures 3C, 3D, and S3F). Hence, expression of CCR2 on endothelial cells was sufficient to partially restore metastasis.

CCR2 Expression on Myeloid Cells Contributes to Tumor Cell Metastasis

To assess the role of CCR2 on myeloid cells during metastasis, we bred *Ccr2*$^{loxP/loxP}$ with *LysMCre* mice (Clausen et al., 1999), resulting in mice with reduced CCR2 expression on myeloid cells. Similar amounts of Ly6C^{hi} monocytes were detected in blood from *LysMCreCcr2*$^{loxP/loxP}$ and C57BL/6 mice by flow cytometry (Figure 4A).

We next challenged *LysMCreCcr2*$^{loxP/loxP}$ mice with MC-38GFP cells and quantified Ly6C^{hi} monocytes in lungs at 6 and 12 hr p.i. (Figures 4B and S4A). Strong reduction (>90%) in the influx of Ly6C^{hi} monocytes to the lungs and a decrease in local recruitment of F4/80^{+} and CD11b^{+} cells to tumor cells were observed (Figure 4C). To determine the effect of reduced CCR2^{+}/Ly6C^{hi} monocyte recruitment on metastasis, *LysMCreCcr2*$^{loxP/loxP}$, *Ccr2*$^{loxP/loxP}$, *Ccr2*$^{-/-}$, and C57BL/6 mice were injected with MC-38GFP and analyzed 28 d.p.i. Lung metastasis was increased in *LysMCreCcr2*$^{loxP/loxP}$ compared to *Ccr2*$^{-/-}$ mice ($p < 0.05$; Figures 4D and S4B). However, in comparison to C57BL/6 mice, metastasis in *LysMCreCcr2*$^{loxP/loxP}$ mice was decreased. This was confirmed by quantification of GFP fluorescence and immunohistochemistry of lung tissues (Figures 4D and S4C). Thus, CCR2 expression on myeloid cells contributes to metastasis of MC-38GFP cells.

Tumor Cell-Derived CCL2 Expression Controls Myeloid Cell Recruitment

Whether CCR2-dependent lung metastasis occurs also with different tumor cells, we injected mice with Lewis lung carcinoma cells (3LL). Similar to MC-38GFP cells, attenuation of metastasis was observed in *Ccr2*$^{-/-}$ when compared to C57BL/6 lungs ($p < 0.05$; Figure 5A, upper panels). Next, we injected B16-BL6 melanoma cells. Of note, similar extent of lung metastasis was observed in C57BL/6 and *Ccr2*$^{-/-}$ mice indicating that B16-BL6 melanoma cells extravasate and metastasize independently of CCR2 (Figure 5A, lower panels).

The dependency of metastasis on host-derived CCR2 expression indicates the involvement of tumor cell-intrinsic factors. We therefore first compared chemokine and chemokine receptor *mRNA* expression levels in lungs of C57BL/6 and *Ccr2*$^{-/-}$ mice injected with MC-38GFP cells. A strong increase in *Ccl2*, *Ccl7*, *Ccl12*, *Cxcl1*, and *Cxcl10* expression was detected at 4 hr p.i. in C57BL/6 lungs (Figure 5B). These transcripts remained abundant 8 and 12 hr p.i. and decreased at 48 hr p.i. (Figure 5B and data not shown). Similar transcriptional changes occurred in lungs of MC-38GFP-injected *Ccr2*$^{-/-}$mice (Figure 5B), suggesting that chemokine induction does not depend on host-derived

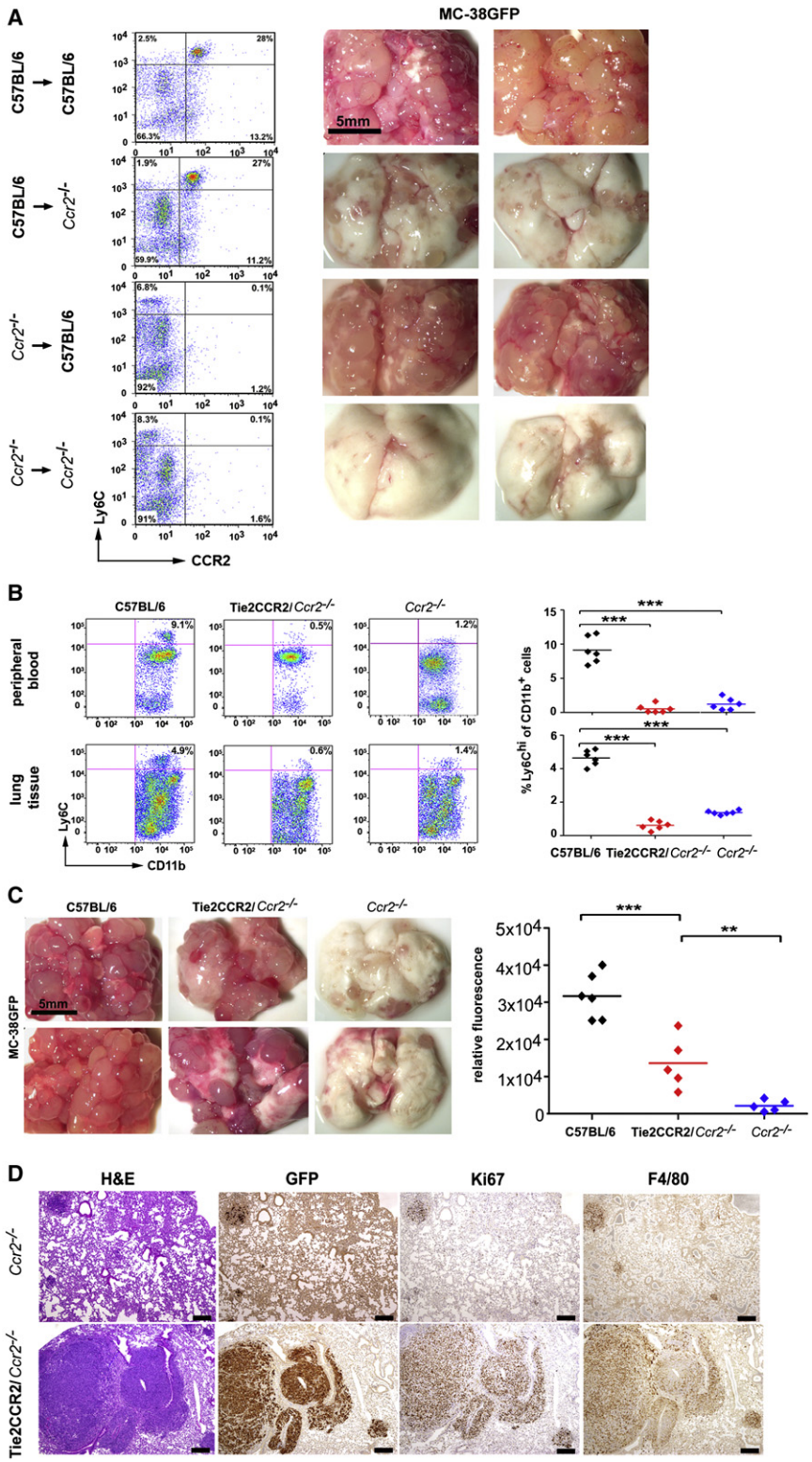

Figure 3. CCR2 Expression on Radio-Resistant Cells Suffices for Tumor Cell Metastasis

(A) Flow cytometry analysis of blood from C57BL/6→C57BL/6 (n = 8), C57BL/6→*Ccr2*$^{-/-}$ (n = 9), *Ccr2*$^{-/-}$→C57BL/6 (n = 7) and *Ccr2*$^{-/-}$→*Ccr2*$^{-/-}$ (n = 5) chimeric mice for the presence of CCR2^{+} Ly6C^{hi} cells (left row). Macroscopy of lungs from MC-38GFP-injected chimeric mice 28 d.p.i. Size of scale bar is indicated (middle/ right row).

(B) Flow cytometry for CD11b^{+}Ly6C^{hi} cells in blood (upper row) and lungs (lower row) of naive C57BL/6, Tie2CCR2/*Ccr2*$^{-/-}$ and *Ccr2*$^{-/-}$ mice (left panel). Quantification of Ly6C^{hi} cells is presented in the right panel (n = 6, each).

(C) Macroscopy of lungs from MC-38GFP-injected C57BL/6, Tie2CCR2/*Ccr2*$^{-/-}$ and *Ccr2*$^{-/-}$ mice 28 d.p.i. Size of scale bar is indicated (left panel). Quantification of GFP fluorescence in lung homogenates of C57BL/6, Tie2CCR2/*Ccr2*$^{-/-}$ and *Ccr2*$^{-/-}$ mice (n = 5, each; right panel).

(D) Histological analysis of MC-38GFP tumors in lungs of Tie2CCR2/*Ccr2*$^{-/-}$ and *Ccr2*$^{-/-}$ mice. H&E: Hematoxylin/Eosin, GFP: tumor cells, Ki67: proliferating cells, F4/80: macrophages. Scale bar: 50 μm; statistics: ***p < 0.001; **p < 0.01.

See also Figure S3.

CCR2. Alternatively, tumor cells may directly cause increased chemokine expression by altering the cellular composition and/or activation status of cells in the lungs of MC-38GFP-injected mice. However, chemokine receptor *mRNA* expression was unaltered in lungs of C57BL/6 and *Ccr2*$^{-/-}$ mice p.i. (Figure 5C). When we compared chemokine expression in MC-38GFP, 3LL, and B16-BL6 cells, elevated levels of *Ccl2*, *Ccl7*, *Cxcl1*, and *Cxcl10* transcripts were detected in MC-38GFP tumor cells compared to C57BL/6 colon (Figure S5A). Of note, *Ccl2 mRNA* and protein levels were elevated in MC-38GFP and 3LL cells and low in B16-BL6 melanoma cells, indicating that CCR2-dependent metastasis relies on tumor cell-derived CCL2 (Figures 5D, S5B, and S5C).

To determine whether MC-38 and 3LL-derived CCL2 was required for tumor cell extravasation and metastasis, CCL2 expression was silenced with small hairpin RNA (shRNA) in MC-38GFP cells (MC-38GFP^{CCL2kd}). *Ccl2 mRNA* was reduced by 75%–90%, CCL2 protein was reduced by 60%–85%, and expression of other chemokines/cytokines remained unaffected (Figure 5D). Cells stably transduced with scrambled shRNA served as control (MC-38GFP^{scr}). MC-38GFP and MC-38GFP^{CCL2kd} cells were injected into C57BL/6 mice, and their ability to recruit Ly6C^{hi} monocytes to the lung at 4 and 12 hr p.i. was assayed by flow cytometry. Similar numbers of Ly6C^{hi} cells were detected at 4 hr p.i. in lungs of C57BL/6 mice injected with MC-38GFP^{CCL2kd} or MC-38GFP cells (Figure 5E). However, no specific recruitment of Ly6C^{hi} monocytes

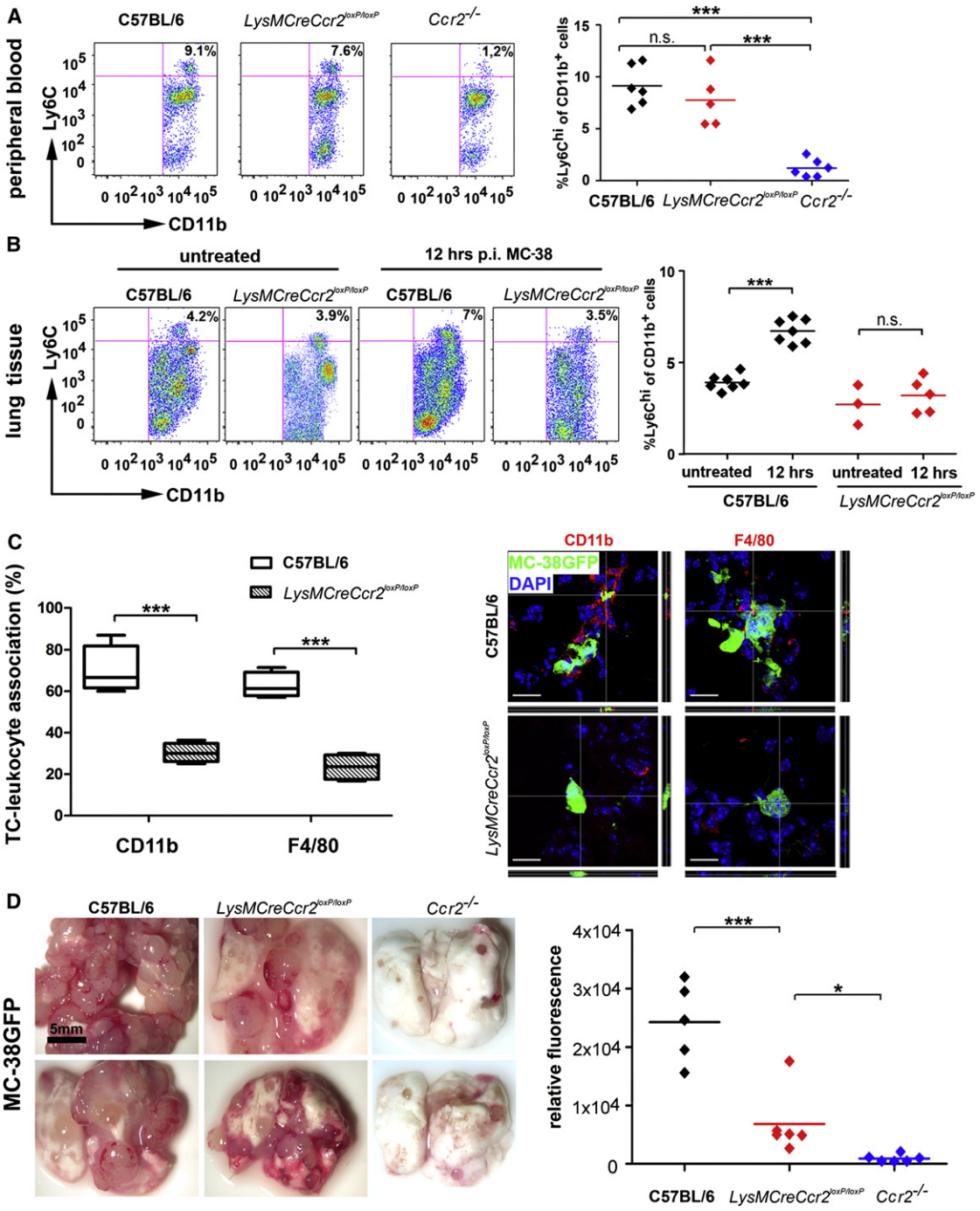

Figure 4. CCR2 Expression on Ly6C^{hi} Monocytes Facilitates Tumor Cell Extravasation

(A) Flow cytometry for CD11b^{+}Ly6C^{hi} cells in blood of C57BL/6, *LysMCreCcr2*$^{loxP/loxP}$ and *Ccr2*$^{-/-}$ mice (n = 5–6; left panel). Quantification of Ly6C^{hi} cells (right panel).

(B) Flow cytometry for CD11b^{+}Ly6C^{hi} cells in lungs of naive C57BL/6 and MC-38-injected C57BL/6 and *LysMCreCcr2*$^{loxP/loxP}$ mice 12 hr p.i. (n = 5–7; left panel). Quantification of Ly6C^{hi} cells (right panel).

(C) Confocal microscopy investigating the interaction of myeloid cells (CD11b, F4/80; red) and tumor cells (green) in lungs of C57BL/6 and *LysMCreCcr2*$^{loxP/loxP}$ mice. Nuclei are stained in blue (DAPI); scale bar: 20 μm; Z-stacks are indicated.

(D) Macroscopy of lungs from C57BL/6, *LysMCreCcr2*$^{loxP/loxP}$ and *Ccr2*$^{-/-}$ mice 28 d.p.i. with MC-38GFP. Size of scale bar is indicated (left panel). Quantification of GFP fluorescence in lung homogenates of C57BL/6 (n = 5), *LysMCreCCR2*$^{loxP/loxP}$ (n = 6), and *Ccr2*$^{-/-}$ (n = 6) mice (right panel). Statistics: ***p < 0.001; *p < 0.05; n.s., not significant.

See also Figure S4.

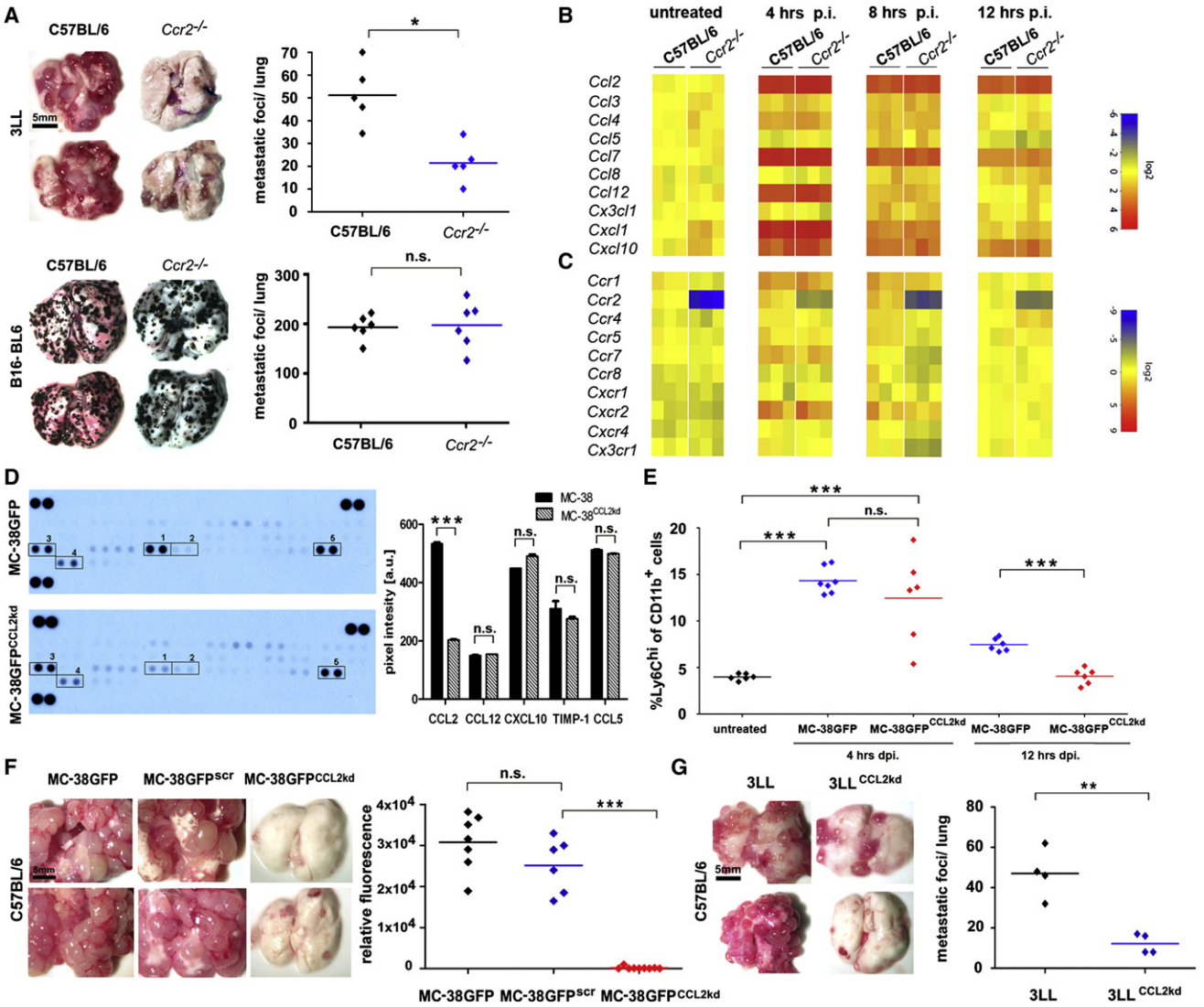

Figure 5. Tumor Cell-Derived CCL2-Dependent and -Independent Mechanisms of Tumor Cell Extravasation

(A) Macroscopy of lungs from C57BL/6 and *Ccr2*$^{-/-}$ mice at 12 d.p.i. with Lewis lung carcinoma cells (3LL) and quantification of tumor nodules (n = 5, each; upper row). Macroscopy of lungs from C57BL/6 and *Ccr2*$^{-/-}$ mice at 14 d.p.i. with melanoma cells (B16-BL6) and quantification of tumor numbers (n = 6, each; lower row).

(B and C) Real-time PCR analysis for the expression of selected chemokines (B) and chemokine receptors (C) in lungs of C57BL/6 and *Ccr2*$^{-/-}$ mice. Untreated, 4 hr p.i., 8 hr p.i., and 12 hr p.i. with MC-38GFP are shown from left to right. Data are presented as ΔΔct values in a log2 scale (red: upregulated; blue: down-regulated). Columns indicate individual mice (n = 3); rows represent particular genes. Each data point reflects the median expression of a particular gene resulting from three to four technical replicates, normalized to the mean expression value of the respective gene in C57BL/6 lungs.

(D) Expression profile of various chemokines and cytokines in MC-38GFP and MC-38GFP^{CCL2kd} cells. 1: CCL2 (silenced); 2: CCL12; 3: CXCL10; 4: TIMP-1; 5: CCL5 remain unaffected. Dots in the upper right and left corners serve as loading controls (left panel). Quantification of pixel density (shown in arbitrary units [a.u.]; mean ± SEM; right panel).

(E) Quantification of CD11b^{+}Ly6C^{hi} cells in lungs of naive C57BL/6 mice and 4 hr and 12 hr p.i. with MC-38GFP and MC-38GFP^{CCL2kd} cells (n = 6–7).

(F) Macroscopy of lungs derived from C57BL/6 mice 28 d.p.i. with MC-38GFP, MC-38GFP^{scr} and MC-38GFP^{CCL2kd} cells. Size of scale bar is indicated. Quantification of GFP fluorescence in lung homogenates of C57BL/6 mice 28 d.p.i. with MC-38GFP (n = 7), MC-38GFP^{scr} (n = 6) and MC-38GFP^{CCL2kd} (n = 9) cells.

(G) Macroscopy of lungs from C57BL/6 mice 12 d.p.i. with 3LL and 3LL^{CCL2kd} cells. Size of scale bar is indicated (left panel). Quantification of tumor nodules (n = 4, each; right panel); statistics: ***p < 0.001; **p < 0.01; *p < 0.05; n.s., not significant.

See also Figure S5.

was detected in lungs of C57BL/6 mice 12 hr p.i. with MC-38GFP^{CCL2kd} cells. Therefore, specific recruitment of Ly6C^{hi} cells is controlled by MC-38-derived CCL2. Next, we analyzed tumor cell extravasation and metastasis in C57BL/6 mice injected with MC-38GFP^{CCL2kd}, MC-38GFP or MC-38GFP^{scr} cells. Reduced lung metastasis was observed in C57BL/6 mice upon

MC-38GFP^{CCL2kd} injection and confirmed by analysis of GFP fluorescence ($p < 0.001$; Figure 5F). Similar results were obtained by silencing of CCL2 in 3LL cells ($p < 0.01$; Figure 5G).

In addition, reduced CCL2 expression in MC-38GFP cells (MC-38GFP^{CCL2kd}) diminished the ability to interact with CD11b$^+$, F4/80$^+$, or Ly6C$^+$ cells ($p < 0.001$). Although MC-38GFP^{CCL2kd} cells showed enhanced interaction with Ly6G$^+$ cells ($p < 0.001$; Figure S5D), they failed to recruit adoptively transferred myeloid cells (Figure S5E). This supports the conclusion that tumor cell-derived CCL2 is required for the association of tumor cells with myeloid cells.

CCR2 Expression on Endothelial Cells Determines Lung Permeability

To determine whether endothelial CCR2 expression was sufficient to induce vascular permeability, we injected Tie2CCR2/*Ccr2*$^{-/-}$ mice with MC-38GFP cells. Elevated levels of Evans blue in Tie2CCR2/*Ccr2*$^{-/-}$ lungs suggest that endothelial CCR2 activation is sufficient to induce lung vascular permeability (Figure 6A). Since host-derived CCL2 has been implicated in metastasis (Qian et al., 2011), we injected *Ccl2*$^{-/-}$ mice with MC-38GFP cells. Interestingly, lung vascular permeability was increased upon tumor cell injection ($p < 0.001$; Figure 6A), indicating that tumor cells induce vascular permeability in the absence of host-derived CCL2. In line, MC-38GFP^{CCL2kd} cells failed to induce vascular permeability in C57BL/6 lungs (Figure 6A). To investigate whether the local microenvironment (e.g., CCL2 expression; monocytes; stromal cells) rescues the inability of CCL2-deficient tumor cells to extravasate and metastasize, we coinjected MC-38 and MC-38GFP^{CCL2kd} cells into C57BL/6 mice. Similar numbers of metastases were observed in lungs of C57BL/6 mice injected with MC-38 versus MC-38GFP^{CCL2kd}/MC-38 cells 28 d.p.i. ($p = 0.6$; Figure 6B). Of note, lungs from C57BL/6 mice injected with MC-38GFP^{CCL2kd}/MC-38 cells displayed mainly GFP-negative tumors, suggesting that tumors mainly originated from CCL2$^+$ tumor cells ($p < 0.001$; Figures 6B and 6C). Therefore, the inability of MC-38GFP^{CCL2kd} cells to metastasize cannot be restored by the local environment.

We next examined lungs from C57BL/6 and *Ccr2*$^{-/-}$ mice 12 hr p.i. with MC-38 cells at ultrastructural level. Injection of MC-38 cells induced changes in C57BL/6 lung tissue including increased thickness of airway epithelial cells in the bronchi and thickened smooth muscle cells. Of note, tumor cells were found inside the alveoli (Figure 6D, left panel) and rarely in the vessels. Alveoli in C57BL/6 lungs appeared shrunken, with numerous alveolar macrophages and type I, II pneumocytes. Moreover, we observed an intimate interaction between MC-38 cells and C57BL/6 endothelia with tumor cell protrusions spanning through the apical side of the endothelium resembling ongoing tumor cell transmigration (Figure 6D, middle panel, inset). In contrast, *Ccr2*$^{-/-}$ lung endothelium appeared to be less affected by the injection of MC-38 tumor cells with no visible indication for endothelial attachment (Figure 6D, right panel, inset).

Endothelial CCR2 Signaling Controls Tumor Cell Extravasation through the JAK2-Stat5 and p38MAPK Pathways

To identify the mechanisms involved in tumor cell extravasation, we next examined transmigration of tumor cells through lung endothelial monolayers in presence or absence of monocytes in vitro. MC-38GFP cells incubated on C57BL/6 endothelial cells for 16 hr transmigrated only minimally toward an FCS gradient. Cocultivation of MC-38GFP cells with BM-derived monocytes induced efficient transmigration of MC-38GFP cells through C57BL/6 endothelia ($p < 0.001$; Figure 7A). In contrast, MC-38GFP cells were unable to transmigrate through endothelial cells isolated from *Ccr2*$^{-/-}$ mice either in the presence or absence of monocytes ($p = 0.6$; Figure 7A). To determine whether tumor cell transmigration depends on tumor cell-derived CCL2, we tested the ability of MC-38GFP^{CCL2kd} cells to transmigrate in vitro. MC-38GFP^{CCL2kd} cells could not transmigrate through a C57BL/6 endothelial monolayer in the presence of monocytes ($p < 0.001$; Figure 7B). Interestingly, neither lack of endothelial nor monocytic CCR2 expression affected efficacy of monocyte transmigration (Figure 7C). Taken together, endothelial CCR2 signaling can specifically enable transmigration of tumor cells without affecting monocytes. Tumor cell-derived CCL2 was sufficient to induce permeability in the CCR2$^+$ endothelial monolayer even in the absence of monocytes. In contrast, MC-38GFP^{CCL2kd} cells induced partial endothelial permeability only in the presence of monocytes (Figure 7D). These findings provide direct evidence for the role of endothelial CCR2 activation during tumor cell extravasation; and for the supportive role of monocytes in this process.

CCL2 is known to activate Janus kinase 2 (JAK2) through CCR2 (Mellado et al., 1998), thereby triggering several downstream pathways such as Stat1, Stat3 and Stat5, p38MAPK, and PI3K (Agrawal et al., 2011; Sanz-Moreno et al., 2011). We first tested whether inhibition of JAK2 phosphorylation would affect tumor cell transmigration. AG490 effectively blocked tumor cell transmigration, demonstrating the requirement of CCR2-JAK2 signaling for tumor cell extravasation ($p < 0.001$; Figure 7E). Inhibition of Stat3 phosphorylation (S3I-201) failed to affect tumor cell migration ($p = 0.8$), while block of Stat5 phosphorylation impeded transmigration of MC-38GFP cells ($p < 0.001$; Figure 7E). PI3K inhibition with Wortmannin did not alter tumor cell transmigration ($p = 0.6$), whereas blocking p38MAPK phosphorylation with SB202190 did ($p < 0.001$, Figure 7F). Therefore, both JAK2-Stat5 and p38MAPK pathways appeared to be involved in transmigration of MC-38GFP cells through CCR2$^+$ endothelium.

We next addressed whether tumor cells, rather than transmigrating through endothelial junctions, might trans-invade endothelial cells (Feng et al., 1998), which was shown to depend on Rac/Rho GTPases. However, inhibition of Rac1 (with NSC23766) failed to block tumor cell transmigration pointing at transmigration through endothelial junctions (Figure 7E).

To provide further evidence that CCR2-JAK2 signaling is involved in tumor cell extravasation, we measured JAK2 phosphorylation in lung homogenates from MC-38-injected mice. Increased JAK2 phosphorylation relative to total JAK2 was observed at 8 and 12 hr p.i. in C57BL/6 lungs which was prevented by AG490. In contrast, inhibition of p38MAPK did not affect JAK2 phosphorylation (Figure 7F). Importantly, no or minor phosphorylation of JAK2 was detected in *Ccr2*$^{-/-}$ mice upon tumor cell injection, confirming that CCR2 expression in lungs is crucial for activation of this signaling cascade. Similarly, p38MAPK and Stat5 were activated in lungs of C57BL/6 mice

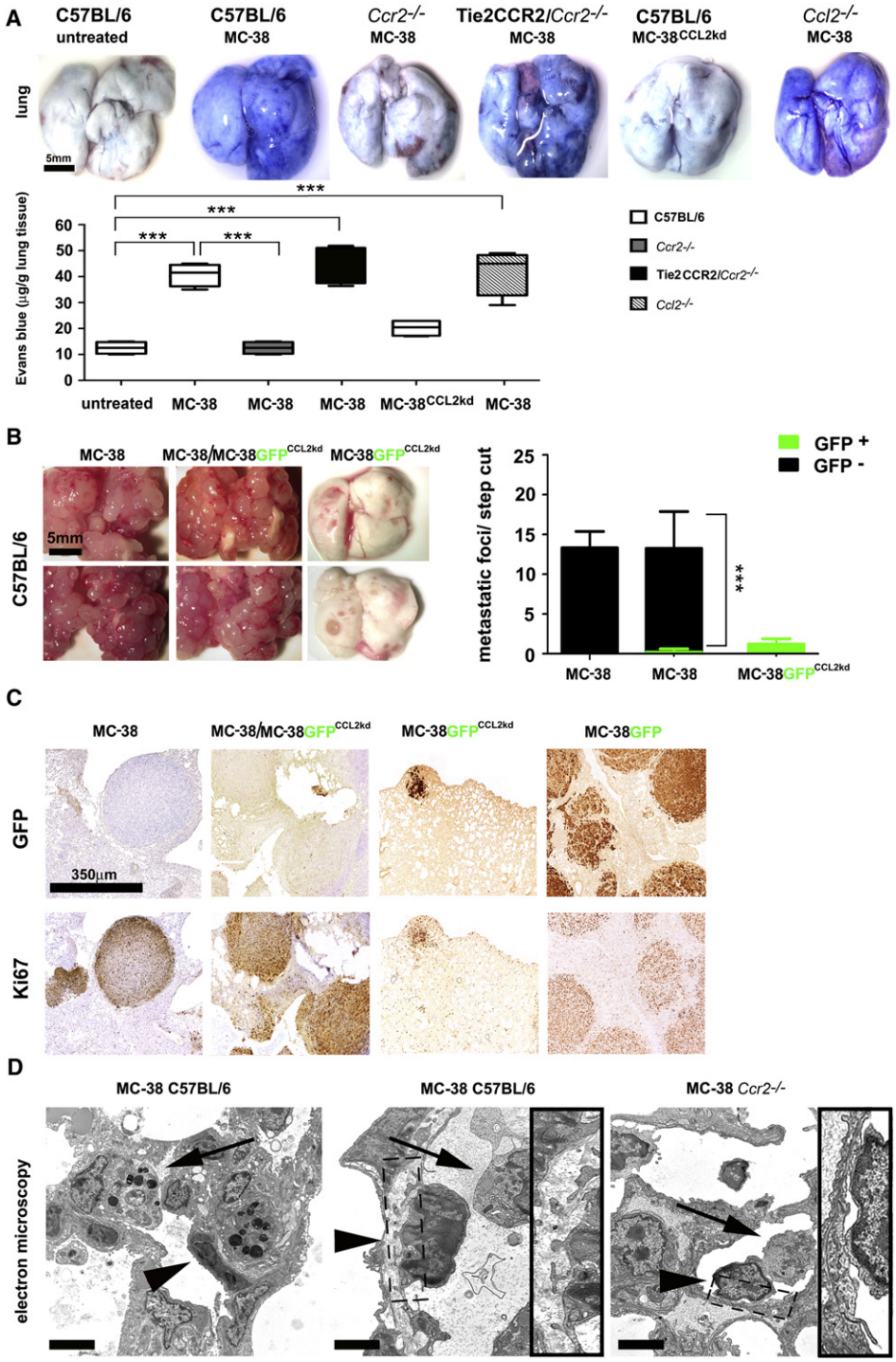

Figure 6. Tumor Cell-Derived CCL2 Is Sufficient to Induce Endothelial Permeability

(A) Macroscopy of lungs with Evans blue accumulation derived from untreated C57BL/6 mice or treated mice of various genotypes 24 hr p.i. with MC-38GFP and MC-38GFP^{CCL2kd} cells. Scale bar is indicated. Spectrophotometric quantification of Evans blue extracted from lung tissue.

(B) Macroscopy of lungs derived from C57BL/6 mice 28 d.p.i. with MC-38 (n = 3), MC-38/MC-38GFP^{CCL2kd} (1:1 ratio; n = 5) and MC-38GFP^{CCL2kd} cells (n = 3; left panel). Quantification of tumor nodules on step cuts through lungs (black bars represent MC-38 cells, green bars MC-38GFP^{CCL2kd} cells; mean ± SEM; right panel).

(C) Immunohistochemistry for the quantification of tumor nodules. GFP and Ki67 served as tumor markers. Size of scale bar is indicated.

(D) Electron microscopy images of lungs of C57BL/6 (left and middle) and *Ccr2*$^{-/-}$ mice (right) 12 hr p.i. with MC-38GFP. Left: arrowhead points toward a tumor cell in the alveolar space, in close contact to a type II pneumocyte (arrow). Middle panel: arrowhead shows an attached and transmigrating tumor cell localized within the vessel. The arrow indicates a monocyte within the vessel. The insert shows the interaction between tumor cell and vessel wall at higher magnification. Right: No visible transmigration of tumor cells (arrow head) in lungs of *Ccr2*$^{-/-}$ mice. Arrow: monocyte within the vessel. Scale bar: 5 µm; statistics: ***$p < 0.001$.

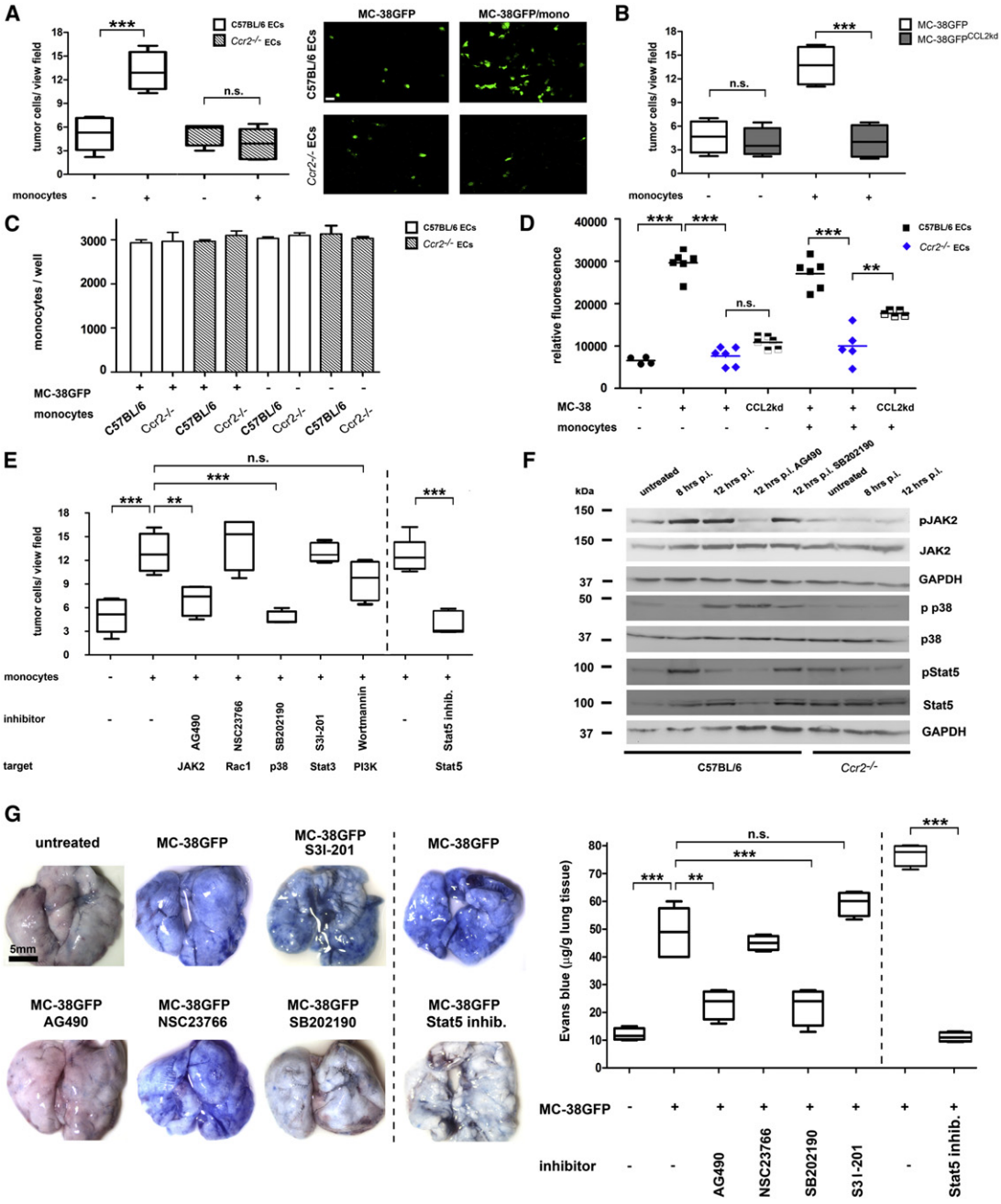

Figure 7. CCL2-CCR2-Mediated Permeabilization of the Endothelium Is Driven by JAK2-Stat5 and p38MAPK activation

(A) MC-38GFP cells were cocultured with monocytes for 16 hr on monolayers of endothelial cells derived either from C57BL/6 or *Ccr2*$^{-/-}$ lungs. Transmigrated GFP^{+} tumor cells in the lower chamber were counted and are presented as percentiles (left panel). Representative images of transmigrated tumor cells for each coculture; scale bar: 10 μm (right panel).

(B) MC-38GFP cells were compared with MC-38GFP^{CCL2kd} cells for their efficiency to migrate through C57BL/6 endothelial cells. Transmigrated GFP^{+} tumor cells were counted and values are presented as percentiles.

(C) Analysis of transmigrated monocytes at 16 hr post coculture with C57BL/6 or *Ccr2*$^{-/-}$ endothelial cells with or without tumor cells (mean ± SEM).

(D) Permeability of the C57BL/6 or *Ccr2*$^{-/-}$ endothelial cell layer for Dextran-FITC was determined at 7 hr post addition of tumor cells with or without monocytes.

(E) Inhibitors for JAK2 (AG490), Rac (NSC23766), p38MAPK (SB201290), Stat3 (S3I-201), PI3K (Wortmannin), and Stat5 pathways were added to the coculture of MC-38GFP cells with monocytes. GFP^{+} tumor cells transmigrated through the C57BL/6 endothelial cell layer were counted in the lower chamber.

(F) Immunoblot analysis of lung samples derived from C57BL/6 and *Ccr2*$^{-/-}$ mice (untreated, 8 and 12 hr p.i.) as well as C57BL/6 mice treated with AG490 or SB202190 (12 hr p.i.). Panel from top to bottom: pJAK2, JAK2, GAPDH, P-p38, p38, pStat5, Stat5, and GAPDH.

(G) Macroscopy of lungs upon Evans blue administration in presence or absence of inhibitors for Stat3, JAK2, Rac1, p38MAPK and Stat5 16 hr p.i. with MC-38GFP cells. Quantification of Evans blue (n = 4, each; right panel; mean with min/max is shown). Statistics: ***p < 0.001; **p < 0.01; n.s., not significant.

See also Figure S6.

upon tumor cell injection (between 8 and 12 hr p.i.) but not in *Ccr2*$^{-/-}$ lungs (Figure 7F).

We next tested the involvement of the above-described signaling pathways in controlling lung permeability. In line with our in vitro data, JAK2, Stat5 and p38MAPK inhibition prevented the increase in vascular permeability induced by MC-38GFP cells in C57BL/6 mice. However, treatment with Rac1 (NSC23766) and Stat3 (S3I-201) inhibitor failed to affect vascular permeability (Figure 7G). Since a specific inhibitor of PI3K did not affect tumor cell transmigration in vitro, it is unlikely that PI3K signaling is involved in tumor cell extravasation. Accordingly, PI3K$\gamma^{-/-}$ mice developed lung metastasis similar to C57BL/6 mice 28 d.p.i. of MC-38GFP cells (data not shown). Thus, inhibition of JAK2-Stat5 and p38MAPK signaling prevents tumor cell-induced vascular permeability in vivo.

We next investigated whether JAK2-Stat5 or p38MAPK inhibition exclusively affects endothelial cells or also monocytes. We therefore analyzed levels of phosphorylated Stat5 and p38MAPK in MC-38GFP-injected Tie2CCR2/*Ccr2*$^{-/-}$ mice (Figures S6A and S6B). Increase in phosphorylation of JAK2, Stat5 and p38MAPK was comparable both in Tie2CCR2/*Ccr2*$^{-/-}$ and C57BL/6 lungs. Therefore, Stat5 and p38MAPK activation in endothelial cells occurs in the absence of Ly6C^{hi} monocytes.

We next determined whether lack of CCR2 signaling in vivo would affect the expression of Stat5 and p38MAPK target genes associated with the vascular integrity of endothelial cells. Significantly decreased expression of *E-selectin* and *Icam-1* ($p < 0.05$; $p < 0.001$) was found in *Ccr2*$^{-/-}$ lungs compared to C57BL/6 at 8 hr p.i. (Figure S6C). This suggested that the proinflammatory endothelial response associated with metastasis was reduced in *Ccr2*$^{-/-}$ mice. Aside from these transcriptional changes, we observed that coincubation of primary endothelial cells with MC-38 cells caused cytoskeletal retraction and disruption of the endothelial layer, as determined by phalloidin-fluorescein isothiocyanate (FITC) staining (Figure S6D).

We next investigated on ultrastructural level, whether the inhibition of CCR2 signaling affects tumor cell behavior in lungs of C57BL/6 mice. In contrast to lungs of naive mice, but similar to C57BL/6 tumor injected mice, thickened airway epithelial cells and smooth muscle cells were found in mice treated with JAK2 inhibitor. However, strongly reduced tumor cell extravasation could be observed in AG490 treated mice (Figure 8A).

Finally, we assessed whether JAK2 and p38MAPK inhibition would also block lung metastasis. Thus, we treated MC-38GFP-injected mice with AG490 or SB202190 during the first 3 d.p.i. Blockade of both, JAK2 and p38MAPK signaling attenuated metastasis ($p < 0.05$; Figures 8B and 8C).

CCL2 Expression Correlates with Metastatic Potential in Human Colon Cancer Tissue

We next analyzed *CCL2* expression in human primary nonmetastasized colon tumors (UICC stages I and II) and in colon tumors that metastasized into the lymph nodes (UICC stage) or into distant organs (UICC stage IV). *CCL2* transcripts were more abundant in primary colon tumors of stages I, II, and III when compared to healthy colon samples. However, *CCL2* expression was particularly high in colon tumors stage IV that developed metastases in distant organs (Figure 8D), indicating that upregulation of *CCL2* correlates with metastatic potential.

DISCUSSION

During the multistep process of metastasis, cytokines and chemokines have been reported to have pro- or antitumorigenic effects (Granot et al., 2011; Qian et al., 2011). Elevated CCL2 levels have been previously linked to malignancy and increased metastasis in a number of cancers (Soria et al., 2011; Yoshidome et al., 2009; Zhang et al., 2010; Zijlmans et al., 2006). Our analysis of primary colon tumors (UICC stages I–IV) confirmed the link between CCL2 upregulation in stage IV colon carcinoma and metastatic capacity. Recent studies have shown that monocyte recruitment by CCL2 contributes to lung metastasis of breast cancer (Lu and Kang, 2009; Qian et al., 2011). Our data provide evidence that tumor cell-derived CCL2 activates CCR2 on endothelial cells, thereby enabling efficient tumor cell extravasation.

To study the mechanisms of tumor cell extravasation, we applied chimeric, transgenic, and knockout mice, as well as in vitro assays. This allowed us to define the role of tumor cell-derived CCL2 in a spatial and temporal manner. Using these models, we determined that enhanced lung vascular permeability, tumor cell extravasation, and recruitment of Ly6C^{hi} monocytes are initiated by tumor cell-derived CCL2 at sites of vascular arrest in a CCR2-dependent manner.

It was previously demonstrated that systemic depletion of CCL2 with neutralizing antibodies could attenuate metastasis, while the origin of CCL2 was identified to be in tumor cells and stromal compartment (Qian et al., 2011). We show that vascular permeability was enhanced in both *Ccl2*$^{-/-}$ and C57BL/6 mice, suggesting that host-derived CCL2 is not required. In addition, silencing of CCL2 expression in two different tumor cell lines (MC-38GFP and 3LL) prevented induction of lung vascular permeability and subsequent metastasis, further demonstrating that tumor cell-derived CCL2 is sufficient for initiation of tumor cell extravasation. Previous observations that CCL2 overexpression in tumor cells enhanced metastasis are in line with our findings (Lu and Kang, 2009). Importantly, recent work indicated that CCR2 deficiency does not affect primary tumor growth (Sawanobori et al., 2008), arguing against the possibility that the observed reduction in metastasis is the result of tumor growth rate.

Which cellular compartment integrates tumor cell-derived CCL2 signaling through CCR2? CCL2-dependent recruitment of monocytes to metastatic sites has been shown to contribute to metastasis (Mizutani et al., 2009; Qian et al., 2011). It is also known that CCL2-expressing breast tumor cells engage CCR2^{+} cells of monocytic origin to facilitate colonization of lung and bone (Lu and Kang, 2009). Consistent with this, we show that recruitment of Ly6C^{hi} monocytes correlates with metastasis. However, depletion of CCR2 from monocytes in *LysMCreCcr2*$^{loxP/loxP}$ mice strongly affected monocyte recruitment and interaction with tumor cells and consequently reduced but did not prevent metastasis. In line, even partial reduction of CCR2 affected monocyte recruitment (Leuschner et al., 2011). Accordingly, the number of metastases in *Ccr2*$^{-/-}$ → C57BL/6 chimeric mice was considerably lower than in C57BL/6 mice. Furthermore, experiments with Tie2CCR2/*Ccr2*$^{-/-}$ mice confirmed that endothelial expression of CCR2 is sufficient for metastasis (Figure 3C). Therefore, Ly6C^{hi} monocytes appear to be necessary but not sufficient for effective metastasis.

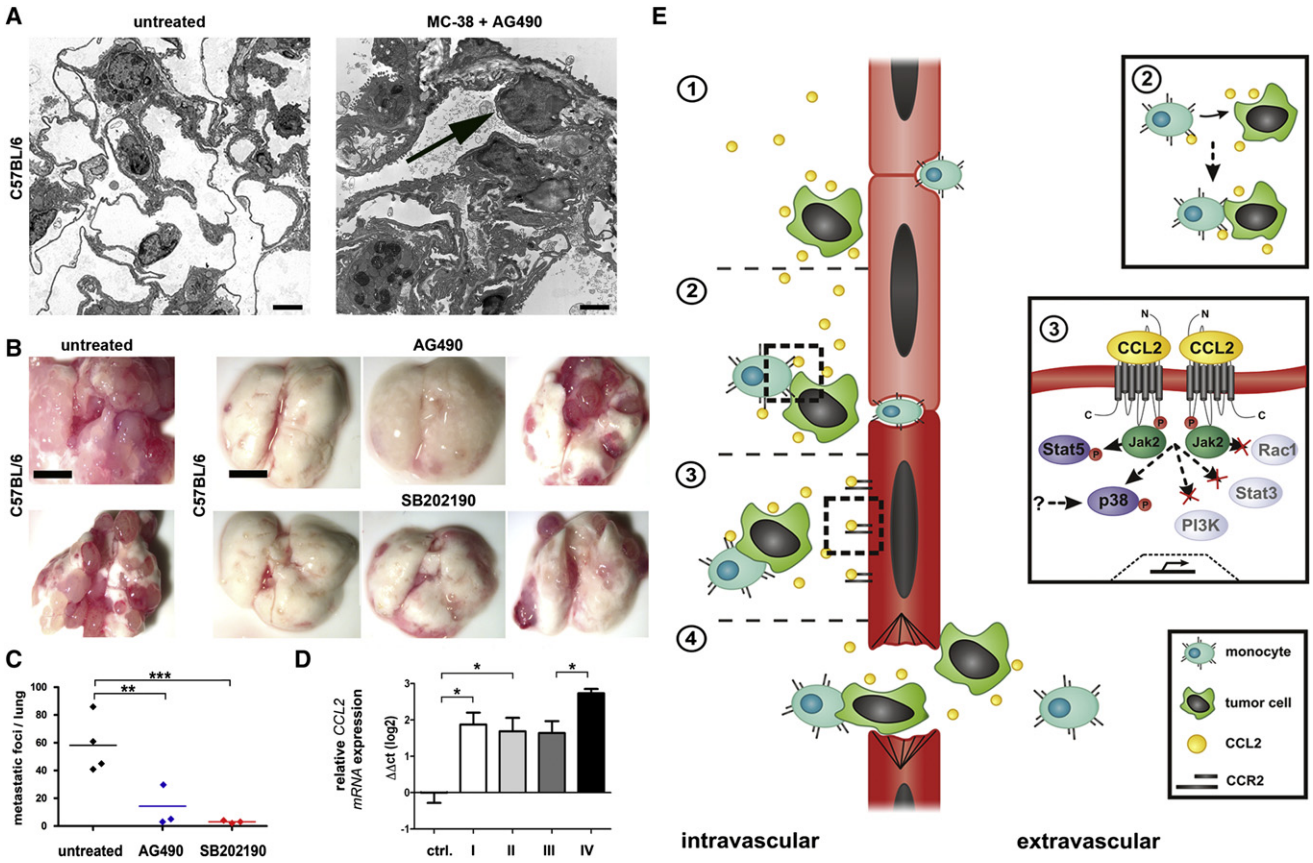

Figure 8. Short-Term Inhibition of JAK2 or p38MAPK Impedes Tumor Cell Metastasis

(A) Electron microscopy images of a naive C57BL/6 lung (left, scale bar: 4 μm) and 12 hr p.i. with MC-38GFP and AG490 treatment (right, scale bar: 2 μm); arrow points toward a tumor cell.

(B) Macroscopy of lungs from C57BL/6 mice 26 d.p.i. with MC-38GFP left untreated or with AG490 or SB202190 treatment during the first 3 d.p.i. Scale bar: 5 mm.

(C) Quantification of tumor nodules in lungs of C57BL/6 mice left untreated (n = 4), SB202190 (n = 3), or AG490 (n = 3) treated upon MC-38GFP injection.

(D) Transcriptional analysis of *CCL2* levels in tissue obtained from colon-cancer patients. *mRNA* expression levels in healthy control tissue (ctrl.; n = 4), in tumor samples classified as stage I (n = 10), stage II (n = 10) both being nonmetastatic; stage III: metastastic in lymph nodes (n = 10), stage IV: metastatic in distant organs (n = 9) colon carcinomas were studied. Data are presented in a log2 scale. Each bar reflects the median expression (mean ± SEM) of a gene resulting from three to four technical replicates, normalized to the mean expression value of *CCL2* in control samples. Statistics: ***$p < 0.001$; **$p < 0.01$; *$p < 0.05$.

(E) Schematic model depicting how CCL2-expressing tumor cells attract monocytes (1 and 2), trigger vascular permeability (3) and transmigrate through the endothelium (4). Tumor cell-dependent activation of CCR2 on the endothelium induces JAK2, Stat5, and p38MAPK phosphorylation but not PI3K, Stat3, and Rac1.

Here, we demonstrate that endothelial CCR2 signaling controls metastasis by promoting tumor cell extravasation. We hypothesize that CCR2 on endothelial cells may resemble a "lock-and-key" signal for opening the vasculature and enabling extravasation of $CCL2^+$ tumor cells. Indeed, we found that expression of CCR2 on endothelial cells is linked to the induction of vascular permeability. This "lock-and-key" relationship was dependent on CCL2 expression solely from the tumor cells, since MC-38^{CCL2kd} cells failed to induce vascular permeability and metastasis in C57BL/6 mice. Since coinjection experiments of MC-38GFP^{CCL2kd}/MC-38 cells only induced efficient metastasis of $CCL2^+$ but not MC-38GFP^{CCL2kd} cells, we suggest that an intimate interaction of $CCL2^+$ colon carcinoma cells with the $CCR2^+$ endothelium is required.

Monocyte transmigration still occurred through CCR2-deficient endothelial monolayers, indicating that CCR2 signaling on endothelial cells specifically enables transmigration of $CCL2^+$ tumor cells.

There are several signaling pathways that participate in endothelial activation associated with diapedesis of leukocytes during inflammation (McIntyre et al., 2003), some of which act downstream of CCR2 (e.g., Stat3, PI3K (Yu et al., 2009). From the panel of inhibitors tested in vitro, we identified the JAK2, Stat5, and p38MAPK signaling pathways as responsible for induction of vascular permeability and extravasation in vivo. Activation of the p38MAPK in endothelial cells by transmigrating tumor cells has been observed previously (Tremblay et al., 2006). The pattern of JAK2 and p38MAPK activation in MC-38-injected C57BL/6 mice suggests that these two pathways act independently of each other, since inhibition of p38MAPK phosphorylation did not block Stat5 or JAK2 phosphorylation. In contrast, JAK2 inhibition blocked Stat5 but not p38MAPK

phosphorylation. Tumor cell-induced phosphorylation of both JAK2-Stat5 and p38MAPK was detected in Tie2CCR2/*Ccr2*$^{-/-}$ lungs, arguing that both signaling pathways are activated in parallel in the endothelial compartment.

Based on our data, we propose the following model describing the role of CCR2 signaling in metastasis: Upon vascular arrest, CCL2^{+} tumor cells induce a local chemokine gradient, recruiting CCR2^{+} monocytes. Concomitantly or subsequently direct activation of CCR2 on the endothelium is triggered by tumor cells, which is critical for metastasis. CCL2 activates JAK2 and p38MAPK signaling, leading to enhanced vascular permeability that along with monocyte recruitment enables efficient tumor cell extravasation (Figure 8E). The exact kinetics and modes of transmigration remain to be described. Our data identify a yet undescribed role for tumor cell-derived chemokines in metastasis that goes beyond the attraction of inflammatory cells.

With increasing interest, chemokines and chemokine receptors are being considered as targets for cancer therapy, including metastasis. Certainly, the CCL2-CCR2 axis is just one possible chemokine-chemokine receptor axis exploited by tumor cells. Nevertheless, further studies will be required to identify which cancers use chemokine-chemokine receptor interactions for efficient tumor cell extravasation and metastasis. Our results identify inhibition of CCR2 and its downstream targets (JAK2/Stat5/p38MAPK) as a potential strategy for preventing CCL2-mediated metastasis therapeutically.

EXPERIMENTAL PROCEDURES

Mice

Animals were maintained under specific pathogen-free conditions, and experiments were approved by Zürich Cantonal Veterinary Committee in accordance to the guidelines of the Swiss Animal Protection Law. C57BL/6 and *Ccl2*$^{-/-}$ mice were purchased from the Jackson Laboratory, *Ccr2*$^{-/-}$ mice (Boring et al., 1997; Kuziel et al., 1997) were either purchased from the Jackson Laboratory or obtained from our own breedings; Tie2CCR2/*Ccr2*$^{-/-}$ were described previously (Mildner et al., 2009); *LysMCreCcr2*$^{loxP/loxP}$ were obtained from M. Pasparakis (G.v.L. and M.P., unpublished data); and BacCCR2GFP and BacCCR2DTCFP mice (Hohl et al., 2009) were obtained from E. Pamer.

Human Colon Cancer Tissue

Patients with colon carcinomas stage UICC I (n = 10), II (n = 10), III (n = 10), and IV (n = 9) were selected from the Erlangen Registry for Colorectal Carcinomas (ERCRC). The local ethics committee approved the study and the regulations of the same committee of the clinical center Erlangen were obeyed; written consent has been obtained (approval nr. 3914).

Experimental Metastasis Assay

Mice were i.v. injected with MC-38GFP cells (3×10^5) and euthanized after 28 days. Metastatic foci were counted, macroscopic pictures of lungs were taken and GFP fluorescence was measured in lung homogenates (Borsig et al., 2002).

Vascular Permeability Assay

Permeability of the lung microvasculature was determined with Evans blue dye extravasation technique (Reutershan et al., 2006). Briefly, mice were injected with tumor cells, and, after 24 hr, 2 mg of Evans blue was i.v. injected followed by euthanasia 30 min later. In experiments using various signaling pathways inhibitors (AG490 and SB202190 [Sigma], NSC23766 [Calbiochem], S3I-201 and Stat5 [Santa Cruz]), inhibitors were i.p. injected 1 hr before and 5 hr post tumor cell injection at concentrations of 10–25 mg/kg. Lungs were perfused with PBS, dissected, photographed and homogenized. Evans blue was extracted by incubation with formamide at 60°C for 18 hr. Evans blue concentration was measured spectrophotometrically (absorbance at 620 nm).

Statistical Analysis

Statistical analysis was performed with the GraphPad Prism software (version 4.0). All data are presented as mean ± SEM and were analyzed by ANOVA with the post hoc Bonferroni multiple comparison test, unless specified differently. Analysis of two samples was performed with Student's t test.

SUPPLEMENTAL INFORMATION

Supplemental Information includes six figures, Supplemental Experimental Procedures, and Supplemental References and can be found with this article online at http://dx.doi.org/10.1016/j.ccr.2012.05.023.

ACKNOWLEDGMENTS

We would like to thank Drs. Anna Lorentzen, Tracy O'Connor, Barbara Stecher, and Prof. Percy Knolle for critically reading the manuscript, Frank Tacke for mice, Yannick Böge, Renaud Maire, Robin Nagel, Silvia Behnke, Jay Tracy, Daniel Kull, Ruth Hillermann, Alexandra Müller, and Prof. Ursus Riede for support. M.H. was supported by an ERC Starting grant (LiverCancerMechanisms), the Helmholtz foundation, the Hofschneider foundation, Oncosuisse, and the Swiss National Foundation (no. 310030-130822). L.B. was supported by Swiss National Foundation (no. 31003A-133025). M.P. was supported by the center of chronic immunodeficiency (CCI) and the DFG (SFB 620, FOR1336, PR 577/8-1). M.S. and R.S.C. were supported by the German Federal Ministry for Education and Research.

Received: October 10, 2011
Revised: January 31, 2012
Accepted: May 18, 2012
Published: July 9, 2012

REFERENCES

Agrawal, S., Gollapudi, S., Su, H., and Gupta, S. (2011). Leptin activates human B cells to secrete TNF-α, IL-6, and IL-10 via JAK2/STAT3 and p38MAPK/ERK1/2 signaling pathway. J. Clin. Immunol. *31*, 472–478.

Allavena, P., Germano, G., Marchesi, F., and Mantovani, A. (2011). Chemokines in cancer related inflammation. Exp. Cell Res. *317*, 664–673.

Boring, L., Gosling, J., Chensue, S.W., Kunkel, S.L., Farese, R.V., Jr., Broxmeyer, H.E., and Charo, I.F. (1997). Impaired monocyte migration and reduced type 1 (Th1) cytokine responses in C-C chemokine receptor 2 knockout mice. J. Clin. Invest. *100*, 2552–2561.

Borsig, L., Wong, R., Hynes, R.O., Varki, N.M., and Varki, A. (2002). Synergistic effects of L- and P-selectin in facilitating tumor metastasis can involve non-mucin ligands and implicate leukocytes as enhancers of metastasis. Proc. Natl. Acad. Sci. USA *99*, 2193–2198.

Chambers, A.F., Groom, A.C., and MacDonald, I.C. (2002). Dissemination and growth of cancer cells in metastatic sites. Nat. Rev. Cancer *2*, 563–572.

Clausen, B.E., Burkhardt, C., Reith, W., Renkawitz, R., and Förster, I. (1999). Conditional gene targeting in macrophages and granulocytes using LysMcre mice. Transgenic Res. *8*, 265–277.

Feng, D., Nagy, J.A., Pyne, K., Dvorak, H.F., and Dvorak, A.M. (1998). Neutrophils emigrate from venules by a transendothelial cell pathway in response to FMLP. J. Exp. Med. *187*, 903–915.

Granot, Z., Henke, E., Comen, E.A., King, T.A., Norton, L., and Benezra, R. (2011). Tumor entrained neutrophils inhibit seeding in the premetastatic lung. Cancer Cell *20*, 300–314.

Gupta, G.P., and Massagué, J. (2006). Cancer metastasis: building a framework. Cell *127*, 679–695.

Hiratsuka, S., Watanabe, A., Aburatani, H., and Maru, Y. (2006). Tumour-mediated upregulation of chemoattractants and recruitment of myeloid cells predetermines lung metastasis. Nat. Cell Biol. *8*, 1369–1375.

Hohl, T.M., Rivera, A., Lipuma, L., Gallegos, A., Shi, C., Mack, M., and Pamer, E.G. (2009). Inflammatory monocytes facilitate adaptive CD4 T cell responses during respiratory fungal infection. Cell Host Microbe *6*, 470–481.

Joyce, J.A., and Pollard, J.W. (2009). Microenvironmental regulation of metastasis. Nat. Rev. Cancer *9*, 239–252.

Kim, S., Takahashi, H., Lin, W.W., Descargues, P., Grivennikov, S., Kim, Y., Luo, J.L., and Karin, M. (2009). Carcinoma-produced factors activate myeloid cells through TLR2 to stimulate metastasis. Nature *457*, 102–106.

Kuziel, W.A., Morgan, S.J., Dawson, T.C., Griffin, S., Smithies, O., Ley, K., and Maeda, N. (1997). Severe reduction in leukocyte adhesion and monocyte extravasation in mice deficient in CC chemokine receptor 2. Proc. Natl. Acad. Sci. USA *94*, 12053–12058.

Läubli, H., and Borsig, L. (2010). Selectins promote tumor metastasis. Semin. Cancer Biol. *20*, 169–177.

Läubli, H., Stevenson, J.L., Varki, A., Varki, N.M., and Borsig, L. (2006). L-selectin facilitation of metastasis involves temporal induction of Fut7-dependent ligands at sites of tumor cell arrest. Cancer Res. *66*, 1536–1542.

Läubli, H., Spanaus, K.S., and Borsig, L. (2009). Selectin-mediated activation of endothelial cells induces expression of CCL5 and promotes metastasis through recruitment of monocytes. Blood *114*, 4583–4591.

Leuschner, F., Dutta, P., Gorbatov, R., Novobrantseva, T.I., Donahoe, J.S., Courties, G., Lee, K.M., Kim, J.I., Markmann, J.F., Marinelli, B., et al. (2011). Therapeutic siRNA silencing in inflammatory monocytes in mice. Nat. Biotechnol. *29*, 1005–1010.

Loberg, R.D., Ying, C., Craig, M., Day, L.L., Sargent, E., Neeley, C., Wojno, K., Snyder, L.A., Yan, L., and Pienta, K.J. (2007). Targeting CCL2 with systemic delivery of neutralizing antibodies induces prostate cancer tumor regression in vivo. Cancer Res. *67*, 9417–9424.

Lu, X., and Kang, Y. (2009). Chemokine (C-C motif) ligand 2 engages CCR2+ stromal cells of monocytic origin to promote breast cancer metastasis to lung and bone. J. Biol. Chem. *284*, 29087–29096.

Mantovani, A., and Sica, A. (2010). Macrophages, innate immunity and cancer: balance, tolerance, and diversity. Curr. Opin. Immunol. *22*, 231–237.

McIntyre, T.M., Prescott, S.M., Weyrich, A.S., and Zimmerman, G.A. (2003). Cell-cell interactions: leukocyte-endothelial interactions. Curr. Opin. Hematol. *10*, 150–158.

Mellado, M., Rodríguez-Frade, J.M., Aragay, A., del Real, G., Martín, A.M., Vila-Coro, A.J., Serrano, A., Mayor, F., Jr., and Martínez-A, C. (1998). The chemokine monocyte chemotactic protein 1 triggers Janus kinase 2 activation and tyrosine phosphorylation of the CCR2B receptor. J. Immunol. *161*, 805–813.

Mildner, A., Mack, M., Schmidt, H., Brück, W., Djukic, M., Zabel, M.D., Hille, A., Priller, J., and Prinz, M. (2009). CCR2+Ly-6Chi monocytes are crucial for the effector phase of autoimmunity in the central nervous system. Brain *132*, 2487–2500.

Mishra, P., Banerjee, D., and Ben-Baruch, A. (2011). Chemokines at the crossroads of tumor-fibroblast interactions that promote malignancy. J. Leukoc. Biol. *89*, 31–39.

Mizutani, K., Sud, S., McGregor, N.A., Martinovski, G., Rice, B.T., Craig, M.J., Varsos, Z.S., Roca, H., and Pienta, K.J. (2009). The chemokine CCL2 increases prostate tumor growth and bone metastasis through macrophage and osteoclast recruitment. Neoplasia *11*, 1235–1242.

O'Hayre, M., Salanga, C.L., Handel, T.M., and Allen, S.J. (2008). Chemokines and cancer: migration, intracellular signalling and intercellular communication in the microenvironment. Biochem. J. *409*, 635–649.

Peinado, H., Lavotshkin, S., and Lyden, D. (2011). The secreted factors responsible for pre-metastatic niche formation: old sayings and new thoughts. Semin. Cancer Biol. *21*, 139–146.

Qian, B.Z., and Pollard, J.W. (2010). Macrophage diversity enhances tumor progression and metastasis. Cell *141*, 39–51.

Qian, B.Z., Li, J., Zhang, H., Kitamura, T., Zhang, J., Campion, L.R., Kaiser, E.A., Snyder, L.A., and Pollard, J.W. (2011). CCL2 recruits inflammatory monocytes to facilitate breast-tumour metastasis. Nature *475*, 222–225.

Reutershan, J., Morris, M.A., Burcin, T.L., Smith, D.F., Chang, D., Saprito, M.S., and Ley, K. (2006). Critical role of endothelial CXCR2 in LPS-induced neutrophil migration into the lung. J. Clin. Invest. *116*, 695–702.

Salcedo, R., Ponce, M.L., Young, H.A., Wasserman, K., Ward, J.M., Kleinman, H.K., Oppenheim, J.J., and Murphy, W.J. (2000). Human endothelial cells express CCR2 and respond to MCP-1: direct role of MCP-1 in angiogenesis and tumor progression. Blood *96*, 34–40.

Sanz-Moreno, V., Gaggioli, C., Yeo, M., Albrengues, J., Wallberg, F., Viros, A., Hooper, S., Mitter, R., Féral, C.C., Cook, M., et al. (2011). ROCK and JAK1 signaling cooperate to control actomyosin contractility in tumor cells and stroma. Cancer Cell *20*, 229–245.

Sawanobori, Y., Ueha, S., Kurachi, M., Shimaoka, T., Talmadge, J.E., Abe, J., Shono, Y., Kitabatake, M., Kakimi, K., Mukaida, N., and Matsushima, K. (2008). Chemokine-mediated rapid turnover of myeloid-derived suppressor cells in tumor-bearing mice. Blood *111*, 5457–5466.

Soria, G., Ofri-Shahak, M., Haas, I., Yaal-Hahoshen, N., Leider-Trejo, L., Leibovich-Rivkin, T., Weitzenfeld, P., Meshel, T., Shabtai, E., Gutman, M., and Ben-Baruch, A. (2011). Inflammatory mediators in breast cancer: coordinated expression of TNFα & IL-1β with CCL2 & CCL5 and effects on epithelial-to-mesenchymal transition. BMC Cancer *11*, 130.

Tremblay, P.L., Auger, F.A., and Huot, J. (2006). Regulation of transendothelial migration of colon cancer cells by E-selectin-mediated activation of p38 and ERK MAP kinases. Oncogene *25*, 6563–6573.

Yoshidome, H., Kohno, H., Shida, T., Kimura, F., Shimizu, H., Ohtsuka, M., Nakatani, Y., and Miyazaki, M. (2009). Significance of monocyte chemoattractant protein-1 in angiogenesis and survival in colorectal liver metastases. Int. J. Oncol. *34*, 923–930.

Yu, H., Pardoll, D., and Jove, R. (2009). STATs in cancer inflammation and immunity: a leading role for STAT3. Nat. Rev. Cancer *9*, 798–809.

Zhang, J., Patel, L., and Pienta, K.J. (2010). CC chemokine ligand 2 (CCL2) promotes prostate cancer tumorigenesis and metastasis. Cytokine Growth Factor Rev. *21*, 41–48.

Zijlmans, H.J., Fleuren, G.J., Baelde, H.J., Eilers, P.H., Kenter, G.G., and Gorter, A. (2006). The absence of CCL2 expression in cervical carcinoma is associated with increased survival and loss of heterozygosity at 17q11.2. J. Pathol. *208*, 507–517.

Cancer Cell
Article

A Distinct Replication Fork Protection Pathway Connects Fanconi Anemia Tumor Suppressors to RAD51-BRCA1/2

Katharina Schlacher,[1,2,*] Hong Wu,[2,3] and Maria Jasin[1,*]
[1]Developmental Biology Program, Memorial Sloan-Kettering Cancer Center, New York, NY 10065, USA
[2]Department of Molecular and Medical Pharmacology
[3]Institute for Molecular Medicine
University of California, Los Angeles, CA 90095, USA
*Correspondence: schlachk@mskcc.org (K.S.), m-jasin@ski.mskcc.org (M.J.)
DOI 10.1016/j.ccr.2012.05.015

SUMMARY

Genes mutated in patients with Fanconi anemia (FA) interact with the DNA repair genes *BRCA1* and *BRCA2/FANCD1* to suppress tumorigenesis, but the molecular functions ascribed to them cannot fully explain all of their cellular roles. Here, we show a repair-independent requirement for FA genes, including *FANCD2*, and *BRCA1* in protecting stalled replication forks from degradation. Fork protection is surprisingly rescued in *FANCD2*-deficient cells by elevated RAD51 levels or stabilized RAD51 filaments. Moreover, *FANCD2*-mediated fork protection is epistatic with *RAD51* functions, revealing an unanticipated fork protection pathway that connects FA genes to *RAD51* and the *BRCA1/2* breast cancer suppressors. Collective results imply a unified molecular mechanism for repair-independent functions of FA, RAD51, and BRCA1/2 proteins in preventing genomic instability and suppressing tumorigenesis.

INTRODUCTION

Replication stalling is central to the mechanism of efficacy of many commonly used cancer chemotherapeutics. These include agents that induce DNA lesions, such as camptothecin and cisplatin, as well as those that stall replication progression by perturbing the composition and/or concentration of nucleotide pools, such as gemcitabine and 5-fluorouracil (Stathis and Moore, 2010). Tumor suppressors mutated in Fanconi anemia (FA) are crucial for preventing genomic instability upon replication stalling (Moldovan and D'Andrea, 2009), thus providing a context in which to understand cellular responses to perturbed DNA replication.

The FA pathway involves monoubiquitination of FANCD2-FANCI proteins by the FA core complex in addition to a parallel or downstream function of homologous recombination (HR) proteins, including the breast cancer suppressor BRCA2/FANCD1 (Moldovan and D'Andrea, 2009) (Figure 1A). Together, FA and HR proteins suppress cellular sensitivity to DNA replication poisons that induce DNA interstrand crosslinks (ICLs), such that mechanistic studies have largely focused on the connection between these proteins in the context of ICL repair. In vitro studies have demonstrated that FANCD2 promotes break formation at ICLs and translesion synthesis by an unknown mechanism, while HR proteins act downstream of ICL processing in repairing the collapsed fork caused by strand breakage (Long et al., 2011).

Paradoxical to these functions in promoting DNA breakage and subsequent break repair, the FA/BRCA protein network is also highly activated by replication stalling from depletion of nucleotide pools, such as from hydroxyurea (HU), which does not elicit physical DNA lesions that require removal (Howlett et al., 2005; Naim and Rosselli, 2009), as well from other lesions (Langevin et al., 2011; Rosado et al., 2011), including UV

Significance

Replication stalling is at the heart of many chemotherapeutic agents, including those that limit nucleotide incorporation into DNA (e.g., gemcitabine) and those that block replication fork progression (e.g., camptothecin and platinum drugs). Replication stalling agents activate the FA/BRCA tumor suppressor pathway and cause genomic instability in cells lacking pathway components. We report here an unexpected function of the FA/BRCA pathway in protecting stalled replication forks from nucleolytic degradation. This finding provides a cellular understanding of expanded roles of these tumor suppressors with significant implications for ongoing research efforts in understanding tumor susceptibility in patients with FA, therapeutic resistance, and emerging therapeutic strategies.

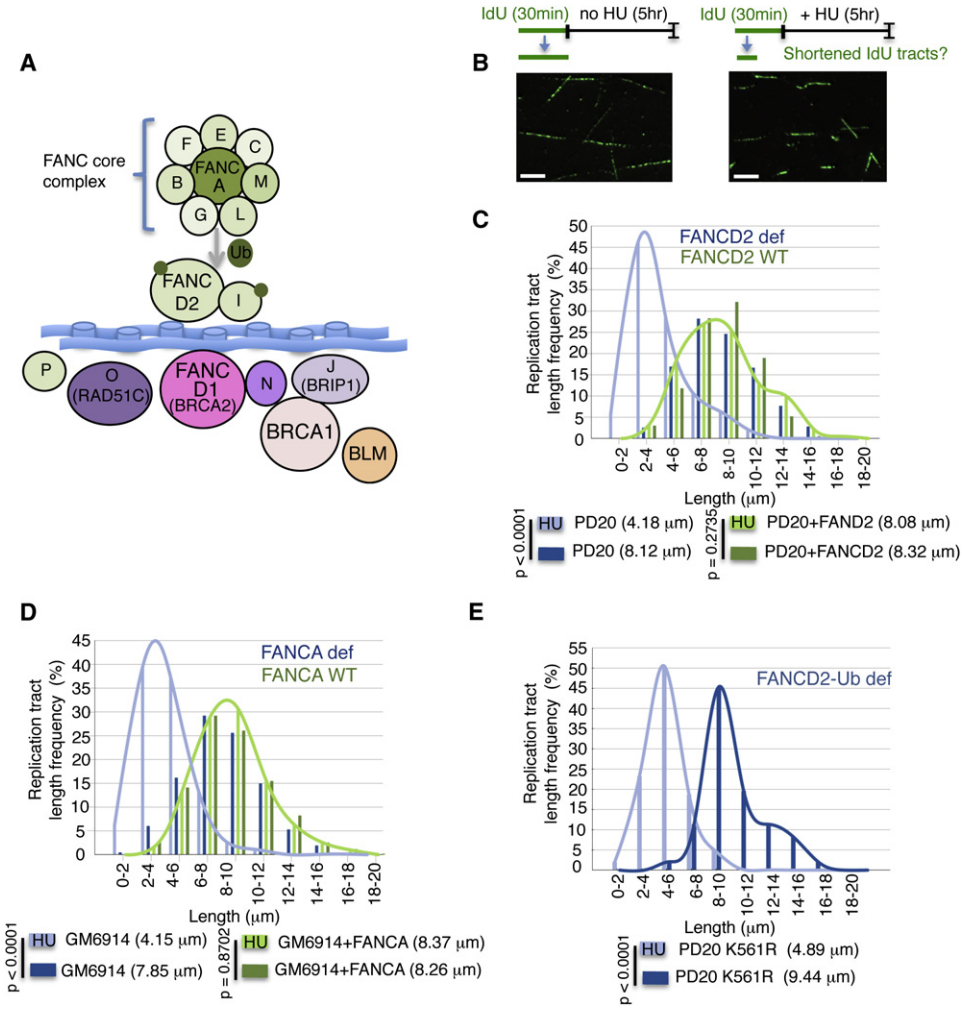

Figure 1. FA/BRCA Gene Network Protects Stalled DNA Replication Forks

(A) A graphical representation of the FA/BRCA gene network depicts FA core complex proteins (FANCA, B, C, E, F, G, L, M), which promote the mono-ubiquitination (Ub) of FANCD2 and FANCI. BRCA-related proteins (FANCD1/BRCA2, FANCN/PALB2, and FANCJ/BRIP1) and recently identified FANCO/RAD51C and FANCP/SLX4 are not required for FANCD2–FANCI monoubiquitination and act downstream or in parallel to canonical FA proteins. While BRCA1 is part of the FA/BRCA gene network, BRCA1 mutations have not been found in FA patients. BLM interacts with the gene network, but its loss causes a distinct syndrome.

(B) Graphical sketch of experimental design of fork protection assay. Lengths of nascent replication tracts (labeled with IdU) are measured by DNA spreading after 5 hr of replication stalling with HU. Representative DNA fiber images are given. Scale bars (white) correspond to 4 μm.

(C) Preformed IdU tract lengths measuring replication fork stability by DNA spreading in patient-derived FANCD2-defective PD20 cells, but not cells complemented with the wild-type protein, shorten with HU. Median IdU tract lengths are given in parentheses here and in subsequent figures.

(D) Nascent tract length distribution curve measured by DNA spreading in patient-derived FANCA-defective GM6914 cells show nascent strand shortening with HU, unlike cells complemented with the wild-type protein.

(E) Nascent tract length distribution curve measured by DNA spreading in PD20 cells expressing the FANCD2 K561R mutant defective for monoubiquitination show nascent strand shortening with HU.

See also Figure S1.

damage, which primarily is removed by other repair pathways. Moreover, FANCD2 functionally interacts with the RAD51-mediator protein BRCA2 (Hussain et al., 2004; Wang et al., 2004). However, FA proteins are not canonical HR factors, as cells derived from FA patients are not severely defective in HR repair of double-strand breaks (Nakanishi et al., 2011). Thus, the functional relationship between FA and HR proteins during replication stalling remains enigmatic. The importance of replication stalling to tumor development is underscored by the observation that oncogene activation in general induces replication stress (Bartkova et al., 2006), and specifically by the recent finding that precancerous oncogene expression reduces nucleotide pools (Bester et al., 2011).

To address general roles of FA/BRCA proteins during perturbed replication and to provide a more accurate and complete appreciation of how these proteins function in replication fork fidelity with implications for therapeutic strategies, we examined the functional connection between FANCD2 and HR proteins at

replication forks stalled by nucleotide depletion with HU as well as replication stalling chemotherapeutic agents.

RESULTS

Fanconi Anemia Proteins Protect Stalled DNA Replication Forks

BRCA2 and RAD51 can act in replication fork stabilization independent of double-strand break repair (Hashimoto et al., 2010; Lomonosov et al., 2003; Schlacher et al., 2011). Specifically, RAD51 recombinase filament stabilization by the BRCA2 C terminus (C-ter) protects against nucleolytic degradation of stalled replication forks. Stalled replication forks that are not protected by BRCA2 lead to chromosomal instability. We reasoned that if this distinct mechanism is involved in disease suppression, defects may be found associated with disease susceptibility genes other than *BRCA2*. Because *BRCA2* is a suppressor of FA and as such is also known as *FANCD1*, we tested a possible function for FA genes in fork stability. Specifically, nascent replication tracts were IdU-labeled before replication stalling with hydroxyurea (HU) (Figure 1B); the retention of the label after HU treatment serves as a measure for fork stability using DNA fiber spreading (Schlacher et al., 2011).

To test an involvement of FA proteins in protecting stalled replication forks, we monitored the stability of nascent replication tracts in FA patient-derived cells defective in FANCD2. Replication stalling causes a dramatic shortening of the median IdU tract length in FANCD2-defective PD20 cells compared either to mock treatment (Figure 1C, 4.18 μm and 8.12 μm, $p < 0.0001$) or to cells complemented with FANCD2 (Figure 1C, 8.08 μm and 8.32 μm, $p = 0.2735$). These results with FANCD2-defective cells are similar to those obtained with BRCA2 (FANCD1)-defective patient cells (Figure S1 available online) and with BRCA2-defective rodent cells (Schlacher et al., 2011).

FA pathway activation involves monoubiquitination of the FANCD2/FANCI proteins by FA core complex proteins (D'Andrea, 2010). Similar to FANCD2-defective cells, we found that patient-derived GM6914 cells defective in the core complex protein FANCA show degradation of newly synthesized DNA strands when treated with HU, but not with mock treatment (Figure 1D, 4.15 μm and 7.85 μm, $p < 0.0001$). Yet nascent strands are maintained intact in FANCA-complemented cells (Figure 1D, 8.37 μm and 8.26 μm, $p = 0.3702$). This suggests a functional requirement for FA proteins upstream of FANCD2 monoubiquitination in maintaining fork stability.

To directly assess if fork protection requires FA pathway activation by monoubiquitination of FANCD2, we analyzed nascent replication tracts in PD20 cells expressing mutant FANCD2-K561R incapable of being ubiquitinated (Ub) (Garcia-Higuera et al., 2001). We found that these cells fail to maintain the integrity of nascent DNA tracts during replication stalling with HU (Figure 1E, 4.89 μm and 9.44 μm, $p < 0.0001$). Thus, in addition to BRCA2, fork stabilization requires FA pathway activation through FANCD2 monoubiquitination.

FA Pathway Suppresses Genomic Instability When Replication Is Stalled

We tested the cellular consequence of replication stalling by nucleotide depletion on FA-defective cells. Metaphase spreads of FANCA-defective GM6914 cells show significantly elevated levels of spontaneous chromosomal aberrations compared to cells that are complemented with wild-type FANCA (Figure 2A, $p = 0.0107$). Upon treatment with HU, the load of DNA breaks and radial structures in GM6914 cells considerably increases from an average of 0.6 to 2.5 aberrations per cell (Figure 2A, $p < 0.0001$), while only a moderate elevation is observed in FANCA-complemented cells from 0.34 to 0.72 aberrations per cell (Figure 2A, $p = 0.0836$). Thus, replication stalling by nucleotide depletion selectively elevates genomic instability in FA-defective cells.

Genomic instability upon HU, however, is not accompanied by acute cell death. While FANCA-defective cells are exquisitely sensitive to ICL-inducing reagents such as mitomycin-C (MMC, Figure S2A), they show no substantial difference in cellular survival rates compared to FANCA-proficient cells upon treatment with HU (Figure 2B). Interestingly, when we tested BRCA2/FANCD1-defective cells for MMC sensitivity, we found that cells containing the BRCA2 S3291A variant, which is proficient for double-strand break repair but cannot protect stalled forks, shows only moderate sensitivity to high concentrations of MMC compared to cells with BRCA2 truncation (Figure S2B), suggesting two separable functions for BRCA2/FANCD1 during ICL repair, one of which involves replication fork protection.

Other replication stalling agents such as the chemotherapeutics gemcitabine (Figure 2C), which inhibits replication elongation, or camptothecin (Figure S2C), a replication poison that prevents DNA ligation and elicits a roadblock to replication by covalently locking topoisomerase I to DNA, show similar results compared to HU with no to very mild acute cellular death. These results suggest that immediate cell death is not an obligate immediate consequence of replication stalling in FA-defective cells.

We next examined if FA proteins are required for fork protection when replication is stalled by agents other than HU. Replication tracts are maintained intact in FANCA-proficient cells when treated with the chemotherapeutic gemcitabine (Figure 2D, $p = 0.612$ with and without gemcitabine). In contrast, the nascent strands shorten dramatically in FANCA-defective GM6914 cells with gemcitabine (Figure 2D, $p < 0.0001$). Likewise, exposure to camptothecin shortens replication tracts in FA-defective cells (Figure 2E, $p < 0.0001$). Thus, replication stalling caused by various agents elicit fork instability in FANCA-defective cells.

Parallel and Downstream Functions of FA-Associated Proteins

Several proteins have been identified to associate with FA components, although they are not considered to be FA proteins as mutations have not been found as yet in FA patients. The BRCA1 breast cancer suppressor associates in complexes with several FANC proteins, including FANCD2 and BRCA2 (Moldovan and D'Andrea, 2009). We found that BRCA1-defective mouse embryonic stem (ES) cells show shortened nascent tracts with replication stalling (Figure 3A, 5.52 μm and 8.88 μm, $p < 0.0001$), unlike cells with a functional BRCA1 (Figure 3A, 8.82 μm and 8.73 μm, $p = 0.831$). Thus, both BRCA1 and BRCA2—the major hereditary breast cancer suppressors—stabilize replication forks, providing a mechanistic link between tumor suppression and the protection of stalled replication forks.

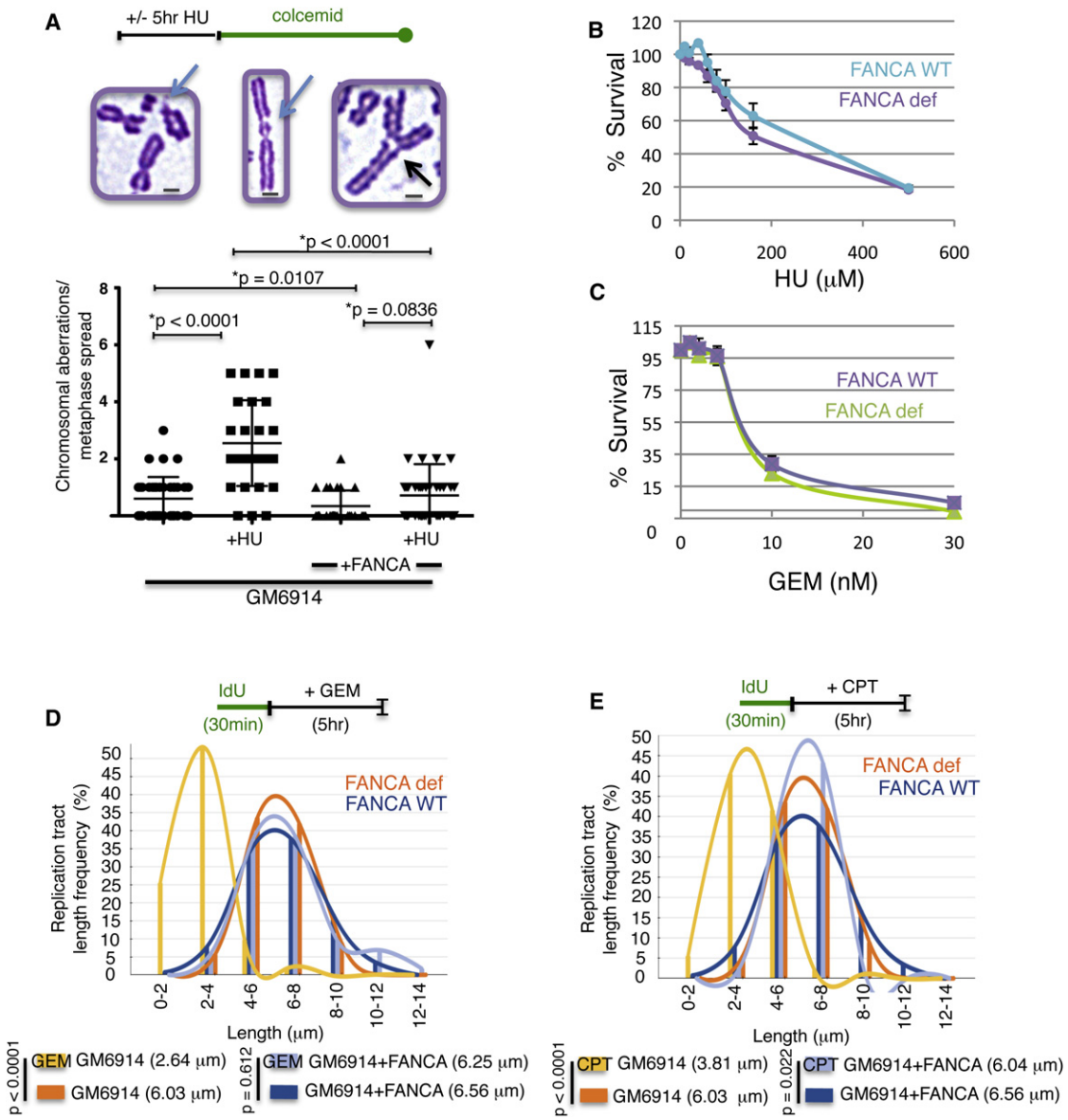

Figure 2. FA Pathway Suppresses Genomic Instability upon Replication Stalling

(A) Chromosomal aberrations measured by metaphase chromosome spreads with FANCA-deficient and –complemented GM6914 cells with HU (± SD, n = 40). Representative images of chromosomal aberrations of metaphase chromosomes are given. Scale bars (gray) correspond to 2 μm.

(B) Cell survival analysis of FANCA-defective, patient-derived GM6914 cells and cells complemented with FANCA upon continuous HU treatment (± SEM, n = 4).

(C) Cell survival analysis of FANCA-defective cells and cells complemented with FANCA upon continuous gemcitabine (GEM) treatment (± SEM, n = 3).

(D and E) Nascent tract length distribution curves measured by DNA spreading in patient-derived FANCA-defective GM6914 cells and cells complemented with the wild-type protein with gemcitabine [GEM, (D)] and camptothecin [CPT, (E)].

See also Figure S2.

BLM helicase interacts with both FA and BRCA networks (Chu and Hickson, 2009; Deans and West, 2009; Moldovan and D'Andrea, 2009). Loss of BLM causes Bloom syndrome, a developmental disorder with high cancer predisposition (Chu and Hickson, 2009), but is phenotypically distinct from FA. On the cellular level, BLM, in partnership with TopIIIα, decatenates fully replicated chromosomes (Chu and Hickson, 2009). We used mouse ES cells expressing BLM under negative doxycycline control (Figure 3B, $Blm^{tet/tet}$ inset) to assess if BLM plays a role in the protection of stalled forks from degradation. BLM-depleted cells maintain IdU tracts intact when exposed to HU (Figure 3B, $Blm^{tet/tet}$+DOX; 7.93 μm and 7.72 μm, p = 0.338), similar to cells expressing BLM (Figure 3B, $Blm^{tet/tet}$; 8.09 μm and 8.12 μm, p = 0.831). Thus, unlike BRCA and FANC deficiency, loss of BLM does not result in degradation of stalled replication forks.

BLM helicase, however, is required for efficient replication restart after HU (Davies et al., 2007) (Figure S3A). Related to

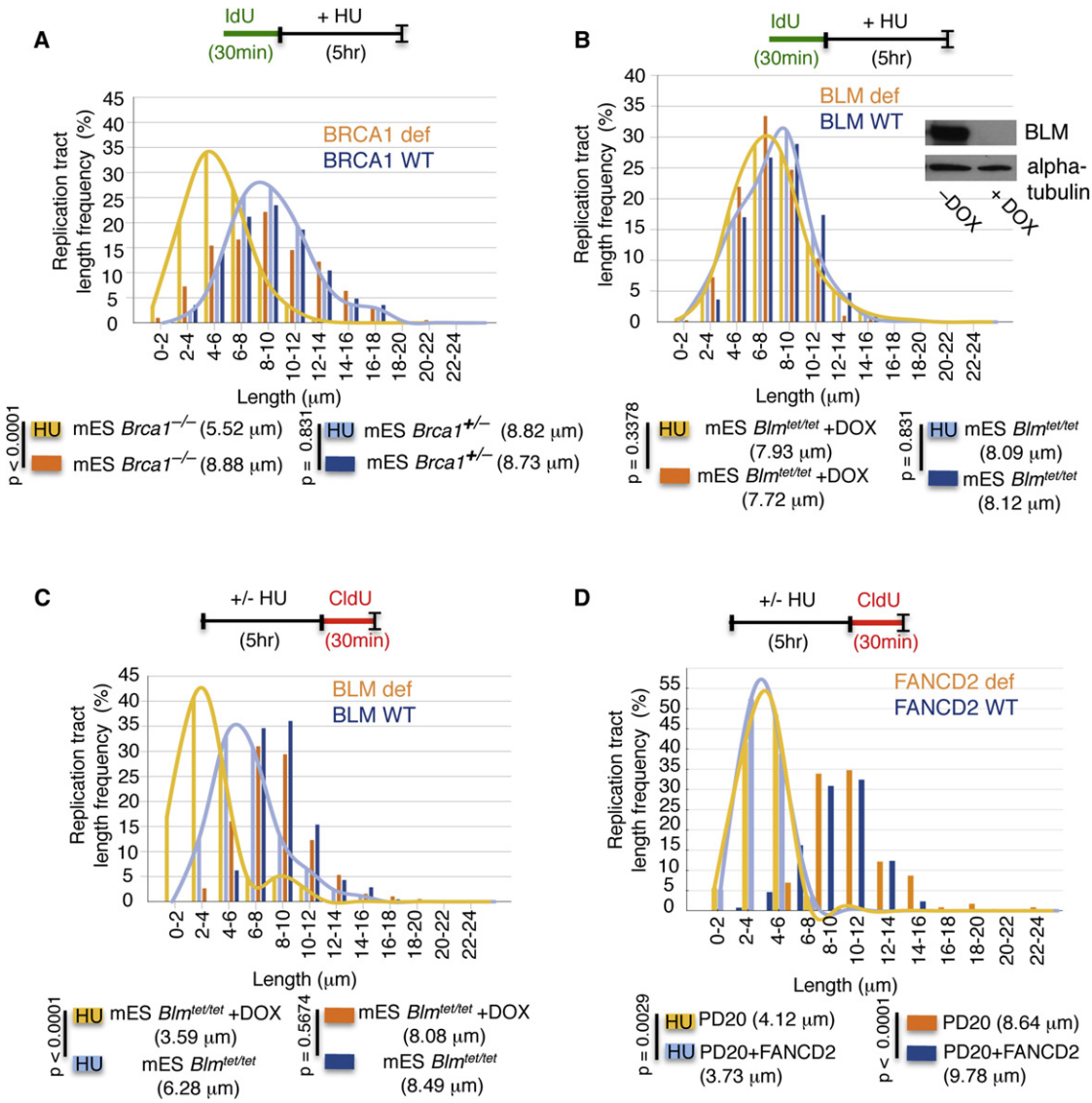

Figure 3. Parallel and Downstream Functions of FA-Associated Proteins

(A) Replication fork stability analysis by DNA spreading of preformed IdU tracts in BRCA1-deficient mouse ES cells (mES *Brca1*$^{-/-}$) and mouse ES cells containing wild-type BRCA1 (mES *Brca1*$^{+/-}$) with HU. Median IdU tract lengths are given in parenthesis here and in subsequent graph panels.

(B) Replication fork stability analysis by DNA spreading of preformed IdU tracts in BLM-depleted mouse ES cells with negative doxycycline (DOX) control of BLM expression (mES *Blm*$^{tet/tet}$ +DOX) and BLM proficient ES cells (mES *Blm*$^{tet/tet}$). See inset, western blot for BLM expression.

(C) Replication recovery analysis after fork stalling with HU as measured by DNA spreading of CldU replication tracts in BLM-depleted (mES *Blm*$^{tet/tet}$ +DOX) and BLM proficient mouse ES cells (mES *Blm*$^{tet/tet}$). Median CldU tract lengths are given in parentheses here and in subsequent graph panel.

(D) Replication recovery analysis (CldU tract length) after fork stalling is in FANCD2-defective and in FANCD2-complemented PD20 cells.

See also Figure S3.

this, we find that BLM-depleted cells have a defect in replication recovery as measured by substantially shorter CldU tracts after exposure to HU when compared with cells expressing wild-type BLM (Figure 3C, 3.59 μm and 6.28 μm, $p < 0.0001$ and Figure S3B). Thus, BLM deficiency results in defects in replication recovery that can be observed by measuring either the length of the replication tracts (Figure 3C) or the frequency of forks that restart (Davies et al., 2007; Figure S3A).

Because BLM interacts with both FA and BRCA networks, we further tested FA (Figure 3D and Figure S3C) and BRCA1-defective cells (Figure S3D) for replication recovery after stalling with HU. Similar to BRCA2 deficiency (Schlacher et al., 2011) but in contrast to BLM deficiency (Figure 3C), no defect in replication recovery is observed: replication tracts formed after HU are similarly short in both FANCD2-defective and -complemented PD20 cells after exposure to HU (Figure 3, 4.12 μm and 3.73 μm, $p = 0.0029$ and Figure S3E). Similar results were obtained for FANCA (Figures S3C and S3F) and BRCA1-defective cells (Figures S3D and S3G). These data suggest that BLM acts downstream of the BRCA and FANC proteins, subsequent to the protection of

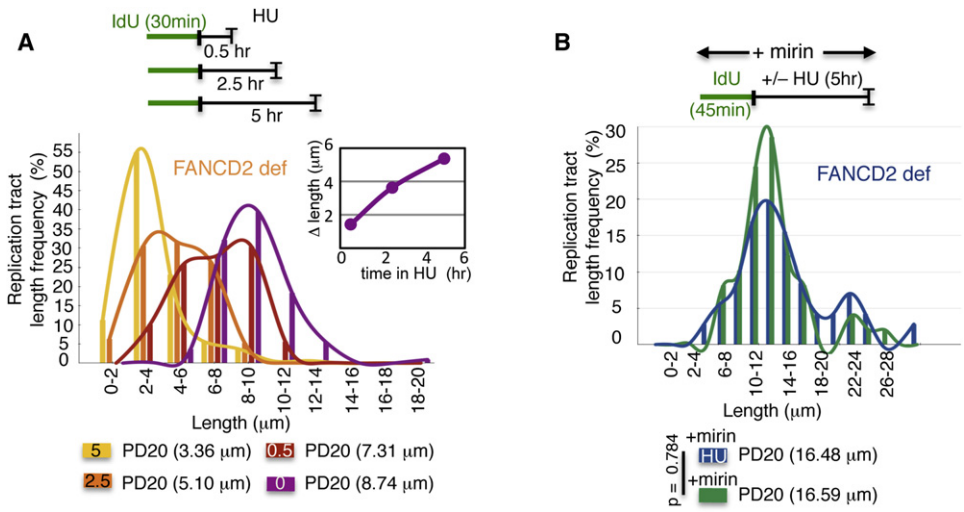

Figure 4. FA Genes Protect Against MRE11-Dependent Fork Degradation

(A) Replication fork stability analysis by DNA spreading of IdU replication tracts in FANCD2-deficient PD20 cells during various exposure times to HU. Inset; the rate of IdU tract length change is 0.87 μm/hr, estimated to be ~2.2 kb/hr.

(B) Replication fork stability analysis by DNA spreading of IdU replication tracts in FANCD2-deficient PD20 with chemical inhibition of MRE11 nuclease by treatment with mirin, with and without HU.

See also Figure S4.

stalled forks, perhaps in decatenation of structures elicited by positive supercoiling ahead of the fork.

FA Genes Protect Against MRE11-Dependent Fork Degradation

MRE11 nuclease promotes degradation of stalled replication forks when either BRCA2 or RAD51 function is impaired (Hashimoto et al., 2010; Schlacher et al., 2011). We found that degradation in FANCD2-defective cells occurs at ~2.2 kb/hr (Figure 4A, inset), which is reminiscent of the slow kinetics of MRE11-dependent degradation in BRCA2-defective cells (Schlacher et al., 2011). Moreover, double-labeling experiments suggest that both leading and lagging strand degradation occurs, as the most recently incorporated nucleotides are excised first (Figures S4A–S4C). These results suggest that MRE11 nuclease, which promotes both 3′–5′ and 5′–3′ end processing (Williams et al., 2008), mediates the nascent replication tract shortening in FA-defective cells. We chemically inhibited MRE11 nuclease with mirin (Dupré et al., 2008), and found that it blocks nascent tract shortening upon fork stalling with HU (Figure 4B, 16.46 μm and 16.59 μm, p = 0.738). Therefore, FANCD2, like BRCA2 and RAD51, protects nascent strands at stalled replication forks from degradation by MRE11.

Functional Interaction of FA and RAD51 Proteins at Stalled Forks

RAD51 was recently shown to act downstream of FANCD2 during ICL repair (Long et al., 2011). Yet, RAD51 is recruited to ICLs prior to FANCD2 such that a second function upstream of ICL incision could not be excluded (Long et al., 2011). We therefore sought to address whether *FANCD2* acts in synergy with RAD51 when protecting stalled forks or whether they act epistatically, within a common pathway. To test this, we expressed the BRC4 peptide (Saeki et al., 2006), which suppresses DNA binding of RAD51 and thus disrupts RAD51 filaments.

Replication tracts are dramatically shortened upon HU in FANCD2-complemented PD20 cells expressing the BRC4 peptide (Figure 5A, 3.86 μm and 8.18 μm $p < 0.0001$), demonstrating efficient RAD51 depletion from filaments leading to fork destabilization. Moreover, RAD51 depletion in PD20 cells complemented with FANCD2 mimics the replication tract shortening seen with deficiency of FANCD2 itself (compare Figure 5A, 3.86 μm, and Figure 5B, 4.17 μm, $p = 0.104$). Although replication tracts are significantly shorter in FANCD2-defective cells with HU compared to without HU (Figure 5B, 4.17 μm and 8.9 μm, $p < 0.0001$), the tract shortening is not exacerbated by depletion of RAD51 from filaments (Figure 5B, 4.11 μm, $p = 0.324$). Taken together, the data suggest that *RAD51* and *BRCA2* act in epistasis with FANCD2 for replication fork stabilization.

Given that perturbing RAD51 in FANCD2-defective cells results in a phenotype comparable to FANCD2 deficiency alone, we hypothesized that FANCD2 may play a role in RAD51 filament stabilization subsequent to RAD51 loading onto DNA. To gain insight into the mechanism of FANCD2-mediated fork stabilization, we expressed the RAD51 K133R mutant. This mutant is devoid of ATPase activity required for dissociation from DNA (Morrison et al., 1999), and thus forms hyperstable filaments. We found that RAD51 K133R renders IdU tracts in PD20 cells resistant to degradation, maintaining replication tract lengths comparable to those observed in PD20 cells expressing wild-type FANCD2 (compare Figure 5C, 7.95 μm, and Figure 5A, 8.18 μm, $p = 0.825$). Thus, fork instability caused by FANCD2 deficiency can be compensated for by RAD51 filament stabilization.

Elevated RAD51 protein levels are often found in tumor cells (Raderschall et al., 2002b; Brown and Holt, 2009), which

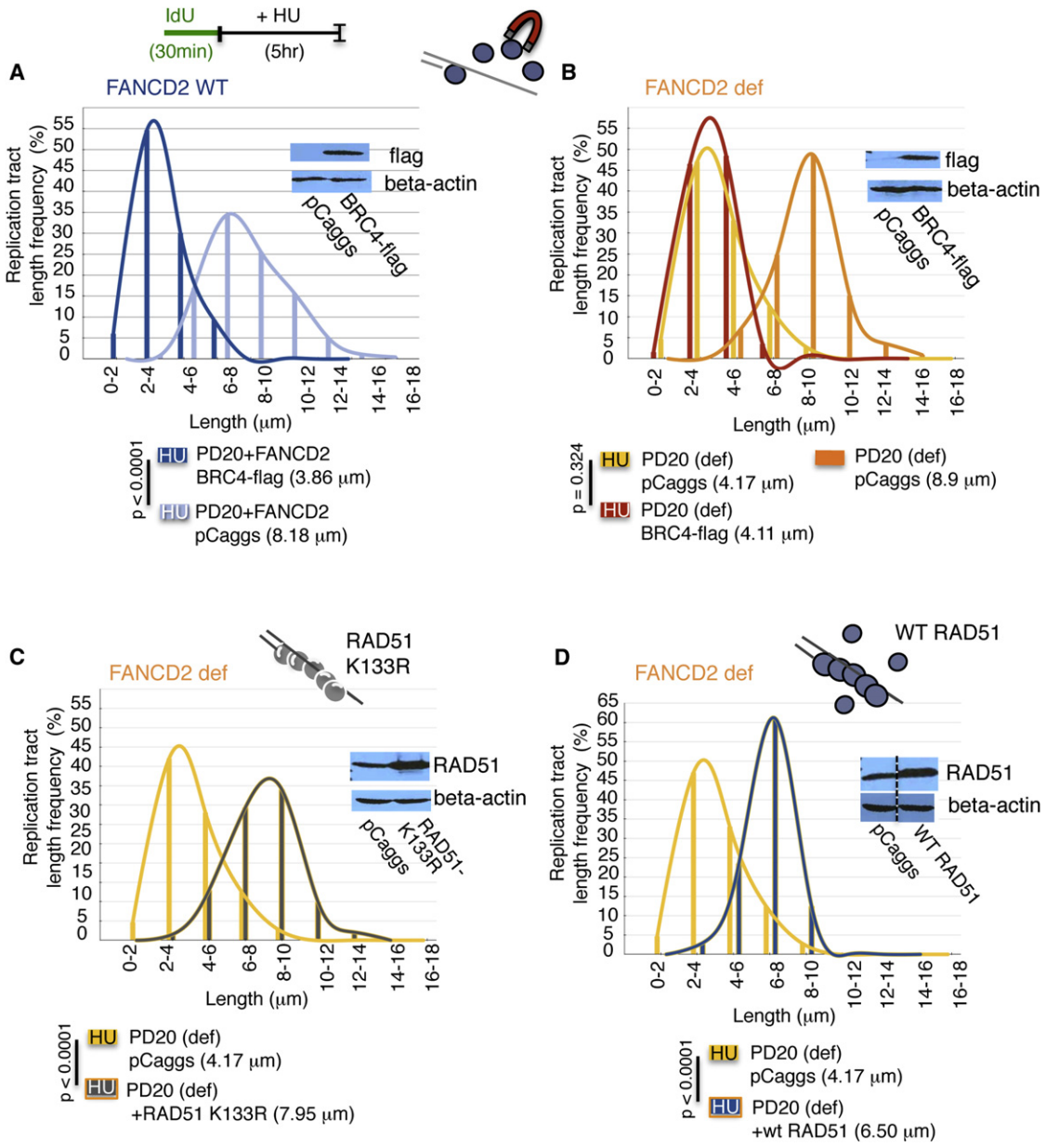

Figure 5. Functional Interaction of FA and RAD51 Proteins at Stalled Forks

(A) Replication fork stability analysis by DNA spreading of IdU replication tracts in FANCD2-complemented PD20 cells expressing flag-tagged BRC4-peptide (see western blot, inset), which disrupts RAD51 binding to DNA.

(B) Replication fork stability analysis by DNA spreading of IdU replication tracts in FANCD2-deficient PD20 cells expressing flag-tagged BRC4-peptide (see western blot, inset).

(C) Replication fork stability analysis by DNA spreading of IdU replication tracts in FANCD2-deficient PD20 cells expressing mutant RAD51 K133R (see western blot, inset), which forms stable filaments, upon fork stalling with HU.

(D) Replication fork stability analysis by DNA spreading of IdU replication tracts in FANCD2-deficient PD20 cells overexpressing wild-type (WT) RAD51 (see western blot, inset), which promotes filament assembly, upon fork stalling with HU.

perhaps drives more stable filament formation (Raderschall et al., 2002a), suggesting the potential for even wild-type RAD51 to effect fork protection. We therefore examined the effect of higher levels of wild-type RAD51 on replication tract stability in FA-defective cells. Strikingly, we found that overexpression of wild-type RAD51 in FANCD2-defective PD20 cells can partially rescue replication fork instability upon HU and primarily maintain replication tracts intact (Figure 5D, 4.17 and 6.50 without and with increased RAD51 expression, $p < 0.0001$). Taken together, the data show that FANCD2 and RAD51 support each other at replication forks such that both FANCD2 and RAD51 positively regulate replication tract stability.

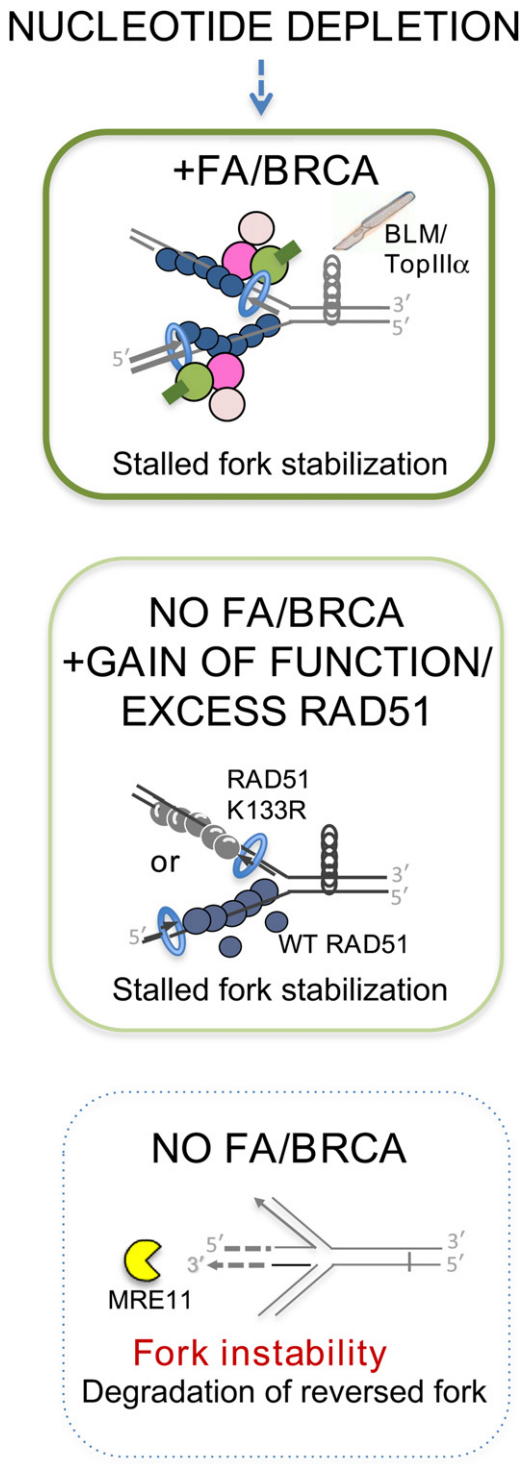

Figure 6. Model of *FA/BRCA* Gene Network Functions in Replication Fork Stability

Nucleotide depletion, as caused by oncogene activation or chemotherapeutic agents, stalls replication forks. FA/BRCA proteins stabilize RAD51 at stalled replication forks to protect nascent strands from MRE11-dependent degradation. RAD51 filament stabilization in the absence of FA/BRCA proteins is sufficient for fork protection. This can be achieved by gain of function mutant RAD51 or overexpression of wild-type RAD51, as commonly seen in tumor cells. BLM-TopIIIα acts downstream in the restart of stalled forks. Protein colors: BRCA2, pink; FANCD2, green; ubiquitin, dark green; BRCA1, light pink; wild-type RAD51, dark blue; RAD51 K133R, steel gray; PCNA, blue (doughnut); MRE11 yellow (pacman). BLM-TopIIIα, scalpel.
See also Figure S5.

DISCUSSION

Because of the exquisite sensitivity of FA genes to ICL lesions, most studies thus far have focused on their role in ICL repair. Yet, the FA machinery prevents genome instability and lethality caused by replication blocks other than ICLs with uncharacterized implications for tumorigenesis (Howlett et al., 2005; Langevin et al., 2011; Naim and Rosselli, 2009; Rosado et al., 2011). Here the discovery of a role for FANCD2-Ub in preventing degradation of nascent DNA strands in vivo independent of ICL processing complements and extends existing results. Notably, FANCD2-Ub functions epistatically with RAD51 at stalled forks within this distinct pathway, as does BRCA2, which provides a more complete understanding of how these proteins maintain replication fork fidelity in the context of ICL and other DNA stresses.

FANCD2 monoubiquitination involves an interaction with the replisome component proliferating cell nuclear antigen (PCNA) (Howlett et al., 2009). Because BRCA2/RAD51 functionally interacts with FANCD2 (Long et al., 2011; Wang et al., 2004) and BRCA2/RAD51 alone is insufficient for fork protection in the absence of FANCD2-Ub, a testable mechanistic model is that as part of a protein supercomplex FANCD2-Ub connects the BRCA and RAD51 proteins to replisome components to stabilize stalled forks and prevent fork collapse (Figure 6). This protection mechanism provides a functional explanation for the observations that upon replication stalling both BRCA1 and BRCA2 rapidly relocalize to replication foci containing PCNA (Chen et al., 1998). Moreover, FANCD2 colocalizes with PCNA and RAD51 to foci in response to HU (Hussain et al., 2004) and FANCD2 is found localized to sister chromatids upon replication stress (Naim and Rosselli, 2009). It recently was reported that an FA component stabilizes a specialized translesion synthesis (TLS) DNA polymerase at nuclear foci upon DNA damage (Kim et al., 2012). Thus, given the data and model presented here, it will be interesting to see if this polymerase stabilizing function could hold true for other DNA polymerases and in particular nonspecialized polymerases, because TLS polymerases are unlikely to be involved when replication is stalled without eliciting DNA lesions such as by HU.

Other FA proteins may be found to act in this distinct pathway of fork stabilization. FANCJ is important in processing DNA secondary structures at G-rich regions (Hiom, 2010). In the context of replication fork stability, disruption of such G-rich structures may be crucial to create single-strand DNA stretches long enough to support sufficiently stable RAD51 filaments. FANCP (SLX4) binds to several endonucleases implicated in ICL processing (Cybulski and Howlett, 2011). However, it is feasible that FANCP (SLX4) may have additional functions that support the structural maintenance of replication fork structures through Smc5/6 (Ohouo and Smolka, 2011), as how Smc5/6 promotes chromosome stability is largely unknown and it may have a role in the maintenance of undamaged chromosomes. Structural destabilization of replication forks and fork

degradation indeed provide feasible mechanisms for both spontaneous fork breakage and deletion mutations, both of which are hallmarks of FA-defective cells (Papadopoulo et al., 1990; Schroeder et al., 1964).

FA is a disease with life-threatening consequences on hematopoiesis, marked by stem cell attrition before the development of tumors. Consistent with a nonlethal phenotype during embryogenesis and the small stature of FA patients, we find that replication stalling does not elicit acute but only marginal cell death in FA-defective cells (Figure 2B). Yet, unprotected replication forks result in DNA damage as indicated by the marked increase in genomic aberrations in FA-defective cells upon treatment with HU (Figure 2A). As DNA damage has recently been shown to promote hematopoietic stem cell aging (Wang et al., 2012), we propose in particular that nonlethal DNA damage may promote hematopoietic stem cell attrition by accumulated differentiation rather than cell death. Nonlethal DNA damage in other tissues on the other hand could eventually promote tumorigensis by prolonged cellular exposure to mutagenesis without cell death and account for the high tumor susceptibility in FA patients. Thus, replication fork protection potentially provides a mechanism to resolve the apparent paradox involving the seemingly opposing phenotypes of stem cell death and mutagenesis promoting tumor predisposition.

Fork stabilization is likely also an important event during ICL repair, consistent with data demonstrating RAD51 recruitment to stalled forks before ICL processing (Long et al., 2011). Our observation that a variant of BRCA2/FANCD1 defective in fork protection sensitizes cells to ICLs, however to a much lesser extent than mutant BRCA2/FANCD1 defective in both DSB repair and fork protection, suggests that both fork protection and DSB repair contribute to the suppression of lethality upon ICL. Intriguingly, a dual role during ICL repair beyond DSB repair was also recently reported for BRCA1 (Bunting et al., 2012). The fork protection role for BRCA1 that we report here could therefore be feasibly related to the DSB repair-independent function of BRCA1 during ICL repair. Likewise, sensitivity of FA-deficient cells to ICLs may involve fork protection. While FA proteins clearly have separate roles during ICL repair (Knipscheer et al., 2009; Kim et al., 2012), fork stabilization may not be essential to ensure the complete removal of this lethal type of lesion. Rather, we suggest that during ICL repair, fork stabilization by BRCA and FA proteins may increase access for nucleases and thus the efficiency for incision and subsequent repair.

However, replisome stalling is far more frequent than ICL processes and has particular significance for rapidly cycling cells such as cells of the hematological system or those responding to mitogenic signals like hormones. Moreover, precancerous oncogene expression by HPV infection can induce replication stress by decreasing nucleotide pools (Bester et al., 2011). This direct connection between tumor initiation and replication stalling together with our data showing that FA proteins suppress genomic instability by protecting stalled forks suggests a mechanistic basis for the observed susceptibility of FA patients to oral cancer upon HPV infection (Park et al., 2010). Protection and stabilization of replication forks has critical implications for the maintenance of genomic integrity and thus likely constitutes an unanticipated mechanism of tumor suppression. In support of this hypothesis, we identified the sporadic breast cancer cell line MCF7 to be defective in protecting stalled forks (Figure S5), which implies that this distinct mechanism is also linked to some sporadic cancers.

Cancer therapeutics target DNA replication and dividing cells, so that DNA damage responses are exploited as therapeutic targets and resistance factors. Our experiments reveal that RAD51 stabilization rescues FANCD2 deficiency in protecting stalled forks, despite the fact that FA proteins are clearly not canonical HR factors. This surprising result underscores the emerging importance of an unappreciated aspect in RAD51 filament mediation, which differs from loading of RAD51 onto DNA to promote strand exchange, to instead utilize RAD51 filaments to stabilize DNA structures. Importantly, wild-type RAD51 is often found overexpressed in tumors that acquired resistance to chemotherapeutic drug treatment (Brown and Holt, 2009), which is sufficient in overcoming genetic defects to restore repair functions in these cells and, as we show here, also replication fork stability to a large extent. While defects in replication fork protection elicit genomic instability that initially contribute to tumorigenesis, restoration of the function by RAD51 overexpression after transformation could benefit the proliferative capacity of the tumor cell. Our results provide a mechanistic link between tumor suppression and the protection of stalled replication forks by showing that both BRCA1 and BRCA2, the major hereditary breast cancer suppressors, stabilize replication forks. Thus, our collective results unite breast cancer and FA susceptibility genes in one common molecular process that protect against genomic instability. This integrated function for the *FA/BRCA* gene network in stabilizing stalled forks is expected to prompt investigations of this distinct pathway in tumorigenesis, stem cell aging and controlling stalled DNA replication processes to suppress genomic instability that will shape emerging therapeutic strategies.

EXPERIMENTAL PROCEDURES

Cell Lines

SV40-transformed FA fibroblasts (GM6914, GM6914+FANCA, PD20F, and PD20F+FANCD2 (Jakobs et al., 1996; Näf et al., 1998; Timmers et al., 2001) were previously described and are also available through the FA Cell Repository at Oregon Health & Science University. Mouse ES cells (*Brca1*$^{-/-}$ and *Brca1*$^{+/-}$ [Gowen et al., 1996; Moynahan et al., 1999]; *Blm*$^{tet/tet}$ [Yusa et al., 2004]) were previously described.

Drugs

5′iodo-2′deoxyuridine (IdU), 5′chloro-2′deoxyuridine (CldU), and HU were purchased from Sigma-Aldrich. Mirin (Dupré et al., 2008) was provided by the MSKCC Organic Synthesis Core Facility.

Cell Transfection

Using Fugene 6 (Roche Applied Science) and following the manufacturer's instructions, 10^5 PD20 or complemented cells were transfected with 2 μg of flag-BRC4, RAD51 K133R, wild-type RAD51 or empty (pCaggs) expression plasmids. Expression of the peptides was tested 40 hr post transfection by standard western blotting using Anti-Flag Clone M2 (Sigma-Aldrich) antibody against flag-BRC4 or anti-RAD51 antibody (Santa Cruz) against RAD51 K133R or wild-type RAD51.

DNA Fiber Spreads

DNA fiber spreads were prepared as previously described (Schlacher et al., 2011). Briefly, replication tracts of log-phase cells were pulse labeled with 50 μM IdU and CldU before or after replication stalling with 4 mM HU, 1 μM

gemcitabine or 0.5 μM camptothecin respectively, as indicated in the sketches. Cells were harvested, lysed and spread to obtain single DNA molecules on microscope slides before standard immunofluorescence with antibodies against IdU and CldU (Novus Biologicals, BD Biosciences).

Statistical Analysis

Between 100 and 1400 nascent DNA tracts were measured using ImageJ software from 1-3 independent experiments. P-values obtained from the Mann-Whitney test and the 95% confidence intervals were calculated using Prism software.

Cellular Survival Assays

For survival assays, 3000 cells were seeded in a 24-well plate the day before continuous treatment with the indicated drugs. The number of viable cells was determined when confluency reached ~80% for the untreated cells using Cell Titer 96 AQueous One Solution Cell Proliferation Assay (Promega).

Metaphase Spread Analysis

For metaphase spreads, 2×10^5 cells were seeded the day before HU treatment (4 mM) and treated with colcemid (0.1 μg/ml, GIBCO), as indicated. For metaphase spreads, cells were swollen with 0.075 M KCL (12 min, 37°C), fixed with methanol/acetic acid (3:1), dropped onto a microscope slide, stained with 5% Giemsa, and mounted with Cytoseal 60 (Fisher Scientific) before imaging with an Olympus BX60 microscope.

SUPPLEMENTAL INFORMATION

Supplemental Information includes five figures and can be found with this article online at doi:10.1016/j.ccr.2012.05.015.

ACKNOWLEDGMENTS

We thank Koji Nakanishi, Jan LaRocque, and other members of the Jasin and Wu labs for reagents and discussions. K.S. is the Berger Foundation Fellow of the Damon Runyon Cancer Research Foundation (DRG 1957-07). This work was supported by NIH grants R01CA121110 (H.W.) and R01GM54668 and P01CA94060 (M.J.).

Received: December 15, 2011
Revised: April 3, 2012
Accepted: May 8, 2012
Published: July 9, 2012

REFERENCES

Bartkova, J., Rezaei, N., Liontos, M., Karakaidos, P., Kletsas, D., Issaeva, N., Vassiliou, L.V., Kolettas, E., Niforou, K., Zoumpourlis, V.C., et al. (2006). Oncogene-induced senescence is part of the tumorigenesis barrier imposed by DNA damage checkpoints. Nature *444*, 633–637.

Bester, A.C., Roniger, M., Oren, Y.S., Im, M.M., Sarni, D., Chaoat, M., Bensimon, A., Zamir, G., Shewach, D.S., and Kerem, B. (2011). Nucleotide deficiency promotes genomic instability in early stages of cancer development. Cell *145*, 435–446.

Brown, E.T., and Holt, J.T. (2009). Rad51 overexpression rescues radiation resistance in BRCA2-defective cancer cells. Mol. Carcinog. *48*, 105–109.

Bunting, S.F., Callen, E., Kozak, M.L., Kim, J.M., Wong, N., Lopez-Contreras, A.J., Ludwig, T., Baer, R., Faryabi, R.B., Malhowski, A., et al. (2012). BRCA1 Functions Independently of Homologous Recombination in DNA Interstrand Crosslink Repair. Mol Cell.

Chen, J., Silver, D.P., Walpita, D., Cantor, S.B., Gazdar, A.F., Tomlinson, G., Couch, F.J., Weber, B.L., Ashley, T., Livingston, D.M., and Scully, R. (1998). Stable interaction between the products of the BRCA1 and BRCA2 tumor suppressor genes in mitotic and meiotic cells. Mol. Cell *2*, 317–328.

Chu, W.K., and Hickson, I.D. (2009). RecQ helicases: multifunctional genome caretakers. Nat. Rev. Cancer *9*, 644–654.

Cybulski, K.E., and Howlett, N.G. (2011). FANCP/SLX4: a Swiss army knife of DNA interstrand crosslink repair. Cell Cycle *10*, 1757–1763.

D'Andrea, A.D. (2010). Susceptibility pathways in Fanconi's anemia and breast cancer. N. Engl. J. Med. *362*, 1909–1919.

Davies, S.L., North, P.S., and Hickson, I.D. (2007). Role for BLM in replication-fork restart and suppression of origin firing after replicative stress. Nat. Struct. Mol. Biol. *14*, 677–679.

Deans, A.J., and West, S.C. (2009). FANCM connects the genome instability disorders Bloom's Syndrome and Fanconi Anemia. Mol. Cell *36*, 943–953.

Dupré, A., Boyer-Chatenet, L., Sattler, R.M., Modi, A.P., Lee, J.H., Nicolette, M.L., Kopelovich, L., Jasin, M., Baer, R., Paull, T.T., and Gautier, J. (2008). A forward chemical genetic screen reveals an inhibitor of the Mre11-Rad50-Nbs1 complex. Nat. Chem. Biol. *4*, 119–125.

Garcia-Higuera, I., Taniguchi, T., Ganesan, S., Meyn, M.S., Timmers, C., Hejna, J., Grompe, M., and D'Andrea, A.D. (2001). Interaction of the Fanconi anemia proteins and BRCA1 in a common pathway. Mol. Cell *7*, 249–262.

Gowen, L.C., Johnson, B.L., Latour, A.M., Sulik, K.K., and Koller, B.H. (1996). Brca1 deficiency results in early embryonic lethality characterized by neuroepithelial abnormalities. Nat. Genet. *12*, 191–194.

Hashimoto, Y., Ray Chaudhuri, A., Lopes, M., and Costanzo, V. (2010). Rad51 protects nascent DNA from Mre11-dependent degradation and promotes continuous DNA synthesis. Nat. Struct. Mol. Biol. *17*, 1305–1311.

Hiom, K. (2010). FANCJ: solving problems in DNA replication. DNA Repair (Amst.) *9*, 250–256.

Howlett, N.G., Taniguchi, T., Durkin, S.G., D'Andrea, A.D., and Glover, T.W. (2005). The Fanconi anemia pathway is required for the DNA replication stress response and for the regulation of common fragile site stability. Hum. Mol. Genet. *14*, 693–701.

Howlett, N.G., Harney, J.A., Rego, M.A., Kolling, F.W., 4th, and Glover, T.W. (2009). Functional interaction between the Fanconi Anemia D2 protein and proliferating cell nuclear antigen (PCNA) via a conserved putative PCNA interaction motif. J. Biol. Chem. *284*, 28935–28942.

Hussain, S., Wilson, J.B., Medhurst, A.L., Hejna, J., Witt, E., Ananth, S., Davies, A., Masson, J.Y., Moses, R., West, S.C., et al. (2004). Direct interaction of FANCD2 with BRCA2 in DNA damage response pathways. Hum. Mol. Genet. *13*, 1241–1248.

Jakobs, P.M., Sahaayaruban, P., Saito, H., Reifsteck, C., Olson, S., Joenje, H., Moses, R.E., and Grompe, M. (1996). Immortalization of four new Fanconi anemia fibroblast cell lines by an improved procedure. Somat. Cell Mol. Genet. *22*, 151–157.

Kim, H., Yang, K., Dejsuphong, D., and D'Andrea, A.D. (2012). Regulation of Rev1 by the Fanconi anemia core complex. Nat. Struct. Mol. Biol. *19*, 164–170.

Knipscheer, P., Räschle, M., Smogorzewska, A., Enoiu, M., Ho, T.V., Schärer, O.D., Elledge, S.J., and Walter, J.C. (2009). The Fanconi anemia pathway promotes replication-dependent DNA interstrand cross-link repair. Science *326*, 1698–1701.

Langevin, F., Crossan, G.P., Rosado, I.V., Arends, M.J., and Patel, K.J. (2011). Fancd2 counteracts the toxic effects of naturally produced aldehydes in mice. Nature *475*, 53–58.

Lomonosov, M., Anand, S., Sangrithi, M., Davies, R., and Venkitaraman, A.R. (2003). Stabilization of stalled DNA replication forks by the BRCA2 breast cancer susceptibility protein. Genes Dev. *17*, 3017–3022.

Long, D.T., Räschle, M., Joukov, V., and Walter, J.C. (2011). Mechanism of RAD51-dependent DNA interstrand cross-link repair. Science *333*, 84–87.

Moldovan, G.L., and D'Andrea, A.D. (2009). How the fanconi anemia pathway guards the genome. Annu. Rev. Genet. *43*, 223–249.

Morrison, C., Shinohara, A., Sonoda, E., Yamaguchi-Iwai, Y., Takata, M., Weichselbaum, R.R., and Takeda, S. (1999). The essential functions of human Rad51 are independent of ATP hydrolysis. Mol. Cell. Biol. *19*, 6891–6897.

Moynahan, M.E., Chiu, J.W., Koller, B.H., and Jasin, M. (1999). Brca1 controls homology-directed DNA repair. Mol. Cell *4*, 511–518.

Näf, D., Kupfer, G.M., Suliman, A., Lambert, K., and D'Andrea, A.D. (1998). Functional activity of the fanconi anemia protein FAA requires FAC binding and nuclear localization. Mol. Cell. Biol. *18*, 5952–5960.

Naim, V., and Rosselli, F. (2009). The FANC pathway and BLM collaborate during mitosis to prevent micro-nucleation and chromosome abnormalities. Nat. Cell Biol. *11*, 761–768.

Nakanishi, K., Cavallo, F., Perrouault, L., Giovannangeli, C., Moynahan, M.E., Barchi, M., Brunet, E., and Jasin, M. (2011). Homology-directed Fanconi anemia pathway cross-link repair is dependent on DNA replication. Nat. Struct. Mol. Biol. *18*, 500–503.

Ohouo, P.Y., and Smolka, M.B. (2011). A touching moment for Smc5/6: from ssDNA binding to repair. Cell Cycle *10*, 1190–1191.

Papadopoulo, D., Guillouf, C., Mohrenweiser, H., and Moustacchi, E. (1990). Hypomutability in Fanconi anemia cells is associated with increased deletion frequency at the *HPRT* locus. Proc. Natl. Acad. Sci. USA *87*, 8383–8387.

Park, J.W., Pitot, H.C., Strati, K., Spardy, N., Duensing, S., Grompe, M., and Lambert, P.F. (2010). Deficiencies in the Fanconi anemia DNA damage response pathway increase sensitivity to HPV-associated head and neck cancer. Cancer Res. *70*, 9959–9968.

Raderschall, E., Bazarov, A., Cao, J., Lurz, R., Smith, A., Mann, W., Ropers, H.H., Sedivy, J.M., Golub, E.I., Fritz, E., and Haaf, T. (2002a). Formation of higher-order nuclear Rad51 structures is functionally linked to p21 expression and protection from DNA damage-induced apoptosis. J. Cell Sci. *115*, 153–164.

Raderschall, E., Stout, K., Freier, S., Suckow, V., Schweiger, S., and Haaf, T. (2002b). Elevated levels of Rad51 recombination protein in tumor cells. Cancer Res. *62*, 219–225.

Rosado, I.V., Langevin, F., Crossan, G.P., Takata, M., and Patel, K.J. (2011). Formaldehyde catabolism is essential in cells deficient for the Fanconi anemia DNA-repair pathway. Nat. Struct. Mol. Biol. *18*, 1432–1434.

Saeki, H., Siaud, N., Christ, N., Wiegant, W.W., van Buul, P.P., Han, M., Zdzienicka, M.Z., Stark, J.M., and Jasin, M. (2006). Suppression of the DNA repair defects of BRCA2-deficient cells with heterologous protein fusions. Proc. Natl. Acad. Sci. USA *103*, 8768–8773.

Schlacher, K., Christ, N., Siaud, N., Egashira, A., Wu, H., and Jasin, M. (2011). Double-strand break repair-independent role for BRCA2 in blocking stalled replication fork degradation by MRE11. Cell *145*, 529–542.

Schroeder, T.M., Anschütz, F., and Knopp, A. (1964). [Spontaneous chromosome aberrations in familial panmyelopathy]. Humangenetik *1*, 194–196.

Stathis, A., and Moore, M.J. (2010). Advanced pancreatic carcinoma: current treatment and future challenges. Nat. Rev. Clin. Oncol. *7*, 163–172.

Timmers, C., Taniguchi, T., Hejna, J., Reifsteck, C., Lucas, L., Bruun, D., Thayer, M., Cox, B., Olson, S., D'Andrea, A.D., et al. (2001). Positional cloning of a novel Fanconi anemia gene, *FANCD2*. Mol. Cell *7*, 241–248.

Wang, J., Sun, Q., Morita, Y., Jiang, H., Gross, A., Lechel, A., Hildner, K., Guachalla, L.M., Gompf, A., Hartmann, D., et al. (2012). A differentiation checkpoint limits hematopoietic stem cell self-renewal in response to DNA damage. Cell *148*, 1001–1014.

Wang, X., Andreassen, P.R., and D'Andrea, A.D. (2004). Functional interaction of monoubiquitinated FANCD2 and BRCA2/FANCD1 in chromatin. Mol. Cell. Biol. *24*, 5850–5862.

Williams, R.S., Moncalian, G., Williams, J.S., Yamada, Y., Limbo, O., Shin, D.S., Groocock, L.M., Cahill, D., Hitomi, C., Guenther, G., et al. (2008). Mre11 dimers coordinate DNA end bridging and nuclease processing in double-strand-break repair. Cell *135*, 97–109.

Yusa, K., Horie, K., Kondoh, G., Kouno, M., Maeda, Y., Kinoshita, T., and Takeda, J. (2004). Genome-wide phenotype analysis in ES cells by regulated disruption of Bloom's syndrome gene. Nature *429*, 896–899.

Cancer Cell
Article

The *ALK*^{F1174L} Mutation Potentiates the Oncogenic Activity of MYCN in Neuroblastoma

Teeara Berry,[1] William Luther,[3] Namrata Bhatnagar,[3] Yann Jamin,[2] Evon Poon,[1] Takaomi Sanda,[3] Desheng Pei,[3] Bandana Sharma,[3] Winston R. Vetharoy,[1] Albert Hallsworth,[1] Zai Ahmad,[1] Karen Barker,[1] Lisa Moreau,[3] Hannah Webber,[1] Wenchao Wang,[3] Qingsong Liu,[4] Antonio Perez-Atayde,[6] Scott Rodig,[5] Nai-Kong Cheung,[7] Florence Raynaud,[1] Bengt Hallberg,[8] Simon P. Robinson,[2] Nathanael S. Gray,[4] Andrew D.J. Pearson,[1,9] Suzanne A. Eccles,[1] Louis Chesler,[1,9,10,*] and Rani E. George[3,10,*]
[1]Divisions of Clinical Studies and Cancer Therapeutics
[2]Division of Radiotherapy and Imaging
The Institute of Cancer Research, Sutton, Surrey SM2 5NG, UK
[3]Department of Pediatric Hematology and Oncology, Dana-Farber Cancer Institute and Children's Hospital Boston
[4]Department of Cancer Biology, Dana-Farber Cancer Institute and Biological Chemistry and Molecular Pharmacology
[5]Department of Pathology, Brigham and Women's Hospital
Harvard Medical School, Boston, MA 02115, USA
[6]Department of Pathology, Children's Hospital Boston, Boston, MA 02115, USA
[7]Department of Pediatrics, Memorial Sloan-Kettering Cancer Center, New York, NY 10065, USA
[8]Department of Molecular Biology, Umeå University, Umeå, Sweden
[9]The Children and Young People's Unit, The Royal Marsden NHS Trust, Sutton, Surrey SM2 5PT, UK
[10]These authors contributed equally to this work
*Correspondence: rani_george@dfci.harvard.edu (R.E.G.), louis.chesler@icr.ac.uk (L.C.)
http://dx.doi.org/10.1016/j.ccr.2012.06.001

SUMMARY

The *ALK*^{F1174L} mutation is associated with intrinsic and acquired resistance to crizotinib and cosegregates with *MYCN* in neuroblastoma. In this study, we generated a mouse model overexpressing *ALK*^{F1174L} in the neural crest. Compared to *ALK*^{F1174L} and *MYCN* alone, co-expression of these two oncogenes led to the development of neuroblastomas with earlier onset, higher penetrance, and enhanced lethality. *ALK*^{F1174L}/*MYCN* tumors exhibited increased MYCN dosage due to ALK^{F1174L}-induced activation of the PI3K/AKT/mTOR and MAPK pathways, coupled with suppression of MYCN pro-apoptotic effects. Combined treatment with the ATP-competitive mTOR inhibitor Torin2 overcame the resistance of *ALK*^{F1174L}/*MYCN* tumors to crizotinib. Our findings demonstrate a pathogenic role for *ALK*^{F1174L} in neuroblastomas overexpressing *MYCN* and suggest a strategy for improving targeted therapy for *ALK*-positive neuroblastoma.

INTRODUCTION

Neuroblastoma, an embryonal tumor derived from the neural crest, is the most common extracranial solid tumor of childhood (National Cancer Institute, 2005). It arises from sympathetic ganglia and adrenal glands, manifesting as thoracic, paraspinous or abdominal tumors, with metastases to bone and bone marrow in high-risk cases. Despite considerable success in the treatment of favorable-biology neuroblastoma, 5-year survival rates for children with high-risk disease, which accounts for over half of all newly diagnosed cases, seldom exceed 40% (Matthay et al., 1999). A typical feature of high-risk neuroblastoma is amplification of *MYCN*, an oncogene encoding a pleiotropic nuclear phosphoprotein in the MYC family of helix-loop-helix transcription factors (Schwab et al., 1984). *MYCN* amplification is the major genetic aberration associated with aggressive tumor phenotype and poor outcome in neuroblastoma (Brodeur et al., 1984; Seeger et al., 1985). Targeted expression of *MYCN* to

Significance

The *ALK*^{F1174L} mutation has particular relevance in cancer, not only because of its role in neuroblastoma, but also because it causes resistance to crizotinib in *ALK*-rearranged tumors in general. Our murine model of high-risk neuroblastoma defined by cooperation between ALK^{F1174L} and MYCN should provide an ideal platform for further dissection of oncogenic ALK-MYCN interactions and for screening candidate agents for their ability to inhibit ALK oncoproteins and related signaling pathways. Our therapeutic strategy of combined ALK and mTOR inhibition may benefit not only neuroblastoma patients with *ALK*^{F1174L}-positive tumors who exhibit de novo resistance, but perhaps also patients with other cancers expressing crizotinib-sensitive *ALK* aberrations that acquire resistance after a favorable initial response.

the neural crest in transgenic mice causes aggressive neuroblastomas and tumorigenesis is positively correlated with *MYCN* transgene dosage or with the development of additional genetic mutations (Hansford et al., 2004; Weiss et al., 1997). Direct inhibition of MYCN has not yet been clinically successful, thus much attention is being directed to the therapeutic targeting of molecules that modulate the activities of this potent oncoprotein.

We and others have identified activating point mutations in the anaplastic lymphoma receptor tyrosine kinase gene (*ALK*) in approximately 8% of primary neuroblastomas (Chen et al., 2008; George et al., 2008; Janoueix-Lerosey et al., 2008; Mossé et al., 2008). In our study, these mutations converted IL-3-dependent Ba/F3 cells to cytokine-independent growth, led to constitutive phosphorylation of ALK and downstream signaling, and were sensitive to the small-molecule ALK inhibitor, TAE684 (George et al., 2008). Drug-induced cytotoxicity was associated with decreased phosphorylation of ALK and its downstream effectors and with the induction of apoptosis. Inhibition of ALK expression in neuroblastoma cells harboring *ALK* mutations resulted in a similar apoptotic phenotype and impaired cell proliferation. Together, these studies suggested that *ALK* mutations may afford therapeutic targets in high-risk neuroblastoma, thus leading to early phase clinical trials of crizotinib, an ALK/MET inhibitor that has been FDA approved for use in adults with *ALK*-translocated cancers (Butrynski et al., 2010; Kwak et al., 2010).

Of several somatic activating *ALK* mutations identified in neuroblastomas, one of the more common is a cytosine-to-adenine change in exon 23, resulting in a phenylalanine-to-leucine substitution at codon 1174 (F1174L) within the kinase domain (Chen et al., 2008; George et al., 2008; Janoueix-Lerosey et al., 2008; Mossé et al., 2008). This mutation appears to be more potent than the others, correlating with a higher degree of autophosphorylation and greater transforming capacity. Moreover, it is preferentially associated with *MYCN* gene amplification in neuroblastoma and defines a subset of ultra-high-risk neuroblastoma patients with distinctly poor outcome (De Brouwer et al., 2010). Finally, ALK^{F1174L} represents one of the sites of secondary kinase domain mutations in cases of *ALK*-rearranged cancers that have become resistant to crizotinib treatment (Sasaki et al., 2010). In particular, cell line and xenograft models of human neuroblastoma with ALK^{F1174L} expression are only minimally sensitive to crizotinib (Bresler et al., 2011), suggesting that effective targeting of ALK^{F1174L} will require innovative means of combating crizotinib resistance or perhaps the development of ALK inhibitors with alternative mechanisms of action.

To determine the pathogenic consequences of ALK^{F1174L}-MYCN interactions in neuroblastoma and to identify strategies that might overcome the resistance of these tumors to crizotinib, we engineered a transgenic mouse model that overexpresses both molecules in neural crest-derived cells.

RESULTS

Generation of the *Th-ALK*^{F1174} Transgenic Tumor Model

To generate mice that overexpress ALK^{F1174L} in the neural crest, we injected blastocysts from the C57BL/6J strain with a *Th-*ALK^{F1174L} construct in which human ALK^{F1174L} cDNA was ligated downstream of the rat tyrosine hydroxylase (*Th*) promoter (Banerjee et al., 1992) (Figure 1A; Figure S1A available online). *Th* is expressed in committed sympathetic precursor cells of the neural crest, and this tissue specificity has facilitated efforts to target *MYCN* overexpression to neuroectodermal cells resulting in tumors that arise in the sympathetic ganglia and adrenal gland (Weiss et al., 1997). We verified expression of the human ALK^{F1174L} protein in 293T cells, which lack endogenous expression of ALK (Figure S1B). Germline positivity for the transgene was demonstrated in multiple founders by PCR genotyping of tail DNA. Tissue-specific expression of ALK^{F1174L} and of the endogenous wild-type (WT) murine *Alk* was confirmed by RT-PCR followed by sequencing of cDNA in the cervical sympathetic ganglia and adrenal glands of 7- to 10-day-old mice (Figure 1B). In four distinct founder lines, ALK^{F1174L} was transmitted in Mendelian ratios and produced no apparent phenotype in either hemi- or homozygotes, not only in the C57BL/6J background but also in the more "tumor-permissive" 129X1/SvJ strain.

Overexpression of ALK^{F1174L} Potentiates the Oncogenic Activity of MYCN In Vivo

A meta-analysis of *ALK* mutations in human neuroblastoma suggested that ALK^{F1174L} may play a role in promoting aggressive tumors in cooperation with *MYCN* amplification (De Brouwer et al., 2010). Otherwise, evidence to support a functional interaction between MYCN and ALK^{F1174L} in vivo is lacking. We therefore investigated the effect of co-expression of ALK^{F1174L} and MYCN in neuroblastoma by crossing *Th-*ALK^{F1174L} mice with *Th-MYCN* mice (Weiss et al., 1997). Mice hemizygotic for both ALK^{F1174L} and *MYCN* exhibited high tumor penetrance with rapid lethality superior to that observed in *MYCN* hemizygotes (Figures 1C and 1D; Table 1). Of the four *Th-*ALK^{F1174L} founder lines that were crossed with *Th-MYCN* mice, the offspring of founders 2 and 4 showed complete tumor penetrance, shorter median time to tumor onset, and decreased survival at 100 days of age compared to that of *Th-MYCN* animals (Figure 1C and Table 1). An additional pattern of complete penetrance with longer latency was obtained in founder lines 1 and 3 (Figure 1D and Table 1). All subsequent experiments described in this study were performed using offspring of founders 2 and 4.

Co-expression of ALK^{F1174L} and *MYCN* (ALK^{F1174L}/*MYCN* compound hemizygotes) led to the development of large, bulky and locally invasive thoracic and abdominal masses that arose in the paraspinal ganglia or adrenals, locations typically seen in human neuroblastoma (Figure 2A). In contrast to *MYCN* tumors that generally arise as single primary tumors, the ALK^{F1174L}/*MYCN* tumors manifested as large, synchronous primary masses (Figure 2A). Focal masses on the forelimb, neck, and shoulder were seen in a minority of animals (data not shown). No evidence of macroscopic tumor spread to other organs (skin, liver, kidney, brain and lung) was detected. Tumor bearing mice exhibited normal peripheral blood counts (data not shown) and immunostaining of bone marrow cytospins for expression of the neural crest marker tyrosine hydroxylase (TH) revealed no evidence of bone marrow metastasis (Figure S2A). The tumors exhibited robust expression of ALK and MYCN at both the RNA and protein levels (Figures 2B and 2C) and also expressed

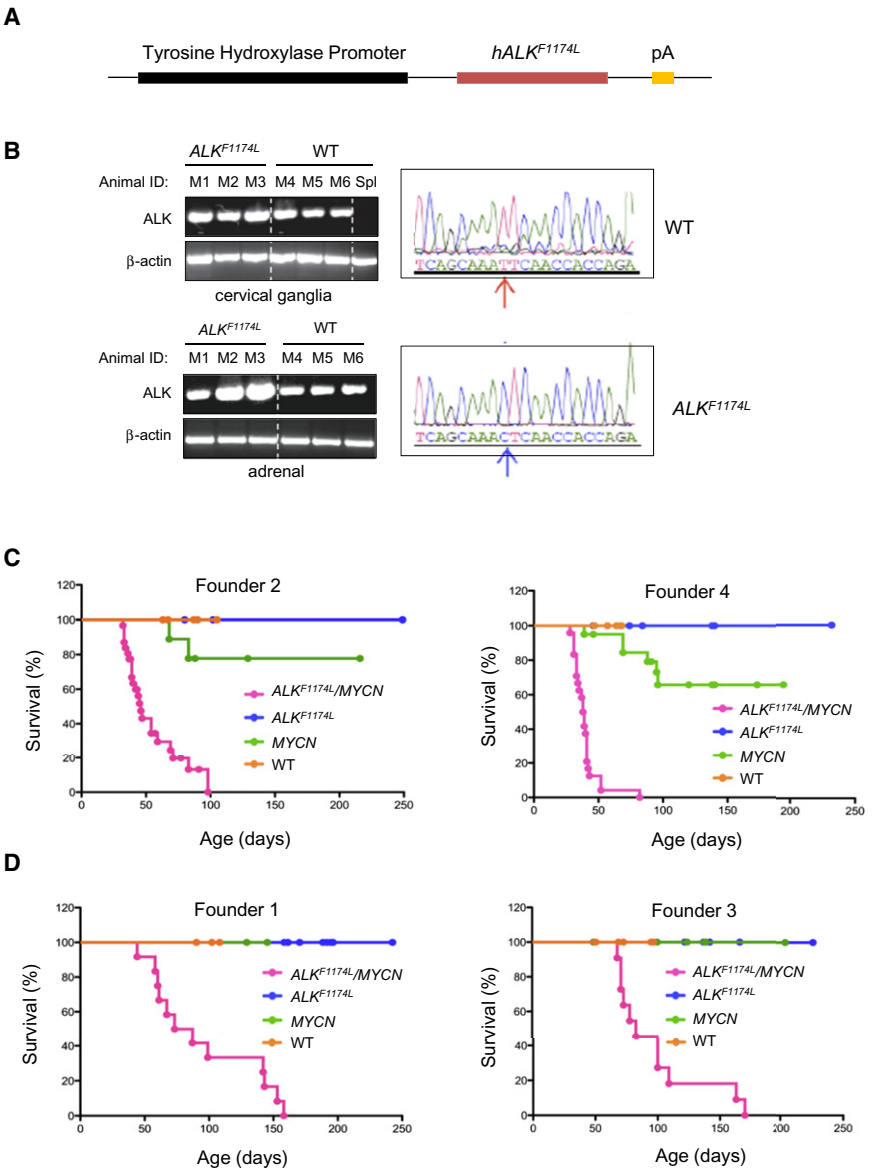

Figure 1. Overexpression of ALK^{F1174L} Potentiates the Oncogenic Activity of MYCN In Vivo

(A) The ALK^{F1174L} cDNA was ligated 3′ to the rat *Th* promoter to generate the p4.5 Th-ALK^{F1174L} transgenic construct (*Th*-ALK^{F1174L}).

(B) RT-PCR analysis of *ALK* expression in cervical ganglia and adrenal glands of 7 to 10-day-old WT mice (M4-M6) or mice transgenic for ALK^{F1174L} (M1-M3) (left panels). Spl, spleen. Electropherogram showing the change in the phenylalanine codon (TTC) in WT *ALK* to leucine (CTC) in the ALK^{F1174L} mutation in ganglia (right panel).

(C and D) Kaplan-Meier survival curves of founder lines resulting from intercrosses of *Th*-ALK^{F1174L} mice and *Th-MYCN* mice. (C) Founder 2 - ALK^{F1174L}/*MYCN*, n = 31; *MYCN*, n = 9; ALK^{F1174L}, n = 4; *WT*, n = 5. Founder 4 - ALK^{F1174L}/*MYCN*, n = 25; *MYCN*, n = 20; ALK^{F1174L}, n = 13; *WT*, n = 6. (D) Founder 1 - ALK^{F1174L}/*MYCN*, n = 12; *MYCN*, n = 6; ALK^{F1174L}, n = 12; *WT*, n = 3. Founder 3 - ALK^{F1174L}/*MYCN*, n = 11; *MYCN*, n = 10; ALK^{F1174L}, n = 11; *WT*, n = 5.

See also Figure S1.

phosphorylated ALK^{F1174L} (Figure 2C). Similar to genotypically verified human neuroblastoma tumors expressing both ALK^{F1174L} and *MYCN*, histologically, the doubly transgenic murine tumors displayed characteristic dense aggregates of poorly differentiated small round blue cells with high mitotic activity in a stroma-poor background (Figure 2D). Both human and murine tumors had similar immunohistochemical profiles of high-level cytoplasmic ALK and nuclear MYCN protein expression (Figure 2D). Positive staining for markers of human neuroblastoma, such as synaptophysin, was also evident (Figure S2B). These results demonstrate the ability of constitutively expressed ALK^{F1174L} to enhance MYCN-driven oncogenesis. Importantly, the early onset and rapid lethality of ALK^{F1174L}/*MYCN* murine tumors are characteristic of the clinical course of high-risk neuroblastoma in humans (De Brouwer et al., 2010) and thus they provide a suitable model in which to dissect ALK^{F1174L}/MYCN interactions in vivo.

ALK^{F1174L}/*MYCN* Tumors Show Differential Activation of Signal Transduction Pathways

To further characterize the aggressive nature of ALK^{F1174L}/*MYCN* tumors, we analyzed the transcriptional profiles of *MYCN*-positive tumors with or without ALK^{F1174} expression. ALK^{F1174L}/*MYCN* and *MYCN* tumors exhibited distinct genetic profiles; of the 684 genes that were differentially expressed, 476 were upregulated in ALK^{F1174L}/*MYCN* tumors (Figure 3A). Gene set enrichment analysis (GSEA) indicated significant upregulation of genes involved in the PI3K/AKT/mTOR and MAPK signal transduction pathways in ALK^{F1174L}/*MYCN* compared to *MYCN* tumors (Figure 3B), suggesting increased utilization of these two pathways in neuroblastoma cells constitutively expressing ALK^{F1174L} together with *MYCN*. This was supported by immunoblot analysis showing greater phosphorylation of AKT, as well as activation of components of the MAPK pathway, MEK and ERK, in ALK^{F1174L}/*MYCN* versus *MYCN* tumor cells (Figure 3C). These differences in activation of downstream signaling were confirmed also by immunohistochemical staining, which in addition showed upregulated mTOR activity as determined by pS6 kinase expression (Figure 3D). Similar upregulation of pS6K and pERK were seen in human ALK^{F1174L}/*MYCN*-expressing tumors compared to those with *MYCN* overexpression only (Figure 3D). Moreover, a number of kinase-associated docking proteins, such as the Src homology 2 domain-containing adaptor molecules GRB2, IRS1 and IRS2, were significantly upregulated in ALK^{F1174L}/*MYCN* tumors (Figure S3). Together, these data attest to the

Table 1. Transgenic Lines Resulting from *Th-ALK*^{F1174L} and *Th-MYCN* Intercrosses

Founder Line[a]	Genotypes	Number of Animals	Penetrance (%)	Latency (days), Median (range)
1	*Th-ALK*^{F1174L}/*MYCN*	12	100	80 (44–185)
	Th-MYCN	6	0	–
	Th-ALK^{F1174L}	12	0	–
	Th-ALK^{F1174L}/*ALK*^{F1174L}	22	0	–
	WT	3	0	–
2	*Th-ALK*^{F1174L}/*MYCN*	31	100[b]	42 (32–98)[c]
	Th-MYCN	9	25	76 (67–88)
	Th-ALK^{F1174L}	4	0	–
	Th-ALK^{F1174L}/*ALK*^{F1174L}	8	0	–
	WT	5	0	–
3	*Th-ALK*^{F1174L}/*MYCN*	11	100	83 (68–163)
	Th-MYCN	10	0	–
	Th-ALK^{F1174L}	11	0	–
	WT	5	0	–
4	*Th-ALK*^{F1174L}/*MYCN*	25	100[b]	39 (28–93)[c]
	Th-MYCN	20	35	79 (39–96)
	Th-ALK^{F1174L}	13	0	–
	Th-ALK^{F1174L}/*ALK*^{F1174L}	10	0	–
	WT	6	0	–

[a]Four *ALK*^{F1174L} founder lines exhibited neural tissue-specific overexpression of *ALK*^{F1174L} (adrenal tissue and superior cervical ganglia). *ALK*^{F1174L} (C57BL/6J) and *MYCN* (129X1/SvJ) hemizygotes were serially intercrossed into the permissive 129X1/SvJ strain. F1 *MYCN* offspring were not tumor prone, but regained 25%–35% penetrance at 100 days in F3–F4, consistent with expectations for this strain background (75%–94% 129X1/SvJ).
[b]Significantly different from penetrance in mice expressing *Th-MYCN* ($p < 0.0001$ by Student's t test).
[c]Significantly different from median (range) days to tumor onset in mice expressing *Th-MYCN* ($p < 0.0001$ by Student's t test).

predominance of these signaling networks in *ALK*^{F1174L}/*MYCN* tumors in comparison to *MYCN* tumors.

ALK^{F1174L} Enhances MYCN Protein Stabilization

Given the roles of both the PI3K/AKT/mTOR and MAPK pathways in post-translational modification of MYCN (Chesler et al., 2006; Gustafson and Weiss, 2010; Marshall et al., 2011), we determined the consequences of their activation on MYCN protein stability in the double transgenic tumors. Indeed, higher levels of MYCN were apparent in *ALK*^{F1174L}/*MYCN* versus *MYCN* tumors by immunohistochemical staining but not by immunoblotting (Figures 4A and 4D). To clarify whether *ALK*^{F1174L} expression influenced MYCN protein levels, we abrogated expression of ALK^{F1174L} in the Kelly human neuroblastoma cell line, which expresses high levels of both genes. Small interfering RNA (siRNA) knockdown of ALK^{F1174L} expression led to a decreased MYCN protein level in these cells (Figure 4B). Moreover, the half-life of MYCN protein was reduced from 90-120 min to 30 min when ALK^{F1174L} was depleted by shRNA knockdown, suggesting that ALK^{F1174L} plays a role in reducing MYCN protein turnover (Figure 4C). To determine whether MYCN stability was enhanced in *ALK*^{F1174L}/*MYCN* tumors, we analyzed the phosphorylation of serine 62 (S62) and threonine 58 (T58), which regulate MYCN protein stability (Gustafson and Weiss, 2010; Sjostrom et al., 2005). We observed decreased pMYCN^{T58} levels in *ALK*^{F1174L}/*MYCN* tumors compared to *MYCN* tumors (Figure 4D). Increased PI3K pathway activity is thought to oncogenically stabilize MYCN in neuroblastoma cells by inactivating glycogen synthase kinase 3β (GSK3β), which mediates phosphorylation of MYCN at T58 (Chesler et al., 2006; Gustafson and Weiss, 2010). The same process appears to occur in *ALK*^{F1174L}/*MYCN* tumors, where GSK3β is phosphorylated (inactivated), in contrast to *MYCN* tumors (Figure 4D). pMYCN^{T58} then binds to the E3 ligase FBXW7 and is targeted for ubiquitination and degradation (Otto et al., 2009). Using a dual-link antibody ligation assay to detect direct physical interactions between MYCN and FBXW7, we observed that knockdown of ALK^{F1174L} in Kelly cells led to increased interactions between the two proteins, further attesting to the role of this mutant in mediating decreased pMYCN^{T58} levels (Figure 4E). Thus, by promoting greater stabilization of MYCN, constitutive signaling mediated by ALK^{F1174L} appears to increase MYCN dosage in the *ALK*^{F1174L}/*MYCN* transgenic tumor model.

Upregulation of Endogenous *Mycn* RNA in *ALK*^{F1174L}/*MYCN* Tumors

A striking observation in the transcriptional signatures was the markedly increased expression of endogenous *Mycn* in *ALK*^{F1174L}/*MYCN* versus *MYCN* tumors; in fact, murine *Mycn* was among the top 25 significantly upregulated genes in our expression arrays (Figure 5A). To pursue this observation, we used qRT-PCR to measure levels of human *MYCN* and murine *Mycn* in the *ALK*^{F1174L}/*MYCN* tumors. While there was no significant difference between the levels of transgenic human *MYCN* in the two types of tumor, the expression of mouse *Mycn* RNA was indeed elevated in the *ALK*^{F1174L}/*MYCN* tumors, equivalent to expression levels of transgenic human *MYCN* (Figure 5B). There was no evidence of amplification of either oncogene on FISH analysis (Figure 5C), eliminating this mechanism as a cause of increased *Mycn* expression. To determine whether ALK^{F1174L} has a role in modulating *MYCN* expression, we measured *MYCN* mRNA levels in Kelly cells upon knockdown of ALK^{F1174L} and observed a decrease in *MYCN* mRNA levels (Figure 5D). This suggests that the constitutively activated *ALK* mutant may also regulate transcription of *MYCN*.

ALK^{F1174L} Activates an Anti-Apoptotic Program in the *ALK*^{F1174L}/*MYCN* Tumors

Ectopic expression of MYCN sensitizes cells to undergo apoptosis (Pelengaris et al., 2002). This means that efficient transformation by MYCN would require concomitant inhibition of apoptosis. Although both *ALK*^{F1174L}/*MYCN* and *MYCN* tumors exhibited similar levels of proliferation by Ki-67 staining, the amount of apoptosis as determined by TUNEL and cleaved

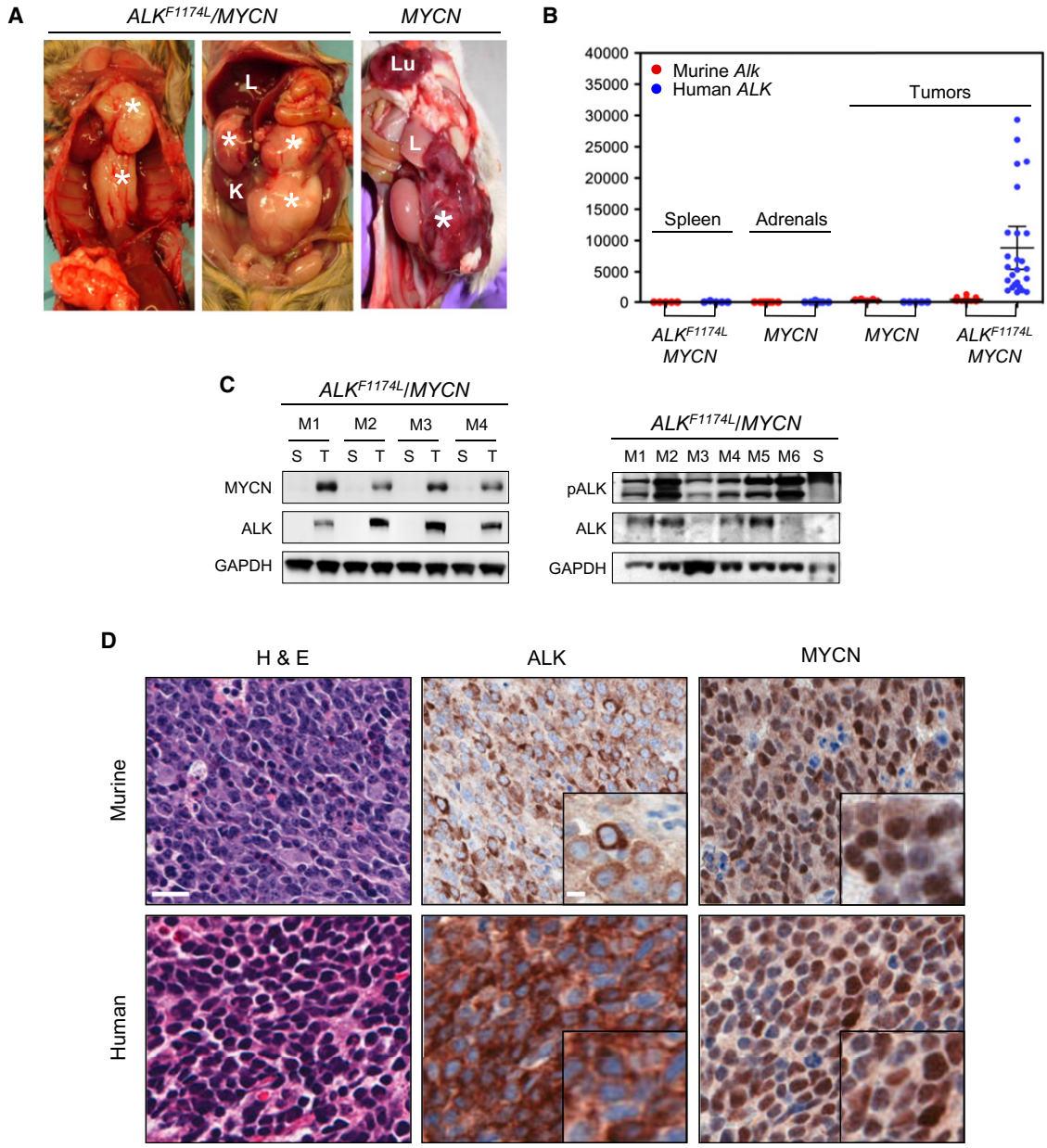

Figure 2. Combined Overexpression of *ALK*^{F1174L} and *MYCN* Results in Multifocal Neuroblastomas

(A) Gross appearance of representative *ALK*^{F1174L}/*MYCN* and *MYCN* tumors. Tumors (*) arise as multifocal primary lesions in *ALK*^{F1174L}/*MYCN* animals: thoracic paraspinous (left panel) and abdominal (right panel) tumors. K, kidney; L, liver; Lu, Lung.

(B) Quantitative RT-PCR analysis of murine and human *ALK* expression in spleen, adrenal glands and tumors from *ALK*^{F1174L}/*MYCN* or *MYCN* mice. Error bars indicate mean values ± 95% confidence interval (CI).

(C) Immunoblotting of *ALK*^{F1174L}/*MYCN* tumors (T, M1-M6) for ALK, MYCN (left panel) and pALK (right panel). pALK was detected using a human-specific ALK^{Y1604} antibody. Matched spleens (S) were used as negative controls and GAPDH was used as a loading control.

(D) H&E and immunohistochemical staining for ALK and MYCN of representative *ALK*^{F1174L}/*MYCN* murine and human neuroblastoma tumor sections. Scale bars, 20 μm, insets 5 μm.

See also Figure S2.

caspase-3 staining was greatly reduced in the *ALK*^{F1174L}/*MYCN* versus *MYCN* tumors (Figures 6A and S4). Similar differences were noted between human neuroblastoma tumors that were positive for both *ALK*^{F1174} and *MYCN* and those that were positive for *MYCN* only (Figure 6A). These findings suggest that constitutive expression of ALK^{F1174L} reduces apoptosis caused by MYCN overexpression. To test this hypothesis, we examined the gene expression profiles of these tumors, noting that expression of *Trp53* was downregulated in the *ALK*^{F1174L}/*MYCN* tumors versus *MYCN* tumors (Figure 6B). However, none of the genes

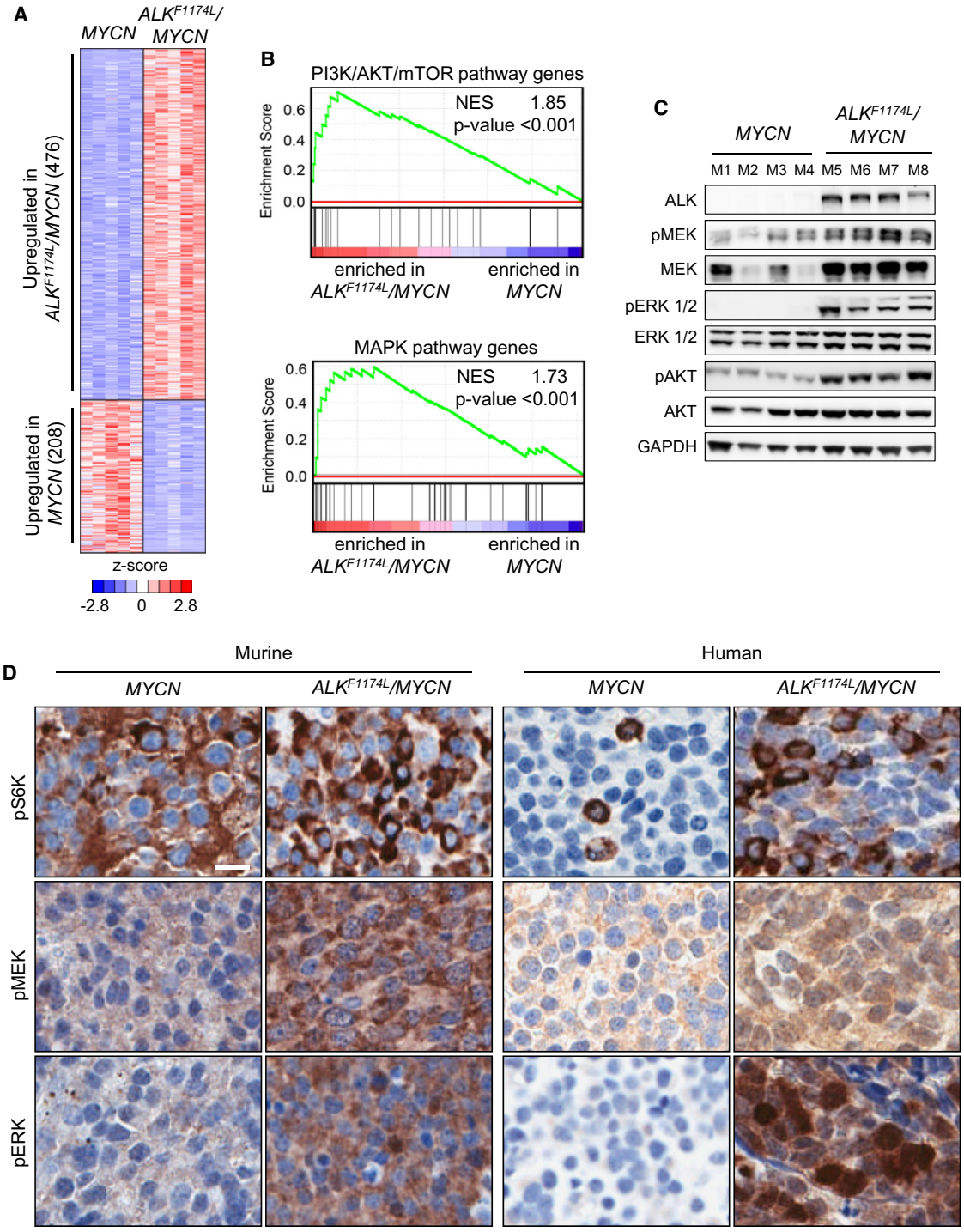

Figure 3. *ALK*^{F1174L}/*MYCN* Tumors Exhibit Distinct Expression Profiles and Downstream Signaling Compared to *MYCN* Tumors

(A) Heat map representation of differentially regulated genes in *ALK*^{F1174L}/*MYCN* versus *MYCN* tumors (fold change ≥ 2.0; corrected p value < 0.05).

(B) GSEA of PI3K/AKT/mTOR and MAPK pathway genes in transcriptional profiles of *ALK*^{F1174L}/*MYCN* and *MYCN* tumors. The normalized enrichment score (NES) and the nominal p values are indicated.

(C) Immunoblotting of PI3K/AKT/mTOR and MAPK signaling pathways in *ALK*^{F1174L}/*MYCN* and *MYCN* tumors.

(D) Immunohistochemical staining for PI3K/AKT/mTOR (pS6K) and MAPK (pMEK and pERK) pathways in *ALK*^{F1174L}/*MYCN* and *MYCN* murine and human tumors (Scale bars, 10 μm).

See also Figure S3.

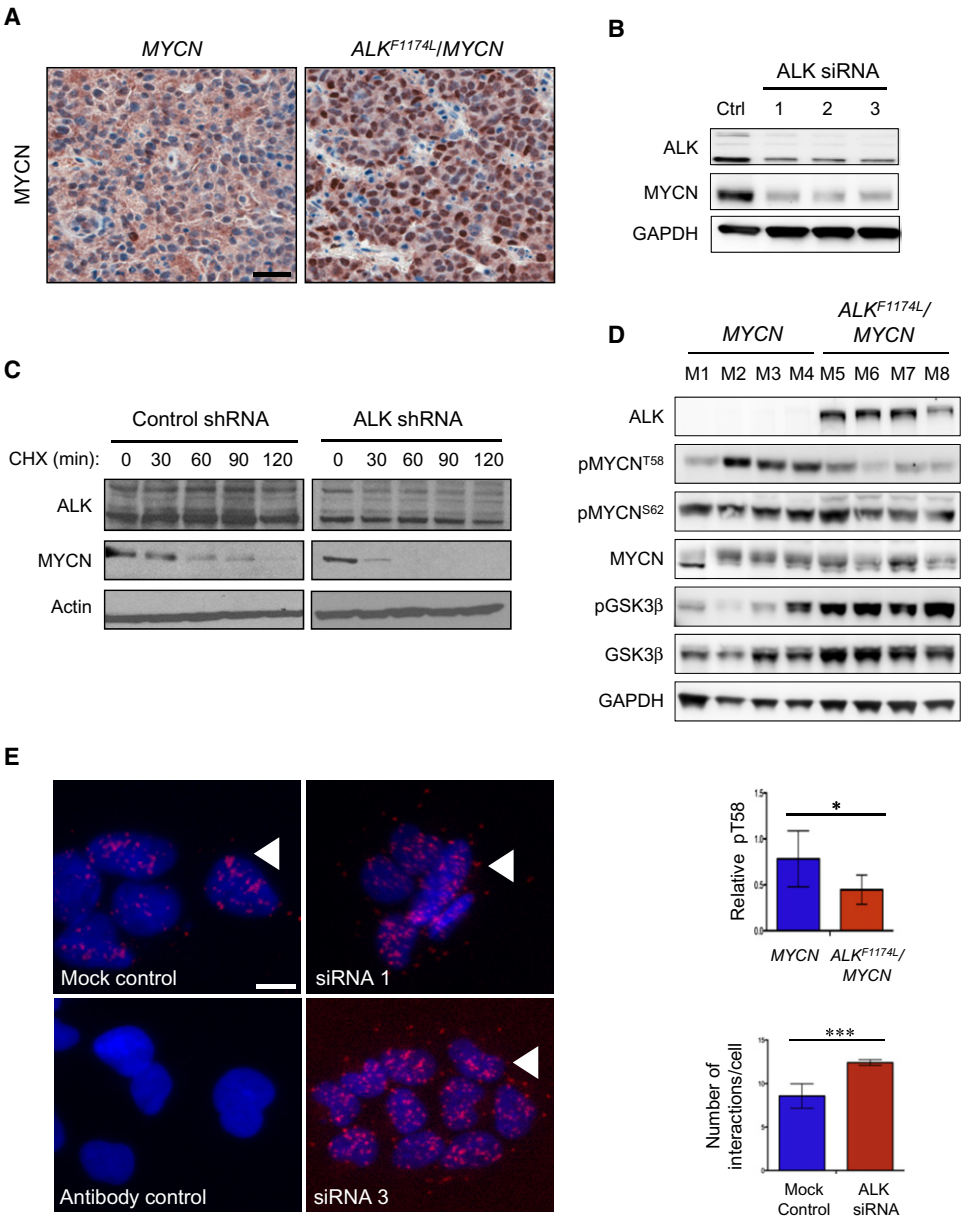

Figure 4. ALK^{F1174L} Enhances MYCN Protein Stabilization

(A) Immunohistochemical staining for MYCN in *ALK*^{F1174L}/*MYCN* and *MYCN* tumors. Scale bars, 20 μm.

(B) Western blot analysis of MYCN protein in Kelly human neuroblastoma cells after ALK^{F1174L} knockdown using three different siRNAs (1, 2, and 3). Ctl, cells expressing a control siRNA.

(C) Western blot analysis of MYCN protein expression in Kelly cells transfected with an *ALK* or control shRNA followed by treatment with 25 μmol/L of cycloheximide (CHX) and harvested at the indicated time points.

(D) Immunoblotting of *ALK*^{F1174L}/*MYCN* and *MYCN* tumors for pMYCN^{S62}, pMYCN^{T58}, and pGSK3β (upper panel). Graph (lower panel) depicts quantification of pMYCN^{T58} expression in the two types of tumors. *p = 0.05 by unpaired t test.

(E) In situ detection of MYCN:FBXW7 complex formation (arrowheads) in untreated Kelly cells (mock control), ALK^{F1174L}-depleted cells (siRNAs 1 and 3), or cells probed with secondary antibody only as a negative control (antibody control). Quantification of the number of MYCN:FBXW7 interactions in untreated Kelly cells and ALK^{F1174L}-depleted Kelly cells (right panel). Data are presented as means ± standard deviation (SD). ***p = 0.009 (Student's t test).

encoding proteins reported to be involved in MYCN-induced apoptosis that regulate p53, such as MDM2, p14^{ARF} or TWIST (Gustafson and Weiss, 2010) were differentially expressed between *ALK*^{F1174L}/*MYCN* tumors and *MYCN* tumors (data not shown). Since various BCL2 family members are direct transcriptional targets of p53 (Hemann and Lowe, 2006), we then compared the expression of BCL2 family proteins between the two tumor types. Both mRNA and protein levels of the pro-survival genes *Bcl2* and *Bclw* (*Bcl2l2*), but not *Mcl1*, were significantly upregulated in *ALK*^{F1174L}/*MYCN* tumors (Figures

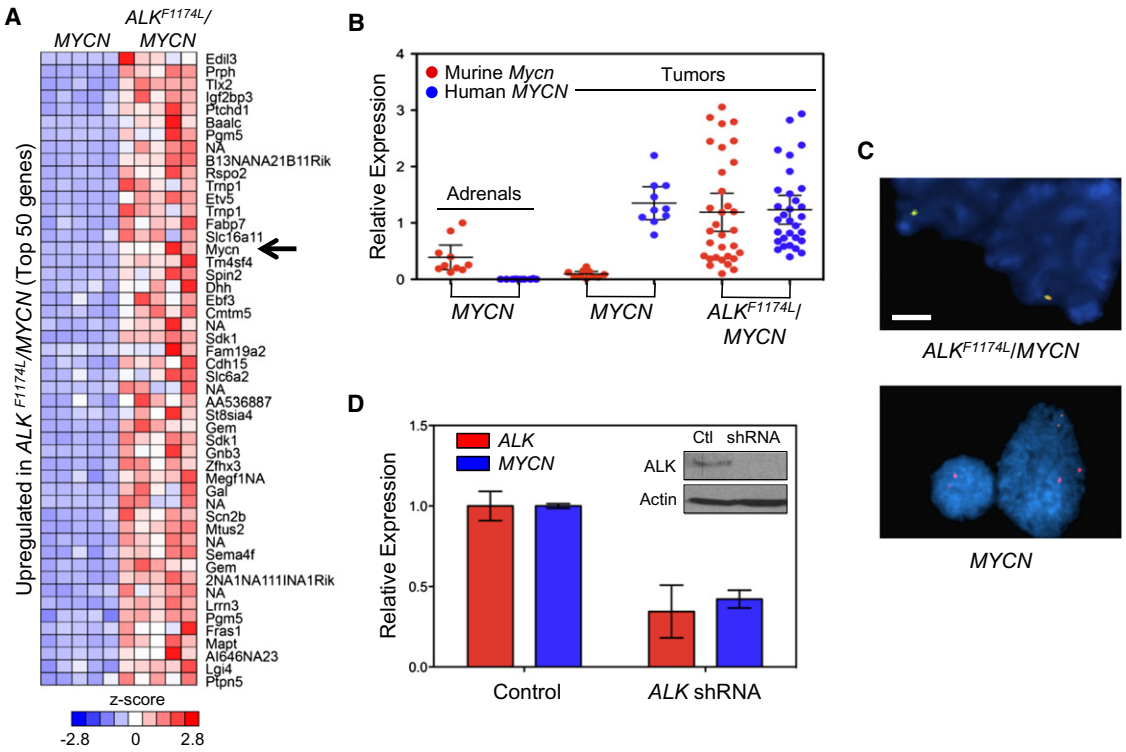

Figure 5. ALK^{F1174L} Induces Expression of Endogenous Murine MYCN

(A) Heat map representing the top 50 upregulated genes (corrected p value < 0.05, fold change ≥ 2.0) in ALK^{F1174L}/*MYCN* tumors compared with *MYCN* tumors.
(B) qRT-PCR analysis of murine and human *MYCN* expression in adrenal glands and tumors from ALK^{F1174L}/*MYCN* and *MYCN* mice. Expression is relative to either murine or human *MYCN* levels in tumors from *MYCN* heterozygotic mice. Mean values ± 95% CI are indicated.
(C) FISH analysis of murine ALK^{F1174L}/*MYCN* tumors using an *ALK* dual-color break-apart probe (upper panel) and a *MYCN* probe (lower panel) (Scale bar, 10 μm).
(D) qRT-PCR analysis of ALK^{F1174L} and *MYCN* expression in Kelly cells in which ALK^{F1174L} expression was depleted using shRNA, compared with cells in which a control shRNA was used. Western blot showing level of ALK^{F1174L} knockdown (inset). Mean ± SEM values for three independent experiments are shown. Ctl, cells expressing a control shRNA.

6B–6D). The pro-apoptotic genes *Bak* and *Bax*, the latter being a key intermediate of MYC-driven apoptosis (Hemann and Lowe, 2006), and the BH3 pro-apoptotic genes *Bik*, *Bid*, and *Noxa* were downregulated in the ALK^{F1174L}/*MYCN* tumors (Figures 6B and 6C). Together, these findings suggest that constitutively expressed ALK^{F1174L} contributes to MYCN-driven neuroblastoma by exerting an anti-apoptotic effect that allows transformed cells to evade MYCN-induced apoptosis.

Combined Inhibition of ALK^{F1174L} and Its Downstream Signaling Pathways Leads to Regression of ALK^{F1174L}/*MYCN* Tumors

Human neuroblastoma cells and xenograft models expressing ALK^{F1174L} are resistant to crizotinib (Bresler et al., 2011). To determine if such resistance was reiterated in our neuroblastoma model, we treated mice bearing ALK^{F1174L}/*MYCN* tumors with crizotinib. After documenting baseline tumor burden by serial MRIs, we treated the animals for 7 days with oral vehicle or crizotinib at a daily dose of 100 mg/kg, which has been used in xenograft models of neuroblastoma (Bresler et al., 2011). Despite partial dephosphorylation of ALK, crizotinib treatment did not appear to have an effect on tumor size (Figures 7A–7C). Histologic analysis confirmed the lack of any significant treatment effect on cellularity, while cleaved caspase-3 staining revealed no evidence of apoptosis (Figure 7D). Thus, our doubly transgenic model recapitulates the crizotinib resistance of human neuroblastoma and ALK-rearranged cancers.

Preclinical studies of crizotinib have shown that both pAKT and pERK are incompletely inhibited with doses of crizotinib that abolish ALK phosphorylation in NPM-ALK-positive lymphoma cells (Christensen et al., 2007). To determine whether the lack of response to crizotinib in the ALK^{F1174L}/*MYCN* tumors could be due to persistent or even paradoxical activation of the signaling pathways utilized by these two interacting oncoproteins, we analyzed the downstream effectors of the PI3K/AKT/mTOR and MAPK pathways. Although treatment with crizotinib led to a minimal decrease in AKT phosphorylation compared with results for vehicle-treated animals, it lacked any discernible effects on mTOR and MAPK signaling, as indicated by the persistent activation of pS6K and p4E-BP1 and of pMEK and pERK, respectively, on both western analysis and immunohistochemistry (Figures 7C and 7D).

We therefore sought to determine if these tumors could be rendered sensitive to crizotinib by adding Torin2, an ATP-competitive inhibitor of mTOR (Liu et al., 2011), a combination that had exhibited efficacy in vitro (A. Azarova and R.E.G., unpublished data). When given alone, Torin2 ablated *MYCN* tumors with reduction in MYCN protein levels and induction of

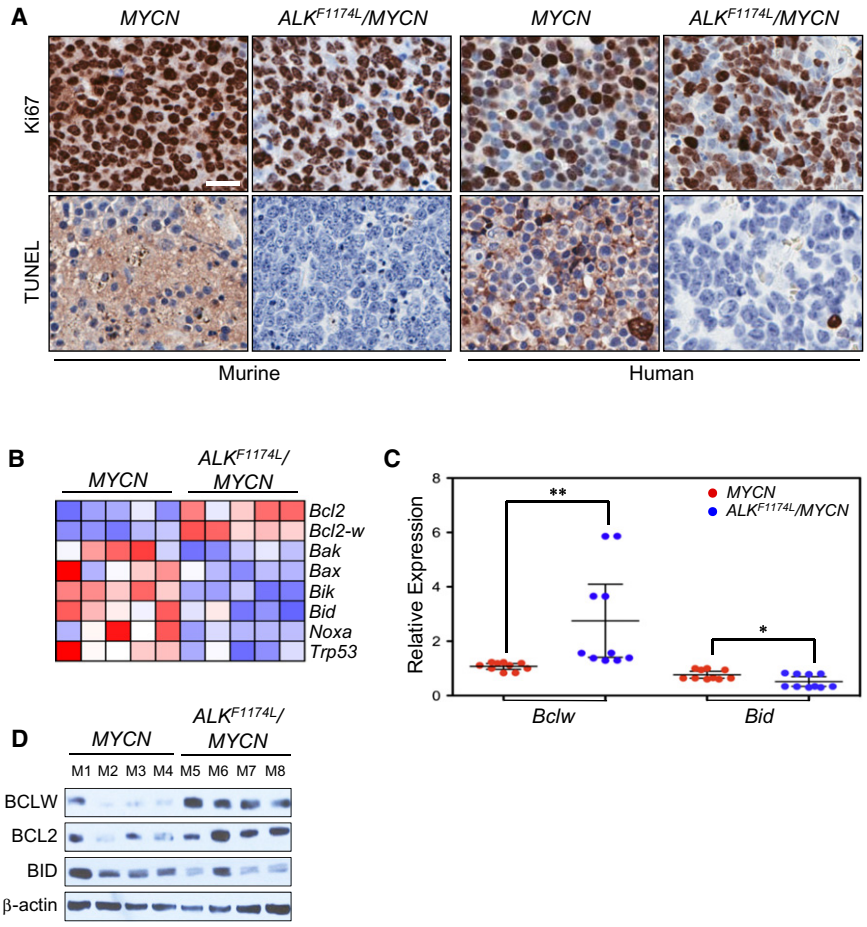

Figure 6. *ALK*^{F1174L} Promotes Anti-Apoptotic Activity in *ALK*^{F1174L}/*MYCN* Neuroblastomas

(A) Immunohistochemical staining for Ki67 and TUNEL of transgenic murine and human *ALK*^{F1174L}/*MYCN* and *MYCN* neuroblastomas. Scale bars, 20 μm.

(B) Heat map representation of the expression levels of pro-survival genes, *Bcl2* and *Bclw*, and the pro-apoptotic genes *Bak*, *Bax*, *Bik*, *Bid*, *Noxa*, and *Trp53*, in *ALK*^{F1174L}/*MYCN* and *MYCN* tumors.

(C) qRT-PCR analysis of *Bclw* and *Bid* expression in *ALK*^{F1174L}/*MYCN* and *MYCN* tumors (n = 10 in each group). Gene expression is relative to that in a *MYCN* tumor. Data are presented as mean ± SEM (*p = 0.03, **p = 0.005).

(D) Immunoblotting of *ALK*^{F1174L}/*MYCN* and *MYCN* tumors depicting expression of BCLW, BCL2, and BID proteins in the *ALK*^{F1174L}/*MYCN* and *MYCN* tumors.

See also Figure S4.

apoptosis (Figures S5A–S5C). However, concomitant expression of ALK^{F1174L} abrogated any efficacy of Torin2, as indicated by essentially stable tumor volumes after 7 days of treatment with this agent at 20 mg/kg/day (Figures 7A and 7B). Predictably, Torin2 treatment of *ALK*^{F1174L}/*MYCN* tumors in large part led to downregulation of the mTORC1 targets, pS6K and p4E-BP1, but did not affect pMEK or pERK, or induce any substantial increase in apoptosis (Figures 7C and 7D). By contrast, combined use of crizotinib (100 mg/kg/day) with Torin2 (20 mg/kg/day) for 7 days significantly reduced tumor size and growth (Figures 7A and 7B). Of the four mice receiving both agents, three had obvious regressions of their tumors, while one showed growth inhibition. The proportion of mice with tumor regression improved to 100% in a subsequent study in which 80% dosage of each drug was given in combination (data not shown). These favorable responses to combination treatment correlated with inhibition of pALK, pAKT, mTOR, and MAPK targets (Figures 7C and 7D). Importantly, the combination also led to a striking increase in apoptosis as determined by cleaved caspase-3 staining (Figure 7D). Since phospho-ALK immunoblotting does not appear to provide a reliable assessment of ALK inhibition, we confirmed by mass spectroscopy that crizotinib was present in tumor tissue at exposure levels in excess of its published IC_{50} for ALK inhibition (Bresler et al., 2011; Schönherr et al., 2012) (Table S1). The variability in total ALK levels on immunoblots of tumors treated with the combination (Figure 7C) likely reflects the significant levels of cell death observed at 7 days post-treatment (Figure 7D, H&E stain), and is not a primary effect of the therapy on ALK levels. Consistent with this possibility, immunohistochemical staining of these tumors showed large regions that stained negatively for ALK (Figure S5D), and in tumors harvested after short-term (3-day) therapy trials, uniform levels of total ALK were seen on immunoblots (Figure S5E).

We next analyzed longer-term survival using a larger number of mice (n = 10 per group) treated for 14 days. Treatment with crizotinib and Torin2 significantly prolonged survival compared to the outcome with use of vehicle or either single agent alone (Figure 7E). Indeed, all mice given the combination remained alive for 10–23 days post-treatment, whereas mice treated with crizotinib and Torin2 as single agents began to die before treatment was stopped, with none surviving for more than 10 days post-treatment. Together, these findings suggest that the failure of crizotinib to inhibit the downstream pathways utilized by ALK^{F1174L} and MYCN can be overcome by adding an effective downstream pathway inhibitor, such as Torin2.

DISCUSSION

Activating mutations in the ALK receptor tyrosine kinase represent potentially useful therapeutic targets in high-risk neuroblastoma. In contrast to MYCN, which has been difficult to target (Gustafson and Weiss, 2010), mutated ALK lends itself to inhibition by small molecules and hence may spawn a generation of targeted therapies for this resistant tumor. Here we used a mouse model of neuroblastoma coexpressing *ALK*^{F1174L} and *MYCN* to demonstrate that constitutive ALK^{F1174L} activity potentiates the oncogenic effects of MYCN, resulting in the formation of aggressive, highly penetrant tumors. Similar cooperativity between ALK^{F1174L} and MYCN was recently observed in a zebrafish

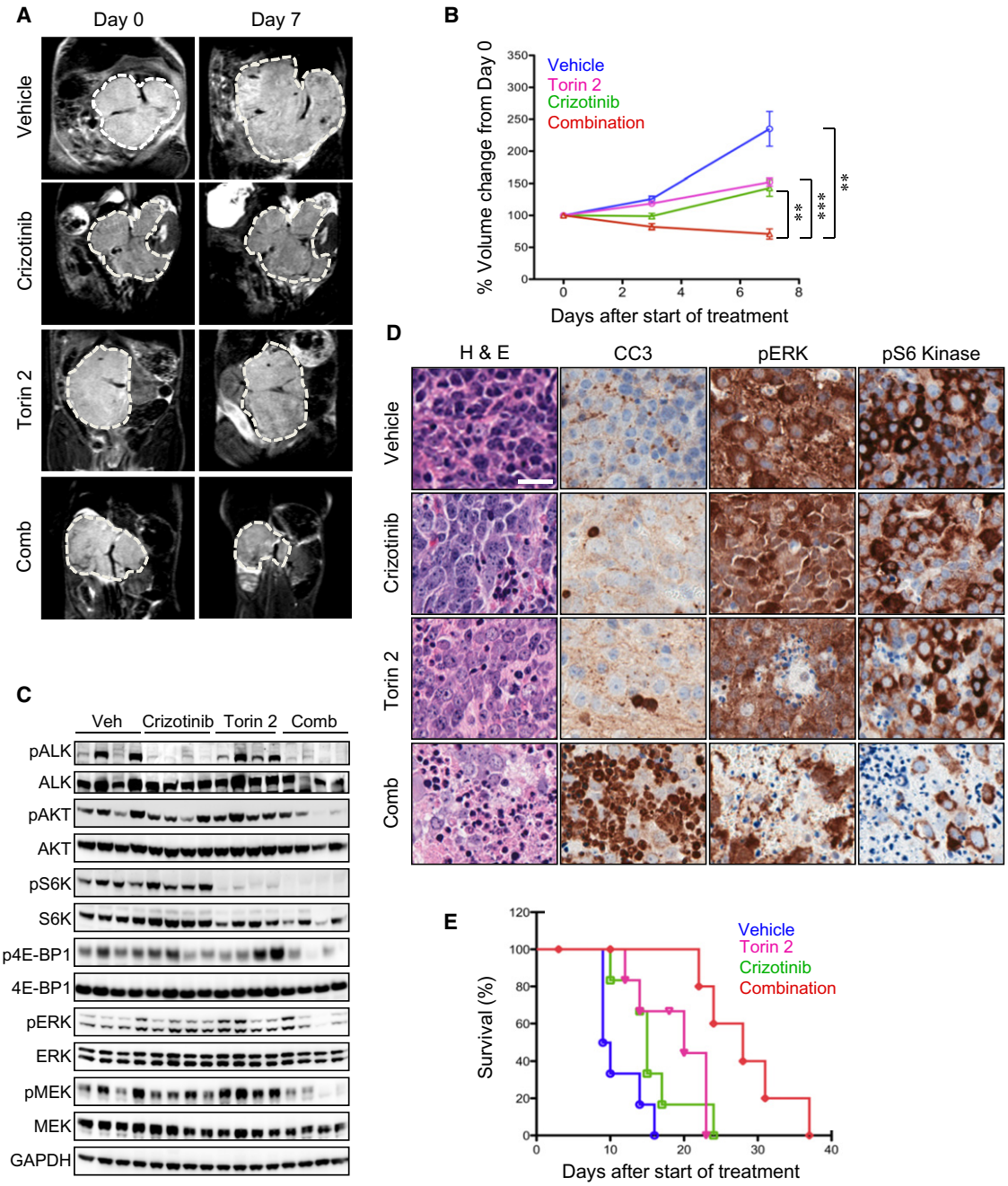

Figure 7. Combined Targeting of ALK^{F1174L} and mTOR Is Effective against ALK^{F1174L}/*MYCN* Neuroblastomas

(A) MRI images depicting a representative tumor response to vehicle or crizotinib (100 mg/kg) and Torin2 (20 mg/kg) as single agents or in combination (at single agent doses) after 7 days of treatment. Comb, combination treatment.

(B) Quantitation of changes in tumor volume in animals treated with crizotinib, Torin2, or combination therapy as measured by MRI on days 0, 3 and 7. Data are presented as means ± SEM (4 animals per treatment group). Crizotinib versus combination, **p = 0.003; Torin2 versus combination; ***p = 0.0002; vehicle versus combination, **p = 0.002; all by Student's t test.

(C) Western blot analysis of the indicated proteins in ALK^{F1174L}/*MYCN* tumors in panels (A) and (B). Veh, vehicle; Comb, combination.

(D) H&E and immunohistochemical staining of tumors in (A) and (B) as indicated. Comb, combination treatment. Scale bars, 10 μm.

(E) Kaplan-Meier survival analysis for ALK^{F1174L}/*MYCN* animals (10 per group) treated for 14 days with crizotinib and Torin2 as single or combined agents. Crizotinib versus combination, p = 0.007; Torin2 versus combination, p = 0.02; both comparisons by log-rank test.

See also Figure S5 and Table S1.

model (Zhu et al., 2012). The acceleration of tumorigenesis by mutant ALK is accompanied by activation of signaling pathways that lead to stabilization of the MYCN protein while countering its pro-apoptotic effects. We also show that our *ALK*^{F1174L}/*MYCN* tumor model recapitulates the in vitro resistance of ALK^{F1174L}–positive tumor cells to crizotinib, but that the combination of crizotinib and an mTOR inhibitor, Torin2, can circumvent this resistance, leading to marked tumor regression and prolongation of survival.

ALK^{F1174L}, although shown to be transforming in NIH 3T3 and Ba/F3 assays (Chen et al., 2008; De Brouwer et al., 2010; George et al., 2008; Janoueix-Lerosey et al., 2008), did not appear to be sufficient by itself to induce tumors in our model. The reasons underlying this are not entirely clear, but given the fact that *ALK* mutations have been identified in both high- and low-stage tumors, it is conceivable that while activated ALK has a role in tumor initiation, cooperation with additional aberrations such as *MYCN* amplification or loss of tumor suppressors on chromosome 1p or 11q are required to specify high- versus low-stage tumors. Serial analysis of developing sympathetic tissues from *Th-ALK*^{F1174L} mice will be useful in determining whether neuroblast cell hyperplasia or even localized tumors develop in these animals, which then regress in the absence of cooperative genetic events.

Of interest, the *ALK*^{F1174L} mutation has not been reported in the germline of patients with familial neuroblastoma. This could indicate that either high levels of activated ALK kinase activity or functions specific to the ALK^{F1174L} mutation are not tolerated during embryogenesis. By contrast, we observed Mendelian distribution of *ALK*^{F1174L} alleles in crosses of our *Th-ALK*^{F1174L} animals suggesting absence of embryonic lethality. The approach we used to generate our murine model does not modify the endogenous *ALK* alleles and therefore the developmentally essential expression of endogenous *ALK* in the CNS and other organs (Vernersson et al., 2006) presumably remains unaltered. Moreover, the *Th*-driven *ALK*^{F1174L} mutation exhibits tissue-specific expression in relatively more differentiated *Th*-positive sympathetic neuronal precursors. To more accurately address these issues, a knock-in modeling strategy replacing an endogenous *Alk* allele with an inducible *ALK*^{F1174L} allele would be required.

In the *Th-MYCN* model, heterozygote animals of the 129X1/SvJ strain develop neuroblastoma within 4 to 5 months accompanied by additional chromosomal gains or losses, whereas homozygous animals show increased penetrance and shorter latency of tumors that approaches 100% at three months, without the requirement for additional chromosomal lesions (Weiss et al., 1997). Thus, a small increase in MYCN dosage is sufficient to augment MYCN-driven tumorigenesis. We observed increased MYCN protein stability in *ALK*^{F1174L}/*MYCN* transgenic tumors. MYCN stability is specifically regulated by sequential phosphorylation of S62 and T58 within MYC Box 1, the former through either CDK1 or the MAPK pathway (Marshall et al., 2011; Sears et al., 2000; Sjostrom et al., 2005), and the latter, through the PI3K/AKT pathway via GSK3β-mediated inhibitory phosphorylation (Sears et al., 2000). AKT- or ERK-mediated mTORC1 signaling also downregulates PP2A, which normally dephosphorylates MYCN at S62, targeting pMYCN^{T58} for ubiquitination and degradation by the E3 ligase FBXW7 (Gustafson and Weiss, 2010). We demonstrate that increased activation of the PI3K/AKT/mTOR pathway and additional recruitment of the MAPK pathway combine to stabilize MYCN in *ALK*^{F1174L}/*MYCN* tumors. We suggest that the discrepancy between MYCN levels on immunohistochemical staining versus immunoblotting reflects the very short half-life and high rate of synthesis of this oncoprotein in vivo. *Th-MYCN* tumors have very high levels of MYCN protein even in the absence of ALK expression (Weiss et al., 1997), and the limited dynamic range of immunoblotting may hinder the detection of increased total MYCN by this method.

We also report that the stabilization of the MYCN protein seen in *ALK*^{F1174L}/*MYCN* tumors is augmented by increased levels of endogenous *Mycn* transcripts, confirming recent in vitro findings that both WT and gain of function *ALK* mutations stimulate *MYCN* transcription (Schönherr et al., 2012). The mechanism underlying this phenomenon is unclear, but could be due to either an indirect effect of ALK^{F1174L} signaling on the *Mycn* promoter (Wierstra and Alves, 2008) or loss of *Mycn* autorepression. Indeed, as reported by Penn et al. (Penn et al., 1990), MYC suppresses transcription from its own promoter when the level of the oncoprotein exceeds 10,000 molecules per cell. It seems reasonable, then, to suggest that signaling mediated by ALK^{F1174L} either prevents or abolishes a block at the *Mycn* promoter, allowing unimpeded gene transcription. Such ALK^{F1174L}-induced regulation of Mycn could occur during early development, leading to sustained high levels of MYCN in sympathetic neuronal precursor cells, which then sets the stage for rapid malignant transformation.

The relative lack of apoptosis in our tumor model suggests that ALK^{F1174L} counteracts MYCN-induced cell death as part of the transformed phenotype. We noted significant downregulation of the pro-apoptotic BCL2 proteins NOXA, BID, and BAX, all transcriptional targets of p53, which itself was downregulated in the *ALK*^{F1174L}/*MYCN* tumors. Accompanying these findings was upregulation of the anti-apoptotic BCLW and, to a lesser extent, BCL2 proteins. The upregulation of BCLW is particularly relevant because it has been shown to counteract apoptosis induced by nerve growth factor deprivation and BAD overexpression in sympathetic neuronal cells (Hamnér et al., 2001). Moreover, the overexpression of BCLW and BCL2, but not MCL1, places the *ALK*^{F1174L}/*MYCN* tumors in the subset of neuroblastomas that are predicted to be sensitive to the BCL2 inhibitor ABT-737 (Goldsmith et al., 2010), thus providing an additional avenue for therapeutic targeting of these tumors. In other receptor tyrosine kinase-activated cancers and in tumors positive for ALK fusion proteins, resistance to apoptosis is mediated through signal transduction pathways that directly enhance the transcription of anti-apoptotic factors such as *BCLXL* while inhibiting pro-apoptotic genes (Chiarle et al., 2008). We therefore suggest that the anti-apoptotic effect seen in *ALK*^{F1174L}/*MYCN* tumors arises from ALK^{F1174L}-mediated activation of both the PI3K/AKT/mTOR and MAPK signaling cascades.

The demonstration that *ALK* cooperates with *MYCN* to accelerate tumorigenesis helps to explain the role of oncogenes such as *MYCN* during tumor initiation. The bulk of evidence suggests that MYC oncoproteins play a critical role during this phase of tumor development, where high levels are required to initiate and expand oncogenic clones (Arvanitis and Felsher, 2006;

Soucek and Evan, 2010), usually in combination with an apoptotic defect (Hansford et al., 2004). We propose that activated *ALK* simultaneously stabilizes MYCN protein and uncouples MYCN-driven apoptosis, potentiating the oncogenic activity of MYCN during early development of neuroblasts. This concept is also relevant to the clinical observation that prognosis in neuroblastoma is strongly associated with *MYCN* gene copy number but only variably with protein levels (Cohn et al., 2000). In contrast to the situation during tumor initiation, low, "threshold" levels of MYC are likely sufficient to maintain progression of oncogene-addicted, established tumors, and prevent the switch from ongoing proliferation to apoptosis/necrosis (Murphy et al., 2008; Shachaf et al., 2008). Therefore, stabilization of MYCN by modulation of MYC Box 1 phosphorylation (Marshall et al., 2011) or inhibition of MYCN protein ubiquitination and degradation (Otto et al., 2009) are both mechanisms by which stoichiometric control of MYC protein levels are achieved during malignant transformation in precancerous cells (Marshall et al., 2011). Pharmacologic modulation of such pathways that stabilize MYCN abrogates neuroblastoma tumor formation in the *Th-MYCN* model, providing experimental validation of this concept (Chanthery et al., 2012; Marshall et al., 2011).

In MYCN-driven neuroblastoma, the PI3K pathway appears to be the major signaling conduit for regulation of MYCN activity, and selective inhibition of this pathway has been shown to lead to MYCN destabilization and subsequent tumor regression (Chesler et al., 2006). Oncogenic transformation caused by ALK fusion proteins, on the other hand, appears to be effected through several interconnected and overlapping pathways that are differentially recruited by the activated ALK kinase based on cell type, context and fusion partner (Chiarle et al., 2008; Palmer et al., 2009). In anaplastic large cell lymphoma, the aberrant growth of the cells expressing the *NPM-ALK* fusion gene, for example, is mainly attributable to activation of the JAK-STAT and MAPK pathways (Pulford et al., 2004). However, in our tumor model, ALK^{F1174L} utilizes both the PI3K/AKT/mTOR and MAPK pathways to instigate downstream signals leading to increased survival. Interestingly, the same signaling pathways are upregulated when the *F1174L* mutation occurs in the background of *ALK* translocations such as *EML4-ALK* and *RANBP2-ALK* (Heuckmann et al., 2011; Sasaki et al., 2010), suggesting that the same mode of downstream signaling is used whether the mutation arises de novo or as an acquired mechanism of resistance. Hence, the treatment strategy that we propose, in which crizotinib is combined with a downstream pathway inhibitor, may be effective against these cancers, delaying or even preventing the onset of resistance to crizotinib.

For a tyrosine kinase inhibitor to be successful, it must abrogate activity of key intracellular pathways that transmit oncogenic activity of the kinase. We determined that the resistance to crizotinib seen in ALK^{F1174L}/*MYCN*-driven murine neuroblastoma relates to incomplete inhibition of key signaling cascades. Crizotinib treatment, while leading to reduced levels of pALK and pAKT at high doses lacked any effect on pERK or activated mTOR signaling in ALK^{F1174L}/*MYCN* tumors. Thus, in crizotinib-treated animals even a minimal amount of ALK^{F1174L} activity appears sufficient to maintain downstream signaling, especially that of mTORC1. We suggest that both the PI3K/AKT and MAPK pathways contribute to mTORC1 activation in these tumors, but as AKT signaling becomes downregulated by crizotinib, mTORC1 signaling is maintained by the MAPK pathway, which would account for the relative insensitivity of the tumor cells to single agent treatment with Torin2. However, combined treatment with crizotinib and Torin2 induced downregulation of all components of the PI3K/AKT/mTOR as well as MAPK pathways, accompanied by the induction of massive apoptosis. Importantly, suppression of these two signaling pathways, together with ALK^{F1174L} activity, effectively inhibited the growth of ALK^{F1174L}/*MYCN* tumors, leading to significant decreases in tumor volumes and a higher proportion of surviving mice.

Our study indicates that the combination of crizotinib and an ATP-competitive mTOR inhibitor, or perhaps a MEK inhibitor, would afford a useful treatment strategy for neuroblastoma with constitutive activation of ALK^{F1174L} and *MYCN*. The reduced susceptibility of *F1174L*-mutated *ALK* to crizotinib inhibition has been reported to arise from an increased ATP-binding affinity, suggesting that higher doses of crizotinib or substitution of higher-affinity inhibitors may surmount this barrier to successful treatment (Bresler et al., 2011). Although a dose-response relationship to crizotinib as a single agent in ALK^{F1174L}-expressing neuroblastoma cell lines (Bresler et al., 2011; A. Azarova and R.E.G., unpublished data) and in our ALK^{F1174L}/*MYCN* model (L.C. and R.E.G., unpublished data) has been observed, whether the doses of crizotinib required to completely eradicate the tumor will be feasible in a clinical setting remains to be determined. Moreover, prolonged use of even the most effective ALK inhibitor by itself would ultimately generate resistance. Hence, simultaneously attacking more than one vulnerable lesion in neuroblastoma cells seems a more promising strategy to prevent or forestall the development of crizotinib resistance. Indeed, further efficacy might be afforded by the addition of therapeutic agents that inhibit the pro-survival proteins BCL2 and BLCW or that disrupt mechanisms active in the synthesis of MYCN. Regardless of the specific combination of targets, the double transgenic model developed in this study would provide an ideal platform for screening candidate small-molecule inhibitors and elucidating interactions among the aberrant signaling cascades that underlie ALK^{F1174L}/*MYCN*-positive neuroblastoma. Finally, we suggest that simultaneous targeting of ALK and its downstream effector molecules may lengthen the duration of response in a larger group of patients with tumors harboring crizotinib-sensitive ALK. This cohort includes those with other point mutations or amplification of *ALK* as in neuroblastoma, or with *ALK* translocations such as non-small cell lung cancer, inflammatory myofibroblastic tumor, anaplastic large cell lymphoma, and several others.

EXPERIMENTAL PROCEDURES

Plasmids

The ALK^{F1174L} mutation was introduced into WT *ALK* cDNA in pcDNA3.1 (Invitrogen) using the QuickChange II Site-Directed Mutagenesis Kit (Stratagene). All mutations were confirmed by sequencing of the entire *ALK* open reading frame. The ALK^{F1174L} cDNA was ligated downstream of the rat tyrosine hydroxylase (*Th*) promoter (Banerjee et al., 1992) in the *Th-MYCN* transgenic construct after excision of *MYCN* with appropriate restriction enzymes to generate the p4.5 *Th-*ALK^{F1174L} construct. For transient transfections, ALK^{F1174L} was introduced into 293T cells (human embryonic kidney transformed cells) using Fugene 6 transfection reagent (Roche) according to the manufacturer's instructions.

Mouse Models

Th-ALK^{F1174L} founders were derived from *CBA* × *C57BL/6J* mice and genetically crossed with *Th-MYCN* mice of the 129/SvJ strain. Tail DNA of all animals was analyzed for *ALK* and *MYCN* transgenes by qRT-PCR (Transnetyx, Inc.). All animal experiments were conducted in accordance with established UK Home Office guidelines per conditions specified in an animal use authorization license (PPL70-6882) that is approved by The Institute of Cancer Research local ethical review committee.

Tumor Histopathology

Animal tumors were harvested at sacrifice, fixed in 10% neutral buffered formalin, and paraffin-embedded for histologic studies. Tissue sections were stained with H&E and assessed histologically by a pediatric pathologist (A.P.A.) for confirmation of tumor type, and specifically for histologic features of neuroblastoma including amount of stroma and neuropil, mitotic/karyorrhectic index, and degree of differentiation. Representative examples from each of the founder lines were analyzed (*ALK*^{F1174L}/*MYCN* tumors, n = 15; *MYCN* tumors, n = 9). For immunohistochemistry, 5 μm sections were stained with antibodies to ALK (Ventana), MYCN (Calbiochem), pMEK, pS6K, pERK, cleaved caspase 3 (Cell Signaling Technology), and TUNEL (Millipore) using standard methods, including heat-induced epitope retrieval using citrate buffer pH 6 (or EDTA buffer for ALK). Formalin-fixed slides from patients with both ALK^{F1174L}/MYCN-positive and MYCN-positive neuroblastoma tumors were stained using the same antibodies. All human tumor specimens were obtained in accordance with the Institutional Review Boards of Memorial Sloan-Kettering Cancer Center and the Dana-Farber Cancer Institute and deidentified before analysis.

Murine Therapy Trials

Th-MYCN hemizygous mice were bred with *Th-ALK*^{F1174L} hemizygous mice, and litters were genotyped to detect the presence of human *MYCN* or *ALK*^{F1174L} transgenes. After weaning, at about day 28, animals hemizygous for both transgenes or *MYCN* alone were palpated for intra-abdominal tumors twice weekly. Animals with palpable tumors (30–70 days old) were randomized to treatment groups. For intervention trials, mice were treated with 100 mg/kg crizotinib or 20 mg/kg Torin2 as single agents, 100 mg/kg crizotinib and 20 mg/kg Torin2 in combination, or vehicle for 7 days. Crizotinib and Torin2 were administered via oral gavage. MRI was performed on a 7T Bruker horizontal bore microimaging system (Bruker Instruments, Ettlingen, Germany) using a 3-cm birdcage coil. Anatomical T_2-weighted coronal images were acquired from twenty contiguous 1 mm thick slices through the mouse abdomen, from which tumor volumes were determined using segmentation from regions of interest drawn on each tumor-containing slice. At sacrifice, tumors were excised, weighed, snap frozen in liquid nitrogen for metabolic assays, or fixed in 10% neutral buffered formalin. For survival trials, mice were treated with 100 mg/kg crizotinib or 20 mg/kg Torin2 as single agents, 100 mg/kg crizotinib (or 80 mg/kg where indicated) and 20 mg/kg Torin2 in combination, or vehicle for 14 days. Mice were monitored daily; tumor size was palpated and animal weights measured. Animals were sacrificed when pathologic signs of tumor burden (predominantly poor mobility) were apparent.

Statistical Analyses

All biochemical experiments were done in triplicate unless otherwise stated. Two-tailed Student's t test was used to test significance. Survival curves were constructed by the Kaplan and Meier method, with differences between curves tested for statistical significance using the log-rank test; s.d., standard deviation; C.I., confidence interval; s.e.m., standard error of the mean.

ACCESSION NUMBERS

The GEO public database accession number for the microarray data is GSE35560.

SUPPLEMENTAL INFORMATION

Supplemental Information includes five figures, one table, Supplemental Experimental Procedures, and Supplemental References and can be found with the article online at http://dx.doi.org/10.1016/j.ccr.2012.06.001.

ACKNOWLEDGMENTS

We thank Terri Bowman for help with immunohistochemistry. We thank J.R. Gilbert for helpful comments on the manuscript. This work was supported by US National Institutes of Health Grant R01 CA148688 (to R.E.G.), Sidney Kimmel Translational Scholar Award (to R.E.G.), Children's Hospital Boston TRP Pilot Grant (to R.E.G.), NIH Grant CA136851-01A1 (to N.S.G. and Q.L.), the Catie Hoch Foundation and the Robert Steel Foundation (to N.K.C.), SPARKS grant 09RMH01 (to L.C.), Neuroblastoma Society Grant NES003X (to L.C.), Medical Research Council (MRC) Grant NC3R-G1000121/94513 (to L.C. and S.A.E.), ICR and Cancer Research UK (CRUK) Grants A14610 (to L.C.), C309/A8274, and C309/A11566 (to S.A.E.), ICR CRUK/EPSRC/MRC and Department of Health (England) Grant C1060/A10334 (to Y.J. and S.P.R.), CRUK Grant A10294 (to A.D.J.P.), and Wellcome Trust Grant 091763Z/10/Z (to Y.J.). We acknowledge NHS funding to the NIHR Biomedical Research Centre.

Received: January 14, 2012
Revised: March 18, 2012
Accepted: June 5, 2012
Published: July 9, 2012

REFERENCES

Arvanitis, C., and Felsher, D.W. (2006). Conditional transgenic models define how MYC initiates and maintains tumorigenesis. Semin. Cancer Biol. *16*, 313–317.

Banerjee, S.A., Hoppe, P., Brilliant, M., and Chikaraishi, D.M. (1992). 5′ flanking sequences of the rat tyrosine hydroxylase gene target accurate tissue-specific, developmental, and transsynaptic expression in transgenic mice. J. Neurosci. *12*, 4460–4467.

Bresler, S.C., Wood, A.C., Haglund, E.A., Courtright, J., Belcastro, L.T., Plegaria, J.S., Cole, K., Toporovskaya, Y., Zhao, H., Carpenter, E.L., et al. (2011). Differential inhibitor sensitivity of anaplastic lymphoma kinase variants found in neuroblastoma. Sci. Transl. Med. *3*, 108–114.

Brodeur, G.M., Seeger, R.C., Schwab, M., Varmus, H.E., and Bishop, J.M. (1984). Amplification of N-*myc* in untreated human neuroblastomas correlates with advanced disease stage. Science *224*, 1121–1124.

Butrynski, J.E., D'Adamo, D.R., Hornick, J.L., Dal Cin, P., Antonescu, C.R., Jhanwar, S.C., Ladanyi, M., Capelletti, M., Rodig, S.J., Ramaiya, N., et al. (2010). Crizotinib in ALK-rearranged inflammatory myofibroblastic tumor. N. Engl. J. Med. *363*, 1727–1733.

Chanthery, Y.H., Gustafson, W.C., Itsara, M., Persson, A., Hackett, C.S., Grimmer, M., Charron, E., Yakovenko, S., Kim, G., Matthay, K.K., and Weiss, W.A. (2012). Paracrine signaling through MYCN enhances tumor-vascular interactions in neuroblastoma. Sci. Transl. Med. *4*, 115–113.

Chen, Y., Takita, J., Choi, Y.L., Kato, M., Ohira, M., Sanada, M., Wang, L., Soda, M., Kikuchi, A., Igarashi, T., et al. (2008). Oncogenic mutations of ALK kinase in neuroblastoma. Nature *455*, 971–974.

Chesler, L., Schlieve, C., Goldenberg, D.D., Kenney, A., Kim, G., McMillan, A., Matthay, K.K., Rowitch, D., and Weiss, W.A. (2006). Inhibition of phosphatidylinositol 3-kinase destabilizes Mycn protein and blocks malignant progression in neuroblastoma. Cancer Res. *66*, 8139–8146.

Chiarle, R., Voena, C., Ambrogio, C., Piva, R., and Inghirami, G. (2008). The anaplastic lymphoma kinase in the pathogenesis of cancer. Nat. Rev. Cancer *8*, 11–23.

Christensen, J.G., Zou, H.Y., Arango, M.E., Li, Q., Lee, J.H., McDonnell, S.R., Yamazaki, S., Alton, G.R., Mroczkowski, B., and Los, G. (2007). Cytoreductive antitumor activity of PF-2341066, a novel inhibitor of anaplastic lymphoma kinase and c-Met, in experimental models of anaplastic large-cell lymphoma. Mol. Cancer Ther. *6*, 3314–3322.

Cohn, S.L., London, W.B., Huang, D., Katzenstein, H.M., Salwen, H.R., Reinhart, T., Madafiglio, J., Marshall, G.M., Norris, M.D., and Haber, M. (2000). MYCN expression is not prognostic of adverse outcome in advanced-stage neuroblastoma with nonamplified MYCN. J. Clin. Oncol. *18*, 3604–3613.

De Brouwer, S., De Preter, K., Kumps, C., Zabrocki, P., Porcu, M., Westerhout, E.M., Lakeman, A., Vandesompele, J., Hoebeeck, J., Van Maerken, T., et al. (2010). Meta-analysis of neuroblastomas reveals a skewed ALK mutation spectrum in tumors with MYCN amplification. Clin. Cancer Res. *16*, 4353–4362.

George, R.E., Sanda, T., Hanna, M., Fröhling, S., Luther, W., 2nd, Zhang, J., Ahn, Y., Zhou, W., London, W.B., McGrady, P., et al. (2008). Activating mutations in ALK provide a therapeutic target in neuroblastoma. Nature *455*, 975–978.

Goldsmith, K.C., Lestini, B.J., Gross, M., Ip, L., Bhumbla, A., Zhang, X., Zhao, H., Liu, X., and Hogarty, M.D. (2010). BH3 response profiles from neuroblastoma mitochondria predict activity of small molecule Bcl-2 family antagonists. Cell Death Differ. *17*, 872–882.

Gustafson, W.C., and Weiss, W.A. (2010). Myc proteins as therapeutic targets. Oncogene *29*, 1249–1259.

Hamnér, S., Arumäe, U., Li-Ying, Y., Sun, Y.F., Saarma, M., and Lindholm, D. (2001). Functional characterization of two splice variants of rat bad and their interaction with Bcl-w in sympathetic neurons. Mol. Cell. Neurosci. *17*, 97–106.

Hansford, L.M., Thomas, W.D., Keating, J.M., Burkhart, C.A., Peaston, A.E., Norris, M.D., Haber, M., Armati, P.J., Weiss, W.A., and Marshall, G.M. (2004). Mechanisms of embryonal tumor initiation: distinct roles for MycN expression and MYCN amplification. Proc. Natl. Acad. Sci. USA *101*, 12664–12669.

Hemann, M.T., and Lowe, S.W. (2006). The p53-Bcl-2 connection. Cell Death Differ. *13*, 1256–1259.

Heuckmann, J.M., Hölzel, M., Sos, M.L., Heynck, S., Balke-Want, H., Koker, M., Peifer, M., Weiss, J., Lovly, C.M., Grütter, C., et al. (2011). ALK mutations conferring differential resistance to structurally diverse ALK inhibitors. Clin. Cancer Res. *17*, 7394–7401.

Janoueix-Lerosey, I., Lequin, D., Brugières, L., Ribeiro, A., de Pontual, L., Combaret, V., Raynal, V., Puisieux, A., Schleiermacher, G., Pierron, G., et al. (2008). Somatic and germline activating mutations of the ALK kinase receptor in neuroblastoma. Nature *455*, 967–970.

Kwak, E.L., Bang, Y.J., Camidge, D.R., Shaw, A.T., Solomon, B., Maki, R.G., Ou, S.H., Dezube, B.J., Jänne, P.A., Costa, D.B., et al. (2010). Anaplastic lymphoma kinase inhibition in non-small-cell lung cancer. N. Engl. J. Med. *363*, 1693–1703.

Liu, Q., Wang, J., Kang, S.A., Thoreen, C.C., Hur, W., Ahmed, T., Sabatini, D.M., and Gray, N.S. (2011). Discovery of 9-(6-aminopyridin-3-yl)-1-(3-(trifluoromethyl)phenyl)benzo[h][1,6]naphthyridin-2(1H)-one (Torin2) as a potent, selective, and orally available mammalian target of rapamycin (mTOR) inhibitor for treatment of cancer. J. Med. Chem. *54*, 1473–1480.

Marshall, G.M., Liu, P.Y., Gherardi, S., Scarlett, C.J., Bedalov, A., Xu, N., Iraci, N., Valli, E., Ling, D., Thomas, W., et al. (2011). SIRT1 promotes N-Myc oncogenesis through a positive feedback loop involving the effects of MKP3 and ERK on N-Myc protein stability. PLoS Genet. *7*, e1002135.

Matthay, K.K., Villablanca, J.G., Seeger, R.C., Stram, D.O., Harris, R.E., Ramsay, N.K., Swift, P., Shimada, H., Black, C.T., Brodeur, G.M., et al; Children's Cancer Group. (1999). Treatment of high-risk neuroblastoma with intensive chemotherapy, radiotherapy, autologous bone marrow transplantation, and 13-cis-retinoic acid. N. Engl. J. Med. *341*, 1165–1173.

Mossé, Y.P., Laudenslager, M., Longo, L., Cole, K.A., Wood, A., Attiyeh, E.F., Laquaglia, M.J., Sennett, R., Lynch, J.E., Perri, P., et al. (2008). Identification of ALK as a major familial neuroblastoma predisposition gene. Nature *455*, 930–935.

Murphy, D.J., Junttila, M.R., Pouyet, L., Karnezis, A., Shchors, K., Bui, D.A., Brown-Swigart, L., Johnson, L., and Evan, G.I. (2008). Distinct thresholds govern Myc's biological output in vivo. Cancer Cell *14*, 447–457.

Otto, T., Horn, S., Brockmann, M., Eilers, U., Schüttrumpf, L., Popov, N., Kenney, A.M., Schulte, J.H., Beijersbergen, R., Christiansen, H., et al. (2009). Stabilization of N-Myc is a critical function of Aurora A in human neuroblastoma. Cancer Cell *15*, 67–78.

National Cancer Institute. (2005). Surveillance, Epidemiology and End Results Database. http://seer.cancer.gov/publications/childhood/sympathetic.pdf.

Palmer, R.H., Vernersson, E., Grabbe, C., and Hallberg, B. (2009). Anaplastic lymphoma kinase: signalling in development and disease. Biochem. J. *420*, 345–361.

Pelengaris, S., Khan, M., and Evan, G. (2002). c-MYC: more than just a matter of life and death. Nat. Rev. Cancer *2*, 764–776.

Penn, L.J., Brooks, M.W., Laufer, E.M., and Land, H. (1990). Negative autoregulation of c-myc transcription. EMBO J. *9*, 1113–1121.

Pulford, K., Morris, S.W., and Turturro, F. (2004). Anaplastic lymphoma kinase proteins in growth control and cancer. J. Cell. Physiol. *199*, 330–358.

Sasaki, T., Okuda, K., Zheng, W., Butrynski, J., Capelletti, M., Wang, L., Gray, N.S., Wilner, K., Christensen, J.G., Demetri, G., et al. (2010). The neuroblastoma-associated F1174L ALK mutation causes resistance to an ALK kinase inhibitor in ALK-translocated cancers. Cancer Res. *70*, 10038–10043.

Schönherr, C., Ruuth, K., Kamaraj, S., Wang, C.L., Yang, H.L., Combaret, V., Djos, A., Martinsson, T., Christensen, J.G., Palmer, R.H., and Hallberg, B. (2012). Anaplastic lymphoma kinase (ALK) regulates initiation of transcription of MYCN in neuroblastoma cells. Oncogene, Jan 30. [Epub ahead of print].

Schwab, M., Varmus, H.E., Bishop, J.M., Grzeschik, K.H., Naylor, S.L., Sakaguchi, A.Y., Brodeur, G., and Trent, J. (1984). Chromosome localization in normal human cells and neuroblastomas of a gene related to c-myc. Nature *308*, 288–291.

Sears, R., Nuckolls, F., Haura, E., Taya, Y., Tamai, K., and Nevins, J.R. (2000). Multiple Ras-dependent phosphorylation pathways regulate Myc protein stability. Genes Dev. *14*, 2501–2514.

Seeger, R.C., Brodeur, G.M., Sather, H., Dalton, A., Siegel, S.E., Wong, K.Y., and Hammond, D. (1985). Association of multiple copies of the N-myc oncogene with rapid progression of neuroblastomas. N. Engl. J. Med. *313*, 1111–1116.

Shachaf, C.M., Gentles, A.J., Elchuri, S., Sahoo, D., Soen, Y., Sharpe, O., Perez, O.D., Chang, M., Mitchel, D., Robinson, W.H., et al. (2008). Genomic and proteomic analysis reveals a threshold level of MYC required for tumor maintenance. Cancer Res. *68*, 5132–5142.

Sjostrom, S.K., Finn, G., Hahn, W.C., Rowitch, D.H., and Kenney, A.M. (2005). The Cdk1 complex plays a prime role in regulating N-myc phosphorylation and turnover in neural precursors. Dev. Cell *9*, 327–338.

Soucek, L., and Evan, G.I. (2010). The ups and downs of Myc biology. Curr. Opin. Genet. Dev. *20*, 91–95.

Vernersson, E., Khoo, N.K., Henriksson, M.L., Roos, G., Palmer, R.H., and Hallberg, B. (2006). Characterization of the expression of the ALK receptor tyrosine kinase in mice. Gene Expr. Patterns *6*, 448–461.

Weiss, W.A., Aldape, K., Mohapatra, G., Feuerstein, B.G., and Bishop, J.M. (1997). Targeted expression of MYCN causes neuroblastoma in transgenic mice. EMBO J. *16*, 2985–2995.

Wierstra, I., and Alves, J. (2008). The c-myc promoter: still MysterY and challenge. Adv. Cancer Res. *99*, 113–333.

Zhu, S., Lee, J.S., Guo, F., Shin, J., Perez-Atayde, A.R., Kutok, J.L., Rodig, S.J., Neuberg, D.S., Helman, D., Feng, H., et al. (2012). Activated ALK collaborates with MYCN in neuroblastoma pathogenesis. Cancer Cell *21*, 362–373.

Cancer Cell
Report

Innate Neural Stem Cell Heterogeneity Determines the Patterning of Glioma Formation in Children

Da Yong Lee,[1] Scott M. Gianino,[1] and David H. Gutmann[1,*]
[1]Department of Neurology, Washington University School of Medicine, St. Louis, MO 63110, USA
*Correspondence: gutmannd@wustl.edu
http://dx.doi.org/10.1016/j.ccr.2012.05.036

SUMMARY

The concept that gliomas comprise a heterogeneous group of diseases distinguished by their developmental origin raises the intriguing possibility that neural stem cells (NSCs) from different germinal zones have differential capacities to respond to glioma-causing genetic changes. We demonstrate that lateral ventricle subventricular zone NSCs are molecularly and functionally distinct from those of the third ventricle. Consistent with a unique origin for pediatric low-grade glioma, third ventricle, but not lateral ventricle, NSCs hyperproliferate in response to mutations characteristic of childhood glioma. Finally, we demonstrate that pediatric optic gliomas in *Nf1* genetically engineered mice arise from the third ventricle. Collectively, these observations establish the importance of innate brain region NSC heterogeneity in the patterning of gliomagenesis in children and adults.

INTRODUCTION

The importance of the cell of origin in tumorigenesis and clinical behavior of brain tumors (Singh et al., 2004; Taylor et al., 2005) has been strengthened by the observation that histologically identical brain tumors are composed of molecularly distinct subtypes that reflect their progenitor cell of origin (Gibson et al., 2010; Johnson et al., 2010; Kalamarides et al., 2011; Sharma et al., 2007). These findings suggest that brain tumors with distinct cellular origins are unique diseases with different growth control regulatory networks, genetic changes, and responses to therapy. Consistent with this, we have shown that mouse neural stem cells (NSCs) from the brainstem, but not the neocortex, exhibit increased proliferation and gliogenesis following inactivation of the neurofibromatosis-1 (NF1) tumor suppressor gene (Lee et al., 2010). This differential sensitivity to *Nf1* loss closely parallels the propensity for pilocytic astrocytomas (PAs) in children with NF1 to form within the optic pathway and brainstem, but rarely in the cortex (Guillamo et al., 2003). A similar geographic pattern of gliomagenesis is observed for sporadic pediatric PAs harboring *KIAA1549:BRAF* fusions (Jacob et al., 2009), which predominantly form in the cerebellum.

Within the brain there are several germinal zones potentially germane to brain tumorigenesis, including the subventricular zone of the lateral ventricle (lv-SVZ), the third ventricle (TVZ), and the fourth ventricle (Quiñones-Hinojosa et al., 2006; Weiss et al., 1996; Xu et al., 2005). Although the lv-SVZ is often considered to be the likely stem cell compartment for cerebral hemisphere glioma formation in mice following the introduction of genetic alterations observed in high-grade human adult gliomas (Alcantara Llaguno et al., 2009; Jacques et al., 2010; Wang et al., 2009), other populations, including $NG2^+$ cells (Assanah et al., 2006; Masui et al., 2010) and oligodendrocyte precursors (Liu et al., 2011; Sugiarto et al., 2011), can serve as potential cells of origin for malignant glioma. However, to our knowledge, the origin of optic glioma, the second-most common low-grade pediatric glioma, remains unresolved. Based on the proximity of the optic nerve/chiasm to the TVZ and that optic nerve oligodendrocyte precursors can originate from the TVZ (Ono et al., 1997), we hypothesized that TVZ may be the progenitor compartment for these pediatric brain tumors.

RESULTS

NSCs from the lv-SVZ and TVZ Are Molecularly Distinct Populations

We obtained several lines of evidence supporting that TVZ is a true stem cell niche. First, cells lining the TVZ in the embryonic

Significance

Whereas some adult malignant cerebral hemispheric gliomas have been shown to arise from neural stem or progenitor cells residing in the subventricular zone of the lateral ventricle (lv-SVZ), to our knowledge, the cellular origin of pediatric low-grade gliomas is unknown. Consistent with the propensity for childhood gliomas to develop in the optic nerve and chiasm, we demonstrate that third ventricle (TVZ) NSCs are molecularly and functionally distinct from their lv-SVZ counterparts and are the likely cell of origin for murine low-grade optic gliomas. These findings establish brain region NSC heterogeneity as a major determinant underlying the patterning of gliomagenesis in children and adults.

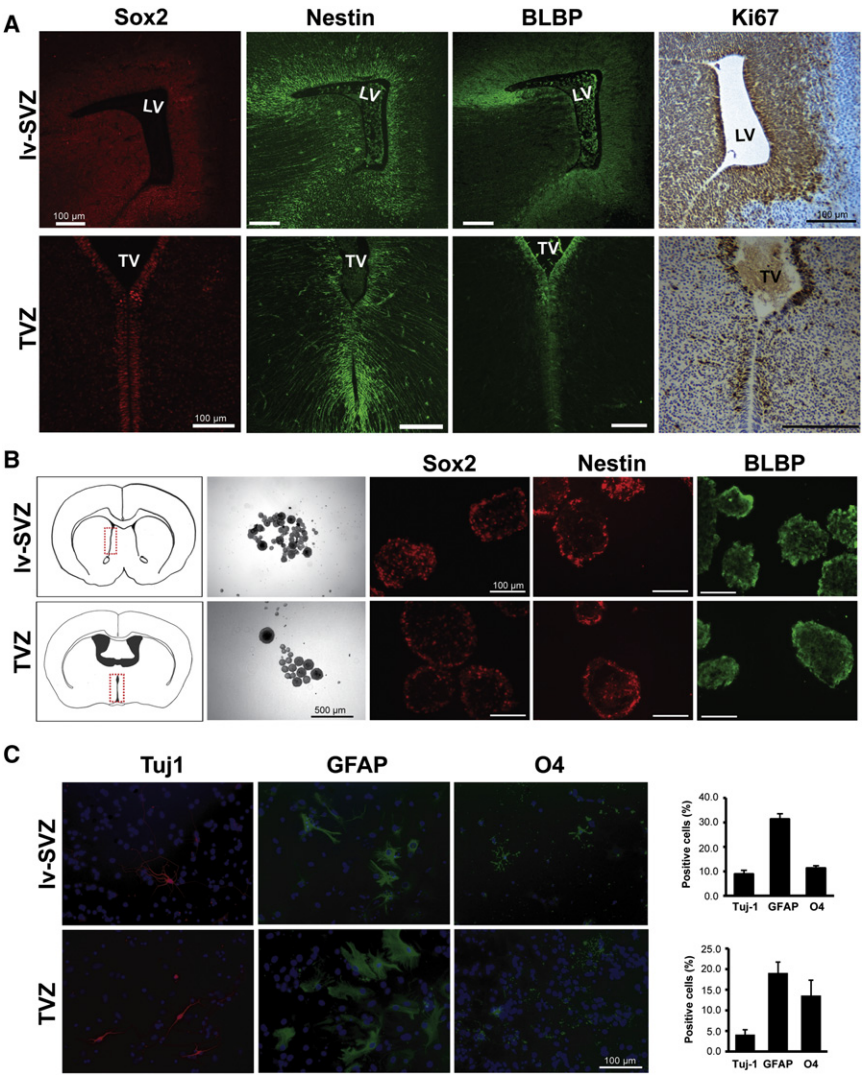

Figure 1. NSCs Can Be Generated from the lv-SVZ and TVZ

(A) Immunostaining of the cells lining the mouse E15.5 TVZ shows expression of the Sox2, nestin, and BLBP NSC markers. LV, lateral ventricle; TV, third ventricle.

(B) Single neurospheres from the lv-SVZ and TVZ form secondary neurospheres in vitro and express Sox2, nestin, and BLBP. The diagrams denote the regions used for NSC cultures.

(C) TVZ NSCs can differentiate into neurons (Tuj-1), astrocytes (GFAP), and oligodendrocytes (O4). Values denote the mean ± SEM.

Scale bars: (A) and (C), 100 μm; (B) phase contrast, 500 μm; (B) fluorescence, 100 μm.

day 15.5 (E15.5) mouse brain express NSC markers Sox2, nestin, and BLBP, and exhibit robust proliferation (Ki67 immunostaining) (Figure 1A). Second, TVZ NSCs can generate Sox2$^+$, nestin$^+$, and BLBP$^+$ neurospheres and undergo self-renewal, similar to their lv-SVZ counterparts (Figure 1B). Third, dissociated single cells from TVZ neurospheres differentiate into neurons, astrocytes, and oligodendrocytes in vitro (Figure 1C).

We then employed gene expression profiling to demonstrate that TVZ NSCs and lv-SVZ NSCs are molecularly distinct populations. Initially, E17.5 TVZ and lv-SVZ NSCs from three females were used for the profiling; however, one outlier lv-SVZ NSC sample, based on principal component analysis (PCA), was eliminated from the following analyses (see Figure S1A available online). Using hierarchical clustering methods, lv-SVZ and TVZ NSCs were easily separable (Figures 2A and S1A). The differential expression of several genes was validated by quantitative reverse-transcription PCR (Figure 2B) and by in situ hybridization (Allen Brain Atlas at http://www.brain-map.org/): *Chl1* and *Slit2* expression was higher in the hypothalamus/TVZ region compared to the anterior forebrain/lv-SVZ region, whereas *Dcx* and *Cntn1* expression was higher in the anterior forebrain/lv-SVZ region relative to the hypothalamus/TVZ region (Figure S1B). A subset of these genes was also similarly differentially expressed in older mice (Figures S1B and S1C). Together, these data demonstrate that TVZ and lv-SVZ contain molecularly distinct NSC populations.

lv-SVZ and TVZ NSCs Exhibit Unique Cell-Autonomous Responses to Glioma-Causing Genetic Mutations

To determine whether TVZ and lv-SVZ NSCs exhibit different responses to glioma-associated genetic events, we measured NSC proliferation in response to *KIAA1549:BRAF* expression, a representative pediatric glioma-causing genetic change (Jones et al., 2008), *PTEN* loss, a representative adult glioma-causing genetic change (Pollack et al., 2006), and *p53* loss, which occurs in both adult and pediatric gliomas (Hayes et al., 1999; Kim et al., 2010). The *KIAA1549:BRAF* mutation is found in 62% of hypothalamus/optic pathway PAs but is uncommon in histologically identical tumors of the cerebral hemispheres (14%) (Jacob et al., 2009). *p53* inactivation increased proliferation and decreased apoptosis of both lv-SVZ and TVZ NSCs (Figure 2C, top, and Figure S1D). *Pten* inactivation increased proliferation of lv-SVZ, but not in TVZ, NSCs, whereas *KIAA1549:BRAF* overexpression increased proliferation of TVZ, but not in lv-SVZ, NSCs, with no effect in apoptosis (Figures 2C and S1D). Decreased apoptosis was observed in both NSC populations following *Pten* loss, whereas *KIAA1549:BRAF* overexpression resulted in no change. These differential responses do not reflect a failure to activate AKT following *Pten* loss in TVZ NSCs or MEK following *KIAA1549:BRAF* expression in lv-SVZ NSCs (Figure S1E).

Mouse Nf1 Optic Gliomas Arise from TVZ

To identify the ventricular zone of origin for optic glioma, we chose NF1 as a model experimental system because gliomas

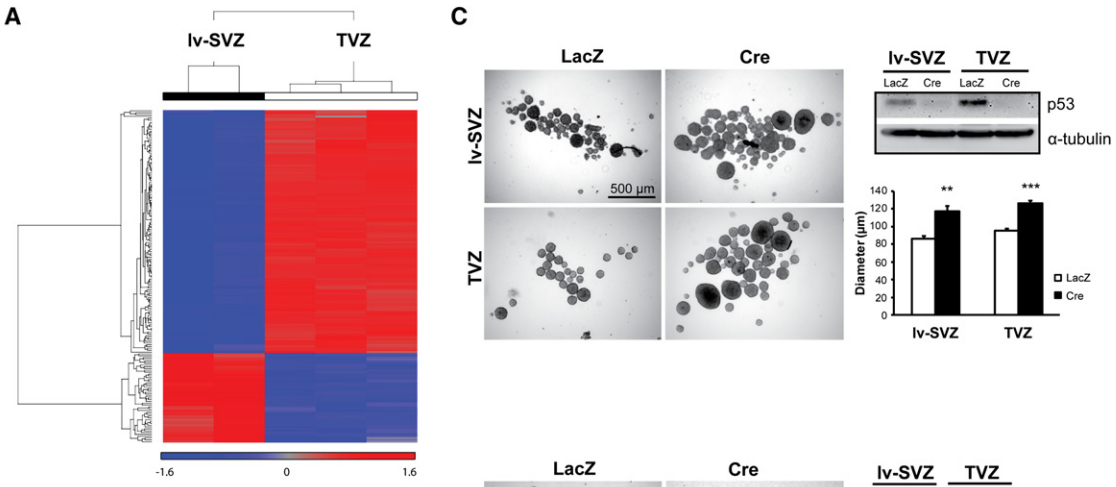

B

Gene Symbol	Microarray FC (TVZ/lv-SVZ)	Microarray p	q-PCR FC (TVZ/lv-SVZ)	q-PCR p
Casc5	3.76268	0.00396	5.17	<0.0001
Chl1	6.07247	0.011865	11.41	0.0333
Ect2	4.20363	0.009195	11.09	0.0005
Fignl1	4.22097	0.007586	5.58	0.0091
Gmnn	3.49677	0.006895	7.73	<0.0001
Hmmr	4.37526	0.001085	3.5	0.0081
Nr2f2	3.73674	0.004442	4.51	0.0064
Pbk	4.25061	0.007103	6.04	0.0008
Shcbp1	3.90795	0.012452	9.24	0.0005
Slit2	3.3639	0.000299	3.36	0.0046
Ttk	4.25887	0.006919	13.61	0.0027

Gene Symbol	Microarray FC (lv-SVZ/TVZ)	Microarray p	q-PCR FC (lv-SVZ/TVZ)	q-PCR p
Apoe	4.12505	0.007103	4.55716	0.0446
Cntn1	4.21629	0.009195	4.08644	0.0013
Dcx	3.77764	0.022158	22.5876	0.0071
Gng3	5.64923	0.000731	2.88	0.0069
Ptsg2	4.8974	0.007586	3.04273	0.0045
Rbp1	14.0755	0.00004	7.14286	0.0032

Figure 2. NSCs from the lv-SVZ and TVZ Are Molecularly Distinct Progenitor Populations with Unique Cell-Autonomous Responses to Glioma-Causing Genetic Mutations

(A) SAM separates lv-SVZ and TVZ NSCs with the expression level represented as standardized values from −1.6 (blue, <1-fold change) to 1.6 (red, >1-fold change). No change (0 value) is denoted by gray.

(B) Validation of select differentially expressed transcripts by quantitative reverse-transcription PCR with fold changes (FC) and p values (p) are shown.

(C) Increased neurosphere diameters were observed in NSCs from both the lv-SVZ and TVZ following *p53* loss. Increased neurosphere diameters were found only in lv-SVZ NSCs following *Pten* loss. Increased neurosphere diameters were observed only in TVZ NSCs following *KIAA1549:BRAF* expression (RT-PCR). Values denote the mean ± SEM. $p^* < 0.01$, $p^{**} < 0.001$, $p^{***} < 0.0001$.

Scale bars, 500 μm.

See also Figure S1.

predominate in the optic pathway of children with this syndrome (Guillamo et al., 2003). Similar to human NF1-associated gliomas, optic gliomas form in the prechiasmatic and chiasmal regions of $Nf1^{+/-}$ mice following complete *Nf1* inactivation in glial progenitors (Figure 3A) (Bajenaru et al., 2003). These gliomas could arise from NSCs in the lv-SVZ, TVZ (Figure 3B), optic nerve, or retina.

We first excluded the retina and optic nerve as cell of origin of these gliomas because true NSCs capable of self-renewal and multilineage differentiation could not be generated from either E17.5 or postnatal day (P) 1 retina cells or the optic nerve (Figure S2A; Cicero et al., 2009; Lee et al., 2010). Additionally, Cre transgene expression ($LacZ^+$ cells) was not detected in the retina

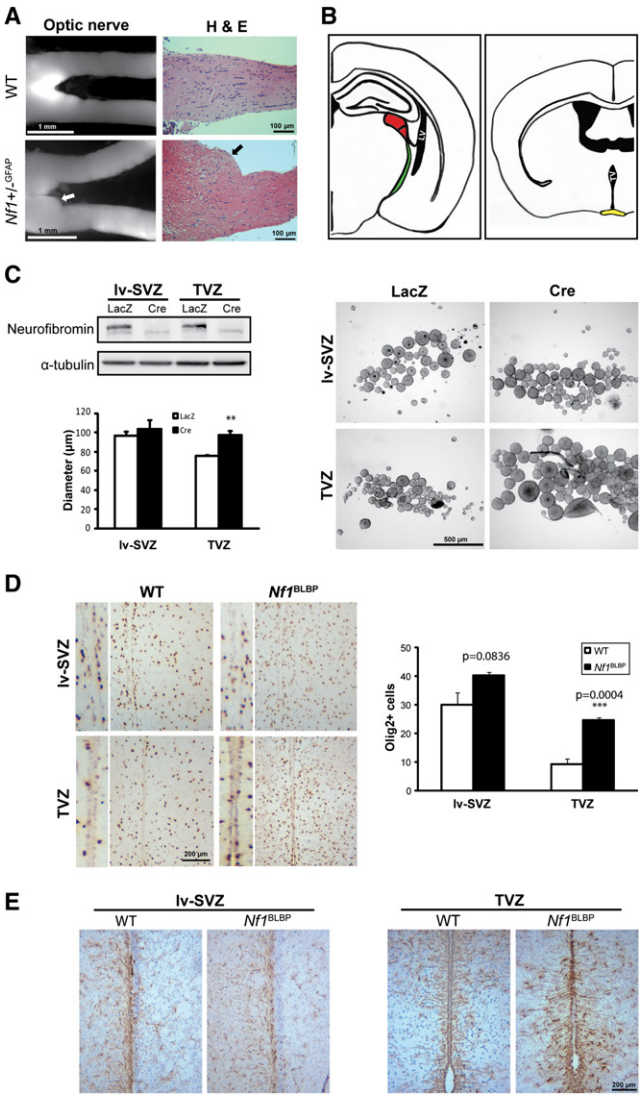

Figure 3. TVZ NSCs Are Preferentially Sensitive to *Nf1* Loss

(A) Increased optic nerve volume (white arrow) and abnormal cell clusters (black arrow) were observed in optic gliomas from 3-month-old $Nf1^{+/-GFAP}$ mice. H&E, hematoxylin and eosin staining; WT, wild-type.

(B) The potential cellular origins (lv-SVZ and TVZ) of optic gliomas in *Nf1* mutant mice are illustrated. Lateral ventricle (LV) is shown in black, lateral geniculate nucleus in red, third ventricle (TV) in black, optic tract in green, and optic chiasm in yellow.

(C) Increased TVZ neurosphere proliferation was seen following *Nf1* loss, with little effect on lv-SVZ NSCs.

(D) There were 3-fold more $Olig2^+$ cells found in the TVZ of $Nf1^{BLBP}$ mice ($p = 0.0004$), but not in the lv-SVZ ($p = 0.0836$), compared to controls.

(E) Increased numbers of $GFAP^+$ cells were found in the TVZ, but not in the lv-SVZ, of $Nf1^{BLBP}$ mice compared to controls.

Values denote the mean ± SEM. Scale bars: (A) left, 1 mm; (A) right, 100 μm; (C), 500 μm; (D) and (E), 200 μm.

See also Figure S2.

or optic nerve until after P2 or E17.5, respectively (Figure S2B). We then show that $Nf1^{-/-}$ NSCs from the TVZ, but not the lv-SVZ, exhibit increased proliferation relative to wild-type NSCs, with no effect on apoptosis in vitro (Figures 3C and S2C).

To provide in vivo support for these in vitro observations, we inactivated *Nf1* in $BLBP^+$ NSCs beginning at E9.5 and found that the numbers of $Olig2^+$ glial progenitors (Figure 3D) and $GFAP^+$ astrocytes (Figure 3E) were increased in the TVZ, but not in the lv-SVZ, of P8 $Nf1^{BLBP}$ mice compared to control littermates in vivo.

To examine whether human hypothalamic/optic gliomas recapitulate the gene expression pattern of TVZ (Sharma et al., 2007), PCA and hierarchical clustering revealed that hypothalamic/optic pathway gliomas were separated from their supratentorial counterparts (Figure S2D). Although some of the differentially expressed genes were not represented on the human Affymetrix Gene Chip, we found that one differentially expressed TVZ transcript (*Slit2*) was significantly higher (3.7-fold; $p = 0.001$) in hypothalamic/optic PAs compared to supratentorial PAs. Two other TVZ-overexpressed transcripts (*Gmnn* and *Nr2f2*) and two lv-SVZ-overexpressed transcripts (*Cntn1* and *Apoe*) also exhibited increased expression in hypothalamic/optic gliomas and supratentorial gliomas, respectively, although not reaching statistical significance, likely due to the small sample size ($p = 0.08–0.1$) (Figure S2D).

Finally, we sought to define a developmental window when optic glioma formation is favored by virtue of the selective proliferative activity of the TVZ and lv-SVZ using three different GFAP-Cre driver lines with distinct patterns of Cre-mediated *Nf1* inactivation in vivo (Figures S3A and 4A). The *GFAP-Cre:IRES-LacZ* strain used to generate $Nf1^{+/-GFAP}$ mouse optic gliomas has detectable LacZ expression in the lv-SVZ and TVZ beginning at E15.5 (Figure 4B). The GFAP-Cre* strain (Zhuo et al., 2001) initiates Cre expression in the anterior part of forebrain by E13.5 (Figures 4A and 4C) and in the hypothalamus, which includes the TVZ, by E16.5 (Figure 4C). $Nf1^{+/-GFAP^*}$ mice also develop optic glioma (Zhu et al., 2005) (Figure 4E). Analysis of the TVZ and lv-SVZ in these mice reveals that $nestin^+$ and $Ki67^+$ progenitor cells reside in both germinal zones at E15.5 (Figure 4B).

To distinguish between these two germinal zones, we employed the GFAP-Cre^{ER} strain, which was similar to the first GFAP-Cre strain, but expressed a tamoxifen-regulatable Cre (Cre^{ER}; Chow et al., 2008). Recombination and inactivation of the *Nf1* gene were verified by recombination PCR (Figure 4D), whereas Cre activity in the brain, optic chiasm, and optic nerve following tamoxifen injection was demonstrated using ROSA-GREEN reporter mice (Figure 4D). Because lv-SVZ contained $nestin^+$ $Ki67^+$ cells at P8–P14, whereas these proliferating progenitors disappeared after P2 in TVZ (Figures 4B, S3B, and S3C), we inactivated *Nf1* either during the first postnatal week of life (P1–P3) or at 2 weeks of age when only the lv-SVZ harbors significant numbers of proliferating ($Ki67^+$) progenitor ($nestin^+$) cells (Figures S3B and S3C). *Nf1* loss at these times did not result in glioma formation at 3 months of age (Figure 4E). As an internal control for the fidelity of the GFAP-Cre^{ER} strain for inducing optic glioma, we treated >20 litters of pregnant females with tamoxifen at E16.5 (50 μg/g i.p.). The vast majority of pregnant dams did not deliver viable mice; however, the one embryonically treated pup that survived to 3 months of age developed an optic glioma (Figure S3D) with increased numbers of $Ki67^+$ cells and increased numbers of $GFAP^+$ astrocytes (Figure S3E). Taken together, these data establish that optic gliomas arise from neural stem/progenitor cells in the proliferative TVZ during

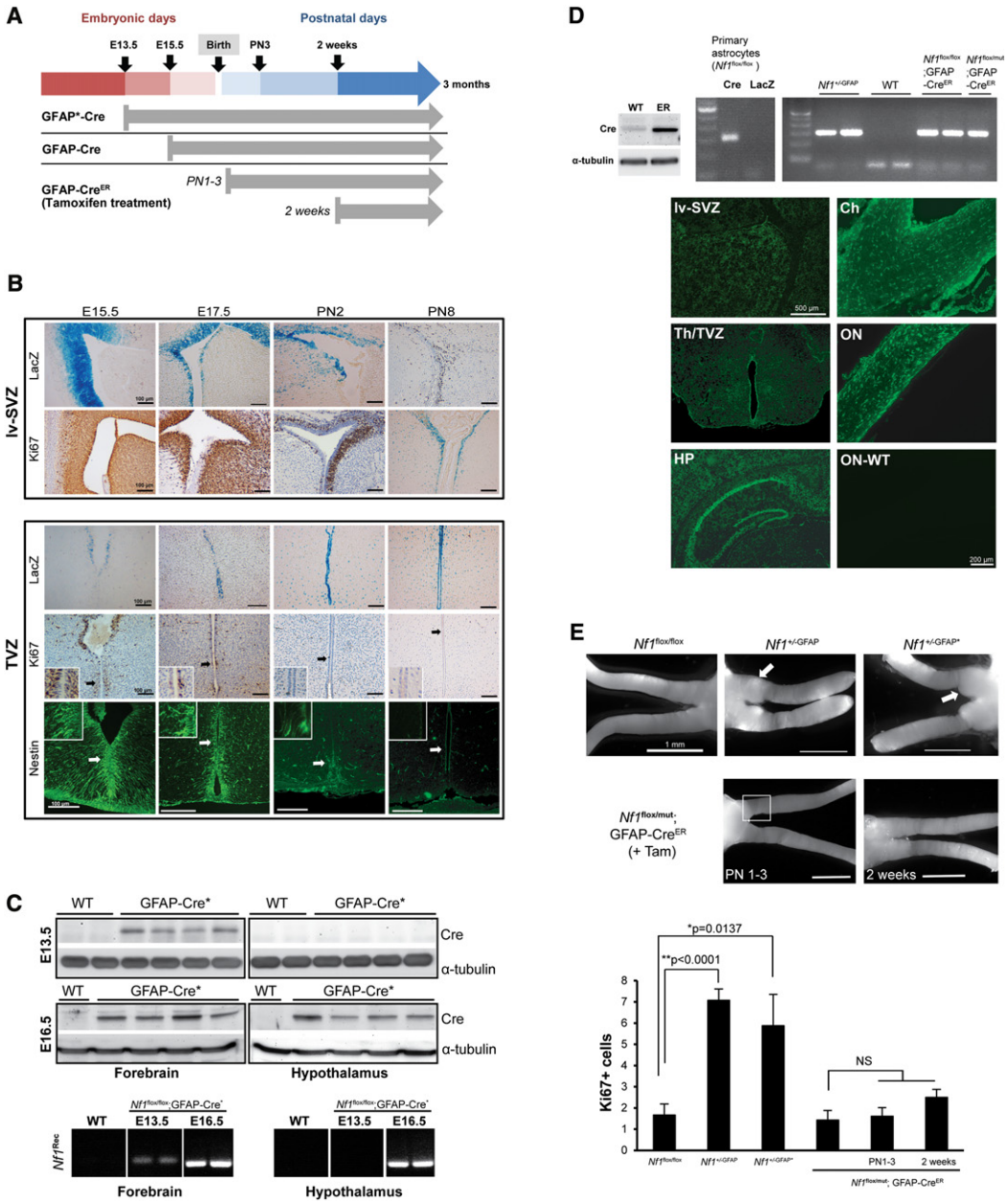

Figure 4. Embryonic *Nf1* Inactivation Is Required for Optic Glioma Formation

(A) The timing of *Nf1* inactivation by Cre-mediated excision is shown for each strain.

(B) X-Gal staining reveals GFAP-Cre transgene expression in the lv-SVZ and TVZ beginning at E15.5. Whereas lv-SVZ cells are Ki67$^+$ from E15.5 through P8, scant numbers of Ki67$^+$ or nestin$^+$ cells are detected in the TVZ by P2.

(C) Cre expression and *Nf1* gene recombination (*Nf1*^{Rec}) are detected by E13.5 in the anterior forebrain/lv-SVZ ("forebrain") and by E16.5 in the hypothalamus/TVZ ("hypothalamus") of GFAP-Cre* mice.

(D) Cre-mediated *Nf1* gene recombination (PCR) in *Nf1*$^{+/-GFAP}$ mice and in tamoxifen-treated *Nf1*$^{flox/flox}$; GFAP-Cre^{ER} and *Nf1*$^{flox/mut}$; GFAP-Cre^{ER} mice was seen. Wild-type (WT) C57BL/6 mouse brain was used as a negative control, whereas Ad5Cre-infected (Cre) and Ad5LacZ-infected (LacZ) *Nf1*$^{flox/flox}$ astrocytes served as positive and WT controls, respectively. Cre-ER fusion protein (~70 kDa) expression was detected in GFAP-Cre^{ER} (ER), but not in WT, mouse brains. EGFP was expressed in tamoxifen-treated ROSA-GREEN; GFAP-Cre^{ER} mouse brains and optic nerves (ON) at 1 month of age, but not in a WT mouse optic nerve (ON-WT). HP, hippocampus; Th, thalamus; Ch, chiasm.

(E) Whereas optic gliomas develop in *Nf1*$^{+/-GFAP}$ and *Nf1*$^{+/-GFAP^*}$ mice, no gliomas formed in *Nf1*$^{flox/flox}$ or *Nf1*$^{flox/mut}$; GFAP-Cre^{ER} treated with tamoxifen (+Tam) beginning at P1 or P14. Increased Ki67$^+$ cells were found in the prechiasmatic and chiasmal regions (square) of *Nf1*$^{+/-GFAP}$ and *Nf1*$^{+/-GFAP^*}$ mice. In contrast, the number of Ki67$^+$ cells in *Nf1*$^{flox/mut}$; GFAP-Cre^{ER} postnatally treated with tamoxifen is indistinguishable from control *Nf1*$^{flox/flox}$ mice. Values denote the mean ± SEM. NS, not significant.

Scale bars: (B), 100 μm; (D) left, 500 μm; (D) right, 200 μm; (E), 1 mm. PN, postnatal days.

See also Figure S3.

embryogenesis rather than from astrocytes at later postnatal stages.

DISCUSSION

Our finding that NSCs from two different germinal zones are molecularly distinct stem cell populations is consistent with previous reports examining mouse embryonic spinal cord and brain NSCs as well as human neural progenitor cells from the developing cortex and ventral midbrain (Johnson et al., 2010; Kelly et al., 2009; Kim et al., 2009; Taylor et al., 2005). In each case the unique genetic signature reflects the regional identity of the progenitors. Importantly, we show that the heterogeneity revealed at the molecular level translates into unique functional responses to glioma-causing genetic changes seen in children and adults. Although, to our knowledge, the precise etiologies for these innate differences are unknown, they likely reflect transcriptional networks and signaling set points unique to these brain regions. For example we have previously shown that the expression of the mTOR component rictor underlies the ability of *Nf1*-deficient NSCs to increase their proliferation and glial differentiation (Lee et al., 2010), whereas basal cAMP levels in specific brain regions partly dictate the spatial pattern of gliomagenesis in NF1 (Warrington et al., 2010).

We also provide several lines of converging evidence that optic gliomas likely originate from stem/progenitor cells residing in the TVZ. Although both TVZ and lv-SVZ germinal zones could provide cells of origin for these tumors, only TVZ, but not lv-SVZ, NSCs exhibit increased proliferation and gliogenesis following *Nf1* inactivation. In addition, optic gliomas do not form in mouse strains following postnatal *Nf1* inactivation when only lv-SVZ NSCs are proliferating. These latter experiments also demonstrate that *Nf1* inactivation in GFAP-expressing astrocytes in young mice does not result in optic gliomagenesis. One report employing immunohistochemical and gene expression analysis similarly suggested that human optic gliomas might derive from third ventricle glial progenitors (Tchoghandjian et al., 2009). This result parallels the developmental origins of another optic nerve glial cell population in which oligodendrocyte precursor cells generated in the floor of the TVZ differentiate and migrate into the optic nerve in response to signaling molecules from retinal ganglion axons (Gao and Miller, 2006; Ono et al., 1997).

Although our mouse experimental data argue that optic gliomas in children with NF1 arise from the TVZ, it is possible that we have modeled only one type of human optic glioma, and that other subtypes of optic glioma originate from different progenitor cells akin to other CNS cancers (Gibson et al., 2010; Johnson et al., 2010). Additional potential progenitors could be $NG2^+$ oligodendrocyte precursor cells recently implicated in malignant gliomagenesis (Assanah et al., 2006; Liu et al., 2011; Masui et al., 2010; Sugiarto et al., 2011). However, *Nf1* inactivation in $NG2^+$ cells of $Nf1^{+/-}$ mice, similar to the *Nf1* mouse models described here, is not sufficient for glioma formation (A. Solga, unpublished data). Future studies aimed at subdividing these common pediatric tumors into molecularly distinct diseases will facilitate the development of brain tumor therapies targeted to the specific growth regulatory pathways that drive cell growth and differentiation in these distinct cancer-initiating cell populations.

EXPERIMENTAL PROCEDURES

Mice

All strains were generated (Supplemental Experimental Procedures), maintained on a C57BL/6 background, and used under an approved Animal Studies Committee protocol at Washington University.

NSC Isolation and Analysis

lv-SVZ and TVZ NSCs from $Nf1^{flox/flox}$, $p53^{flox/flox}$, and $Pten^{flox/flox}$ P1 mouse pups were infected with adenovirus containing LacZ or Cre, and protein loss was confirmed by western blotting (Lee et al., 2010). NSCs expressing *KIAA1549:BRAF* were generated following retrovirus infection (Peter Collins, University of Cambridge) and verified by RT-PCR (Supplemental Experimental Procedures). pBABE-puro retrovirus was used as control. NSC proliferation and multilineage differentiation assays were performed as described previously by Lee et al. (2010).

Immunohistochemistry and Immunocytochemistry

Tissues and cells were prepared as previously reported by Hegedus et al. (2007) prior to staining with appropriate antibodies (Supplemental Experimental Procedures).

Microarray Analysis

RNA from three independent litters of E17.5 C57BL/6 lv-SVZ and TVZ NSCs was subjected to microarray profiling (Supplemental Experimental Procedures), and differentially expressed probe sets ($p < 0.05$; fold change >3-fold increase or decrease) were prioritized for validation.

Quantitative Reverse-Transcription PCR

mRNA expression was determined by quantitative reverse-transcription PCR using NSCs from independently generated litters as described previously by Yeh et al. (2009) (Supplemental Experimental Procedures).

X-Gal Staining

Six micrometer frozen sections were stained with X-Gal (Gold Biotechnology, St. Louis) (Hegedus et al., 2007).

Tamoxifen Injection and Recombination PCR

Tamoxifen was injected into lactating females (1 mg/50 μl i.p.) at P1–P3 or P14–P18 (Supplemental Experimental Procedures), and *Nf1* recombination was determined by recombination PCR (Mayes et al., 2011).

Western Blotting

Western blotting was performed as reported previously by Lee et al. (2010) (Supplemental Experimental Procedures).

Statistical Analyses

Each experiment was performed with samples from at least three independent litters. Statistical significance ($p < 0.05$) was determined (Student's t test) using GraphPad Prism 5.0 software (GraphPad).

ACCESSION NUMBERS

Human PA (GSE5675) and mouse NSC (GSE37832) microarray data were deposited in the Gene Expression Omnibus (http://www.ncbi.nlm.nih.gov/geo/).

SUPPLEMENTAL INFORMATION

Supplemental Information includes three figures, Supplemental Experimental Procedures, and Supplemental Referneces and can be found with this article online at http://dx.doi.org/10.1016/j.ccr.2012.05.036.

ACKNOWLEDGMENTS

We thank Crystal White-Worsena and Madelyn Reynolds for technical assistance and Suzanne Baker (St. Jude Children's Research Hospital, Memphis,

TN) for the GFAP-Cre^{ER} mice. This work was funded by grants from the NIH (NS065547-01 to D.H.G.), NCI (CA141549-01 to D.H.G.), and the NEI (EY02687).

Received: December 8, 2011
Revised: April 7, 2012
Accepted: May 31, 2012
Published: July 9, 2012

REFERENCES

Alcantara Llaguno, S., Chen, J., Kwon, C.H., Jackson, E.L., Li, Y., Burns, D.K., Alvarez-Buylla, A., and Parada, L.F. (2009). Malignant astrocytomas originate from neural stem/progenitor cells in a somatic tumor suppressor mouse model. Cancer Cell *15*, 45–56.

Assanah, M., Lochhead, R., Ogden, A., Bruce, J., Goldman, J., and Canoll, P. (2006). Glial progenitors in adult white matter are driven to form malignant gliomas by platelet-derived growth factor-expressing retroviruses. J. Neurosci. *26*, 6781–6790.

Bajenaru, M.L., Hernandez, M.R., Perry, A., Zhu, Y., Parada, L.F., Garbow, J.R., and Gutmann, D.H. (2003). Optic nerve glioma in mice requires astrocyte Nf1 gene inactivation and Nf1 brain heterozygosity. Cancer Res. *63*, 8573–8577.

Chow, L.M., Zhang, J., and Baker, S.J. (2008). Inducible Cre recombinase activity in mouse mature astrocytes and adult neural precursor cells. Transgenic Res. *17*, 919–928.

Cicero, S.A., Johnson, D., Reyntjens, S., Frase, S., Connell, S., Chow, L.M., Baker, S.J., Sorrentino, B.P., and Dyer, M.A. (2009). Cells previously identified as retinal stem cells are pigmented ciliary epithelial cells. Proc. Natl. Acad. Sci. USA *106*, 6685–6690.

Gao, L., and Miller, R.H. (2006). Specification of optic nerve oligodendrocyte precursors by retinal ganglion cell axons. J. Neurosci. *26*, 7619–7628.

Gibson, P., Tong, Y., Robinson, G., Thompson, M.C., Currle, D.S., Eden, C., Kranenburg, T.A., Hogg, T., Poppleton, H., Martin, J., et al. (2010). Subtypes of medulloblastoma have distinct developmental origins. Nature *468*, 1095–1099.

Guillamo, J.S., Créange, A., Kalifa, C., Grill, J., Rodriguez, D., Doz, F., Barbarot, S., Zerah, M., Sanson, M., Bastuji-Garin, S., and Wolkenstein, P.; Réseau NF France. (2003). Prognostic factors of CNS tumours in Neurofibromatosis 1 (NF1): a retrospective study of 104 patients. Brain *126*, 152–160.

Hayes, V.M., Dirven, C.M., Dam, A., Verlind, E., Molenaar, W.M., Mooij, J.J., Hofstra, R.M., and Buys, C.H. (1999). High frequency of TP53 mutations in juvenile pilocytic astrocytomas indicates role of TP53 in the development of these tumors. Brain Pathol. *9*, 463–467.

Hegedus, B., Dasgupta, B., Shin, J.E., Emnett, R.J., Hart-Mahon, E.K., Elghazi, L., Bernal-Mizrachi, E., and Gutmann, D.H. (2007). Neurofibromatosis-1 regulates neuronal and glial cell differentiation from neuroglial progenitors in vivo by both cAMP- and Ras-dependent mechanisms. Cell Stem Cell *1*, 443–457.

Jacob, K., Albrecht, S., Sollier, C., Faury, D., Sader, E., Montpetit, A., Serre, D., Hauser, P., Garami, M., Bognar, L., et al. (2009). Duplication of 7q34 is specific to juvenile pilocytic astrocytomas and a hallmark of cerebellar and optic pathway tumours. Br. J. Cancer *101*, 722–733.

Jacques, T.S., Swales, A., Brzozowski, M.J., Henriquez, N.V., Linehan, J.M., Mirzadeh, Z., O' Malley, C., Naumann, H., Alvarez-Buylla, A., and Brandner, S. (2010). Combinations of genetic mutations in the adult neural stem cell compartment determine brain tumour phenotypes. EMBO J. *29*, 222–235.

Johnson, R.A., Wright, K.D., Poppleton, H., Mohankumar, K.M., Finkelstein, D., Pounds, S.B., Rand, V., Leary, S.E., White, E., Eden, C., et al. (2010). Cross-species genomics matches driver mutations and cell compartments to model ependymoma. Nature *466*, 632–636.

Jones, D.T., Kocialkowski, S., Liu, L., Pearson, D.M., Bäcklund, L.M., Ichimura, K., and Collins, V.P. (2008). Tandem duplication producing a novel oncogenic BRAF fusion gene defines the majority of pilocytic astrocytomas. Cancer Res. *68*, 8673–8677.

Kalamarides, M., Stemmer-Rachamimov, A.O., Niwa-Kawakita, M., Chareyre, F., Taranchon, E., Han, Z.Y., Martinelli, C., Lusis, E.A., Hegedus, B., Gutmann, D.H., and Giovannini, M. (2011). Identification of a progenitor cell of origin capable of generating diverse meningioma histological subtypes. Oncogene *30*, 2333–2344.

Kelly, T.K., Karsten, S.L., Geschwind, D.H., and Kornblum, H.I. (2009). Cell lineage and regional identity of cultured spinal cord neural stem cells and comparison to brain-derived neural stem cells. PLoS One *4*, e4213.

Kim, H.J., McMillan, E., Han, F., and Svendsen, C.N. (2009). Regionally specified human neural progenitor cells derived from the mesencephalon and forebrain undergo increased neurogenesis following overexpression of ASCL1. Stem Cells *27*, 390–398.

Kim, Y.H., Nobusawa, S., Mittelbronn, M., Paulus, W., Brokinkel, B., Keyvani, K., Sure, U., Wrede, K., Nakazato, Y., Tanaka, Y., et al. (2010). Molecular classification of low-grade diffuse gliomas. Am. J. Pathol. *177*, 2708–2714.

Lee, Y., Yeh, T.H., Emnett, R.J., White, C.R., and Gutmann, D.H. (2010). Neurofibromatosis-1 regulates neuroglial progenitor proliferation and glial differentiation in a brain region-specific manner. Genes Dev. *24*, 2317–2329.

Liu, C., Sage, J.C., Miller, M.R., Verhaak, R.G., Hippenmeyer, S., Vogel, H., Foreman, O., Bronson, R.T., Nishiyama, A., Luo, L., and Zong, H. (2011). Mosaic analysis with double markers reveals tumor cell of origin in glioma. Cell *146*, 209–221.

Masui, K., Suzuki, S.O., Torisu, R., Goldman, J.E., Canoll, P., and Iwaki, T. (2010). Glial progenitors in the brainstem give rise to malignant gliomas by platelet-derived growth factor stimulation. Glia *58*, 1050–1065.

Mayes, D.A., Rizvi, T.A., Cancelas, J.A., Kolasinski, N.T., Ciraolo, G.M., Stemmer-Rachamimov, A.O., and Ratner, N. (2011). Perinatal or adult Nf1 inactivation using tamoxifen-inducible PlpCre each cause neurofibroma formation. Cancer Res. *71*, 4675–4685.

Ono, K., Yasui, Y., Rutishauser, U., and Miller, R.H. (1997). Focal ventricular origin and migration of oligodendrocyte precursors into the chick optic nerve. Neuron *19*, 283–292.

Pollack, I.F., Hamilton, R.L., James, C.D., Finkelstein, S.D., Burnham, J., Yates, A.J., Holmes, E.J., Zhou, T., and Finlay, J.L.; Children's Oncology Group. (2006). Rarity of PTEN deletions and EGFR amplification in malignant gliomas of childhood: results from the Children's Cancer Group 945 cohort. J. Neurosurg. Suppl. *105*, 418–424.

Quiñones-Hinojosa, A., Sanai, N., Soriano-Navarro, M., Gonzalez-Perez, O., Mirzadeh, Z., Gil-Perotin, S., Romero-Rodriguez, R., Berger, M.S., Garcia-Verdugo, J.M., and Alvarez-Buylla, A. (2006). Cellular composition and cytoarchitecture of the adult human subventricular zone: a niche of neural stem cells. J. Comp. Neurol. *494*, 415–434.

Sharma, M.K., Mansur, D.B., Reifenberger, G., Perry, A., Leonard, J.R., Aldape, K.D., Albin, M.G., Emnett, R.J., Loeser, S., Watson, M.A., et al. (2007). Distinct genetic signatures among pilocytic astrocytomas relate to their brain region origin. Cancer Res. *67*, 890–900.

Singh, S.K., Hawkins, C., Clarke, I.D., Squire, J.A., Bayani, J., Hide, T., Henkelman, R.M., Cusimano, M.D., and Dirks, P.B. (2004). Identification of human brain tumour initiating cells. Nature *432*, 396–401.

Sugiarto, S., Persson, A.I., Munoz, E.G., Waldhuber, M., Lamagna, C., Andor, N., Hanecker, P., Ayers-Ringler, J., Phillips, J., Siu, J., et al. (2011). Asymmetry-defective oligodendrocyte progenitors are glioma precursors. Cancer Cell *20*, 328–340.

Taylor, M.D., Poppleton, H., Fuller, C., Su, X., Liu, Y., Jensen, P., Magdaleno, S., Dalton, J., Calabrese, C., Board, J., et al. (2005). Radial glia cells are candidate stem cells of ependymoma. Cancer Cell *8*, 323–335.

Tchoghandjian, A., Fernandez, C., Colin, C., El Ayachi, I., Voutsinos-Porche, B., Fina, F., Scavarda, D., Piercecchi-Marti, M.D., Intagliata, D., Ouafik, L., et al. (2009). Pilocytic astrocytoma of the optic pathway: a tumour deriving from radial glia cells with a specific gene signature. Brain *132*, 1523–1535.

Wang, Y., Yang, J., Zheng, H., Tomasek, G.J., Zhang, P., McKeever, P.E., Lee, E.Y., and Zhu, Y. (2009). Expression of mutant p53 proteins implicates a lineage relationship between neural stem cells and malignant astrocytic glioma in a murine model. Cancer Cell *15*, 514–526.

Warrington, N.M., Gianino, S.M., Jackson, E., Goldhoff, P., Garbow, J.R., Piwnica-Worms, D., Gutmann, D.H., and Rubin, J.B. (2010). Cyclic AMP suppression is sufficient to induce gliomagenesis in a mouse model of neurofibromatosis-1. Cancer Res. *70*, 5717–5727.

Weiss, S., Dunne, C., Hewson, J., Wohl, C., Wheatley, M., Peterson, A.C., and Reynolds, B.A. (1996). Multipotent CNS stem cells are present in the adult mammalian spinal cord and ventricular neuroaxis. J. Neurosci. *16*, 7599–7609.

Xu, Y., Tamamaki, N., Noda, T., Kimura, K., Itokazu, Y., Matsumoto, N., Dezawa, M., and Ide, C. (2005). Neurogenesis in the ependymal layer of the adult rat 3rd ventricle. Exp. Neurol. *192*, 251–264.

Yeh, T.H., Lee da, Y., Gianino, S.M., and Gutmann, D.H. (2009). Microarray analyses reveal regional astrocyte heterogeneity with implications for neurofibromatosis type 1 (NF1)-regulated glial proliferation. Glia *57*, 1239–1249.

Zhu, Y., Harada, T., Liu, L., Lush, M.E., Guignard, F., Harada, C., Burns, D.K., Bajenaru, M.L., Gutmann, D.H., and Parada, L.F. (2005). Inactivation of NF1 in CNS causes increased glial progenitor proliferation and optic glioma formation. Development *132*, 5577–5588.

Zhuo, L., Theis, M., Alvarez-Maya, I., Brenner, M., Willecke, K., and Messing, A. (2001). hGFAP-cre transgenic mice for manipulation of glial and neuronal function in vivo. Genesis *31*, 85–94.